

Springer Series  
in Biophysics 12

R. Rigler  
H. Vogel (Eds.)

# Single Molecules and Nanotechnology

 Springer

Springer Series in Biophysics 12

R. Rigler • H. Vogel  
Editors

# Single Molecules and Nanotechnology

 Springer

Professor Dr. Rudolf Rigler  
Laboratory of Medical Biophysics, MBB  
Karolinska Institute  
S-171 77 Stockholm  
Sweden

Professor Dr. Horst Vogel  
Laboratory of Physical Chemistry of Polymers and Membranes  
Institute of Chemical Sciences and Engineering  
Swiss Federal Institute of Technology (EPFL)  
CH-1015 Lausanne  
Switzerland

ISSN 0932-2353  
ISBN: 978-3-540-73923-4 e-ISBN: 978-3-540-73924-1

Library of Congress Control Number: 2007932191

This work is subject to copyright. All rights are reserved, whether the whole or part of the material is concerned, specifically the rights of translation, reprinting, reuse of illustrations, recitation, broadcasting, reproduction on microfilm or in any other way, and storage in data banks. Duplication of this publication or parts thereof is permitted only under the provisions of the German Copyright Law of September 9, 1965, in its current version, and permission for use must always be obtained from Springer. Violations are liable to prosecution under the German Copyright Law.

Springer-Verlag is a part of Springer Science+Business Media

[springer.com](http://springer.com)

© Springer-Verlag Berlin Heidelberg 2008

The use of general descriptive names, registered names, trademarks, etc. in this publication does not imply, even in the absence of a specific statement, that such names are exempt from the relevant protective laws and regulations and therefore free for general use.

Printed on acid-free paper 5 4 3 2 1 0

## Preface

The investigation of molecules as individuals has grown rapidly in recent years, and in the process has uncovered molecular properties not normally accessible by ensemble experiments. In particular, the direct characterization of biologically important molecules such as enzymes, molecular motors, or receptors and entire signaling complexes in action, for example in a live biological cell, yielded unexpected insights. Common approaches for studying single molecules include the electrical detection of ion channels in membranes, the measurement of the dynamics of (bio)chemical reactions between individual molecules, the imaging of individual molecules by scanning probe techniques or by fluorescence correlation spectroscopy, and the direct monitoring of single molecules by optical microscopies, to mention a few. The application of these techniques in physics, chemistry, and biology has opened new areas of nanotechnology. This book provides a representative selection of recent developments in the rapidly evolving field of single molecule techniques of importance in life sciences and will have future impact on the quantitative description of biological processes. The editors of this book hope that the chapters, written by leading scientists in the field, will attract students and scientists from different disciplines, provide them with an authentic insight into this young field of research, allow them to evaluate experimental methods and results, and thereby give them support for their own research.

Lausanne  
September 2007

Rudolf Rigler  
Horst Vogel

# Contents

<b>1 Nanophotonics and Single Molecules</b> . . . . .	1
W.E. Moerner, P. James Schuck, David P. Fromm, Anika Kinkhabwala, Samuel J. Lord, Stefanie Y. Nishimura, Katherine A. Willets, Arvind Sundaramurthy, Gordon Kino, Meng He, Zhikuan Lu, and Robert J. Twieg	
<b>2 Single Biomolecules at Cryogenic Temperatures: From Structure to Dynamics</b> . . . . .	25
Clemens Hofmann, Florian Kulzer, Rob Zondervan, Jürgen Köhler, and Michel Orrit	
<b>3 Quantum Optics: Colloidal Fluorescent Semiconductor Nanocrystals (Quantum Dots) in Single-Molecule Detection and Imaging</b> . . . . .	51
Laurent A. Bentolila, Xavier Michalet, and Shimon Weiss	
<b>4 Scanning Fluorescence Correlation Spectroscopy</b> . . . . .	81
Zdeněk Petrášek and Petra Schwill	
<b>5 Single-Molecule Imaging of Cellular Signaling</b> . . . . .	107
Sandra de Keijzer, B. Ewa Snaar-Jagalska, Herman P. Spink, and Thomas Schmidt	
<b>6 Mobility and Signaling of Single Receptor Proteins</b> . . . . .	131
Michael Prummer and Horst Vogel	
<b>7 Single Enzyme Kinetics: A Study of the Yeast Enzyme <i>Candida Antarctica</i> Lipase B</b> . . . . .	163
Wendy Verheijen, Davey Loos, Frans C. De Schryver, and Johan Hofkens	

<b>8 Protein Folding and Dynamics from Optical Single Molecule Spectroscopy</b> .....	181
Benjamin Schuler and Gilad Haran	
<b>9 Single Molecules and Nanoscale Surfactant Networks</b> .....	217
Aldo Jesorka, Michal Tokarz, and Owe Orwar	
<b>10 Single-Molecule Covalent Chemistry in a Protein Nanoreactor</b> .....	251
Hagan Bayley, Tudor Luchian, Seong-Ho Shin, and Mackay Steffensen	
<b>11 Single-Molecule Microscopy and Force Spectroscopy of Membrane Proteins</b> .....	279
Andreas Engel, Harald Janovjak, Dimtrios Fotiadis, Alexej Kedrov, David Cisneros, and Daniel J. Müller	
<b>Index</b> .....	313

## Contributors

Bayley, Hagan

Department of Chemistry, University of Oxford, Oxford OX1 3TA, UK,  
hagan.bayley@chem.ox.ac.uk

Bentolila, Laurent A.

Department of Chemistry and Biochemistry, University of California  
at Los Angeles, Los Angeles, CA 90095-1569, USA, lbento@chem.ucla.edu  
California NanoSystems Institute, University of California at Los Angeles,  
Los Angeles, CA 90095-1569, USA,  
LBENTO@chem.ucla.edu

Cisneros, David

Center of Biotechnology, University of Technology, Tatzberg 47-51, Dresden,  
Germany

De Schryver, Frans C.

Department of Chemistry, Katholieke Universiteit Leuven, Celestijnenlaan 200F,  
3001 Heverlee, Belgium,  
frans.deschyver@chem.kuleuven.ac.be

Engel, Andreas

M.E. Müller Institute for Structural Biology, Biozentrum, University of Basel,  
Klingelbergstrasse 70, 4056 Basel, Switzerland,  
andreas.engel@unibas.ch

Fotiadis, Dimtrios

M.E. Müller Institute for Structural Biology, Biozentrum, University of Basel,  
Klingelbergstrasse 70, 4056 Basel, Switzerland

Fromm, David P.

Department of Chemistry, Stanford University, Stanford, CA 94305-5080, USA

Haran, Gilad

Department of Chemical Physics, Weizmann Institute of Science, Rehovot 76100,  
Israel, gilad.haran@weizmann.ac.il



He, Meng

Department of Chemistry, Kent State University, Kent, OH 44242, USA

Hofkens, Johan

Department of Chemistry, Katholieke Universiteit Leuven, Celestijnenlaan 200F,  
3001 Heverlee, Belgium

Unité Chimie des Matériaux Inorganiques et Organiques, Université Catholique  
de Louvain, Bâtiment Lavoisier Place L. Pasteur 1, 1348 Louvain-la-Neuve,  
Belgium

Hofmann, Clemens

Molecular Nano-Optics and Spins (MoNOS), Huygens Laboratory,  
Leiden University, Postbus 9504, 2333 CA Leiden, The Netherlands

Janovjak, Harald

Center of Biotechnology, University of Technology, Tatzberg 47-51, Dresden,  
Germany

Jesorka, Aldo

Department of Chemistry and Bioscience, Chalmers University of Technology,  
Kemivägen 10, SE-41296 Göteborg, Sweden

Kedrov, Alexej

Center of Biotechnology, University of Technology, Tatzberg 47-51, Dresden,  
Germany

Keijzer, Sandra de

Physics of Life Processes, Leiden Institute of Physics, Leiden University,  
P.O. Box 9504, 2300 RA, The Netherlands

Cell Biology, Leiden Institute of Biology, Leiden University, P.O. Box 9504, 2300  
RA, The Netherlands

Kinkhabwala, Anika

Department of Chemistry, Stanford University, Stanford, CA 94305-5080, USA

Kino, Gordon

Department of Electrical Engineering, Stanford University, Stanford,  
CA 94305-5080, USA

Köhler, Jürgen

Experimental Physics IV and BIMF, University of Bayreuth, 95440 Bayreuth,  
Germany, juergen.koehler@uni-bayreuth.de

Kulzer, Florian

Molecular Nano-Optics and Spins (MoNOS), Huygens Laboratory, Leiden  
University, Postbus 9504, 2333 CA Leiden, The Netherlands

Lord, Samuel J.

Department of Chemistry, Stanford University, Stanford, CA 94305-5080, USA

Loos, Davey

Department of Chemistry, Katholieke Universiteit Leuven, Celestijnenlaan 200F,  
3001 Heverlee, Belgium

Lu, Zhikuan

Department of Chemistry, Kent State University, Kent, OH 44242, USA

Luchian, Tudor

Dept. of Biophysics & Medical Physics, Alexandru I. Cuza University Iasi-6,  
Romania

Michalet, Xavier

Department of Chemistry and Biochemistry, University of California  
at Los Angeles, Los Angeles, CA 90095-1569, USA

Moerner, W.E.

Department of Chemistry, Stanford University, Stanford, CA 94305-5080, USA,  
wmoerner@stanford.edu

Müller, Daniel J.

Center of Biotechnology, University of Technology, Tatzberg 47-51, Dresden,  
Germany

Nishimura, Stefanie Y.

Department of Chemistry, Stanford University, Stanford, CA 94305-5080, USA

Orrit, Michel

Molecular Nano-Optics and Spins (MoNOS), Huygens Laboratory,  
Leiden University, Postbus 9504, 2333 CA Leiden, The Netherlands,  
orrit@molphys.leidenuniv.nl

Orwar, Owe

Department of Chemistry and Bioscience, Chalmers University of Technology,  
Kemivägen 10, SE-41296 Göteborg, Sweden, orwar@chembio.chalmers.se

Petrášek, Zdeněk

Institut für Biophysik, Technische Universität Dresden, Tatzberg 47-51,  
01307 Dresden, Germany

Prummer, Michael

Institute of Chemical Sciences and Engineering, Swiss Federal Institute  
of Technology (EPFL), CH-1015 Lausanne, Switzerland

Schmidt, Thomas

Physics of Life Processes, Leiden Institute of Physics, Leiden University,  
P.O. Box 9504, 2300 RA, The Netherlands,  
Schmidt@Physics.LeidenUniv.nl

Schuck, P. James

Department of Chemistry, Stanford University, Stanford, CA 94305-5080, USA

Schuler, Benjamin

Biochemisches Institut, Universität Zürich, Winterthurerstr. 190, 8057 Zürich,  
Switzerland, schuler@bioc.unizh.ch

Schwille, Petra

Institut für Biophysik, Technische Universität Dresden, Tatzberg 47–51,  
01307 Dresden, Germany, petra.schwille@biotec.tu-dresden.de

Shin, Seong-Ho

Materials Sciences Division, Lawrence Berkeley National Laboratory, Berkeley,  
CA 94720, USA

Snaar-Jagalska, B. Ewa

Cell Biology, Leiden Institute of Biology, Leiden University, P.O. Box 9504, 2300  
RA, The Netherlands

Spaank, Herman P.

Cell Biology, Leiden Institute of Biology, Leiden University, P.O. Box 9504, 2300  
RA, The Netherlands

Steffensen, Mackay

Department of Chemistry, University of Oxford, Oxford, OX1 3TA, UK

Sundaramurthy, Arvind

Department of Electrical Engineering, Stanford University, Stanford,  
CA 94305-5080, USA

Tokarz, Michal

Department of Chemistry and Bioscience, Chalmers University of Technology,  
Kemivägen 10, SE-41296 Göteborg, Sweden

Twieg, Robert J.

Department of Chemistry, Kent State University, Kent, OH 44242, USA

Verheijen, Wendy

Department of Chemistry, Katholieke Universiteit Leuven, Celestijnenlaan 200F,  
3001 Heverlee, Belgium

Vogel, Horst

Institute of Chemical Sciences and Engineering, Swiss Federal Institute  
of Technology (EPFL), CH-1015 Lausanne, Switzerland,  
horst.vogel@epfl.ch

Weiss, Shimon

Department of Chemistry and Biochemistry, University of California  
at Los Angeles, Los Angeles, CA 90095-1569, USA, sweiss@chem.ucla.edu  
California NanoSystems Institute, University of California at Los Angeles,  
Los Angeles, CA 90095-1569, United States of America

Department of Physiology, David Geffen School of Medicine, University  
of California at Los Angeles, Los Angeles, CA 90095-1569, USA

A. Willets, Katherine

Department of Chemistry, Stanford University, Stanford, CA 94305-5080, USA

Zondervan, Rob

Molecular Nano-Optics and Spins (MoNOS), Huygens Laboratory, Leiden  
University, Postbus 9504, 2333 CA Leiden, The Netherlands

# Chapter 1

## Nanophotonics and Single Molecules

W.E. Moerner(✉), P. James Schuck, David P. Fromm,  
Anika Kinkhabwala, Samuel J. Lord, Stefanie Y. Nishimura,  
Katherine A. Willets, Arvind Sundaramurthy, Gordon Kino,  
Meng He, Zhikuan Lu, and Robert J. Twieg

### Contents

1.1	Introduction.....	2
1.2	Development of Single-Molecule Fluorophores with Alternate Readout Capabilities .....	3
1.2.1	Motivations .....	3
1.2.2	The DCDHF Single-Molecule Fluorophores.....	3
1.2.3	Comparing DCDHF Molecules to Well-Known Single-Molecule Fluorophores .....	5
1.2.4	Lifetimes in Different Environments .....	6
1.2.5	Labeling of Cellular Membranes .....	7
1.2.6	Two-Photon Fluorescence Excitation .....	10
1.3	Toward Improving the Mismatch Between Light and Single Molecules .....	11
1.3.1	Motivation.....	11
1.3.2	Optically Resonant Metallic Bowtie Nanoantennas .....	13
1.3.3	Optical Resonances of Metallic Bowtie Nanoantennas.....	13
1.3.4	Local Enhancement of the Optical Fields Near the Nanoantenna .....	14
1.3.5	Exploring the Chemical Enhancement for Surface-Enhanced Raman Scattering with Au Bowtie Nanoantennas .....	16
1.4	Summary and Prospects.....	19
1.4.1	Single-Molecule Fluorophores .....	19
1.4.2	Metallic Bowtie Nanoantennas .....	19
	References.....	20

**Abstract** Single emitting molecules are currently providing a new window into nanoscale systems ranging from biology to materials science. The amount of information that can be extracted from each single molecule depends upon the specific photophysical properties of the fluorophore and how these properties are affected by the nearby environment. For this reason, it is necessary to develop single-molecule emitters with as many different reporter functions as possible. The first part of this chapter describes a relatively new class of single-molecule fluorophores which offer

---

W.E. Moerner  
Department of Chemistry, Stanford University, Stanford, CA, 94305-5080 USA  
wmoerner@stanford.edu

R. Rigler and H. Vogel (eds.), *Single Molecules and Nanotechnology*. 1  
*Springer Series in Biophysics 12*.  
© Springer-Verlag Berlin Heidelberg 2008

tunable photophysical properties and, in turn, improved local reporting functionality on the nanometer length scale. The second part of this chapter presents metallic nanostructures which can address a second issue: the mismatch between the typical size of a single fluorophore ( $\sim 1$  nm along a long dimension) and the wavelength of light ( $\sim 500$  nm). Such nanostructures could lead to more efficient excitation of single molecules, in particular, higher excitation probability as well as reduced backgrounds, and effectively higher spatial resolution. Metallic nanostructures based on two triangles formed into a bowtie shape feature large enhancements of the local electromagnetic field and give rise to strong surface-enhanced Raman scattering of molecules. In future work, enhanced electromagnetic structures can be combined with single-molecule reporters in a variety of applications.

## 1.1 Introduction

In recent decades, the ability to perform optical spectroscopy and microscopy of single molecules in condensed phase samples (Moerner and Orrit 1999) has fascinated scientists in fields ranging from biophysics (Zhuang and Rief 2000; Weiss 1999; Lu 2005; Rasnik et al. 2005), to cellular biology (Moerner 2003), to materials and polymer science (Cotlet et al. 2004; Barbara et al. 2005; Lee et al. 2005), and even to quantum-mechanical single-photon sources (Moerner 2004; Lounis and Orrit 2005). Using now-standard experimental methods (Ha et al. 1999; Ha 2001; Moerner and Fromm 2003), information on local interactions can be extracted, molecule by molecule, by the measurement of excited state lifetimes, spectra, orientations, brightness, degree of energy transfer, and photon correlations, thus removing ensemble averaging and allowing exploration of heterogeneity. Single-molecule studies often reveal complex statistical fluctuations, which allow useful comparison with theoretical models in a variety of cases (Barkai et al. 2004; Watkins and Yang 2004; Hummer and Szabo 2005).

A continuing need exists for the improvement and extension of these efforts in order to increase the variety and amount of information that may be obtained from single-molecule studies. For example, at room temperature, eventual photobleaching limits the knowledge that may be extracted from each individual molecule. To compensate for this, it is necessary to continually develop new reporter functions for robust fluorophores that provide sufficiently strong signals at the single-molecule level.

The first part of this chapter describes a relatively new class of single-molecule fluorophores which offer tunable photophysical properties and, in turn, improved local reporting functionality on the nanometer length scale. While a single molecule can report on its immediate nanoenvironment, in most experiments, there is a large mismatch between the size of a single fluorophore ( $\sim 1$  nm along a long dimension) and the wavelength of light ( $\sim 500$  nm). Developing ways to overcome this would lead to more efficient excitation of single molecules, in particular, higher excitation probability as well as reduced backgrounds, and effectively higher spatial resolution.

One approach for overcoming the mismatch involves nanoscale metallic structures that concentrate light to subwavelength regions. We have explored this idea with metallic “bowtie” nanoantennas in which the enhancement of the local electromagnetic field can be directly measured. In the second part of this chapter we describe the optical properties of bowties, and illustrate their use in spectroscopy for the case of surface-enhanced Raman scattering of molecules. In future work, enhanced electromagnetic structures can be combined with single-molecule reporters in a variety of applications.

## **1.2 Development of Single-Molecule Fluorophores with Alternate Readout Capabilities**

### ***1.2.1 Motivations***

Over the years, it is certainly true that a large number of fluorescent dyes (Tsien and Waggoner 1995) have become available for labeling applications, for example, from commercial sources such as Molecular Probes (Invitrogen Corp.), Dyomics GmbH, and many others. Of particular interest here are the fluorophores that show environmental sensitivity, that is, those which show alterations in emission spectra, fluorescence lifetimes, or fluorescence quantum yields that vary based on the polarity or the viscosity of the environment. For example, dyes such as laurdan, prodan, dansyl, NBD, merocyanines, and the recently reported di-4-ANEPPHQ have all been utilized in various reporter applications in biological systems (Parasassi et al. 1998; Maier et al. 2002; Touthkine et al. 2003; Jin et al. 2005), but this list is by no means exhaustive. For the most part, experiments using environmentally sensitive fluorophores have focused on high concentration imaging, as only a subset of the larger group of fluorophores shows the high quantum yield, weak triplet bottlenecks, and high photostability to allow detection at the single-molecule level. For this reason, it is necessary to continue research efforts to develop single-molecule emitters with as many different reporter functions as possible.

### ***1.2.2 The DCDHF Single-Molecule Fluorophores***

Recent work in the Moerner and Twieg laboratories has focused on a new class of fluorophores that meet the strict demands for single-molecule imaging and offer additional interesting properties such as a large ground state dipole moment  $\mu_g$ , moderate hyperpolarizability  $\beta$ , and sensitivity to the rigidity of the local environment (Willets et al. 2003a, 2005). The molecules within this class all contain an amine donor and a dicyanodihydrofuran (DCDHF) acceptor linked by a conjugated unit (benzene, thiophene, styrene, etc.). These molecules are named DCDHF fluorophores after the acceptor unit (Melikian et al. 1995), which is constant among the

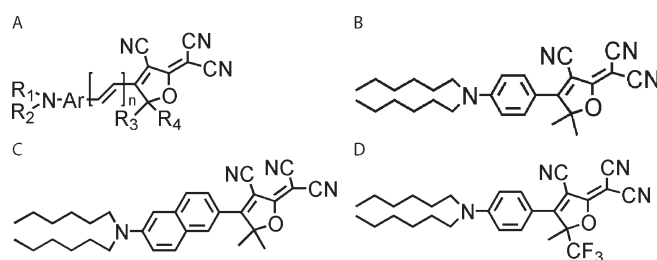


**Figure 1.1** Representative structures of the DCDHF fluorophore class. In the general structure **A**, the aromatic group (Ar) may be one or more benzene or thiophene groups, and different substituents may be added at the positions R1–R4 to modify the properties of the molecule. The structure **B** shows the first molecule studied in this class, DCDHF-6. Structure **C**, DCDHF-N-6, is a long-wavelength version; structure **D**, DCDHF-CF<sub>3</sub>, has been used in membrane labeling studies as described in the text

class. Figure 1.1A shows the general structure of these molecules, and Figure 1.1B shows the molecule DCDHF-6, the first and most studied compound in this group. The DCDHF molecules are examples of nonlinear optical chromophores possessing large second-order nonlinearity by virtue of the asymmetric donor–acceptor structure and high degree of conjugation (Nicoud and Twieg 1987; Kanis et al. 1994; Zyss 1994; Zhang et al. 2001).

Nonlinear optical chromophores at high concentrations in polymers have received much attention from the chemical community in recent decades owing to the utility of such materials for second-harmonic generation, electro-optic phase modulation, and many other potential applications (Prasad and Williams 1991; Burland et al. 1994; Nalwa and Miyata 1997; Kuzyk and Dirk 1998). The DCDHF molecules were originally designed for and utilized extensively in high-performance photorefractive polymer materials (Wright et al. 2001; He et al. 2002; Ostroverkhova et al. 2002; Ostroverkhova and Moerner 2004).

Usually, nonlinear optical chromophores are not thought to be particularly fluorescent, inasmuch as the strong charge-transfer transition producing the optical nonlinearity is often accompanied by considerable excited-state distortion of the molecule. In spite of this, the DCDHF fluorophores are surprisingly well-suited for single-molecule fluorescence detection (Willets et al. 2003). This may be a result of the fact that their earlier optimization for photorefractive applications rested more upon producing a large polarizability anisotropy and dipole moment rather than a large hyperpolarizability (Kippelen et al. 1997). Figure 1.2A shows an epifluorescence image of single molecules of DCDHF-6 in a poly(methyl methacrylate) thin film at room temperature. Observing the time-dependent emission from single spots (Figures 1.2B, 1.2C) shows clear single-step photobleaching. The blinking event for Figure 1.2C near 3 seconds is a property common to many single molecules (Moerner 1997), but in this system, 85% of the molecules observed did not show blinking on the time scale of the measurement (100 ms), itself a surprising result.



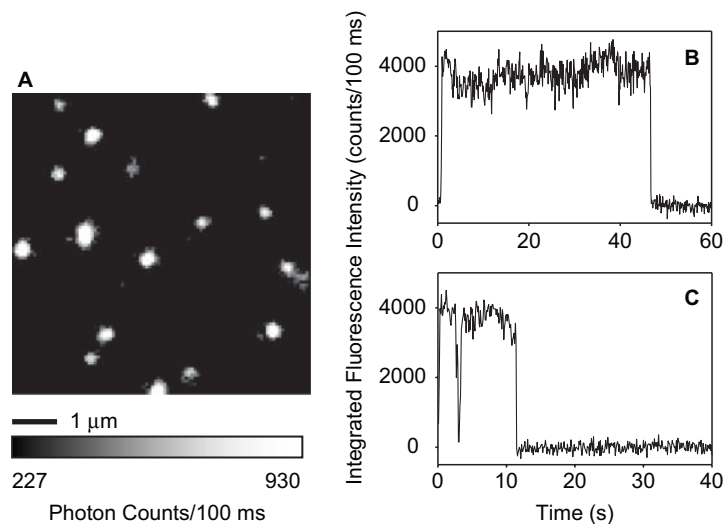


**Figure 1.2** (A) Epifluorescence image of single molecules of DCDHF-6 in a thin film of PMMA at room temperature. The time traces in (B) and (C) show single-step photobleaching. (Reprinted by permission from Willets et al. (2003a))

### 1.2.3 Comparing DCDHF Molecules to Well-Known Single-Molecule Fluorophores

To illustrate some of the properties of molecules in the DCDHF class compared to conventional fluorophores, Table 1.1 shows the properties of three DCDHFs compared to Rhodamine 6G (R6G) and Texas Red.

Although the absorption and emission of R6G and Texas Red are at longer wavelengths than for DCDHF-6, the synthetic flexibility of the DCDHFs at the conjugated linker (Ar plus  $n$  vinyl groups; Figure 1.1A) has allowed derivatives to be produced with absorption as long as 700 nm (for a thiophene–thiophene–vinyl linker) while maintaining the advantageous characteristics of the parent molecule. The fourth entry in the table for DCDHF-N-6 (see Figure 1.1C) is an example of one of the long-wavelength emitters where the aromatic coupling group is a naphthalene (Lord et al. 2007). The fifth entry is for DCDHF-A-6, the anthracene analogue to DCDHF-N-6. Comparing the first three rows in the table, the extinction coefficients  $\epsilon$  for R6G and Texas Red are larger than for DCDHF-6, but this parameter too is larger for other longer wavelength versions of the DCDHF molecules not shown here.

Surprisingly, in toluene liquid solution, the fluorescence quantum yield  $\Phi_F$  for DCDHF-6 is quite small. The first clue that these molecules have strong environmental sensitivity came from the observation that in the relatively more rigid PMMA environment, the fluorescence quantum yield is much higher, comparable to R6G and Texas Red. It is important to note that the bulk photobleaching quantum yields  $\Phi_B$  are

**Table 1.1** Properties of three DCDHFs compared to rhodamine 6G (R6G) and Texas Red

	$\lambda_{\text{abs}}$ (nm)	$\lambda_{\text{em}}$ (nm)	$\epsilon$ ( $\text{M}^{-1}\text{cm}^{-1}$ )	$\Phi_{\text{F}}$	$\Phi_{\text{B}}$	$N_{\text{tot,e}}$	$\mu_{\text{g}}$ (D)
R6G	530	556	105,000	0.95	$5 \times 10^{-7\text{a}}$ $1 \times 10^{-5\text{b}}$	$1.9 \times 10^6$	cation
Texas Red	576	592	177,000	0.93	$7 \times 10^{-7\text{a}}$ $4 \times 10^{-5\text{b}}$	$1.4 \times 10^6$	anion
DCDHF-6	486	505	71,000	0.044 <sup>c</sup> 0.92 <sup>d</sup>	$9 \times 10^{-7\text{d}}$	$2.4 \times 10^{6\text{d,e}}$	11.4
DCDHF-N-6	526	579	42,000	0.85 <sup>c</sup> 0.98 <sup>d</sup>	$2 \times 10^{-6\text{b}}$	$1.4 \times 10^{6\text{d,f}}$	–
DCDHF-A-6	585	689	35,000	0.54 <sup>c</sup> 0.71 <sup>d</sup>	$1 \times 10^{-5\text{b}}$	$2.2 \times 10^{6\text{d,g}}$	–

<sup>a</sup>In ethanol (Soper et al. 1993)<sup>b</sup>In aqueous gelatin<sup>c</sup>In toluene<sup>d</sup>In a PMMA film<sup>e</sup>Corrected for a detection efficiency of 8%<sup>f</sup>Corrected for a detection efficiency of 9%<sup>g</sup>Corrected for a detection efficiency of 10%

also quite comparable, and superior when compared in an aqueous environment. The inverse of this parameter is approximately related to the average number of emitted photons before photobleaching in the single-molecule experiments,  $N_{\text{tot,e}}$ . Again, the DCDHF-6 dye is quite comparable to the conventional fluorophores. Finally, although DCDHF-6 has a large ground state dipole moment, R6G and Texas Red are charged.

The mechanism for the increase in fluorescence emission in more rigid environments has been explored by quantum chemical calculations of the energy level structure of the molecule as a function of various intramolecular twists (Willets et al. 2004). By calculating the various excited state geometries that could be easily reached upon a Franck–Condon excitation, two relaxed forms were found, one with a more planar molecular structure, and one with a large twist around the dicyanomethylene bond. The former is likely to be emissive, whereas the latter is not far in energy from a similar structure on the ground state manifold, and hence would be expected to be nonradiative. The model was considered that the varying emission from the molecule results from changing the partitioning between the two de-excitation pathways. Presumably, in a more rigid environment that restricts the dicyanomethylene twist, the molecule cannot access the nonradiative pathway. The fact that the  $\Phi_{\text{F}}$  value for the DCDHF-6 molecule shows a strong correlation with the viscosity when in hydrogen-bonding solvents might be a result of local steric hindrance from the immediate H-bond network. These ideas are subjects of future theoretical and experimental verification.

### 1.2.4 Lifetimes in Different Environments

The reporter properties of the DCDHF fluorophores can be exploited in single-molecule experiments to reveal inherent differences in local environments or to

monitor time-dependent changes in the host. Because the fluorescence quantum yield is related to the excited state lifetime ( $\tau_F$ ) of a molecule ( $\Phi_F = \tau_F / \tau_{rad}$ , with  $\tau_{rad}$  the radiative lifetime; Lakowicz 1999), the  $\tau_F$  value should also provide a sensitive measure of the local environment. Using conventional time-correlated single photon counting (TCSPC) methods to record delay times between excitation by a pulsed laser source and emission from a single molecule (Lakowicz 1999), the excited state lifetimes of the DCDHF-6 molecules in different hosts can be measured. In toluene, where the measured quantum yield was quite low, the bulk excited state lifetime was limited by the response time of the instrument ( $<400$  ps); on the other hand, in PMMA where the quantum yield was near unity, the lifetime was several ns (Willets et al. 2003, 2004).

Bulk studies of DCDHF-6 in different methacrylate polymer hosts revealed that the average excited state lifetime of the molecule increased with increasing glass transition temperature ( $T_g$ ) of the host. However, ensemble studies do not directly yield insight into the overall heterogeneity of the environment, because only the average value of the lifetime is measured. For single-molecule experiments, dilute samples of DCDHF-6 were prepared in PMMA ( $T_g \sim 120^\circ\text{C}$ ) and an (*n*-butyl methacrylate)/(iso-butyl methacrylate) copolymer ( $T_g \sim 35^\circ\text{C}$ ), and both samples were studied at room temperature. Figure 1.3A shows an example of a lifetime measurement for a single molecule in PMMA, which fits a single exponential very well. Figure 1.3B shows the distribution of single-molecule lifetimes in the two different hosts as well as fits to a Gaussian profile.

Consistent with the bulk results, the average lifetime in the copolymer is shorter than in the PMMA. The widths of both distributions, however, are greater than the statistically expected measurement error of 100 ps, which can be attributed to the microscopic heterogeneity of the polymer films. The distribution of lifetimes is broader in the copolymer host, suggesting that a greater variety of microscopic local environments exists in this matrix.

Recent work has shown that the lifetime of a twisted perylene derivative reports on the free volume of its host polymer matrix (Vallee et al. 2004); this idea may also apply to the DCDHF results. The local free volume in the copolymer is expected to be higher than that in the PMMA (Vallee et al. 2004) and thus our results suggest that the free volume is not only larger but also more broadly distributed in the copolymer. This example shows that these dyes may prove useful for sensing dynamic changes in the local environment, simply by monitoring changes in the excited state lifetime of an individual molecule as its host environment is perturbed. Such measurements are useful not only for studying polymers, but for any situation in which dynamic changes in environment are expected.

### 1.2.5 Labeling of Cellular Membranes

Many types of dynamic environments exist in biological systems, where many dynamical processes and heterogeneous environments can be found. Although synthetic modifications to optimize interaction of the DCDHF dyes with specific

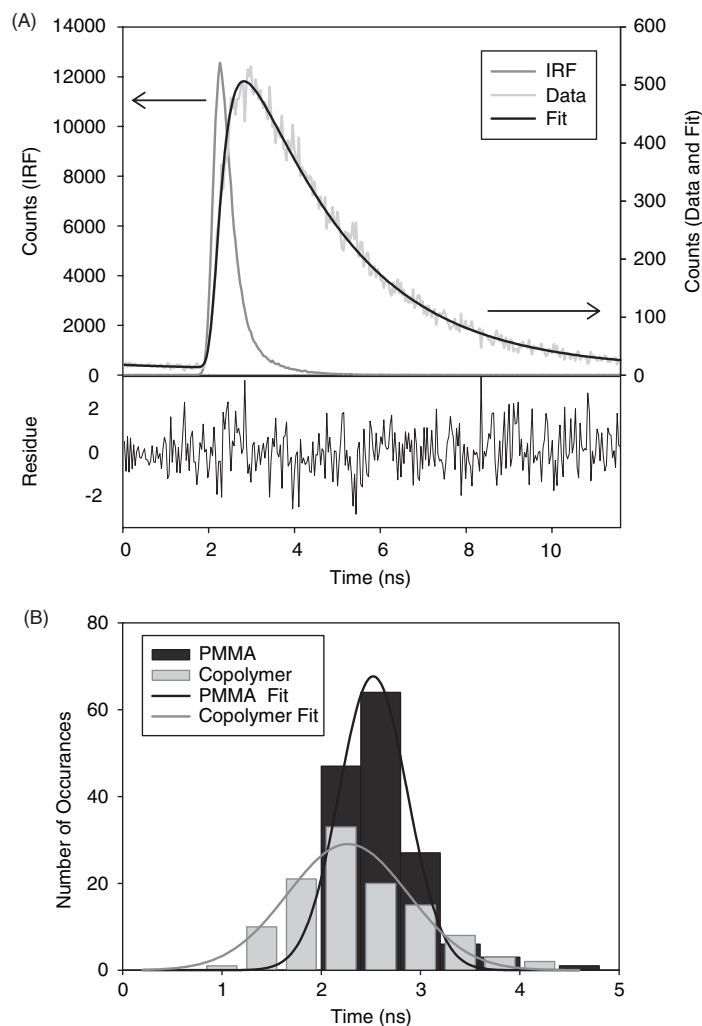


**Figure 1.3** (A) Excited state lifetime measurement (light gray line) of a single molecule of DCDHF-6 in PMMA. Also shown are the instrument response function (dark gray line) and a single exponential fit to the data (black line) with a characteristic decay time of 2.42 ns. The residuals of the fit are also shown. (Reprinted by permission from Willets et al. (2003b)). (B) Histogram of single molecule fluorescence lifetimes of DCDHF-6 in a BM/iBM copolymer (light gray) and in PMMA (dark gray). For both datasets, 400 ps bins are used. The error of the individual lifetime determinations is 100 ps. (Reprinted by permission from Willets et al. (2005))

biological targets are underway, the fluorophores in their current form are directly useful in the study of cellular membranes. The molecules have an amphiphilic structure with a polar dicyanomethylenedihydrofuran group at one end and a non-polar hydrocarbon tail on the amine. Thus, the DCDHF dyes can act as fluorescent

lipid analogues, and the relatively constrained environment of the membrane bilayer can lead to bright emission.

Using egg phosphatidylcholine vesicles to deliver the fluorophores to a cell membrane (Schütz et al. 2000) or by dissolution in a small amount of ethanol, single-molecule concentrations of DCDHF probes have been successfully inserted into the plasma membrane of Chinese hamster ovary (CHO) cells. To illustrate, part A of Figure 1.4 shows a white-light transmission image of a CHO cell (typical dimensions  $\sim 10 \times 25 \mu\text{m}$  in the image plane, and  $\sim 5 \mu\text{m}$  thick). Figure 1.4B shows a wide-field fluorescence image of single molecules of DCDHF6-CF3 in the upper plasma membrane of this CHO cell. Each molecule is rapidly diffusing in the membrane, and by recording positional trajectories as a function of time, the diffusion coefficient for the DCDHF molecules in the membrane can be calculated (Vrljic et al. 2002). The observed diffusion coefficient of  $2.1 \mu\text{m}^2\text{s}^{-1}$  is consistent with measured diffusion coefficients of other fluorescent lipid analogues such as Cy5-labeled DOPE (Schütz et al. 2000) in the plasma membrane, which suggests that the DCDHF molecules are integrated into the lipid bilayer.

The compatibility of the DCDHF dyes with cells as well as the synthetic flexibility to add reactive functional groups for site-specific labeling should allow the DCDHF fluorophores to be useful for a variety of in vitro and in vivo biological labeling experiments. In addition, future studies should also be able to detect changes in the

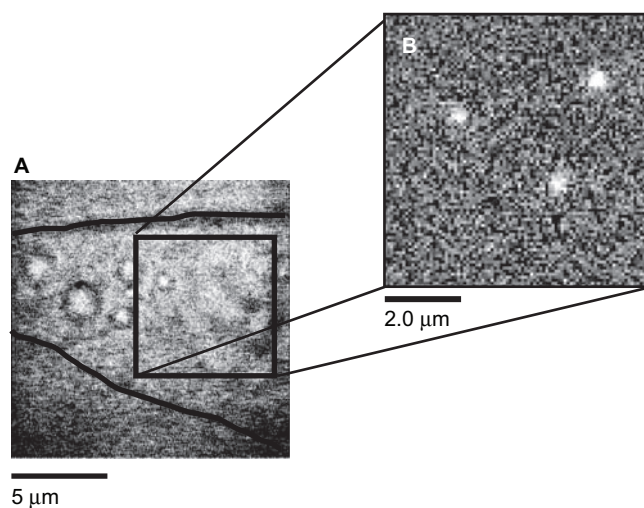


**Figure 1.4** (A) White-light transmission image of a CHO cell showing the sketched cell edges (black) and the region of interest. (B) Epifluorescence image of single molecules of DCDHF6-CF3 in the upper membrane of the cell excited at 532 nm with an 18 ms integration time. (Parts (A) (B) reprinted by permission from Willets et al. (2005))

emission properties arising from local heterogeneity in the plasma membrane (Nishimura et al. 2006).

### ***1.2.6 Two-Photon Fluorescence Excitation***

One of the challenges of labeling live cells with single-molecule reporters is the large autofluorescence background arising from natively fluorescent molecules such as flavins. Because these interfering fluorescent molecules are so plentiful, their emission can overwhelm the relatively small fluorescence signal from single-molecule labels. One solution to this problem involves preparation of long-wavelength emitters, and the DCDHF molecules do allow for this possibility.

Alternatively, many researchers have turned to two-photon fluorescence in order to avoid the naturally occurring background (Denk et al. 1990; Xu et al. 1996). In these experiments, two (typically infrared) photons of frequency  $\omega$  are used to excite the molecule rather than a single photon with the optically resonant frequency  $2\omega$ . Infrared excitation can reduce signals from the autofluorescent species in the cell, however, two-photon absorption is a low probability event, typically requiring high intensity excitation with  $\sim 100$  fs laser pulses, and therefore the single emitter of interest needs to have a large two-photon absorption cross-section  $\delta$ . For example, the  $\delta$  value for R6G in methanol, considered a fairly strong two-photon emitter, is 30 GM at 800 nm (where 1 GM =  $10^{-50}$  cm<sup>4</sup> s photon<sup>-1</sup>; Albota et al. 1998).

The natural optical nonlinearity of the DCDHF dyes suggests that they too may be useful two-photon emitters, and our recent measurements find two-photon cross-sections reaching more than 44 GM for DCDHF-6, slightly larger than that for R6G (Schuck et al. 2005b). Figure 1.5a shows the expected quadratic behavior of the bulk DCDHF-6 two-photon absorption signal versus input cw laser power from 930 nm pulses from a mode-locked Ti:Sapphire laser (pulse widths  $\sim 125$  fs). In Figure 1.5b, the fluorescence spectra arising from one- and two-photon excitation are shown to be roughly identical. The TPF excitation spectrum peaks at 945 nm and approximately mirrors the shape of the single-photon absorption spectrum with double the wavelength. As with many two-photon dyes (Xu and Webb 1996a; Schuck et al. 2005b), the spectrum is blue-shifted by more than 40 nm relative to the expectation from single-photon absorption. In Figure 1.5c, for a single-molecule concentration sample of DCDHF-6 in PMMA, the two-photon excited fluorescence from individual molecules is easily observed, with clear single-step photobleaching (Figure 1.5d). The ability to observe single molecules of DCDHF-6 using two-photon fluorescence expands the range of usefulness of these dyes, suggesting that they are candidates for applications where autofluorescence provides excessive background.

Overall, these studies and others in progress show that the DCDHF dyes are excellent single-molecule emitters with a degree of synthetic flexibility that should allow them to be tailored for a variety of applications.

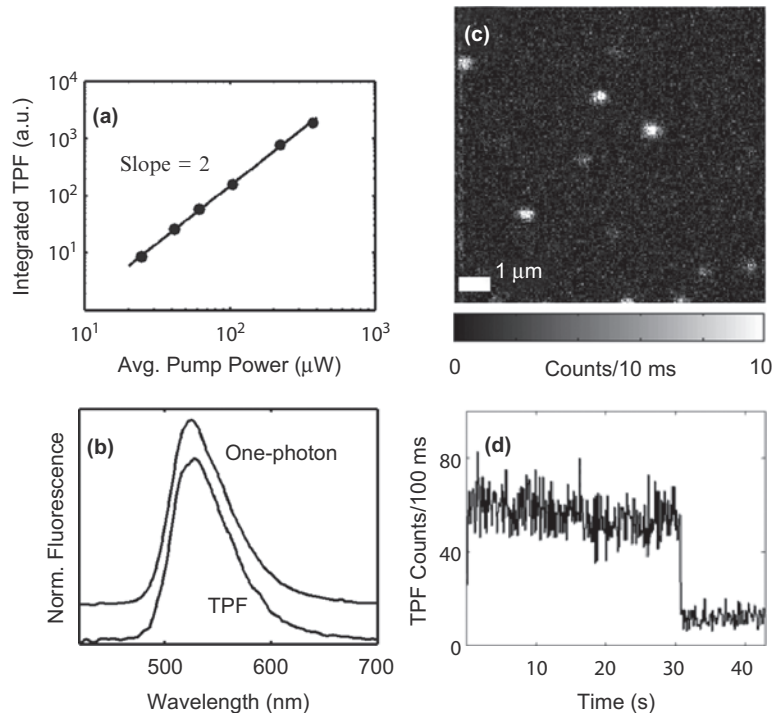


**Figure 1.5** (a) A log–log plot demonstrating the quadratic dependence of TPF on average excitation power for a bulk sample of DCDHF-6 in PMMA. (b) One- and two-photon fluorescence spectra from DCDHF-6, where the one-photon spectrum has been vertically offset for clarity. (c) TPF scanning confocal image of single DCDHF-6 molecules in a PMMA film. (d) Area-integrated TPF intensity of a single molecule as a function of time, 100 ms averaging interval. (Reprinted by permission from Schuck et al. (2005b))

### 1.3 Toward Improving the Mismatch Between Light and Single Molecules

#### 1.3.1 Motivation

When light of wavelength  $\lambda$  is focused into a medium of refractive index  $n$ , the minimum spot size due to diffraction is of the order of  $\lambda/(2n)$ . For example, at a wavelength of 405 nm, at the edge of the visible band, diffraction limits the minimum spot size to be greater than  $\sim 150$  nm. Typical single-molecule emitters are far smaller, and it would be far more efficient to couple the single molecule to a near-field light source far smaller than the diffraction-limited value. Aperture-based near-field techniques, where light is squeezed through a tiny hole, can achieve lateral spatial resolution on the order of the hole diameter (Betzig et al. 1991). In practice, near-field microscopic images have been recorded by pulled and metal-coated optical fiber tips, but these are fragile and plagued by poor transmission, on the order of  $10^{-3}$  to  $10^{-6}$  (Zenhausern et al. 1995).

Electromagnetic theory predicts that electric fields (E-fields) are enhanced in close proximity to sharp metal points with a radius of curvature much smaller than the incident illumination wavelength, the so-called lightning-rod effect that has been recently applied at optical frequencies, producing lateral resolution on the order of the curvature of the point (Bohn et al. 2001). The highly localized E-field enhancement in apertureless near-field systems has been exploited to produce an ultra-small, ultra-intense light source that has applications in high-density optical storage, high-resolution optical imaging, and laser spectroscopy, including enhanced fluorescence (Novotny et al. 1998) and Raman scattering (Hartschuh et al. 2003).

Small metallic particles with sharp points also produce locally enhanced E-fields, and rod-shaped and triangular antennas have recently been made resonant in the infrared (Crozier et al. 2003). In the microwave regime, it has been shown that a “bowtie”-shaped antenna, where two metallic triangles facing tip to tip are separated by a small gap, produces a large E-field confined to the area near the gap (Grober et al. 1997). Small gaps between two nanometer-scale particles have also been implicated in producing electromagnetically enhanced “hot spots,” enabling the detection of surface enhanced Raman scattering (SERS) of single molecules (Kneipp et al. 1997; Nie and Emory 1997; Michaels et al. 2000).

Investigators have suggested that the ultra-intense fields required for SERS are created by strong plasmonic coupling between pairs of small metallic spheres (Michaels et al. 2000; Kneipp et al. 2002; Xu and Kaelin 2003). However, all single-molecule SERS studies to date have used randomly deposited colloidal particles. These findings motivated renewed interest in optically resonant nanoantennas that can be reproducibly fabricated (Haynes et al. 2003; Jackson et al. 2003; Rechberger et al. 2003; Su et al. 2003; Genov et al. 2004; Hao and Schatz 2004), which in turn led to our emphasis on metallic bowtie nanoantennas (see Figure 1.6) that are controllably produced using electron-beam lithography (EBL). Bowtie nanoantennas, designed to combine both the lightning-rod and coupled-plasmon resonant enhancement effects, should greatly improve the mismatch between conventional optical excitation and nanoscale objects, enabling progress in the area of nanophotonics.

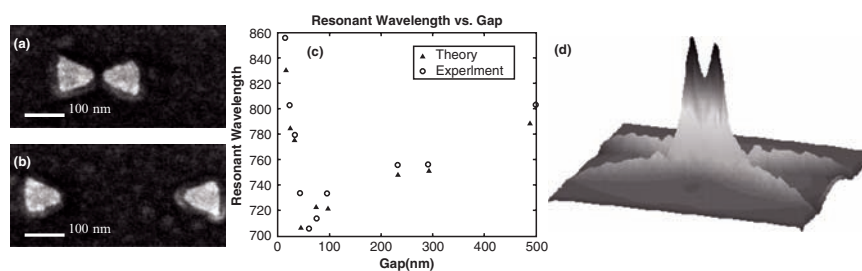


**Figure 1.6** SEM images of two representative gold bowties on a fused silica-ITO substrate (a) and (b). The variation of resonant wavelength with gap for light polarized along the line between the two triangles, with experiment shown as open circles and FDTD simulations as filled triangles (c). (After Sundaramurthy et al. (2005), used by permission.) FDTD simulation of field intensity ( $I$ ) enhancement near a 16 nm-gap bowtie (d) pumped at  $\lambda = 830$  nm. Maximum  $I$  enhancement is  $\sim 1500$ .



### ***1.3.2 Optically Resonant Metallic Bowtie Nanoantennas***

Initial studies were aimed at making reproducible sub-100 nm-sized metallic bowties that could be located at specified positions. To achieve this, Au bowties were fabricated with electron beam lithography (EBL) on transparent substrates. Details of bowtie nanoantenna fabrication can be found in Fromm et al. 2004 and scanning electron microscope (SEM) images of two representative bowties with different gap sizes are shown in Figure 1.6a,b. Each triangle of a bowtie is  $75 \pm 5$  nm in length (perpendicular bisector), has a tip radius of curvature of  $18 \pm 2$  nm, an Au thickness of  $\sim 18$  nm, and a 3.0 nm Ti adhesion sticking layer. Objects of this size are at the limit of current EBL fabrication methods.

Due to the complex behavior of metals at optical frequencies (Palik 1985), it is important to note that optically resonant nanoantennas are not “scaled-down” versions of their microwave and radiowave counterparts. The utilization of plasmon resonance effects is required to achieve antenna behavior in the optical regime, which results in antenna sizes that are much smaller than might be expected if “ideal” metallic properties are assumed.

### ***1.3.3 Optical Resonances of Metallic Bowtie Nanoantennas***

Because localized plasmon resonances are extremely dependent on geometry and material properties, we investigated the spectral scattering behavior of bowtie nanoantennas in detail, both experimentally (Fromm et al. 2004) and theoretically (Sundaramurthy et al. 2005) using finite-difference time-domain (FDTD) calculations of the local electromagnetic field. Single bowtie scattering spectra were measured experimentally as a function of gap size with far-field total internal reflection (TIR) microscopy. This method has the advantage that the excitation beam is trapped in the evanescent field until scattered toward the detector by the bowtie. The excitation light was broadband and s-polarized so that the axis of each bowtie was carefully oriented parallel to the polarization axis. (The perpendicular polarization leads to unremarkable results, similar to the scattering from isolated triangles (Fromm et al. 2004)).

Many bowties with varying gaps were fabricated and measured on a single substrate to record the peak scattering wavelength versus gap, with the results shown in Figure 1.6c. The measured results (open circles) were compared to three-dimensional FDTD calculations of the spectra, and the resonant wavelengths are shown as closed triangles. The FDTD simulations used measured frequency-dependent dielectric properties of the Au and simulated the exact structure fabricated, making no approximations to compute the final field intensity in the vicinity of the bowties.

Plotting the peak resonant wavelength as a function of gap size provides insight into the interparticle coupling behavior of single bowtie nanoantennas. Figure 1.6c shows the resonant scattering wavelength for 27 individual bowties, with gaps ranging from 16 to 488 nm, plotted against gap size. For light polarized along the line between the two triangles, the plasmon scattering resonance first blue-shifts with

increasing gap, and then red-shifts as the particles become more and more uncoupled; this was a surprising result as observations of the blue-shift followed by red-shift had not previously been reported in the literature.

This behavior may be approximately understood in a coupled-dipole approximation as changes in the phase between static dipole–dipole interactions and dipole radiative interaction effects (Zhao et al. 2003; Fromm et al. 2004). The peak resonance wavelengths from the FDTD simulations (closed triangles) agree quite well with the experimental observations, suggesting the utility of FDTD in predicting the behavior of coupled nanoparticle systems. Moreover, the calculations give information about the local electric fields and currents, which leads to the following interpretation of the resonant wavelength shifts. For gaps less than 60 nm, as shown in Figure 1.6a, the dominant field is between the tips. The gap capacity and the inductance due to plasmon propagation near the tip cause a resonance that shifts to the red as the gap size is decreased and the capacity increases. For gaps greater than 60 nm, the fields are predominantly in the  $y$ -direction normal to the triangles and flow back to the triangle from which they left. The device tends to behave more as a single triangle and has a resonance that shifts slowly to the red as the gap increases (Sundaramurthy et al. 2005).

### ***1.3.4 Local Enhancement of the Optical Fields Near the Nanoantenna***

Theoretical calculations suggest the plasmon resonances of such bowtie structures should be accompanied by extremely localized, greatly enhanced optical fields, which may be useful for a diverse range of future nanoscale applications. An FDTD-calculated field intensity distribution just above the bowtie surface is shown in Fig. 1.6d for a 16 nm-gap bowtie pumped near resonance with  $\lambda = 830$  nm radiation. According to the simulation, the fields are confined to regions approximately 20 nm in diameter ( $\sim\lambda/40$ ) near the tip of each triangle and should be enhanced by more than 1500 times relative to the intensity of the incident beam!

It had previously proven difficult to directly measure the electromagnetic fields in the gaps between plasmonically coupled structures because the incident pumping field extends over a much larger (diffraction-limited) area and tends to leak into the detector. To address this, we have found it useful to use two-photon effects that only appreciably occur in the regions where the optical fields are very strong. Using this approach, we have experimentally determined (Schuck et al. 2005a) the optical intensity enhancement values for the fields in the metal of these structures, which closely approximate the fields outside the metal near the surface.

Strongly enhanced local fields due to the excitation of surface plasmons in rough films, sharp tips, and nanoparticles give rise to detectable two-photon absorption in Au (Chen et al. 1981; Boyd et al. 1986; Beversluis et al. 2003). The resulting excitation of electrons from the  $d$  valence band to the  $sp$  conduction band leads to a broadband emission continuum, termed two-photon-excited photoluminescence (TPPL) in Au. Due to its nonlinear (intensity squared) dependence on excitation intensity, TPPL is an extremely sensitive probe of excitation field strength and

distribution. Variations between the TPPL spectra from differently shaped Au nanoparticles provide evidence for the localized origin of the absorption and subsequent emission (Bouhelier et al. 2003).

We have used TPPL to directly determine absolute values for optical field enhancements of single Au bowties by comparing the strength of TPPL from bowties with TPPL from a smooth Au film (Schuck et al. 2005a). The TPPL from individual bowties was measured with a sample-scanning microscope. A mode-locked Ti:sapphire laser producing high peak intensity 120 fs pulses at  $\lambda = 830$  nm with a repetition rate of 75 MHz was used for excitation. The value  $\lambda = 830$  nm was chosen because the smallest gap bowties were measured to be resonant close to this wavelength (see Figure 1.6c).

Using a diffraction-limited focus from an inverted microscope, arrays of single bowties with various gap sizes were scanned, and Au TPPL was focused onto a single-photon counting avalanche photodiode (APD) for broadband collection, creating TPPL images such as those shown in Figures 1.7a,b. Figures 1.7d,e show that the TPPL is strongly polarization-dependent. After optical experiments, the sample was coated with a thin Cr layer ( $\sim 4$  nm) to enable careful measurement of nanoantenna gap size in a scanning electron microscope (SEM).

The intensity enhancement factor in the metal of the bowtie  $i$ ,  $\alpha_{br}^i$ , can be calculated by carefully measuring the ratio of TPPL intensities from the bowtie and a smooth reference film and taking into the account the different excitation areas in the two cases (Schuck et al. 2005a). As shown in Figure 1.7c, the experimentally determined TPPL intensities yield  $E^2$  enhancement factors of greater than  $10^3$ , or greater than  $10^6$  in  $E^4$  (i.e.,  $\alpha^2$ ) for bowties with the smallest gaps. These are the largest such factors reported to date for lithographically produced nanoantennas. It should be noted that with gap spacings smaller than 16 nm and smaller tip radii of curvature than 12 nm, it should be possible in principle to obtain still stronger fields. However, smaller and well-controlled gap spacings and tip radii may be difficult to reliably fabricate in practice.

A comparison of Figure 1.7a with 1.7b demonstrates the practical limitations of EBL when attempting to produce ever-smaller gap sizes and features. Figure 1.7a is a TPPL image of four bowties, each designed to have 24 nm gaps. Note the general uniformity of the TPPL, evidence of consistent bowtie shape and gap size. There is a large variation in TPPL intensities, however, from the four bowties in the TPPL image in Figure 1.7b, which are from an array designed to contain bowties with significantly smaller (19 nm) gaps. In Figure 1.7b, the inhomogeneity in brightness results from variations in the actual gap width (gaps ranging from 0 to 28 nm were measured for this array), and bowties that appear dark were later found to be shorted using SEM.

### ***1.3.5 Exploring the Chemical Enhancement for Surface-Enhanced Raman Scattering with Au Bowtie Nanoantennas***

Over 30 years ago, it was first observed that the Raman signal of pyridine dramatically increases when adsorbed on a roughened Ag electrode (Fleischmann et al.

1974; Jeanmaire and Van Duyne 1977), and the detailed origins of surface-enhanced Raman scattering (SERS) arising from nanostructured metals have remained a topic of debate. Researchers have divided the SERS enhancements into two factors (Michaels, et al. 2000): an electromagnetic (EM) enhancement, where illumination intensity is enhanced due to sharp metal edges or plasmon effects, and a chemical enhancement (CE), where the Raman cross-section of adsorbed molecules is increased above the solution value (Moskovits 1985).

Interest in the SERS mechanism blossomed with the recent observation of Raman lines apparently arising from single molecules adsorbed onto colloidal Ag and Au particles (Kneipp et al. 1997; Nie and Emory 1997; Michaels et al. 2000). To obtain the 14-order of magnitude enhancement required to make Raman signals competitive with single-molecule fluorescence, it was believed that an enormous EM enhancement at “hot spots” was combined with a modest CE in these systems.

Michaels et al. (2000) suggested that coupled colloidal particles locally enhance the incident laser pump intensity and SERS detection probability, yielding a total EM enhancement potentially as high as  $10^{10}$ . However, uncertainty about the relative importance of the chemical effect, which has been estimated to enhance SERS signals by factors anywhere from 10 to as high as  $10^6$  (Otto 2002; Haran 2004), has motivated our use of bowties as an electromagnetically calibrated SERS-active substrate. Because bowties provide a coupled plasmon system with lithographically controllable gap and known (measured) EM enhancement (Schuck et al. 2005a), they allow direct exploration of the role of CE in SERS (Fromm et al. 2006).

For this study, bowties were coated with p-mercaptoaniline (pMA), which is known to form a self-assembled monolayer (SAM) upon binding to Au through the thiol. Using the known values for the monolayer packing area of pMA ( $19\text{\AA}^2/\text{molecule}$ ), the surface area of the bowtie experiencing enhanced E-fields ( $3000\text{nm}^2$ ) as predicted by electromagnetic calculations (Sundaramurthy et al. 2005), the solution-phase pMA Raman scattering cross-section for nonresonant, infrared pumping ( $10^{-29}\text{cm}^2$ ), and excitation and detection parameters, total SERS enhancement (TE) for pMA on the bowtie was estimated to be  $7 \times 10^7$  per molecule, assuming all  $10^4$  molecules in the enhanced field contribute equally to SERS. The TE value is often broken into EM and CE contributions in the following manner:  $\text{TE} = (|E|_{\text{pump}}^2 / |E_0|^2) \cdot (|E|_{\text{transmit}}^2 / |E_0|^2) \cdot \text{CE}$ , where  $E_0$  is the incident electric field. In our bowties,  $|E|_{\text{pump}}^2$  is measured (Schuck et al. 2005a) to be  $\sim 1500 \cdot |E_0|^2$ . Assuming that  $|E|_{\text{transmit}}^2$  is also  $\sim 1500 \cdot |E_0|^2$ , reasonable for Stokes radiation considering the fairly broad antenna resonance (Fromm et al. 2004), a value of CE  $\sim 30$  is obtained, consistent with previous estimates.

Closer examination of the SERS spectra reveals that there are intriguing and unexpected dynamics; particular lines “blink” and their mode frequencies shift discontinuously, even though an entire monolayer of pMA covers the bowtie. Behavior like this has been reported previously (Kneipp et al. 1997; Nie and Emory 1997; Michaels et al. 2000; Haran 2004), but only at concentrations of a few molecules per nanoparticle.

It is immediately obvious in the spectral waterfall plot in Figure 1.8A that the intensity and frequency of some Raman lines are stable, but vary significantly for other modes. Using previous pMA mode assignments (Osawa et al. 1994), modes

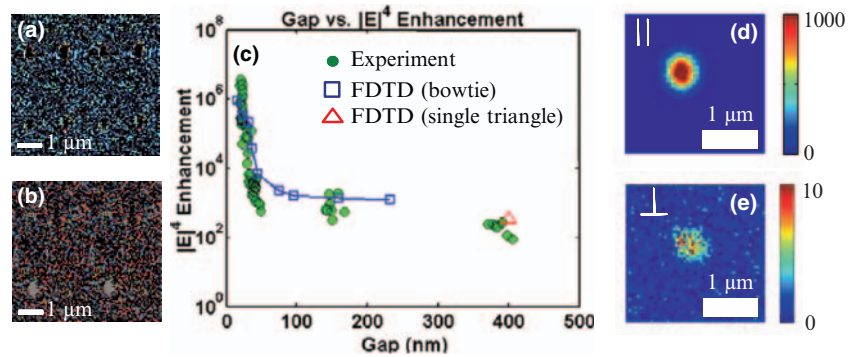


**Figure 1.7** TPPL images of bowties from arrays with nominal gap sizes of (a) 24 nm and (b) 19 nm. Comparison of experimental (circles) and theoretical (open squares and triangle) values of the square of intensity enhancement,  $(\alpha_{\text{pl}})^2$ , for bowties with gaps of 16 nm to 406 nm (c). FDTD simulations for  $(\alpha_{\text{pl}})^2$  from an individual triangle are used for comparison to the bowties with nominal gap size of 400 nm. Incident polarization dependence is shown in (c) and (d) for a 20 nm gap bowtie (note different scales). (After Schuck et al. (2005a), used by permission)

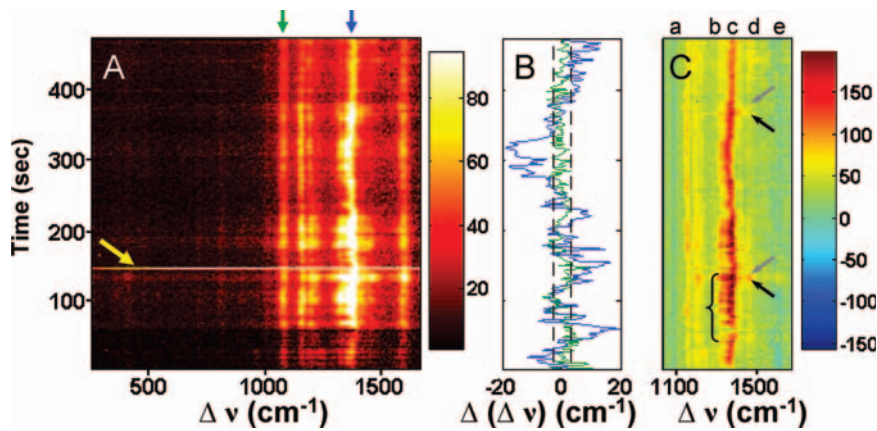


**Figure 1.8** (A) Waterfall plot showing the evolution of SERS spectra with time (2 s integration).  $I = 11 \text{ kW/cm}^2$  for  $t = 0 - 57 \text{ s}$ , and  $I = 38 \text{ kW/cm}^2$  for  $t = 57 - 460 \text{ s}$ . Notice the intense flash of continuum fluorescence at  $t \sim 150 \text{ s}$  (yellow arrow), the relatively stable modes at  $1077 \text{ cm}^{-1}$  and  $1590 \text{ cm}^{-1}$ , and fluctuations of both frequency and amplitude for the  $1160$ ,  $1195$ ,  $1325$ ,  $1380$ , and  $1450 \text{ cm}^{-1}$  Raman modes. (B) Mode center frequency fluctuations for  $1077 \text{ cm}^{-1}$  (green) and  $1380 \text{ cm}^{-1}$  (blue) lines, with error bar shown as dashed lines. Only modes with  $b_2$  symmetry fluctuate significantly. (C) A waterfall plot of difference spectra showing discrete intensity fluctuations evident for  $b_2$  modes. Note the blinking in the  $1325 \text{ cm}^{-1}$  mode (bracket, mode “b”) and “on” (black arrows) “off” (gray arrows) switching for mode “d,”  $1450 \text{ cm}^{-1}$ . Mode “c” ( $1380 \text{ cm}^{-1}$ ) also fluctuates. Modes (“a,”  $1077 \text{ cm}^{-1}$  and “e,”  $1590 \text{ cm}^{-1}$ ) having  $a_1$  symmetry are suppressed by the subtraction (see text and Fromm et al. (2006) for details). (After Fromm et al. (2006), used by permission)

at 1077 and 1590  $\text{cm}^{-1}$ , assigned to  $a_1$  symmetry, are stable in their frequency, and their intensity varies by less than a factor of 2 over the entire spectral series. For this reason, we use the  $a_1$  modes as key reference modes in our analysis below. Conversely, peaks at 1160, 1195, 1325, 1380, and 1450  $\text{cm}^{-1}$ , which have  $b_2$  symmetry and have been interpreted as charge transfer (CT) modes for pMA (Hill and Wehling 1993; Osawa et al. 1994), display large frequency and intensity fluctuations. For frequency fluctuations, Figure 1.8B displays the center frequency time trajectory of one mode in each of the two classes, determined by fitting the peaks to Lorentzian profiles. The  $a_1$  1077  $\text{cm}^{-1}$  reference mode (green) displays little change within the noise (dashed lines), whereas the  $b_2$  1380  $\text{cm}^{-1}$  mode (blue) varies significantly, often “jumping” as much as  $\pm 20 \text{ cm}^{-1}$  from its average value.

One may assume that the Raman spectra include contributions from a large number of molecules with the small enhancement calculated above, plus a contribution from a small number of molecules with large (possibly huge) enhancement. To highlight the latter contribution, we use the strength of the 1077  $\text{cm}^{-1}$  reference mode to scale a bulk pMA SERS calibration spectrum (measured elsewhere; Fromm et al. (2006)) and subtract it from the observed spectra, generating the difference spectra in Figure 1.8C. Note that scaling by the 1077  $\text{cm}^{-1}$  mode automatically makes the other  $a_1$  mode at 1590  $\text{cm}^{-1}$  disappear. Figure 1.8C shows strong on/off amplitude fluctuations in several  $b_2$  modes (designated “b” and “d”), for example, at the arrows and bracket. Because the  $b_2$  modes have been shown to be strongly affected by charge transfer (CT) from the metal (Osawa et al. 1994), the discrete fluctuations of the  $b_2$  modes suggest a dynamic CT process is occurring.

Due to the difficulty in synchronizing even a small number of molecules, discrete intensity fluctuations (blinking) and spectral jumping are often used as two spectroscopic signatures of single molecules (Moerner and Orrit 1999). We note that blinking alone is not necessarily a fair indicator of single-molecule SERS, because the EM enhancement could rapidly change, leading to temporary fluctuations of SERS signals for all molecules near the gap. The stability of the reference  $a_1$  modes shows that large EM changes are not occurring here.

Because the frequency and/or amplitude of the  $b_2$  modes often discontinuously “jump,” and in any one 2 s spectrum, a single frequency is observed, this observation implies that there is either a synchronization of a huge fraction of the  $10^4$  molecules near the gap (Fromm et al. 2006), or that a very small subset of molecules is responsible for the discontinuous changes, with the possibility that the fluctuating difference SERS signature is from just a few molecules. If this is true, the varying frequencies (Figure 1.8B) and amplitudes (Figure 1.8C) of the CT  $b_2$  modes suggest that selected molecule(s) are subject to a huge variation in their CE, from  $\sim 30$  to as much as  $\sim 10^7$ , whereupon CT temporarily increases the Raman cross-section of affected modes. Apparently, the signal from a small subset may be comparable, even exceeding (by more than an order of magnitude) that of the remaining  $10^4$  molecules near the bowtie gap, even though both are subject to the same EM value, not an unreasonable possibility (Wang 2005). This fascinating behavior may be possibly understood using existing CT theory, in which we suggest that an increase in wavefunction mixing between  $\pi$ -orbitals in the benzene ring and Au occurs when

a pMA molecule lies down at the surface. Tests of this idea would require careful imaging of the SAM in future studies.

## 1.4 Summary and Prospects

### 1.4.1 *Single-Molecule Fluorophores*

The DCDHF single-molecule fluorophores have been used in polymer hosts to report on local free volume through differences in the excited-state lifetime. The dyes have also been incorporated into the membranes of live cells for use as lipid analogues, and single copies can be observed diffusing in the cell membrane. Two-photon fluorescence has been observed for single DCDHF fluorophores as well. In future studies, the DCDHF fluorophores can be considered for situations where the molecule is specifically attached to a biomolecule or polymer or binds strongly to a biomolecule. When the molecule is located in a relatively rigid environment, the emission would be much brighter compared to the case where the molecule is unbound or is in a more flexible local environment. Another class of studies envisioned can take advantage of the large ground-state dipole moment; in particular, one would expect to be able to turn the molecule using an external electric field or a strong, time-varying local electric field such as that from the bowties. In addition, the optical nonlinearity of these molecules is a third local reporter variable that is waiting to be explored in imaging applications.

### 1.4.2 *Metallic Bowtie Nanoantennas*

In order to explore the regime where optical fields much smaller than the diffraction limit are used to probe molecules, we have fabricated Au bowtie nanoantennas by e-beam lithography that have tunable resonances in the visible/near-IR wavelength range. FDTD calculations have been used to predict resonance frequencies, field profiles, and local field enhancements. Experimental measurements of peak scattering wavelength by TIR microscopy for bowties with a range of gap sizes from 20 to 500 nm are in good agreement with theory. We have also experimentally measured optical intensity enhancements at Au bowtie nanoantennas of various gap sizes using TPPL, and the field intensity enhancement is  $>10^3$  confined to a region  $\sim 650 \text{ nm}^2$ . Because the electromagnetic enhancement is known for bowties, they have provided the first calibrated substrate for the direct investigation of the chemical enhancement effect in SERS, which may be as large as  $10^7$  for a few molecules.

It is to be expected that with optimization of the fabrication, Au bowties will be reproducibly manufactured either individually on a scanning probe or in large arrays on a single substrate. This would yield extremely intense near-field optical light sources with high local contrast that have applications ranging from ultra-sensitive

biological detection, single-molecule spectroscopy, and nanometer-scale lithography to high-resolution optical microscopy and spectroscopy.

Already, in recent work, the bowties have been used to fabricate ultra-small islands of photoresist by two-photon polymerization (Sundaramurthy et al. 2006). Using a bowtie to pump single molecules would be a dramatic improvement in the mismatch between conventional optical excitations and nanoscale structures. However, it will be essential to treat the molecule–bowtie system as a coupled near-field object in order to understand the observed effects, especially because there may be perturbation of the molecular properties by the proximity to the metal (Ambrose et al. 1994; Trautman et al. 1994; Bian et al. 1995). Eventually, these light sources will be combined with the ultimate small emitter, a nm-sized single molecule.

**Acknowledgments** This work was supported in part over the years by the U. S. Department of Energy Grant No. DE-FG03-00ER45815, by the National Institutes of Health Grant Nos. 1R21-GM65331 and 1P20-HG003638, and by the National Science Foundation Grant Nos. DMR-0237247 and DMR-0507296.

## References

- Albota, M.A., C. Xu, et al. (1998). Two-photon fluorescence excitation cross sections of biomolecular probes from 690 to 960 nm. *Appl. Opt.* **37**: 7352–7356.
- Ambrose, W.P., P.M. Goodwin, et al. (1994). Alterations of single molecule fluorescence lifetimes in near-field optical microscopy. *Science* **265**: 364–367.
- Barbara, P.F., A.J. Gesquiere, et al. (2005). Single-molecule spectroscopy of conjugated polymers. *Acc. Chem. Res.* **38**: 602–610.
- Barkai, E., Y.-J. Jung, et al. (2004). Theory of single-molecule spectroscopy: Beyond the ensemble average. *Annu. Rev. Phys. Chem.* **55**: 457–507.
- Betzig, E., J.K. Trautman, et al. (1991). Breaking the diffraction barrier: Optical microscopy on a nanometric scale. *Science* **251**: 1468–1470.
- Beyersluis, M.R., A. Bouhelier, et al. (2003). Continuum generation from single gold nanostructures through near-field mediated intraband transitions. *Phys. Rev. B* **68**: 115433.
- Bian, R.X., R.C. Dunn, et al. (1995). Single molecule emission characteristics in near field microscopy. *Phys. Rev. Lett.* **75**: 4772–4775.
- Bohn, J.L., D.J. Nesbitt, et al. (2001). Field enhancement in apertureless near-field scanning optical microscopy. *J. Opt. Soc. Amer. A* **18**(12): 2998–3006.
- Bouhelier, A., M.R. Beyersluis, et al. (2003). Characterization of nanoplasmonic structures by locally excited photoluminescence. *Appl. Phys. Lett.* **83**: 5041–5043.
- Boyd, G.T., Z.H. Yu, et al. (1986). Photoinduced luminescence from the noble metals and its enhancement on roughened surfaces. *Phys. Rev. B* **33**: 7923–7936.
- Burland, D.M., R.D. Miller, et al. (1994). Second-order nonlinearity of poled-polymer systems. *Chem. Rev.* **94**: 31–75.
- Chen, C.K., A.R.B. de Castro, et al. (1981). Surface enhanced second-harmonic generation. *Phys. Rev. Lett.* **46**: 145–148.
- Cotlet, M., S. Masuo, et al. (2004). Probing conformational dynamics in single donor–acceptor synthetic molecules by means of photoinduced reversible electron transfer. *Proc. Nat. Acad. Sci. USA* **101**: 13343–13348.
- Crozier, K.B., A. Sundaramurthy, et al. (2003). Optical antennas: Resonators for local field enhancement. *J. Appl. Phys.* **94**: 4632–4642.



- Denk, W., J.H. Strickler, et al. (1990). Two-photon laser scanning fluorescence microscopy. *Science* **248**: 73–76.
- Fleischmann, M., P.J. Hendra, et al. (1974). Raman spectra of pyridine adsorbed at a silver electrode. *Chem. Phys. Lett.* **26**(2): 163–166.
- Fromm, D.P., A. Sundaramurthy, et al. (2004). Gap-dependent optical coupling of single “bowtie” nanoantennas resonant in the visible. *Nano Lett.* **4**: 957–961.
- Fromm, D.P., A. Sundaramurthy, et al. (2006). Exploring the chemical enhancement for surface-enhanced Raman scattering with Au bowtie nanoantennas. *J. Chem. Phys. Commun.* **124**(6): 061101.
- Genov, D.A., A.K. Sarychev, et al. (2004). Resonant field enhancement from metal nanoparticle arrays. *Nano Lett.* **4**: 153–158.
- Grober, R.D., R.J. Schoelkopf, et al. (1997). Optical antenna: Towards a unity efficiency near-field optical probe. *Appl. Phys. Lett.* **70**: 1354–1356.
- Ha, T. (2001). Single-molecule fluorescence resonant energy transfer. *Methods* **25**: 78–86.
- Ha, T., T.A. Laurence, et al. (1999). Polarization spectroscopy of single fluorescent molecules. *J. Phys. Chem. B* **103**: 6839–6850.
- Hao, E. and G.C. Schatz (2004). Electromagnetic fields around silver nanoparticles and dimers. *J. Chem. Phys.* **120**: 357–366.
- Haran, G. (2004). Single molecule-Raman spectroscopy and local work function fluctuations. *Israel J. Chem.* **44**: 385–390.
- Hartschuh, A., E.J. Sanchez, et al. (2003). High-resolution near-field Raman microscopy of single-walled carbon nanotubes. *Phys. Rev. Lett.* **90**: 95503.
- Haynes, C.L., A.D. McFarland, et al. (2003). Nanoparticle optics: The importance of radiative dipole coupling in two-dimensional nanoparticle arrays. *J. Phys. Chem. B* **107**: 7337–7342.
- He, M., R. Twieg, et al. (2002). Dicyanomethylenedihydrofuran photorefractive materials. *Proc. SPIE* **4802**: 9–20.
- Hill, W. and B. Wehling (1993). Potential- and pH-dependent surface-enhanced Raman scattering of p-mercapto aniline on silver and gold substrates. *J. Phys. Chem.* **97**: 9451–9455.
- Hummer, G. and A. Szabo (2005). Free energy surfaces from single-molecule force spectroscopy. *Acc. Chem. Res.* **38**: 504–513.
- Jackson, J.B., S.L. Westcott, et al. (2003). Controlling the surface enhanced Raman effect via the nanoshell geometry. *Appl. Phys. Lett.* **82**: 257–259.
- Jeanmaire, D.L. and R.P. Van Duyne (1977). Surface Raman spectroelectrochemistry Part I. Heterocyclic, aromatic, and aliphatic amines adsorbed on the anodized silver electrode. *J. Electroanal. Chem.* **84**(1): 1–20.
- Jin, L., A.C. Millard, et al. (2005). Cholesterol-enriched lipid domains can be visualized by di-4-ANEPPDHQ with linear and nonlinear optics. *Biophys. J.* **89**(1): L04–6.
- Kanis, D.R., M.A. Ratner, et al. (1994). Design and construction of molecular assemblies with large second-order optical nonlinearities. Quantum chemical aspects. *Chem. Rev.* **94**: 195–242.
- Kippelen, B., F. Meyers, et al. (1997). Chromophore design for photorefractive applications. *J. Amer. Chem. Soc.* **119**(19): 4559–4560.
- Kneipp, K., H. Kneipp, et al. (2002). Surface-enhanced Raman scattering and biophysics. *J. Phys. Condens. Mat.* **14**: R597–R624.
- Kneipp, K., Y. Wang, et al. (1997). Single molecule detection using surface-enhanced Raman scattering. *Phys. Rev. Lett.* **78**: 1667–1105.
- Kuzyk, M.G. and C.W. Dirk (1998). *Characterization Techniques and Tabulations for Organic Nonlinear Optical Materials*. New York: Dekker-CRC Press.
- Lakowicz, J.R. (1999). *Principles of Fluorescence Spectroscopy*. New York: Kluwer Academic.
- Lee, T.-H., J.I. Gonzales, et al. (2005). Single-molecule optoelectronics. *Acc. Chem. Res.* **38**: 534–541.
- Lord, S.J., Z. Lu, et al. (2007). Photophysical properties of acene DCDHF fluorophores: Long-wavelength single-molecule emitters designed for cellular imaging. *J. Phys. Chem. A* published on Web 8/24/2007, “<http://dx.doi.org/10.1021/jp0712598>” 10.1021/jp0712598.

- Lounis, B.L. and M. Orrit (2005). Single-photon sources. *Rep. Prog. Phys.* **68**: 1129–1179.
- Lu, H.P. (2005). Probing single-molecule protein dynamics. *Acc. Chem. Res.* **38**: 557–565.
- Maier, O., V. Oberle, et al. (2002). Fluorescent lipid probes: Some properties and applications. *Chem. Phys. Lipids* **116**: 3–18.
- Melikian, G., F.P. Rouessac, et al. (1995). Synthesis of substituted dicyanomethylendihydrofurans. *Synth. Commun.* **25**(19): 3045–3051.
- Michaels, A.M., J. Jiang, et al. (2000). Ag nanocrystal junctions as the site for surface-enhanced Raman scattering of single rhodamine 6G molecules. *J. Phys. Chem. B* **104**: 11965–11971.
- Moerner, W.E. (1997). Those blinking single molecules. *Science* **277**: 1059.
- Moerner, W.E. (2003). Optical measurements of single molecules in cells. *Trends Analyt. Chem.* **22**: 544–548.
- Moerner, W.E. (2004). Single-photon sources based on single molecules in solids. *New J. Phys.* **6**: 88.
- Moerner, W.E. and D.P. Fromm (2003). Methods of single-molecule fluorescence spectroscopy and microscopy. *Rev. Sci. Instrum.* **74**: 3597–3619.
- Moerner, W.E. and M. Orrit (1999). Illuminating single molecules in condensed matter. *Science* **283**: 1670–1676.
- Moskovits, M. (1985). Surface-enhanced spectroscopy. *Rev. Mod. Phys.* **57**: 783–826.
- Nalwa, H.S. and S. Miyata (Eds.) (1997). *Nonlinear Optics of Organic Molecules and Polymers*. Boca Raton, FL: CRC Press.
- Nicoud, J.F. and R.J. Twieg (1987). *Design and Synthesis of Organic Molecular Compounds for Efficient Second Harmonic Generation. Nonlinear Optical Properties of Organic Molecules and Crystals*. D. S. Chemla and J. Zyss. New York: Academic Press. **1**: 227–296.
- Nie, S. and S.R. Emory (1997). Probing single molecules and single nanoparticles by surface-enhanced Raman scattering. *Science* **275**: 1102–1106.
- Nishimura, S.Y., S.J. Lord, L.O. Klein, K.A. Willets, M. He, Z. Lu, R.J. Twieg, and W.E. Moerner (2006). Diffusion of lipid-like single-molecule fluorophores in the cell membrane. *J. Phys. Chem. B* **110**: 8151–8157.
- Novotny, L., E.J. Sanchez, et al. (1998). Near-field optical imaging using metal tips illuminated by higher-order Hermite–Gaussian beams. *Ultramicroscopy* **71**: 21–29.
- Osawa, M., N. Matsuda, et al. (1994). Charge transfer resonance Raman process in surface-enhanced Raman scattering from p-aminothiophenol adsorbed on silver: Herzberg-Teller contribution. *J. Phys. Chem.* **98**: 12702–12707.
- Ostroverkhova, O. and W.E. Moerner (2004). Organic photorefractives: Mechanisms, materials, and applications. *Chem. Revs.* **104**: 3267–3314.
- Ostroverkhova, O., D. Wright, et al. (2002). Recent advances in the understanding and development of photorefractive polymers and glasses. *Adv. Funct. Mater.* **12**(9): 621–629.
- Otto, A. (2002). What is observed in single molecule SERS, and why? *J. Raman Spectrosc.* **33**(8): 593–598.
- Palik, E.D. (1985). *Handbook of Optical Constants*. Orlando, FL: Academic Press.
- Parasassi, T., E.K. Krasnowska, et al. (1998). Laurdan and prodan as polarity-sensitive fluorescent membrane probes. *J. Fluoresc.* **8**: 365–373.
- Prasad, P.N. and D.J. Williams (1991). *Introduction to Nonlinear Optical Effects in Molecules and Polymers*. New York: John Wiley.
- Rasnik, I., S.A. McKinney, et al. (2005). Surfaces and orientations: Much to FRET about? *Acc. Chem. Res.* **38**: 542–548.
- Rechberger, W., A. Hohenau, et al. (2003). Optical properties of two interacting gold nanoparticles. *Opt. Commun.* **220**: 137–141.
- Schuck, P.J., D.P. Fromm, et al. (2005a). Improving the mismatch between light and nanoscale objects with gold bowtie nanoantennas. *Phys. Rev. Lett.* **94**: 017402.
- Schuck, P.J., K.A. Willets, et al. (2005b). A novel fluorophore for two-photon-excited single-molecule fluorescence. *Chem. Phys.* **318**: 7–11.
- Schütz, G.J., G. Kada, et al. (2000). Properties of lipid microdomains in a muscle cell membrane visualized by single molecule microscopy. *EMBO J.* **19**: 892–901.

- Soper, S.A., H.L. Nutter, et al. (1993). The photophysical constants of several fluorescent dyes pertaining to ultrasensitive fluorescence spectroscopy. *Photochem. Photobiol.* **57**: 972–977.
- Su, K.H., Q.-H. Wei, et al. (2003). Interparticle coupling effects on plasmon resonances of nanogold particles. *Nano Lett.* **3**: 1087–1090.
- Sundaramurthy, A., K.B. Crozier, et al. (2005). Field enhancement and gap-dependent resonance in a system of two opposing tip-to-tip Au nanotriangles. *Phys. Rev. B* **72**: 165409.
- Sundaramurthy, A., P.J. Schuck, et al. (2006). Toward nanometer-scale optical photolithography: Using the near-field of bowtie optical nanoantennas. *Nano Lett.* **6**: 355–360.
- Toutchkine, A., V. Kraynov, et al. (2003). Solvent-sensitive dyes to report protein conformational changes in living cells. *J. Amer. Chem. Soc.* **125**: 4132–4145.
- Trautman, J.K., J.J. Macklin, et al. (1994). Near-field spectroscopy of single molecules at room temperature. *Nature* **369**: 40–42.
- Tsien, R.Y. and A. Waggoner (1995). Fluorophores for confocal microscopy. *Handbook of Biological Confocal Microscopy 2nd ed.* J.B. Pawley. New York: Plenum Press, 267–279.
- Vallee, R.A.L., M. Cotlet, et al. (2004). Single-molecule conformations probe free volume in polymers. *J. Amer. Chem. Soc.* **126**: 2296–2297.
- Vrljic, M., S.Y. Nishimura, et al. (2002). Translational diffusion of individual class II MHC membrane proteins in cells. *Biophys. J.* **83**: 2681–2692.
- Wang, Z., Rothberg, L.J. (2005). Origins of blinking in single-molecule raman spectroscopy. *J Chem Phys B*: jp0460947.
- Watkins, L.P. and H. Yang (2004). Information bounds and optimal analysis of dynamic single-molecule measurements. *Biophys. J.* **86**: 4015–4029.
- Weiss, S. (1999). Fluorescence spectroscopy of single biomolecules. *Science* **283**: 1676–1683.
- Willetts, K.A., P.R. Callis, et al. (2004). Experimental and theoretical investigations of environmentally sensitive single-molecule fluorophores. *J. Phys. Chem. B* **108**: 10465–10473.
- Willetts, K.A., S.Y. Nishimura, et al. (2005). Nonlinear optical chromophores as nanoscale emitters for single-molecule spectroscopy. *Acc. Chem. Res.* **38**(7): 549–556.
- Willetts, K.A., O. Ostroverkhova, et al. (2003a). New fluorophores for single-molecule spectroscopy. *J. Amer. Chem. Soc.* **125**: 1174–1175.
- Willetts, K.A., O. Ostroverkhova, et al. (2003b). Novel fluorophores for single-molecule imaging. *Proc. SPIE* **5222**: 150–157.
- Wright, D., U. Gubler, et al. (2001). A high performance photorefractive polymer composite with 2-dicyanomethylene-3-cyano-2,5-dihydrofuran chromophore. *Appl. Phys. Lett.* **79**(26): 4274–4276.
- Xu, C. and W.W. Webb (1996a). Measurement of two-photon excitation cross sections of molecular fluorophores with data from 690 to 1050 nm. *J. Opt. Soc. Amer. B* **13**: 481–491.
- Xu, C., W. Zipfel, et al. (1996b). Multiphoton fluorescence excitation: New spectral windows for biological nonlinear spectroscopy. *Proc. Nat. Acad. Sci. USA* **93**: 10763–10768.
- Xu, H. and M. Kaell (2003). Polarization-dependent surface-enhanced Raman spectroscopy of isolated silver nanoaggregates. *Chem. Phys. Chem.* **4**: 1001–1005.
- Zenhausen, F., Y. Martin, et al. (1995). Scanning interferometric apertureless microscopy: Optical imaging at 10 angstrom resolution. *Science* **269**: 1083–1085.
- Zhang, C., C.G. Wang, et al. (2001). Progress toward device-quality second-order nonlinear optical materials. 4. A trilink high mu beta NLO chromophore in thermoset polyurethane: A “guest-host” approach to larger electrooptic coefficients. *Macromol.* **34**: 253–261.
- Zhao, L., K.L. Kelly, et al. (2003). The extinction spectra of silver nanoparticle arrays: Influence of array structure on plasmon resonance wavelength and width. *J. Phys. Chem. B*, **107**: 7343–7350.
- Zhuang, X. and M. Rief (2000). Single-molecule protein folding. *Curr. Opin. Struct. Biol.* **13**: 88–97.
- Zyss, J., Ed. (1994). *Molecular Nonlinear Optics*. New York: Academic Press.

## Chapter 2

# Single Biomolecules at Cryogenic Temperatures: From Structure to Dynamics

Clemens Hofmann, Florian Kulzer, Rob Zondervan, Jürgen Köhler,  
and Michel Orrit(✉)

2.1	Introduction.....	26
2.1.1	Cryogenic Conditions and Structure.....	26
2.1.2	Cryogenic Conditions and Dynamics.....	26
2.1.3	Single Biomolecules at Room Temperature: Success Stories and Limitations.....	28
2.1.4	Single-Molecule Optics Under Cryogenic Conditions.....	29
2.2	Spectroscopy of Single Light-Harvesting Complexes.....	30
2.2.1	Photosynthesis in Purple Bacteria.....	30
2.2.2	The Static Electronic Structure of LH2 from <i>Rps. acidophila</i> .....	34
2.2.3	Dynamics in the B800 Band of LH2 from <i>Rs. molischianum</i> .....	38
2.2.4	Outlook of Light-Harvesting Complex Spectroscopy.....	42
2.3	From Structure to Dynamics.....	42
2.4	Conclusions.....	47
	References.....	48

**Abstract** Elucidating the dynamics of proteins remains a central and daunting challenge of molecular biology. In our contribution we discuss the relevance of low-temperature observations not only to structure, but also to dynamics, and thereby to the function of proteins. We first review investigations on light-harvesting complexes to illustrate how increased photostability at low temperatures and spectral selection provide a deeper insight into the excitonic interactions of the chromophores and the dynamics of the protein scaffold. Furthermore, we introduce a novel technique that achieves controlled, reproducible temperature cycles of a microscopic sample on microsecond timescales. We discuss the potential of this technique as a tool to achieve repeatable single-molecule freeze-trapping and to overcome some of the limitations of single-molecule experiments at room temperature.

---

Michel Orrit  
Molecular Nano-Optics and Spins (MoNOS), Huygens Laboratory, Leiden University,  
Postbus 9504, 2333 CA Leiden, The Netherlands  
orrit@molphys.leidenuniv.nl

Jürgen Köhler  
Experimental Physics IV and BIMF,  
University of Bayreuth, 95440 Bayreuth, Germany  
juergen.koehler@uni-bayreuth.de

R. Rigler and H. Vogel (eds.), *Single Molecules and Nanotechnology*.  
*Springer Series in Biophysics 12*.  
© Springer-Verlag Berlin Heidelberg 2008

## 2.1 Introduction

### 2.1.1 *Cryogenic Conditions and Structure*

New protein structures enter the Protein Data Bank at an exponentially growing rate, exceeding 5000 for the year 2004 alone. Much of this progress is owed to the high luminosity and to the tunability of synchrotron sources, which have reduced recording times for diffraction patterns of protein crystals from months with a conventional rotating anode to minutes at an undulator beamline. These spectacular gains are unfortunately paralleled by increased radiation damage to the crystal and to its protein units. Cooling a protein crystal to temperatures around 100 K considerably reduces molecular mobility and reactivity. The two main benefits of cryogenic conditions are a reduction of thermal fluctuations, whereby Bragg peaks grow and sharpen, and, more important, a hardening of the soft organic assemblies against X-ray damage, providing much longer integration times (Garman 2003). The same benefits are also exploited in electron microscopy, where low temperatures improve the sharpness of the images, but also resistance to electron irradiation, allowing one to average high-quality images from many single molecules (van Heel et al. 2000). Cryogenic conditions are therefore crucial to protect protein structures against damage, and to obtain longer observation times as well as better resolution. Modern three-dimensional protein structures, on which our understanding of protein function and interactions builds, are therefore essentially low-temperature structures. How well do these protein structures in crystals match those at room temperature and at physiological conditions (Halle 2004)? Although temperature, entropy, and interactions with a fluid environment are inseparably part of the structure and dynamics of any biomolecule, one usually assumes that the main structural features do not dramatically change upon cooling down, at least in a broad majority of cases, and that structures obtained at cryogenic conditions are relevant to physiologic conditions. We adopt this point of view in the rest of this chapter.

### 2.1.2 *Cryogenic Conditions and Dynamics*

A protein structure derived from X-ray crystallography is necessarily an oversimplification. The crystal environment severely reduces structural fluctuations, which are central to function. To this day, information about the dynamics of proteins, their folding, conformational fluctuations, reaction pathways, and so on, remains fragmentary. Elucidating the dynamics of proteins remains a central and daunting challenge of molecular biology. In this chapter, we plead for the relevance of low-temperature observations not only to structure, but also to dynamics, and thereby to functions of proteins. This is a rather counterintuitive contention. After all, most, if not all, forms of life cease to operate below the freezing point of water solutions. Molecular motion, exchange of reactants, transport, and the like need a fluid environment to proceed at realistic physiological rates. Even proton exchange, one of the fastest chemical

reactions, often involving tunnelling, dramatically slows down when thermal fluctuations are suppressed. Obviously, most dynamical processes will either be utterly frozen, or at least severely hampered at low enough temperatures. Yet, as we later argue, freeze-quenching of dynamical processes can be turned into an advantage.

At least one kind of chemical processes still remains active at cryogenic temperatures, indeed nearly as active as at room temperature: the processes involving movements of charges only, electrons or holes. Because electrons are very light particles, tunnelling dominates the first steps of charge transfer within small molecules, and often dominates transfer between neighboring molecules as well. In other words, cryogenic conditions will give a good first approximation of the electronic structure of biomolecules, that is, of the spatial distribution of relevant electronic wavefunctions, and of the relaxation pathways and intermediate states between different redox states. Spectroscopy at cryogenic conditions is facilitated by the improved spectral resolution and by the longer relaxation times of all other processes, that is, those involving molecular rearrangements. Low-temperature studies therefore form a reliable basis for the discussion of electronic properties in physiological conditions. In Section 2.2, we illustrate this point with single-molecule studies of the light-harvesting protein complex LH2 of purple bacteria.

A second important field of application of cryogenic techniques to the dynamics of biomolecules is physical trapping. Isolating and identifying intermediates at different stages of a biochemical reaction is a powerful method to shed light on its kinetics, and on the complex dynamics of the biomolecules involved. An insightful discussion of different methods for trapping biological reaction intermediates is given by Moffat and Henderson (1995). “Chemical trapping” relies on suddenly modifying the chemical environment (i.e., concentration, pH, redox potential, etc.) to stabilize intermediates. “Physical trapping,” which involves quickly freezing a system down to a temperature where further evolution is blocked, has the advantages that reactions to a temperature change are rapid, and that the system remains closer to authentic conditions than with chemical trapping. For fast enough freezing, and for reactions slower than the freezing time, high-temperature intermediates will be kinetically trapped, and their structures will be immobilized at low temperature. As Frauenfelder and colleagues have shown in their pioneering experiments on myoglobin, a protein’s structure is not unique (Austin et al. 1975). The same primary sequence may present many possible conformations with nearly the same energy. Relaxation between the different conformational substates is governed by a broad distribution of activation barriers in a complex, hierarchically arranged multidimensional space. Diffusion in this complex space is described by the potential energy landscape. As we propose and discuss in Section 2.3, a combination of physical trapping with single-molecule microscopy would provide a powerful approach to explore the potential energy landscape of proteins. As the different conformational substates can be trapped and observed during long times, one could map the potential energy landscape in a detailed fashion. Moreover, by repeatedly cycling a single protein molecule between room and low temperatures, one could let it hop from substate to substate, and in this way reconstruct the typical relaxation pathways in the energy landscape. Section 3 describes some ideas and reports preliminary results in this direction.

Before we review experiments and perspectives for the microscopy of single biomolecules under cryogenic conditions, we briefly recall the particular features, advantages, and limitations of single-molecule spectroscopy.

### ***2.1.3 Single Biomolecules at Room Temperature: Success Stories and Limitations***

Single-molecule optics at room temperature has been a rapidly growing field in the past ten years, as testified by a number of recent review articles (Nie and Zare 1997; Xie and Trautman 1998; Weiss 1999, 2000; Kelley et al. 2001; Deniz et al. 2000; Moerner 2002; Michalet and Weiss 2002; Moerner and Fromm 2003; Peterman et al. 2004; Tinnefeld 2005) and two books (Rigler et al. 2001; Zander et al. 2002). Much effort has been devoted to single biomolecules, in order to address key questions in molecular biology. A common approach is to translate structural information into an optical property, often by means of fluorescent dyes attached to the biomolecule. These fluorophores can be linked with a high degree of control by several biochemical techniques, such as site-specific mutagenesis or fusion/co-expression with fluorescent proteins. Such fluorescent constructs have been used for position and orientation tracking and for co-localization studies. As “spectroscopic rulers,” they enable measurements of distances up to several nanometers by energy transfer, electron transfer, or fluorescence quenching.

Many different issues have been addressed at the single-molecule level: enzymatic dynamics (Lu et al. 1998; Ha et al. 1999; Edman et al. 1999; Zhuang et al. 2000, 2002; Edman and Rigler 2000; van Oijen et al. 2003; Yang et al. 2003), the motion of the motor proteins myosin (Vale et al. 1996; Kitamura et al. 1999; Yildiz et al. 2003; Funatsu et al. 1995) and kinesin (Nishiyama et al. 2001, 2002; Sosa et al. 2001; Peterman et al. 2001; Yildiz et al. 2004; Kapitein et al. 2005; Kural et al. 2005), conformational dynamics of ATP-ase (Börsch et al. 1998, 2002; Sambongi et al. 1999; Diez et al. 2004), chemotactic signaling (Veda et al. 2001), folding of proteins (Deniz et al. 2000; Schuler et al. 2002; Lipman et al. 2003; Rhoades et al. 2004) and RNA (Bokinsky et al. 2003; Rueda et al. 2004), and DNA sequencing (Goodwin et al. 1997; Sauer et al. 1999; Stephan et al. 2001). All these successes notwithstanding, a few inherent problems remain in room-temperature studies of single molecules.

1. The temporal resolution is limited by photon counting statistics: A single fluorophore’s emission rate is limited by the lifetime of the excited state. For a given signal-to-noise ratio, a minimum number of photons  $N$  should be counted, in order to overcome shot noise, which scales with  $1/\sqrt{N}$ , even under the best possible experimental conditions. This makes it very difficult in practice to directly follow changes of single-molecule properties (position, emission spectrum, lifetime, energy transfer efficiency, etc.) on submillisecond timescales, even though each individual photon is in principle detected with subnanosecond timing accuracy (only limited by the response of the detector).

2. Single-molecule fluorescence is intermittent and often exhibits extended dark periods during which no photon can be detected. This ubiquitous phenomenon, commonly referred to as “photoblinking,” is caused by photophysical processes such as intersystem crossing to the triplet state and radical formation by electron transfer (Zondervan et al. 2003). Although photoblinking processes are reversible, and although fluorescence eventually recovers, any useful signal about the system is irretrievably lost during the “off” periods.
3. The total observation time for each molecule is limited by photobleaching: To be detected, a single fluorophore must be excited efficiently, and hence must spend a significant amount of time in optically excited states. This opens many reaction pathways, which may lead to bleaching (Zondervan et al. 2004; Eggeling et al. 2005), that is, to an irreversible loss of fluorescence, for example by self-sensitized photo-oxidation with singlet oxygen (Christ et al. 2001). Photobleaching makes it very difficult to observe processes at the single-molecule level on timescales longer than a few seconds or tens of seconds.

A number of attempts succeeded in mitigating the problems outlined above. First of all, oxygen-scavengers in biological assays greatly improve the photostability of traditional fluorophores such as Cy3 (Yildiz et al. 2003). At the same time, new classes of durable labels appear: semiconductor quantum dots provide longer observation times (Dahan et al. 2003; Michalet et al. 2005); their blinking can also be largely suppressed under certain conditions (Hohng and Ha 2004). Nanometer-sized gold particles are photostable labels that can be detected with high sensitivity and selectivity by means of photothermal (Boyer et al. 2002; Berciaud et al. 2004, 2005) and other techniques (Lindfors et al. 2004). Yet other approaches sidestep photobleaching by relying on diffusion in solution to provide a steady stream of “fresh” molecules. These can be probed in the stationary detection volume one after the other with high temporal resolution (Zander et al. 2002; Hess et al. 2002; Medina and Schwille 2002; Vokojevic et al. 2005). This method, however, comes at the price of reintroducing some degree of ensemble averaging, and/or of being limited to processes faster than milliseconds, the characteristic diffusion time through the detection volume.

### ***2.1.4 Single-Molecule Optics Under Cryogenic Conditions***

We later review experiments on single biomolecules at low temperatures, and propose perspectives for at least partly solving the experimental problems discussed above, therefore we conclude this introduction by giving a brief summary of basic concepts and current topics in single-molecule optics at low temperatures.

Looking back with our present-day knowledge of room-temperature single-molecule microscopy, it seems paradoxical that the first single molecules were optically detected at liquid helium temperatures. What justified the additional experimental investment of cryogeny was, first, a dramatic enhancement of the absorption cross-section by optical resonance, and second, an equally dramatic enhancement of the stability and photoresistance of molecular systems at cryogenic conditions. The first effect was well known



in the field of high-resolution spectroscopy, from fluorescence line-narrowing and persistent spectral hole-burning (Moerner 1989): The narrow zero-phonon line of a single molecule's electronic transition provides an absorption signal strong enough to be detected directly by a double-heterodyne absorption technique (Moerner and Kador 1989) or indirectly by fluorescence-excitation spectroscopy (Orrit and Bernard 1990). Both approaches mainly exploited a spectral selection of individual chromophores via their narrow zero-phonon lines, so that no spatial resolution was required (note, however, that single-molecule microscopy in far-field was nevertheless first demonstrated at low temperatures (Güttler et al. 1994)). The second advantage of cryogenic conditions, photostability, enabled lengthy accumulation of weak but stable signals.

Cryogenic single-molecule experiments traditionally have two main themes: they open studies of the interaction of a single quantum system with light and thus give direct access to quantum-optical phenomena. On the other hand, the single fluorophores can be used as sensitive nanoprobe for structural dynamics of the host matrix, making it possible to address many questions in low-temperature solid-state physics (Tamarat et al. 2000). Here, we only want to mention a few aspects that are important for the following discussion on single biomolecules at low temperatures:

1. Owing to spectral selection, the narrow lines of many single molecules can be distinguished in each focal spot, even when the individual chromophores would be too close to each other for far-field microscopy at room temperature. This is of considerable advantage for complex biological systems such as light-harvesting complexes, whose function requires a high concentration of chromophores, which could not be reduced without damage. Furthermore, valuable structural information can be extracted from spectral dynamics, which would be hidden in the broad room-temperature spectra.
2. The photostability of fluorophores is generally improved at low temperatures, providing opportunities for much longer effective observation times with one and the same absorber.
3. The intrinsic dynamics of biomolecules are dramatically slowed down, and are completely frozen out at a sufficiently low observation temperature. This loosens the aforementioned trade-off between temporal resolution and photon-counting statistics. Varying the temperature furthermore provides access to the hierarchy of thermal activation barriers for conformational changes, thus giving insight into the energy landscape of the studied species.

In the next section, we review low-temperature studies on single light-harvesting complexes, which illustrate the points outlined above.

## 2.2 Spectroscopy of Single Light-Harvesting Complexes

### 2.2.1 *Photosynthesis in Purple Bacteria*

In purple bacteria sunlight is absorbed by a network of antenna pigment proteins. The photosynthetic apparatus of purple bacteria contains two types of antenna complexes, the central light-harvesting complex 1 (LH1) and the peripheral light-harvesting

complex 2 (LH2) (Law et al. 2004). LH1 and the reaction center (RC) are closely associated and form the so-called core complex, whereas LH2 is not in direct contact with the RC but transfers the energy to the RC via the LH1 complex. LH2 is known to comprise two distinct bacteriochlorophyll *a* (BChl *a*) pigment pools which are labeled B800 and B850, whereas the LH1 complex comprises only one pigment pool labeled B870 (Hu et al. 1998). The denotations of the pigment assemblies correspond to their room-temperature absorption maxima in the near infrared.

The first steps of photosynthesis are depicted in Figure 2.1A. After the absorption of a photon, for instance by the B800 pigment pool in the peripheral LH2 complex, energy is transferred to the B850 pigments in 1 to 2 ps (de Caro et al. 1994; Kennis et al. 1997; Wendling et al. 2003; Wu et al. 1996) whereas energy transfer among the B850 molecules is at least an order of magnitude faster (Chachisvilis et al. 1997; Jimenez et al. 1996; Vulto et al. 1999). In the case of isolated LH2, (i.e., in the absence of LH1 and the RC) the lowest excited state of the B850 pigment pool has a relatively long fluorescence lifetime of approximately 1 ns (Monshouwer et al. 1997). Otherwise, the energy is further transferred to the B870 assembly of LH1 and on to the reaction center in which the energy is stored by means of a long-lived (>100 ms (Francia et al. 2004)) charge separation. This is necessary as the excited states of the pigments decay very rapidly, in less than a few nanoseconds. This charge separation is ultimately used for the synthesis of even longer lived chemical storages such as the major energy source in biological systems, adenosine triphosphate (ATP) or the major electron donor in reductive biosynthesis, nicotinamide-adenine

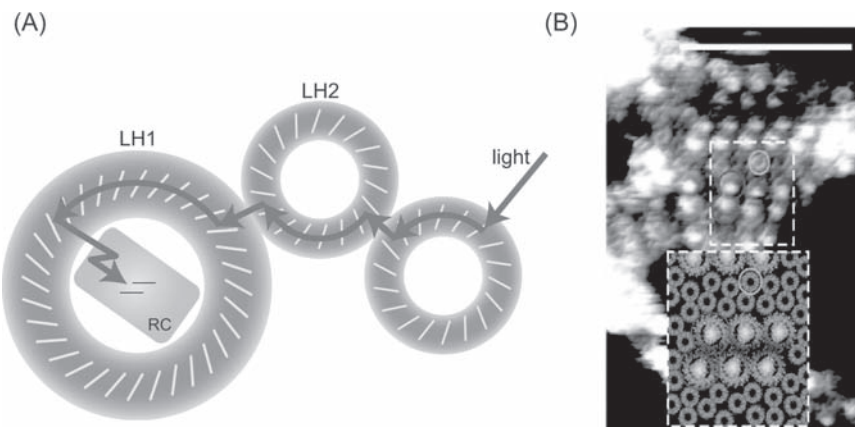


**Figure 2.1** (A) Sketch of the photosynthetic unit of purple bacteria. It comprises the reaction center (RC) and two types of photosynthetic membrane complexes: the light-harvesting 1 (LH1) and the peripheral light-harvesting 2 (LH2) complex. LH1 and the RC are closely associated to form the core complex, whereas LH2 transfers the excitation energy to the RC via the LH1 complex as indicated by the arrows. The light bars indicate the BChl *a* molecules which are held in place by the grey protein scaffold. (Reprinted by permission from Macmillan Publishers Ltd: *Nature*, (Kühlbrandt 1995), copyright 1995.) (B) AFM image of a core complex array surrounded by LH2 complexes in a native photosynthetic membrane. The inset at the bottom represents the same region as the dashed box in the center using model structures that are based on atomic resolution data. (Reprinted by permission from Macmillan Publishers Ltd: *Nature*, (Bahatyrova et al. 2004), copyright 2004)

dinucleotide phosphate (NADPH) (Stryer 2000; van Grondelle et al. 1994). It is thought that a protein called PufX acts as a gate in the LH1 ring through which the charge-carrying proton can leave the RC.

In recent years, AFM has provided unique insight into biological systems. Images of the photosynthetic apparatus in native membranes show an arrangement of the photosynthetic unit in which the core complex is surrounded by several LH2 complexes in a two dimensional structure, Figure 2.1B (Bahatyrova et al. 2004; Scheuring et al. 2004).

### The Geometric Structure of the Light Harvesting Complex 2

The structures of LH2 complexes from several species were determined by X-ray crystallography or electron-microscopy (McDermott 1995; Papiz et al. 2003; Koepke et al. 1996; Walz et al. 1998). Remarkably, all peripheral LH complexes form circular oligomers of the two hydrophobic  $\alpha$ - and  $\beta$ -apoproteins, which noncovalently bind three BChl *a* molecules and one or two carotenoids, featuring a nonameric (*Rps. acidophila*, *Rb. sphaeroides*) or octameric (*Rs. molischanum*) quaternary protein structure.

In the left part of Figure 2.2 the structure of the LH2 pigment-protein complex of *Rps. acidophila* derived from X-ray crystallography with a resolution of 2.0 Å is

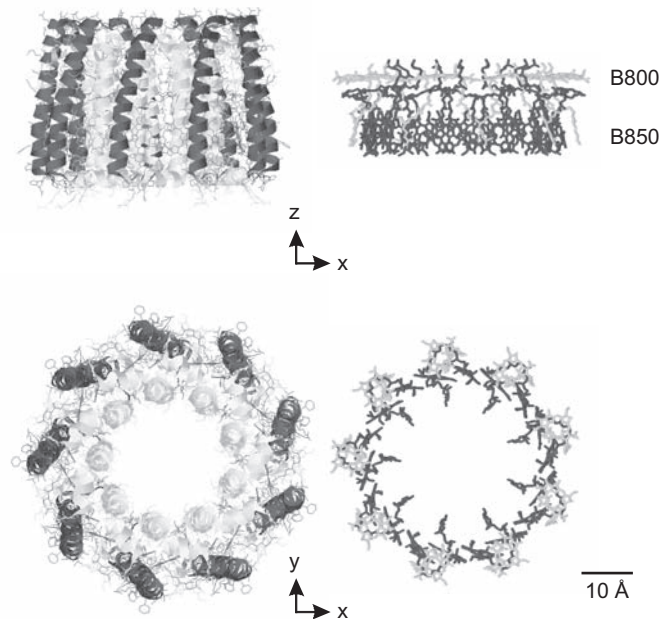


**Figure 2.2** X-ray structure of the LH2 complex from *Rps. acidophila*. The left part displays the whole pigment–protein complex whereas in the right part only the BChl *a* molecules are drawn. The upper part shows a side view, the lower part a top view. The pigments are arranged in two concentric rings commonly termed B800 (light-grey) and B850 (black). The atomic coordinates were taken from the Protein Data Bank, identification code 1NKZ.

shown as a whole, whereas in the right part only the BChl *a* molecules are depicted. The two rings of BChl *a* molecules can be distinguished. The B850 ring consists of nine repeating pairs of one  $\alpha$ - and one  $\beta$ -bound pigment which are arranged as the blades of a turbine. The B800 ring consists of nine well-separated pigments that have their molecular planes perpendicular to the symmetry axis—each bound by a heterodimer—arranged in a  $C_9$  symmetry.

## The Electronic Structure of the Light Harvesting Complex 2

By now, it has been established that the spatial structure of photosynthetic complexes, especially the mutual orientation of the pigments, determines to a large extent their spectroscopic features and excited-state dynamics (van Amerongen et al. 2002). These assemblies of repeating noncovalently bound molecular units show intermediate features between an individual molecule and a crystal, which makes them suitable model systems to study different types of intermolecular interactions in great detail (Fidder et al. 1991; Juzeliunas and Reinek 1997; Cory et al. 1999; De Rossi et al. 1998; Mostovoy and Knoester 2000; Scheblykin et al. 2000; Dempster et al. 2001; Vacha et al. 2001).

Without any interaction the absorption line shape of a pure electronic transition (e.g.,  $S_1 \rightarrow S_0$ ) would be Lorentzian and its homogeneous line width ( $\Gamma_{\text{hom}} = 1/2\pi\tau_1$ ) would be determined by its excited state lifetime  $\tau_1$ . However, the interaction of the probe molecule with its surrounding causes frequency fluctuations  $\delta\nu$  of the absorption whose contributions to the optical line shape depend on the time scale  $\delta t$  of the fluctuations.

Fast fluctuations  $\delta\nu \delta t < 1$  such as the coupling of the vibrational motions of the proteins (i.e., phonons) to the electronic transitions of the pigment will lead to a temperature-dependent broadening of the absorption line. These dephasing processes lead to a homogeneous broadening of the absorption line. In contrast, slow fluctuations  $\delta\nu \delta t > 1$  of the environment—such as structural changes of the proteins—cause spectral diffusion represented by gradual spectral drifts or abrupt jumps of the absorption frequency that results in an inhomogeneously broadened absorption. In principle for a spectrally diffusing line the individual frequency jumps could be observed with a sufficiently fast and sensitive detection system (Tamarat et al. 2000).

For an assembly of  $N$  molecules the electronically excited states can be described in Heitler–London approximation by the following Hamiltonian,

$$H = \underbrace{\sum_n (E_0 + \delta E_n) |n\rangle \langle n|}_{\text{energy}} + \underbrace{\sum_{n,m} (V_{n-m} + \delta V_{n,m}) |n\rangle \langle m|}_{\text{interaction}}. \quad (2.1)$$

Here  $E_0$  denotes the average excited state energy of an individual pigment and  $V_{n-m}$  the average interaction between two pigments separated by  $|n-m|$  BChl *a* molecules.  $\delta E_n$  and  $\delta V_{n,m}$  represent the deviations and are commonly referred to as diagonal and off-diagonal disorder, respectively. The former is usually characterized by the width  $\Delta$  of a Gaussian distribution of site energies. These deviations can be

ascribed to subtle differences in the pigment–protein interaction. The interaction between a chromophore and a molecule in its surroundings depends on distance through different terms varying as  $R^{-n}$ , including dipole–dipole ( $n = 3$ ), dispersion ( $n = 6$ ), repulsion ( $n = 12$ ), and so on. Fluctuations in the local environment of the chromophore correspond to distance changes between neighboring molecules, resulting in fluctuations of the absorption frequency of the chromophore.

Two limiting cases can be distinguished for the description of the electronically excited states of such a molecular aggregate. In the limit  $V/\delta E \ll 1$  the description of the excited states in terms of excitations localized on the individual molecules is a good approximation. For  $V/\delta E \gg 1$  the electronically excited states of the aggregate are described more appropriately as excitations that are coherently delocalized over the whole aggregate.

### Single-Molecule Spectroscopy on LH2

For single-molecule experiments LH2 complexes were isolated from intact bacteria and subsequently purified (McDermott et al. 1995; Germeroth et al. 1993). The samples were prepared by spincoating a highly diluted LH2–detergent solution on a Li-fluoride substrate, and then cooled in a liquid He bath–cryostat to 1.4 K. The Ti–sapphire–laser-excited fluorescence (spectral window: 20 nm, bandwidth of detection:  $1 \text{ cm}^{-1}$ ) around 880 nm was detected with an avalanche photodiode (SPCM–AQR–16, EG&G). To examine the polarization dependence of the spectra, a  $\frac{1}{2}\lambda$  plate was put in the confocal excitation path. A detailed description of the experimental setup can be found in (Hofmann et al. 2004a).

#### 2.2.2 The Static Electronic Structure of LH2 from *Rps. acidophila*

Five examples of fluorescence-excitation spectra of individual LH2 complexes from *Rps. acidophila* are shown in Figure 2.3. In the top two traces the sum of 19 spectra from individual complexes (solid line) is compared with the spectrum from a large ensemble of pigment protein complexes (dashed line). Both spectra are in good agreement, indicating that the experimental selection procedure is not biased towards a subensemble.

When observing the single complexes, the ensemble averaging in these bands is removed and remarkable new spectral features become visible. The striking differences between the two absorption bands can be rationalized by considering the intermolecular interaction strength  $V$  between neighboring BChl  $a$  molecules in a ring and the spread in transition energies  $\Delta E_n$ .

#### The B800 Band, Localized Excitations

The BChl  $a$  molecules in the B800 ring feature an interaction energy of about  $24 \text{ cm}^{-1}$  whereas the width of the Gaussian distribution of site energies  $\Delta \approx 120 \text{ cm}^{-1}$ .

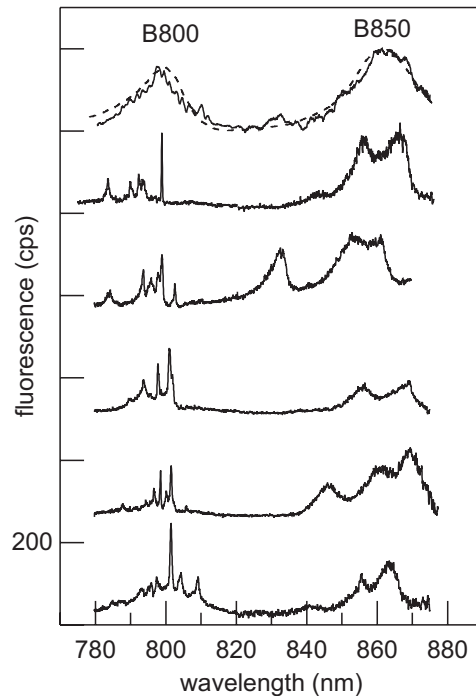


**Figure 2.3** Fluorescence-excitation spectra of LH2 from *Rps. acidophila*. The top traces show the comparison between an ensemble spectrum (dashed line) and the sum of 19 spectra recorded from individual complexes (solid line). The lower five traces display spectra from single LH2 complexes. (Reprinted from (Ketelaars et al. 2001), with permission from the Biophysical Society)

This yields  $V/\Delta \approx 0.2$  which falls into the regime of weak to intermediate coupling. These numbers suggest a slight delocalization of the B800 excited states over 2–3 neighboring BChl *a* molecules in the B800 manifold with a concomitant redistribution of oscillator strength (van Grondelle 1994; Hofmann et al. 2003a; Sundström et al. 1999; Sauer et al. 1996).

This conjecture is supported by the spectra of the B800 ring. For strict localization one would expect 9 absorption lines, however, the spectra typically feature a discrete pattern of 4–6 narrow absorption lines with a spread of several nanometers around the peak absorption of the ensemble value (Figure 2.3). The variations with respect to the number of lines and the spectral positions of the absorptions is caused by the energetic disorder in these biological systems, as discussed in the previous section.

### The B850 Band, Frenkel Excitons

In contrast to the weak coupling in the B800 ring, the smaller spatial distance of the BChl *a* molecules in the B850 ring of about 10 Å (compared to 20 Å in the B800 ring) leads to strong coupling of about  $250 \text{ cm}^{-1}$ . With a disorder of  $\Delta \approx 250 \text{ cm}^{-1}$

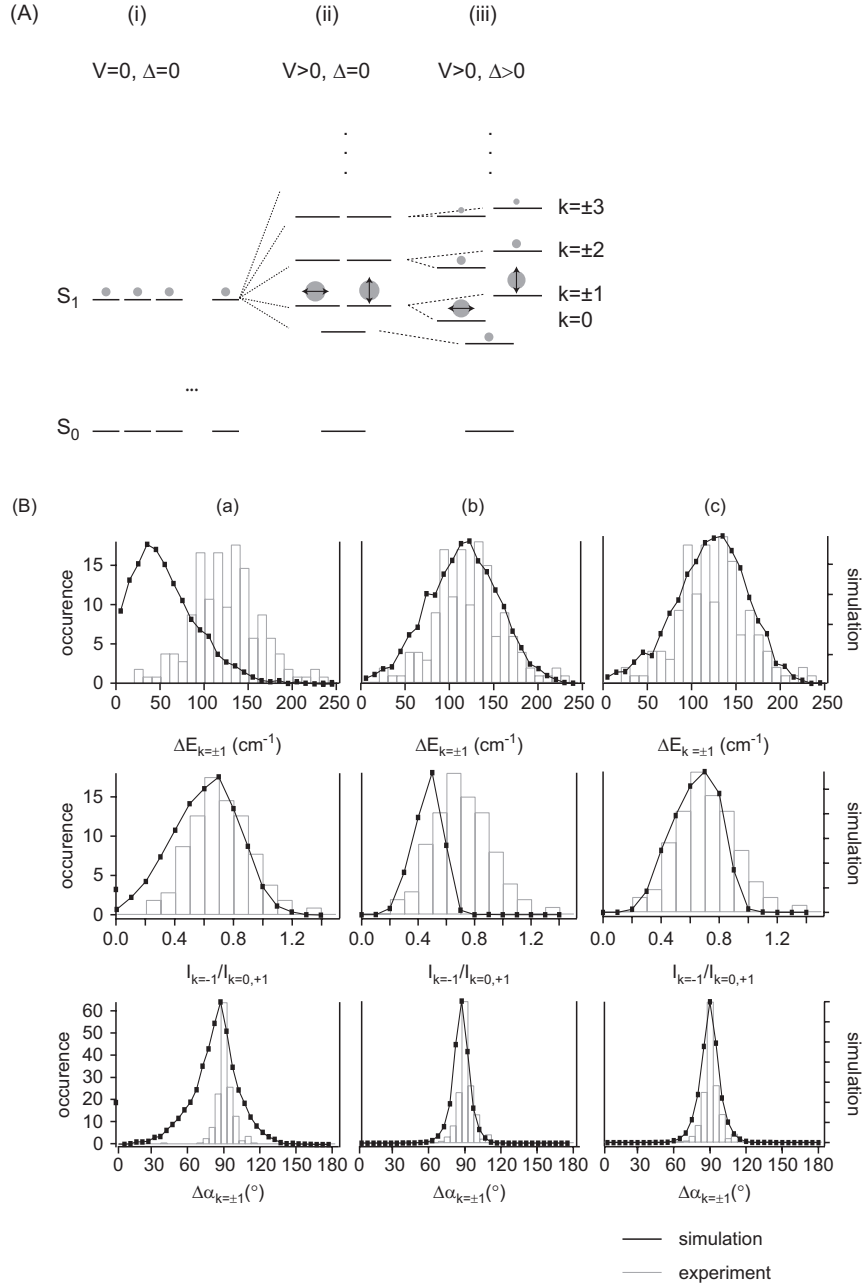


**Figure 2.4** (A) Energy diagram of the strongly coupled B850 pigment pool. (i) Energy diagram for the case of no interaction ( $V = 0$ ) between the pigments and no disorder ( $\Delta = 0$ ). (ii) Situation for the case of interacting pigments ( $V > 0$ ) but no energetic nor structural heterogeneity ( $\Delta = 0$ ). (iii) Exciton states for the case of interacting pigments ( $V > 0$ ) that feature energetic and/or structural disorder ( $\Delta > 0$ ). The size of the grey circles reflects the oscillator strength of the

we get  $V/\Delta \approx 1$  which suggests that the electronic excitations in the B850 are strongly delocalized among the pigments (Jimenez et al. 1996; Monshouwer et al. 1997; Mostovoy and Knoester 2000; Sauer et al. 1996; Pullerits et al. 1996).

If we treat the system in  $C_{18}$ -symmetry (i.e., neglecting a slight dimerization of the BChl *a* molecules) and assume as a starting point no disorder (i.e.,  $\delta E_n = \delta V_{n,m} = 0$ ), diagonalization of the Hamilton operator (Equation 2.1) leads to so-called Frenkel excitons

$$|k\rangle = \frac{1}{\sqrt{N}} \sum_{n=1}^N e^{i2\pi k \frac{n}{N}} |n\rangle, \quad (2.2)$$

which are completely delocalized over the whole ring (van Oijen et al. 1999). In contrast to the energy diagram for the uncoupled molecules (Figure 2.4A, (i)) the energy scheme for the strongly coupled system comprises a lowest excited state  $k = 0$ , eight pairwise degenerate states  $k = \pm 1 \dots \pm 4$  and  $k = \pm 5 \dots \pm 8$  and on top a single state  $k = 9$ , at least for the example of the B850 ring in LH2 from *Rps. acidophila* for which  $N = 18$  (Matsushita et al. 2001). However, only the exciton states  $k = \pm 1$ , which are circularly polarized right and left (or their orthogonally polarized linear combinations) carry significant oscillator strength. For the other states, the linear combinations of the individual transition-dipole moments cancel out, resulting in a zero net transition-dipole moment (Matsushita et al. 2001). The energy scheme for the lowest exciton states is depicted in Figure 2.4A (ii), in which the oscillator strength is indicated by the grey circles.

If energetic and structural disorders are present, the degeneracy of the exciton states is lifted and oscillator strength is redistributed from the  $k = \pm 1$  states to neighboring levels as is depicted in Figure 2.4A, (iii) (Matsushita et al. 2001; Hu et al. 2002).

The single complex spectra of the B850 ring in Figure 2.3 present a limited number of broad bands, of which the two low-energy ones are approximately orthogonally polarized (not shown). These spectral features are consistent with the Frenkel exciton model in the presence of disorder. More detailed information on the type of disorder in the B850 band can be obtained by comparing the experimental data with numerical simulations. Especially interesting are spectral features of the  $k = \pm 1$  pair of exciton states such as their energetic separation  $\Delta E_{\text{blue,red}}$ , the ratio of the integrated intensities  $I_{\text{blue}}/I_{\text{red}}$ , and the relative orientation of the transition-dipole moments  $\Delta\alpha_{\text{blue,red}}$ . Blue (red) refers to the energetically higher (lower) absorption band.

Figure 2.4B shows a comparison between the experimental distributions (histograms) and the numerical simulation (lines) for these parameters from top to bottom.

←

**Figure 2.4** (continued) transition-dipole moments and the arrows indicate their orientation. **(B)** Comparison between the experimental distributions (histograms) and numerical simulations (solid squares) of different types of disorder. The experimental data refer to the left vertical scale, whereas the simulations refer to the right vertical scale. For details see text. (Reprinted from (Hofmann et al. 2004b), with permission from Elsevier)



In the numerical simulations, three different types of disorder were compared: (a) random diagonal disorder which suggests that all disorder comes from a statistical distribution of the pigment's site energies, (b) random diagonal disorder together with correlated off-diagonal disorder which assumes a contribution to the disorder from a correlated modulation of the interaction strengths between the pigments, and (c) random and correlated diagonal disorder which assumes a contribution to the disorder from a correlated modulation of the site energies of the pigments.

The simulations show that the experimental histograms can be reproduced best by model (c), assuming a width of  $\Delta = 250 \text{ cm}^{-1}$  for the Gaussian distribution of diagonal random disorder and a cosinelike modulation of the site energies with a modulation amplitude  $E_{\text{mod}} = 180 \text{ cm}^{-1}$ . Such a modulation of the site energies could be interpreted as a modulation of the interaction of the pigments with protein residues in their binding pocket resulting from a small geometrical deviation of the circular geometry into an ellipse.

### 2.2.3 Dynamics in the B800 Band of LH2 from *Rs. molischanum*

Apart from static variations in the absorptions, temporal fluctuations of the spectra were also observed. These dynamics comprise distinct and/ or gradual changes of the spectral position of the absorption lines. The broad bands in the B850 spectrum resulting from the strongly coupled pigment manifold do not allow for detailed analysis of the dynamics. In contrast, fluctuations of the narrow absorption lines of the localized excitations in the B800 band can be followed more easily. Therefore the individual BChl *a* molecules in the B800 ring can serve as sensitive probes for changes in the pigment–pigment interaction as well as for structural dynamics of the protein residues in their vicinity.

In order to study such effects in more detail the B800 spectra are recorded in rapid succession by scanning the laser repetitively between 770 nm and 820 nm ( $12987 \text{ cm}^{-1}$ – $12195 \text{ cm}^{-1}$ ) at a scan speed of 3 nm/s ( $\approx 50 \text{ cm}^{-1}/\text{s}$ ) and by storing the resulting traces separately. Because the line width of the excitation laser is  $1 \text{ cm}^{-1}$ , this procedure allows one to follow the temporal development of the individual B800 absorptions with a time resolution of about 50 ms (i.e., the time required to scan the laser across the resonance). Spectral diffusion events that occur on a faster time scale cannot be resolved and contribute to the line width of the features observed. In the following, the registered spectra are displayed in a two-dimensional representation, where the horizontal axis corresponds to wavenumber, the vertical axis to time and the grey scale to the intensity of absorption.

#### Pigment–Pigment Interaction, Probing Pigment Coupling

An example of temporal changes in the absorption frequency of a B800 excitation is given in Figure 2.5. Part (A) shows a stack of consecutively recorded spectra of

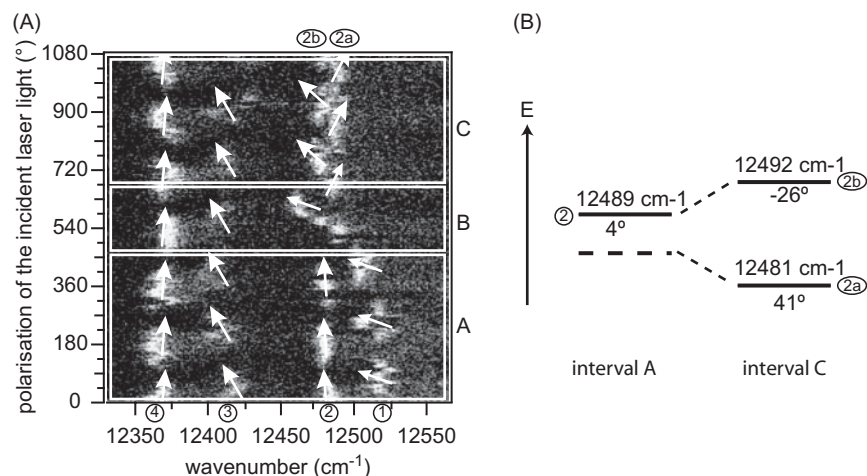


**Figure 2.5** (A) Two-dimensional representation of fluorescence-excitation spectra from an individual B800 ring. Between successive scans the polarization has been turned by  $1.8^\circ$ . The arrows show the orientation of the transition-dipole moments of the individual absorptions with respect to the laboratory frame. (B) Diagram of the absorption energies and orientations of the transition-dipole moments from some absorptions in part (A). (Reprinted with permission from (Hofmann et al. 2003a), copyright 2003 by the American Physical Society)

the B800 band of an individual LH2 complex from *Rhodospirillum molischianum*. Between two successive scans the polarization of the excitation laser has been turned by  $1.8^\circ$ . The fluorescence intensity is proportional to  $\cos^2\theta$ , where  $\theta$  defines the angle between the electric field vector and the transition-dipole moment. The arrows in Figure 2.5 visualize the orientations of the transition-dipole moments with respect to the lab frame.

The spectral pattern can be divided into three parts as indicated by the boxes. In intervals A and C all absorption lines are stable in frequency and phase angle, whereas in part B lines 1 and 2 seem to disappear and lines 2a and 2b appear. The analysis of all spectral positions and orientations of the involved transition-dipole moments leads to the conjecture that the absorption labeled 2 in interval A results from an uncoupled molecule that couples to another molecule during interval B resulting in the absorptions labeled 2a and 2b in interval C as sketched in Figure 2.5B. The fluctuations in the electronic coupling during interval B could be caused by changes in the protein backbone or rearrangements of the BChl *a* molecules in their binding pocket. Such changes alter the electrostatic environment of the individual pigments and result in a shift of their absorption energies and consequently in changes of their interaction strength.

This experiment demonstrated that the B800 pigments act as sensitive probes to monitor the pigment–pigment interaction and that the electronic coupling strength for this assembly falls into the regime of weak to intermediate coupling.

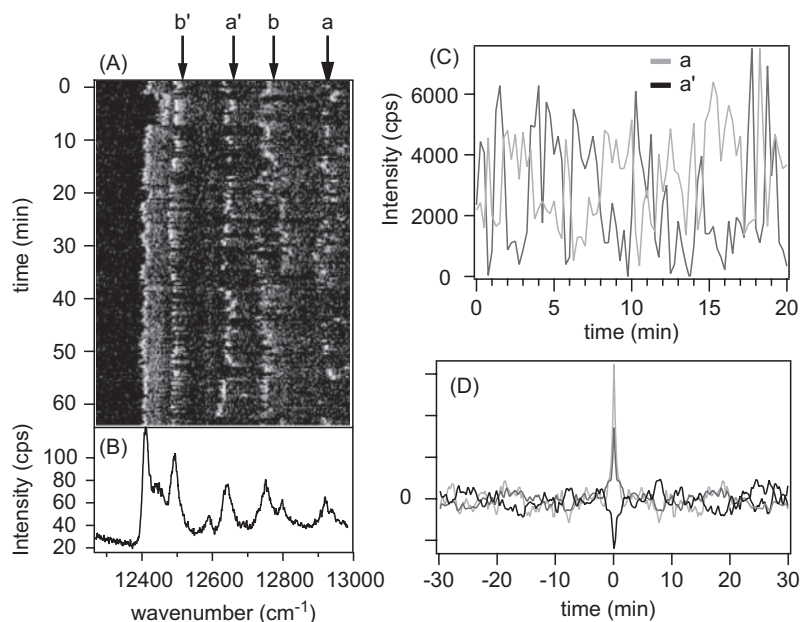


**Figure 2.6** (A) Two-dimensional representation of fluorescence-excitation spectra from an individual B800 ring. The averaged spectrum is depicted in (B). The fluorescence intensity of the two spectral features labeled a and a' is shown versus time in (C). Their autocorrelation (upper grey, a, and black, a', lines) and cross-correlation (lower black line) are shown in (D). (Reprinted from (Hofmann et al. 2003b), copyright 2003 National Academy of Sciences, U.S.A.)

### Pigment-Protein Interaction, Probing Protein Dynamics

Besides the random spectral wandering of a single absorption line, large discrete spectral jumps were observed for some complexes. These were characterized by the recurrent disappearance of one line and the appearance of one new line at a different spectral position. An example of this behavior is shown in Figure 2.6. Part (A) shows a stack of consecutively recorded spectra, and the spectrum that results when the whole sequence is averaged is shown in Figure 2.6B. If one follows the intensities of the spectral features labeled a and a' in time (Figure 2.6C), strong intensity fluctuations can be observed which turn out to be anticorrelated (Figure 2.6D). This behavior clearly shows that the two absorption lines separated by  $278\text{cm}^{-1}$  are closely associated. Similar changes in transition energy by several hundred wavenumbers have been observed for the b/b' pair of absorptions and for three pairs of absorption from another LH2 complex. Those spectral changes occur at rates of about  $10^{-2}$ – $10^{-3}\text{ s}^{-1}$ .

Looking closer at the individual absorption lines, it becomes obvious that their spectral position changes slightly from scan to scan. The energetic span that is sampled by the spectral positions of the absorption ranges from  $10$ – $100\text{cm}^{-1}$  at rates of  $0.03$ – $1\text{ s}^{-1}$ . Contributions to the line width from faster unresolved spectral dynamics of the chromophore, while the laser is scanned through the resonance, cannot be excluded. Taking the measured line widths and the scan speed of the laser into account these contributions have to occur at rates larger than  $5$ – $10\text{ s}^{-1}$  and cover at most a few wavenumbers.

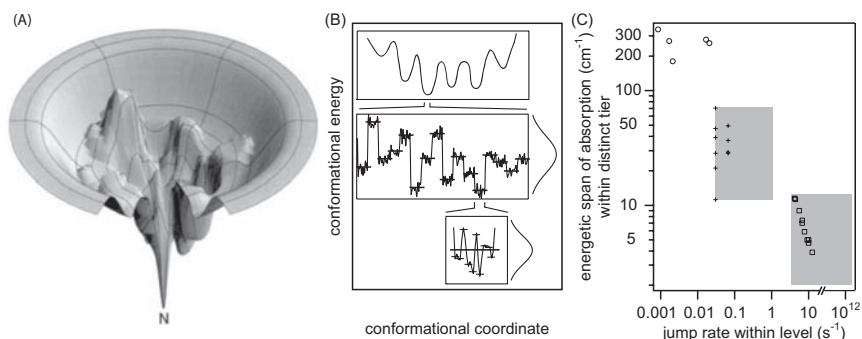


**Figure 2.7** (A) Sketch of a protein energy landscape. (Reprinted by permission from Macmillan Publishers Ltd: Nature Structural Biology, (Dill and Chan 1997), copyright 1997.) (B) Schematic sketch of three subsequent tiers of the potential energy hypersurface of a protein as a function of an arbitrary conformational coordinate. (C) Width of the spectral region that is covered by the spectral fluctuations of the chromophore within a certain time window—termed the energetic span—versus the rate of these fluctuations in the three tiers found. Circles correspond to data from large spectral jumps, crosses to data from spectral diffusion, boxes to possibly unresolved small spectral fluctuations; see text for details. (Panels (B) and (C) are reprinted from (Hofmann et al. 2003b), copyright 2003 National Academy of Sciences, U.S.A.)

How can these different types of spectral fluctuations of the chromophores be related to conformational changes of the proteins? Due to the weak interactions that stabilize the proteins and the many degrees of freedom of such a large molecule, the lowest energy state is not unique and can more appropriately be described in terms of a rugged energy landscape. This energy landscape features a large number of minima, maxima and saddle points as depicted in Figure 2.7A. Each minimum in this landscape represents a different conformational substate (CS) that corresponds to a different arrangement of the atoms.

Following the pioneering work of Frauenfelder and coworkers, a model has been put forward which proposes that this energy landscape is arranged in hierarchical tiers. On each level of the hierarchy the CS are characterized by an average energy barrier between the CS that decreases with descending hierarchy (Frauenfelder et al. 1991, 1994; Nienhau and Young 1996). A consequence of this idea is that structural fluctuations of a protein become hierarchically organized, and that biological processes are described in terms of characteristic temperature-dependent rate distributions associated with different tiers.

Consequently, the three observed time categories of spectral diffusion were interpreted as the representation of three distinct energy tiers in the energy landscape of the protein. In Figure 2.7C the observed spectral fluctuations are tentatively drawn in a way in which the different types of spectral diffusion are level with different tiers in a schematic illustration of such an energy landscape in Figure 2.7B.

The observed spectral fluctuations were ascribed to modulations of the pigment–protein interactions of the chromophore. These modulations result in changes of the excited state energies as discussed in Section 2.1. Support for this conjecture comes from several investigations. Theoretical estimations show that the site energy of a BChl *a* molecule can shift up to  $500\text{cm}^{-1}$  due to perturbations of the  $\pi$ -conjugation of the bacteriochlorin macrocycle (Gudowska-Novak et al. 1990).

Site-directed mutagenesis has shown that fluctuations in the strength of a hydrogen bond between a protein residue in the binding pocket and the C<sub>2</sub> acetyl group of the BChl *a* molecule lead to spectral shifts of 100–200 cm<sup>-1</sup> of the B800 ensemble absorption (Gall et al. 1997). And by spectral hole-burning spectroscopy it has been found that relative distance changes of  $\Delta R/R \approx 10^{-4} - 10^{-2}$  are already sufficient to result in spectral shifts of 1–100 cm<sup>-1</sup> for the B800 absorptions (Zazubovich et al. 2002).

### **2.2.4 Outlook of Light-Harvesting Complex Spectroscopy**

These experiments demonstrate that pigment–protein complexes are convenient model systems to probe protein dynamics and to reveal the organization of the potential energy landscape of a protein. An advantage is certainly that no biological mutation and/or chemical processing is needed to equip these complexes with sensitive probes for protein dynamics. The low-temperature approach is compulsory for the detection of the small spectral fluctuations and also to slow down the dynamics to time scales that are accessible with today’s experimental equipment.

Apart from various studies of individual LH2 complexes, also LH1 complexes have been studied (Ketelaars et al. 2002; Gerken 2003a, b). In the strongly coupled B870 pigment pool structural disorder plays a much larger role than in the B850 ring, which blurs the clear spectral characteristics of the undisturbed Frenkel exciton manifold. However, comparing spectra of individual LH1 complexes with numerical simulations that take high-resolution AFM images as a starting point could clarify the role of a small protein, PufX, mentioned earlier (Section 2.1).

## **2.3 From Structure to Dynamics**

The combination of physical trapping with single-molecule fluorescence has the potential to overcome two of the most serious obstacles in today’s single-molecule measurements, photobleaching and limitations in time-resolution. As discussed in the introduction, cryogenic conditions reduce the rate of photo-induced reactions, and provide long periods of time to investigate the structures of frozen configurations with a high signal-to-noise ratio. Repeating many freeze–thaw cycles of a single biomolecule, while optically observing it during the cold periods, one would obtain a series of snapshots of the observed quantities, such as orientations of transition moments, fluorescence lifetimes, distances within FRET pairs, and so on. The time resolution of such a movie would only be limited by the cooling and heating rates. The volume of the heated sample should therefore be chosen as small as possible. One could imagine reducing sample sizes to dimensions as tiny as a few tens of nm, which are still significantly larger than the size of many protein molecules. However, we conservatively consider a volume of a few  $\mu\text{m}$  in size, such as

the focal region of an optical microscope. With a size of a few  $\mu\text{m}$ , cooling rates as high as  $1\text{ K}/\mu\text{s}$  can be achieved. As an additional benefit, such extreme cooling rates directly quench liquid water into amorphous ice, thus minimizing stress and damage to biomolecules. Incidentally, we point out that single-molecule microscopy is the only method with the potential to combine fluorescence with ultrafast temperature cycles (including fast cooling as well as fast heating). A single molecule can always be placed close to the warmest point of a temperature distribution, where temperature is well defined, and where the gradient vanishes. On the contrary, for an ensemble of molecules in the focal spot, the local temperatures would be broadly distributed. Thermal and temporal heterogeneity would make the ensemble version of the method much less attractive.

Temperature jumps of a few Kelvin can be induced by short laser pulses: DNA, RNA, polypeptides, or proteins were unfolded at room temperature by such moderate temperature changes (Phillips et al. 1995; Ballew et al. 1996; Munoz et al. 1997; Callender et al. 1998; Gruebele 1999; Eaton et al. 2000; Ansari et al. 2001; Rabl et al. 2002; Dimitriadis et al. 2004; Chung et al. 2005). In these experiments, the heating rate, being limited by pulse duration only, can be very high. Cooling, however, is limited by heat diffusion out of the large heated volume. It is usually very slow. In the scheme explored here, the sample is placed in a cold cryostat. We select a diffraction-limited hot spot by locally heating the sample up to room temperature with a continuous-wave near-infrared laser focused on an absorbing metal film. The laser power can be switched on and off in nanoseconds. As soon as the heating laser is switched off, the heated volume quickly reverts to the surrounding cryostat temperature. We can repeat the temperature cycle between a low and a high value, as schematically presented in Figure 2.8. With a diffraction-limited hot spot about  $1\text{ }\mu\text{m}$  in size, the expected heating and cooling times are on the order of a microsecond.

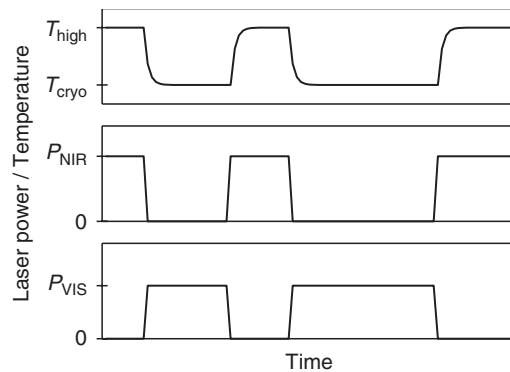


**Figure 2.8** Scheme of the proposed thermal cycles between cryogenic and room temperatures. A focused near-infrared (NIR) laser beam with power  $P_{\text{NIR}}$  (middle graph) rapidly raises the local focus temperature to  $T_{\text{high}}$  (top graph). The moment the NIR laser is switched off, the temperature quickly drops back to the surrounding temperature  $T_{\text{cryo}}$ . In the proposed method, a visible laser (bottom graph) with power  $P_{\text{VIS}}$  will excite fluorescent labels during the cold periods at  $T_{\text{cryo}}$  exclusively, to prevent photobleaching. (Reprinted from (Zondervan et al. 2006), with permission from the Biophysical Society)

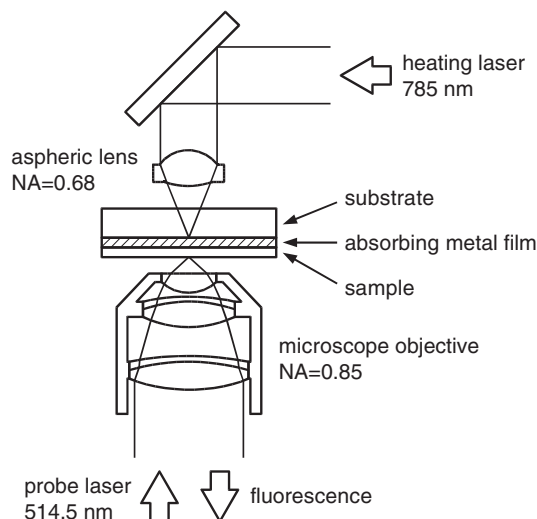


**Figure 2.9** Scheme of the optical paths around the sample plate in the cryostat. The sample plate is a glass substrate (thickness 0.17 mm), coated with a thin, absorbing metal film (thickness 50 nm), itself covered with the fluorescent solution layer. Fluorescence is excited (514.5 nm) and collected by a custom-made ten-lens objective (NA = 0.85, represented here by a simplified five-lens scheme) beneath the sample. Above it, a mirror at 45 degrees and an aspheric singlet lens (NA = 0.68) direct and focus the NIR beam (785 nm) onto the metal film right above the visible focus. (Reprinted from (Zondervan et al. 2006), with permission from the Biophysical Society)

In the present section, we briefly describe recent experiments, which have demonstrated the feasibility of fast temperature cycles in the focus of a microscope (Zondervan et al. 2006). We achieved repeated temperature cycles between 130 K and ambient temperature. The optical setup, schematically shown in Figure 2.9, is built around a variable-temperature confocal microscope with single-molecule sensitivity that is placed in a cryostat. The sample, which can be moved in three dimensions by piezo-driven inchworm motors, is excited through a high-quality microscope objective. This objective, which also collects the sample fluorescence, is placed below the sample. An infrared path is added above the sample to drive the fast thermal cycles. The heating infrared beam (785 nm) is focused by an aspheric singlet lens, and its power can be modulated at a high rate by an acousto-optical modulator. In our first demonstration experiments, the sample was a fluorophore-doped glycerol film spin-coated on an absorbing 50 nm thick metal layer.

We chose glycerol as a solvent because of the steep dependence of its physical properties on temperature. Between room temperature and the glass transition temperature (about 190 K), its viscosity varies by 10 orders of magnitude. We measured the local temperature through the viscosity-dependent rotational diffusion of fluorescent molecules. For very short rotational diffusion times, we used steady-state fluorescence anisotropy. At the lowest temperatures (200 to 240 K), we measured the fluctuations of the polarized fluorescence of small numbers of molecules (by fluorescence anisotropy correlation spectroscopy, FACS, a method related to FCS).

Between 240 and 280 K, we could deduce temperature from the fluorescence of the dye, rhodamine 6G. Owing to photoblinking processes, its fluorescence intensity continuously varies in this range (Zondervan et al. 2003). Armed with those various calibration methods, we could image the spatial temperature profile around the focused heating spot, as can be seen in Figure 2.10. At a cryostat temperature of 130 K, a few tens of mW were sufficient to exceed room temperature at the center of the spot: The heating efficiency was 30 K/mW with a 50-nm NiCr film, as can be seen in Figure 2.11, which confirms the expected linear dependence of the temperature on the power of the heating beam. The dark central spot in the rightmost panel of Figure 2.10 indicates the onset of fast molecular reorientation during the fluorescence lifetime, a signature of the low viscosity of the room-temperature phase. The anisotropy increase at lower power and/or larger distances from the center is exclusively due to photoblinking kinetics. The diameter of the hot spot deduced from Figure 2.10 is approximately  $5\ \mu\text{m}$ . It corresponds to an enormous temperature gradient of about  $50\ \text{K}/\mu\text{m}$ , a prerequisite for fast cooling.

In order to demonstrate that heating and cooling times indeed are as short as microseconds, we investigated the thermal kinetics of the hot spot using fluorescence anisotropy of rhodamine 6G in glycerol. To achieve a satisfactory signal/noise ratio with a time resolution of  $1\ \mu\text{s}$ , we periodically chopped the NIR intensity at 2.5 kHz, and averaged the heating and cooling transients of many bright and dark periods with photon-counting electronics. We then converted the anisotropy plots into temperature traces, neglecting slow photoblinking effects and considering only rotational diffusion. Figure 2.12 shows the temperature responses during heating

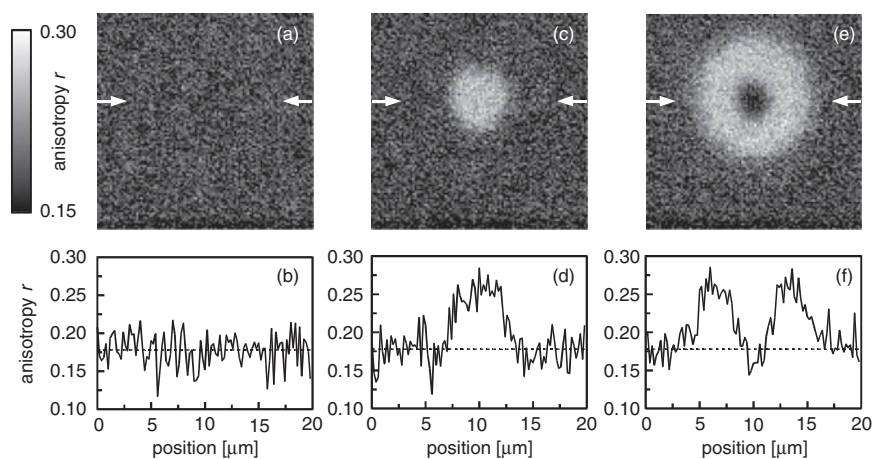


**Figure 2.10** Anisotropy images: Polarized fluorescence images are recorded in the region around the infrared focus. Graphs (b), (d), and (f) show cross-sections of images (a), (c), and (e) through the center of the heating spot. At low power (5 mW), image (c) shows a high-anisotropy spot, arising from polarization-dependent photoblinking. At the highest power (8.5 mW), the anisotropy decreases in the center because of orientational diffusion in the hot spot. This feature shows that room temperature has been reached. From a previous temperature calibration, we deduced the temperature in the center, 280 K for (c) and 335 K for (e). (Reprinted from (Zondervan et al. 2006), with permission from the Biophysical Society)



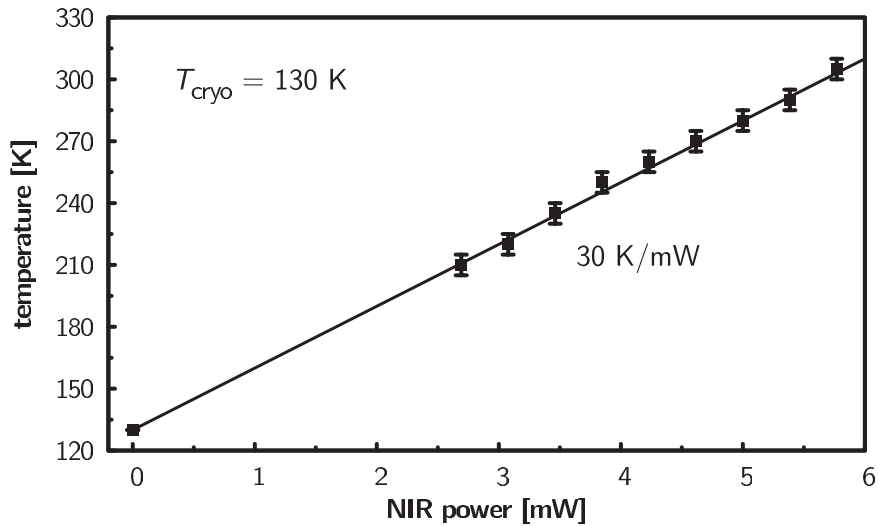


**Figure 2.11** Variation with heating power of the temperature at the center of the hot spot, as deduced from an analysis of fluorescence anisotropy. The temperature scales linearly with applied power with a slope of 30 K/mW (solid line). The accuracy of the calibration is  $\pm 5$  K, indicated by error bars. (Adapted from (Zondervan et al. 2006))

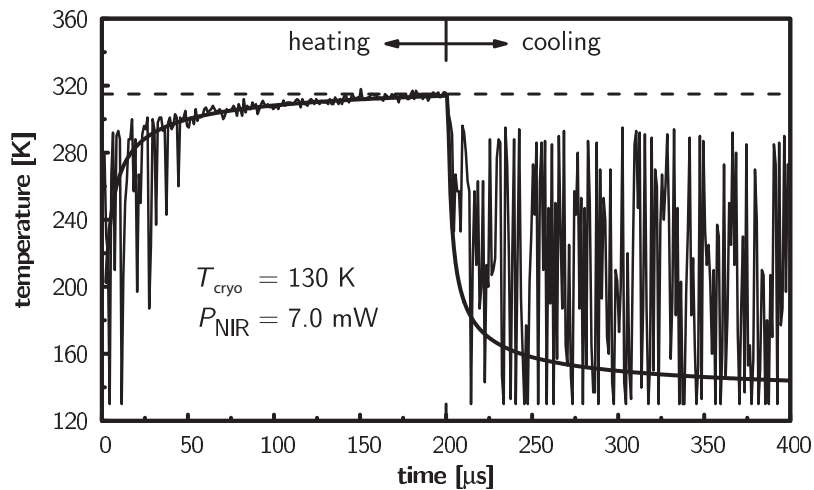


**Figure 2.12** Temperature response during heating (first 200  $\mu$ s) and cooling (second 200  $\mu$ s) for an infrared heating power of 7.0 mW. The noisy trace is derived from a fluorescence anisotropy trace in the center of the spot, translated into temperatures by means of a previous temperature calibration. The time resolution is 1  $\mu$ s. The smooth line is a theoretical model of the temperature response with the heat equation. The fit of the data is excellent in the high-temperature part of the transient, although no parameter was adjusted. The half-change time is about 3.5  $\mu$ s. (Reprinted from (Zondervan et al. 2006), with permission from the Biophysical Society)

and cooling for 7.0 mW, calculated from the anisotropy data. The range of our local thermometer is limited by rotational diffusion. Below 280 K, the temperature cannot be determined and the plots are very noisy. Between 280 and 300 K the accuracy is low because of the large uncertainty in  $r_0$ . Above 300 K rotational diffusion is fast enough, and the temperature determination is very accurate, to within a few K. The last part of the heating transient as well as the beginning of the cooling transient are in excellent agreement with a theoretical model based on the heat equation, without adjustable parameters. The first part of the cooling trace confirms the calculated cooling time of 3–4  $\mu$ s.

These initial experiments establish that temperature jumps of hundreds of Kelvin are possible within a few microseconds, for cooling as well as for heating. Such cooling rates are sufficient to supercool pure water, and a fortiori water with cryoprotectants such as glycerol or trehalose (Angell and Choi 1986; Sutton 1991; Branca et al. 1997). This ability to supercool water is of great experimental interest, because it opens the possibility to reversibly cycle large biomolecules such as nucleic acids and proteins between high and low temperatures, without damage from expanding ice crystals. A further appealing feature of the thermal cycles is that the higher temperature is adjustable. By independently varying the higher temperature of the cycle and the dwell time in that warmer bath, one could explore the potential energy landscape. Of particular interest would be the determination of the most favorable pathways between conformational substates. In a next step, we intend to apply the temperature cycles to studies of the dynamics of single molecules at room temperature. The dynamical process of interest will be decomposed into a series of freeze–measure–thaw evolution cycles, where the duration of the steps will be variable (see Figure 2.8). Such temperature-cycle experiments seem particularly promising for the single-molecule analysis of protein folding, a process extending over many time scales (Dill and Chan 1997). By following repeated folding events of one and the same single protein, one could study preferred folding pathways and possible long-term memory effects.

## 2.4 Conclusions

Cryogenic conditions are already in widespread use for structural analysis, in X-ray crystallography as well as in high-resolution electron microscopy. In that case the main drive to resort to low temperatures is the dramatic improvement in the photoresistance of biological structures. The main message of this chapter is that low temperatures present an additional benefit in the study of dynamics. This conclusion clearly applies to electronic dynamical processes, which are mainly determined by structure, and for which a low-temperature analysis forms a good basis for the understanding of room-temperature dynamics. Cryogenic conditions have the advantage of providing high resolution and a natural hierarchy of temperature-activated barriers, as was illustrated by the spectroscopy of individual light-harvesting complexes.

More generally, single-molecule methods bring with them the unique possibility to control temperature in the molecular environment with microsecond time resolution. Such short cooling times are out of reach for large ensembles of molecules. In conventional freeze–quench experiments, the cooling step can at best be performed once, usually by projection of micrometer-sized droplets onto a cold substrate. The optical selection of a small volume of sample in a cold environment offers the possibility of repeated and fast temperature cycles. One could thus take advantage of the improved photostability of the chromophores at low temperatures while using temperature as a control parameter to probe the height of activation barriers and without being limited in temporal resolution by the requirements of photon counting statistics. We have reported some preliminary results in this direction by demonstrating controlled and reproducible temperature cycles of several hundreds of Kelvins on a timescale of microseconds, and we hope that this method can be developed further and applied to the dynamics of protein folding in the near future.

## References

- C. A. Angell, Y. Choi: *J. Microsc.- Oxf.* **141**, 251–261 (1986)  
A. Ansari, S. V. Kuznetsov, Y. Q. Shen: *Proc. Natl. Acad. Sci. U. S. A.* **98**, 7771–7776 (2001)  
R. Austin, R. Beeson, L. Eisenstein, et al.: *Biochemistry* **14**, 5355–5373 (1975)  
S. Bahatyrova, R. N. Frese, C. A. Siebert, et al.: *Nature* **430**, 1058–1062 (2004)  
R. M. Ballew, J. Sabelko, M. Gruebele: *Proc. Natl. Acad. Sci. U. S. A.* **93**, 5759–5764 (1996)  
S. Berciaud, L. Cognet, G. A. Blab, B. Lounis: *Phys. Rev. Lett.* **93**, 257402 (2004)  
S. Berciaud, L. Cognet, P. Tamarat, B. Lounis: *Nano Lett.* **5**, 515–518 (2005)  
G. Bokinsky, D. Rueda, V. K. Misra, et al.: *Proc. Natl. Acad. Sci. U. S. A.* **100**, 9302–9307 (2003)  
M. Börsch, P. Turina, C. Eggeling, et al.: *FEBS Lett.* **437**, 251–254 (1998)  
M. Börsch, M. Diez, B. Zimmermann, et al.: *FEBS Lett.* **527**, 147–152 (2002)  
D. Boyer, P. Tamarat, A. Maali, et al.: *Science* **297**, 1160–1164 (2002)  
C. Branca, S. Magazu, G. Maisano, P. Migliardo: *J. Chem. Phys.* **111**, 281–287 (1999)  
R. H. Callender, R. B. Dyer, R. Gilmanshin, W. H. Woodruff: *Annu. Rev. Phys. Chem.* **49**, 173–202 (1998)  
M. Chachisvilis, O. Kühn, T. Pullerits, V. Sundström: *J. Phys. Chem. B* **101**, 7275–7283 (1997)  
T. Christ, F. Kulzer, P. Bordat, T. Basché: *Angew. Chem.-Int. Edit.* **40**, 4192–4195 (2001)  
H. S. Chung, M. Khalil, A. W. Smith, et al.: *Proc. Natl. Acad. Sci. U. S. A.* **102**, 612–617 (2005)  
M. Cory, M. Zerner, X. Hu, K. Schulten: *J. Phys. Chem. B* **102**, 7640–7650 (1998)  
M. Dahan, S. Levi, C. Luccardini, et al.: *Science* **302**, 442–445 (2003)  
C. de Caro, R. W. Visschers, R. van Grondelle, S. Völker: *J. Phys. Chem.* **98**, 10584–10590 (1994)  
S. E. Dempster, S. J. Jang, R. J. Silbey: *J. Chem. Phys.* **114**, 10015–10023 (2001)  
A. A. Deniz, T. A. Laurence, G. S. Beligere, et al.: *Proc. Natl. Acad. Sci. U. S. A.* **97**, 5179–5184 (2000)  
A. A. Deniz, T. A. Laurence, M. Dahan, et al.: *Annu. Rev. Phys. Chem.* **52**, 233–257 (2001)  
U. De Rossi, S. Dähne, U. Gomez, H. Port: *Chem. Phys. Lett.* **287**, 395–402 (1998)  
M. Diez, B. Zimmermann, M. Börsch, et al.: *Nat. Struct. Mol. Biol.* **11**, 135–141 (2004)  
K. A. Dill, H. S. Chan: *Nat. Struct. Biol.* **4**, 10–19 (1997)  
G. Dimitriadis, A. Drysdale, J. K. Myers, et al.: *Proc. Natl. Acad. Sci. U. S. A.* **101**, 3809–3814 (2004)  
W. A. Eaton, V. Munoz, S. J. Hagen, et al.: *Annu. Rev. Biophys. Biomol. Struct.* **29**, 327–359 (2000)

- L. Edman, R. Rigler: Proc. Natl. Acad. Sci. U. S. A. **97**, 8266–8271 (2000)
- L. Edman, Z. Földes-Papp, S. Wennmalm, R. Rigler: Chem. Phys. **247**, 11–22 (1999)
- C. Eggeling, A. Volkmer, C. A. M. Seidel: ChemPhysChem **6**, 791–804 (2005)
- H. Fidder, J. Knoester, D. A. Wiersma: J. Chem. Phys. **95**, 7880–7890 (1991)
- F. Francia, M. Dezi, A. Rebecchi, et al.: Biochemistry **43**, 14199–14210 (2004)
- H. Frauenfelder, S. Sligar, P. Wolynes: Science **254**, 1598–1603 (1991)
- H. Frauenfelder, G. Nienhaus, R. Young: Relaxation and Disorder in Proteins in: *Disorder effects in relaxational processes*, edited by R. Richert (Springer Verlag Berlin, Berlin, 1994) pp. 591–614
- T. Funatsu, Y. Harada, M. Tokunaga, et al.: Nature **374**, 555–559 (1995)
- A. Gall, G. Fowler, C. Hunter, B. Robert: Biochemistry **36**, 16282–16287 (1997)
- E. Garman: Curr. Opin. Struct. Biol. **13**, 545–551 (2003)
- U. Gerken, D. Lupo, C. Tietz, et al.: Biochemistry **42**, 10354–10360 (2003a)
- U. Gerken, F. Jelezko, B. Götze, et al.: J. Phys. Chem. B **107**, 338–343 (2003b)
- L. Germeroth, F. Lottspeich, B. Robert, H. Michel: Biochemistry **32**, 5615–5621 (1993)
- P. M. Goodwin, H. Cai, J. H. Jett, et al.: Nucleosides Nucleotides **16**, 543–550 (1997)
- M. Gruebele: Annu. Rev. Phys. Chem. **50**, 485–516 (1999)
- E. Gudowska-Novak, M. Newton, J. Fajer: J. Phys. Chem. **94**, 5795–5801 (1990)
- F. Güttler, T. Irrgartinger, T. Plakhotnik, et al.: Chem. Phys. Lett. **217**, 393–397 (1994)
- T. Ha, A. Y. Ting, J. Liang, et al.: Proc. Natl. Acad. Sci. USA **96**, 893–898 (1999)
- B. Halle: Proc. Natl. Acad. Sci. U. S. A. **101**, 4793–4798 (2004)
- S. T. Hess, S. H. Huang, A. A. Heikal, W. W. Webb: Biochemistry **41**, 697–705 (2002)
- C. Hofmann, M. Ketelaars, M. Matsushita, et al.: Phys. Rev. Lett. **90**, 13004 (2003a)
- C. Hofmann, T. J. Aartsma, H. Michel, J. Köhler: Proc. Natl. Acad. Sci. U. S. A. **100**, 15534–15538 (2003)
- C. Hofmann, T. Aartsma, H. Michel, J. Köhler: New J. Phys. **6**, 8 (2004a)
- C. Hofmann, T. J. Aartsma, J. Köhler: Chem. Phys. Lett. **395**, 373–378 (2004b)
- S. Hohng, T. Ha: J. Am. Chem. Soc. **126**, 1324–1325 (2004)
- X. C. Hu, A. Damjanovic, T. Ritz, K. Schulten: Proc. Natl. Acad. Sci. U. S. A. **95**, 5935–5941 (1998)
- X. C. Hu, T. Ritz, A. Damjanovic, et al.: Q. Rev. Biophys. **35**, 1–62 (2002)
- R. Jimenez, S. N. Dikshit, S. E. Bradforth, G. R. Fleming: J. Phys. Chem. **100**, 6825–6834 (1996)
- G. Juzeliunas, P. Reineker: J. Chem. Phys. **107**, 9801–9806 (1997)
- L. C. Kapitein, E. J. G. Peterman, B. H. Kwok, et al.: Nature **435**, 114–118 (2005)
- A. M. Kelley, X. Michalet, S. Weiss: Science **292**, 1671–1672 (2001)
- J. T. M. Kennis, A. M. Streltsov, H. Permentier, et al.: J. Phys. Chem. B **101**, 8369–8374 (1997)
- M. Ketelaars, A. M. van Oijen, M. Matsushita, et al.: Biophys. J. **80**, 1591–1603 (2001)
- M. Ketelaars, C. Hofmann, J. Köhler, et al.: Biophys. J. **83**, 1701–1715 (2002)
- K. Kitamura, M. Tokunaga, A. H. Iwane, T. Yanagida: Nature **397**, 129–134 (1999)
- J. Koepke, X. C. Hu, C. Muenke, et al.: Structure **4**, 581–597 (1996)
- W. Kühlbrandt: Nature **374**, 497–498 (1995)
- C. Kural, H. Kim, S. Syed, et al.: Science **308**, 1469–1472 (2005)
- C. J. Law, A. W. Roszak, J. Southall, et al.: Mol. Membr. Biol. **21**, 183–191 (2004)
- K. Lindfors, T. Kalkbrenner, P. Stoller, V. Sandoghdar: Phys. Rev. Lett. **93**, 037401 (2004)
- E. A. Lipman, B. Schuler, O. Bakajin, W. A. Eaton: Science **301**, 1233–1235 (2003)
- H. P. Lu, L. Y. Xun, X. S. Xie: Science **282**, 1877–1882 (1998)
- M. Matsushita, M. Ketelaars, A. M. van Oijen, et al.: Biophys. J. **80**, 1604–1614 (2001)
- G. McDermott, S. M. Prince, A. A. Freer, et al.: Nature **374**, 517–521 (1995)
- M. A. Medina, P. Schwille: Bioessays **24**, 758–764 (2002)
- X. Michalet, S. Weiss: C. R. Phys. **3**, 619–644 (2002)
- X. Michalet, F. F. Pinaud, L. A. Bentolila, et al.: Science **307**, 538–544 (2005)
- W. E. Moerner (ed.): *Persistent Spectral Hole-Burning: Science and Applications* (Springer, Berlin, 1989)
- W. E. Moerner: J. Phys. Chem. B **106**, 910–927 (2002)

- W. E. Moerner, D. P. Fromm: *Rev. Sci. Instrum.* **74**, 3597–3619 (2003)
- W. E. Moerner, L. Kador: *Phys. Rev. Lett.* **62**, 2535–2538 (1989)
- K. Moffat, R. Henderson: *Curr. Opin. Struct. Biol.* **5**, 656–663 (1995)
- R. Monshouwer, M. Abrahamsson, F. van Mourik, R. van Grondelle: *J. Phys. Chem. B* **101**, 7241–7248 (1997)
- M. V. Mostovoy, J. Knoester: *J. Phys. Chem. B* **104**, 12355–12364 (2000)
- V. Munoz, P. A. Thompson, J. Hofrichter, W. A. Eaton: *Nature* **390**, 196–199 (1997)
- S. M. Nie, R. N. Zare: *Annu. Rev. Biophys. Biomolec. Struct.* **26**, 567–596 (1997)
- G. Nienhaus, R. Young: Protein Dynamics in: *Encyclopedia of Applied Physics Volume 15: Power Electronics to Raman Scattering*, edited by G. Trigg, E. Immergut (Wiley VCH, New York, 1996) vol. 15 of *Encyclopedia of Applied Physics* pp. 163–184
- M. Nishiyama, E. Muto, Y. Inoue, et al.: *Nat. Cell Biol.* **3**, 425–428 (2001)
- M. Nishiyama, H. Higuchi, T. Yanagida: *Nat. Cell Biol.* **4**, 790–797 (2002)
- M. Orrit, J. Bernard: *Phys. Rev. Lett.* **65**, 2716–2719 (1990)
- M. Z. Papiz, S. M. Prince, T. Howard, et al.: *J. Mol. Biol.* **326**, 1523–1538 (2003)
- E. J. G. Peterman, H. Sosa, L. S. B. Goldstein, W. E. Moerner: *Biophys. J.* **81**, 2851–2863 (2001)
- E. J. G. Peterman, H. Sosa, W. E. Moerner: *Annu. Rev. Phys. Chem.* **55**, 79–96 (2004)
- C. M. Phillips, Y. Mizutani, R. M. Hochstrasser: *Proc. Natl. Acad. Sci. U. S. A.* **92**, 7292–7296 (1995)
- T. Pullerits, M. Chachisvilis, V. Sundström: *J. Phys. Chem.* **100**, 10787–10792 (1996)
- C. R. Rabl, S. R. Martin, E. Neumann, P. M. Bayley: *Biophys. Chem.* **101**, 553–564 (2002)
- E. Rhoades, M. Cohen, B. Schuler, G. Haran: *J. Am. Chem. Soc.* **126**, 14686–14687 (2004)
- R. Rigler, M. Orrit, T. Basché (eds.): *Single Molecule Spectroscopy: Nobel Conference Lectures* Springer Series in Chemical Physics (Springer, Berlin, 2001)
- D. Rueda, G. Bokinsky, M. M. Rhodes, et al.: *Proc. Natl. Acad. Sci. U. S. A.* **101**, 10066–10071 (2004)
- Y. Sambongi, Y. Iko, M. Tanabe, et al.: *Science* **286**, 1722–1724 (1999)
- K. Sauer, R. J. Cogdell, S. M. Prince, et al.: *Photochem. Photobiol.* **64**, 564–576 (1996)
- M. Sauer, B. Angerer, K. T. Han, C. Zander: *PCCP Phys. Chem. Chem. Phys.* **1**, 2471–2477 (1999)
- I. G. Scheblykin, O. Y. Sliusarenko, L. S. Lepnev, et al.: *J. Phys. Chem. B* **104**, 10949–10951 (2000)
- S. Scheuring, J. N. Sturgis, V. Prima, et al.: *Proc. Natl. Acad. Sci. U. S. A.* **101**, 11293–11297 (2004)
- B. Schuler, E. A. Lipman, W. A. Eaton: *Nature* **419**, 743–747 (2002)
- H. Sosa, E. J. G. Peterman, W. E. Moerner, L. S. B. Goldstein: *Nat. Struct. Biol.* **8**, 540–544 (2001)
- J. Stephan, K. Dorre, S. Brakmann, et al.: *J. Biotechnol.* **86**, 255–267 (2001)
- L. Stryer: *Biochemistry* (W. H. Freeman and Company, New York, 2000) 4th edn.
- V. Sundström, T. Pullerits, R. van Grondelle: *J. Phys. Chem. B* **103**, 2327–2346 (1999)
- R. L. Sutton: *J. Chem. Soc. Faraday Trans.* **87**, 101–105 (1991)
- P. Tamarat, A. Maali, B. Lounis, M. Orrit: *J. Phys. Chem. A* **104**, 1–16 (2000)
- P. Tinnefeld, M. Sauer: *Angew. Chem.-Int. Edit.* **44**, 2642–2671 (2005)
- M. Ueda, Y. Sako, T. Tanaka, et al.: *Science* **294**, 864–867 (2001)
- M. Vacha, M. Saeki, O. Isobe, et al.: *J. Chem. Phys.* **115**, 4973–4976 (2001)
- R. D. Vale, T. Funatsu, D. W. Pierce, et al.: *Nature* **380**, 451–453 (1996)
- H. van Amerongen, L. Valkunas, R. van Grondelle: *Photosynthetic excitons* (World Scientific Publishing Co. Pte. Ltd., Singapore, New Jersey, London, Hong Kong, 2000)
- R. van Grondelle, J. P. Dekker, T. Gillbro, V. Sundström: *Biochim. Biophys. Acta-Bioenerg.* **1187**, 1–65 (1994)
- M. van Heel, B. Gowen, R. Matadeen, et al.: *Q. Rev. Biophys.* **33**, 307–369 (2000)
- A. M. van Oijen, M. Ketelaars, J. Köhler, et al.: *Science* **285**, 400–402 (1999)
- A. M. van Oijen, P. C. Blainey, D. J. Crampton, et al.: *Science* **301**, 1235–1238 (2003)
- V. Vukojevic, A. Pramanik, T. Yakovleva, et al.: *Cell. Mol. Life Sci.* **62**, 535–550 (2005)
- S. I. E. Vulto, J. T. M. Kennis, A. M. Streltsov, et al.: *J. Phys. Chem. B* **103**, 878–883 (1999)
- T. Walz, S. J. Jamieson, C. M. Bowers, et al.: *J. Mol. Biol.* **282**, 833–845 (1998)
- S. Weiss: *Science* **283**, 1676–1683 (1999)

- S. Weiss: *Nat. Struct. Biol.* **7**, 724–729 (2000)
- M. Wendling, F. van Mourik, I. H. M. van Stokkum, et al.: *Biophys. J.* **84**, 440–449 (2003)
- H. M. Wu, S. Savikhin, N. R. S. Reddy, et al.: *J. Phys. Chem.* **100**, 12022–12033 (1996)
- X. S. Xie, J. K. Trautman: *Annu. Rev. Phys. Chem.* **49**, 441–480 (1998)
- H. Yang, G. B. Luo, P. Karnchanaphanurach, et al.: *Science* **302**, 262–266 (2003)
- A. Yildiz, J. N. Forkey, S. A. McKinney, et al.: *Science* **300**, 2061–2065 (2003)
- A. Yildiz, M. Tomishige, R. D. Vale, P. R. Selvin: *Science* **303**, 676–678 (2004)
- C. Zander, J. Enderlein, R. A. Keller (eds.): *Single Molecule Detection in Solution* (Wiley–VCH, Berlin, 2002)
- V. Zazubovich, R. Jankowiak, G. Small: *J. Phys. Chem. B* **106**, 6802–6814 (2002)
- X. W. Zhuang, L. E. Bartley, H. P. Babcock, et al.: *Science* **288**, 2048–2052 (2000)
- X. W. Zhuang, H. Kim, M. J. B. Pereira, et al.: *Science* **296**, 1473–1476 (2002)
- R. Zondervan, F. Kulzer, S. B. Orlinskii, M. Orrit: *J. Phys. Chem. A* **107**, 6770–6776 (2003)
- R. Zondervan, F. Kulzer, M. A. Kol'chenko, M. Orrit: *J. Phys. Chem. A* **108**, 1657–1665 (2004)
- R. Zondervan, F. Kulzer, H. van der Meer, et al.: *Biophys. J.* **90**, 2958–2969 (2006)

# Chapter 3

## Quantum Optics: Colloidal Fluorescent Semiconductor Nanocrystals (Quantum Dots) in Single-Molecule Detection and Imaging

Laurent A. Bentolila(✉), Xavier Michalet, and Shimon Weiss

3.1	Introduction.....	54
3.2	Quantum Dots: Semiconductor Systems of Reduced Dimensionality .....	56
3.2.1	Energy Bandgap.....	56
3.2.2	Exciton States, Quantum Confinement, and Quantization of Energy .....	57
3.2.3	Optical Properties of Quantum Dots.....	58
3.3	Quantum Dots: From Physical Chemistry to Bioimaging .....	60
3.3.1	Colloidal Nanocrystal Synthesis.....	60
3.3.2	Quantum Dots Bioconjugates for Imaging .....	61
3.4	Quantum Dot Imaging: From Ensemble to Single-Molecule Sensitivity.....	63
3.4.1	Techniques for Single-Molecule Fluorescence Visualization.....	64
3.4.2	Single-Molecule Sensitivity Requirements.....	65
3.5	Quantum Dots: Applications in Single-Molecule Optical Imaging.....	71
3.5.1	Quantum Dot Imaging of Protein Conformational Changes .....	71
3.5.2	Quantum Dot Tracking of Cell-Surface Membrane Receptors .....	73
3.6	Future Directions .....	74
3.7	Concluding Remarks.....	75
	References.....	75

**Abstract** Coming from the electronic material sciences, semiconductor nanocrystals, called quantum dots (QDs), have emerged as new powerful fluorescent probes for in vitro and in vivo biological labeling and single-molecule experiments. QDs possess several unique optical properties that make them very attractive over conventional fluorescent dyes and genetically encoded proteins technologies. They have precise emission color tunability by size due to quantum confinement effects, better photostability and brightness, wide absorption band and very narrow emission band for multiplexing, and increased fluorescence lifetimes. These characteristics, combined with some dramatic progresses achieved in surface chemistry, biocompatibility and targeting strategies have allowed their recent advances in the field of single-molecule detection and imaging using diverse microscope geometries like confocal microscopy, total internal

---

Laurent A. Bentolila  
Department of Chemistry and Biochemistry, University of California at Los Angeles, Los Angeles,  
CA 90095-1569, USA  
LBENTO@chem.ucla.edu

R. Rigler and H. Vogel (eds.), *Single Molecules and Nanotechnology*. 53  
*Springer Series in Biophysics 12*.  
© Springer-Verlag Berlin Heidelberg 2008

reflection (TIR) microscopy or basic wide-field epifluorescence microscopy. This chapter reviews the basic principles of QDs' electronic structure necessary to understand their fundamental optical and physical properties and goes on to present recent QDs' uses in biological imaging with an emphasis on single-molecule detection.

### 3.1 Introduction

In its visionary lecture delivered at Caltech in 1959, Richard Feynman suggested that "strange phenomena" would occur when a material's size is reduced to the nanometer scale (Feynman 1961). For semiconductor material, these radical changes occur when quantum-size phenomena (quantum confinement) take over conventional bulk properties. As the material's size is reduced in at least one dimension (in the 1 to 10 nm range), new material's properties start to emerge. These mesoscopic semiconductor structures of reduced dimensions (2-D quantum wells, 1-D quantum wires, and 0-D quantum dots) show unique size-dependent optical and electrical properties due to quantum confinement. Quantum dots (QD) are often dubbed "qdots," "quantum crystallites," or more simply "nanocrystals."

Predating our modern solid-state physics understanding of this phenomenon, centuries-old color-stained glass artworks decorating medieval cathedral windows are a vivid example of quantum confinement. These glass-melts contain colloidal particles made of zinc, cadmium sulfides, and selenides. It is only recently that the size-dependent optical properties of nanocrystals have been described within the framework of quantum confinement due to the pioneering work of the St. Petersburg school in Russia (Efros and Efros 1982; Ekimov and Onuschenko 1982; Ekimov et al. 1980) and the Bell Labs in the United States (Rossetti et al. 1983).

Nanocrystals of semiconductor material used in biological applications (e.g., CdSe, PbS) are synthesized in solution using colloidal chemistry (Yin and Alivisatos 2005). They are in general spherical faceted crystals characterized by a diameter smaller than their exciton Bohr radius, a length scale that characterizes the typical electron-hole distance in the bulk material. The QDs small size (about 2 to 10 nm wide which corresponds to a few hundreds to a few thousands of atoms (Kadavanich et al. 2001)) imparts to them useful electronic and optical properties, very different from the properties of the bulk material on which they are based, most notably fluorescence. They behave as single "atom-like" quantum entities and adopt new properties that depend directly on their size (Alivisatos 1996a). Therefore, QDs are sometimes referred to as "artificial atoms" and even have their own periodic table (Ashoori 1996).

Their most useful property for imaging is the tunability of the absorption and emission spectra, which are related to the QD diameter, a parameter that can be precisely controlled by the duration of the nanocrystal growth. This simple control, as well as the availability of a variety of materials with significantly different properties allows for the synthesis of a continuous palette of emission colors spanning the soft ultraviolet (UV), the visible, and the near-infrared (NIR) portion of the light spectrum. These and several other unique QD optical properties have recently galvanized



the biological sciences and include improved signal brightness, resistance against photobleaching, and simultaneous excitation of multiple fluorescence colors.

Since the first experiments demonstrating their potential uses as optical probes in biological imaging (Bruchez et al. 1998; Chan and Nie 1998), QDs have been applied in most biotechnological applications using fluorescence, including DNA array technology, immunofluorescence assays (reviewed in Alivisatos (2004)), and cell and animal biology (reviewed in Medintz et al. (2005) and Michalet et al. (2005)).

A survey of the recent literature testifies to the ever-growing interest of QD-based technologies in the biosciences. Publications using QD imaging probes in biological research have increased exponentially as robust QD sources became commercially available and readily formulated for the needs of the experimentalists. However, despite this current enthusiasm, QD technology will most likely not replace the well-established fluorescent dye technologies but rather will complement some of their shortcomings in niche applications (Michalet et al. 2005). For example, QDs emitting in the far-red and NIR regions of the spectrum could be of great utility for *in vivo* biological imaging, diagnostic, and possibly even therapeutics, due to their good separation from autofluorescence background and increased penetration of excitation and light emission through thick tissues.

Kim et al. (2004) have recently demonstrated in pigs and mice the superiority of NIR QDs in sentinel lymph node (SLN) mapping, a major procedure in breast cancer surgery. Because the QDs allowed image guidance throughout the procedure, virtually free of any background, the size of the incision that ensured the successful removal of the SLN was reduced. The imaging of SLN in real-time without the need of traditional dyes or radioactive tracers is a significant breakthrough that suggests that NIR imaging of QDs could possibly aid surgical procedures in humans (Kim et al. 2004). QDs are also proving to be excellent probes for two-photon confocal microscopy and deep-tissue imaging given their large absorption cross-section (Larson et al. 2003). But when combined with ultrasensitive microscopy techniques, QDs are showing their true potential by allowing visualization of cellular processes at a molecular scale (Dahan et al. 2003; Lidke et al. 2005; Warshaw et al. 2005).

Single-molecule microscopy is a novel high-resolution, high-sensitivity optical technique that is revealing a wealth of new information about the dynamics of isolated molecules, *in vitro* and in their cellular environment (Harms et al. 2001; Iino et al. 2001; Schutz et al. 2000; Seisenberger et al. 2001; Ueda et al. 2001). The ability to watch one molecule at a time can unravel subtle and discrete subpopulations and/or rare events that would otherwise be hidden in heterogeneous samples because of the statistical and temporal averaging from which those ensemble measurements suffer (Michalet et al. 2003). Because of their unmatched photostability, QDs are the probes of choice for long observation of individual cellular proteins, reconciling the inherent incompatibility in time scales of organic dyes' photobleaching lifetime and desired observation time (Weiss 1999). Additionally, single-molecule fluorescence microscopy can be combined with electron microscopy (EM) given QDs high electronic density as it has been demonstrated recently (Dahan et al. 2003). Thus, QDs have the unique potential to provide spatial, temporal, and structural information at all length scales: from the whole-body down to nanometer resolution with a single probe.

This chapter begins by setting out the basic principles of QDs' electronic structure necessary to understand their fundamental optical and physical properties. It then gives a brief review of the dramatic progress achieved in surface chemistry, biocompatibility, and targeting strategies that allowed their recent advances in imaging applications. It then goes on to present recent QDs' uses in biological imaging with an emphasis on single-molecule detection. QD in vitro assay labeling and sensing are discussed elsewhere (Alivisatos 2004; Medintz et al. 2005; Michalet et al. 2005). Finally, it outlines the future directions and potentials of QD technology in fluorescence spectroscopy of single-biomolecules.

## 3.2 Quantum Dots: Semiconductor Systems of Reduced Dimensionality

This section outlines the essential concepts of low-dimensional semiconductor structures and provides a framework to understand why QDs demonstrate desirable optical properties for imaging. Interested readers should consult textbooks on quantum mechanics, solid-state physics, or QDs (Atkins and Friedman 1997; Gaponenko 1998; Kittel 1996) for an in-depth discussion.

### 3.2.1 Energy Bandgap

Electrons in atoms and molecules have defined energies, described by quantum mechanics as "energy levels". Only two electrons can exist in any one energy level (Pauli exclusion principle) with the consequence that electrons will start filling energy levels from the lowest energies upwards. In crystalline solids (such as metals, semiconductors, and insulators), however, electrons are arranged in a near continuum of energy levels known as energy bands due to the overlap of their atomic orbitals in the closely packed crystalline arrangements (Kittel 1996).

The highest filled band at  $T = 0\text{ K}$  is known as the valence band and the first unfilled band above the valence band is referred to as the conduction band. Regions in energy for which no wavelike electron orbitals exist separate valence and conduction bands. Such forbidden regions are called energy gaps ( $E_g$ ) or band gaps, and result from the interaction of the conduction electron wavefunctions with the ion cores of the crystal.

The band theory of materials explains qualitatively the difference among conductors, semiconductors, and insulators. In conductors (e.g., metals), valence and conduction bands overlap ( $E_g = 0$ ), allowing free electrons to participate in the conduction process. To the contrary, bulk semiconductors have a filled valence band and a mostly empty conduction band separated by an  $E_g$  typically of about 1–2 electron volt (eV) ( $3.8\text{e-}23$  to  $7.6\text{e-}23$  kcal). Insulators are not different from semiconductors except for the fact that in insulators,  $E_g$  is far greater than the thermal energy of the electron ( $E_g > 2\text{ eV}$ , Figure 3.1).

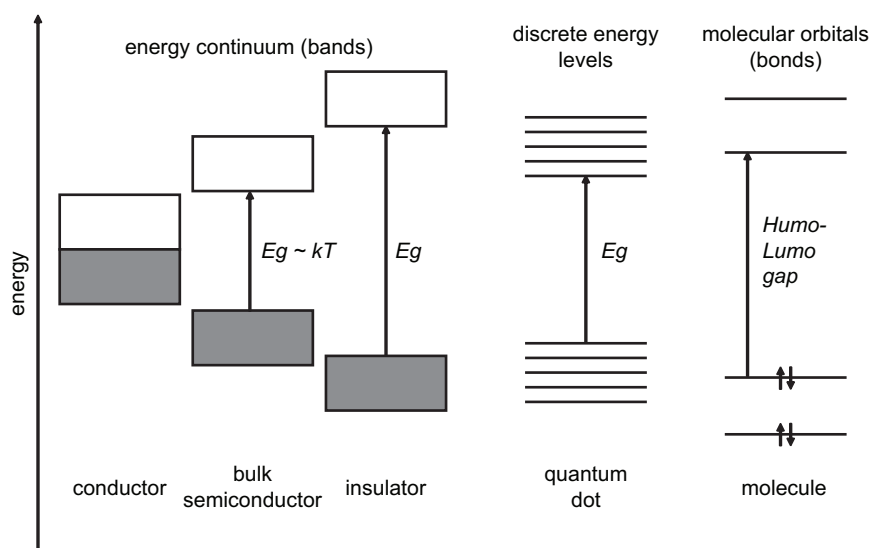


**Figure 3.1** Simplified energy level diagram for crystalline inorganic solids and molecules. Grey boxes: filled valence bands; empty boxes: empty conduction bands (at 0 K). The vertical arrow represents the bandgap energy  $E_g$  for the solids, and the highest occupied molecular orbital–lowest unoccupied molecular orbital (HOMO–LUMO) energy gap in the molecule. The electronic structure of semiconductor QD is in the intermediate regime between bands and bonds. (Adapted from Murphy (2002) and Kittel (1996))

### 3.2.2 Exciton States, Quantum Confinement, and Quantization of Energy

Upon photon absorption of light with energy  $h\nu > E_g$ , an electron is promoted from the filled valence band to the (mostly) empty conduction band, leaving a positively charged vacancy, or “hole”, which can be described as a quasiparticle with a mass, momentum, and energy interacting with its surrounding. The excited electron in the conduction band and the hole in the valence band are of opposite signs and therefore interact with each other via Coulomb interaction, similarly to the proton and electron of a hydrogen atom. As in the hydrogen atom, the distance separating the electron–hole pair (such a bound pair is referred to as an “exciton”) is described by the Bohr radius ( $a_{ex}$ ) and is characteristic of the material under consideration:

$$a_{ex} = \epsilon \hbar^2 / \pi m_{ex} e^2 \quad (1)$$

where  $\epsilon$  is the semiconductor permittivity,  $m_{ex}$  is the reduced exciton mass (as determined by ion cyclotron resonance (Gaponenko 1998; Hannay 1959; Mahan 2000)),  $h$  is Planck’s constant, and  $e$  the electron charge. The exciton’s Bohr radius is

typically about 1 to 10 nm (Gaponenko 1998) for most semiconductors (e.g.,  $a_{\text{CuCl}} \sim 7 \text{ \AA}$ ,  $a_{\text{GaAs}} \sim 100 \text{ \AA}$ , and  $a_{\text{CdSe}} \sim 56 \text{ \AA}$ ).

For semiconductor dimensions smaller than the exciton's Bohr radius, the motion of the excitons becomes obviously confined in space. Confinement in one dimension gives rise to quantum wells, in two dimensions to quantum wires and when all three spatial dimensions are confined, a quasi-zero-dimensional dot (quantum dot) structure is produced (Alivisatos 1996a,b; Empedocles and Bawendi 1999; Steigerwald and Brus 1990; Weller 1993a,b, 1998; Zhang 1997). The confined exciton behaves as a particle trapped in a spherical three-dimensional potential box (i.e., classical particle-in-a-box problem). Practically, calculations and experiments show that the three-dimensional reduction of the QD nanocrystal dimensions results in the appearance of discrete energy levels at the edges of the conduction and valence bands reminiscent of that of atoms or that of the familiar HOMO-LUMO-energy gap for small molecules (Figure 3.1). QD nanocrystals therefore exhibit a mixture of properties in this mesoscopic regime, transitioning from bulk semiconductor (i.e., with energy bands) properties to single atom-like properties (i.e., with discrete energy levels). QDs are thus also referred to as "artificial atoms" or "hyperatoms".

### 3.2.3 *Optical Properties of Quantum Dots*

#### 3.2.3.1 Tunable Bandgap and Size-Dependent Photoluminescence

The separation of the last discrete electronic level of the valence band and the first discrete level of the conduction band, or first exciton energy is related to the bulk bandgap energy  $E_g$  and the size of the QD in such a way that  $E_g$  increases as the dimensions of the particle decreases (Alivisatos 1996a,b; Brus 1984; Weller 1998; Zhang 1997). This first exciton energy of a nanocrystal is often referred to as its bandgap energy, and this is the terminology that is used henceforth.

Because particle size directly relates to the QD's bandgap energy, QDs have size- and composition-dependent absorption and emission (Figure 3.2A). Photoluminescence in QDs is essentially described in terms of the annihilation of the exciton by radiative recombination. Therefore the emission wavelength follows the size-dependent changes in the bandgap; that is, the smaller the QD, the bluer is its emission (tunable emission). In practice, it is possible to continuously tune the spectroscopic properties of QDs by precisely controlling the duration, temperature, and ligand molecules used during the colloidal chemical synthesis (Alivisatos 1996a).

As in the case of bulk semiconductors, the QD's absorption has an increased probability at higher energies (i.e., shorter wavelength), and is characterized by a broad-band absorption spectrum, in marked difference with standard fluorophores (Figure 3.2B). Also, the ensuing ensemble emission spectrum is slightly Stokes-shifted with respect to the excitation band edge and consists of a narrow and symmetric Lorentzian band (30–40 nm full-width-at-half maximum (FWHM) or less) in sharp contrast with

the red-tailed emission spectra of most fluorophores (Figure 3.2B). The width of the ensemble spectrum is due to both the size dispersion of the QD particles inherent to their synthesis (as we discuss in Section 3.3.1) and spectral jumps caused by local changes on the QD's surface. Spectral jumps are another illustration of the atom-like nature of QDs and their similarities to molecules, for which similar phenomenon have been described (Ambrose and Moerner 1991; Orrit and Bernard 1990).

### 3.2.3.2 Bandgap and Wavefunction Engineering

The fate of the photo-generated electron–hole pair is influenced by unpassivated surface defects in the crystal structure, which can act as temporary “traps” for the electron or hole, preventing their radiative recombination. The alternation of trapping and untrapping events results in intermittent fluorescence, or blinking typical of QDs, visible at the single-molecule level (Nirmal et al. 1996) and reduces the overall quantum yield (QY), defined as the ratio of emitted to absorbed photons.

One way to eliminate these “trap” states and protect surface atoms from photo-oxidation and other chemical reactions is to grow a few atomic layers thick protective

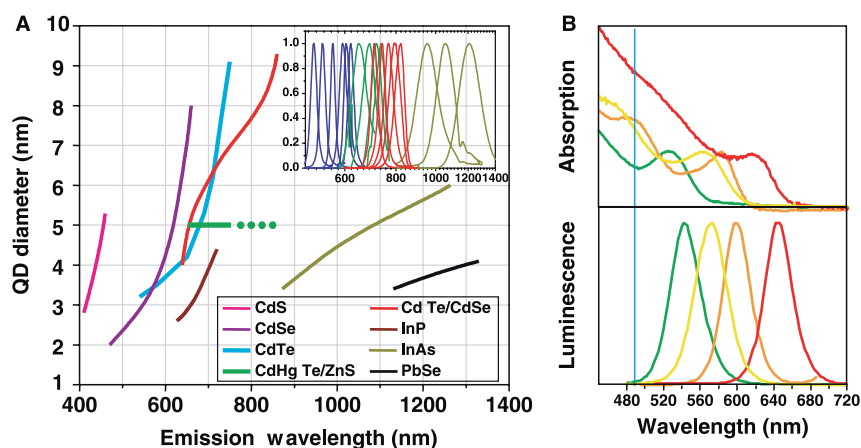


**Figure 3.2** (A) Emission maxima and sizes of quantum dots of different composition. QDs can be synthesized from various types of semiconductor materials (II-VI: CdS, CdSe, CdTe...; III-V: InP, InAs...; IV-VI: PbSe...) characterized by different bulk bandgap energies. The curves represent experimental data from the literature on the dependence of peak emission wavelength on QD diameter. The range of emission wavelength is 400 to 1350 nm, with size varying from 2 to 9.5 nm (organic passivation/solubilization layer not included). All spectra are typically around 30 to 50 nm (FWHM). Inset: Representative emission spectra for some materials. (B) Absorption (upper curves) and emission (lower curves) spectra of four CdSe/ZnS QD samples. The blue vertical line indicates the 488 nm line of an argon-ion laser, which can be used to efficiently excite all four types of QDs simultaneously. ((A) Reprinted with permission from Michalet et al. (2005). Copyright 2005 AAAS. (B) Reprinted with permission from Gerion et al. (2001). Copyright 2001 American Chemical Society)

shell of a larger bandgap material and similar crystalline mesh on top of the nanocrystal core (Dabbousi et al. 1997; Eychmüller et al. 1993; Kortan et al. 1990; Mews et al. 1994; Peng et al. 1997). This “shell” layer can increase the QY to values up to ~90 % (Reiss et al. 2002) by eliminating surface traps and better confining the exciton into the core. This step also enhances QDs’ photostability by several orders of magnitude relative to conventional dyes (Sukhanova et al. 2004).

A typical example is a ZnS shell ( $E_g = 3.8$  eV corresponding to absorption onsets at ~325 nm (Dabbousi et al. 1997, Hines and Guyot-Sionnest 1996)) used to cap CdSe cores ( $E_g = 1.7$  eV ~720 nm; Murphy (2002) in a so-called band alignment of type-I. CdS ( $E_g = 2.4$  eV ~520 nm; Peng et al. (1997)) is better lattice-matched to CdSe, but ZnS has a larger band offset (Böer 1990) resulting in better confinement. Leakage of the wavefunction into the shell results in a slightly red-shifted spectra of the “core-shell” structure as compared to the core alone (Peng et al. 1997).

Recently, atomic layer-by-layer successive shell deposition has revealed systematic changes of lifetime with shell growth of type-II CdTe/CdSe QDs (Li et al. 2005). This demonstrates the high-level of wavefunction manipulation and radiative recombination control that can be achieved in the quantum size regime.

One can take advantage of the long QDs’ lifetime (>10 ns; Efros and Rosen (2000) to separate their signal from background autofluorescence encountered in cells by time-gated imaging detection (Dahan et al. 2001) as discussed in Sections 3.4 and 3.6.

### 3.3 Quantum Dots: From Physical Chemistry to Bioimaging

QDs have been obtained using various technologies; from “top-down” techniques by means of reducing a quantum wells in the two lateral dimensions to “bottom-up” precision growth techniques borrowed from glass technology and colloidal chemistry (Gaponenko 1998). Here, we provide a brief overview of the state-of-the-art fabrication of fluorescent colloidal QDs, a class of QDs exclusively used for biological labeling.

#### 3.3.1 Colloidal Nanocrystal Synthesis

“Bottom-up” approaches allow the most precise growth control of the QDs, providing very narrow size distributions (<5% standard deviation in diameter) necessary for imaging applications. In the colloidal approach, QDs are grown in a solvent solution. Molecular or ionic QD precursors are reacted at high temperature (300°C) in a single vessel, together with a stabilizing agent (an organic surfactant) that stabilizes the growing particles. Typically, a mixture of surfactants such as trioctylphosphine oxide (TOPO) and trioctylphosphine (TOP) is used to coat the growing crystallite cores and prevent their aggregation, as well as the dissolution of smaller nanocrystals in favor of larger ones (a process known as Ostwald ripening).

Murray, Norris, and Bawendi (1993) first introduced this concept for the growth of CdSe nanocrystals in TOPO.

Size tuning (from 2.0 to 8.0 nm) is precisely controlled by factors such as the duration, temperature, relative concentration, and rate of addition of ligand molecules (Alivisatos 1996a; Yin and Alivisatos 2005) and is monitored by absorption and photoluminescence spectra of aliquots taken along the time-course of the reaction (Bowen Katari et al. 1994). Cooling down the reaction vial eventually stops the growth altogether. QD cores are then purified through successive “size-selective precipitation” and washing steps, which further improve their size distribution (Murray et al. 1993; Vossmeier et al. 1994). They are kept in nonpolar solvents such as butanol or toluene. High-resolution TEM indicates that the cores obtained by these methods are made of a few hundred to a few thousand atoms (Kadavanich et al. 2001; Murray et al. 1993). The QY of the resulting core is generally modest (a few percent only) until an outer shell of higher bandgap material is added (see below).

### 3.3.2 *Quantum Dots Bioconjugates for Imaging*

The use of semiconductor QDs as biological fluorescent probes requires that they: (i) are water soluble; (ii) offer reactive groups on their surface for subsequent bioconjugation; (iii) maintain all their photophysical properties when transferred into aqueous buffers (wide excitation band, narrow emission, long fluorescence lifetime, high quantum yield, high photochemical and photophysical stability); (iv) remain monodispersed; and (v) have a reasonable final small size. Therefore, continuing research efforts focus on further developing and improving the organic–inorganic interface.

#### 3.3.2.1 **Quantum Dot Solubilization**

Inasmuch as QDs are mostly synthesized in nonpolar organic solvents, their hydrophobic surface must be converted to a hydrophilic one in order to solubilize them in aqueous buffers. This can be achieved by either surfactant exchange, a process primarily driven by mass-action in which the native TOP/TOPO is substituted with bifunctional ligands or by insulation of the original hydrophobic QD within a heterofunctional amphiphilic coating (Figure 3.3).

These various QD solubilization strategies include: (i) ligand exchange with simple thiol-containing molecules (Chan and Nie 1998; Pathak et al. 2001) or more sophisticated ones such as oligomeric phosphines (Kim and Bawendi 2003), dendrons (Guo et al. 2003), and peptides (Akerman et al. 2002; Pinaud et al. 2004); (ii) encapsulation by a layer of amphiphilic diblock (Wu et al. 2003), or triblock copolymers (Gao et al. 2004), in silica shells (Bruchez et al. 1998; Gerion et al. 2001), phospholipid micelles (Dubertret et al. 2002), polymer beads (Gao et al. 2002), polymer shells (Pellegrino et al. 2004), amphiphilic polysaccharides (Osaki et al. 2004); and (iii) combination of

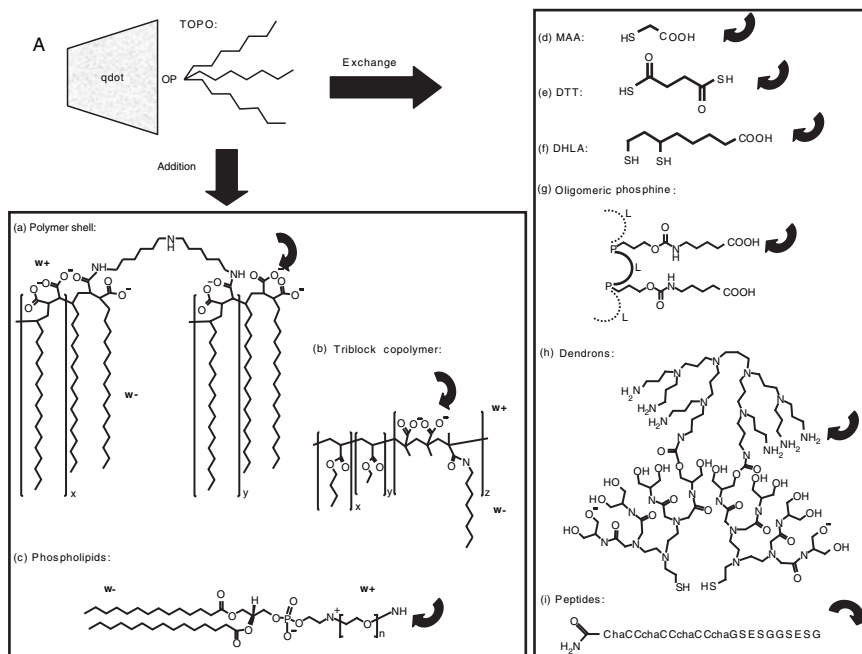


**Figure 3.3** Quantum dot solubilization and functionalization. (A) Surface chemistries. TOPO (trioctylphosphine oxide)-passivated QDs can be solubilized in aqueous buffer by addition of a layer of amphiphilic molecules containing hydrophilic (w+) and hydrophobic (w-) moieties, or by exchange of TOPO with molecules that have a Zn-coordinating end (usually a thiol group, SH) and a hydrophilic end. Examples of addition include (a) formation of a cross-linked polymer shell, (b) coating with a layer of amphiphilic triblock copolymer, and (c) encapsulation in phospholipid micelles. Examples of exchange include (d) mercaptoacetic acid (MAA), (e) dithiothreitol (DTT), (f) dihydrolipoic acid (DHLA), (g) oligomeric phosphines, (h) cross-linked dendrons, and (i) peptides. The curved arrow indicates sites available for further functionalization. (Reprinted with permission from Michalet et al. (2005). Copyright 2005 AAAS)

layers of different molecules conferring the required colloidal stability to QDs (Mattoussi et al. 2000; Sukhanova et al. 2004). Recently, some groups have developed promising water-based synthesis (Gaponik et al. 2002; Rogach et al. 2001) yielding particles emitting from the visible to the NIR spectrum that are intrinsically water-soluble, but have yet to be tested in biological environments.

### 3.3.2.2 Quantum Dot Functionalization

Surface functionalization with hydrophilic ligands serves as a point of chemical attachment for biomolecules. QD ligands containing either an amine or a carboxyl group offer the possibility to cross-link molecules containing a thiol group (Akerman et al. 2002; Dubertret et al. 2002; Mitchell et al. 1999) or an *N*-hydroxy-succinimyl-ester moiety (Bruchez et al. 1998; Pinaud et al. 2004) using standard



bioconjugation reactions. Another approach uses electrostatic interactions between QDs and charged adapter molecules, or proteins modified to incorporate charged domains (Goldman et al. 2002). These functionalization steps can be repeated to add or change functionality. For instance, streptavidin-coated QDs can be used in combination with biotinylated proteins, antibodies, or nucleic acids (Bentolila and Weiss 2006; Chan et al. 2005; Dahan et al. 2003; Jaiswal et al. 2003; Mansson et al. 2004; Pinaud et al. 2004; Wu et al. 2003). By extension, a generic three-layer approach using (i) an antibody against a specific target, (ii) a biotinylated secondary antibody against the first, and (iii) a streptavidin-coated QD, allows QD labeling of most types of target (Dahan et al. 2003; Wu et al. 2003). However, the “sandwich” approach results in large structures that may impede further use of QDs in some applications.

To circumvent that problem, our laboratory has developed a unique peptide-based solubilization and functionalization approach that maintains the small size of the particles. This is achieved by exchanging the surfactants with synthetic phytochelatin-like  $\alpha$ -peptides (Pinaud et al. 2004) that mimic the natural formation of peptide-coated QDs during heavy metal detoxification processes in plants and yeasts (Cobbett 2001; Dameron et al. 1989; Dameron and Winge 1990a,b; Stillman 1995). These peptides comprise a metal-chelating and hydrophobic domain ensuring binding to the QD surface, and a hydrophilic tail that provide solubilization and stability in buffers (Figure 3.3i). A single binding domain of the peptide containing cysteines (C) and hydrophobic unnatural amino acids 3-cyclohexylalanines (Cha) is responsible for surface recognition and attachment to QDs, whereas the variable hydrophilic domain provides solubilization and functional groups for bioconjugation. This surface chemistry is very simple and achieved in a single reaction step. The resulting particles have excellent colloidal and photophysical properties (Doose et al. 2005, Pinaud et al. 2004) suitable for single-molecule techniques, as we discuss in Section 3.4. It is important to note that our peptide-coating approach maintains the overall size of the QDs relatively small (8 to 13 nm) as compared to ~18 nm for phospholipid-coated QDs, and 30 nm for commercial nanorods protected by a polymer coat (Doose et al. 2005).

### **3.4 Quantum Dot Imaging: From Ensemble to Single-Molecule Sensitivity**

The successful developments of a wide range of methods for bioconjugating fluorescent colloidal QDs have accelerated their use in biological imaging and ultrasensitive detection in vitro applications, in live cells and in whole organisms (reviewed in Alivisatos (2004), Medintz et al. (2005), and Michalet et al. (2005)). Most appealing for the biosciences, are the high brightness, high resistance to photobleaching, and the ability to size-tune fluorescent emission of these inorganic–biological hybrid nanostructures. When combined with ultrasensitive optical techniques the enhanced photophysical properties of QDs fulfill the stringent requirements needed to achieve single-molecule sensitivity to study complex

dynamic cellular processes. In the following, we discuss the experimental layouts and the physical observables of these microscopy techniques.

### 3.4.1 Techniques for Single-Molecule Fluorescence Visualization

The first single protein visualized by fluorescence microscopy was an antibody molecule labeled with about 100 fluorophores (Hirschfeld 1976). Since then, progress in molecular imaging has advanced the boundary of detection down to the single-molecule–single-fluorophore complexes in their native cellular environment (Harms et al. 2001; Iino et al. 2001; Schutz et al. 2000; Seisenberger et al. 2001; Ueda et al. 2001). These advances have been critically dependent upon three main factors: (i) the introduction of enhanced indicator probes (new variants of genetically encoded fluorescent proteins, novel inorganic nanomaterials and novel organic fluorophores); (ii) the innovation of new optics and detectors allowing steady gain in microscope collection optics, detector sensitivity and dynamic range; and (iii) the enhanced computer capabilities to process an ever-growing flow of data.

Single-molecule fluorescence imaging techniques rely mainly on two schemes: wide-field excitation/detection and point excitation/detection geometries (Figure 3.4). The wide-field format uses epifluorescence illumination with high-power arc lamps (e.g., mercury) in a Kohler-illumination arrangement (Goulian and Simon 2000) or defocused laser excitation (Schmidt et al. 1996), or total internal reflection excitation (TIR; Axelrod 2003; Funatsu et al. 1995) and a wide area detector (camera).

TIR differs from the first two wide-field methods in limiting the excitation light to the “evanescent field” region at the boundary between the coverslip and water (or

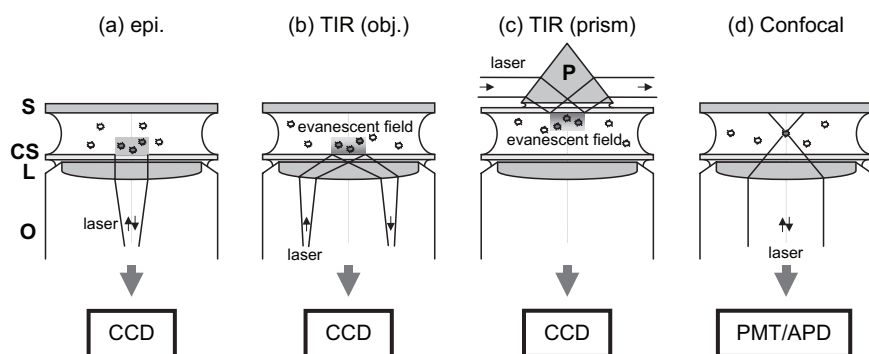


**Figure 3.4** Different excitation/detection geometries utilized in single-molecule microscopy: (a) epifluorescence, (b) through-the-objective TIR, (c) prism TIR, and (d) confocal microscopy (laser scanning beam or scanning stage). S: slide; CS: coverslip; L: lens; O: objective, typically high NA oil-immersion ( $>1.4$  for TIR); P: prism. Area (CCD) or point (PMT or APD) detectors are shown. The filled and empty circles represent fluorescent molecules that are visible and invisible, respectively. Figure is not to scale. (Adapted from Moerner (2003) and Kellermayer (2005))

air) (Figures 3.4b and c). The intensity of the evanescent field decays exponentially as the distance from the boundary increases, thus limiting the excitation depth to a very narrow layer, typically one hundred to a few hundreds of nanometers (Axelrod 2003). Because TIR is a proximity imaging method its application is limited to molecules immobilized on the surface, molecules diffusing close to the surface, or cell surface (the plasma membrane) near the solid support.

The large area detectors used with wide-field excitation geometries include cooled back-thinned CCD cameras, intensified CCD cameras (ICCD; for instance SIT cameras), or electron-multiplying CCD cameras (EMCCD), with detection quantum efficiencies (QE) ranging from 40 to 90% in the visible spectral range. Such detectors allow the simultaneous observation of multiple single molecules scattered over a relatively large field of view (Goulian and Simon 2000; Michalet et al. 2003; Schmidt et al. 1996).

In recent years, single QDs have been successfully observed and tracked over extended period of times (up to a few hours) using TIR microscopy (Michalet et al. 2001b) or basic wide-field epifluorescence microscopy (Figure 3.5 and Dahan et al. (2003), Hohng and Ha (2004), Lidke et al. (2005), and Warshaw et al. (2005)).

The point excitation/detection scheme is based on a confocal laser scanning or stage scanning microscopy (CLSM or CSSM, respectively). The laser beam is focused through an objective lens onto the specimen (Pawley 1995; Webb 1999). The diffraction-limited focal spot defines the excitation volume, which is on the order of a few femtoliters ( $10^{-15}$  l). In CLSM, the laser beam is raster-scanned across the field of view and the image is acquired pixel by pixel using a point-detector (typically a photomultiplier tube of QE <20%) and reconstructed by software. This scheme, however, provides relatively poor sensitivity. In CSSM, the excitation beam is stationary on the optical axis and the sample-stage is raster-scanned across the field of view to produce the pixel-by-pixel image.

Ultrasensitive avalanche photodiode point detectors (APD, QE <90%) are typically used for this scheme, which is usually slower and therefore adapted to very low light level imaging (Michalet et al. 2001a). The CSSM approach is suited for the acquisition of fluorescence time traces of immobilized molecules (Macklin et al. 1996) or isolated QDs (Lacoste et al. 2000) and provides high spatial and temporal resolution, as well as access to fluorescence lifetime information but is inadequate to simultaneously study dynamic processes of many molecules. Wide-field methods are therefore necessary for the high-throughput accumulation of a statistically significant number of single molecule trajectories (Funatsu et al. 1995; Schmidt et al. 1996).

### **3.4.2 *Single-Molecule Sensitivity Requirements***

#### **3.4.2.1 *Signal and Noise***

A prerequisite to achieving single-molecule sensitivity is a careful optimization of background, signal, and noise emission which are manifested in the signal-to-noise

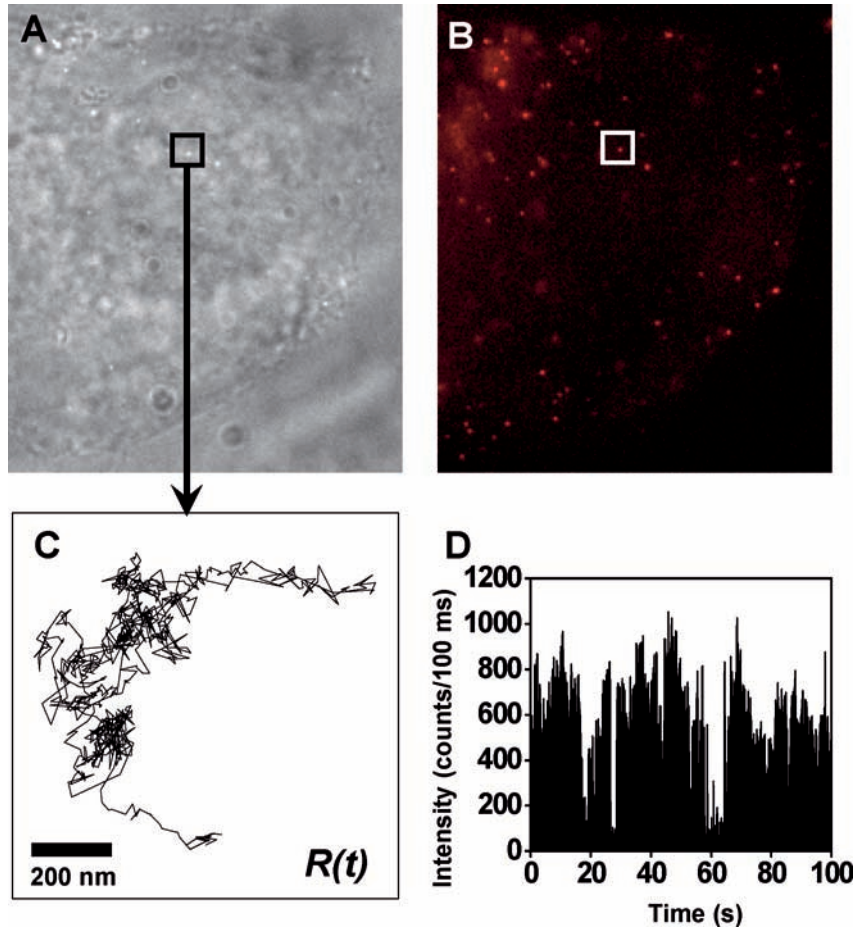


**Figure 3.5** Single-particle tracking in a live-cell. The brightness and photostability of QDs permits single QD observation over a long period of time. Live HeLa cells stably transfected with a plasmid expressing a chimeric avidin-CD14 receptor were grown on fibronectin-coated glass coverslips, incubated with biotin-QDs (emission: 630nm), and washed with the observation medium. The cells were observed in DIC (A) and epifluorescence (B) on an inverted microscope (Axiovert 100, Zeiss) using a simple Hg lamp and imaged with a cooled monochrome CCD camera (CoolSnap HQ, Roper Scientific). Single-QDs were observed to diffuse at characteristically different rates in different regions of the membrane or inside the cytosol (data not shown). C: The 1000 steps (100ms/step) trajectory,  $R(t)$ , of the QD localized in the region marked in panel (A, B), with (D) the corresponding QD intensity,  $I(t)$ . The blinking pattern (succession of on and off emission) demonstrates that a single QD was observed. (Reprinted with permission from Michalet et al. (2005). Copyright 2005 AAAS)

ratio (SNR) and the signal-to-background ratio (SBR) (Michalet et al. 2003; Paige et al. 2001)) defined as

$$SNR = \frac{Signal}{RMS (Signal + Background + Electronic Noise)} \quad (3.2)$$

and

$$SBR = \frac{Signal}{Background}. \quad (3.3)$$

On the instrument side, improving the collection efficiency can increase both SNR and SBR whereas using a higher excitation power and longer integration time will only improve the SNR. SBR can be increased by reducing the excitation volume through combination of focusing (as in CLSM) and/or specialized optical excitation (as with the evanescent field in TIR; Michalet et al. (2003), Paige et al. (2001)).

On the probe (fluorophore) side, desirable properties include high extinction (absorption) coefficient, high fluorescence QY, minimal intersystem crossing to triplet state, and high photostability (Kapanidis and Weiss 2002). QDs indeed fulfill these requirements.

QDs' high molar extinction coefficient ( $\epsilon$ ), on the order of  $10^6 \text{ M}^{-1} \text{ cm}^{-1}$  in the visible, is  $\sim 10$ – $100$  times larger than that of standard organic dyes or genetically encoded fluorescent protein (Dabbousi et al. 1997; Leatherdale et al. 2002) and is the prime contributor to QDs' high SNR.

$\epsilon$  directly relates to the number of photons  $N$  (i.e., the “signal” in Equations (3.2) and (3.3)) emitted from a single QD in a given acquisition time  $\tau$  as follows,

$$N = \alpha q \cdot (2.303 \epsilon / N_A) (I \lambda / hc) \tau \quad (3.4)$$

where  $\alpha$  is the detection efficiency ( $\sim 0.1$ – $5\%$ ),  $q$  the emission quantum yield (30–80%),  $\lambda$  the QD emission wavelength,  $h$  the Planck constant ( $h = 6.63 \times 10^{-34} \text{ J s}$ ),  $c$  the speed of light,  $I$  the excitation power per unit area, and  $N_A$  the Avogadro number.

Practically, this means that at comparable quantum yields and similar emission saturation levels (Doose et al. 2005), QDs are much brighter than dyes. In addition, because they are very photostable, they emit many more photons per particle prior to photobleaching compared to organic dyes (Ballou et al. 2004; Dubertret et al. 2002). These properties allow the detection of QDs' fluorescent signal way above background with the ultimate high sensitivity of one QD per target molecule (Figures 3.5, 3.8, Dahan et al. (2003), and Lidke et al. (2005)).

### 3.4.2.2 Resolution and Localization

An important issue in the quantitative data analysis of single-molecule microscopy/spectroscopy relates to the accuracy with which the position of a single molecule can be determined.

In wide-field microscopy, TIR or CLSM, the ability to detect single molecules depends on those molecules being spaced far enough apart from each other (which means working at low dilution, usually within the ten to hundred picomolar concentration range). This is due to the fact that in light microscopy, spatial resolution (the ability to distinguish identical fluorescent point-sources at high density) is

fundamentally limited by the diffraction of light. Indeed, the focusing of light produces a finite-size focal volume of about 250–300 nm in  $x$ - $y$  and 700–800 nm in  $z$  in the visible range (Abbe 1873). This volume is mathematically described by diffraction theory and is called the point-spread-function (PSF; Pawley (1995)).

At the transverse focal plane ( $x$ - $y$ ) the full-width-at-half-maximum (FWHM) of the focal spot is:

$$\Delta x, \Delta y \approx \frac{\lambda}{2n \sin \alpha} \quad (3.5)$$

and along the optical axis ( $z$ ) is:

$$\Delta z \approx \frac{2\lambda}{n \sin^2 \alpha} \quad (3.6)$$

where  $\lambda$  is the excitation wavelength,  $n$  the refractive index, and  $\alpha$  the semiaperture angle of the objective lens. It is customary to use the FWHM of the PSF as a direct measure of the resolution (Rayleigh criterion). Without resorting to super-resolution techniques (as we discuss later) fluorescent microscopes can thus resolve at best,  $\lambda/2 \sim 200$  nm at the focal ( $x$ - $y$ ) plane and only 500–800 nm along the optic axis ( $z$ ) with visible light (Pawley 1995). As an example, in order to resolve two individual and identical QDs that emit 630 nm light, they need to be at least 240 nm apart in the  $x$ - $y$  plane when imaged with an oil-immersion objective with a numerical aperture (NA) of 1.3. This means that spatial resolution is first intrinsically limited by wavelength not by molecule concentration. Therefore, resolution must be confused neither with single-molecule sensitivity (Weiss 1999) nor with positioning accuracy and distance measurement between two spectrally distinct single-fluorescent molecules (Lacoste et al. 2000).

In fact, the localization of a fluorescent point-source (i.e., the center of the PSF) can be determined with much better precision (in a sense overcoming the diffraction limit) without improving the imaging resolution by fitting the PSF with a two-dimensional Gaussian curve or using centroid-finding algorithms (Gelles et al. 1988), if a sufficient number of photons  $N$  can be collected from the spot (Bobroff 1986, Michalet et al. 2001a; Snyder et al. 2004, Yildiz et al. 2003). In the case of QDs, the high number of emitted (and collected) photons  $N$  affords high localization accuracy. With signal high enough to overcome background, Equation (3.2) can be approximated by:

$$SNR \approx \frac{Signal}{RMS(Signal)} \quad (3.7)$$

The localization precision is solely limited by the SNR as calculated by many authors (Bobroff 1986; Michalet et al. 2001a; Ober et al. 2004; Snyder et al. 2004; Thompson et al. 2002; Yildiz et al. 2003). The exact expression of the localization accuracy depends on the theoretical framework used to describe the experimental situation. We give here the formula derived in Michalet et al. (2001a) which reads in the absence of background:

$$\sigma = \frac{1}{\sqrt{2\pi}} \frac{\delta x}{\text{SNR}} \quad (3.8)$$

where  $\delta x$  is the image pixel size.

Dahan et al. (2003) have shown that it is possible to observe QD's SNR of about  $\sim 50$  under physiological conditions resulting in accuracy as high as 5–10 nm.

Similarly, Figure 3.5 illustrates how QD's high SNR, brightness, and resistance to photobleaching allow tracking the diffusion of individual QD-tagged CD14 receptors in the membrane of live human HeLa cells (Michalet et al. 2005).

This high-localization accuracy principle together with the broad excitation spectrum of QDs (single excitation, multiple emission, Figure 3.2B) allow us to measure the relative position of two spectrally distinct QDs with nanometer accuracy as well (Lacoste et al. 2000; Michalet et al. 2001a). Figure 3.6 presents an example of closely spaced QDs, where centroid-fitting algorithms allow subpixel localization with nanometer accuracy of multiple-color individual QDs (Lacoste et al. 2000). In conclusion, QDs can improve positioning accuracy and distance measurement beyond the diffraction limit imposed by the optical resolution of the microscope, although without increasing the imaging resolution per se.

Improving the optical imaging resolution in  $x$ ,  $y$ , and  $z$  requires “breaking” the diffraction limit of light. This can only be done by effectively reducing the volume of the PSF. Several methods have been proposed and demonstrated: (i) near-field scanning optical microscopy (NSOM; Betzig and Chichester (1993), Betzig and Trautman (1992); Enderle et al. (1997)) or interference methods such as (ii) standing-wave microscopy (Bailey et al. 1993; Frohn et al. 2000), (iii) I<sup>2</sup>M (Gustafsson 2005; Gustafsson et al. 1999), (iv) 4Pi microscopy (Egner and Hell 2005; Hell 2003; Hell and Stelzer 1992), and (v) stimulated emission (STED) microscopy (Dyba and Hell 2002; Hofmann et al. 2005; Klar et al. 2000) although the applicability of some of these techniques remain to be demonstrated with QDs.

### 3.4.2.3 Singleness and Blinking

Because the diffraction-limited volume (typically, several hundred nanometers across,  $\sim 1$  fl in volume) is much larger than the dimensions of single molecule emitters (dyes and QDs), one has to rule out the possibility that the observed signal originates from two or more emitters. Working at low concentration reduces the probability of finding more than one molecule in the excitation volume. Also, we have seen that the excitation volume could be further reduced by super-resolution methods. Nonetheless, one can only conclude that the observed signal emanates from a single molecule (QD) if the following criteria are met (Betzig and Chichester 1993; Michalet et al. 2003):

The observed (surface or volume) density of emitters correlates with the known concentration of molecules used to prepare the sample.

The observed fluorescence intensity level is consistent with that of a single emitting molecule (according to (Equation 3.2)).

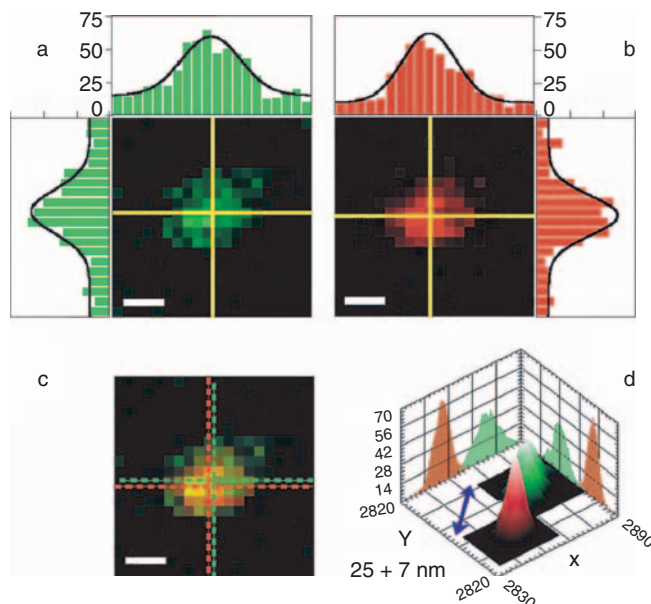


**Figure 3.6** Ultrahigh-resolution colocalization of individual nanocrystals. Mixture of green (Em: 540 nm) and red (Em: 620 nm) QDs excited at 488 nm (excitation power: 200 nW incident or 320 W/cm<sup>2</sup> peak irradiance; integration time: 50 ms). (a), (b) Green and red channel images of a 1 × 1 μm<sup>2</sup> scan obtained by raster scanning the sample through the fixed excitation PSF and recording the respective signals on two different APDs (pixel size: 50 nm; scale bar: 200 nm). As visible from the intensity profiles along two orthogonal lines passing through the PSFs centers, the count rates are similar in both channels. Black curves indicate the corresponding cross-sections of the fitted PSFs. (c) Overlay of the two channels with indication of the determined PSFs centers. (d) Bootstrap replicas of the datasets were fitted in order to estimate the uncertainty of the position determination (Efron and Tibshirani 1994). The figure shows the histograms of the fitted centers distribution obtained from 1000 simulations. The measured distance is 25 nm with a corresponding uncertainty of 7 nm (68% confidence limit). (Reprinted with permission from Lacoste et al. (2000). Copyright 2000, the National Academy of Sciences USA)

When immobilized, each dye or nanocrystal rod emitter has a well-defined absorption or emission dipole (Hu et al. 2001).

Fluorescence emission exhibits only two levels: on/off behavior due to blinking, intersystem crossing to triplet state or photobleaching.

If two or more emission levels exist, they must correlate to changes in photophysical properties (Neuhauser et al. 2000).

The emitted light exhibits antibunching, that is, no simultaneous emission of two photons (Basché et al. 1992). For QDs this is true for low excitation levels only since multiple exciton generation has been recently reported (Ellingson et al. 2005).

Lastly, single QDs can be identified by their characteristic blinking (intermittency) behavior that occurs at all time scales (Banin et al. 1999; Nirmal et al. 1996).



Intermittency is readily seen by the naked eye using a standard fluorescent microscope. The diffraction-limited spots are seen as alternating between “on” and “off” emission states. Figure 3.5D shows a typical single QD blinking time trace. QD’s intermittency has been used as the main criterion for the detection of single QDs in live cells (Chan and Nie 1998; Dahan et al. 2003; Howarth et al. 2005) and fluorescence in situ hybridization (FISH) experiments in fixed cells (Bentolila and Weiss 2006, Crut et al. 2005).

### **3.5 Quantum Dots: Applications in Single-Molecule Optical Imaging**

The main benefit of utilizing QDs for single molecule imaging is their enhanced brightness and photostability, that is, the ability to image and observe individual molecules for long periods of time. Up to now this has been exploited to study the dynamics of two classes of molecules: the translocation and conformational changes of mechanochemical transducers (molecular motors), and the diffusion and transport of receptor proteins in the plasma membrane. In the following, we review these recent achievements and speculate on future advances.

#### ***3.5.1 Quantum Dot Imaging of Protein Conformational Changes***

Myosin V is a double-headed molecular motor that delivers intracellular cargo over long distances by moving processively along actin filament tracks. Single-molecule fluorescence polarization (Forkey et al. 2003) and high-accuracy fluorophores localization methods (FIONA; Yildiz et al. (2003)) have suggested that myosin V is likely to walk with a hand-over-hand mechanism where the heads alternate between “leading” and “trailing” positions. Although very convincing, these experiments have, however, relied on monitoring the movement of a single-labeled myosin head with no direct visualization of the movements of the two heads.

Warshaw et al. (2005) used TIR microscopy and the ability to differentially label each head of a single myosin molecule with a QD of a different color to characterize how myosin generates motion under load. The high spatial and temporal resolution afforded in QD imaging allowed the first time observation of each head alternating positions in a hand-over-hand fashion during processive movement. Single-laser excitation and simultaneous detection of the two QD emission spectra allowed precise positioning measurements of the myosin heads in the  $x,y$  focal plane with 6 nm resolution at the 83 ms integration time (Figure 3.7). These data, through direct observation, confirmed myosin V’s hand-over-hand mode of walking along an actin filament. The authors demonstrated that the QD load did not affect the overall velocity of the motor. They also observed hidden substeps suggesting that

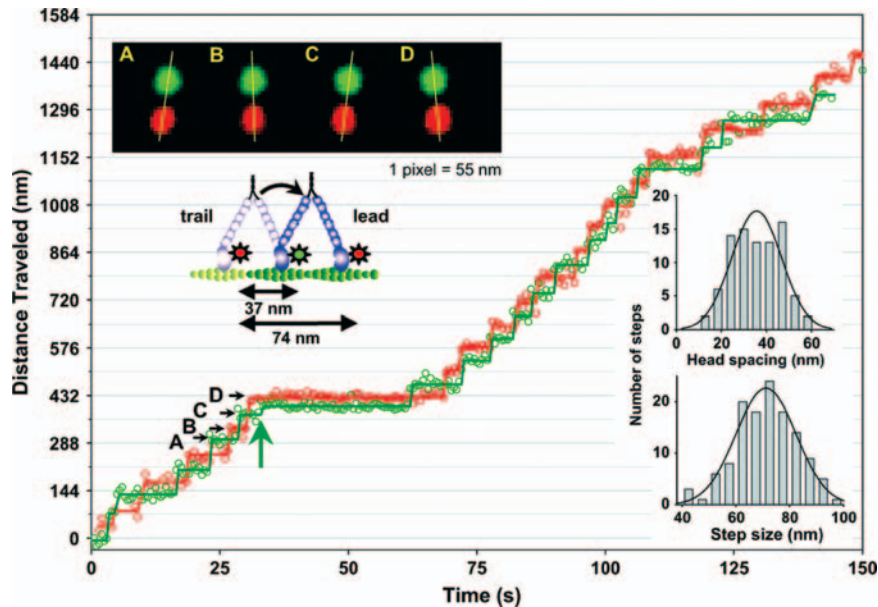


**Figure 3.7** Myosin V processive run with heads labeled with different colored quantum dots. Green and red open circles are the  $QD_{565}$  and  $QD_{655}$  positions, respectively, determined by Gaussian fits. Solid lines are the average QD positions between steps with the onset of steps determined by eye. Upper left are averaged QD images for steps labeled A–D, with red and green images offset by 12 pixels in y for clarity. The yellow lines connect QD centers emphasizing alternating relative head positions. Green arrow identifies substep. Lower right are histograms of interhead spacing and step size. (Reprinted with permission from (Warshaw et al. 2005). Copyright 2005 American Biophysical Society)

once the head has stably attached to an actin monomer, it can detach and reattach before taking its following step.

Another important issue is to understand how motor proteins carry out their functions in living cells under physiological conditions. Beside a single report using a green fluorescence protein (GFP), high background noise, rapid photobleaching, and poor spatial resolution have so far precluded resolving the individual steps of molecular motor proteins *in vivo*. To circumvent these limitations, Nan et al. (2005) have taken advantage of the exceptional brightness and photostability of QDs and recently reported the first observation of individual microtubule motor steps in living cells by following the movements of endocytic vesicles loaded with QDs. The authors showed that QDs allowed them to record motor displacement traces with 300  $\mu$ s time resolution and 1.5 nm spatial precision. They also documented new aspects of microtubule motor movements that had been previously undetected using conventional dye technology.

These results demonstrate the ability of QDs to monitor motor proteins at the molecular level in living cells with higher resolution and will certainly be followed by studies on other motor proteins and systems.

### 3.5.2 *Quantum Dot Tracking of Cell-Surface Membrane Receptors*

Monitoring the trajectories of individual proteins in the plasma membrane of cells has been limited so far by either the size of the probe (40 nm gold nanoparticles or 500 nm latex beads) that may interfere with protein dynamic (Saxton and Jacobson 1997) or by the rapid photobleaching of small (1 to 4 nm) fluorescent organic labels (Ueda et al. 2001).

To circumvent these two main limitations, Dahan et al. (2003) have used antibody-conjugated QDs to track individual glycine receptors at the surface of living neurons. The authors used a standard wide-field microscope and a sensitive CCD camera to identify individual QD-tagged membrane receptors according to their blinking properties. The distance separating neighboring QDs (i.e., the density of membrane receptor labeling) was carefully optimized to make sure that individual QDs could be distinguished optically (i.e., less than one labeled receptor per diffraction-limited resolved spot).

Although the trajectory of an individual receptor could not necessarily be tracked continuously due to blinking (Figure 3.8), the advantages of using QDs were evident. QDs' photostability allowed the observation of individual receptor trajectory for at least 20 min compared to ~5 s with Cy3-labeled antibodies. The brightness of the QDs allowed the spots to be detected with a SNR of about 50 (integration time 75 ms), an increase of almost a factor of 10. This directly translated into a better positioning accuracy of ~5–10 nm (see Equation (3.8)). These experiments also revealed that extrasynaptic receptors were far more mobile than previously considered by single-particle tracking using micrometer-sized beads (Meier et al. 2001), further confirming that the larger load size does influence diffusion properties. Finally, the authors demonstrated the ability to combine the high-temporal dynamics afforded by single-molecule fluorescence microscopy

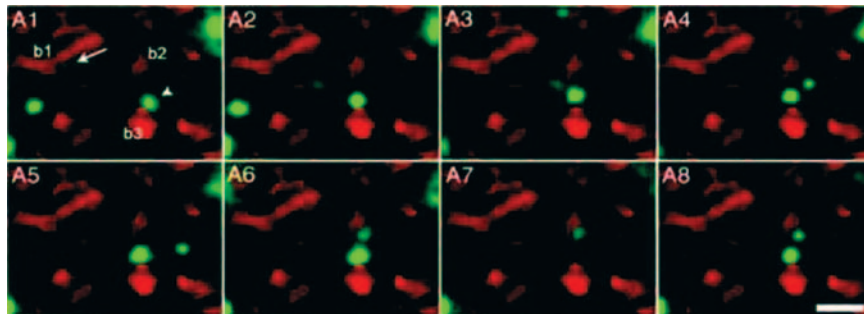


**Figure 3.8** Motion of individual glycine receptors diffusing in the membrane of live neurons. Red spots correspond to synaptic boutons labeled with FM 4-64. One QD (*arrow*), initially located in bouton b1 diffuses in the extrasynaptic domain and then associates with bouton b2. A second QD (*arrowhead*) diffuses while remaining associated with bouton b3. Scale bar is 2  $\mu\text{m}$ . (Reprinted with permission from Dahan et al. (2003). Copyright 2003 AAAS)

with high-resolution cellular localization afforded by electron microscopy on the same QD-labeled samples.

### 3.6 Future Directions

The two previous examples clearly illustrate the unmatched potential of QD technology for single-molecule microscopy and spectroscopy. It is reasonable to expect that with further experimental optimization (microscope geometries, QD photophysical properties, and/or development of new detectors) high positioning accuracy measurement could be approaching or surpass the one-and-half nanometer precision that has been achieved with single-color organic dyes (Snyder et al. 2004, Yildiz et al. 2003). Furthermore, the demonstration that a polarization microscope allows the detection of the QDs and nanorods orientation in three-dimensional space (Empedocles et al. 1999; Hu, 2001, p.131) suggests new methods to study protein undergoing conformational changes in real-time by enlisting the use of end-specific functionalized nanorods (Mokari et al. 2004).

QDs may also be instrumental in achieving single-molecule visualization of the motion of intracellular proteins involved in signaling pathways. Indeed, the observation of single molecules inside living cells has remained challenging partially due to the cellular autofluorescence originating from natural cellular fluorophores present in organelles (flavins, NADH, etc.). This inherent limitation might be alleviated by imaging long-wavelength QDs (extending to the NIR spectrum where autofluorescence is reduced) and/or by taking advantage of the long QD fluorescence lifetime ( $>5$  ns; Efros and Rosen (2000)) to combine the power of time-gated detection (Dahan et al. 2001) to further separate the QD fluorescent signal from that of the cellular background fluorescence (constituted mostly of shorter-lived species).

A prerequisite for QD intracellular applications is the determination of reproducible conditions to deliver monodisperse QDs inside the cell cytoplasm that avoid aggregation in the endosomes (Chen and Gerion 2004; Derfus et al. 2004). It might be also necessary to associate QDs with a fluorescence-quenching molecule that can dissociate upon binding to the target (Chang et al. 2005) to allow discriminating between bound and unbound QDs. Finally, a new software/hardware combination might be needed to track the motion of intracellular molecules that is likely to take place within the three-dimensional space of the cytosol (Levi et al. 2005; Speidel et al. 2003).

Although not achieving single-molecule detection yet, Lidke et al. (2004, 2005) have provided “proof-of-concept” studies showing that QDs are indeed powerful tools to continuously monitor complex signaling pathways, from the cell membrane to specific organelles in the cytoplasm. Lidke et al. used QD-tagged epidermal growth factor (EGF) to directly image the ligand-induced activation process as well as the homo- and heterodimerization of members of the erbB receptor family. QD’s photostability over more than 60 min allowed continuous tracking of ErbB1 receptors from the cell membrane, through endocytosis and the subsequent pathways of vesicular trafficking and fusion.

It is important to note that when single-molecule sensitivity could be achieved at the surface of the filipodia, the authors discovered a new retrograde transport of the erbB1 receptor associated with the cytoskeleton. This retrograde transport preceded receptor endocytosis, which occurs at the base of the filipodia (Lidke et al. 2005).

### 3.7 Concluding Remarks

Since their introduction in 1998 (Bruchez et al. 1998; Chan and Nie 1998), fluorescent semiconductor nanocrystals have been widely accepted by the scientific community and the biotechnology industry as new fluorescent, nonisotopic labels of unmatched potential. Although QDs are here to stay, they are not likely to replace fluorescent dyes and genetically encoded proteins technologies. Rather, they will complement some of their shortcomings in niche applications requiring better photostability, NIR emission, multiplexing (multicolor) capabilities, and single-molecule sensitivity over long periods of time. Quite remarkably, quantum confinement phenomena in nanoscale materials, first predicted and studied by physicists, next synthesized and implemented by inorganic chemists, are now being harnessed and utilized by biologists as a new tool to visualize and study functional molecules down to the single-molecule level within cells and organisms.

**Acknowledgments** The development of QDs and SM microscopy were made possible thanks to the contribution of past and present members of our laboratory and our valuable colleagues in the field. We would also like to thank Tal Paley for her editorial assistance. Fluorescent microscopy images in Figure 3.5 were obtained at the California NanoSystems Institute Advanced Light Microscopy/Spectroscopy Shared Facility, Department of Chemistry and Biochemistry, at UCLA. This work was supported by funds from the National Institute of Health, Grant No. 5-R01-EB000312-04 and by the Department of Energy, Grant No. ER63421-0008273.

### References

- Abbe E (1873) Beitrage zur Theorie des Mikroskops und der mikroskopischen Wahrnehmung. *Arch. f. Mikroskop. Anat.* 9: 413–420
- Akerman ME, Chan WCW, Laakkonen P, Bhatia SN, and Ruoslahti E (2002) Nanocrystal targeting in vivo. *Proc. Natl. Acad. Sci. USA* 99 (20): 12617–12621
- Alivisatos AP (1996a) Semiconductor clusters, nanocrystals, and quantum dots. *Science* 271 (5251): 933–937
- Alivisatos AP (1996b) Perspectives on the physical chemistry of semiconductor nanocrystals. *J. Phys. Chem.* 100 (31): 13226–13239
- Alivisatos P (2004) The use of nanocrystals in biological detection. *Nat. Biotechnol.* 22 (1): 47–52
- Ambrose WP and Moerner WE (1991) Fluorescence spectroscopy and spectral diffusion of single impurity molecules in a crystal. *Nature* 349: 225–227
- Ashoori RC (1996) Electrons in artificial atoms. *Nature* 379: 413–419

- Atkins PW and Friedman RS (1997) *Molecular Quantum Mechanics*. Oxford University Press, New York
- Axelrod D (2003) Total internal reflection fluorescence microscopy in cell biology. *Meth. Enzymol.* 361: 1–33
- Bailey B, Farkas DL, Taylor DL, and Lanni F (1993) Enhancement of axial resolution in fluorescence microscopy by standing-wave excitation. *Nature* 366 (6450): 44–48
- Ballou B, Lagerholm BC, Ernst LA, Bruchez MP, and Waggoner AS (2004) Noninvasive imaging of quantum dots in mice. *Bioconjug. Chem.* 15 (1): 79–86
- Banin U, Bruchez M, Alivisatos AP, Ha T, Weiss S, and Chemla DS (1999) Evidence for a thermal contribution to emission intermittency in single CdSe/CdS core/shell nanocrystals. *J. Chem. Phys.* 110 (2): 1195–1201
- Basché T, Moerner WE, Orrit M, and Talon H (1992) Photon antibunching in the fluorescence of a single dye molecule trapped in a solid. *Phys. Rev. Lett.* 69: 1516–1519
- Bentolila LA and Weiss S (2006) Single-step multicolor fluorescent in situ hybridization analysis using semiconductor quantum dot-DNA conjugates. *Cell Biochem. Biophys.* 45 (1): 59–70
- Betzig E and Chichester RJ (1993) Single molecules observed by near-field scanning optical microscopy. *Science* 262: 1422–1425
- Betzig E and Trautman JK (1992) Near-field optics: Microscopy, spectroscopy, and surface modification beyond the diffraction limit. *Science* 257: 189–195
- Bobroff N (1986) Position measurement with a noise-limited instrument. *Rev. Sci. Instrum.* 57 (6): 1152–1157
- Böer KW (1990) *Survey of Semiconductor Physics. Electrons and Other Particles in Bulk Semiconductors*. Van Nostrand Reinhold, New York
- Bowen Katari JEB, Colvin VL, and Alivisatos AP (1994) X-ray photoelectron spectroscopy of CdSe nanocrystals with applications to studies of the nanocrystal surface. *J. Phys. Chem.* 98: 4109–4117
- Bruchez M, Moronne M, Gin P, Weiss S and Alivisatos AP (1998) Semiconductor nanocrystals as fluorescent biological labels. *Science* 281: 2013–2015
- Brus LE (1984) Electron-electron and electron-hole interactions in small semiconductor crystallites: the size dependence of the lowest excited electronic state. *J. Chem. Phys.* 80 (9): 4403–9
- Chan P, Yuen T, Ruf F, Gonzalez-Maeso J, and Sealfon SC (2005) Method for multiplex cellular detection of mRNAs using quantum dot fluorescent in situ hybridization. *Nucleic Acids Res.* 33 (18): e161
- Chan WCW and Nie SM (1998) Quantum dot bioconjugates for ultrasensitive nonisotopic detection. *Science* 281 (5385): 2016–2018
- Chang E, Miller JS, Sun J, Yu WW, Colvin VL, Drezek R, and West JL (2005) Protease-activated quantum dot probes. *Biochem. Biophys. Res. Commun.* 334 (4): 1317–1321.
- Chen F and Gerion D (2004) Fluorescent CdSe/ZnS nanocrystal-peptide conjugates for long-term, nontoxic imaging and nuclear targeting in living cells. *Nano Lett.* 4: 1827–1832
- Cobbett CS (2001) Heavy metal detoxification in plants: Phytochelatin biosynthesis and function. *Int J. Mol. Biol.* 51 (3): 183–188
- Crut A, Geron-Landre B, Bonnet I, Bonneau S, Desbiolles P, and Escude C (2005) Detection of single DNA molecules by multicolor quantum-dot end-labeling. *Nucleic Acids Res.* 33 (11): e98
- Dabbousi RO, Rodriguez-Viejo J, Mikulec FV, Heine JR, Mattoussi H, Ober R, Jensen KF, and Bawendi MG (1997) (CdSe)ZnS core-shell quantum dots: Synthesis and characterization of a size series of highly luminescent nanocrystallites. *J. Phys. Chem. B* 101: 9463–9475
- Dahan M, Laurence T, Pinaud F, Chemla DS, Alivisatos AP, Sauer M, and Weiss S (2001) Time-gated biological imaging by use of colloidal quantum dots. *Optics Lett.* 26 (11): 825–827
- Dahan M, Levi S, Luccardini C, Rostaing P, Riveau B, and Triller A (2003) Diffusion dynamics of glycine receptors revealed by single-quantum dot tracking. *Science* 302 (5644): 442–445
- Dameron CT and Winge DR (1990a) Characterization of peptide-coated cadmium-sulfide crystallites. *Inorg. Chem.* 29 (7): 1343–1348

- Dameron CT and Winge DR (1990b) Peptide-mediated formation of quantum semiconductors. *Trends Biotechnol.* 8 (1): 3–6
- Dameron CT, Reese RN, Mehra RK, Kortan AR, J. CP, Steigerwald ML, Brus LE, and Winge DR (1989) Biosynthesis of cadmium sulphide quantum semiconductor crystallites. *Nature* 338: 596–597
- Derfus AM, Chan WCW, and Bhatia SN (2004) Intracellular delivery of quantum dots for live cell labeling and organelle tracking. *Adv. Mater.* 16 (12): 961–966
- Doose S, Tsay JM, Pinaud F, and Weiss S (2005) Comparison of photophysical and colloidal properties of biocompatible semiconductor nanocrystals using fluorescence correlation spectroscopy. *Anal. Chem.* 77 (7): 2235–2242
- Dubertret B, Skourides P, Norris DJ, Noireaux V, Brivanlou AH, and Libchaber A (2002) In vivo imaging of quantum dots encapsulated in phospholipid micelles. *Science* 298 (5599): 1759–1762
- Dyba M and Hell SW (2002) Focal spots of size  $\lambda/23$  open up far-field fluorescence microscopy at 33 nm axial resolution. *Phys. Rev. Lett.* 88 (16): 163901
- Efron B and Tibshirani RJ (1994) *An Introduction to the Bootstrap*. CRC Press, Boca Raton, FL.
- Efros AL and Efros AL (1982) Interband absorption of light in a semiconductor sphere. *Sov. Phys. Semicond.* 16 (7): 1209–1214
- Efros AL and Rosen M (2000) The electronic structure of semiconductor nanocrystals. *Ann. Rev. Mat. Sci.* 30: 475–521
- Egner A and Hell SW (2005) Fluorescence microscopy with super-resolved optical sections. *Trends Cell Biol.* 15 (4): 207–215
- Ekimov AI and Onuschenko AA (1982) Quantum size effect in the optical spectra of semiconductor microcrystals. *Sov. Phys. Semicond.* 16 (7): 1215–1219
- Ekimov AI, Onuschenko AA, and Tsekhomskii VA (1980) Exciton light absorption by CuCl microcrystals in glass matrix. *Sov. Glass Phys. Chem.* 6: 511–512
- Ellingson RJ, Beard MC, Johnson JC, Yu P, Micic OI, Nozik AJ, Shabaev A, and Efros AL (2005) Highly efficient multiple exciton generation in colloidal PbSe and PbS quantum dots. *Nano Lett.* 5 (5): 865–871
- Empedocles S and Bawendi M (1999) Spectroscopy of single CdSe nanocrystallites. *Accounts Chem. Res.* 32 (5): 389–396
- Empedocles SA, Neuhauser R, Shimizu K, and Bawendi MG (1999) Photoluminescence from single semiconductor nanostructures. *Adv. Mater.* 11: 1243–1256
- Enderle T, Ha T, Ogletree DF, Chemla DS, Magowan C, and Weiss S (1997) Membrane specific mapping and colocalization of malarial and host skeletal proteins in the Plasmodium falciparum infected erythrocyte by dual-color near-field scanning optical microscopy. *Proc Natl Acad Sci U S A* 94 (2): 520–525
- Eychmüller A, Mews A, and Weller H (1993) A quantum dot quantum well: CdS/HgS/CdS. *Chem. Phys. Lett.* 208: 59–62
- Feynman, R. (1961) in *Miniaturization*, ed. Gilbert, HD, Reinhold, New York, 282–296
- Forkey JN, Quinlan ME, Shaw MA, Corrie JE, and Goldman YE (2003) Three-dimensional structural dynamics of myosin V by single-molecule fluorescence polarization. *Nature* 422 (6930): 399–404
- Frohn JT, Knapp HF, and Stemmer A (2000) True optical resolution beyond the Rayleigh limit achieved by standing wave illumination. *Proc Natl Acad Sci U S A* 97 (13): 7232–7236
- Funatsu T, Harada Y, Tokunaga M, Saito K, and Yanagida T (1995) Imaging of single fluorescent molecules and individual ATP turnovers by single myosin molecules in aqueous solution. *Nature* 374 (6522): 555–559
- Gao X, Chan WCW, and Nie S (2002) Quantum-dot nanocrystals for ultrasensitive biological labeling and multicolor optical encoding. *J. Biomed. Opt.* 7 (4): 532–537
- Gao X, Cui Y, Levenson RM, Chung LWK, and Nie S (2004) In vivo cancer targeting and imaging with semiconductor quantum dots. *Nature Biotechnol.* 22: 969
- Gaponenko SV (1998) *Optical Properties of Semiconductor Nanocrystals*. Cambridge University Press, Cambridge

- Gaponik N, Talapin DV, Rogach AL, Hoppe K, Shevchenko EV, Kornowski A, Eychmüller A, and Weller H (2002) Thiol-capping of CdTe nanocrystals: an alternative to organometallic synthetic routes. *J. Phys. Chem. B* 106: 7177–7185
- Gelles J, Schnapp BJ, and Sheetz MP (1988) Tracking kinesin-driven movements with nanometer scale precision. *Nature* 331: 450–453
- Gerion D, Pinaud F, Williams SC, Parak WJ, Zanchet D, Weiss S, and Alivisatos AP (2001) Synthesis and properties of biocompatible water-soluble silica-coated CdSe/ZnS semiconductor quantum dots. *J. Phys. Chem. B* 105 (37): 8861–8871
- Goldman ER, Anderson GP, Tran PT, Mattoussi H, Charles PT, and Mauro JM (2002) Conjugation of luminescent quantum dots with antibodies using an engineered adaptor protein to provide new reagents for fluoroimmunoassays. *Anal. Chem.* 74 (4): 841–847
- Goulian M and Simon SM (2000) Tracking single proteins within cells. *Biophys. J.* 79: 2188–2198
- Guo W, Li JJ, Wang YA, and Peng XG (2003) Conjugation chemistry and bioapplications of semiconductor box nanocrystals prepared via dendrimer bridging. *Chem. Mater.* 15 (16): 3125–3133
- Gustafsson MG (2005) Nonlinear structured-illumination microscopy: wide-field fluorescence imaging with theoretically unlimited resolution. *Proc. Natl. Acad. Sci. USA* 102 (37): 13081–6
- Gustafsson MG, Agard DA, and Sedat JW (1999) I5M: 3D widefield light microscopy with better than 100nm axial resolution. *J. Microsc.* 195 (Pt 1): 10–16
- Hannay NB (1959) *Semiconductor*. Reinhold, New York
- Harms GS, Cognet L, Lommerse PH, Blab GA, Kahr H, Gamsjäger R, Spaink HP, Soldatov NM, Romanin C, and Schmidt T (2001) Single-molecule imaging of I-type Ca(2+) channels in live cells. *Biophys J.* 81 (5): 2639–2646
- Hell SW (2003) Toward fluorescence nanoscopy. *Nature Biotechnol.* 21 (11): 1347–1355
- Hell SW and Stelzer EHK (1992) Properties of a 4Pi confocal fluorescence microscope. *J. Optic. Soc. Amer.* 9: 2159–2166
- Hines MA and Guyot-Sionnest P (1996) Synthesis and characterization of strongly luminescing ZnS-capped CdSe nanocrystals. *J. Phys. Chem.* 100 468–471
- Hirschfeld T (1976) Optical microscopic observation of single small molecules. *Appl. Optics* 15 (12): 2965–2966
- Hofmann M, Eggeling C, Jakobs S, and Hell SW (2005) Breaking the diffraction barrier in fluorescence microscopy at low light intensities by using reversibly photoswitchable proteins. *Proc. Natl. Acad. Sci. USA* 102 (49): 17565–17569
- Hohng S and Ha T (2004) Near-complete suppression of quantum dot blinking in ambient conditions. *J. Am. Chem. Soc.* 126 (5): 1324–5
- Howarth M, Takao K, Hayashi Y and Ting AY (2005) Targeting quantum dots to surface proteins in living cells with biotin ligase. *Proc. Natl. Acad. Sci. USA* 102 (21): 7583–7588
- Hu J, Li L, Yang W, Manna L, Wang L, and Alivisatos AP (2001) Linearly polarized emission from colloidal semiconductor quantum rods. *Science* 292 (5524): 2060–3
- Iino R, Koyama I and Kusumi A (2001) Single molecule imaging of green fluorescent proteins in living cells: E-cadherin forms oligomers on the free cell surface. *Biophys. J.* 80 (6): 2667–2677
- Jaiswal JK, Mattoussi H, Mauro JM, and Simon SM (2003) Long-term multiple color imaging of live cells using quantum dot bioconjugates. *Nature Biotechnol.* 21 (1): 47–51
- Kadavanich A, V., Kippeny TC, Erwin MM, Pennycook SJ and Rosenthal SJ (2001) Sublattice resolution structural and chemical analysis of individual CdSe nanocrystals using atomic number contrast scanning transmission electron microscopy and electron energy loss spectroscopy. *J. Phys. Chem. B* 105 361–369
- Kapanidis A and Weiss S (2002) Fluorescent probes and bioconjugation chemistries for single-molecule fluorescence analysis of biomolecules. *J. Chem. Phys.* 117 10953–10964
- Kellermayer MS (2005) Visualizing and manipulating individual protein molecules. *Physiol. Meas.* 26 (4): R119–153



- Kim S and Bawendi MG (2003) Oligomeric ligands for luminescent and stable nanocrystal quantum dots. *J. Am. Chem. Soc.* 125 (48): 14652–14653
- Kim S, Lim YT, Soltesz EG, De Grand AM, Lee J, Nakayama A, Parker JA, Mihaljevic T, Laurence RG, Dor DM, Cohn LH, Bawendi MG, and Frangioni JV (2004) Near-infrared fluorescent type II quantum dots for sentinel lymph node mapping. *Nature Biotechnol.* 22 (1): 93–97
- Kittel C (1996) *Introduction to Solid State Physics*. John Wiley, New York
- Klar TA, Jakobs S, Dyba M, Egner A, and Hell SW (2000) Fluorescence microscopy with diffraction resolution barrier broken by stimulated emission. *Proc. Natl. Acad. Sci. USA* 97: 8206–8210
- Kortan AR, Hull R, Opila RL, Bawendi MG, Steigerwald ML, Carroll PJ, and Brus LE (1990) Nucleation and growth of CdSe on ZnS quantum crystallite seeds, and vice versa, in inverse micelle media. *J. Amer. Chem. Soc.* 112: 1327–1332
- Lacoste TD, Michalet X, Pinaud F, Chemla DS, Alivisatos AP, and Weiss S (2000) Ultrahigh-resolution multicolor colocalization of single fluorescent probes. *Proc. Natl. Acad. Sci. USA* 97 (17): 9461–9466
- Larson D, Zipfel W, Williams R, Clark S, Bruchez M, Wise F, and Webb WW (2003) Water-soluble quantum dots for multiphoton fluorescence imaging in vivo. *Science* 300: 1434–1436
- Leatherdale CA, Woo WK, Mikulec FV, and Bawendi MG (2002) On the absorption cross section of CdSe nanocrystal quantum dots. *J. Phys. Chem. B* 106: 7619–7622
- Levi V, Ruan Q, and Gratton E (2005) 3-D particle tracking in a two-photon microscope: Application to the study of molecular dynamics in cells. *Biophys. J.* 88 (4): 2919–2928
- Li JJ, Tsay JM, Michalet X, and Weiss S (2005) Wavefunction engineering: From quantum wells to near-infrared type-II colloidal quantum dots synthesized by layer-by-layer colloidal epitaxy. *Chem. Phys.* 318 (1–2): 82–90
- Lidke DS, Lidke KA, Rieger B, Jovin TM, and Arndt-Jovin DJ (2005) Reaching out for signals: Filopodia sense EGF and respond by directed retrograde transport of activated receptors. *J. Cell Biol.* 170 (4): 619–26
- Lidke DS, Nagy P, Heintzmann R, Arndt-Jovin DJ, Post JN, Grecco HE, Jares-Erijman EA, and Jovin TM (2004) Quantum dot ligands provide new insights into erbB/HER receptor-mediated signal transduction. *Nat. Biotechnol.* 22 (2): 198–203
- Macklin JJ, Trautman JK, Harris TD, and Brus LE (1996) Imaging and time-resolved spectroscopy of single molecules at an interface. *Science* 272: 255–258
- Mahan GD (2000) *Many-Particle Physics*. Kluwer Academic/Plenum, New York
- Mansson A, Sundberg M, Balaz M, Bunk R, Nicholls IA, Omling P, Tagerud S, and Montelius L (2004) In vitro sliding of actin filaments labelled with single quantum dots. *Biochem. Biophys. Res. Commun.* 314 (2): 529–534
- Mattoussi H, Mauro JM, Goldman ER, Anderson GP, Sundar VC, Mikulec FV, and Bawendi MG (2000) Self-assembly of CdSe-ZnS quantum dot bioconjugates using an engineered recombinant protein. *J. Am. Chem. Soc.* 122 (49): 12142–12150
- Medintz IL, Uyeda HT, Goldman ER, and Mattoussi H (2005) Quantum dot bioconjugates for imaging, labelling and sensing. *Nat. Mater.* 4 (6): 435–46
- Meier J, Vannier C, Serge A, Triller A, and Choquet D (2001) Fast and reversible trapping of surface glycine receptors by gephyrin. *Nat. Neurosci.* 4 (3): 253–60
- Mews A, Eychmüller A, Giersig M, Schoos D, and Weller H (1994) Preparation, characterization, and photophysics of the quantum dot quantum well system CdS/HgS/CdS. *J. Phys. Chem.* 98: 934–941
- Michalet X, Kapanidis AN, Laurence T, Pinaud F, Doose S, Pflughoeft M, and Weiss S (2003) The power and prospects of fluorescence microscopies and spectroscopies. *Ann. Rev. Biophys. Biomol. Struct.* 32: 161–182
- Michalet X, Lacoste TD, and Weiss S (2001a) Ultrahigh-resolution colocalization of spectrally resolvable point-like fluorescent probes. *Methods* 25 (1):
- Michalet X, Pinaud F, Lacoste TD, Dahan M, Bruchez MP, Alivisatos AP, and Weiss S (2001b) Properties of fluorescent semiconductor nanocrystals and their application to biological labeling. *Single Mol.* 2 (4): 261–276

- Michalet X, Pinaud FF, Bentolila LA, Tsay JM, Doose S, Li JJ, Sundaresan G, Wu AM, Gambhir SS, and Weiss S (2005) Quantum dots for live cells, in vivo imaging, and diagnostics. *Science* 307 (5709): 538–544
- Mitchell GP, Mirkin CA, and Letsinger RL (1999) Programmed assembly of DNA functionalized quantum dots. *J. Am. Chem. Soc.* 121 (35): 8122–8123
- Moerner WE (2003) Optical measurements of single molecules in cells. *Trends Anal. Chem.* 22 (9): 544–548
- Mokari T, Rothenberg E, Popov I, Costi R, and Banin U (2004) Selective growth of metal tips onto semiconductor quantum rods and tetrapods. *Science* 304 (5678): 1787–1790
- Murphy CJaC, J.L. (2002) Quantum dots: A primer. *Appl. Spectroscopy* 56 (1): 16A–27A
- Murray CB, Norris DJ, and Bawendi MG (1993) Synthesis and characterization of nearly monodisperse CdE (E = S, Se, Te) semiconductor nanocrystallites. *J. Amer. Chem. Soc.* 115: 8706–8715
- Nan X, Sims PA, Chen P, and Xie XS (2005) Observation of individual microtubule motor steps in living cells with endocytosed quantum dots. *J. Phys. Chem. B Condens. Matter Mater. Surf. Interfaces Biophys.* 109 (51): 24220–24224
- Neuhauser RG, Shimizu KT, Woo WK, Empedocles SA, and Bawendi MG (2000) Correlation between fluorescence intermittency and spectral diffusion in single semiconductor quantum dots. *Phys. Rev. Lett.* 85 (15): 3301–3304
- Nirmal M, Dabbousi BO, Bawendi MG, Macklin JJ, Trautman JK, Harris TD, and Brus LE (1996) Fluorescence intermittency in single cadmium selenide nanocrystals. *Nature* 383: 802–804
- Ober RJ, Ram S, and Ward ES (2004) Localization accuracy in single-molecule microscopy. *Biophys. J.* 86 (2): 1185–1200
- Orrit M and Bernard J (1990) Single pentacene molecules detected by fluorescence excitation in a p-terphenyl crystal. *Phys. Rev. Lett.* 65 (21): 2716–2719
- Osaki F, Kanamori T, Sando S, Sera T, and Aoyama Y (2004) A quantum dot conjugated sugar ball and its cellular uptake. On the size effects of endocytosis in the subviral region. *J. Am. Chem. Soc.* 126: 6520–6521
- Paige MF, Bjerneld EJ, and Moerner WE (2001) A comparison of through-the-objective total internal reflection microscopy and epifluorescence microscopy for single-molecule fluorescence imaging. *Single Molec.* 2: 191–201
- Pathak S, Choi SK, Arnheim N, and Thompson ME (2001) Hydroxylated quantum dots as luminescent probes for in situ hybridization. *J. Am. Chem. Soc.* 123 (17): 4103–4104
- Pawley, JB (1995) Handbook of biological confocal microscopy, 2<sup>nd</sup> edition, Plenum Press, New York
- Pellegrino T, Manna L, Kudera S, Liedl T, Koktysh D, Rogach AL, Keller S, Radler J, Natile G, and Parak WJ (2004) Hydrophobic nanocrystals coated with an amphiphilic polymer shell: A general route to water soluble nanocrystals. *Nano Lett.* 4 (4): 703–707
- Peng X, Schlamp MC, Kadavanich AV, and Alivisatos AP (1997) Epitaxial growth of highly luminescent CdSe/CdS core/shell nanocrystals with photostability and electronic accessibility. *J. Amer. Chem. Soc.* 119 (30): 7019–7029
- Pinaud F, King D, Moore H-P, and Weiss S (2004) Bioactivation and cell targeting of semiconductor CdSe/ZnS nanocrystals with phytochelatin-related peptides. *J. Am. Chem. Soc.* 126 6115–6123
- Reiss P, Bleuse J, and Pron A (2002) Highly luminescent CdSe/ZnSe core/shell nanocrystals of low size dispersion. *Nano Lett.* 2 (7): 781–784
- Rogach AL, Harrison MT, Kershaw SV, Kornowski A, Burt MG, Eychmuller A, and Weller H (2001) Colloidally prepared CdHgTe and HgTe quantum dots with strong near-infrared luminescence. *Phys. Status Solidi B* 224 (1): 153–158
- Rossetti R, Nakahara S, and Brus LE (1983) Quantum size effects in the redox potentials, resonance Raman spectra, and electronic spectra of CdS crystallites in aqueous solution. *J. Chem. Phys.* 79: 1086–1088
- Saxton MJ and Jacobson K (1997) Single-particle tracking: Applications to membrane dynamics. *Ann. Rev. Biophys. Biomol. Struct.* 26: 373–399

- Schmidt T, Schütz GJ, Baumgartner W, Gruber HJ, and Schindler H (1996) Imaging of single molecule diffusion. *Proc. Nat. Acad. Sci. USA* 93: 2926–2929
- Schutz GJ, Kada G, Pastushenko VP, and Schindler H (2000) Properties of lipid microdomains in a muscle cell membrane visualized by single molecule microscopy. *Embo. J.* 19 (5): 892–901
- Seisenberger G, Ried MU, Endress T, Buning H, Hallek M, and Brauchle C (2001) Real-time single-molecule imaging of the infection pathway of an adeno-associated virus. *Science* 294 (5548): 1929–32
- Snyder GE, Sakamoto T, Hammer JA, 3rd, Sellers JR, and Selvin PR (2004) Nanometer localization of single green fluorescent proteins: Evidence that myosin V walks hand-over-hand via telemark configuration. *Biophys. J.* 87 (3): 1776–1783
- Speidel M, Jonas A, and Florin EL (2003) Three-dimensional tracking of fluorescent nanoparticles with subnanometer precision by use of off-focus imaging. *Opt. Lett.* 28 (2): 69–71
- Steigerwald ML and Brus LE (1990) Semiconductor crystallites: A class of large molecules. *Acc. Chem. Res.* 23 (6): 183–8
- Stillman MJ (1995) Metallothioneins. *Coord. Chem. Rev.* 144: 461–511
- Sukhanova A, Devy M, Venteo L, Kaplan H, Artemyev M, Oleinikov V, Klinov D, Pluot M, Cohen JHM, and Nabiev I (2004) Biocompatible fluorescent nanocrystals for immunolabeling of membrane proteins and cells. *Anal. Biochem.* 324 (1): 60–67
- Thompson RE, Larson DR, and Webb WW (2002) Precise nanometer localization analysis for individual fluorescent probes. *Biophys. J.* 82 (5): 2775–83
- Ueda M, Sako Y, Tanaka T, Devreotes P, and Yanagida T (2001) Single-molecule analysis of chemotactic signaling in Dictyostelium cells. *Science* 294 (5543): 864–7
- Vossmeyer T, Katsikas L, Giersig M, Popovic IG, Diesner K, Chemseddine A, Eychmüller A, and Weller H (1994) CdS nanoclusters: Synthesis, characterization, size dependent oscillator strength, temperature shift of the excitonic transition energy, and reversible absorbance shift. *J. Phys. Chem.* 98: 7665–7673
- Warshaw DM, Kennedy GG, Work SS, Kremmentsova EB, Beck S, and Trybus KM (2005) Differential labeling of myosin V heads with quantum dots allows direct visualization of hand-over-hand processivity. *Biophys. J.* 88 (5): L30–32
- Webb RH (1999) Theoretical basis of confocal microscopy. *Methods Enzymol.* 307: 3–20
- Weiss S (1999) Fluorescence spectroscopy of single biomolecules. *Science* 283: 1676–1683
- Weller H (1993a) Quantized semiconductor particles: A novel state of matter for materials science. *Adv. Mater.* (Weinheim, Germany) 5 (2): 88–95
- Weller H (1993b) Colloidal semiconductor Q-particles: Chemistry in the transition region between solid and molecular states. *Angewandte Chemie* 105 (1): 43–55 (See also *Angew. Chem., Int. Ed. Engl.*, 1993, 32(1), 41–53)
- Weller H (1998) Quantum size colloids: From size-dependent properties of discrete particles to self-organized superstructures. *Curr. Opin. Colloid Interface Sci.* 3 (2): 194–199
- Wu XY, Liu HJ, Liu JQ, Haley KN, Treadway JA, Larson JP, Ge NF, Peale F, and Bruchez MP (2003) Immunofluorescent labeling of cancer marker Her2 and other cellular targets with semiconductor quantum dots. *Nature Biotechnol.* 21 (1): 41–46
- Yildiz A, Forkey JN, McKinney SA, Ha T, Goldman YE, and Selvin PR (2003) Myosin V walks hand-over-hand: Single fluorophore imaging with 1.5-nm localization. *Science* 300 (5628): 2061–2065
- Yin Y and Alivisatos AP (2005) Colloidal nanocrystal synthesis and the organic-inorganic interface. *Nature* 437 (7059): 664–70
- Zhang JZ (1997) Ultrafast studies of electron dynamics in semiconductor and metal colloidal nanoparticles: Effects of size and surface. *Acc. Chem. Res.* 30 (10): 423–429

# Chapter 4

## Scanning Fluorescence Correlation Spectroscopy

Zdeněk Petrášek and Petra Schwille(✉)

4.1	Introduction.....	84
4.2	Theory.....	85
4.2.1	Fluorescence Correlation Methods.....	85
4.2.2	Fluorescence Correlation Spectroscopy.....	85
4.2.3	Image Correlation Spectroscopy.....	87
4.2.4	Spatiotemporal Image Correlation Spectroscopy.....	87
4.2.5	Scanning Fluorescence Correlation Spectroscopy.....	88
4.3	Applications.....	94
4.4	Implementation.....	97
4.4.1	Light Source.....	98
4.4.2	Optical Part.....	98
4.4.3	Electronics.....	99
4.4.4	Software.....	100
4.4.5	Data analysis.....	101
4.5	Conclusion.....	102
	References.....	103

**Abstract** Fluorescence correlation techniques are used to investigate photophysical, photochemical, interaction and transport properties of fluorescent or fluorescently labelled molecules at extremely low concentrations by analyzing the fluctuations of the measured fluorescence signal. Since their introduction more than thirty years ago, many variations of fluorescence correlation techniques have been developed. They range from the original and the most widely applied Fluorescence Correlation Spectroscopy analyzing temporal fluctuations at a fixed position and suitable for the investigation of molecules in motion to Image Correlation Spectroscopy analyzing spatial correlations of immobile species. Scanning Fluorescence Correlation Spectroscopy is a group of correlation techniques where the measurement volume is moved across the sample in a defined way, resulting in a spatiotemporal correlation of the detected fluorescence. Scanning improves the accuracy of measurements on slowly moving molecules, diminishes the negative effects of photobleaching, and allows measurements on systems where other fluorescence correlation approaches

---

Petra Schwille  
Institut für Biophysik, Technische Universität Dresden, Tatzberg 47–51, 01307 Dresden, Germany  
petra.schwille@biotec.tu-dresden.de

R. Rigler and H. Vogel (eds.), *Single Molecules and Nanotechnology*. 83  
*Springer Series in Biophysics 12*.  
© Springer-Verlag Berlin Heidelberg 2008

perform poorly or are not possible. This chapter discusses scanning FCS in its relation to other fluorescence correlation methods, describes different variations of scanning FCS, summarizes some of the applications, and finally presents an example of experimental setup designed for two-photon scanning FCS.

## 4.1 Introduction

Fluorescence correlation techniques obtain information about the investigated system by measuring the magnitude of spontaneous microscopic fluctuations and their relaxation while the system is in equilibrium from the macroscopic point of view. The actually measured quantity reflecting the fluctuations of the parameter of interest (e.g., the mean number of particles) is the fluorescence intensity. In other fluctuation methods this “reporting” quantity can be, for example, scattered light or conductivity (Weissman 1981).

Fluorescence fluctuations typically encountered in fluorescence correlation methods arise due to Brownian translational and rotational particle diffusion, particle interactions (such as association/dissociation in chemical reactions in equilibrium), as well as intramolecular processes, for example, transitions between singlet and triplet energy states, radical ion formation, and the like. All these processes giving rise to fluorescence fluctuations can therefore be studied with fluorescence correlation methods.

The most widely used fluorescence fluctuation method is fluorescence correlation spectroscopy (FCS) (Rigler and Elson 2001; Krichevsky and Bonnet 2002; Thompson et al. 2002) which measures the signal fluctuations in one stationary volume with a size usually limited by light diffraction. Fluorescence correlation spectroscopy has been applied to studies of many biological processes involving single molecules (Schwille 2001; Hess et al. 2002; Bacia and Schwille 2003). The suitability of FCS for applications in biology can be linked to its high sensitivity, noninvasiveness, high spatial resolution, and the fact that the investigated system is not disturbed from equilibrium as in some other methods, such as fluorescence recovery after photobleaching (FRAP).

In many cases the investigated molecules are immobile or diffuse too slowly to cause sufficient temporal fluorescence fluctuations needed for FCS analysis. Still, fluctuation analysis can be performed on such systems. In this case the spatial rather than the temporal fluctuations provide information on molecular concentrations, aggregation, association, and so on. The method analyzing spatial fluorescence distributions is known as image correlation spectroscopy (ICS) (Petersen et al. 1993).

Scanning fluorescence correlation spectroscopy (SFCS), presented in this contribution, could be broadly defined as FCS with relative movement of the sample and the measurement volume. It combines the high temporal resolution of FCS with the measurement in many locations encountered in ICS, therefore it can be logically grouped somewhere between these two methods. Combining the advantages of both, SFCS expands the range of the systems that can be studied with fluorescence fluctuation analysis.

## 4.2 Theory

### 4.2.1 Fluorescence Correlation Methods

A typical fluorescence correlation experiment constitutes the measurement of a fluorescence signal  $F(p)$  as a function of some parameter  $p$ . The fluctuations of the fluorescence signal reflect fluctuations of some quantity of interest; for example, the average number of molecules in the measurement volume, and their proper evaluation yields the desired quantity values. The parameter  $p$  can be any combination of the spatial coordinates  $x$ ,  $y$ ,  $z$  and time  $t$ . The fluorescence correlation methods can be classified on the basis of the choice of the parameter  $p$ .

The fluctuations are quantified by means of the autocorrelation function  $G(\Delta p)$  of the measured signal  $F(p)$ :

$$G(\Delta p) = \langle F(p)F(p + \Delta p) \rangle, \quad (4.1)$$

or the normalized autocorrelation function  $g(\Delta p)$ :

$$g(\Delta p) = \frac{\langle F(p)F(p + \Delta p) \rangle}{\langle F(p) \rangle^2} - 1, \quad (4.2)$$

which can be understood as an autocorrelation of the fluctuations  $\delta F(p)$  of  $F(p)$ :  $\delta F(p) = F(p) - \langle F(p) \rangle$ . The averaging  $\langle \cdot \rangle$  in the above equations is performed over the set or subset of the experimental values  $F(p)$ . The calculated correlation function is then fitted to a model function based on the theoretical model of the investigated system. The average  $\langle \cdot \rangle$  in the derivation of the model correlation function is calculated as an ensemble average.

One can imagine an idealized experiment where  $F(p)$  is measured as a function of all spatial coordinates and time ( $p = x, y, z, t$ ) with high resolution in all four dimensions. The four-dimensional autocorrelation function would then reflect correlations over all possible combinations of dimensions. However, such a measurement is not yet technically possible and even not necessary due to high information redundancy in such a hypothetical dataset in a typical investigated system. In practice, the parameter  $p$  corresponds to one or two (max. three) coordinates out of  $x$ ,  $y$ ,  $z$ , and  $t$ .

### 4.2.2 Fluorescence Correlation Spectroscopy

The most common choice of the parameter  $p$  in  $F(p)$  is the time  $t$  and the method is then called fluorescence correlation spectroscopy. Although FCS is sometimes used to denote the whole family of fluorescence correlation techniques, it is used here in a narrower sense, as a method where temporal correlation of the fluorescence from one location is calculated. The correlation function depends on one parameter: the correlation (lag) time  $\tau = \Delta t$ .

In the simplest case a FCS experiment provides two parameters describing the investigated system: the average number of independently diffusing fluorescent particles  $\bar{n}$ . in the measurement volume, and the diffusion coefficient of the particles. The average number of particles  $\bar{n}$ . can be obtained directly from the value of the autocorrelation function at  $\tau = 0$ , assuming proportionality between the number of particles  $n$  and the fluorescence intensity  $F(t)$  at any time:  $F = kn$ , and a Poisson distribution of the number of particles  $n$ , namely the fact that the variance of particle number is equal to the mean:  $\sigma_n^2 = \bar{n}$ . From Equation 4.2 then follows,

$$g(0) = \frac{\langle F(t)^2 \rangle}{\langle F(t) \rangle^2} - 1 = \frac{\sigma_F^2}{\langle F \rangle^2} = \frac{\sigma_n^2}{\langle n \rangle^2} = \frac{1}{\bar{n}}. \quad (4.3)$$

The above expression represents a comparison between the size of the fluctuations of the fluorescence signal  $\sigma_F^2$  and the mean signal size itself  $\langle F \rangle$ . The inverse dependence of the amplitude  $g(0)$  on the average number of particles  $\bar{n}$ . is a mathematical representation of the intuitive fact that the relative magnitude of fluctuations decreases with increasing number of particles.

The diffusion coefficient can be obtained by fitting the experimentally determined autocorrelation (Equation 4.2) to the appropriate model function (see, e.g., Krichevsky and Bonnet 2002). A more realistic model taking into account the excitation intensity profile results in an additional proportionality factor in Equation 4.3.

In a practical realization of a FCS experiment the fluorescence intensity  $F(t)$  is measured in a small (diffraction-limited) stationary sample volume with high temporal resolution going down to the nanosecond time range. In combination with time-correlated single photon counting (TCSPC) technique the temporal resolution can be extended to the picosecond time range (Felekyan et al. 2005). The other end of the useful measurement range, the long correlation times, is limited only by the possibility/ability to maintain the investigated system and the experimental setup stationary and undisturbed over a long time period. The practically attainable time range spans many orders of magnitude which makes FCS applicable to the studies of a large range of diffusional and inter- and intramolecular processes.

Inasmuch as the fluorescence  $F(t)$  in FCS is measured as a function of time, the averaging in the definition of the autocorrelation (Eq. 2) is a time average. The averaging has to be performed over a sufficient number of independent “fluctuation events” in order to provide a reasonably precise estimate of the desired parameters (number of particles, diffusion time) by comparison with the model function calculated using ensemble average. If the particles are immobile and the average number of particles is the parameter of interest, time-averaging in Equation 4.2 does not lead to an accurate estimate because the fluctuations of the number of particles in the measurement volume are practically nonexistent ( $\sigma_n^2 \rightarrow 0$ ; see Equation 4.3). One solution to this problem is offered by image correlation spectroscopy.

### 4.2.3 *Image Correlation Spectroscopy*

In many biologically relevant applications the molecules of interest bind to membranes and other cellular structures that may significantly reduce their mobility. Although in some cases of slow diffusion FCS measurements are possible by extending the measurement time, in other cases photobleaching of the labels prevents measurements over longer periods of time.

As a solution to this problem image correlation spectroscopy has been introduced (Petersen et al. 1993). In ICS the fluorescence image of the sample is recorded; that is, the measured fluorescence  $F(p)$  is a function of spatial coordinates:  $p = x, y$ . The image is autocorrelated according to Equation 4.2. Similarly to FCS, the amplitude of the autocorrelation function  $g(0,0)$  reflects the average number of independent fluorescent particles (Equation 4.3). The average number of particles together with fluorescence intensity per particle can be used to characterize aggregation (Brown and Petersen 1998). The shape of the autocorrelation function reflects the excitation beam profile and the particle size, if the particles are comparable to or larger than the beam waist diameter, and may also be affected by the particle diffusion if this cannot be neglected during the used exposure time.

The average in the definition of the autocorrelation function (Equation 4.2) is calculated over the pixels of the acquired image and can be thus regarded as an approximation of an ensemble average. The number of independent sample volumes, corresponding to the number of independent fluctuation events in FCS, can be estimated as the image size divided by the size of the measurement volume.

In ICS, the spatial correlation is performed to assure sufficient averaging in estimation of  $g(0, 0)$ , and not to obtain autocorrelation of fixed features in the image. On the contrary, the image has to be uniform on the scale larger than the measurement volume size to avoid artefacts. This prerequisite is equivalent to the requirement that the fluorescence signal be stationary in a FCS measurement. Methods dealing with analysis of ICS data containing unwanted features were introduced (Rocheleau et al. 2003). An exception is applications where ICS is used to characterize changes in image structures, for example, the measurement of extension fluctuations of a stretched DNA molecule (Reisner et al. 2005).

### 4.2.4 *Spatiotemporal Image Correlation Spectroscopy*

Image correlation spectroscopy as described above does not provide any temporal information. If dynamic information is required, ICS can be extended by acquiring a series of images in rapid succession. In the formalism introduced above this corresponds to measuring the fluorescence  $F(p)$  as a function of space and time:  $p = x, y, t$ . The correlation analysis can then be performed separately on spatial and temporal coordinates (Wiseman et al. 2000; Srivastava and Petersen 1996; Wiseman et al. 2004) or fully as defined by Equations 4.1 and 4.2. The latter approach has been called spatiotemporal image correlation spectroscopy (STICS) (Hebert et al. 2005). Spatiotemporal



ICS allows, in addition to concentration and aggregation measurements, the measurements of slow diffusion and magnitude and directions of flows. If parts of the image are analyzed separately, diffusion coefficient- or velocity-mapping are possible. The spatial-temporal correlation offers more than a simple combination of FCS and ICS. For example, the direction and magnitude of flow cannot be determined by FCS or ICS alone, but a spatial cross-correlation analysis among at least three measurement volumes is necessary (Brinkmeier et al. 1999; Gosch and Rigler 2005).

Compared with FCS, STICS suffers from lower temporal resolution which is determined by the maximum rate of image acquisition. Thus, only relatively slow dynamics can be studied.

#### 4.2.5 Scanning Fluorescence Correlation Spectroscopy

In scanning fluorescence correlation spectroscopy the fluorescence is recorded from a small measurement volume defined by the focused illuminating beam as in FCS, and this measurement volume is moved relative to the sample in a controlled way. Because the movement of the measurement volume in the sample is the only principal difference from FCS, all other features of FCS are preserved in SFCS, most importantly the high temporal resolution. The fluorescence signal  $F(t)$  is measured as a function of spatial and temporal coordinates:  $p = x, y, t$ , however, contrary to STICS, not the whole  $xyt$  space is sampled. At any time  $t$  only one point in  $xy$  is probed. Consequently, the correlation function calculated according to Equation 4.2 cannot be evaluated in the whole correlation space  $\xi, \theta, \tau (= \Delta x, \Delta y, \Delta t)$  but only at some points. This is schematically illustrated in Figure 4.1.

The diagram in Figure 4.1A describes a line-scan SFCS where the measurement volume is moved repeatedly along the  $x$ -axis in the positive direction (the flyback period is neglected in the figure). The bold lines represent the sampled points in the

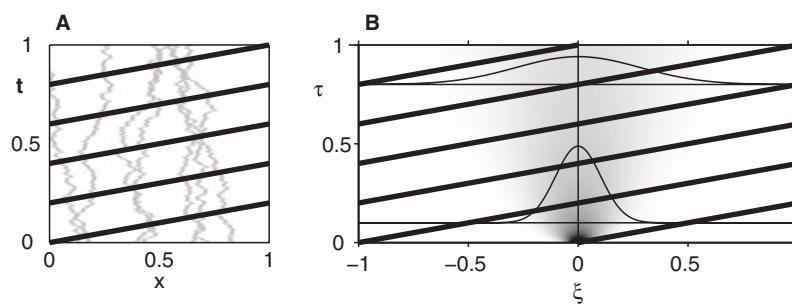


**Figure 4.1** A schematic description of the line scan. **A:** the measurement volume position along the  $x$  axis in time is marked by bold lines; traces of several diffusing particles are shown in grey; **B:** the correlation coordinates  $\xi$  and  $\tau$  at which the autocorrelation can be calculated from the measurement depicted in A are marked by bold lines; the full two-dimensional autocorrelation is shown in grey together with two profiles at early and late correlation times  $\tau$

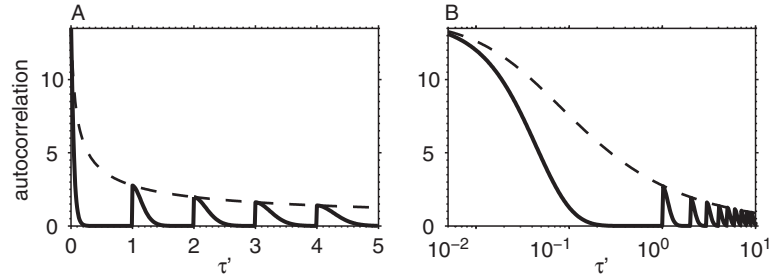


**Figure 4.2** The theoretical autocorrelation function from the line scan depicted in Figure 4.1A; the bold curve corresponds to the profile along the bold lines in Figure 4.1B for  $\xi > 0$ ; the dashed curve is a profile for  $\xi = 0$  and represents a point-FCS measurement: **A**: linear time axis, **B**: logarithmic time axis

$xy$  space. The gray curves symbolize the positions of several diffusing particles. The diagram in Figure 4.1B shows the corresponding spatiotemporal autocorrelation  $g(\xi, \tau)$ . The gray values correspond to the theoretical autocorrelation function. Two profiles of the autocorrelation along the spatial axis at early and late times are shown. They are of Gaussian shape with the width increasing with time due to diffusion. The bold lines show the parts of the two-dimensional autocorrelation function obtainable from the line scan measurement. The autocorrelation profile along the bold lines (for positive  $\xi$  values), which is the actual result of the depicted line-scan SFCS measurement, is shown in Figure 4.2. The Figures 4.1 and 4.2 essentially describe the experiment of Koppel et al. (1994).

It can be seen from Figures 4.1 and 4.2 that although SFCS does not yield the full two-dimensional autocorrelation, a suitable choice of the measured profiles of the  $g(\xi, \tau)$  (determined by the scan amplitude and period) provides a large amount of information about the autocorrelation. The high spatiotemporal resolution of SFCS may be preferable to the full, albeit lower-resolution, two-dimensional autocorrelation obtainable with STICS because of high information redundancy in  $g(\xi, \tau)$ . This redundancy is most apparent in case of pure diffusion, where the temporal profile at  $\xi = 0$  (a standard FCS curve) contains full information about the particle concentration and diffusion process. The redundancy is also present in more complex processes, for example, diffusion combined with flow.

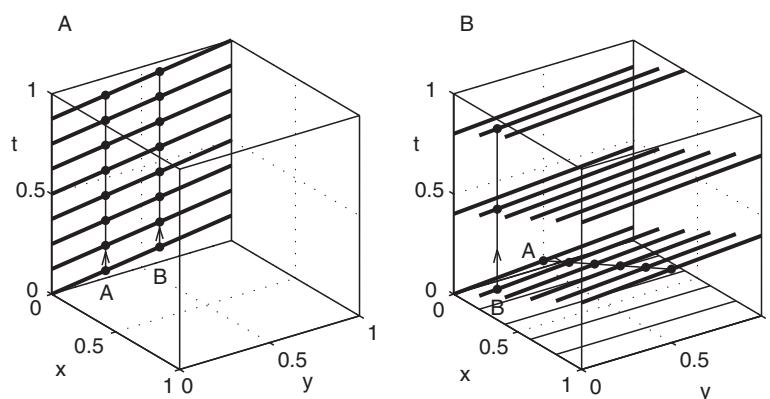
A usual FCS experiment would be represented in Figure 4.1A by a vertical line at a selected location  $x$ , and the obtained autocorrelation would correspond to a temporal profile at  $\xi = 0$  in Figure 4.1B and the dashed curve envelope in Figure 4.2. In some sense SFCS suffers from lower temporal resolution because only the points separated by the scan period ( $\tau = nT$ ) are sampled from the full FCS curve. This does not pose a problem when the diffusion is slow and when the sampling of the correlation function by the scan period  $T$  is sufficiently fine. Additionally, the missing information is partially contained in the shape (width) of the peaks of the SFCS curve (Figure 4.2).

Figure 4.1 also shows that the moving beam collects the signal from all particles along the scan path, whereas a stationary beam (FCS) would detect only the

particles that happen to diffuse to its position. There are even some positions in the shown example where no particle would be detected. This demonstrates how SFCS increases the number of independent sampling volumes which determines the effective number of independent points over which the averaging in Equation (4.2) takes place. In this way SFCS can increase the statistical accuracy of the averaging process. The scanned area (amplitude) and the scan speed (period) and their relation to the diffusion time determine the gain in accuracy due to the increase of the number of independent sample volumes and the loss of time resolution due to the probe volume “escaping” the particles before they can diffuse out and thus leave a trace about their diffusion time. The experimental parameters have to be carefully chosen depending on the diffusion characteristics and the expectations placed on the recovered parameters: whereas for slowly diffusing particles the scanned area will be large, leading to reduction in time resolution (which is not a problem for slowly diffusing or stationary particles), for fast diffusion the scanned area can be smaller allowing for the necessary higher temporal resolution, or the scanning can be abandoned altogether.

Figures 4.3 and 4.4 show several examples of scanning patterns in two spatial dimensions: a line scan, a raster scan, a circle scan, and a spiral scan. The line scan (Figure 4.3A) represents the same scenario as shown in Figure 4.1. In addition to the already discussed motivation for employing SFCS, scanning provides a way of measuring fluorescence signal autocorrelation from multiple locations simultaneously. This is done by dividing the acquired data to parts based on spatial location (points A and B in Figure 4.3A) and autocorrelating them separately. The reduced temporal resolution given by the line scan period then determines the range of measurable diffusional processes. In addition, the signals from different locations can be cross-correlated, allowing, for example, detection of uniform flows.

The raster scan (Figure 4.3B) extends the probed space to two dimensions. The signal can then be correlated along three different directions giving in principle access to three different time scales on which diffusion can be studied. Autocorrelation



**Figure 4.3** Two examples of scanning patterns: **A**: line scan, **B**: raster scan

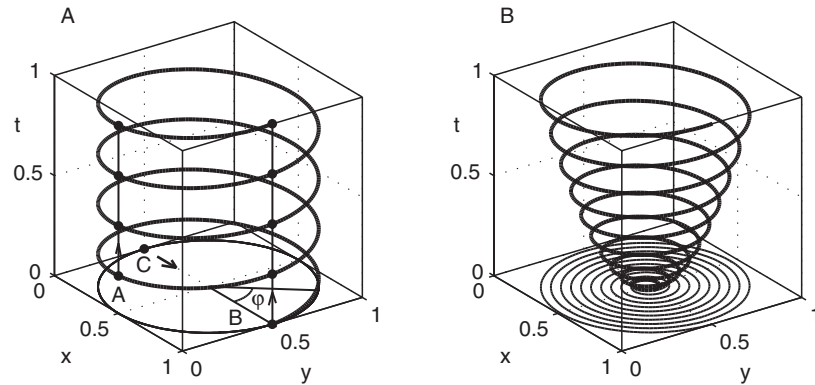


**Figure 4.4** Two examples of scanning patterns: **A**: circle scan, **B**: spiral scan

along the scanned line monitors the diffusion and other processes causing fluctuations that are faster than the scan speed. Slower diffusion will be reflected in the autocorrelation across the scan lines (line A in Figure 4.3B) and very slow diffusion can be monitored by correlating the signal across the frames (line B in Figure 4.3B). Neglecting the temporal differences between different points within one frame and performing spatiotemporal correlation across the frames reduces the raster scan SFCS to STICS.

As in line scan SFCS, individual correlation analysis of parts of the data corresponding to different spatial locations produces a map monitoring slow diffusion. This may however be problematic to realize in practice because of poor signal-to-noise ratio. Spatial mapping of flow vectors has been achieved using STICS (Hebert et al. 2005), and a similar approach is used in particle imaging velocimetry (PIV) where, however, the signal quality is better due to the far larger than molecular scales (Adrian 1991).

The line scan and raster scan modes or their variations can be easily implemented on a commercial confocal laser scanning microscope (CLSM). The presence of turning points in line and raster scan modes, and of the return period in one-directional scan means that accurate synchronization between the measurement volume position and data acquisition is necessary for correct calculation of the autocorrelation because parts of the signal stream have to be excluded from the analysis. This synchronization is to some extent implemented in CLSMs as it is the basis of the image formation.

Circle scan SFCS (Figure 4.4A) has the advantage that no turning points or dead times are present. Therefore, in the simplest case, no synchronization is necessary and the data stream can be correlated as in a usual FCS experiment. However, if circle scan SFCS is used to obtain spatially resolved information, for example, diffusion coefficients along the perimeter of the circle, accurate synchronization is obviously needed.

The knowledge of the scanning beam position at all times opens up a possibility for the measurement of magnitudes and directions of uniform flows across the

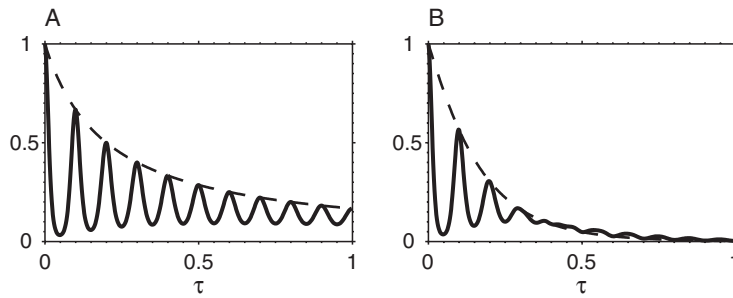
scanned region, as demonstrated by Skinner et al. (2005). The fluorescence signal is recorded as a function of time that uniquely determines the phase angle  $\varphi(t)$  of the focal point position. The fluorescence signal can then be autocorrelated with respect to a particular angle  $\varphi_0 \in (0, 2\pi)$  producing a phase angle-dependent autocorrelation function  $g(\varphi_0, \tau)$ . The autocorrelation of the data is calculated according to a modified Equation (4.2):

$$g(\varphi_0, \tau) = \frac{\langle F(t)F(t+\tau) \rangle_{\varphi_0}}{\langle F(t) \rangle_{\varphi_0}^2} - 1, \quad (4.4)$$

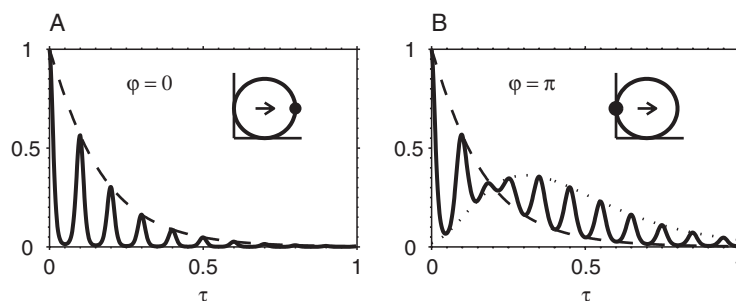
where the calculation of the average  $\langle \tau \rangle_{\varphi_0}$  is restricted to angles  $\varphi = \varphi_0 + 2\pi n$ ; that is, the averaging is done only over times  $t$  at which the focal point was at the position determined by the phase  $\varphi_0$ .

Figure 4.5 shows the theoretical autocorrelation functions of circle scan SFCS in the presence of only diffusion (Figure 4.5A) and in the presence of diffusion and directional flow (Figure 4.5B) together with usual FCS curves (dashed envelopes). Although the existence of flow can be seen in Figure 4.5B, the autocorrelation curve contains only information about its magnitude but not its direction.

Figure 4.6 shows position-sensitive autocorrelation curves calculated for angles  $\varphi_0 = 0$  (Figure 4.6A) and  $\varphi_0 = \pi$  (Figure 4.6B), for diffusion and flow in the positive  $x$ -axis direction (bold arrow in Figure 4.4A). The angle  $\varphi_0 = 0$  corresponds to the point B in Figure 4.4A and the angle  $\varphi_0 = \pi$  to the point C. The particles detected at the point B are flowing away from the scanned region, therefore they do not contribute to the autocorrelation at later times due to their flow, and the autocorrelation is fully enveloped by a standard point FCS curve (Figure 4.6A). The particles detected at position C cross the scanning path again after flowing across the circle diameter, which results in a higher correlation values at corresponding times compared to a point FCS (Figure 4.6B). The dotted envelope represents a correlation curve that would be obtained in a spatial cross-correlation experiment with the two measurement volumes positioned at points C and B. This experiment, however,



**Figure 4.5** Theoretical autocorrelation functions obtained with a circle scan: **A**: in the presence of diffusion only; **B**: in the presence of diffusion and uniform flow; this curve represents the average of the position-sensitive autocorrelation (Figure 4.6) over all angles  $\varphi$



**Figure 4.6** Theoretical position-sensitive autocorrelation functions obtained with a circle scan in the presence of diffusion and uniform flow: **A**: autocorrelation for  $\varphi = 0$ , that is, for the point where the flowing molecules leave the scanned region; **B**: autocorrelation for  $\varphi = \pi$ , that is, for the point where the flowing molecules enter the scanned region

allows one to determine only the projection of the velocity vector onto the line connecting the two points, not the flow direction in the  $xy$ -plane. The advantage of the circle scan SFCS lies in the fact that one measurement dataset is used to calculate autocorrelation for all phase angles  $\varphi_0$  allowing accurate determination of the direction of flow without any a priori knowledge.

Scanning FCS has the potential to diminish the negative effects of photobleaching, which is an important limiting factor in FCS, especially when two-photon excitation is employed. The local depletion of fluorescent molecules and apparent shortening of diffusion times due to photodestruction are encountered when high excitation powers are used. The use of high excitation powers is motivated by the fact that the signal-to-noise ratio in the experimental curves increases with the fluorescence count rate per molecule.

In SFCS the total excitation light dose is distributed over the scanned region. In addition, the depleted concentration of fluorescent molecules at one location can be partially recovered due to the diffusional influx of intact molecules before the same spot is revisited by the excitation beam in the next scan cycle. Scanning FCS does not reduce the total photobleaching (if linear dependence between excitation dose and photobleaching yield is assumed) but alleviates its effects on the autocorrelation by “escaping” the regions containing photobleached molecules and spreading the photobleached molecules over a larger area. The circle scan lowers the excitation dose at any position by a factor equal to the ratio between the circle circumference and the measurement spot diameter. Alternatively, the spiral scan with a constant speed (Figure 4.4B) can be applied to further decrease the excitation dose at any location. This approach then comes close to ICS if the molecules are immobile.

An interesting question is whether photobleaching itself could be reduced, not only its negative consequences. If photobleaching is mediated by the triplet states, as shown in some cases (Widengren and Rigler 1996; Dittrich and Schwille 2001), exciting one location for a time shorter than the time needed for a significant build-up of the triplet state population (determined by the rates of transitions between the molecular energy

states) and revisiting the same location after all the triplet states have decayed back to the ground state would lower the possibility of triplet–triplet absorption, and therefore photobleaching. However, rather high scanning speeds, possibly achievable with acousto-optical deflectors, would be necessary to explore this possibility.

Scanning FCS can be combined with all variations of FCS. For example, the cross-correlation analysis of fluorescence fluctuations in two detection channels defined by different emission wavelengths (Schwille et al. 1997) or emission polarizations (Barcellona et al. 2004) could benefit from the combination with scanning. The applications of cross-correlation analysis often focus on the relative amplitudes of the autocorrelation and cross-correlation of the signal rather than on the diffusion kinetics, therefore a partial loss of the information on diffusion kinetics present in some SFCS implementations is not a problem. Scanning FCS can be also combined with the analysis of distribution of photocounts in the binned fluorescence signal  $F(p)$  (photon counting histogram (Chen et al. 1999), fluorescence intensity distribution analysis (Kask et al. 1999)), or higher-order auto/cross-correlation analysis (Palmer and Thompson 1987, 1989; Thompson 1991).

### 4.3 Applications

The early applications of SFCS aimed mainly at the determination of the concentration and the diffusion of the molecules was considered negligible. The reason for scanning was the need to record the fluorescence signal from a sufficient number of statistically independent volumes in systems where the diffusion of the molecules was too slow to guarantee fast turnover of the molecules in the measurement volume. Initially, the sample rather than the excitation beam was moved.

In 1976 Weissman et al. (1976) used a technique that could be regarded as the first application of SFCS to measure molecular weights of DNA molecules stained with ethidium bromide. Because of the relatively large measurement volume and slow diffusion of DNA molecules the sample was placed in a cylindrical cell and rotated with a period of 4 s while the measurement volume was stationary. In this way sampling from approximately 400 independent volumes was achieved and proved to be sufficient for the calculation of the average magnitude of fluctuations necessary to obtain the DNA concentration and subsequently the molecular weight.

The technique of Weissman et al. was modified by Nicoli et al. (1980) who moved the sample placed in a thin cylindrical tube linearly up and down by mounting it on a loudspeaker. The goal of the measurement was to investigate the binding between antibody and antigen attached to a bead of 3–5  $\mu\text{m}$  diameter. The two populations of fluorescently labeled antibodies—free in solution and bound to the antigen on the bead—are then distinguished on basis of their different diffusion times. After a suitably chosen scan period  $T$  the correlation of unbound antibodies disappears and the correlation of slowly diffusing bound molecules is still present.

A line scan SFCS was introduced by Petersen in 1984 (Petersen 1984, 1986; Petersen et al. 1986) as a modification of FCS for slowly diffusing species in cell

membranes. The goal was to measure aggregation, that is, to estimate the number of monomers per aggregate, or to obtain information about the distribution of aggregate sizes. The fluorescence signal was recorded while translating the sample linearly with a constant velocity, and then autocorrelated. In the theoretical treatment (Petersen 1986) a formula is presented relating the amplitude of the autocorrelation to the mean number and variance of the number of monomers per aggregate. Several special cases of multimodal distributions (sums of unimodal distributions characterized by the mean and the variance) are discussed, for example, the simple aggregation reaction  $nA \rightarrow A_n$  where only monomers and aggregates of degree  $n$  are present, or the situation with monomers and aggregates with Poisson-distributed sizes. The line-scanning SFCS was applied to measure the mean number of aggregates of Sindbis virus and vesicular stomatitis virus glycoproteins on the membrane of fibroblasts. The same SFCS implementation was used by St-Pierre and Petersen (1990) to study ligand binding to aggregated receptors, or more precisely, to find the relationship between the degree of ligand binding and the state of receptor aggregation. Another application involved the measurement of epidermal growth factor receptor distribution on A431 cells (St-Pierre and Petersen 1992).

The applications of SFCS described so far were concerned only with the amplitude of the correlation function and did not attempt to obtain any information about the diffusion of the fluorescent species. Meyer and Schindler (1988) used circular scanning to measure particle concentration and diffusion coefficient. The circular path was achieved by rotating an optical unit holding a tilted objective. The autocorrelation of the measured fluorescence exhibited periodic peaks at times corresponding to the period  $T$  of rotation. The amplitude of the peak at time  $\tau = 0$  provided the particle number, and the decrease of the amplitude and the broadening of the peaks at longer lag times  $\tau = nT$  was used to determine the diffusion coefficient. The method was applied to study concentration- and calcium-dependent aggregation of lipid vesicles, and the time course of aggregation of a membrane matrix protein from *E. coli* in lipid monolayer. The range of diffusion coefficients  $D$  that can be determined with the used setup is  $10^{-7}$ – $10^{-10}$   $\text{cm}^2\text{s}^{-1}$ .

Koppel et al. (1994) used a commercial confocal laser scanning microscope (CLSM) to perform SFCS by repeatedly scanning a single line across the sample. The major advantage of using a CLSM compared to the above-described techniques is a smaller detection volume and the possibility of faster scanning. The correlation curves were fitted to a model of two-dimensional diffusion plus uniform flow (representing in this case the moving excitation beam) which yielded the particle number and the diffusion coefficient. The method has been applied to the measurement of the diffusion coefficient of ethidium bromide-stained DNA of different sizes in solution, and to the analysis of diffusion of colloidal gold particles in suspension and bound to PE in supported planar bilayers. In case of the gold particles scattered light rather than fluorescence was used to detect the particles. The maximum diffusion coefficient measurable with this method is on the order of  $10^{-7}$   $\text{cm}^2\text{s}^{-1}$ . Separate analysis of parts of the recorded data was demonstrated, allowing the detection of variations in particle concentrations or diffusion coefficients at different regions along the scanned line.



Berland et al. (1996) demonstrated the use of two-photon excitation with a circle scan SFCS on a home-built CLSM for the measurement of particle concentrations. The method was applied to studying protein aggregation and dissociation in solution. Measuring the dependence of the number of independent particles (dimers and tetramers) on the total protein concentration and assuming equilibrium between dimers and tetramers dissociation constant was determined. Kinetic measurements of dissociation upon dilution and measurements of pH-dependent dissociation were also performed.

An approach similar to SFCS has been applied by Winkler et al. (1999) to confocal fluorescence coincidence analysis, where association between two molecular fragments labeled with different fluorophores is identified by coincident detection of photons in two spectral detection channels. The results demonstrate that moving the sample with frequencies as low as 3 Hz significantly improves the S/N ratio, thus allowing shorter measurement times required for high-throughput screening applications.

Amediek et al. (2002) combined dual-color cross-correlation analysis with scanning. The authors used piezo-driven sample stage moving in several scanning patterns: line, spiral, and a random scan, and investigated their effects on the auto- and cross-correlation curves recorded from immobile samples. The investigated systems were GFP-DsRed fusion proteins immobilized in a gel and double-labeled cholera holotoxin bound to immobile receptors on a cell membrane. Scanning the sample allowed autocorrelation and cross-correlation curves to be recorded and to identify co-localization on basis of the cross-correlation amplitude, a task practically impossible with a standard FCS because of photobleaching of very slowly diffusing or immobile molecules. Among the employed scanning patterns the random scan proved to be most suitable, possibly due to the absence of artefacts arising from the periodicity in the other patterns.

Ruan et al. (2004) applied circle scan SFCS to study slow diffusion of membrane proteins in giant unilamellar vesicles (GUV). The geometry of the experiment was such that the circular path of the measurement volume intersected the surface of the GUV twice, one half of the scan path laid outside the GUV and one half inside. The detected fluorescence signal was processed in such a way that autocorrelation curve for every point along the circular path was obtained. With this approach fast diffusion of the labeled antibody in the outer solution and slow diffusion of the antibody bound to the membrane protein were measured. The application of SFCS in this case does not increase the number of independently sampled volumes on the membrane (only two locations are measured) but allows simultaneous measurement of autocorrelation in different locations, the points along the circular path. Additionally, small movements of the GUV which can prevent point FCS measurements on moving membrane can be compensated for by shifting the signal records from subsequent scans relative to each other, before the data are correlated.

Xiao et al. (2005) used a sample-scanning CLSM to image fluorescent molecules immobilized on a surface and in polystyrene films, and to measure autocorrelation of their fluorescence via line scan SFCS. The authors were interested in the bright/dark state transitions (triplet or radical ion state) on the microsecond time scale. It was

suggested that this method could be applied to determination of the rates of association and dissociation of freely diffusing molecules with immobilized molecules, for example in screening of surface-patterned peptide and nucleic acid microarrays.

Digman et al. (2005a,b) performed autocorrelation analysis on images obtained with a commercial CLSM and a home-built two-photon scanning microscope. The two-dimensional autocorrelation of the raster-scan images provided information about fast diffusion (or scan speed and measurement volume size) along the fast scan axis, as in the line scan SFCS. The autocorrelation decay along the slow scan axis reflects diffusion on a longer time scale. Raster- and line-scan SFCS were demonstrated on paxillin-EGFP diffusing in cytosol of CHOK1 cells.

The most detailed and comprehensive analysis of the possibilities of circular-scan SFCS so far has been presented by Skinner et al. (2005). Taking advantage of synchronization between the beam position along the circular path characterized by the phase angle  $\varphi$  and the data acquisition the authors introduce position-sensitive SFCS (PSFCS). This variation of SFCS allows calculation of the autocorrelation as a function of the phase  $\varphi$  and lag time  $\tau$  which can be used to measure, in addition to diffusion, the direction and speed of flow and the position of immobile particles (see Figures 4.5 and 4.6). If required, an appropriate normalization procedure eliminates unwanted effects in autocorrelation caused by immobile particles. The circular-scan SFCS was shown to be less sensitive to photobleaching than standard FCS. The method has been demonstrated on freely diffusing and uniformly flowing dye in solution and EGFP diffusing in cells.

## 4.4 Implementation

The first applications of SFCS used special experimental setups designed and suitable only for a particular type of experiment (Weissman et al. 1976; Nicoli et al. 1980; Meyer and Schindler 1988). The disadvantages of most of these setups are inflexibility, relatively large measurement volume, and the need to move the sample, which could lead to sample distortions due to its inertia and elastic properties.

With the development of laser scanning microscopy a home-built or a commercial multipurpose CLSM has become the most common instrument used for SFCS. Although a line or a raster scan is easily realizable with a commercial CLSM, the inaccessibility of the control software source code makes the implementation of other scan modes practically impossible. The advantage of a home-built system is the full control over the scanner movement. Furthermore, the emission collection efficiency and the profile of the excitation laser beam at the objective back aperture are perhaps more crucial parameters in fluorescence correlation measurements than in imaging applications. A custom-built setup allows for optimization of these parameters.

We present here a two-photon laser scanning setup built in our laboratory as an example of a versatile instrument for two-photon imaging and SFCS applications.

#### 4.4.1 Light Source

A tunable Ti:Sapph laser Mira 900-F (Coherent, Santa Clara, USA; 76 MHz, 700–1000 nm, 100–150 fs pulse length) pumped by frequency doubled 10 W Nd:YVO<sub>4</sub> laser Verdi V10 (Coherent; 532 nm) is used as the excitation source. Two-photon excitation has certain advantages over one-photon excitation: the excitation is limited to a well-confined volume, therefore no additional volume reduction with the help of a pinhole is needed, and, for the same reason, the total photobleaching in the sample is lower. This fact, together with weaker scattering of light of longer wavelengths makes two-photon excitation particularly suitable for measurements in deeper tissue (König 2000).

The drawback of two-photon excitation is stronger photobleaching in the focal point with the consequence that significantly lower count rates per molecule, and therefore a lower signal-to-noise ratio, can be achieved compared to one-photon excitation.

The described setup could in principle be modified to a one-photon excitation mode by exchanging the laser, using an appropriate beamsplitter and emission filters, and installing a pinhole in the emission path. This could be realized, for example, by coupling the avalanche photodiodes (APD) with an optical fiber of selected core diameter, and placing the entry of the fiber, playing the role of the pinhole, to the present position of APDs.

#### 4.4.2 Optical Part

The optical path of the excitation and emitted light in the microscope is shown in Figure 4.7. The laser beam is initially expanded by the combination of lenses L1 and L2 in order to overfill the entrance aperture of the objective after having passed through

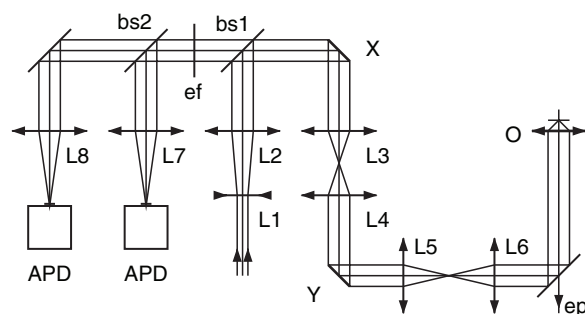


**Figure 4.7** Optical part of the two-photon laser scanning microscope: L1–L8: lenses; bs1, bs2: beam splitters; ef: emission filter; X, Y: scanners with mounted mirrors; O: objective; ep: eyepieces; APD: avalanche photodiode

the rest of the scanning optics. Optionally, the laser beam can be passed through a prism group velocity dispersion compensator before expansion if the pulse duration in the focal point of the objective needs to be optimized (Müller et al. 1998).

The beamsplitter bs1 reflects the infrared excitation beam and transmits the fluorescence collected by the objective. The lenses L3 and L4 image the fast scanner X onto the slow scanner Y and the lenses L5 and L6 image the slow scanner onto the back objective aperture while collimating the beam. The objective then focuses the excitation beam into a diffraction-limited spot and collects the fluorescence which is descanned by following the same path as the excitation beam in the opposite direction. After having been transmitted by the beamsplitter bs1 the fluorescence can be divided into two spectral channels by the beamsplitter bs2 or, alternatively, divided by a polarizing beamsplitter into two polarization components. With the help of the lenses L7 and L8 the fluorescence is focused onto the active area of the avalanche photodiodes (APD; type SPCM-CD2801, PerkinElmer, Wellesley, USA).

The scanning optics is built around an inverted IX 71 microscope (Olympus, Tokyo, Japan). The light enters via a side hole in the revolver holding the filter cubes and is reflected upwards by a mirror mounted in a custom-made filter cube. The light therefore does not pass through the microscope tube lens.

The beam is steered by two mirrors mounted on shafts of closed-loop galvanometer scanners (VM2000, GSI Lumonics GmbH, Unterschleißheim, Germany). The maximum scan frequency is limited to 50–500 Hz, depending on the amplitude of the scan. Faster scanning could be achieved by resonant scanners, however, at the cost of losing the flexibility of choosing the scan pattern. As an alternative to mechanical scanners, much faster acousto-optical deflectors (AOD) can be used to steer the beam (Roodra et al. 2004).

### 4.4.3 *Electronics*

A diagram depicting the electronic components of the experimental setup and their connections is shown in Figure 4.8. The central part of the microscope electronics is formed by the ADWin Gold system (Jäger GmbH, Lorsch, Germany), a general-purpose microprocessor-controlled unit containing several analog and digital inputs and outputs, and counters. The ADWin module generates an arbitrary voltage waveform which, via the scanner drivers (MiniSax, GSI Lumonics), determines the angular deflection of the scanners. The scanners contain a position sensor generating a signal that is provided to the user by the MiniSax drivers. This signal can be recorded by the ADWin module to monitor the real scanner position.

In the imaging mode, the fast scanner X is driven with a voltage waveform of a sawlike shape with rounded turning points formed by fragments of a parabola. The waveform shape has been optimized to maximize the linearity of the scan and to minimize the time needed for changing the direction. The sample is illuminated for the whole time of the scanning cycle (no beam blocking takes place) and the signal is recorded while scanning in both directions (bidirectional scan). The slow scanner Y is moved stepwise during the reversal period of the fast mirror.

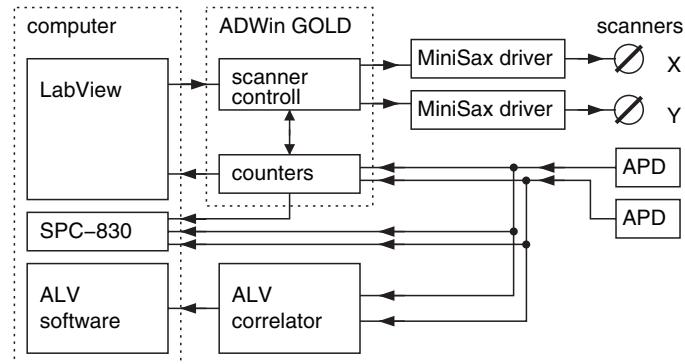


**Figure 4.8** Electrical part of the two-photon laser scanning microscope

The output signal of the APD detectors consists of a sequence of 40 ns TTL pulses, each corresponding to a detected photon. The pulses are counted by the counters in the ADWin module and arranged accordingly into pixels of the image.

The APD outputs are also passed to a hardware correlator ALV-6000 (ALV GmbH, Langen, Germany). This correlator is able to process two input signals and calculate their autocorrelations or a cross-correlation, although not both simultaneously. Alternatively, the APD outputs can be processed by a SPC-830 photon counting module (Becker & Hickl GmbH, Berlin, Germany). The SPC-830 module measures the photon arrival time of every photon and stores the data stream into a file. The complete fluorescence intensity trace is then available for offline analysis.

With the help of pixel, line, and frame clock signals generated by the ADWin module and a laser synchronization signal, the SPC-830 can construct fluorescence images, and thanks to precise picosecond timing provided by the time-correlated single photon counting (TCSPC) method fluorescence lifetime imaging (FLIM) can be performed.

The position of the observed section of the sample along the optical axis (z-section) is controlled by a piezo nano-positioning device PIFOC P-721.10 (Physik Instrumente GmbH, Waldbronn, Germany) on which the objective is mounted.

#### 4.4.4 Software

The user interface and the control of the ADWin module and the PIFOC device is provided by a program written in the LabView environment (National Instruments, Austin, USA). Based on the user-defined parameters the waveforms for either the image acquisition or for the SFCS measurement are calculated and passed as an array of values from LabView to ADWin Gold which then generates the actual driving voltage signal. LabView reads the pixel count values from ADWin when they become available, and uses them to create the fluorescence image.

The processor in the ADWin module is capable of running several processes (programs) in a real-time mode. In the presented application four processes are used: one low-priority process checking the status of the scanners and three high-priority processes: one for image acquisition, one for waveform generation for the SFCS measurements and one for positioning the laser beam to any location selected by the user. The execution of these processes is again controlled by LabView.

Due to the finite time response of the mechanical scanners there is a time lag between the driving voltage signal and the actual scanner position. This time lag can lead to synchronization artefacts between the lines scanned in opposite directions which are manifested as a relative shift of the odd and even lines in the image. The time lag occurring with the particular waveform used in the described scanning design varies only slightly with the scan speed and amplitude and is largely taken into account during the image reconstruction. However, a small residual variation of the time lag may still be apparent in the image. The remaining line shift can be easily corrected for by maximizing the overlap between the neighboring lines by finding an optimal value of the line shift  $d$ . Expressed mathematically, the following function has to be minimized by varying  $d$ :

$$f(d) = \frac{1}{\lfloor n/2 \rfloor (n-d)} \sum_{j=0}^{\lfloor n/2 \rfloor - 1} \sum_{i=0}^{n-d-1} (c(i, 2j) - c(i+d, 2j+1))^2, \quad (4.5)$$

where  $c(i, j)$  is the number of counts in the image pixel  $(i, j)$ ,  $i$  and  $j$  are the column and row indices, respectively, and the size of the image is  $n \times n$ .

The synchronization problem is not immediately apparent in a one-directional scan system, because all lines are shifted in the same direction resulting in the shift of the whole image. Although this does not pose a problem in purely imaging applications, in our case, where we want to perform measurement in a well-defined location, be it a point-FCS or a more complex SFCS experiment, exact synchronization between the image on the screen and the beam position within the sample is necessary. From this point of view the one-directional scan is not easier to implement, and because it involves more dead time, the bidirectional scan was chosen for the described device. Figure 4.9 demonstrates the measurement of the fluorescence autocorrelation at a defined location within a cell.

Both the ALV autocorrelator and the SPC-830 photon counting module are supplied with software fully controlling the instruments. The two devices are operating independently, without any interface to the main LabView program.

#### 4.4.5 Data analysis

The ALV autocorrelator provides directly the autocorrelation and cross-correlation functions but not a full photon sequence with high temporal resolution making a more advanced analysis needed in some SFCS applications impossible. The SPC-830

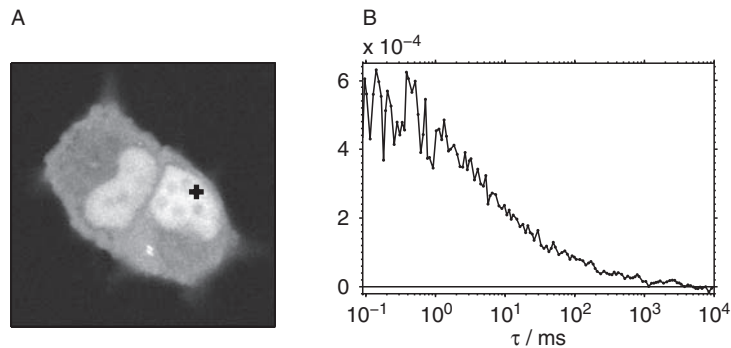


**Figure 4.9** Two-photon excitation fluorescence image of a GFP-expressing cell (**A**) and the fluorescence autocorrelation curve measured at the point indicated by the cross (**B**)

module provides a full photon sequence that is correlated offline with a custom-written software (C++) using the multiple-tau approach (Magatti and Ferri 2001). Because the complete fluorescence intensity signal  $F(p)$  is available, various ways of data processing as described above can be implemented.

## 4.5 Conclusion

Scanning FCS is not a single technique but rather a whole family of techniques spanning the gap between the most widely used one-point FCS on one side and ICS on the other side. We have tried to present here various SFCS approaches in relation to FCS and ICS, and to identify the reasons why they are preferable to other fluorescence correlation methods in certain situations. The choice of a particular SFCS implementation is governed by two factors: the information we want to obtain about the sample and the sample properties limiting the range of applicable techniques.

The main reasons that can make SFCS the method of choice instead of FCS or other correlation techniques can be summarized as follows.

- Improve signal-to-noise ratio by increasing the number of statistically independent samples where time averaging is not satisfactory (immobile or slowly diffusing molecules)
- Diminish or avoid the effects of photobleaching (mainly with two-photon excitation)
- Measure correlation at more locations (pseudo-) simultaneously; measure diffusion and flows simultaneously (position-sensitive SFCS)

There are certainly limits to the applicability of SFCS. For example, the scanned region should be homogeneous on a large scale, otherwise a fixed pattern in the detected fluorescence intensity gives rise to unwanted correlations. These effects can

perhaps be eliminated by procedures similar to those dealing with background in ICS (Wiseman and Petersen 1999). Alternatively, they can be taken advantage of in determining the position of immobile molecules (Skinner et al. 2005). Another limitation is the partial loss of diffusion information. This is not likely to be a major hindrance inasmuch as slow diffusion is reflected in the autocorrelation obtained by scanning with a periodic pattern, and other applications may not be interested in diffusion at all, such as cross-correlation binding studies or measurements on immobile molecules.

## References

- R. J. Adrian. Particle-imaging techniques for experimental fluid-mechanics. *Annu. Rev. Fluid Mech.*, 23:261–304, 1991.
- A. Amediek, E. Haustein, D. Scherfeld, and P. Schwille. Scanning dual-color cross-correlation analysis for dynamic co-localization studies of immobile molecules. *Single Molecules*, 3(4):201–210, 2002.
- K. Bacia and P. Schwille. A dynamic view of cellular processes by in vivo fluorescence auto- and cross-correlation spectroscopy. *Methods*, 29(1):74–85, 2003.
- M. L. Barcellona, S. Gammon, T. Hazlett, M. A. Digman, and E. Gratton. Polarized fluorescence correlation spectroscopy of DNA-DAPI complexes. *Microsc. Res. Tech.*, 65(4–5):205–217, 2004.
- K. M. Berland, P. T. C. So, Y. Chen, W. W. Mantulin, and E. Gratton. Scanning two-photon fluctuation correlation spectroscopy: Particle counting measurements for detection of molecular aggregation. *Biophys. J.*, 71(1):410–420, 1996.
- M. Brinkmeier, K. Dorre, J. Stephan, and M. Eigen. Two beam cross correlation: A method to characterize transport phenomena in micrometer-sized structures. *Anal. Chem.*, 71(3):609–616, 1999.
- C. M. Brown and N. O. Petersen. An image correlation analysis of the distribution of clathrin associated adaptor protein (AP-2) at the plasma membrane. *J. Cell Sci.*, 111:271–281, 1998.
- Y. Chen, J. D. Müller, P. T. C. So, and E. Gratton. The photon counting histogram in fluorescence fluctuation spectroscopy. *Biophys. J.*, 77(1):553–567, 1999.
- M. A. Digman, C. M. Brown, P. Sengupta, P. W. Wiseman, A. R. Horwitz, and E. Gratton. Measuring fast dynamics in solutions and cells with a laser scanning microscope. *Biophys. J.*, 89(2):1317–1327, 2005a.
- M. A. Digman, P. Sengupta, P. W. Wiseman, C. M. Brown, A. R. Horwitz, and E. Gratton. Fluctuation correlation spectroscopy with a laser-scanning microscope: Exploiting the hidden time structure. *Biophys. J.*, 88(5):L33–L36, 2005b.
- P. S. Dittrich and P. Schwille. Photobleaching and stabilization of fluorophores used for single-molecule analysis with one- and two-photon excitation. *Appl. Phys. B*, 73(8):829–837, 2001.
- S. Felekyan, R. Kuhnemuth, V. Kudryavtsev, C. Sandhagen, W. Becker, and C. A. M. Seidel. Full correlation from picoseconds to seconds by time-resolved and time-correlated single photon detection. *Rev. Sci. Instrum.*, 76(8):083104, 2005.
- M. Gosch and R. Rigler. Fluorescence correlation spectroscopy of molecular motions and kinetics. *Adv. Drug Deliv. Rev.*, 57(1):169–190, 2005.
- B. Hebert, S. Costantino, and P. W. Wiseman. Spatiotemporal image correlation spectroscopy (STICS) theory, verification, and application to protein velocity mapping in living CHO cells. *Biophys. J.*, 88(5):3601–3614, 2005.
- S. T. Hess, S. H. Huang, A. A. Heikal, and W. W. Webb. Biological and chemical applications of fluorescence correlation spectroscopy: A review. *Biochemistry*, 41(3):697–705, 2002.
- P. Kask, K. Palo, D. Ullmann, and K. Gall. Fluorescence-intensity distribution analysis and its application in biomolecular detection technology. *Proc. Natl. Acad. Sci. U.S.A.*, 96(24):13756–13761, 1999.
- K. König. Multiphoton microscopy in life sciences. *J. Microsc.*, 200:83–104, 2000.



- D. E. Koppel, F. Morgan, A. E. Cowan, and J. H. Carson. Scanning concentration correlation spectroscopy using the confocal laser microscope. *Biophys. J.*, 66(2):502–507, 1994.
- O. Krichevsky and G. Bonnet. Fluorescence correlation spectroscopy: The technique and its applications. *Rep. Prog. Phys.*, 65(2):251–297, 2002.
- D. Magatti and F. Ferri. Fast multi-tau real-time software correlator for dynamic light scattering. *Appl. Opt.*, 40(24):4011–4021, 2001.
- T. Meyer and H. Schindler. Particle counting by fluorescence correlation spectroscopy - simultaneous measurement of aggregation and diffusion of molecules in solutions and in membranes. *Biophys. J.*, 54(6):983–993, 1988.
- M. Müller, J. Squier, R. Wolleschensky, U. Simon, and G. J. Brakenhoff. Dispersion precompensation of 15 femtosecond optical pulses for high-numerical-aperture objectives. *J. Microsc.*, 191:141–150, 1998.
- D. F. Nicoli, J. Briggs, and V. B. Elings. Fluorescence immunoassay based on long-time correlations of number fluctuations. *Proc. Natl. Acad. Sci. U.S.A.*, 77(8):4904–4908, 1980.
- A. G. Palmer and N. L. Thompson. Molecular aggregation characterized by high-order auto-correlation in fluorescence correlation spectroscopy. *Biophys. J.*, 52(2):257–270, 1987.
- A. G. Palmer and N. L. Thompson. High-order fluorescence fluctuation analysis of model protein clusters. *Proc. Natl. Acad. Sci. U.S.A.*, 86(16):6148–6152, 1989.
- N. O. Petersen. Diffusion and aggregation in biological membranes. *Can. J. Biochem. Cell Biol.*, 62(11):1158–1166, 1984.
- N. O. Petersen. Scanning fluorescence correlation spectroscopy 1. Theory and simulation of aggregation measurements. *Biophys. J.*, 49(4):809–815, 1986.
- N. O. Petersen, D. C. Johnson, and M. J. Schlessinger. Scanning fluorescence correlation spectroscopy 2. Application to virus glycoprotein aggregation. *Biophys. J.*, 49(4):817–820, 1986.
- N. O. Petersen, P. L. Hoddellius, P. W. Wiseman, O. Seger, and K. E. Magnusson. Quantitation of membrane-receptor distributions by image correlation spectroscopy—Concept and application. *Biophys. J.*, 65(3):1135–1146, 1993.
- W. Reisner, K. J. Morton, R. Riehn, Y. M. Wang, Z. N. Yu, M. Rosen, J. C. Sturm, S. Y. Chou, E. Frey, and R. H. Austin. Statics and dynamics of single DNA molecules confined in nanochannels. *Phys. Rev. Lett.*, 94(19):196101, 2005.
- R. Rigler and E. S. Elson, editors. *Fluorescence Correlation Spectroscopy. Theory and Application*. Chemical Physics Series. Springer Verlag, Berlin, 1st edition, 2001.
- J. V. Rocheleau, P. W. Wiseman, and N. O. Petersen. Isolation of bright aggregate fluctuations in a multipopulation image correlation spectroscopy system using intensity subtraction. *Biophys. J.*, 84(6):4011–4022, 2003.
- R. D. Roorda, T. M. Hohl, R. Toledo-Crow, and G. Miesenbock. Video-rate nonlinear microscopy of neuronal membrane dynamics with genetically encoded probes. *J. Neurophysiol.*, 92(1):609–621, 2004.
- Q. Q. Ruan, M. A. Cheng, M. Levi, E. Gratton, and W. W. Mantulin. Spatial-temporal studies of membrane dynamics: Scanning fluorescence correlation spectroscopy (SFCS). *Biophys. J.*, 87(2):1260–1267, 2004.
- P. Schwille. Fluorescence correlation spectroscopy and its potential for intracellular applications. *Cell Biochem. Biophys.*, 34(3):383–408, 2001.
- P. Schwille, F. J. Meyer-Almes, and R. Rigler. Dual-color fluorescence cross-correlation spectroscopy for multicomponent diffusional analysis in solution. *Biophys. J.*, 72(4):1878–1886, 1997.
- J. P. Skinner, Y. Chen, and J. D. Muller. Position-sensitive scanning fluorescence correlation spectroscopy. *Biophys. J.*, 89(2):1288–1301, 2005.
- M. Srivastava and N. O. Petersen. Image cross-correlation spectroscopy: A new experimental biophysical approach to measurement of slow diffusion of fluorescent molecules. *Methods Cell Sci.*, 18:47–54, 1996.
- P. R. St-Pierre and N. O. Petersen. Relative ligand-binding to small or large aggregates measured by scanning correlation spectroscopy. *Biophys. J.*, 58(2):503–511, 1990.

- P. R. St-Pierre and N. O. Petersen. Average density and size of microclusters of epidermal growth-factor receptors on A431 cells. *Biochemistry*, 31(9):2459–2463, 1992.
- N. L. Thompson. Fluorescence correlation spectroscopy. In J. R. Lakowicz, editor, *Topics in Fluorescence Spectroscopy, Volume I: Techniques*, pages 337–378. Plenum Press, New York, 1991.
- N. L. Thompson, A. M. Lieto, and N. W. Allen. Recent advances in fluorescence correlation spectroscopy. *Curr. Opin. Struct. Biol.*, 12(5):634–641, 2002.
- M. B. Weissman. Fluctuation spectroscopy. *Annu. Rev. Phys. Chem.*, 32:205–232, 1981.
- M. Weissman, H. Schindler, and G. Feher. Determination of molecular-weights by fluctuation spectroscopy - application to DNA. *Proc. Natl. Acad. Sci. U.S.A.*, 73(8):2776–2780, 1976.
- J. Widengren and R. Rigler. Mechanisms of photobleaching investigated by fluorescence correlation spectroscopy. *Bioimaging*, 4:149–157, 1996.
- T. Winkler, U. Kettling, A. Koltermann, and M. Eigen. Confocal fluorescence coincidence analysis: An approach to ultra high-throughput screening. *Proc. Natl. Acad. Sci. U.S.A.*, 96(4):1375–1378, 1999.
- P. W. Wiseman and N. O. Petersen. Image correlation spectroscopy. II. Optimization for ultrasensitive detection of preexisting platelet-derived growth factor-beta receptor oligomers on intact cells. *Biophys. J.*, 76(2):963–977, 1999.
- P. W. Wiseman, J. A. Squier, M. H. Ellisman, and K. R. Wilson. Two-photon image correlation spectroscopy and image cross-correlation spectroscopy. *J. Microsc.*, 200:14–25, 2000.
- P. W. Wiseman, C. M. Brown, D. J. Webb, B. Hebert, N. L. Johnson, J. A. Squier, M. H. Ellisman, and A. F. Horwitz. Spatial mapping of integrin interactions and dynamics during cell migration by image correlation microscopy. *J. Cell Sci.*, 117(23):5521–5534, 2004.
- Y. Xiao, V. Buschmann, and K. D. Weston. Scanning fluorescence correlation spectroscopy: A tool for probing microsecond dynamics of surface-bound fluorescent species. *Anal. Chem.*, 77(1):36–46, 2005.

## Chapter 5

# Single-Molecule Imaging of Cellular Signaling

Sandra de Keijzer, B. Ewa Snaar-Jagalska, Herman P. Spaink,  
and Thomas Schmidt(✉)

5.1	Single-Molecule Fluorescence Microscopy in Living Cells.....	108
5.2	Model Organism for Studying Signal Transduction.....	110
5.3	Optical Set-Up and Data Acquisition.....	111
5.4	Autofluorescence of <i>Dictyostelium Discoideum</i> Cells.....	112
5.5	Data Analysis.....	114
5.5.1	Background Subtraction.....	114
5.5.2	Identification of Single Molecules.....	116
5.5.3	Tracing Single Molecules.....	116
5.6	Stoichiometry of Receptors in the Plasma Membrane.....	119
5.7	Membrane Organization.....	121
5.7.1	Fluorescent Lipid Insertion.....	122
5.7.2	Fluorescent Membrane Markers.....	122
5.7.3	cAR1 Mobility.....	123
5.8	Prospects.....	125
	References.....	126

**Abstract** Single-molecule microscopy is an emerging technique to understand the function of a protein in the context of its natural environment. In our laboratory this technique has been used to study the dynamics of signal transduction in vivo. A multitude of signal transduction cascades are initiated by interactions between proteins in the plasma membrane. These cascades start by binding a ligand to its receptor, thereby activating downstream signaling pathways which finally result in complex cellular responses. To fully understand these processes it is important to study the initial steps of the signaling cascades. Standard biological assays mostly call for overexpression of the proteins and high concentrations of ligand. This sets severe limits to the interpretation of, for instance, the time-course of the observations, given the large temporal spread caused by the diffusion-limited binding processes. Methods and limitations of single-molecule microscopy for the study

---

Thomas Schmidt  
Physics of Life Processes, Leiden Institute of Physics, Leiden University, P.O. Box 9504, 2300 RA,  
The Netherlands, Schmidt@Physics.LeidenUniv.nl

R. Rigler and H. Vogel (eds.), *Single Molecules and Nanotechnology*. 107  
*Springer Series in Biophysics 12*.  
© Springer-Verlag Berlin Heidelberg 2008

of cell signaling are discussed on the example of the chemotactic signaling of the slime-mold *Dictyostelium discoideum*. Single-molecule studies, as reviewed in this chapter, appear to be one of the essential methodologies for the full spatiotemporal clarification of cellular signaling, one of the ultimate goals in cell biology.

## 5.1 Single-Molecule Fluorescence Microscopy in Living Cells

Ultimately, signal transduction is based on specific reactions between one molecule and a second. As such interactions are usually not completely synchronized in time, bulk studies will only yield information on the average properties of the interactions. In order to obtain more detailed information about the existence of subpopulations, local stoichiometries, and substeps in the interaction processes, it is necessary to follow the processes at a single-molecule level in real-time. The first optical detection of single-dye molecules at ambient conditions was achieved by a method called scanning near-field optical microscopy (SNOM) (Betzig et al. 1993). SNOM is a technique based on scanning a very small light source, with dimensions smaller than the wavelength of light, very close (in the near-field) to the specimen. With this method a spatial resolution of 14 nm was obtained and it has been extended to spectroscopy on fluorescent dyes in polymer matrices or crystals (Ambrose et al., 1994; Trautman et al., 1994; Xie and Dunn, 1994) and biological membranes (Dunn et al., 1994; de Bakker et al., 2001)). The method is, however, restricted in its application to basically immobile objects. The time resolution is too low to follow dynamical processes such as motion and redistribution of components in biological membranes. For those purposes, microscopy had to be extended to visualize single fluorophores in motion. Parallel to the SNOM techniques groups started to develop single-molecule confocal fluorescence microscopy to obtain information on immobilized molecules at very high temporal resolution (for a review see Weiss, 1999). However, the imaging capabilities of single-molecule confocal fluorescence microscopy is rather limited in terms of faster moving objects. The motion of individual dye molecules was visualized with conventional fluorescence microscopy by extending the time resolution to the millisecond range. By using epifluorescence wide-field microscopy with argon-ion laser excitation and imaging of the fluorescence onto a highly-sensitive liquid nitrogen-cooled camera this was achieved (Figure 5.1).

The first demonstration of such an approach was the visualization of the diffusion of individual fluorescently labeled lipids (Schmidt et al., 1996a). Rhodamine was tagged to lipids in a synthetic-membrane plane and diluted until individual molecules could be resolved. The fluorescence intensity profile obtained in these images was fitted to a two-dimensional Gaussian surface. Because of the high image contrast accomplished in those experiments, characterized by a signal-noise

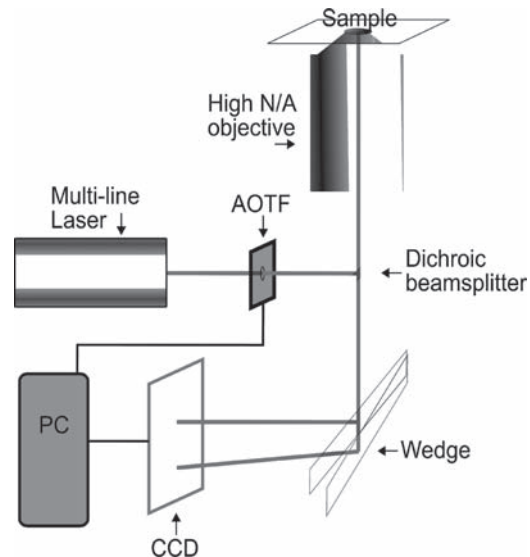


**Figure 5.1** A schematic drawing of the setup. The acousto-optic tunable filter (AOTF) and the camera are controlled by a PC synchronizing the following cycle: (1) 5 ms laser illumination from a chosen laser line excites fluorophores; (2) camera detects signal; (3) camera is read out while laser light is blocked by AOTF. The dichroic beamsplitter separates excitation light from emitted light allowing only photons emitted by the fluorophore to reach the CCD. Using a dichroic wedge mirror, two spectrally different fluorophores can be imaged at once because the emission wavelengths are separated in space and imaged on different areas on the CCD

ratio of 28, a positional accuracy of the individual lipids of 30 nm was achieved (Schmidt et al., 1996a). This same method was used later to investigate the highly specific ligand–receptor recognition between biotin and streptavidin. In this experiment a dual-wavelength approach (Betzig, 1995a,b; Enderle et al., 1997) was used, which allowed determination of the spatial organization of multi-component systems on length scales of ~40 nm (Schütz et al., 1998). The possibilities to observe individual biomolecules with high spatial and temporal resolution was extended by fusing the protein of interest to an autofluorescent protein such as the green fluorescent protein, GFP (Tsien, 1998). The combination of these techniques provided us with the tools to study cellular reactions at the single-molecule level in living cells. The power of single-molecule studies for signal transduction research has been convincingly demonstrated for the first time in experiments that yielded new insight into the dynamical processes occurring in a ligand–receptor system: the epidermal growth factor and its receptor (Sako et al., 2000). The first in vivo fluorescence single-molecule wide-field microscopy experiments showed aggregation of L-type  $\text{Ca}^{2+}$  channels into large clusters (20–40) on the plasma membrane (Harms et al., 2001a).

## 5.2 Model Organism for Studying Signal Transduction

The slime mould *Dictyostelium discoideum* shows high genetic sequence similarities to higher vertebrates and has unique advantages for studying fundamental cellular processes. Studies of *D. discoideum* have provided many of the key insights into the signal transduction pathways of analogous processes such as cytokinesis, motility, phagocytosis, embryogenesis, and chemotaxis. These cellular processes and the coupled biochemical mechanisms are either absent or less accessible in other model organisms. The cells are easy to grow, are especially suitable for microscopic studies because the cells are transparent, and the simplicity of the lifecycle facilitates mutant selection. *D. discoideum* has an intriguing lifecycle consisting of a growth stage in which it lives as a unicellular organism and a developmental stage in which the individual cells interact to form multicellular structures. These aggregates undergo cell differentiation and morphogenesis. Switching from the growth stage to the developmental stage is triggered by removal of nutrients. The aggregation of individual *D. discoideum* cells occurs by chemotaxis to periodic waves of the chemoattractant cyclic adenosine monophosphate, cAMP (Konijn and Vanhaastert, 1987).

Upon binding of cAMP to the seven-transmembrane-G-protein-coupled cAMP receptor, cAR1, the cells respond in two ways, first by the movement towards the cAMP signal, the process called chemotaxis, and second by the production and secretion of more cAMP, the process called relay. The effect of the latter is to transmit the signal throughout the nearby population of amoebae which will cause inward movement of the population to the area of highest cAMP concentration. Remarkably these cells are able to respond to a cAMP gradient of only 2% across the cell body (10  $\mu\text{m}$ ). Evidence suggests that dynamic organization of proteins and lipids plays an important role in chemotaxis (Parent et al., 1998). Based on confocal fluorescence imaging, some of the signaling components of the chemotaxis pathway (such as phosphoinositide 3-kinase, PTEN phosphatase, adenylyl cyclase, cytosolic regulator of adenylyl cyclase, Akt/protein kinase B, PH domain-containing protein A, and small GTPases) in *D. discoideum* have a polarized distribution upon cAMP stimulation (Kimmel and Firtel, 2004; Parent, 2004). In contrast, the proteins in the first activation level in the pathway, the cAMP receptor and its coupled G-protein, are uniformly distributed along the cell surface (Xiao et al., 1997; Jin et al., 2000).

Because localization is not the only dynamic property of a receptor, we wanted to obtain high-resolution lateral and temporal information on the dynamics of the reorganization of cAR1 in the cell membrane upon cAMP stimulation. cAR1 receptors as being G-protein coupled receptors are predicted to form dimers (or higher-order oligomers) as part of their activation. Furthermore, cAR1 receptors are anticipated to redistribute to domains in the plasma membrane where they can form protein–protein and protein–lipid networks. The localization of G-protein coupled receptors in such compartments might control their accessibility to ligands and to downstream signaling proteins, hence forming an important regulatory mechanism for cellular signaling. Single-molecule microscopy offers the opportunity to observe in real-time the

dynamics of an individual cAR1 receptor in the plasma membrane of *D. discoideum* upon stimulation. The information obtained from these studies may shed light on the complex reactions associated with cAR1 signaling and, in general on the primary steps in GPCR signaling in living cells.

### 5.3 Optical Set-Up and Data Acquisition

*Dictyostelium discoideum* cells adherent to either glass slides or, preferentially, to 2-well chambered cover-glasses (1.5 Borosilicate Sterile, Lab Tek II) were mounted onto an inverted microscope (Zeiss) equipped with a 100 $\times$  objective (NA = 1.4, Zeiss) (Figure 5.1). Through the epi-port of the microscope the sample was illuminated for 3–5 ms at 514 nm by an Ar<sup>+</sup>-laser (Spectra physics) and by the 640 nm output of an Ar<sup>+</sup>-pumped dye laser (Spectra Physics). A 200 mm lens in front of the dichroic mirror created a laser spot on the sample of Gaussian profile with  $17.6 \pm 2.2 \mu\text{m}$  (at 514 nm) and  $19.8 \pm 2.2$  (at 640 nm)  $\mu\text{m}$  full-width at half-maximum (fwhm), respectively. The intensity of the laser was set to 1–2 kW/cm<sup>2</sup> as defined by the laser power measured at the objective divided by the illumination area. An acousto-optic tunable filter (AOTF, A.A. Electro Optique), in combination with a function generator (HM8130, Hameg) was used to provide exact timing of the illumination time, intensity, and wavelength. The fluorescence was monitored through a dichroic mirror (DCLP 530 for 514 nm and Cy3/Cy5 for 640 nm, Chroma Technologies) in combination with a band-pass (HQ570/580 for 514 nm, Chroma Technologies) and a low-pass filter (OG 530 for 514 nm, Schott) by a liquid-N<sub>2</sub> cooled slow-scan CCD-camera system (Princeton Instruments). For dual-color experiments two fluorescence signals are separated by means of a dichroic wedge mirror (custom-made, Chroma Technologies) (Cognet et al., 2000). The total collection efficiency for the fluorescence was  $\eta_{\text{det}} = 5\text{--}12\%$  depending on the fluorophore used. Data acquisition was performed on a PC. Parts of the CCD-chip were covered with a mechanical shutter restricting illumination onto the CCD to a small region of the full array (typically  $50 \times 50$  pixels, i.e.,  $11 \times 11 \mu\text{m}^2$  in the image plane, of a total  $1340 \times 400$  pixels). By programming the hardware and by slight modification of the camera electronics it was possible to vary the time-lag between images from a minimal value of 4 ms in a fast frameshift mode and a minimum value of 40 ms in a slow continuous read-out mode of the camera. In the fast mode sequences of images were taken depending on the illuminated area and the storage capacity of the CCD-chip. In principle the only restriction to the length of the sequence in the frame-shift mode is the size of the images and the parallel chip size which was 400 pixels. In general 8 images are taken with a size of  $50 \times 50$  pixels<sup>2</sup> in the fast mode. The slow mode permits continuous imaging limited by computer memory only. In what follows all the images were taken in the slow continuous mode. This decision was based on the predicted diffusion constant of a receptor in the plasma membrane which is on the order of  $0.1 \mu\text{m}^2/\text{s}$ . Before each acquisition cycle 100 images were taken without laser illumination from which an

average dark-image was determined. This average dark-image was subtracted from each image in subsequent acquisitions.

#### 5.4 Autofluorescence of *Dictyostelium Discoideum* Cells

To identify fluorescence signals from individual molecules, their fluorescence has to be distinguishable from the background. Because the detection volume in the sample using wide-field epi-fluorescence microscopy is large, intrinsic fluorescence in living cells will severely interfere with the fluorescence-based imaging. The main source of fluorescence background is due to endogenous molecules such as nicotinamide adenine dinucleotide (NADH), flavins (such as FAD, FMD and flavoproteins), collagen, and elastin. Flavinoids are abundant at high concentrations of  $10^6$ – $10^8$  molecules/cell (Benson et al., 1979) and are a major hurdle for single-molecule measurements. Therefore protocols had to be established in order to make *D. discoideum* accessible for single-molecule experiments. In a modified form those protocols were also applicable to other cell types.

For characterization the autofluorescence was investigated at various wavelengths. The autofluorescence of wild-type cells was measured by illumination at 514 nm and at 640 nm with an intensity of 2 kW/cm<sup>2</sup>, respectively. The autofluorescence was located mainly inside the cells for both wavelengths, and was concentrated in unresolved structures. It was not possible to measure *D. discoideum* cells in the common axenic medium (HL-5) (Watts and Ashworth, 1970) in which they are cultured, because the medium was exceedingly fluorescent, almost independent on wavelength.

One way to reduce the background was to starve cells prior to measurement for different periods of time in phosphate buffer (PB, 3.8 mM Na<sub>2</sub>HPO<sub>4</sub>, 7 mM KH<sub>2</sub>PO<sub>4</sub>, pH 6.5), thereby allowing the exchange of the highly fluorescent medium with the low fluorescent PB. This exchange is facilitated by fluid-phase uptake via large structures, termed macropinosomes (Hacker et al., 1997). The optimal condition for fluid exchange was 6–8 hours in PB at 22°C. The average background intensity was drastically reduced to  $342 \pm 131$  counts/pixel at 514 nm, and to  $72 \pm 33$  counts/pixel at 640 nm (Table 5.1). Additional photobleaching by a short exposure (10 s) to a continuous intensity of 2 KW/cm<sup>2</sup> further reduced the autofluorescence at 514 nm, although less at 640 nm (Table 5.1). This latter finding could be indicative that the signal measured at 640 nm is not due to autofluorescence but due to residual scattering not rejected by the filters.

A severe disadvantage of the 6–8 hours PB incubation is that this procedure triggers the developmental program of the amoeba and cAMP is secreted by the cells. Hence we sought to find another solution to circumvent this disadvantage. The development of a low-fluorescence medium (LF; Liu et al., (2002)) provided us with a tool to further lower the autofluorescence without triggering the starvation program. This medium lacks the highly fluorescent compounds originating from yeast extract in axenic medium, but still contains glucose, that cells would not be



**Table 5.1** Autofluorescence from living cells under different conditions<sup>a</sup>

	514 nm		640 nm	
	Before Photobleaching	After Photobleaching	Before Photobleaching	After Photobleaching
HL-5	—	—	—	—
PB	342 ± 131 (21)	48 ± 12 (21)	72 ± 33 (21)	55 ± 44 (21)
LF+PB	175 ± 103 (20)	30 ± 12 (18)	62 ± 49 (20)	55 ± 37 (18)

<sup>a</sup>Average intensity of autofluorescence in a living *Dictyostelium* cell at 514 and 640nm in counts/pixel (5 ms), followed by the number of cells measured in brackets. Cells were cultured in axenic medium and starved in phosphate buffer (PB) for 7 hours or 16 hours in low fluorescence medium and 1–2 hours PB at 22°C

expected to exit the growth phase and go into development within several hours (Marin et al., 1980). Although the autofluorescence (514nm) for cells cultured in the low-fluorescence medium was lower compared to cells cultured in the axenic medium, they reacted more sensitively to the light. This reaction found expression in the loss of polarity of the cells. The cells also grew more slowly in the low-fluorescence medium and were smaller than the cells from the axenic medium.

The optimal condition for single-molecule experiments with *D. discoideum* cells ultimately, was growing cells in axenic medium and transferring them to a low-fluorescence medium for 15–20 hours to allow the exchange of high-fluorescent axenic medium for the low-fluorescent medium without triggering the developmental stage. Subsequently the cells were transferred to PB 1–2 hours before measurement. The difference between before and after photobleaching for cells under these conditions was 175 ± 103 versus 30 ± 12 counts/pixel and 62 ± 49 versus 55 ± 37 counts/pixel for 514nm and 640nm, respectively (Table 5.1).

The latter data show that the problem of autofluorescence and the need for photobleaching can be avoided by using a fluorophore with an excitation maximum that is red-shifted compared to that of flavins. The spectral and photophysical characteristics for the autofluorescent proteins, mutants of the green fluorescent protein, have been investigated for use in single-molecule microscopy in live cell imaging (Harms et al., 2001b). The yellow-fluorescent protein mutant, eYFP, was shown to be superior compared to all the fluorescent proteins for single-molecule studies in vivo, due to its brightness, resistance to photobleaching and detection ratio as defined by its distance to cellular autofluorescence. Furthermore the absorption spectrum of eYFP shows less overlap with the absorption spectrum of the flavins than GFP (Figure 5.2). Hence, to visualize the receptor in *D. discoideum* a fusion protein of cAR1 with eYFP has been constructed and used. An even better choice would be a red fluorescent protein DsRed (Matz et al., 1999), the spectrum of which is well outside the range of that of the flavins. However, this protein originating from the coral *Discosoma*, has the natural tendency to form tetramers and was found to impair the function of many proteins. Recently an enhanced mRFP was generated for *D. discoideum*, the mRFPmars (Fischer et al., 2004), which has proven to be suitable for monitoring the dynamics of cytoskeletal proteins, but has still to be tested for single-molecule microscopy.

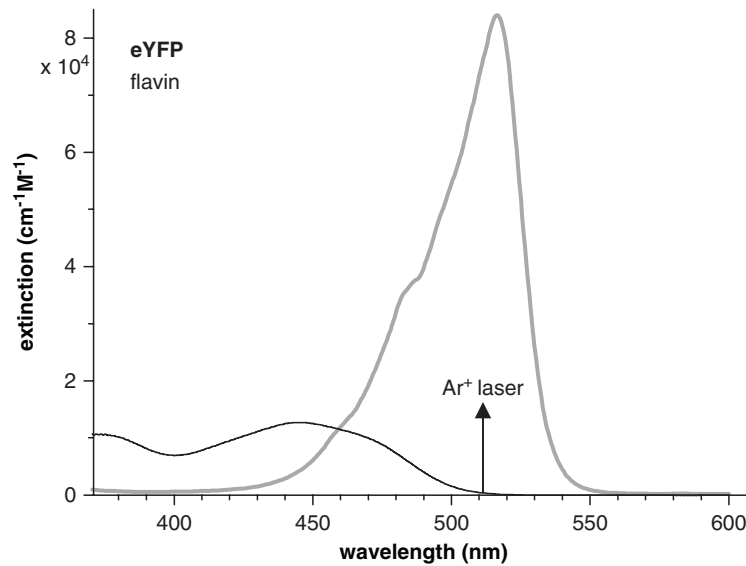


**Figure 5.2** Cellular autofluorescence. Excitation spectra of flavin di-nucleotide compared to that of the enhanced yellow fluorescent protein, eYFP

## 5.5 Data Analysis

The images (Figure 5.3) were analyzed using a software package (Baumgartner 1995) written in Matlab (Mathworks). A sliding mean image was generated from the stack of images with Gaussian weighing around the current image (Figure 5.3A). This background image was subtracted from each image and the resulting background-subtracted image was subsequently filtered using a Gaussian correlation filter. A threshold criterion, determined from the noise in the original image, yielded starting values for a nonlinear fitting procedure of two-dimensional Gaussian profiles to the signals in the unfiltered background-subtracted images. The result of the fitting yielded the position, the intensity, the background, and the width of the fluorescence signal. A detailed description of the image analysis is given in the following subsections.

### 5.5.1 Background Subtraction

In spite of optimization of the culture conditions the autofluorescence in *D. discoideum* remained significant and turned out to be highly inhomogeneous within the cell. Therefore an algorithm was developed to subtract an inhomogeneous, time-varying

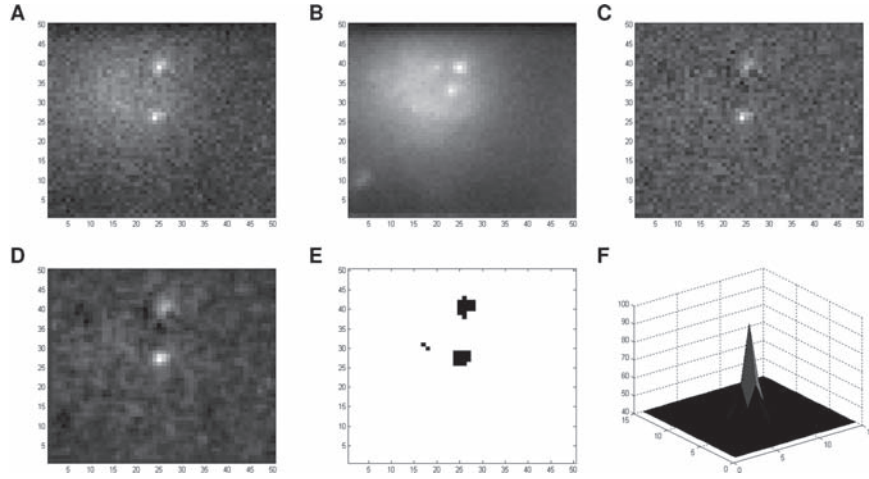


**Figure 5.3** Data analysis. (A) A  $50 \times 50$  pixel image from an image stack of 100 images taken at the apical membrane of an unstimulated *D. discoideum* cell. (B) Sliding mean image from the image stack generated with Gaussian weight around the current image. (C) The mean image is subtracted from the current image. (D) The background-subtracted image was filtered using a Gaussian correlation filter. (E) A threshold criterion determined from the image noise yielded starting values for a nonlinear fitting procedure of two-dimensional Gaussian profiles to the original images. (F) The fitting results yielded the position, signal, and background of an individual fluorescence peak. The position of a molecule was determined with an accuracy of 40 nm and its fluorescence intensity with an uncertainty of <20%

background from the images (de Keijzer et al. submitted). Each image of a stack contains fluorescence signals originating from individual eYFP molecules, contaminated by autofluorescence from the cell including for example, highly fluorescent vesicles slowly diffusing through the cytosol. The algorithm computes a sliding mean image  $m_j$  (Figure 5.3 B) for each image  $j$  of the image stack of length  $N$ .

$$m_j = \sum_{i=1}^N x_i \left( \exp \frac{-(j-i)^2}{\sigma^2} - \exp \frac{-(j-i)^2}{\Delta^2} \right), \quad (5.1)$$

Note that  $m_j$  and  $x_i$  denote two-dimensional image data. The Gaussian weighing around the current image of width  $\sigma = 40$  effectively removes the slowly varying autofluorescence (Figure 5.3 C). Images in the close vicinity of the current image are not subtracted ( $\Delta = 3$ ) which ensures that fast moving objects such as individual molecules and objects that undergo photobleaching at a mean rate of 3 images (typical bleaching time for eYFP) are preserved. In consequence, signals from, for example, bright vesicles are removed whereas those of individual molecules last. The algorithm was validated by simulation, containing Brownian objects, typical autofluorescence features obtained from actual experiments, and the full noise of the detection system. The algorithms with and without mean image subtraction were compared on the simulations, concerning the signal intensity, the width of the

signals, the position of the signals, the mean bleaching time, and the goodness of the fit. The mean-image subtraction globally improved the results. In combination with the new protocol of cell culturing for lowered autofluorescence, a reasonable signal noise ratio (>15) was obtained.

### 5.5.2 Identification of Single Molecules

After background subtraction, the images were filtered using a Gaussian correlation filter (Gelles et al. 1988) (Figure 5.3 D). A threshold criterion was subsequently applied taking into account the noise in each image. Typically signals that exceed the noise by a factor of 1.5 were further investigated (Figure 5.3 E). This initial analysis provided the starting values for a nonlinear fitting procedure of two-dimensional Gaussian profiles to the original images (Marquard 1963). Chi-square, exponential, and  $F$ -tests (Bevington et al. 1992), applied to the fitting results, yielded an unbiased criterion for the final acceptance of individual fluorescence signals as individual molecular entities. The high image contrast characterized by the signal-to-noise ratio,  $S/N > 15$ , allowed for determination of the position of each molecule with an accuracy of 40 nm and its fluorescence intensity with an uncertainty of <20% (Figure 5.3 F).

It should be noted that the noise in each image is fully determined by the photon statistics of the fluorescence signal, the photon statistics of the background, and the small additional readout noise of the CCD camera ( $\sigma_{\text{CCD}} = 6 \text{ cnts/pxl} = 10 \text{ cnts/molecule}$ ):

$$N = \sqrt{\text{signal} + \text{background} + \sigma_{\text{CCD}}^2}. \quad (5.2)$$

When the background signal is homogeneously distributed (or subtracted from the image), the signal can be distinguished from the background if the intensity of the signal is larger than the noise. From Equation (5.2) it becomes obvious that an exceeding background signal will render single-molecule detection impossible. At typical signal levels of 200 cnts/molecule a background signal of ~50 cnts/pxl is still acceptable leading to a  $S/N = 11$ . Finally, cut-off criteria regarding the intensity, the width, and the relative errors in all fitting parameters were used to validate the signal as an individual emitting eYFP molecule.

### 5.5.3 Tracing Single Molecules

The determination of cAR1-eYFP molecule positions was used to analyze their motion from the positional shifts in consecutive images (Figure 5.4A). From this analysis the two-dimensional trajectories of individual cAR1-eYFP receptors in the apical membrane was constructed (Figure 5.4C). Assuming that the receptor moves by a random walk characterized by a diffusion constant  $D_m$ , then the probability for connection of two molecules in consecutive images is given by

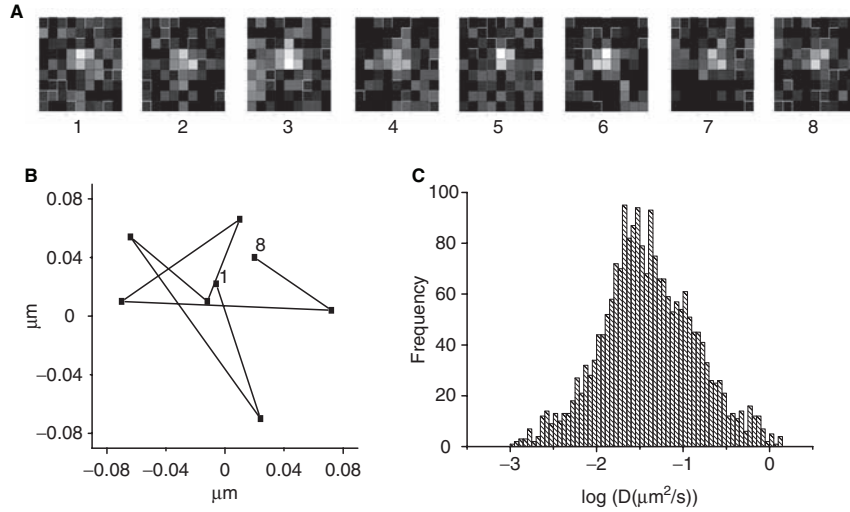


**Figure 5.4** Tracing a single cAR1-eYFP. **(A)** A signal in the apical membrane was followed through eight consecutive images. **(B)** The two-dimensional trajectory of the signal was reconstructed by correlating the images of identical molecules in subsequent observations with a delay time of 39 ms. **(C)** Distribution of the diffusion constant ( $\mu\text{m}^2/\text{s}$ ) of traces observed in the apical membrane of *D. discoideum* cells

$$p(r) = \frac{1}{4D_{in}t} \exp \frac{-\Delta r^2}{4D_{in}t}. \quad (5.3)$$

Signals were recognized as being identical in subsequent images when the probability  $p(r)$  was  $>1\%$ . In general multiple molecules had to be followed in the image sequence. For that the total probability for all molecules,

$$P_{total} = \prod_i p_i, \quad (5.4)$$

was minimized at once by a Vogel algorithm, yielding the connectivity map between two consecutive images. From those pairwise connectivity maps trajectories of all molecules were constructed

The trajectories were up to 14 steps in length, mainly limited by the blinking and photobleaching of the fluorophore (Harms et al., 2001b). For every trajectory a mean square displacement,  $MSD$ , was calculated for various time-lags,  $t_{lag}$  (number of images between two observations). By the relation  $MSD = 4Dt_{lag}$  the diffusion constant  $D$  was determined for each molecule. Because of the limited length of the trajectory the distribution of the diffusion constants was found to be very broad making further analysis very unreliable (Figure 5.4C); for example, any subpopulations were completely washed out by that analysis. Therefore a statistical method for the analysis of multiple trajectories was used (Schütz et al., 1997b):

$$\tilde{P}(r^2, t) = 1 - \exp\left(-\frac{r^2}{r_0^2}\right). \quad (5.5)$$

Equation (5.5) describes the cumulative probability that a particle is found within a circle of radius  $r$  at time  $t$  if it was at the origin at time  $t = 0$ . This method allows one to fit the cumulative probability distributions of the measured squared displacements. The fit yielded a mean square displacement from which the diffusion coefficient for a given time-lag was calculated. Equation (5.5) was further expanded to a two 2-component model in which a fast moving population and a slow moving population were mixed (Schütz et al., 1997a):

$$\tilde{P}(r^2, t) = 1 - \left[ \alpha \cdot \exp\left(-\frac{r^2}{r_1^2(t)}\right) + (1 - \alpha) \cdot \exp\left(-\frac{r^2}{r_2^2(t)}\right) \right], \quad (5.6)$$

With  $r_i^2(t) = 4D_i t$  providing 2 components characterized by diffusion constants  $D_1$  and  $D_2$ , and relative fractions  $\alpha$  and  $(1 - \alpha)$ , respectively. In principle Equation (5.5) could be extended to study more than 2 components, however, in practice the number of data needed for such analysis (2 components, >100 data points; 3 components, >1000 data points) prohibits further analysis.

The data for the analysis according to Equation (5.6) were generated by determining for each trajectory (Figure 5.4B) a set of values of square displacements  $r^2$  between two observations separated by the time lag  $t_{\text{lag}}$  with

$$r^2(t_{\text{lag}}) = (\vec{r}(t + t_{\text{lag}}) - \vec{r}(t))^2. \quad (5.7)$$

The time lag is given by  $t_{\text{lag}} = m(t_{\text{ill}} + t_{\text{delay}})$ , where  $t_{\text{ill}}$  is the illumination time and  $t_{\text{delay}}$  the time between two consecutive images (Schütz et al., 1997c).  $m$  takes on values of 1, 2, ...,  $M - 1$  counting the number of images between two observations.  $M$  denotes the total number of observations of the molecule (on average  $M = 5$  in our experiments). For each value of  $t_{\text{lag}}$ , the probability was constructed from multiple trajectories by counting the number of square displacements with values  $\leq r^2$  normalized by the total number of data points. Because of the limited number of data points available for construction of the distribution, characterized by a maximal value of the square displacement,  $r_{\text{max}}^2$ , Equations (5.5) and (5.6) convert to the experimental probability distribution  $P(r^2, t_{\text{lag}})$

$$P(r^2, t_{\text{lag}}) = \frac{\tilde{P}(r^2, t_{\text{lag}})}{\tilde{P}(r_{\text{max}}^2, t_{\text{lag}})}. \quad (5.8)$$

All experimental cumulative probability distributions of  $r^2$  were plotted and fitted according to Equation 5.8 yielding values for the two mean square displacements and fractions, respectively.

## 5.6 Stoichiometry of Receptors in the Plasma Membrane

G-protein coupled receptors in the plasma membrane, like the cAR1 in *D. discoideum*, are thought to coexist in different stoichiometry states, mainly as monomer and as dimer (Bouvier, 2001; Angers et al., 2002), oscillating between these by association–dissociation equilibria (Figure 5.5A). The different stoichiometric states can be identified by an analysis of the fluorescence intensity distribution of the monomer and that of the colocalized eYFP molecules. The fluorescence intensity distribution of eYFP monomers was determined experimentally for eYFP-his6: Ni<sup>2+</sup>-NTA chelated lipids on an artificial lipid membrane (Harms et al., 2001b). From this the corresponding intensity distribution of  $n$  colocalized eYFP molecules was calculated recursively as a series of convolution integrals (Schmidt et al., 1996b) (Figure 8.5B):

$$\rho_n(I) = \int dI' \rho_1(I') \rho_{n-1}(I - I'), \quad (5.9)$$

with  $\rho_1$  the intensity distribution of individual fluorophores and  $\rho_n$  the corresponding intensity distribution of  $n$  colocalized fluorophores.

The observation of dimers by single-molecule fluorescence microscopy, however, has to be interpreted with care. Indeed, signals corresponding to two YFPs were identified in our experiments. But proximity in this case only means that both signals appeared as a single, unresolved fluorescence peak. Their distance is still smaller than the diffraction limit of  $1.22 \lambda / (2 \text{ NA}) = 370 \text{ nm}$ . This distance is still much larger than the size of the receptors ( $\sim 7 \text{ nm}$ ), hence a dimeric stoichiometry does not necessarily reflect a direct molecular interaction. Studying stoichiometry by intensity distribution analysis is further complicated by the width of the intensity distribution attributed to image noise, blinking of the fluorophores during the recording of an image, and to molecular orientation, each leading to a broadening of the fluorescence intensity distribution.

The strategy as outlined above was applied to the cAR1 receptor in *D. discoideum*. The intensity distribution measured for 36 cells (Figure 5.5B) contained values above 300 cts a distinct difference to that of the YFP monomer distribution. High signals were associated with the dimeric state of the receptor. The distribution in Figure 5.5B was fit to a weighted sum of distributions  $\rho_n$ , each weight giving the corresponding relative fraction,  $\alpha_i$  (Figure 5.5C).

$$\rho_{total} = \left( 1 - \sum_{n=2}^N \alpha_n \right) \rho_1 + \sum_{n=2}^N \alpha_n \rho_n. \quad (5.10)$$

The dimer fraction in Figure 5.5B amounted to 5%, with no significant trimer fraction identified. In the case of the cAR1 receptor in *D. discoideum*, stoichiometric analysis is further hampered by the initial photobleaching procedure. In order to be able to observe individual molecules 99.9% of the receptors were photobleached before measurement. This photobleaching procedure makes extrapolation of stoichiometry

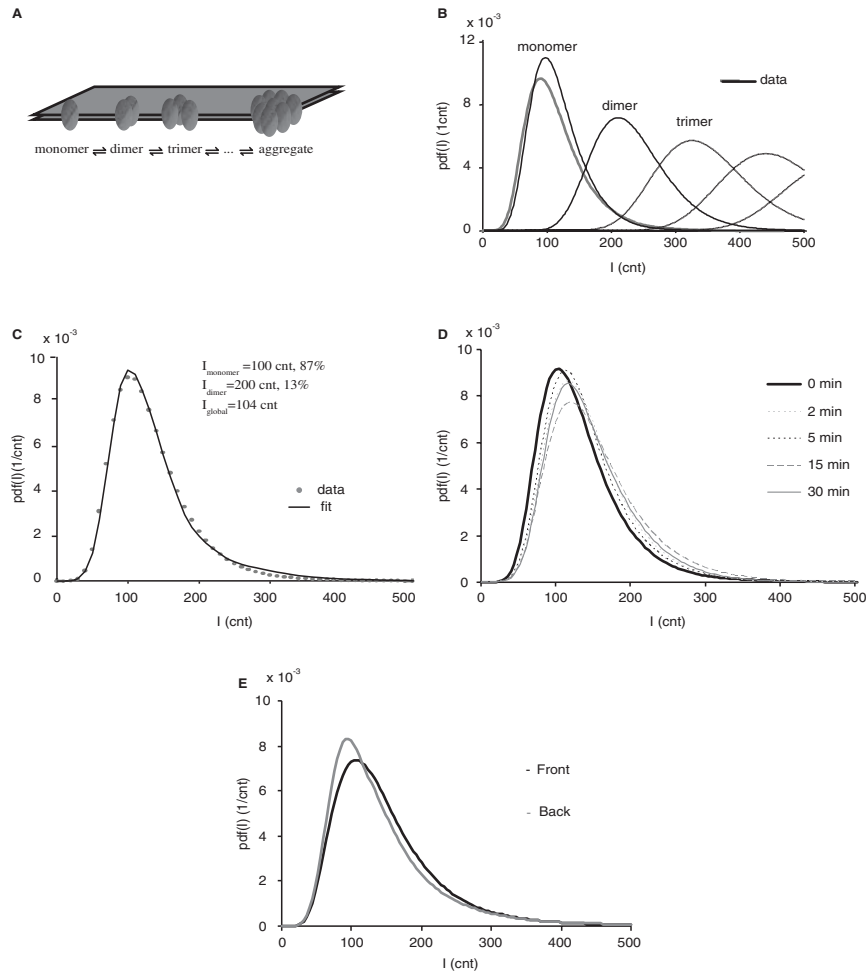


**Figure 5.5** Intensity distributions of cAR1-YFP. **(A)** Model of receptor stoichiometry at the membrane. **(B)** Predicted intensity distributions for eYFP-monomers, eYFP-dimers, and so on are compared to the intensity distribution for cAR1-eYFP data (grey). **(C)** Intensity distribution obtained for cAR1-YFP at the apical membrane of nonstimulated cells (grey dots,  $N = 36$ ). The high signal levels were associated with monomers and dimers, as shown by fitting the distribution with a weighted sum of the distributions expected in Figure 5.5B (black curve). **(D)** Intensity distributions of cAR1-YFP for the different time of continued stimulation ( $N = 36, 29, 20, 25, 22$  for respectively 0, 2, 5, 15, and 30 min, respectively). **(E)** Intensity distributions of cAR1-YFP for the front (black,  $N = 9$ ) and the back (grey,  $N = 9$ ) of the cells. The distributions were fit to a mixture of monomers and dimers. The intensity distributions are equivalent at the front and the back. Front  $\alpha_1 = 71\%$ ,  $\alpha_2 = 29\%$ ; and back  $\alpha_1 = 71\%$ ,  $\alpha_2 = 29\%$

before photobleaching very unreliable because most cAR1-eYFP molecules from multimers were bleached and only the resulting monomers were observed. Assuming that photobleaching is a statistical process, the apparent stoichiometry distribution measured,  $\tilde{n}$ , is related to the original distribution by a binomial



$$\bar{n} = \text{binomial}(n, p), \quad (5.11)$$

in which the survival probability in the case of *D. discoideum* is  $p = 0.001$ . Hence, the small dimer contribution found for cAR1 reflects a larger aggregate of receptors prior to bleaching. A technical solution to obtain a correct measurement of stoichiometry would be to utilize a fluorophore in the red range where photobleaching is not required.

Despite the fact that the precise initial stoichiometry is unavailable, comparative studies of the stoichiometry of cAR1-eYFP under different physiological conditions is a viable approach, because the photobleaching time and photobleaching intensity is under exact control. By this comparative assay we found that the intensity distributions did not change, neither after global stimulation with the ligand (Figure 5.5D), nor by stimulation in a gradient in which we compared the front with the back of the cell (Figure 5.5E). From this we concluded that cAMP stimulation has no effect on the stoichiometric state of the cAR1 receptor during chemotaxis.

## 5.7 Membrane Organization

The Singer and Nicolson model (Singer and Nicolson, 1972) of a homogeneous plasma membrane is currently challenged by the idea that the plasma membrane of eukaryotes consists of a variety of microdomains (Sheetz, 1995; Jacobson et al., 1995; Kusumi and Sako, 1996; Edidin, 1997; Maxfield, 2002; Vereb et al., 2003). The membrane is thought to compartmentalize via (i) the actin-based membrane cytoskeleton which forms a barrier in the plasma membrane; (ii) caveolae, membrane invaginations rich of caveolins which bind to cholesterol (Anderson, 1998); and (iii) lipid rafts, defined by detergent-resistant, liquid-ordered domains on the cell membrane that have a unique lipid composition characterized by a high percentage of cholesterol and sphingolipids (Simons and Ikonen, 1997). It has been proposed that these liquid-ordered domains function as signaling depots, also called signalosomes or transducisomes, where G-protein coupled receptors and their associated G-proteins are clustered and attached or recruited to membranes via lipids (Jacobson et al., 1995; Casey, 1995; Song et al., 1997). Biochemical studies have indicated that point mutations that abolish myristoylation (irreversible modification) and/or palmitoylation (reversible modification) of the  $G\gamma$ -subunit prevent the association of G-proteins with caveolin-enriched membrane fractions (Song et al., 1997). Palmitoylation is required for a productive interaction between GPCR and the  $G\alpha$ -subunits. It has been further shown, that caveolin binding to  $G\alpha$ -subunits is sufficient to maintain the G-protein in the inactive, GDP-conformation and G-proteins become activated when GPCRs are recruited to caveolae upon ligand stimulation (Smart et al., 1999). Although there are no caveolae found in *D. dictyostelium* yet it has been shown that detergent resistant fractions exists which are enriched in signaling proteins including cAR1 (Xiao and Devreotes, 1997). We have shown in earlier studies on mammalian cells that the existence of domains in the plasma

membrane can be revealed by single-molecule microscopy studies of the diffusion behavior of individual molecules. Hence, we set out to apply single-molecule microscopy for a detailed study of the mobility of individual cAR1 in search for domains in the plasma membrane of *D. dictyostelium*.

### 5.7.1 *Fluorescent Lipid Insertion*

In mammalian cells it has been shown that insertion of fluorescence-labeled lipids from vesicles into the plasma membrane can be used for investigation of the membrane organization (Schütz et al., 2000). Saturated lipids (DMPE) are supposedly restricted into microdomains, whereas unsaturated lipids (DOPE) showed free diffusion throughout the membrane. For single-molecule imaging, lipid vesicles were prepared from a mixture of labeled and unlabeled 1-palmitoyl-2-oleoyl-*sn*-glycero-3-phosphocholine (POPC) lipid at a molar ratio of  $10^{-3}$  or from pure labeled lipid for high-concentration imaging. *D. discoideum* wild type cells were incubated for 20 min with a vesicle solution of 50  $\mu\text{g}/\text{ml}$  (Schütz et al., 2000) in phosphate buffer at room temperature to reveal possible domain formation. The pure fluorescent lipid vesicles were used to reveal potential lipid domains by regular confocal fluorescence imaging, whereas the vesicles with a low concentration of fluorescent lipids were used to study the diffusion of individual lipids in potential domains. The latter assay was earlier used in human aorta smooth muscle cells (Schütz et al., 2000), and in human embryo kidney cells (personal communications with P. Lommerse). However, no clear membrane-localized fluorescence was observed after incubation of *D. discoideum* with either of the lipid vesicles. Confocal microscopy revealed that the labeled lipids were not inserted into the plasma membrane but rapidly internalized probably by phagocytosis. Hence, labeling the membrane with fluorescent lipid vesicle insertion is a good tool for mammalian cells; the same approach in *D. discoideum* is largely hampered by the fast membrane turnover in the slime-molds.

### 5.7.2 *Fluorescent Membrane Markers*

In order to set a reference frame for further diffusion studies on the cAMP-receptor, membrane constituents which carry specific sugar moieties were labeled by fluorescence-labeled concanavalin A. The concanavalin A / Alexa647 conjugate binds selectively to  $\alpha$ -mannopyranosyl and  $\alpha$ -glucopyranosyl residues of membrane proteins. It was found that in this way the plasma membrane labeling was stable for up to 15 min, sufficient to study mobility at the single-molecule level. On a length scale  $<200\text{nm}$  the labeled membrane constituents diffused freely in the plasma membrane characterized by a diffusion constant of  $0.2\mu\text{m}^2/\text{s}$ , a typical value for small membrane proteins. Observations for longer periods than 15 min were impaired by

rapid membrane turnover. As with typical membrane markers as the dye FM4-64, concavilin A in *D. discoideum* was also only very transient positioned at the plasma membrane and rapidly translocated to the cytosol. This finding was not too surprising because the water-soluble FM-dyes have been successfully used to study vacuolization in *D. discoideum* in the past (Heuser et al., 1993). The fluid-phase uptake via (macro) pinocytosis of *D. discoideum* cells results in such a high membrane turnover rate that FM-dyes and other membrane-markers have only a limited suitability for plasma membrane localization studies.

### 5.7.3 cAR1 Mobility

The mobility of cAMP-receptors was in turn investigated to test the possibility of receptor subpopulations. Trajectories of individual cAR1-eYFP molecules in unstimulated cells were used to calculate the probability distribution of the square displacements (Equation (5.8)). Figure 5.6A shows the cumulative probability distributions for a time lag of 44 ms ( $t_{\text{delay}} = 39$  ms,  $t_{\text{ill}} = 5$  ms). The data exhibited a biphasic behavior that could not be described by a monoexponential according to Equation (5.5) (dashed line, Figure 5.6A). The data of the cAR1 receptor had to be described by the 2-component model of Equation (5.6) (solid line, Figure 5.6A). A fit of the model to the data yielded  $r_1^2 = 0.03 \pm 0.003 \mu\text{m}^2$ ,  $r_2^2 = (6.7 \pm 1) 10^{-3} \mu\text{m}^2$ , and  $\alpha = 0.38 \pm 0.04$ , respectively. The second component reflected the limited positional accuracy of our measurements ( $\sim 40$  nm). Determination of molecule positions by a fitting algorithm is a random process that leads to a diffusionlike mobility of an immobile object. Given the positional accuracy this apparent mobility is characterized by  $r_2^2 = 4 \times (40 \text{ nm})^2 = 6.4 10^{-3} \mu\text{m}^2$ , the minimal detectable square displacement.

This first determination of the mobility of cAR1 receptors in the plasma membrane of *D. discoideum* cells triggered subsequent studies on the nature of the two mobility components and their biological role. Changes in the mobility upon cAMP stimulation have been observed and a mechanism on how the mobility is linked to downstream signaling components such as the coupled G-protein has been proposed (de Keijzer et al., submitted).

The diffusion of the mobile population was further studied by the characteristics of the mean squared displacement  $r_1^2$  versus the time lag  $t_{\text{lag}}$ . Thereby, the  $r_1^2$  values for different time lags were acquired in two different ways: first at fixed imaging frequency, or delay time  $t_{\text{delay}}$ , the 1-step, 2-step up to the  $n$ -step displacements were analyzed; second, the 1-step displacements were analyzed for different imaging frequency, that is, different delay times  $t_{\text{delay}}$ . For the first method long trajectories are necessary, whereas the second also allows for shorter trajectories such as those of the cAR1-eYFP receptor (Figure 5.6B). Simulations revealed that at least 200 data points of displacement values per  $t_{\text{lag}}$  were needed to get an accurate fit to Equation (5.8). Subsequently the  $(r_1^2, t_{\text{lag}})$  datasets were plotted and fitted to various diffusion models. In the case of normal diffusion the mean squared displacement varies linear with time lag

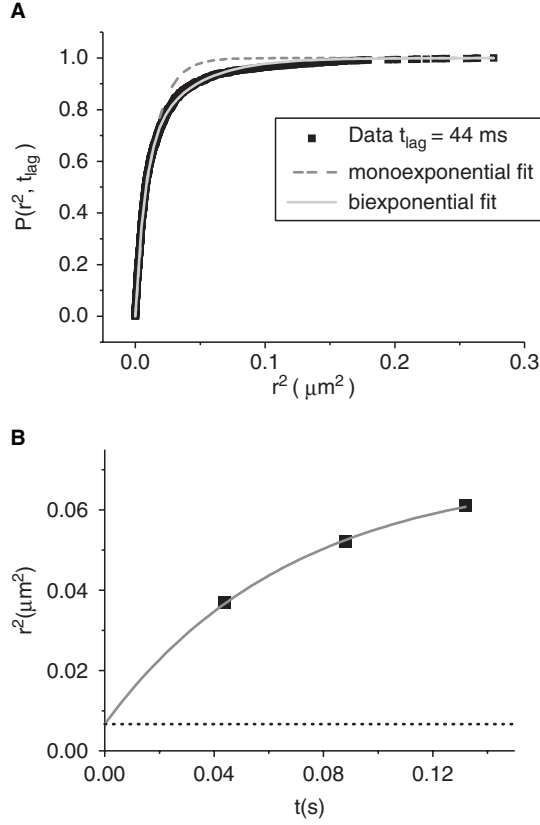


**Figure 5.6** cAR1-eYFP mobility. (A) Cumulative probability  $P(r_1^2, 44 \text{ ms})$  plotted versus the square displacement ( $N = 2060$ ). This distribution was fit with a one-component (dashed line) and a two-component (solid line) model. (B) Fitting of the square displacement distribution to Equation (5.8) yielded a fraction of mobile and immobile receptors. Mean square displacement data for the mobile receptors versus  $t_{lag}$ , generated by taking multiple stepsizes, and fitted according to a confined diffusion model, Equation 5.14. The dotted line represents the offset due to the limited positional accuracy

$$r_1^2(t_{lag}) = 4Dt_{lag}, \quad (5.12)$$

with diffusion constant  $D$ .

When the diffusion is hindered by obstructions or by trapping, the mean square displacement will grow slower with time lag and is characterized by a power law dependence with exponent  $\alpha < 1$ . Such behavior is called anomalous subdiffusion and Equation 5.12 becomes (Feder et al., 1996):

$$r_1^2(t_{lag}) = \Gamma t_{lag}^\alpha \quad (5.13)$$

with a diffusion parameter  $\Gamma$  of unit  $\mu\text{m}^2/\text{s}^\alpha$ . For regular diffusion  $\alpha = 1$ , the diffusion parameter is given by the regular diffusion constant  $\Gamma = 4D$ .

Yet another type of diffusion behavior is called confined diffusion. In that case the mean square displacement initially increases with time but levels off to a constant value for longer time lags. Assuming that diffusion is free within a square of side length  $L$  surrounded by an impermeable reflecting barrier the mean square displacement depends on  $L$  and the initial diffusion coefficient  $D_0$  as (Kusumi et al., 1993):

$$r_1^2(t_{\text{lag}}) = \frac{L^2}{3} \cdot \left[ 1 - \exp\left(\frac{-12D_0 t_{\text{lag}}}{L^2}\right) \right]. \quad (5.14)$$

Data for the cAMP receptor in *D. discoideum*, as shown in Figure 5.4B, were fit according to Equations (5.12) to (5.14). Although more data points will have to be acquired to get an accurate fit, those initial data already suggest that cAR1s were confined to domains of size  $436 \pm 44 \text{ nm}$  and their diffusion within the domain was characterized by an initial diffusion coefficient  $D_0 = 0.23 \pm 0.02 \mu\text{m}^2/\text{s}$ . To validate this finding and unravel the nature of the domains more data are currently being acquired in time, as well in different genetic backgrounds. In any case, data seem to indicate the existence of membrane microdomains in *D. discoideum* like those that have been found for mammalian cells. It should be stressed here that this kind of information was only achievable by in vivo single-molecule microscopy because of its superior lateral resolution as compared to regular fluorescence microscopy techniques.

## 5.8 Prospects

A hallmark in the study of regulation processes of cells would be that all the molecular players in the system are identified, by, for example, genomics techniques, and that all of them are followed and tracked in real-time. Although this general aim seems infeasible one could get a long way ahead in a sequential molecule-by-molecule manner. For that single-molecule microscopy has to be further developed as a universal tool in cell biology. In this review we have outlined, at hand of the model system *Dictyostelium discoideum*, which information can be obtained in general from single-molecule techniques and we have outlined the technique's limitations.

Real-time information about the dynamics of individual cAMP-receptors was obtained for different physiological conditions. A positional accuracy of 40 nm and a time-resolution as small as 7 ms was achieved. Using single-molecule microscopy with this spatial and time resolution we were able to study the effect of ligand stimulation on the dynamics of the receptor in terms of aggregation, in terms of mobility (de Keijzer et al., submitted), and in terms of localization. The dynamics of ligand binding ( $k_{on}$ ,  $k_{off}$ ) and of ligand-receptor interactions can be studied by an straightforward extension of the imaging technique to a dual-wavelength approach. In this way colocalization experiments with a red-labeled ligand, Cy5-cAMP, and

the cAR1-eYFP are feasible (Hemert et al, manuscript in prep.) leading to a direct discrimination of ligand-bound versus unbound receptor molecules.

*Dictyostelium discoideum* appeared to be an ideal system for the development of the general techniques needed towards the ultimate goal. *D. discoideum* is a genetically well-defined organism, plasmids containing downstream proteins of most signaling pathways are available and many fusion proteins with autofluorescent proteins have been made. One can study these downstream signaling proteins by single-molecule techniques as described in this review. When a suitable red-fluorescent protein for single-molecule microscopy becomes available, reactions between multiple signaling components will be studied in two-color experiments. Knock-out mutants or constitutive active mutants are also available. Working with *D. discoideum* has the advantage that mutants can be easily tested in terms of functionality as assayed by rescue of its development cycle. cAR1-eYFP and most other signaling molecules are investigated in knock-out backgrounds rendering results more clear-cut compared to overexpression methods in undefined genetic background (de Keijzer et al, submitted).

Besides the dynamics of the cAR1-YFP receptor in the plasma membrane, it is also possible to follow the trafficking of the receptor into the cytosol upon ligand stimulation at the single-molecule level. Receptor internalization after continued stimulation is a general mechanism by which G-protein coupled receptors modulate their availability. This process is known as adaptation for mammalian systems (Ferguson, 2001). For *D. discoideum* the literature on whether the cAR1 receptor showed ligand-induced internalized was conflicting and this matter was solved using single-molecule microscopy (Serge *et al.*, submitted).

In conclusion single-molecule microscopy studies, as described in this review, provide a powerful tool to investigate the complex processes of signal transduction. The first steps in the challenge to obtain a fully spatial-temporal picture of cellular signaling have been taken. *Dictyostelium discoideum* turned out to provide an ideal model organism in such studies because most cell biological mechanisms are highly conserved in eukaryotes and the single-molecule microscopy studies as described here can be easily transferred for studies in mammalian cells.

## References

- Ambrose, W.P., Goodwin, P.M., Martin, J.C., Keller, R.A. (1994). Single-molecule detection and photochemistry on a surface using near-field optical-excitation. *Physical Review Letters* 72, 160–163.
- Anderson, R.G.W. (1998). The caveolae membrane system. *Annual Review of Biochemistry* 67, 199–225.
- Angers, S., Salahpour, A., Bouvier, M. (2002). Dimerization: An emerging concept for G protein-coupled receptor ontogeny and function. *Annual Review of Pharmacology and Toxicology* 42, 409–435.
- Baumgatner, W. (1995). 'Statistical Methods in Single-Molecule Biophysics', PhD thesis, University of Linz, Austria.
- Benson, R.C., Meyer, R.A., Zaruba, M.E., Mckhann, G.M. (1979). Cellular autofluorescence—is it due to flavins. *Journal of Histochemistry & Cytochemistry* 27, 44–48.

- Betzig, E. (1995). Proposed method for molecular optical imaging. *Optics Letters* 20, 237–239.
- Bevington, P.R., Robinson, D.K. (2003). *Data Reduction and Error Analysis*, Boston: McGraw Hill.
- Bouvier, M. (2001). Oligomerization of G-protein-coupled transmitter receptors. *Nature Reviews Neuroscience* 2, 274–286.
- Casey, P.J. (1995). Protein lipidation in cell signaling. *Science* 268, 221–225.
- Cognet, L., Harms, G.S., Blab, G.A., Lommerse, P.H.M., Schmidt, T. (2000). Simultaneous dual-color and dual-polarization imaging of single molecules. *Applied Physics Letters* 77, 4052–4054.
- de Bakker, B.I., Garcia-Parajo, M.F., Rensen, W.H.J., van Hulst, N.F., de Lange, F., Cambi, A., Figdor, C.G. (2001). Study of individual transmembrane proteins using a combined confocal/near field optical microscope. *Biophysical Journal* 80, 149A–150A.
- Dunn, R.C., Holtom, G.R., Mets, L., Xie, X.S. (1994). Near-field fluorescence imaging and fluorescence lifetime measurement of light-harvesting complexes in intact photosynthetic membranes. *Journal of Physical Chemistry* 98, 3094–3098.
- Edidin, M. (1997). Lipid microdomains in cell surface membranes. *Current Opinion in Structural Biology* 7, 528–532.
- Enderle, T., Ha, T., Ogletree, D.F., Chemla, D.S., Magowan, C., Weiss, S. (1997). Membrane specific mapping and colocalization of malarial and host skeletal proteins in the *Plasmodium falciparum* infected erythrocyte by dual-color near-field scanning optical microscopy. *Proceedings of the National Academy of Sciences of the United States of America* 94, 520–525.
- Feder, T.J., BrustMascher, I., Slattery, J.P., Baird, B., Webb, W.W. (1996). Constrained diffusion or immobile fraction on cell surfaces: A new interpretation. *Biophysical Journal* 70, 2767–2773.
- Ferguson, S.S. (2001). Evolving concepts in G protein-coupled receptor endocytosis: the role in receptor desensitization and signaling. *Pharmacology Review* 53, 1–24.
- Fischer, M., Haase, I., Simmeth, E., Gerisch, G., Muller-Taubenberger, A. (2004). A brilliant monomeric red fluorescent protein to visualize cytoskeleton dynamics in *Dictyostelium*. *Febs Letters* 577, 227–232.
- Gelles, J., Schnapp, B.J., Sheetz, M.P. (1988). Tracking kinesin-driven movements with nanometer-scale precision. *Nature* 331, 450.
- Hacker, U., Albrecht, R., Maniak, M. (1997). Fluid-phase uptake by macropinocytosis in *Dictyostelium*. *Journal of Cell Science* 110, 105–112.
- Harms, G.S., Cognet, L., Lommerse, P.H., Blab, G.A., Kahr, H., Gamsjager, R., Spaink, H.P., Soldatov, N.M., Romanin, C., Schmidt, T. (2001a). Single-molecule imaging of l-type Ca(2+) channels in live cells. *Biophysics Journal JID - 0370626* 81, 2639–2646.
- Harms, G.S., Cognet, L., Lommerse, P.H., Blab, G.A., Schmidt, T. (2001b). Autofluorescent proteins in single-molecule research: applications to live cell imaging microscopy. *Biophysics Journal* 80, 2396–2408.
- Heuser, J., Zhu, Q.L., Clarke, M. (1993). Proton pumps populate the contractile vacuoles of *Dictyostelium* amoebas. *Journal of Cell Biology* 121, 1311–1327.
- Jacobson, K., Sheets, E.D., Simson, R. (1995). Revisiting the fluid mosaic model of membranes. *Science* 268, 1441–1442.
- Jin, T., Zhang, N., Long, Y., Parent, C.A., Devreotes, P.N. (2000). Localization of the G protein betagamma complex in living cells during chemotaxis. *Science* 287, 1034–1036.
- Kimmel, A.R., Firtel, R.A. (2004). Breaking symmetries: Regulation of *Dictyostelium* development through chemoattractant and morphogen signal-response. *Current Opinion in Genetics & Development* 14, 540–549.
- Konijn, T.M., Vanhaastert, P.J.M. (1987). Measurement of chemotaxis in *Dictyostelium*. *Methods in Cell Biology* 28, 283–298.
- Kusumi, A., Sako, Y. (1996). Cell surface organization by the membrane skeleton. *Current Opinion in Cell Biology* 8, 566–574.
- Kusumi, A., Sako, Y., Yamamoto, M. (1993). Confined Lateral Diffusion of Membrane-receptors as studied by single-particle tracking (nanovid microscopy) — Effects of calcium-induced differentiation in cultured epithelial cells. *Biophysical Journal* 65, 2021–2040.

- Liu, T., Mirschberger, C., Chooback, L., Arana, Q., Dal Sacco, Z., MacWilliams, H., Clarke, M. (2002). Altered expression of the 100kDa subunit of the Dictyostelium vacuolar proton pump impairs enzyme assembly, endocytic function and cytosolic pH regulation. *Journal of Cell Science* 115, 1907–1918.
- Marin, F.T., Goyetteboulay, M., Rothman, F.G. (1980). Regulation of development in Dictyostelium-Discoideum .3. Carbohydrate-specific inter-cellular interactions in early development. *Developmental Biology* 80, 301–312.
- Marquardt, D.W. (1963). An algorithm for least-squares estimation of nonlinear parameters. *J. soc. Ind. appl.* 11, 431.
- Matz, M.V., Fradkov, A.F., Labas, Y.A., Savitsky, A.P., Zaraisky, A.G., Markelov, M.L., Lukyanov, S.A. (1999). Fluorescent proteins from nonbioluminescent Anthozoa species. *Nature Biotechnology* 17, 969–973.
- Maxfield, F.R. (2002). Plasma membrane microdomains. *Current Opinion in Cell Biology* 14, 483–487.
- Moerner, W.E., Orrit, M., Weiss, S., Gimzewski, J.K., Joachim, C., Mehta, A.D., Rief, M., Spudich, J.A. Smith, D.A., Simmons, R.M. (1999). Single Molecules. Anonymous. *Science* 283, 1667–1695.
- Parent, C.A. (2004). Making all the right moves: Chemotaxis in neutrophils and Dictyostelium. *Current Opinion in Cell Biology* 16, 4–13.
- Parent, C.A., Blacklock, B.J., Froehlich, W.M., Murphy, D.B., Devreotes, P.N. (1998). G protein signaling events are activated at the leading edge of chemotactic cells. *Cell* 95, 81–91.
- Sako, Y., Minoghchi, S., Yanagida, T. (2000). Single-molecule imaging of EGFR signalling on the surface of living cells. *Nat Cell Biol* 2, 168–72.
- Schmidt, T., Schütz, G.J., Baumgartner, W., Gruber, H.J., Schindler, H. (1996a). Imaging of single molecule diffusion. *Proc Natl Acad Sci U S A* 93, 2926–9.
- Schmidt, T., Schütz, G.J., Gruber, H.J., Schindler, H. (1996b). Local stoichiometries determined by counting individual molecules. *Analytical Chemistry* 68, 4397–4401.
- Schütz, G.J., Kada, G., Pastushenko, V.P., Schindler, H. (2000). Properties of lipid microdomains in a muscle cell membrane visualized by single molecule microscopy. *Embo J* 19, 892–901.
- Schütz, G.J., Schindler, H., Schmidt, T. (1997). Single-molecule microscopy on model membranes reveals anomalous diffusion. *Biophysical Journal* 73, 1073–1080.
- Schütz, G.J., Trabesinger, W., Schmidt, T. (1998). Direct observation of ligand colocalization on individual receptor molecules. *Biophys J* 74, 2223–2226.
- Shaner, N.C., Campbell, R.E., Steinbach, P.A., Giepmans, B.N.G., Palmer, A.E., Tsien, R.Y. (2004). Improved monomeric red, orange and yellow fluorescent proteins derived from *Discosoma* sp red fluorescent protein. *Nature Biotechnology* 22, 1567–1572.
- Sheetz, M.P. (1995). Cellular plasma membrane domains. *Molecular Membrane Biology* 12, 89–91.
- Simons, K., Ikonen, E. (1997). Functional rafts in cell membranes. *Nature* 387, 569–572.
- Singer, S.J., Nicolson, G.L. (1972). The fluid mosaic model of the structure of cell membranes. *Science* 175, 720–731.
- Smart, E.J., Graf, G.A., McNiven, M.A., Sessa, W.C., Engelman, J.A., Scherer, P.E., Okamoto, T., Lisanti, M.P. (1999). Caveolins, liquid-ordered domains, and signal transduction. *Molecular and Cellular Biology* 19, 7289–7304.
- Song, K.S., Sargiacomo, M., Galbiati, F., Parenti, M., Lisanti, M.P. (1997). Targeting of a G(alpha) subunit (G(i)l alpha) and c-Src tyrosine kinase to caveolae membranes: Clarifying the role of N-myristoylation. *Cellular and Molecular Biology* 43, 293–303.
- Trautman, J.K., Macklin, J.J., Brus, L.E., Betzig, E. (1994). Near-field spectroscopy of single molecules at room temperature. *Nature* 369, 40–42.
- Tsien, R.Y. (1998). The green fluorescent protein. *Annual Review of Biochemistry* 67, 509–544.
- Vereb, G., Szollosi, J., Matko, J., Nagy, P., Farkas, T., Vigh, L., Matyus, L., Waldmann, T.A., Damjanovich, S. (2003). Dynamic, yet structured: The cell membrane three decades after the Singer–Nicolson model. *Proceedings of the National Academy of Sciences of the United States of America* 100, 8053–8058.



- Watts, D.J., Ashworth, J.M. (1970). Growth of Myxamoebae of cellular slime mould Dictyostelium-discoideum in axenic culture. *Biochemical Journal* 119, 171.
- Xiao, Z., Devreotes, P.N. (1997). Identification of detergent-resistant plasma membrane microdomains in Dictyostelium: Enrichment of signal transduction proteins. *Molecular Biology of the Cell* 8, 855–869.
- Xiao, Z., Zhang, N., Murphy, D.B., Devreotes, P.N. (1997). Dynamic distribution of chemoattractant receptors in living cells during chemotaxis and persistent stimulation. *Journal of Cell Biology* JID - 0375356 139, 365–374.
- Xie, X.S., Dunn, R.C. (1994). Probing single-molecule dynamics. *Science* 265, 361–364.
- Weiss, S (1999). Single molecules. *Science* 283, 1667–1695.

# Chapter 6

## Mobility and Signaling of Single Receptor Proteins

Michael Prummer and Horst Vogel(✉)

6.1	Introduction.....	132
6.2	Concepts.....	132
6.2.1	Mobility is Important for Cellular Function .....	132
6.3	Techniques .....	133
6.3.1	Fluorescence Correlation Spectroscopy.....	133
6.3.2	Single-Particle Tracking .....	135
6.3.3	Advanced Fluorescence Labeling.....	139
6.3.4	Statistical Analysis.....	144
6.4	Investigations .....	148
6.4.1	Membrane Receptors .....	148
6.5	Outlook .....	156
	References.....	157

**Abstract** Because many central cellular signaling processes are initiated by receptor mediated detection of single or few physical or molecular stimuli, such processes are ideally suited to be investigated by single-molecule techniques.. This review concerns imaging of cellular signaling processes by single molecule microscopies concentrating on cell surface membrane receptors and nuclear receptors. First we give a comprehensive overview on novel developments to label proteins selectively in live cells. Then we discuss in detail how individual membrane proteins labeled with small organic fluorophores, quantum dots, or gold nanoparticles can be imaged in real-time on the upper cell surface with nanometer precision by single-particle tracking, or inside of live cells, by fluorescence correlation spectroscopy at native low expression levels. We report how single-molecule microscopies and spectroscopies can offer substantial new quantitative information to decipher the complex cellular biochemistries with exceptional spatial and temporal resolution.

---

Horst Vogel  
Institute of Chemical Sciences and Engineering, Swiss Federal Institute of Technology (EPFL),  
CH-1015 Lausanne, Switzerland  
horst.vogel@epfl.ch

R. Rigler and H. Vogel (eds.), *Single Molecules and Nanotechnology*. 131  
*Springer Series in Biophysics 12*.  
© Springer-Verlag Berlin Heidelberg 2008

## 6.1 Introduction

Many central cellular signal transduction and amplification processes are initiated by receptor mediated detection of single or few physical or molecular stimuli. Examples include single photon detection by rhodopsin (Doan et al. 2006), detection of single or few molecules of pheromones by specific insect olfactory receptors (Boeckh et al. 1965; Angioy et al. 2003), single-molecule detection by T cells in the immunologic defense system (Fooksman et al. 2006; Irvine et al. 2002; Purbhoo et al. 2004), and the detection of neurotransmitter molecules by neuronal receptors leading to an electrical transmembrane response at synapses (Matsuzaki et al. 2001; Nimchinsky et al. 2004; Lata et al. 2006).

Because the interaction between a single ligand and a single receptor is often sufficient to trigger a cellular response, such processes are ideally suited to be investigated by single-molecule techniques. There are many more situations, however, for which single-molecule experiments are superior to conventional ensemble techniques. In general, the obtained information is more complete and easier to interpret: static and dynamic heterogeneities can be identified and distinguished, and rare events and small populations are not hidden as is the case in ensemble and time-averaged measurements. Most important, fluctuation between different protein structures which finally might induce biological responses and which are hidden in ensembles, are accessible.

This review covers live-cell investigations of membrane receptors and nuclear receptors using single-molecule microscopies. The trajectories of individual membrane proteins labeled with small organic fluorophores, quantum dots, or gold nanoparticles can be imaged in real-time on the upper cell surface with nanometer precision. Thus far, single-particle tracking (SPT) of three-dimensional trajectories inside the lumen of a cell has not been reported. But protein mobility in the cell's interior as well as on its surface can be analyzed, for example, with fluorescence correlation spectroscopy (FCS). In contrast to fluorescence recovery after photo-bleaching (FRAP), which works better the higher the (baseline) intensity is, the optimal concentration regime for FCS is one dye molecule or less in the focal volume at a time and is thus ideally suited to study protein dynamics at native (low) expression levels.

## 6.2 Concepts

### 6.2.1 *Mobility is Important for Cellular Function*

The fluid mosaic model of Singer and Nicolson (1972) and its subsequent extensions (Simons and Vaz 2004; Jacobson et al. 2007; Kusumi et al. 2005) point to the importance of mobile membrane components and intracellular membrane flow for the proper function of biological cells. Molecular interaction partners, especially those involved in signaling cascades, must diffuse laterally to be able to meet and interact, and thereby initiate chemical reactions (Khan and Pessin 2002; Pierce et al. 2002). Certain membrane-bound receptors (homo- or hetero-) dimerize after

ligand binding to become activated. Classical examples are receptor tyrosine kinases such as insulin and EGF receptors (Schlessinger 2000). There are an increasing number of recent reports indicating that seven-transmembrane-helix (7TM) receptors (also named G protein coupled receptors, GPCRs) also form homo- and heterodimers whose functional importance is presently a matter of debate (Bulenger et al. 2005; Chabre and le Maire 2005). The role of diffusing neuroreceptors for development and plasticity of synaptic transmission was demonstrated using single particle imaging by Choquet and Triller (2003).

The fact that the components of biological membranes are heterogeneously distributed in space and time was already noted in the classical fluid mosaic model of Singer and Nicolson. Recent models describe biological membranes as comprising (sub)micrometer-sized lipid assemblies, sometimes termed rafts, which might provide fluid platforms that segregate membrane components, dynamically compartmentalize and enrich, for example, certain proteins and thereby modulate cellular signaling reactions (Simons and Vaz 2004, Jacobson et al. 2007; Kusumi et al. 2005). Compartmentalization in the form of such nano- or microdomains has been proposed to explain the efficiency of signal transduction and amplification at low physiological membrane concentrations of the signaling partners, due to their enrichment in the specialized signaling platforms (Ostrom and Insel 2004). The mobility of the membrane components inside compartments is by definition temporarily restricted, and may be different outside the compartments. The compartments themselves might be mobile or immobile, and might continuously change size and composition. Reliable quantitative data on size, composition, and dynamical changes of such domains, and especially their relevance for biological function in live cells are still very rare.

For example, after activating cellular signaling events, receptors undergo a number of deactivating processes including desensitization, internalization, degradation, or recycling. Mobility might be different in each of these receptor states and particular ligands or ligand classes might have further specific modulating effects. Further complexities are introduced by the interaction of receptors, signaling complexes, and platforms with intracellular proteins structures such as the cytoskeleton, or with components that modulate internalization and degradation pathways.

Although the different processes for signaling appear conceptually very reasonable, there are surprisingly few hard quantitative data available. Single-molecule microscopy and spectroscopy can in this context offer substantial new quantitative information to decipher the complex cellular biochemistries with exceptional spatial and temporal resolution.

## 6.3 Techniques

### 6.3.1 *Fluorescence Correlation Spectroscopy*

Fluorescence correlation spectroscopy (FCS) is a time-averaging fluctuation analysis of small molecular ensembles that combines high sensitivity with high statistical confidence (Vukjevic et al. 2005). Although not strictly a single-molecule technique,

and more a one-molecule-after-the-other technique, FCS requires less stringent conditions than true single-molecule detection and hence can cope better with autofluorescence, limited dye photostability and brightness, and concentrations up to tens of nanomolar, in latest developments even micromolar (Levene et al. 2003). FCS was developed in the early 1970s (Ehrenberg and Rigler 1974; Elson and Magde 1974; Magde et al. 1972), but experimental difficulties precluded its practical development until the 1990s (Eigen and Rigler 1994; Rigler et al. 1993). Since then, practical applications have quickly multiplied. In an FCS experiment fluorescence intensity is measured from an open probe volume in a sample that contains a low concentrated solution of fluorescent particles of interest. The probe volume is usually determined by a diffraction-limited confocal element that is defined by the focal volume of a collimated laser beam and a pinhole that spatially filters the emitted fluorescence light to ensure that only light from the focus is detected (Figure 6.1). Fluorescence intensity fluctuations are recorded with high time-resolution and sensitivity, and analyzed in terms of their autocorrelation function (ACF). These intensity fluctuations arise from concentration fluctuations of particles diffusing in and out of the focal volume, and from any (photophysical) process changing the emission intensity of the particles. Thus, the correlation times obtained from appropriate models give access to the diffusion coefficient of the observed species and to the kinetics of photophysical and chemical reactions. Because of its high sensitivity in the nanomolar range FCS can yield information on biomolecular interactions at natural expression levels without the need to separate the reacting molecules from the formed complexes.

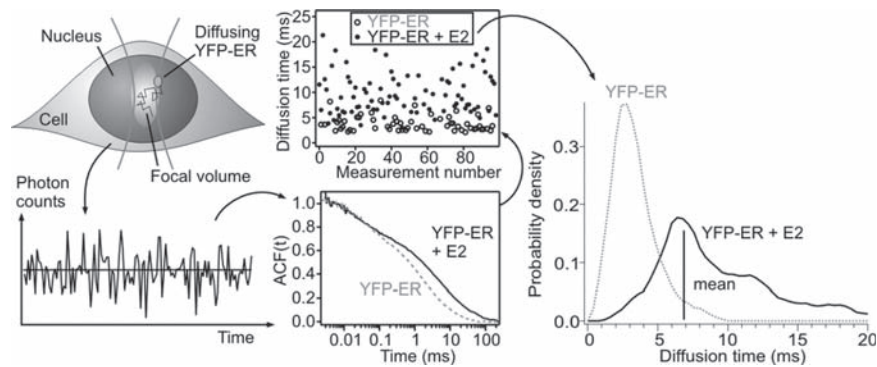


**Figure 6.1** Schematics of a fluorescence correlation spectroscopy experiment in living cells and the diffusion-time distribution analysis. From top left following the arrows: The focus of a confocal microscope is placed inside a cell at the location of interest, here the nucleus. Diffusing labeled proteins (here, a YFP-estrogen receptor construct) at low concentration give rise to a fluctuating fluorescence intensity (bottom left). The characteristic time scale of the slowest fluctuations, determined by autocorrelation techniques (bottom middle), is related to the transit time through the focal volume and thus called the diffusion time. From a series of diffusion times obtained from one or several cells (top middle), diffusion-time distributions can be constructed (right panel). As illustrated, knowing the shape of this distribution can provide much more detailed information than just knowing the mean value

Another technique to determine molecular mobility in living cells is fluorescence recovery after photobleaching (FRAP). Briefly, a predefined area in a cell loaded with fluorescently tagged biomolecules (e.g., proteins or lipids) is bleached by illumination with a high-intensity light pulse. Subsequently, the same area is illuminated again with a low-intensity (read) beam to monitor the recovery of the fluorescence intensity due to diffusion of unbleached dye molecules into this area. The reason for its widespread use is the fact that it can be implemented with standard laser scanning confocal fluorescence microscopes without hardware modification, rather than due to a fundamental superiority. Using FRAP, it is relatively easy to obtain a half-life time of recovery, which depends on the illumination geometry, the shape of the focus, and bleaching speed relative to the diffusion rate, but difficult to relate it to an absolute diffusion coefficient of the labeled particle. The theory of FCS is well established and allows quantitative measurement of the protein concentration, average diffusion coefficients, and physicochemical blinking rates (Krichevsky and Bonnet 2002; Bohmer and Enderlein 2003). FCS is most sensitive at very low concentrations of the fluorophores (i.e., natural expression levels of proteins), whereas FRAP requires much higher concentrations. FCS has microsecond time-resolution, FRAP has usually three orders of magnitude less. Although there is no fundamental limitation, the spatial resolution in FRAP experiments is typically 100 times lower than in FCS experiments. Large-scale spatial averaging can be crucial in live-cell experiments, where quite a number of different microenvironments (e.g., organelles) can reside within the area of interest. Because of the general superiority of FCS compared to FRAP, we concentrate here on the former. However, FCS has also some disadvantages: conventional FCS is rather too insensitive to reveal several modes of diffusion or to resolve multiple mobile components simultaneously, because it averages over time and ensemble, as compared to true single-molecule techniques, such as single-particle or single-molecule tracking (cf. next section). An extension of FCS to more complex samples is presented later (DDA).

The principles and applications of FCS are explained in great detail in a number of articles (Krichevsky and Bonnet 2002; Rigler and Elson 2001; Meseth et al. 1999; Thompson 1991), to which we refer the more interested reader. Fluorescence cross-correlation spectroscopy (FCCS) has been reviewed extensively by Petra Schwille and coworkers, for example, in Bacia et al. (2006), Schwille et al. (1997), and Chapter 4 in this book.

### **6.3.2 *Single-Particle Tracking***

In single-particle tracking (SPT), usually wide-field microscopy is used to image the motion of proteins or lipids on the cell surface (Saxton and Jacobson 1997). Individual molecules or small clusters are observed, with a typical spatial resolution of tens of nanometers and a typical time resolution of tens of milliseconds. To discriminate one individual molecule among often thousands of the same kind and many more of other molecules, the molecule must be labeled with an optically

detectable probe. The motion of labeled molecules is often recorded with a CCD camera and the data are stored for offline analysis. Labels of different types and sizes require specific illumination and detection methods.

Historically, a multifluorophore-labeled lipoprotein was used in the first SPT experiment (Barak and Webb 1982). DeBrabander et al. developed the technique of nanovid microscopy, in which a highly scattering colloidal gold label (~20 nm diameter) is used with bright-field microscopy (de Brabander et al. 1991), which is still the most widely used version for SPT. Larger, several hundred nanometer-sized latex or glass nanospheres are easier to detect but impose a stronger perturbation on the system. For instance, it is still a matter of fierce debate if and to what extent larger particles interact with the cellular membrane and the extracellular matrix, thus dominating the dynamics of the proteins to which they are attached. Particles with radii of less than 10 nm are less disruptive but more difficult to detect as the scattering cross-section scales with  $r^6$ . Recently, new optical methods based on interference (Lindfors et al. 2004) and absorption (Cognet et al. 2003; Berciaud et al. 2004) have been developed to overcome this size barrier, although with considerable instrumental effort.

In scattering SPT, typically gold nanoparticles are exposed with dark-field or DIC illumination, or with coherent single-frequency or white-light laser fields. Detection in DIC is usually done in transmission mode; scattered light can be detected also in reflection. Depending on the size and the material of the particle and the illumination wavelength, the scattering process may be of Rayleigh- or Mie-type and may involve plasmon resonance enhancement. But light cannot only be scattered by the probe particle but also by any localized refractive index inhomogeneity, such as that arising from intracellular organelles, vesicles, or membrane extrusions.

The most common detection method involves high-speed CCD cameras with moderate sensitivity. As a rule of thumb, the faster the camera, the higher is the read-out noise. But because the scattering amplitude is to a large extent simply proportional to the illumination intensity, there is virtually no limit to the signal amplitude that can be obtained, except for heating and destroying of the sample. Therefore, background noise is usually accepted for the sake of speed, and a position resolution of 10 nm in 30 ms is routinely achieved. At this point it should be noted that even though the distance between two particles can be measured with nanometer accuracy, the diffraction limit still determines whether they can be resolved. An even better position and time resolution (0.1 nm in 10  $\mu$ s) is obtained with quadrant photodiode (QPD) detection of the forward scattered light (Pralle et al. 1999). Unfortunately, this resolution comes at the cost of reducing the number of simultaneously observed particles from as many as 100 down to 1 because whereas a CCD camera detects in parallel, QPD detection is serial.

For specific labeling of membrane proteins the (typically) metallic NPs are chemically functionalized and also passivated to avoid unspecific sticking to any surface, for instance, the plasma membrane. Functionalization is conventionally achieved using monoclonal antibodies, which are unspecifically adsorbed to the NP surface. Usually only a fraction of the antibodies will retain the ability to bind their target. This is nevertheless no limitation inasmuch as only a single bond between the NP and one target molecule is required; thus the density of active antibodies should be small.

Two target proteins bound to one NP can lead to serious artifacts. For example, close proximity of membrane receptors can inadvertently trigger signaling cascades. Also, the mobility of a double-targeted NP can be completely different from a single-targeted NP: One impenetrable barrier between two anchors completely immobilizes the doubly bound NP whereas a singly bound NP would be free to move in each of the two half-spaces. Therefore, great care is required to control the linker surface density on the NP. On the other hand, a small surface fraction of specific interaction leaves a large surface fraction of potential unspecific interaction. And as the name suggests, there is no specific protocol to block unspecific interactions. These aspects make surface passivation the greatest challenge in any bionanotechnological application.

In single-chromophore tracking, instead of the scattered illumination light, Stokes shifted fluorescence is used to detect a label (Figure 6.2). Typically, an area of 10–30  $\mu\text{m}$  diameter is illuminated by collimated laser light (intensity  $\sim 1 \text{ kWcm}^{-1}$ ). The excitation light is absorbed by the chromophore that enters the first electronically excited state. After fast relaxation (the Stokes or solvent shift) and after an exponential residence time (the fluorescence lifetime) the emitted red-shifted fluorescence light is detected by a camera. The two characteristic properties of fluorescence with respect to the excitation, red shifted and delayed, can be exploited to efficiently block the excitation light by dichroic mirrors and spectral filters, and also by employing time criteria, that is, pulsed laser sources and time-gated detection. For these reasons, fluorescence has the potential of being a “background-free” technique. In reality, however, autofluorescence from intracellular fluorescent molecules, such as flavins, or from any material in the optical path, such as sparse color centers in glass, is ubiquitous. In order to facilitate single fluorophore detection, the fluorescence from one target molecule has to be greater than the sum over all autofluorescence sources. Even if “nonfluorescent” molecules in cells have a brightness (absorption cross-section  $\times$  fluorescence quantum yield) that is  $10^6$  times less than that of good fluorophores, the presence of only  $10^6$  of such molecules makes single-molecule detection impossible. Therefore, great care is usually taken in reducing autofluorescent background by the selection of low-background medium, chemicals, glass, and even cell types, and by the use of strong fluorophores with extinction coefficients  $\sim 10^5 \text{ M}^{-1}\text{cm}^{-1}$ , quantum yields  $\sim 1$ , and efficient and long excitation wavelengths.

Two modes of wide-field microscopy are most often used for SPT (Figure 6.2): conventional epi-fluorescence microscopy and total internal reflection microscopy (TIRM). In TIRM, the excitation laser beam reaches the sample-carrying glass–water interface at an angle larger than the critical angle of total internal reflection  $\alpha = 61^\circ$ , defined by  $\sin(\alpha) = n_w/n_g$ , the ratio of the refractive indices of water and glass, respectively. The traveling light waves are reflected back into the high refractive index medium at the interface but an evanescent electric field penetrates into the low refractive index medium, with an angle- and wavelength-dependent exponentially decaying penetration depth (Axelrod et al. 1984). This evanescent electric field is able to excite fluorescent molecules in a very thin slab of about 100 nm, thereby reducing substantially the amount of laser-induced background signal. TIRM is thus a superior tool with excellent SBR to study protein motion at the lower plasma membrane or model membranes, which are in contact with the glass surface (Ueda et al. 2001). Transmembrane proteins may experience strong interaction



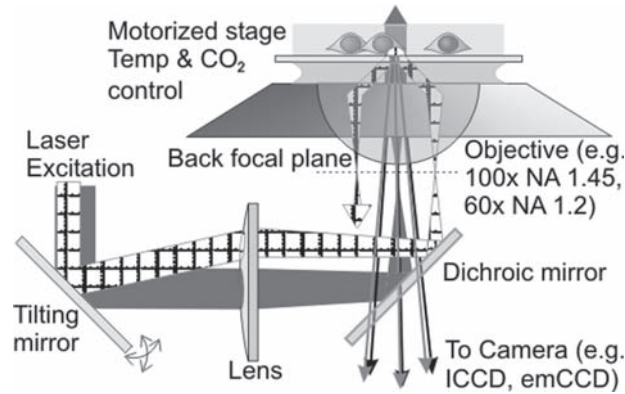


**Figure 6.2** Schematic drawing of a combined total internal reflection (TIR) and epi-fluorescence wide-field microscope used for single-particle tracking. The excitation laser is focused to the back focal plane of a high-NA objective, either on-axis (epi) or off-axis (TIR) relative to the optical axis, to create an illumination area of several tens of micrometers. The TIR-mode is used to illuminate selectively the lower cell membrane up to a distance of  $\sim 100$  nm from the cover slip, thus avoiding most of the cellular background fluorescence. The epi-fluorescence mode is used to illuminate the top surface of the cell that has no contact with the solid support and where proteins experience no artificial hindrance. The drawback is, that by shining light through the whole cell, substantial autofluorescence is created, especially when low wavelength excitation light is used ( $< 550$  nm). The fluorescence photons are collected by the same objective and separated from the excitation light by a dichroic mirror; steep-edge long-pass filters are used to block residual stray and Raman-shifted light. Sensitive cameras are used for imaging, such as intensified or electron-multiplying CCD cameras. For long-term observations of cellular signaling processes, the sample is kept at a controlled temperature and  $\text{CO}_2$  level

with and perturbation by the glass surface, but inner-leaflet proteins attached by lipid anchors are suitable targets for TIRM. Transmembrane proteins are better observed at the upper plasma membrane by epi-fluorescence microscopy at the cost of higher background, because the whole cell is illuminated. It seems that the detection of single GFP molecules (excitation at 488 nm) is possible in TIR geometry (Murakoshi et al. 2004), whereas YFP (excitation at 514 nm) can be detected also at the upper cell surface (Lommerse et al. 2004), and longer excitation wavelengths (561, 568, 633, or 647 nm) are more useful and cause much less background. Going farther into the near-infrared spectral region starts to interfere with the spectral response of current cameras and the transmission of the optical components.

Not many different types of cameras available are useful for single dye tracing. Historically, image intensifiers were used first, owing to their single-photon sensitivity. But the much higher detection quantum yield of silicon-based CCD chips ( $\sim 90\%$  compared to  $\sim 30\%$ ) and the lower noise compensates for the absence of any amplification. In the last couple of years, electron multiplying CCD cameras have become the experimentalists' favorite, unifying the best of both worlds: high QY photoconversion of the CCD and single-photon sensitivity by on-chip amplification above the read-out noise level. In fact, the amplification can be tuned continuously from 1 (normal CCD mode) to 20,000.

To end this section we compare SPT using scattering and using fluorescence. One major difference between the two approaches is the size of the labels that can be used. In the case of fluorescence, markers can be as small as a few nanometers (organic dyes) and as large as 20 nm in the case of fully functionalized and passivated nanocrystalline semiconductor quantum dots (QDs), the same size or slightly smaller than gold NPs used in scattering SPT. Autofluorescent proteins (AFPs) and labeled Fv antibody fragments range in size somewhere in between. In terms of photostability, the order from most stable to fast bleaching is from scattering NPs (no bleaching), QDs (virtually infinitely stable) via organic dyes ( $\sim 10^4$  detected photons), to AFPs ( $<1000$  detected photons). These numbers result in average observed trace lengths of typically  $>1000$  frames (NPs),  $>100$  frames (QDs), 10–50 frames (organic dyes) and 2–5 frames (AFPs), respectively (our own estimate).

In summary, the limitations of the different labels/techniques are: low ( $\sim 100$  ms) time resolution (AFPs, organic dyes), photobleaching (AFPs, organic dyes), cellular autofluorescence (AFPs), aggregation (QDs, NPs, some AFPs), unspecific binding (QDs, NPs, organic dyes), cross-linking (QDs, NPs), intrinsic cellular scattering by organelles (NPs), and interaction with extracellular matrix (QDs, NPs). In comparison, the advantages of the labels/techniques described are: high ( $\sim 10$   $\mu$ s) time-resolution (NPs), stability (NPs, QDs), 1:1 labeling (AFPs),  $<1:1$  labeling (dyes), low perturbation (dyes), multiplexing/selectivity (QDs, dyes, AFPs), and no cytotoxicity (NPs, AFPs, dyes).

The principles and applications of SPT are explained in more detail in an excellent review article (Saxton and Jacobson 1997) and in the work of deKeijzer et al. in Chapter 5 of this book, to which we refer the more interested reader. In order to gather information on protein mobility in cell membranes from SPT, a large number of particle traces must be analyzed using statistical methods, due to the stochastic nature of Brownian motion, as described in a later section. The next section is devoted to a summary of state-of-the-art labeling strategies that have emerged in recent years and that complement more traditional approaches.

### 6.3.3 *Advanced Fluorescence Labeling*

Current orthogonal labeling strategies already in practice or potentially suited for SMI and FCS of proteins and other components in living cells or in vitro involve the use of (i) fluorescent analogues of ligands, (ii) fluorescent antibodies binding to selective epitopes on the target protein or fluorescent streptavidin binding to strept-tags or biotin on the target protein, (iii) the fusion to autofluorescent proteins (AFPs), or the direct labeling of proteins either (iv) posttranslationally by chemical reactions of activated chromophores (chemical labeling of OH, -COOH, -NH<sub>2</sub> or -SH comprising amino acid side chains; reversible labeling of polyhistidine sequences by NTA containing chromophores) or (v) during protein synthesis by introducing nonnatural fluorescent amino acids using the suppressor tRNA technology, and finally (vi) the posttranslational labeling of carrier proteins fused to the protein

under investigation. Each labeling technique has particular advantages and disadvantages (for a recent review on labeling, see (Hovius et al. 2006)).

- (i) Receptor ligands can be coupled to diverse high-performance organic fluorophores but it is a cost- and labor-intensive process requiring a different synthesis strategy for each particular ligand. The conjugate often has properties substantially modified from the unlabeled ligand and only allows for the study of the ligand-bound state of the receptor. Nevertheless, a number of groups have undertaken this approach with some effort but with considerable success (Lill et al. 2005; Hegener et al. 2004; Briddon et al. 2004; Meissner and Haberlein 2003; Maier et al. 2005; Wohland et al. 1999; Grandl et al. 2007; Freudenthaler 2002).
- (ii) Fluorescent antibodies are available for a broad range of epitopes, but they are often larger than the protein of interest, and may cross-link the target proteins thereby interfering with their mobility and functionality. In addition to antibodies raised against epitopes specific for a particular protein (Bouzigues and Dahan 2007), there are antibodies against generally used sequence-tags, for instance, those used for protein purification such as strep-, myc-, flag- or polyhistidine-tags (Ehrensperger et al. 2007; Hassaine et al. 2006). Carefully chosen examples, once they are known not to interfere with the function of the target, also constitute convenient labels in situations where signal strength is an issue, because they can carry multiple fluorophores (on the order of two to ten). In a comparable approach, target proteins have been selectively labeled by fluorescent streptavidin either at strep-tags (Hassaine et al. 2006) or at biotinylated protein sites (Ehrensperger et al. 2007; Charbonniere et al. 2006). Also in this case the size of the probe and its potential cross-linking capability may change the functionality of the target proteins. These disadvantages might be circumvented by using so-called anticallins, small ca. 20kDa proteins derived from human lipocalins where artificial ligand binding sites have been introduced by protein engineering (Skerra 2007).
- (iii) Green fluorescent protein (GFP) and its variants (Shaner et al. 2005; Giepmans et al. 2006) can be attached genetically at different positions to the target protein in a 1:1 stoichiometry, but it suffers from poor photostability, the tendency to form oligomers and spectral overlap with other cellular luminescent compounds leading to substantial autofluorescence. Also, for the study of proteins in the plasma membrane it is preferable to label only the properly translocated fraction, especially in cases where this fraction is small. Although AFPs are not the best choice for SPT in terms of their photophysical properties, their beneficial biochemical properties are responsible for their impact in intracellular FCS applications (Bacia and Schwille 2003).
- (iv) Direct covalent labeling of particular amino acid side chains bearing -COOH, -OH, -SH, and -NH<sub>2</sub> groups by activated chromophores are an ideal method for imaging purified single proteins but usually lack selectivity in the case of live cells due to the high abundance of these groups, resulting in large fluorescence background (Asamoah et al. 2003). Nevertheless, single voltage-gated ion channels labeled by this approach have been investigated in living frog oocytes to detect structural changes of the channel during voltage-gating (Sonnleitner 2002). For technical details we refer to the exceptional comprehensive collection

of examples, mostly on ensemble measurements, in *The Handbook—A Guide to Fluorescence and Labeling Technologies* from Molecular Probes/Invitrogen (<http://probes.invitrogen.com/handbook/>).

A novel covalent labeling of specific tetracystein sequences by biarsenical-bearing chromophores was developed by Tsien and coworkers (Griffin et al. 1998; Martin et al. 2005). Although it has thus far been applied only to ensemble imaging, the method offers interesting potential for single-molecule microscopy. The reactive yet unfluorescent chromophore permeates the cellular membrane and becomes fluorescent after reacting with the tetracystein sequence motif on a particular target protein inside of a living cell.

Several strategies have been developed in recent years to overcome some of the limitations of the methods mentioned above. A few recent reviews summarize these efforts (Miller and Cornish 2005; Johnsson and Johnsson 2007; Foley and Burkart 2007). In the following we summarize our own efforts to use the novel approaches for single molecule microscopy.

### Suppressor tRNA Technology

Several methods have been developed to incorporate unnatural amino acids site-specifically into proteins in mammalian cells. Chemically aminoacylated suppressor tRNAs have been microinjected or electroporated into CHO cells and neurons, respectively, and used to suppress nonsense amber mutations with a series of unnatural amino acids (Wang et al. 2006). It was thus possible to incorporate unnatural amino acids with diverse physicochemical and biological properties into defined positions of the sequence of target proteins expressed in mammalian cells. This method has been widely used to probe channel proteins by electrophysiology (Monahan et al. 2003) and was used for the first time by Turcatti et al. (1996) to insert nonnatural fluorescent amino acids at specific sites in a GPCR (NK2 receptor) in frog oocytes for exploring by FRET the receptor structure. Meanwhile, Schultz and coworkers extended the method in an elegant general approach (Liu et al. 2007): a mutant *Escherichia coli* aminoacyl-tRNA synthase (aaRS) is first evolved in yeast to selectively aminoacylate its tRNA with the unnatural amino acid of interest. This mutant aaRS together with an amber suppressor tRNA is then used to site-specifically incorporate the unnatural amino acid into a protein in mammalian cells in response to an amber nonsense codon. This and other approaches (Ilegems et al. 2002) overcome the originally low efficiency of expression.

### AGT-Labeling

This method is based on the irreversible and specific reaction of human O<sup>6</sup>-alkylguanine–DNA alkyltransferase (hAGT) with fluorescent derivatives of O<sup>6</sup>-benzylguanine (BG), leading to the transfer of the synthetic probe to a reactive cysteine residue on hAGT which is fused to a protein of interest (Keppler et al. 2003, 2004).

Wild-type hAGT is a monomeric protein of 207 aa, the 30 C-terminal residues of which can be deleted without affecting the reactivity against BG, making it smaller than autofluorescent proteins. It is important to note that the rate of the reaction of AGT fusion proteins with BG derivatives is independent of the nature of the label, making it possible to label a single AGT fusion protein with a variety of different probes. Specific labeling of AGT fusion proteins in mammalian cells can be achieved by using AGT-deficient cell lines, and it has been shown that nuclear-localized AGT can be labeled specifically with fluorescein in such cells (Keppler et al. 2003, 2004). Synthetic BG derivatives can be used for the sequential labeling of AGT fusion proteins with a variety of different fluorophores in live mammalian cells; the approach can be used for multicolor analysis of cellular processes and fluorescence resonance energy transfer (FRET) measurements (Meyer et al. 2006). A mutant form of AGT was recently created that can be specifically labeled with substrates that are not accepted by wild-type AGT (Heinis et al. 2006). This permits the labeling of two different AGT fusion proteins with various fluorophores in the same cell or in vitro.

### **ACP-Labeling**

This approach comprises the enzymatic transfer (using specific phosphopanteyl transferases) of the phosphopantetheine of a fluorescent Coenzyme A (CoA) conjugate to an acyl-carrier protein (ACP) fused to the target protein (George et al. 2004; Yin et al. 2004). This technique enabled us to track single G protein-coupled receptors during signaling (Meyer et al. 2006; Jacquier et al. 2006) because several obstacles had been overcome: (i) proteins not properly inserted in the plasma membrane were not labeled and hence did not contribute to out-of-focus background fluorescence. (ii) The fraction of labeled protein could be precisely controlled in time (pulse labeling), with the possibility of repetitive labeling, ensuring a low and well-defined dye concentration required for single-molecule detection. (iii) Free choice of probes allows protein labeling with long-wavelength dyes (e.g., Cy5, Atto dyes) of high absorption cross-section, high quantum yield, and high photostability that were used to improve signal-to-background ratio and observation time. (iv) Multicolor labeling of defined ratio(s) between different probes is easily possible by controlling the composition of substrates in the bulk medium; this is ideally suited for controlling donor-acceptor ratios for FRET measurements of membrane proteins in living cells. (v) Nonspecific binding of the label to the plasma membrane, the most crucial obstacle for a successful application of single molecule microscopy, was reduced by the presence of the hydrophilic CoA-moiety. (vi) Recently, the size of the ACP tag was reduced from 76 to 11 residues without losing too much specificity and efficiency of the labeling reactions, making this approach even more attractive (Yin et al. 2005).

### **Native Protein Ligation**

Native chemical ligation using protein segments prepared by recombinant protein expression has opened the way for the generation of tailor-made large proteins in an

approach called expressed protein ligation (EPL) (Muir 2003). EPL has recently been used to site-specifically label several recombinant proteins with fluorescent groups suitable for single molecule spectroscopy and microscopy (Becker et al. 2006).

### **NTA-Labeling**

This is a generic method to label proteins *in vivo* (and *in vitro*) selectively, rapidly (within seconds), and reversibly, with small molecular probes that can have a wide variety of properties (Guignet 2004). The probes comprise a chromophore and a metal-ion-chelating nitrilotriacetate (NTA) moiety, which binds reversibly and specifically to engineered oligohistidine sequences in proteins of interest. The feasibility of the approach was demonstrated by binding NTA-chromophore conjugates to a representative ligand-gated ion channel and a G protein-coupled receptor, each containing a polyhistidine sequence. By producing different mutant receptors, each comprising the polyhistidine sequence at a different position in the protein, it was possible to vary the probe's position and thereby obtain information on the structure and the location of the receptor in the membrane. In contrast to the transient binding of such a conventional mono-NTA, multivalent-NTA bearing fluorophores form complexes with oligohistidine sequences in proteins which show increased lifetimes of more than an hour (Lata et al. 2006; Hauser and Tsien 2007). Hence, the residence time of the NTA label can be tuned according to the specific needs from seconds to hours.

### **Ligands, Reversible Sequential Labeling (ReSeq)**

A novel method for performing reversible sequential (ReSeq)-binding assays on particular neuroreceptors has recently been developed (Guignet et al. 2007; Schreiter et al. 2005). With this assay, a series of investigations can be performed on the same cell by repetitively applying specific, fluorescently labeled ligands that have fast association–dissociation kinetics. Complete saturation ligand-binding and competition ligand-binding assays have been obtained on a single cell with excellent accuracy and reproducibility. This new approach offers several advantages as it (i) substantially reduces the number of cells needed, (ii) allows the investigation of cell-to-cell variations because extensive data can be collected with individual cells, and (iii) circumvents problems related to low expression levels of receptors and photobleaching of fluorescent ligands, because measurements can be repetitively performed on the same cell to enhance accuracy. Moreover, ReSeq-binding assays can be easily automated and implemented in on-chip analysis which offers a substantial improvement on reliability, efficiency, and reduction of sample consumption. In a typical single-molecule imaging experiment, tens of frames are recorded before fluorophore photobleaching occurs. Because a reversibly binding fluorescent ligand can be washed off completely and added fresh once again, single-molecule experiments can be repeated more than 30 times with one cell, and data with excellent statistics can be collected.

All posttranslational labeling technologies can be used for organic fluorophores and for fluorescent QDs or scattering nanoparticles, and of course equally well for immobilizing proteins, membrane fragments and whole intact cells to surfaces.

### 6.3.4 Statistical Analysis

The relevant questions to be answered with SPT are the following. Is the motion of molecules in a 2D biological membrane Brownian, anomalous or confined? What are the characteristic parameters of the particular mode of motion, for example, the diffusion coefficient, the degree of anomaly, or the confinement size? Are these properties invariant or do they depend on the state of the molecule or the environment such as the state of development of the cell? Is the ensemble of molecules homogeneous or does it consist of subensembles? If yes, of how many and in which composition? Does the composition depend on the state of the ensemble? From these directly observable properties of target molecules submersed in a membrane, indirect information on the surrounding environment and the detailed composition of the membrane can be inferred, as far as it is reflected in the mobility of the particles. This includes structural heterogeneities of cell membranes, that is, nanoscopic lipid domains (“rafts”), attached cytoskeletal elements, or the extent of protein–protein interaction.

The connection of the macroscopic diffusion coefficient  $D$  and the microscopic and molecular world is described by the Einstein relation  $D = k_B T / \gamma$  with  $k_B$  the Boltzmann factor,  $T$  the temperature, and the viscous drag coefficient  $\gamma = 6\pi\eta a$  (for a sphere of radius  $a$  in a homogeneous medium of viscosity  $\eta$ ). In special cases, corrections to the normal Stokes friction force may become relevant (Lukic et al. 2005). Diffusion of cylindrically shaped membrane proteins in two dimensions is described by the exceptionally successful Saffman–Delbrück theory (Staffman and Delbrück 1975), which nevertheless has often been and is still being revised (Gambin et al. 2006). Different modes of motion are anticipated in biological systems: free Brownian motion (Vrljic et al. 2002), directed motion, for example, particles pulled by molecular motors (Nan et al. 2005), confined diffusion, for example, in submicron domains (Suzuki et al. 2005; Jacquier et al. 2006), and anomalous diffusion, for example, due to motion through a region of obstacles (Schutz et al. 1997). They can be distinguished by their different temporal evolution of the mean-square displacement (MSD)  $\langle r^2(t) \rangle$ . Detailed basics of the statistical analysis of SPT data can be found in (Saxton and Jacobson 1997; Saxton 1993; Qian et al. 1991; Chandrasekhar 1943).

We stress one more peculiarity of SPT data analysis, because it is different from what is known to most experimentalists. In conventional data analysis the measurement process leads to a certain statistical variation of the observed (average) value, which decreases rapidly as the number of observations increases and converges eventually to the true time-independent expectation value. In the analysis of diffusion, the expectation value  $D$  itself is not constant but varies stochastically

and approaches its steady-state limit  $D_\infty$  as  $t \rightarrow \infty$ . The result of the two stochastic processes, the measurement process and the random walk, is that any average value converges very slowly to a time-independent expectation value. We have learned this lesson from many computer simulations performed by Saxton in the 1990s (Saxton and Jacobson 1997; Saxton 1993). The result is simply that in SPT longer measurement times and many more data points are needed in order to arrive at statistically meaningful results than in other single-particle observations.

### Single-Molecule Analysis of SPT

In scattering SPT it has become common practice to compute the *MSD* directly from the recorded trajectories containing often several thousand observations (Figure 6.3). From *MSD(t)* one can compute without assuming any model the so-called instantaneous or microscopic diffusion coefficient  $D_{\text{inst}}$  from the linear slope of *MSD(t)* during the first three data points. This was initially motivated by the difficulty in providing a valid model for protein diffusion in a medium as complex as the cell membrane. The concept of  $D_{\text{inst}}$  was the smallest common denominator assuming that on short time and length scales the motion is always Brownian and that no a priori knowledge is available for the longer timescale (Murakoshi et al. 2004). Another theoretically and philosophically well-supported strategy to analyze data without fixing an a priori model is to provide the results for a whole collection of models. The interpretation of the invariable data is then subject to the preference of the reader and to new information acquired in the future.

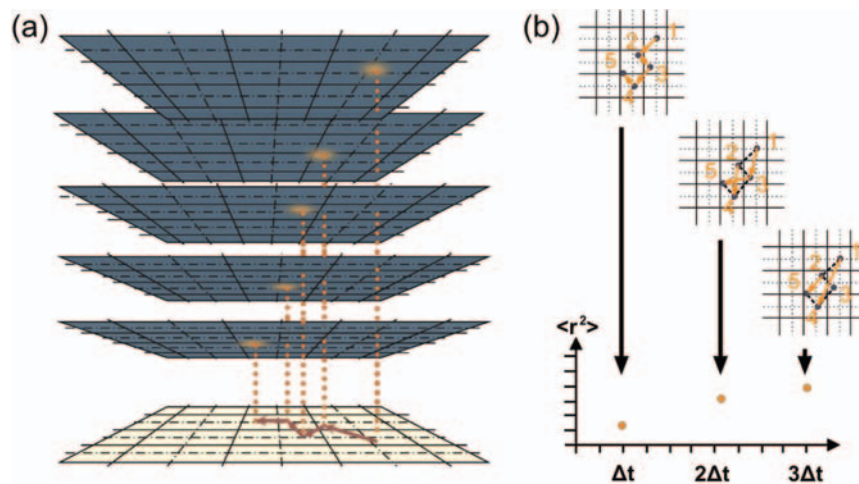


**Figure 6.3** Connectivity algorithm in single-particle tracking. **(a)** Centroids of particle positions are determined in each movie frame, usually by least-square fitting of a 2D-Gaussian. Adjacent positions in consecutive frames are connected to build up a trajectory. **(b)** Squared displacements between frames with increasing time lag are computed and averaged over all frames



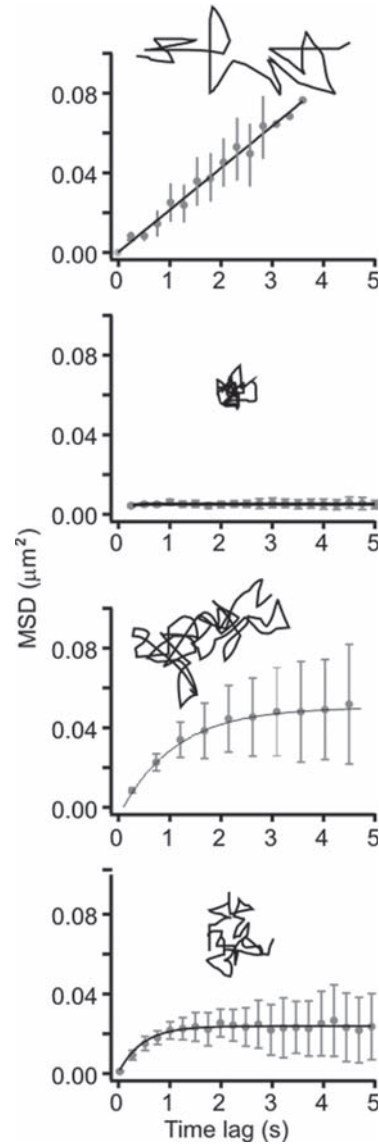
Anomalous diffusion arises from the interaction of the probe particle with other particles that do not completely confine its motion but that slow it down considerably. This vague phrasing is a reflection of the variety of molecular processes all leading to the nonlinear, nonlimited  $MSD(t)$  of anomalous subdiffusion, which makes further interpretation possible only in well-controlled model systems. In more complex and less-controlled conditions, such as the membrane of a living cell, the model of confined diffusion offers several advantages over the minimalistic  $D_{inst}$  approach without constraining too much towards a particular model because it is still fairly phenomenological: confined diffusion describes the  $MSD(t)$  in terms of two parameters, the diffusion coefficient  $D$  and the observed (apparent) confinement size  $L$ . In the limit of  $L \rightarrow \infty$ , diffusion approaches free Brownian motion and in any other case  $L$  characterizes the size of the area the particle was constrained to during the time of observation. Introduction of the confinement allows for a correct determination of the diffusion coefficient in the presence of subdiffusion and a further discrimination of otherwise hidden subensembles. To account for the broadening of single-particle point-spread functions due to the finite integration time of the acquisition setup and the mobility of the particle, Salome and coworkers have derived an important correction because generally the diffusion coefficient and the confinement size are underestimated (Destainville and Salome 2006).

Whereas the depth of data in scattering SPT in principle allows the determination of the most probable model underlying the trace of each single particle, the short trajectories in fluorescence SPT render an unambiguous assignment of a particular set of fitted parameters to single-molecule traces much more difficult. In cases where an analysis of each individual trace is impossible because they are too short, cumulative analysis might be applicable (see next subsection). In only a couple of reports to date, highly photostable fluorescent markers facilitated the recording of sufficiently long trajectories to obtain  $MSD(t)$  traces (Figure 6.4) and histograms of single particle-derived diffusion coefficients (Kusumi et al. 2005; Vrljic et al. 2002; Jacquier et al. 2006; Nakada et al. 2003; Prummer et al. 2006; Seisenberger et al. 2001), which contain of course much more information than just their average.

### Cumulative Analysis of SPT

In single-particle tracking of single dye molecules it is common practice to construct the probability distribution  $P(r^2; t_{lag})$  for the occurrence of a square displacement smaller than  $r^2$  for each time-lag  $t_{lag}$  (100). For molecules with identical (2D) diffusion behavior,  $P(r^2; t_{lag}) = 1 - \exp(-r^2 / 4D t_{lag})$ , and the presence of several subpopulations leads to an equivalent expression containing the sum of weighted exponentials (Schutz et al. 1997; Schmidt et al. 1996; Kusumi et al. 1993). This way, the composition of a mixed ensemble and the different diffusion coefficients can be retrieved from the collected recordings of many molecules, even if each individual trajectory is very short (cf. deKeijzer et al., Chapter 5 in this volume). This represents a considerable advantage over the single-molecule analysis for inferior experimental conditions, such as low photostability or brightness. The disadvantage of the cumulative analysis

**Figure 6.4** Different types of trajectories and resulting  $MSD(t)$  found in living cells. Typical behavior of membrane proteins include free diffusion (1st), immobile molecules (2nd), where the fluctuations are due to instrumental noise  $< (100\text{ nm})^2$ , and confined diffusion of different domain sizes (3rd and 4th). (After Jacquier et al. (2006) and Prummer et al. (2006))



is that in practice it is difficult to resolve more than two species from an ensemble, such as one mobile and one immobile species. Moreover, the mathematical expression mentioned above is, strictly speaking, valid only for free Brownian motion. The treatment of confined diffusion would require introducing some cutoff radius  $r_\infty$ , such that  $P(r^2; t_{\text{lag}}) = 1$  for  $r > r_\infty$  for any  $t_{\text{lag}}$ . Unfortunately, up to now any theoretical description of the cumulative probability distribution of confined diffusion in the framework of SPT is missing. It turns out, however, that the conventional treatment for free diffusion, when applied to confined diffusion, leads only to minor errors, as

seen from computer simulations. In summary, whereas the current situation is somewhat unsatisfying from a theoretical point of view, the practical value of the cumulative analysis has led to its widespread use.

### **Diffusion-Time Distribution Analysis of FCS**

In highly heterogeneous samples, such as the nucleus of a living cell, it is superior to analyze a distribution of diffusion times of very short time intervals (diffusion-time distribution analysis, DDA; Figure 6.1), as opposed to the determination of a set of mean diffusion times from a multispecies model, averaged over a long time and over the whole ensemble (Jankevics et al. 2005). The latter also includes maximum-entropy fitting of a multicomponent model to a single ACF (Sengupta et al. 2003), which often gives much less pronounced results, probably due to the less robust fitting procedure. The time intervals in DDA should be kept as short as possible to obtain a very small subset of the whole distribution of diffusion times present in the sample, but long enough to collect a sufficiently long photon stream for a reliable determination of the diffusion time (in our case 5 s). Short time intervals also reduce the effect of bleaching in each individual ACF, which is especially useful for intracellular measurements using YFP, where bleaching is often rather high.

In order to construct diffusion-time distributions the ambiguity commonly associated with the building of histograms (i.e., the choice of bin size and bin position) can be avoided by averaging over several realizations of a histogram. By this and by choosing the bin size  $b$  according to  $b = 1.06 \min(\sigma, R/1.34) n^{-1/5}$ , we derived the optimal nonparametric estimator for the probability density function from our data (Venables and Ripley 1997). Here,  $\sigma$  is the standard deviation,  $R$  the interquartile range, and  $n$  the number of points entering the histogram. The crucial advantage of DDA compared to conventional bioanalytical tools is that it allows for the determination not only of binding partners, but also of their equilibrium distributions, in living cells, at native expression levels. Diffusion-time distribution analysis thus provides a general approach to monitor biochemical networks in individual living cells and a new tool in the emerging field of live-cell proteomics.

## **6.4 Investigations**

### **6.4.1 Membrane Receptors**

#### **6.4.1.1 G Protein-Coupled Receptors**

##### Neurokinin-1 Receptor

Recently, Lill et al. performed in vivo single-dye tracking of the signaling kinetics of the Neurokinin-1 receptor (NK1R), a G protein-coupled receptor (GPCR) involved in nociception and inflammation (Lill et al. 2005). The signaling cascade

of NK1R is initiated by the specific binding of a fluorescently labeled agonist, Substance P (SP). The diffusion of single receptor–ligand complexes in the plasma membrane of living HEK293 cells was imaged using single-molecule wide-field fluorescence microscopy at 100 ms time resolution. To investigate universal patterns in the diffusion trajectories, the authors defined the ligand-binding event as the common starting point. This synchronization allows the observation of changes in the mode of diffusion. Diffusion of ligand–receptor complexes is slowed significantly and becomes more constrained as a function of time during the first 1000 ms. The decelerated and more constrained diffusion is attributed to an increasing interaction of the GPCR with cellular structures after ligand binding.

We have complemented this investigation by tracking the labeled receptor without any ligand (98). By utilizing ACP-labeling with the small organic fluorophore Cy5, we were able to retrieve an unusually heterogeneous and broad distribution of NK1R diffusion coefficients even in the absence of ligand. In this study we provided first evidence that the ACP-labeling technology is compatible with single-molecule live-cell imaging. Moreover, only with the help of ACP-labeling was it possible to overcome cellular autofluorescence, to image GPCRs at a sufficient signal to background ratio, and to obtain much longer traces than those obtained with AFP-labeling.

#### $\mu$ -Opioid Receptor

Daumas et al. used SPT of nanoscopic gold colloids to study the diffusion of the  $\mu$ -opioid receptor, target of many analgesic drugs including opiates, in living rat kidney fibroblast cells (Daumas et al. 2003). A compartmentalization of the receptors and/or the other partners was suggested as accounting for the rapidity and specificity of signaling, but experimental studies devoted to the question of the membrane organization and dynamics of the components of this signal transduction pathway are still very scarce. The specific labeling of the receptor coupled to a T7-tag at its *N*-terminus, stably expressed in fibroblastic cells, was achieved by colloidal gold coupled to a monoclonal anti T7-tag antibody. The lateral movements of the particles were followed at room temperature by DIC video microscopy at 40 ms time resolution during 2 min with a spatial precision of 15 nm. The receptors were found to have either a slow or directed diffusion mode (10%) or a “walking confined” diffusion mode (90%) composed of a long-term random diffusion and a short-term confined diffusion, and corresponding to a diffusion confined within a domain that itself diffuses. The results indicate that the confinement is due to an effective harmonic potential generated by long-range attraction between the membrane proteins. A simple model for the diffusion of interacting membrane proteins is proposed that explains the variations with the domain size of the short-term and long-term diffusion coefficients.

In contradiction to this work, Suzuki et al. (2005) found that  $\mu$ OR undergoes rapid hop diffusion at a rate comparable to that for transferrin receptor (every 45 and 760 ms on average, respectively). They assume that their fence and picket models may also be applicable to G-protein coupled receptors and found membrane

compartments (210nm and 730nm nested double compartments in the case of normal rat kidney cell line), that are likely delimited by the actin-based membrane-skeleton “fence or corrals” and its associated transmembrane protein “pickets”. Furthermore, they found that strong confinement of gold-labeled  $\mu$ OR could be induced by a prolonged on-ice preincubation of the gold probe with the cells. On the basis of the dense long trajectories of  $\mu$ OR obtained by high-speed single-particle tracking, the membrane compartments apposed and adjoined to each other were found to be delimited by rather straight boundaries, consistent with the involvement of actin filaments in membrane compartmentalization.

### Odorant Receptors

In our laboratory, we are investigating odorant receptor mobility and its relation to signaling events (Jacquier et al. 2006). We focused on functional properties and the spatio-temporal distribution of the human olfactory receptor OR17-40 in living HEK cells using two complementary fluorescence labeling methods: GFP-labeling at the intracellular C-terminus and posttranslational ACP-labeling at the extracellular N-terminus. The fluorescent tags did not interfere with the biological function and enabled us to optically distinguish and quantitatively compare surface (ACP label) and total (GFP) receptor pools at any time in living cells. As the small fluorophore added by ACP labeling did not prevent receptor endocytosis, we could reveal constitutive receptor internalization in the absence of an agonist. ACP-labeling allowed imaging of the complex mobility pattern of single OR molecules in the cell membrane. We analyzed the  $MSD(t)$  profile of each individual molecule in terms of the confined diffusion model and obtained estimated probability densities of ORs under different conditions. Although mobile receptors initially diffused either freely or within domains of various sizes, binding of an agonist or an antagonist increased partitioning of receptors into small domains of  $\sim 190$ nm, which most likely are precursors of clathrin-coated pits (Figure 6.5). The binding of a ligand therefore resulted in a modulation of the continuous constitutive internalization. After endocytosis, receptors were directed to early endosomes for recycling. This unique mechanism of continuous internalization and recycling of OR17-40 might be instrumental to allow rapid recovery of odor perception.

### Metabotropic Glutamate Receptor

Receptors for neurotransmitters are concentrated and stabilized at given sites such as synapses through interactions with scaffolding proteins and cytoskeletal elements. The transport of receptors first involves directed vesicular trafficking of intracellularly stored receptors followed by their targeting to the plasma membrane. Once expressed at the cell surface, receptors are thought to reach their final location by random Brownian diffusion in the plasma membrane plane.

Serge et al. investigated whether the metabotropic glutamate receptor mGluR5 can also be transported actively on the cell surface (Serge et al. 2002, 2003).

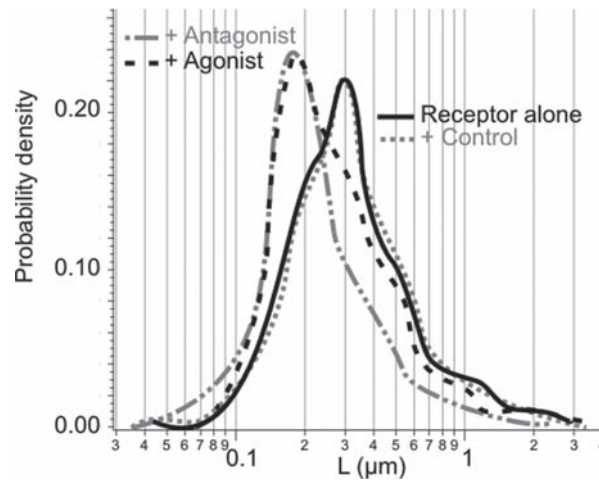


**Figure 6.5** Confinement size distributions found for odorant receptors upon addition of various ligands. The distributions are broad and heterogeneous; the experimental resolution was determined to be  $\pm 1.2$  (constant on the log scale). Both agonist and antagonist induced a reduction of the typical confinement size from 300 nm to 200 nm. (After Jacquier et al. (2006))

Using SPT they followed mGluR5 movement in real-time at the surface of neuronal growth cones or fibroblast lamellipodia, both of which bear a particularly active cytoskeleton. After a certain lag time mGluR5 experienced directed rearward transport, which depended on actin flow. On actin depolymerization, directed movement was suppressed, but receptors were still bound to a rigid structure. In contrast, receptor transport and immobilization was fully suppressed by microtubule depolymerization but was favored by microtubule stabilization. Furthermore, mGluR5 could be immunoprecipitated with tubulin from rat brains, confirming the ability of mGluR5 to bind to microtubules. The authors propose that mGluR5 can be transported on the cell surface through actin-mediated retrograde transport of microtubules. This process may play a role in receptor targeting and organization during synapse formation or during glutamate-mediated growth cone chemotaxis.

### $\beta$ 2-Adrenergic Receptor

Hegener et al. examined the agonist-induced dynamic regulation of the  $\beta$ 2-adrenergic receptor ( $\beta$ 2-AR) on living cells by FCS (Hegener et al. 2004) using a fluorescence-labeled arterenol derivative (Alexa-NA) in hippocampal neurons and in alveolar epithelial type II cells (A549). In addition to the free ligand, in both cell types receptor–ligand complexes with two distinct diffusion coefficients were observed, showing a fast lateral mobility and a hindered mobility. Fast lateral mobility of the receptor–ligand complex was detected immediately after addition of the ligand,

whereas hindered mobility was observed only after a delay of 5 min in neurons (up to 38% of total binding) and of 15–20 min in A549 cells (up to 40% of total binding). Thus, the receptor–ligand complexes with low mobility were formed during receptor regulation. Consistently, stimulation of receptor internalization using the adenylate cyclase activator forskolin shifted the ratio of receptor–ligand complexes toward the bound population. Intracellular FCS measurements and immunocytochemical studies confirmed the appearance of endocytosed receptor–ligand complexes in the cytoplasm subjacent to the plasma membrane after stimulation with the agonist terbutaline. This regulatory receptor internalization was blocked after preincubation with propranolol and with a cholesterol-complexing saponin  $\alpha$ -hederin.

### Adenosine Receptor

The A<sub>1</sub>-adenosine receptor (A<sub>1</sub>-AR) is a G protein-coupled receptor that mediates many of the physiological effects of adenosine as a hormone, autocrine factor, and neuromodulator in the brain, heart, kidney, and adipocytes. A major obstacle to the detailed investigation of ligand interactions with the A<sub>1</sub>-AR in health and disease has been the inability to study its pharmacology directly at the single-cell level. This is crucial because changes in A<sub>1</sub>-AR localization, ligand-binding characteristics, and signaling in membrane compartments of individual cells may be important in a number of different pathologies. It is also clear that GPCRs, including the A<sub>1</sub>-AR, are not distributed uniformly over the cell surface but are localized in discrete membrane microdomains such as caveolae or cholesterol-rich lipid rafts. The exact nature and function of these domains are not yet clear, but they do appear to have an important role in the signaling, desensitization, and intracellular trafficking of a number of receptors. Currently, ligand interactions with the A<sub>1</sub>-AR can be quantified on large cell populations only by using radio-ligand binding.

To increase the resolution of these measurements, Briddon et al. have designed a fluorescent antagonist for the A<sub>1</sub>-AR, XAC-BY630, and used the compound to quantify ligand–receptor binding at a single cell level using FCS (Briddon et al. 2004). XAC-BY630 was a competitive antagonist of A<sub>1</sub>-AR-mediated inhibition of cAMP accumulation and stimulation of inositol phosphate accumulation. Specific binding of XAC-BY630 to cell surface A<sub>1</sub>-AR could also be visualized in living Chinese hamster ovary (CHO)-A1 cells by using confocal microscopy. FCS analysis of XAC-BY630 binding to the membrane of CHO-A1 cells revealed three diffusing components, the free ligand ( $\tau_1$ ), A<sub>1</sub>-AR-bound ligand ( $\tau_2$ ), and nonspecifically membrane-adsorbed ligand ( $\tau_3$ ). Confirmation that  $\tau_2$  resulted from the diffusion of ligand–receptor complexes came from the similar diffusion time observed for the fluorescent A<sub>1</sub>-AR-Topaz fusion protein. Quantification of  $\tau_2$  showed that the number of receptor–ligand complexes increased with increasing free ligand concentration and was decreased by the selective A<sub>1</sub>-AR antagonist, 8-cyclopentyl-1,3-dipropylxanthine. The combination of FCS with XAC-BY630 will be a powerful tool for the characterization of ligand-A<sub>1</sub>-AR interactions in single living cells in health and disease contexts.

### GABA Receptor

Meissner et al. describe a GABA<sub>A</sub> receptor binding assay at the surface of living hippocampal neurons using FCS and a fluorescently labeled muscimol derivative, which provides novel information about the lateral mobility of the GABA<sub>A</sub> receptor–ligand complex (Meissner and Haberlein 2003). They demonstrate the potential of the FCS technique as a highly sensitive and noninvasive method for investigating receptor–ligand binding properties in living cells. They claim that the simultaneous discrimination of different states of mobility of the receptor–ligand complex in the cell membrane as provided by FCS creates a new approach for comparing the mobility of such receptor–ligand complexes with subcellular mechanisms of receptor regulation and signaling. A concentration-dependent increase in the level of specific Mu-Alexa binding was demonstrated by the positive cooperative activity of co-incubated midazolam, which was selectively found in GABA<sub>A</sub> receptor–ligand complexes with hindered mobility.

### G Protein-Coupled Glucocorticoid Receptor

Rapid nongenomic actions of glucocorticoids (GCs) have been well documented, but information about putative membrane receptors that mediate them is scarce. Maier et al. used FCS to search for membrane GC-binding in the mouse pituitary cell line AtT-20 (Maier 2005). A slowly diffusing fraction of fluorescein-labeled dexamethasone on the cell membrane corresponds to fluorescein-dexamethasone binding. Preincubation experiments were performed to test binding specificity: a 500-fold excess of unlabeled dexamethasone abolished subsequent fluorescein-dexamethasone membrane binding, the natural ligand corticosterone prevented it partially, and the sex steroids estradiol and progesterone and the GC-receptor antagonist RU486 had no effect. Preincubation with pertussis toxin resulted in disappearance of the slowest diffusion component suggesting association of the receptor with a G-protein. Taken together, these results demonstrate high-affinity GC-binding on the cell membrane of AtT-20 cells with characteristics distinct from intracellular binding. This study demonstrated for the first time the existence of specific, positively cooperative and G protein-coupled membrane glucocorticoid receptors distinct from their intracellular counterparts.

#### 6.4.1.2 Ligand-Gated Ion Channels

##### Serotonin Receptor (5HT<sub>3</sub>)

The 5-hydroxytryptamine receptor of type 3 was investigated with FCS by Wohland et al. (1999). Binding constants of fluorescently labeled ligands, the stoichiometry, and the mass of the receptor were accessible and the duration of the measurement was on the order of seconds to minutes. The receptor antagonist GR-H was labeled



with the fluorophores rhodamine 6G, fluorescein, N-[7-nitrobenz-2-oxa-1,3-diazol-4-yl], and the cyanine dye Cy5. It was shown that the photophysical and chemical properties have a direct influence on the measurement quality (duration of measurement, signal-to-noise ratio) and the ligand–receptor interactions (dissociation constants), respectively. It was concluded that it is necessary to choose a suitable label or a combination of labels for receptor studies. The affinities of the fluorescently labeled ligands determined by FCS were virtually identical to the values obtained by radio ligand binding experiments. In addition, the dissociation constant of a nonfluorescent receptor ligand was determined successfully by an FCS competition assay. The experimental results showed that only one antagonist binds to the receptor, in agreement with measurements previously published.

### Glutamate-Activated Cationic Channels

The basis for differences in activity-dependent trafficking of AMPA receptors (AMPA receptors) and NMDA receptors (NMDARs) is currently under debate. Using single-molecule tracking, Groc et al. found different lateral mobilities for AMPARs and NMDARs: changes in neuronal activity modified AMPAR but not NMDAR mobility, whereas protein kinase C activation modified both (Groc et al. 2004). Differences in mobility were detected mainly for extrasynaptic AMPARs, suggesting that receptor diffusion between synaptic and extrasynaptic domains was involved in plasticity processes. Their data further strengthen the hypothesis that the pool of extrasynaptic receptors may act as a reserve that can be mobilized on demand, making the extrasynaptic domain a trafficking hallway. The relative instability of the AMPAR with respect to the NMDAR synaptic component during plasticity may originate from greater lateral exchange of AMPARs at equilibrium between the synaptic and extrasynaptic domains.

### Glycine Receptor

Variations in receptor number at a given synapse are known to contribute to synaptic plasticity, but methods used to establish this idea usually do not allow for the determination of the dynamics of these phenomena. Meier, Choquet, and coworkers used single-particle tracking to follow movements of the glycine receptor (GlyR) on the cell surface in real time, with or without the GlyR stabilizing protein gephyrin (Meier et al. 2001). GlyR alternated between diffusive and confined states within seconds. In the absence of gephyrin, GlyR was mostly freely diffusing. Gephyrin induced long confinement periods spatially associated with submembrane clusters of gephyrin. However, even when most receptors were stabilized, they still frequently made transitions through the diffusive state. These data showed that the number of receptors in a cluster results from a dynamic equilibrium between the pools of stabilized and freely mobile receptors. Modification of this equilibrium could be involved in the regulation of the receptor density at synapses.

### 6.4.1.3 Nuclear Receptors

Nuclear receptors are transcription factors that are activated via ligand binding and/or phosphorylation. Upon activation they directly modulate gene expression by binding to specific response elements present in the promoter region of target genes. In addition, nuclear receptors function only within a complex biochemical network of numerous proteins (Metivier et al. 2003; Mckenna and O'Malley 2002). Because nuclear receptors control many aspects of cellular metabolism, they have become the focus of intensive research to develop therapeutics in prevalent diseases such as diabetes or cancer (Tsai and O'Malley 1994). Nuclear receptors are also sensitively influenced by drugs or exogenous pollutants such as herbicides and plasticizers. In this context, protection of humans, animals, and the ecosystem against endocrine disruptors has gained considerable attention (Markey et al. 2002).

In spite of their wide-ranging consequences, for instance, in the development of more effective medicines, the quantitative details of nuclear receptor mediated signaling are largely unknown. Such protein interaction networks are currently investigated in proteomics and systems biology research. The methods presently available to detect stable multiprotein complexes, such as yeast two-hybrid screens, 2D gel electrophoresis followed by mass spectrometry or chromatin immunoprecipitation, show some limitations: these extracellular, *in vitro* proteomic assays are neither able to detect transient (weak) interactions nor are they free from the uncertainty that the detected interactions are artificially induced by high protein concentrations. Even more important, they cannot deliver a quantitative thermodynamic and kinetic description of the underlying biochemical reactions, which is the key to understanding cellular functions on a molecular basis. Therefore, optical microscopy and selective fluorescence labeling has gained increasing attention because of the possibility to image proteins and molecular complexes in living cells with high spatial and temporal resolution, thus enabling the disentanglement of biochemical networks *in vivo*.

#### Estrogen Receptor

Jankevics et al. investigated in living cells the complex and dynamic nature of molecular interactions of a prototypic nuclear hormone receptor, the human estrogen receptor- $\alpha$  (ER) (Jankevics et al. 2005). By analyzing distributions of diffusion times using DDA, they were able to reveal a complex mobility pattern of ER that arises when agonists or antagonists are applied to MCF-7 breast cancer cells. The diffusion times were determined in the nuclei of living cells by FCS of ER fused to YFP. Even in the absence of ligand the mobility distribution of YFP-ER was not completely homogeneous, which provides evidence that ER is present in the nucleus not in one single state but rather in at least two different states as a result of either hindered diffusion or additional interactions. The authors found that upon addition of the agonist estrogen, ER forms a limited number of distinct complexes of varying population by dynamic interaction with other nuclear components, such as cofactor proteins and chromatin. Several ligands caused similar but not identical

interaction patterns. For each of the ligand-induced ER complexes distinct dose–response curves were obtained. The potential to identify interacting proteins was demonstrated by comparing DDA of the YFP-fused ER cofactor YFP-SRC-3 with those of YFP-ER and the result that a small amount of ER-SRC-3 complexes exist already in the absence of ligand.

#### Peroxisome Proliferator-Activated Receptor

In a global approach combining FRAP, FCS, and fluorescence resonance energy transfer (FRET), Feige et al. addressed the behavior in living cells of the peroxisome proliferator-activated receptors (PPARs), a family of nuclear receptors involved in lipid and glucose metabolism, inflammation control, and wound healing (Feige et al. 2005). Interestingly and in contrast to a general assumption, PPARs readily heterodimerized with retinoid X receptor (RXR) in the absence of ligand in living cells. PPAR diffusion coefficients indicate that all the receptors are engaged in complexes of very high molecular mass and/or interact with relatively immobile nuclear components. PPARs are not immobilized by ligand binding, but exhibit a ligand-induced reduction of mobility, probably due to enhanced interactions with cofactors and/or chromatin. This study draws attention to the limitations and pitfalls of fluorescent chimera imaging and demonstrates the usefulness of the combination of FCS, FRAP, and FRET to assess the behavior of nuclear receptors and their mode of action in living cells.

## 6.5 Outlook

As outlined in a recent review by Kholodenko (2006), the activation of cell surface receptors is known to induce spatiotemporal activation profiles of a certain repertoire of signaling proteins which finally result in different gene-expression patterns and diverse physiological responses. For some simple cases, computational models suggest that there is a complex interplay between receptor stimuli and cellular responses that depends on the precise temporal control and relative spatial distribution of activated signal transducers. In spite of the importance of a detailed description and in turn an understanding of cellular signaling in the framework of a complex, spatiotemporal dynamic network of cellular biochemical reactions, quantitative data are available only for a few simple cases (references in Kholodenko (2006)), but for no complex cases such as GPCR-mediated cellular signaling. The lack of such quantitative data is due to the fact that until recently proper techniques were lacking to detect and count corresponding proteins and their molecular complexes (as individuals or in ensemble) in living (e.g., primary) cells at physiological low concentrations with high spatial (down to a few nanometer positional accuracy) and temporal resolution from microseconds to days. Thus it was not possible to decipher *in vivo* the dynamic network of molecular interactions quantitatively in terms of thermodynamic and kinetic reaction parameters.

The situation has changed recently due to the following key developments. Novel *in vivo* labeling of proteins in living cells enables the selective tagging of proteins with extremely photostable, small unperturbing fluorophores which in combination with ultrasensitive optical microscopy allow the imaging of a few or even single molecules in living cells. This opens for the first time the possibility to investigate molecular interactions at physiological concentrations without artifacts due to overexpression of the corresponding species. The approaches outlined in this chapter and elsewhere in this book herald a new era of quantitative biology and are essential for understanding cellular functions on a quantitative chemical basis. Such an understanding has wide-ranging consequences for fundamental sciences, the development of novel medicines, and novel bioanalytical techniques.

**Acknowledgments** The work reviewed here involved many members of our own and other groups. Because of the limited space we were unfortunately not able to include many more important endeavors of others. We would like to thank all members of our group for their contributions reviewed here and Raissa Trend for carefully reading the manuscript. The work from our group was supported by grants of the TopNano21 program, the Swiss National Science Foundation, the NRP50 program and the European Commission (contract LSHG-CT-2004-504601, E-Mep).

## References

- Angioy, A. M., A. Desogus, I. T. Barbarossa, P. Anderson, and B. S. Hansson (2003). Extreme sensitivity in an olfactory system. *Chem Senses* 28:279–284.
- Asamoah, O. K., J. P. Wuskell, L. M. Loew, and F. Bezanilla (2003). A fluorometric approach to local electric field measurements in a voltage-gated ion channel. *Neuron* 37:85–97.
- Axelrod, D., T. P. Burghardt, and N. L. Thompson (1984). Total internal reflection fluorescence. *Annu Rev Biophys Bioeng* 13:247–268.
- Bacia, K., S. A. Kim, and P. Schuille (2006). Fluorescence cross-correlation spectroscopy in living cells. *Nat Methods* 3:83–89.
- Barak, L. S., and W. W. Webb (1982). Diffusion of low density lipoprotein-receptor complex on human fibroblasts. *J Cell Biol* 95:846–852.
- Becker, C. F., R. Seidel, M. Jahnz, K. Bacia, T. Niederhausen, K. Alexandrov, P. Schuille, R. S. Goody, and M. Engelhard (2006). C-terminal fluorescence labeling of proteins for interaction studies on the single-molecule level. *ChemBiochem* 7:891–895.
- Berciaud, S., L. Cognet, G. A. Blab, and B. Lounis (2004). Photothermal heterodyne imaging of individual nonfluorescent nanoclusters and nanocrystals. *Phys Rev Lett* 93:257402.
- Boeckh, J., K. E. Kaissling, and D. Schneider (1965). Insect olfactory receptors. *Cold Spring Harb Symp Quant Biol* 30:263–280.
- Bohmer, M., and J. Enderlein (2003). Fluorescence spectroscopy of single molecules under ambient conditions: Methodology and technology. *Chemphyschem* 4:793–808.
- Bouzigues, C., and M. Dahan (2007). Transient directed motions of GABA(A) receptors in growth cones detected by a speed correlation index. *Biophys J* 92:654–660.
- Briddon, S. J., R. J. Middleton, Y. Cordeaux, F. M. Flavin, J. A. Weinstein, M. W. George, B. Kellam, and S. J. Hill (2004). Quantitative analysis of the formation and diffusion of A1-adenosine receptor-antagonist complexes in single living cells. *Proc Natl Acad Sci USA* 101:4673–4678.
- Bulenger, S., S. Marullo, and M. Bouvier (2005). Emerging role of homo- and heterodimerization in G-protein-coupled receptor biosynthesis and maturation. *Trends Pharmacol Sci* 26:131–137.

- Chabre, M., and M. le Maire (2005). Monomeric G-protein-coupled receptor as a functional unit. *Biochemistry* 44:9395–9403.
- Chandrasekhar, S. (1943). Stochastic problems in physics and astronomy. *Review of Modern Physics* 15:1–89.
- Charbonniere, L. J., N. Hildebrandt, R. F. Ziessel, and H. G. Lohmannsroben (2006). Lanthanides to quantum dots resonance energy transfer in time-resolved fluoro-immunoassays and luminescence microscopy. *J Am Chem Soc* 128:12800–12809.
- Choquet, D., and A. Triller (2003). The role of receptor diffusion in the organization of the postsynaptic membrane. *Nat Rev Neurosci* 4:251–265.
- Cognet, L., C. Tardin, D. Boyer, D. Choquet, P. Tamarat, and B. Lounis (2003). Single metallic nanoparticle imaging for protein detection in cells. *Proc Natl Acad Sci USA* 100:11350–11355.
- Daumas, F., N. Destainville, C. Millot, A. Lopez, D. Dean, and L. Salome (2003). Confined diffusion without fences of a g-protein-coupled receptor as revealed by single particle tracking. *Biophys J* 84:356–366.
- de Brabander, M., R. Nuydens, A. Ishihara, B. Holifield, K. Jacobson, and H. Geerts (1991). Lateral diffusion and retrograde movements of individual cell surface components on single motile cells observed with Nanovid microscopy. *J Cell Biol* 112:111–124.
- Destainville, N., and L. Salome (2006). Quantification and correction of systematic errors due to detector time-averaging in single-molecule tracking experiments. *Biophys J* 90:L17–19.
- Doan, T., A. Mendez, P. B. Detwiler, J. Chen, and F. Rieke (2006). Multiple phosphorylation sites confer reproducibility of the rod's single-photon responses. *Science* 313:530–533.
- Ehrensparger, M. V., C. Hanus, C. Vannier, A. Triller, and M. Dahan (2007). Multiple association states between glycine receptors and gephyrin identified by SPT analysis. *Biophys J* 92:3706–3718.
- Ehrenberg, M., and R. Rigler (1974). Rotational Brownian motion and fluorescence intensity fluctuations. *Chem Phys* 4:390–401.
- Eigen, M., and R. Rigler (1994). Sorting single molecules – Application to diagnostics and evolutionary biotechnology. *Proc Natl Acad Sci USA* 91:5740–5747.
- Elson, E. L., and D. Magde (1974). Fluorescence correlation spectroscopy. 1. Conceptual basis and theory. *Biopolymers* 13:1–27.
- Foley, T. L., and M. D. Burkart (2007). Site-specific protein modification: advances and applications. *Curr Opin Chem Biol* 11:12–19.
- Feige, J. N., L. Gelman, C. Tudor, Y. Engelborghs, W. Wahli, and B. Desvergne (2005). Fluorescence imaging reveals the nuclear behavior of peroxisome proliferator-activated receptor/retinoid X receptor heterodimers in the absence and presence of ligand. *J Biol Chem* 280:17880–17890.
- Fooksman, D. R., G. K. Gronvall, Q. Tang, and M. Edidin (2006). Clustering class I MHC modulates sensitivity of T cell recognition. *J Immunol* 176:6673–6680.
- Freudenthaler, G., M. Axmann, H. Schindler, B. Pragl, H. G. Knaus, and G. J. Schutz (2002). Ultrasensitive pharmacological characterisation of the voltage-gated potassium channel K(V)1.3 studied by single-molecule fluorescence microscopy. *Histochem Cell Biol* 117:197–202.
- Gambin, Y., R. Lopez-Esparza, M. Reffay, E. Sierrecki, N. S. Gov, M. Genest, R. S. Hodges, and W. Urbach (2006). Lateral mobility of proteins in liquid membranes revisited. *Proc Natl Acad Sci U S A* 103:2098–2102.
- George, N., H. Pick, H. Vogel, N. Johnsson, and K. Johnsson (2004). Specific labeling of cell surface proteins with chemically diverse compounds. *J Am Chem Soc* 126:8896–8897.
- Giepmans, B. N., S. R. Adams, M. H. Ellisman, and R. Y. Tsien (2006). The fluorescent toolbox for assessing protein location and function. *Science* 312:217–224.
- Grandl, J., E. Sakr, F. Kotzyba-Hibert, F. Krieger, S. Bertrand, D. Bertrand, H. Vogel, M. Goeldner, and R. Hovius (2007). Fluorescent epibatidine agonists for neuronal and muscle-type nicotinic acetylcholine receptors. *Angew Chem Int Ed Engl* 46:3505–3508.
- Griffin, B. A., S. R. Adams, and R. Y. Tsien (1998). Specific covalent labeling of recombinant protein molecules inside live cells. *Science* 281:269–272.
- Groc, L., M. Heine, L. Cognet, K. Brickley, F. A. Stephenson, B. Lounis, and D. Choquet (2004). Differential activity-dependent regulation of the lateral mobilities of AMPA and NMDA receptors. *Nat Neurosci* 7:695–696.

- Guignet, E. G., R. Hovius, and H. Vogel (2004). Reversible site-selective labeling of membrane proteins in live cells. *Nat Biotechnol* 22:440–444.
- Guignet, E. G., J. M. Segura, R. Hovius, and H. Vogel (2007). Repetitive reversible labeling of proteins at polyhistidine sequences for single-molecule imaging in live cells. *Chemphyschem* 8:1221–1227.
- Hassaine, G., R. Wagner, J. Kempf, N. Cherouati, N. Hassaine, C. Prual, N. Andre, C. Reinhart, F. Pattus, and K. Lundstrom (2006). Semliki Forest virus vectors for overexpression of 101 G protein-coupled receptors in mammalian host cells. *Protein Expr Purif* 45:343–351.
- Hauser, C. T., and R. Y. Tsien (2007). A hexahistidine-Zn<sup>2+</sup>-dye label reveals STIM1 surface exposure. *Proc Natl Acad Sci U S A* 104:3693–3697.
- Hegener, O., L. Prenner, F. Runkel, S. L. Baader, J. Kappler, and H. Haberlein (2004). Dynamics of beta2-adrenergic receptor-ligand complexes on living cells. *Biochemistry* 43:6190–6199.
- Heinis, C., S. Schmitt, M. Kindermann, G. Godin, and K. Johnsson (2006). Evolving the substrate specificity of O6-alkylguanine-DNA alkyltransferase through loop insertion for applications in molecular imaging. *ACS Chem Biol* 1:575–584.
- Hovius, R., B. H. Meyer, E. G. Guignet, and H. Vogel. 2006. Fluorescent labelling of membrane proteins in living cells. In: Lundstrom K, editor. *Structural Genomics on Membrane Proteins*. Boca Raton, FL: CRC/Taylor & Francis.
- Ilegems, E., H. M. Pick, and H. Vogel (2002). Monitoring mis-acylated tRNA suppression efficiency in mammalian cells via EGFP fluorescence recovery. *Nucleic Acids Res* 30:e128.
- Irvine, D. J., M. A. Purbhoo, M. Krogsgaard, and M. M. Davis (2002). Direct observation of ligand recognition by T cells. *Nature* 419:845–849.
- Jacobson, K., O. G. Mouritsen, and R. G. Anderson (2007). Lipid rafts: at a crossroad between cell biology and physics. *Nat Cell Biol* 9:7–14.
- Jacquier, V., M. Prummer, J. M. Segura, H. Pick, and H. Vogel (2006). Visualizing odorant receptor trafficking in living cells down to the single-molecule level. *Proc Natl Acad Sci USA* 103:14325–14330.
- Jankevics, H., M. Prummer, P. Izewska, H. Pick, K. Leufgen, and H. Vogel (2005). Diffusion-time distribution analysis reveals characteristic ligand-dependent interaction patterns of nuclear receptors in living cells. *Biochemistry* 44:11676–11683.
- Johnsson, N., and K. Johnsson (2007). Chemical tools for biomolecular imaging. *ACS Chem Biol* 2:31–38.
- Keppler, A., H. Pick, C. Arrivoli, H. Vogel, and K. Johnsson (2004). Labeling of fusion proteins with synthetic fluorophores in live cells. *Proc Natl Acad Sci USA* 101:9955–9959.
- Keppler, A., S. Gendreizig, T. Gronemeyer, H. Pick, H. Vogel, and K. Johnsson (2003). A general method for the covalent labeling of fusion proteins with small molecules in vivo. *Nat Biotechnol* 21:86–89.
- Khan, A. H., and J. E. Pessin (2002). Insulin regulation of glucose uptake: a complex interplay of intracellular signalling pathways. *Diabetologia* 45:1475–1483.
- Kholodenko, B. N. (2006). Cell-signalling dynamics in time and space. *Nat Rev Mol Cell Biol* 7:165–176.
- Kinjo, M., and R. Rigler (1995). Ultrasensitive hybridization analysis using fluorescence correlation spectroscopy. *Nucleic Acids Res* 23:1795–1799.
- Kusumi, A., Y. Sako, and M. Yamamoto (1993). Confined lateral diffusion of membrane receptors as studied by single particle tracking (nanovid microscopy). Effects of calcium-induced differentiation in cultured epithelial cells. *Biophys J* 65:2021–2040.
- Kusumi, A., C. Nakada, K. Ritchie, K. Murase, K. Suzuki, H. Murakoshi, R. S. Kasai, J. Kondo, and T. Fujiwara (2005). Paradigm shift of the plasma membrane concept from the two-dimensional continuum fluid to the partitioned fluid: High-speed single-molecule tracking of membrane molecules. *Annu Rev Biophys Biomol Struct* 34:351–378.
- Krichevsky, O., and G. Bonnet (2002). Fluorescence correlation spectroscopy: The technique and its applications. *Rep. Prog. Phys.* 65:251–297.

- Lata, S., M. Gavutis, R. Tampe, and J. Piehler (2006). Specific and stable fluorescence labeling of histidine-tagged proteins for dissecting multi-protein complex formation. *J Am Chem Soc* 128:2365–2372.
- Levene, M. J., J. Korch, S. W. Turner, M. Foquet, H. G. Craighead, and W. W. Webb (2003). Zero-mode waveguides for single-molecule analysis at high concentrations. *Science* 299:682–686.
- Lommerse, P. H., G. A. Blab, L. Cognet, G. S. Harms, B. E. Snaar-Jagalska, H. P. Spaank, and T. Schmidt (2004). Single-molecule imaging of the h-ras membrane-anchor reveals domains in the cytoplasmic leaflet of the cell membrane. *Biophys J* 86:609–616.
- Lill, Y., K. L. Martinez, M. A. Lill, B. H. Meyer, H. Vogel, and B. Hecht (2005). Kinetics of the initial steps of G protein-coupled receptor-mediated cellular signaling revealed by single-molecule imaging. *Chemphyschem* 6:1633–1640.
- Lindfors, K., T. Kalkbrenner, P. Stoller, and V. Sandoghdar (2004). Detection and spectroscopy of gold nanoparticles using supercontinuum white light confocal microscopy. *Phys Rev Lett* 93:037401.
- Liu, W., A. Brock, S. Chen, and P. G. Schultz (2007). Genetic incorporation of unnatural amino acids into proteins in mammalian cells. *Nat Methods* 4:239–244.
- Lommerse, P. H., G. A. Blab, L. Cognet, G. S. Harms, B. E. Snaar-Jagalska, H. P. Spaank, and T. Schmidt (2004). Single-molecule imaging of the h-ras membrane-anchor reveals domains in the cytoplasmic leaflet of the cell membrane. *Biophys J* 86:609–616.
- Lukic, B., S. Jeney, C. Tischer, A. J. Kulik, L. Forro, and E. L. Florin (2005). Direct observation of nondiffusive motion of a Brownian particle. *Phys Rev Lett* 95:160601.
- Magde, D., E. Elson, and W. W. Webb (1972). Thermodynamic fluctuations in a reacting system – Measurement by fluorescence correlation spectroscopy. *Phys Rev Lett* 29:705–708.
- Markey, C. M., B. S. Rubin, A. M. Soto, and C. Sonnenschein (2002). Endocrine disruptors: From Wingspread to environmental developmental biology. *J. Steroid Biochem. Mol. Biol.* 83:235–244.
- Matsuzaki, M., G. C. Ellis-Davies, T. Nemoto, Y. Miyashita, M. Iino, and H. Kasai (2001). Dendritic spine geometry is critical for AMPA receptor expression in hippocampal CA1 pyramidal neurons. *Nat Neurosci* 4:1086–1092.
- Maier, C., D. Runzler, J. Schindelar, G. Grabner, W. Waldhausl, G. Kohler, and A. Luger (2005). G-protein-coupled glucocorticoid receptors on the pituitary cell membrane. *J Cell Sci* 118:3353–3361.
- Martin, B. R., B. N. Giepmans, S. R. Adams, and R. Y. Tsien (2005). Mammalian cell-based optimization of the biarsenical-binding tetracysteine motif for improved fluorescence and affinity. *Nat Biotechnol* 23:1308–1314.
- McKenna, N. J., and B. W. O'Malley (2002). Combinatorial control of gene expression by nuclear receptors and coregulators. *Cell* 108:465–474.
- Meier, J., C. Vannier, A. Serge, A. Triller, and D. Choquet (2001). Fast and reversible trapping of surface glycine receptors by gephyrin. *Nat Neurosci* 4:253–260.
- Meissner, O., and H. Haberlein (2003). Lateral mobility and specific binding to GABA(A) receptors on hippocampal neurons monitored by fluorescence correlation spectroscopy. *Biochemistry* 42:1667–1672.
- Meseth, U., T. Wohland, R. Rigler, and H. Vogel (1999). Resolution of fluorescence correlation measurements. *Biophys J* 76:1619–1631.
- Metivier, R., G. Penot, M. R. Hubner, G. Reid, H. Brand, M. Kos, and F. Gannon (2003). Estrogen receptor- $\alpha$  directs ordered, cyclical, and combinatorial recruitment of cofactors on a natural target promoter. *Cell* 115:751–763.
- Meyer, B. H., J. M. Segura, K. L. Martinez, R. Hovius, N. George, K. Johnsson, and H. Vogel (2006). FRET imaging reveals that functional neurokinin-1 receptors are monomeric and reside in membrane microdomains of live cells. *Proc Natl Acad Sci USA* 103:2138–2143.
- Murakoshi, H., R. Iino, T. Kobayashi, T. Fujiwara, C. Ohshima, A. Yoshimura, and A. Kusumi (2004). Single-molecule imaging analysis of Ras activation in living cells. *Proc Natl Acad Sci USA* 101:7317–7322.
- Miller, L. W., and V. W. Cornish (2005). Selective chemical labeling of proteins in living cells. *Curr Opin Chem Biol* 9:56–61.

- Muir, T. W. (2003). Semisynthesis of proteins by expressed protein ligation. *Annu Rev Biochem* 72:249–289.
- Monahan, S. L., H. A. Lester, and D. A. Dougherty (2003). Site-specific incorporation of unnatural amino acids into receptors expressed in mammalian cells. *Chem Biol* 10:573–580.
- Nan, X., P. A. Sims, P. Chen, and X. S. Xie (2005). Observation of individual microtubule motor steps in living cells with endocytosed quantum dots. *J Phys Chem B Condens Matter Mater Surf Interfaces Biophys* 109:24220–24224.
- Nakada, C., K. Ritchie, Y. Oba, M. Nakamura, Y. Hotta, R. Iino, R. S. Kasai, K. Yamaguchi, T. Fujiwara, and A. Kusumi (2003). Accumulation of anchored proteins forms membrane diffusion barriers during neuronal polarization. *Nat Cell Biol* 5:626–632.
- Nimchinsky, E. A., R. Yasuda, T. G. Oertner, and K. Svoboda (2004). The number of glutamate receptors opened by synaptic stimulation in single hippocampal spines. *J Neurosci* 24: 2054–2064.
- Ostrom, R. S., and P. A. Insel (2004). The evolving role of lipid rafts and caveolae in G protein-coupled receptor signaling: implications for molecular pharmacology. *Br J Pharmacol* 143:235–245.
- Pierce, K. L., R. T. Premont, and R. J. Lefkowitz (2002). Seven-transmembrane receptors. *Nat Rev Mol Cell Biol* 3:639–650.
- Pralle, A., M. Prummer, E. L. Florin, E. H. Stelzer, and J. K. Horber (1999). Three-dimensional high-resolution particle tracking for optical tweezers by forward scattered light. *Microsc Res Tech* 44:378–386.
- Prummer, M., B. H. Meyer, R. Franzini, J. M. Segura, N. George, K. Johnsson, and H. Vogel (2006). Post-translational covalent labeling reveals heterogeneous mobility of individual G protein-coupled receptors in living cells. *Chembiochem* 7:908–911.
- Purbhoo, M. A., D. J. Irvine, J. B. Huppa, and M. M. Davis (2004). T cell killing does not require the formation of a stable mature immunological synapse. *Nat Immunol* 5:524–530.
- Qian, H., M. P. Sheetz, and E. L. Elson (1991). Single particle tracking. Analysis of diffusion and flow in two-dimensional systems. *Biophys J* 60:910–921.
- Rigler, R., and E. S. Elson. 2001. *Fluorescence Correlation Spectroscopy: Theory and Applications*. Schäfer FP, Toennies JP, Zinth W, editors. Berlin: Springer Verlag. 487 p.
- Rigler, R., U. Mets, J. Widengren et al. (1993). Fluorescence correlation spectroscopy with high count rate and low-background – Analysis of translational diffusion. *Eur Biophys J with Biophys Lett* 22(3):169–175.
- Rigler, R. (1995). Fluorescence correlations, single molecule detection and large number screening. Applications in biotechnology. *J Biotechnol* 41:177–186.
- Saffman, P. G., and M. Delbruck (1975). Brownian motion in biological membranes. *Proc Natl Acad Sci U S A* 72:3111–3113.
- Saxton, M. J. (1993). Lateral diffusion in an archipelago. Single-particle diffusion. *Biophys J* 64:1766–1780.
- Saxton, M. J., and K. Jacobson (1997). Single-particle tracking: Applications to membrane dynamics. *Annu Rev Biophys Biomol Struct* 26:373–399.
- Schlessinger, J. (2000). Cell signaling by receptor tyrosine kinases. *Cell* 103:211–225.
- Schmidt, T., G. J. Schutz, W. Baumgartner, H. J. Gruber, and H. Schindler (1996). Imaging of single molecule diffusion. *Proc Natl Acad Sci U S A* 93:2926–2929.
- Schreiter, C., M. Gjoni, R. Hovius, K. L. Martinez, J. M. Segura, and H. Vogel (2005). Reversible sequential-binding probe receptor-ligand interactions in single cells. *Chembiochem* 6:2187–2194.
- Schutz, G. J., H. Schindler, and T. Schmidt (1997). Single-molecule microscopy on model membranes reveals anomalous diffusion. *Biophys J* 73:1073–1080.
- Schwille, P., F. J. Meyer-Almes, and R. Rigler (1997). Dual-color fluorescence cross-correlation spectroscopy for multicomponent diffusional analysis in solution. *Biophys J* 72:1878–1886.
- Serge, A., L. Fourgeaud, A. Hemar, and D. Choquet (2002). Receptor activation and homer differentially control the lateral mobility of metabotropic glutamate receptor 5 in the neuronal membrane. *J Neurosci* 22:3910–3920.
- Serge, A., L. Fourgeaud, A. Hemar, and D. Choquet (2003). Active surface transport of metabotropic glutamate receptors through binding to microtubules and actin flow. *J Cell Sci* 116:5015–5022.



- Seisenberger, G., M. U. Ried, T. Endress, H. Buning, M. Hallek, and C. Brauchle (2001). Real-time single-molecule imaging of the infection pathway of an adeno-associated virus. *Science* 294:1929–1932.
- Sengupta, P., K. Garai, J. Balaji, N. Periasamy, and S. Maiti (2003). Measuring size distribution in highly heterogeneous systems with fluorescence correlation spectroscopy. *Biophys. J.* 84:1977–1984.
- Shaner, N. C., P. A. Steinbach, and R. Y. Tsien (2005). A guide to choosing fluorescent proteins. *Nat Methods* 2:905–909.
- Singer, S. J., and G. L. Nicolson (1972). The fluid mosaic model of the structure of cell membranes. *Science* 175:720–731.
- Simons, K., and W. L. Vaz (2004). Model systems, lipid rafts, and cell membranes. *Annu Rev Biophys Biomol Struct* 33:269–295.
- Skerra, A. (2001). ‘Anticalins’: a new class of engineered ligand-binding proteins with antibody-like properties. *J Biotechnol* 74:257–275.
- Sonnleitner, A., L. M. Mannuzzu, S. Terakawa, and E. Y. Isacoff (2002). Structural rearrangements in single ion channels detected optically in living cells. *Proc Natl Acad Sci USA* 99:12759–12764.
- Suzuki, K., K. Ritchie, E. Kajikawa, T. Fujiwara, and A. Kusumi (2005). Rapid hop diffusion of a G-protein-coupled receptor in the plasma membrane as revealed by single-molecule techniques. *Biophys J* 88:3659–3680.
- Thompson, N. L. 1991. Fluorescence Correlation Spectroscopy. In: Lakowicz JR, editor. *Topics in Fluorescence Spectroscopy*. New York: Plenum Press, pp. 337–378.
- Tsai, M. J., and B. W. O’Malley (1994). Molecular mechanisms of action of steroid/thyroid receptor superfamily members. *Annu. Rev. Biochem.* 63:451–486.
- Turcatti, G., K. Nemeth, M. D. Edgerton, U. Meseth, F. Talabot, M. Peitsch, J. Knowles, H. Vogel, and A. Chollet (1996). Probing the structure and function of the tachykinin neurokinin-2 receptor through biosynthetic incorporation of fluorescent amino acids at specific sites. *J Biol Chem* 271:19991–19998.
- Ueda, M., Y. Sako, T. Tanaka, P. Devreotes, and T. Yanagida (2001). Single-molecule analysis of chemotactic signaling in Dictyostelium cells. *Science* 294:864–867.
- Venables, W. N., and B. D. Ripley. 1997. *Modern Applied Statistics with S-PLUS*. Chambers Jea, editor. New York: Springer Verlag.
- Vukojevic, V., A. Pramanik, T. Yakovleva, R. Rigler, L. Terenius, and G. Bakalkin (2005). Study of molecular events in cells by fluorescence correlation spectroscopy. *Cell Mol Life Sci* 62:535–550.
- Vrljic, M., S. Y. Nishimura, S. Brasselet, W. E. Moerner, and H. M. McConnell (2002). Translational diffusion of individual class II MHC membrane proteins in cells. *Biophys J* 83:2681–2692.
- Wang, L., J. Xie, and P. G. Schultz (2006). Expanding the genetic code. *Annu Rev Biophys Biomol Struct* 35:225–249.
- Wohland, T., K. Friedrich, R. Hovius, and H. Vogel (1999). Study of ligand-receptor interactions by fluorescence correlation spectroscopy with different fluorophores: Evidence that the homopentameric 5-hydroxytryptamine type 3As receptor binds only one ligand. *Biochemistry* 38:8671–8681.
- Yin, J., F. Liu, X. Li, and C. T. Walsh (2004). Labeling proteins with small molecules by site-specific posttranslational modification. *J Am Chem Soc* 126:7754–7755.
- Yin, J., P. D. Straight, S. M. McLoughlin, Z. Zhou, A. J. Lin, D. E. Golan, N. L. Kelleher, R. Kolter, and C. T. Walsh (2005). Genetically encoded short peptide tag for versatile protein labeling by Sfp phosphotransferase. *Proc Natl Acad Sci USA* 102:15815–15820.

# Chapter 7

## Single Enzyme Kinetics: A Study of the Yeast Enzyme *Candida Antarctica* Lipase B

Wendy Verheijen, Davey Loos, Frans C. De Schryver(✉),  
and Johan Hofkens

7.1	Introduction.....	163
7.2	The Lipase B from <i>Candida Antarctica</i> .....	165
7.2.1	Structure of the Enzyme .....	165
7.2.2	Applications of CalB .....	165
7.2.3	Strategy .....	166
7.3	Results and Discussion .....	166
7.3.1	Properties of the Fluorescent Product; BCECF Acid .....	166
7.3.2	Labeling and Immobilization of Enzymes.....	168
7.3.3	Enzymatic Turnover Experiments.....	168
7.3.4	Analysis of the Fluorescence Intensity Transients.....	170
7.3.5	The Model.....	176
7.4	Conclusions and Perspectives .....	177
	References.....	178

### 7.1 Introduction

Enzymes are a class of (bio)molecules that function as catalysts of (bio)chemical reactions. They highly accelerate the rate of (bio)chemical reactions (Fersht 1985). During the past decades, our knowledge about enzymes has greatly increased. Enzymes are almost always proteins which are very complex structures having many degrees of motional freedom. Much insight into the structures of these and other biomolecules is obtained by X-ray crystallography (Fersht 1985), nuclear magnetic resonance (NMR; Matthews and Van Holde (1996)), and molecular dynamics simulations (MDS) studies (Jensen et al. 2002). Most of the information available on enzymes has been primarily obtained by means of ensemble measurements. Unfortunately, these data do not give further insight in the static and dynamic heterogeneities. This is important as enzymes are not static molecules. The primary structure can fold into many slightly different conformations with different chemical activity (Frauenfelder et al. 1991). A well-studied process, for example, is the binding

---

Frans C. De Schryver  
Department of Chemistry, Katholieke Universiteit Leuven, Celestijnenlaan 200F, 3001 Everlee,  
Belgium  
frans.deschryver@chem.kuleuven.ac.be

R. Rigler and H. Vogel (eds.), *Single Molecules and Nanotechnology*. 163  
*Springer Series in Biophysics 12*.  
© Springer-Verlag Berlin Heidelberg 2008

of carbon monoxide (CO) to myoglobin (Mb). It has been shown that the rate constant of binding of CO to Mb is nonexponential, indicating that Mb does not exist in a single conformation. Other studies have shown that it exists in a number of conformational substates (Ansari et al. 1985; Frauenfelder et al. 2001).

The recent advances in single-molecule detection (SMD) make it possible to unravel information on links between conformational heterogeneity (structure) and the biological function that are usually hidden in ensemble measurements. The first measurements on the activity of single enzymes, and hence probably the first single molecule measurements, were performed by Rotman in 1961 (Rotman 1961, 1973). Thirty years later, Xue and Yeung were the first to detect experimentally differences in the activities of individual enzyme molecules (static disorder). They discovered that the activities among different lactate dehydrogenase (LDH-1) enzymes can vary with a factor up to four. They were, however, unable to detect dynamic disorder (the time-dependent fluctuation of the catalytic activity of a single enzyme) at that time (Xue and Yeung 1995).

The first serious attempt to detect dynamic disorder came from the group of X. S. Xie. In this case, the enzymatic cycle of individual cholesterol oxidase (COx) molecules was studied by detecting the intrinsic fluorescence emitted by the fluorescent cofactor flavin adenine dinucleotide (FAD; Lu et al. (1998) and Xie and Lu (1999)). Dynamic disorder was detected as a fluctuation of the turnover constant  $k_{\text{cat}}$  of single-enzyme molecules in the time regime of seconds. The fluctuation of the turnover constant was related to the existence of at least two conformational states of the enzyme. A new concept that emerged from this study was the so-called 'memory effect.' When the enzyme resides in a conformation that has a 'high' catalytic activity, the probability that a fast turnover is followed by another fast turnover is rather high. On the other hand, when the enzyme resides in a conformation that has a 'low' catalytic activity, a slow turnover tends to be followed by another slow turnover. It seems as if the enzyme has a memory of its previous turnovers.

SMD can be of particular interest for the study of individual enzymes because it can probe differences in the catalytic activity of different enzyme molecules and it can also monitor the fluctuations of the catalytic activity of a single enzyme molecule as a function of time. Experimental reports are focused on the detection of fluctuations in the catalytic activity of enzymes as a function of time (Lu et al. 1998; Xie and Lu 1999; Xie 2002; Lee and Brody 2005; Velonia et al. 2005; Flomenbom et al. 2005). Theoretical papers are more concerned with the development of statistical methods that can be used to interpret the single-molecule data, as well as with the development of a model for the observed dynamic behaviour (Agmon 2000; Yang and Cao 2002; Yang and Xie 2002; Onuchic et al. 1999; Geva and Skinner 1998; Ross and Vlad 1999; Cao 2000; Berezhkovskii et al. 1999, 2002; Astumian 2002; Flomenbom et al. 2005).

Recently Xie and coworkers derived single-molecule Michaelis–Menten equations with and without dynamic disorder (Kou et al. 2005). Rigler and co-workers suggest that functional conformational motions representing ordered sequences of transitions between a set of conformational substates along with equilibrium conformational fluctuations in the turnover cycle are involved in the explanation of the strong correlations between subsequent turnover cycles of cholesterol oxidase

(Lerch et al. 2005). The key question is whether fluctuations in the catalytic activity of a single enzyme is restricted to this particular enzyme or whether it is a general phenomenon that can be observed for all enzymes.

## 7.2 The Lipase B from *Candida Antarctica*

### 7.2.1 Structure of the Enzyme

The lipase B from *Candida antarctica* (CalB) consists of 317 amino acids and is a globular 33 kDa enzyme that has been isolated from the yeast *Candida antarctica*. Its dimensions are roughly  $30 \times 40 \times 50 \text{ \AA}$  and the polypeptide backbone adopts a conformation that is often referred to as the  $\alpha/\beta$ -hydrolase fold (Ollis et al. 1992).

In contrast with most lipases that show 'interfacial activation,' (Fernández-Lorente 2001; Van Tilbeurgh et al. 1993) that is, a mechanism whereby the enzyme is activated when it is exposed to an oil/water (hydrophobic/hydrophilic) interface, the properties of CalB have led scientists to classify the enzyme as an intermediate between an esterase (catalyzing hydrolysis of esters in aqueous solution) and a real interfacially activated lipase (operating at water-lipid interfaces). CalB does not have a real lid covering the active site and hence displays a limited form of interfacial activation. Furthermore a short helix ( $\alpha 5$ ) in close proximity to the active site has some mobility and probably still allows for some conformational changes. The active site of CalB that is buried at the core of the enzyme is accessible by a flat hydrophobic region with an area of approximately  $450 \text{ \AA}^2$ . This region is in contact with the lipid surface during catalysis. The active site serine is accessible through a channel, approximately  $10 \times 4 \text{ \AA}$  wide and  $12 \text{ \AA}$  length. The actual catalytic 'machinery' is located at the bottom of the active site and consists of a catalytic triad (active site serine, histidine, and aspartate) and the oxyanion hole (Brady et al. 1990).

### 7.2.2 Applications of CalB

In vivo, the function of CalB consists of the hydrolytic decomposition of triglycerides into fatty acids and glycerol (Rogalska et al. 1993). However, depending on the reaction conditions, CalB can be used to catalyze a variety of reactions (Anderson et al. 1998). When it is used in aqueous solutions, the reaction is mostly driven towards the hydrolysis of esters, however, in anhydrous reaction conditions, the reaction can be steered into the synthetic direction: direct esterifications or transesterifications. Therefore, CalB is a valuable biocatalyst in organic synthesis. It has a remarkable stability in organic solvents and it was successfully used, for example, in both apolar as well as relatively polar solvents such as hexane, iso-octane, *tert*-butanol, acetone, and acetonitrile (Ljunger et al. 1994; Cao et al. 1996, 1997; Córdova et al. 1997).

Many applications in the fat and oil producing industry (i.e., both hydrolysis and synthesis of fats and oils) are known (Garcia et al. 1996; Nelson et al. 1996). CalB can also be used for the synthesis and hydrolysis of simple esters (Mattson et al. 1993;

Martinelle et al. 1995; Partali et al. 1994). Examples are the production of isopropyl myristate and myristyl myristate which are both valuable products in the cosmetic industry.

The success of lipases in organic synthesis is also due to their regioselectivity and enantioselectivity. Adelhorst et al. demonstrated that CalB can be used to selectively acylate the 6-O-position of ethylglucoside in solvent free conditions at 70°C (Adelhorst et al. 1990). In aqueous conditions, the reverse hydrolytic reaction can be used to selectively deacylate glucose esters (Kirk et al. 1995). Also other special applications have been reported such as the synthesis of polyesters (Taylor and Binns 1994) that can be achieved by polymerization of a mixture of suitable di- or poly-ols and aliphatic di-acids. A recently documented example is the condensation polymerization of a mixture of adipic acid and 1,8-octanediol in solvent free conditions (Mahapatro et al. 2004).

Alternatively, CalB has also been used as a catalyst to form unique monomers that are otherwise difficult to produce via classical organic synthesis. Standard radical polymerization of these monomers then yields new functional polymers with unique properties such as a high capacity to absorb water. An example is the CalB catalyzed synthesis of 11-metacryloyl aminoundecanoic acid esters of 1- and 3-O-methyl- $\alpha$ -D-glucose and the subsequent AIBN initiated polymerization of these unique monomers (Geyer et al. 1995). Finally, it should be stated at this point that preferably, CalB should be immobilized in an appropriate carrier when using it as a catalyst, inasmuch as immobilization has a highly stabilizing effect on the enzyme (Anderson et al. 1998). Literature reports show that the enzyme is usually immobilized in a macroporous carrier material. Heldt-Hansen et al. demonstrated that at 60–80°C, CalB retains its activity for several hours without experiencing a drop in activity (Heldt-Hansen et al. 1989).

### 7.2.3 Strategy

The concept of this work is the detection of the fluorescence emitted by a single molecule. As a substrate, we chose a nonfluorescent ester that can be converted to a fluorescent product by the specific action of the enzyme, a strategy similar to what was previously reported by Rigler and coworkers (Figure 7.1; Edman and Rigler (2000); Edman et al. (1999)). The profluorescent ester BCECF-AM was selected from the Molecular Probes catalogue. It is converted into the corresponding fluorescent acid product by CalB. In this way, the fluorescence that is monitored after addition of a substrate solution to a single enzyme molecule, will show on–off blinking because of the turnover cycle of the enzyme.

## 7.3 Results and Discussion

### 7.3.1 Properties of the Fluorescent Product; BCECF Acid

Steady-state spectra of BCECF acid in a PBS buffer of pH 7.4 were measured (Figure 7.2). The fluorescent product has an absorption maximum at 500 nm and an emission maximum at 525 nm and thus it can be easily excited using the 488 nm

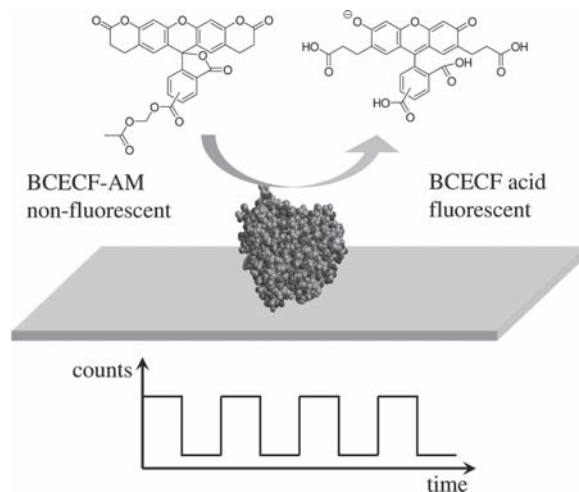


**Figure 7.1** A drop of substrate solution is added on top of the immobilized enzyme molecules, the substrate molecules can reach the active site of the enzymes by diffusion. The fluorescence time trace of a single enzyme molecule that is collected by a confocal microscope setup, is expected to show on-off blinking

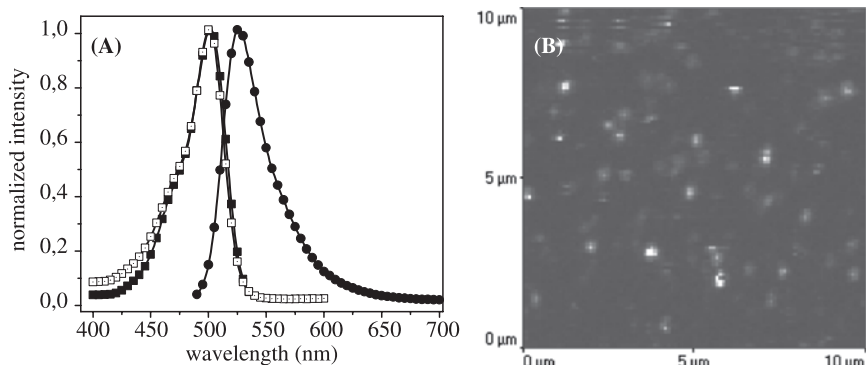


**Figure 7.2** (A) Steady-state spectra of BCECF acid in a PBS buffer, pH 7.4. Solid squares: excitation spectrum, solid circles: emission spectrum, open squares: absorption spectrum. (B) Confocal fluorescence image of individual BCECF acid product molecules. A 1 nM solution of BCECF was spincoated on a glass coverslip. The laser power in front of the microscope was 400 nW, the bin time per pixel was 2.5 ms. The image was taken with a resolution of  $200 \times 200$  pixels. The maximum count rate that was observed for individual BCECF acid molecules was 150 counts per bin

laser line from an Ar-ion laser. To check the visibility of the fluorescent product at the single molecule level, a drop of a 1 nM solution of BCECF acid was spincoated on a carefully cleaned coverslip. Figure 7.2B shows a confocal fluorescence image of the BCECF acid form. Bright fluorescent spots were observed that are attributed to fluorescent product molecules.

### 7.3.2 *Labeling and Immobilization of Enzymes*

In order to localize the enzymes that are not autofluorescent, they were coupled to Alexa-488 dyes with an absorption maximum at 492 nm and an emission maximum at 517 nm. Because of the low photostability of the label at single-molecule excitation conditions, no interference of its emission with the emission of the BCECF product molecules is ensured by photobleaching them before starting addition of the substrate. In order to study the enzymatic conversion for a certain period of time, the labelled enzyme molecules have to be efficiently immobilized. Several immobilization methods have been tried out but the only method that proved to be successful was the immobilization of the enzymes on hydrophobic glass surfaces (Bosley and Peilow 1997). Coverslips were rendered hydrophobic by derivatizing the surface with dichlorodimethylsilane. A 5 nM solution of enzyme was deposited on top of the coverslip and allowed to adsorb to the surface for some minutes. Afterwards the coverslip was extensively rinsed with MilliQ water in order to remove the weakly adsorbed enzymes. Even after addition of a droplet of a solution on top of the cover glass, the enzymes still stay immobilized.

### 7.3.3 *Enzymatic Turnover Experiments*

#### **Ensemble Enzyme Kinetics**

The hydrolysis of an 850 nM solution of the ester both in the presence (Figure 7.3A, black curve) and absence (Figure 7.3A, grey curve) of enzymes are compared by monitoring the fluorescence intensity as a function of time. The initial reaction rate can be plotted as a function of substrate concentration (Figure 7.3B).

These reaction rates show a saturation profile that is a classical outcome for ensemble enzyme kinetics. From these data, a turnover constant  $k_{\text{cat}} = 0.001 \text{ s}^{-1}$  (in solution) was determined.

#### **Single Enzyme Experiments**

To perform single molecule experiments, 100  $\mu\text{l}$  of a 3 nM Alexa-labelled enzyme solution was deposited on a coverslip for 5–10 minutes. The coverslips were then extensively rinsed with water (three times) in order to remove the weakly bound enzymes. On top of this, we applied 5  $\mu\text{l}$  of a 300 nM solution of the substrate. Sequential imaging of a  $10 \times 10 \mu\text{m}^2$  area during approximately 30 minutes revealed an increase of fluorescence originating on the single enzyme molecules as well as a steady increase of the background fluorescence (Figure 7.4) that is attributed to the accumulation of the fluorescent product.

Control experiments were performed whereby no enzymes were present, but no increase in fluorescence intensity was observed. Also control experiments were performed on native CalB with similar results as for the labeled enzymes. In order

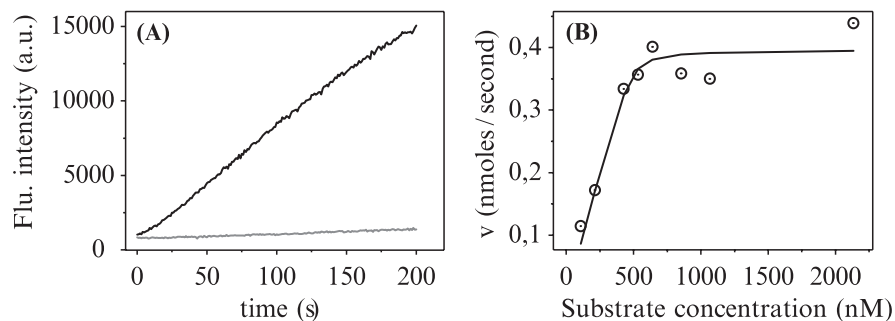


**Figure 7.3** (A) The CalB catalyzed conversion of an 850 nM solution of the ester into the fluorescent product results in an increase of the fluorescence intensity as a function of time (black curve). The enzyme catalyzed conversion is much faster than the self-hydrolysis of an 850 nM substrate solution in water without enzymes (grey curve). (B) The initial slopes of different time traces, similar to the one shown in (A), are plotted as a function of substrate concentration. Fitting this curve yields a  $k_{\text{cat}} = 0.001 \text{ s}^{-1}$

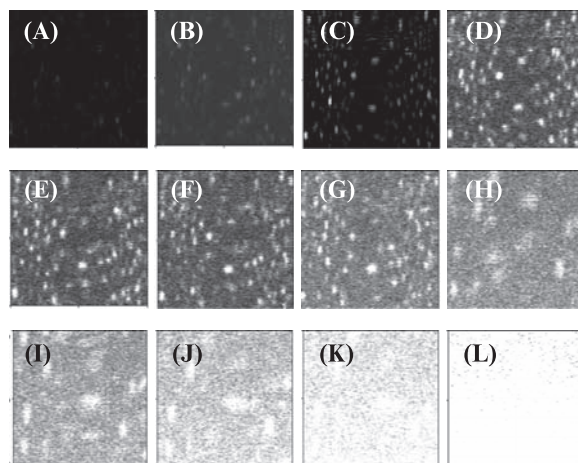


**Figure 7.4** (A), (B): Labelled enzyme molecules were deposited on a hydrophobic coverslip. A  $10 \times 10 \mu\text{m}^2$  area was imaged in order to localize the enzymes. (C)–(L): During imaging, a 300 nM solution of the substrate was added on top of the laser focus. A gradual increase of fluorescence can be observed that we attribute to the formation of fluorescent product molecules by enzymatic hydrolysis of substrate molecules. Note that starting from (H), the area is a  $4,35 \times 4,35 \mu\text{m}^2$  zoom of (G)

to study enzymatic dynamics, single labelled enzyme molecules were positioned in the laser focus and fluorescence transients were recorded. Prior to the addition of substrate, the Alexa-dyes were photobleached.

The fluorescence transients show an increasing background emission due to the continuous generation of fluorescent product by the enzyme molecules. Furthermore, bright spikes are also visible with a signal appreciably higher than the background signal (Figure 7.5). Assuming that each of these spikes can be attributed to a single enzymatic



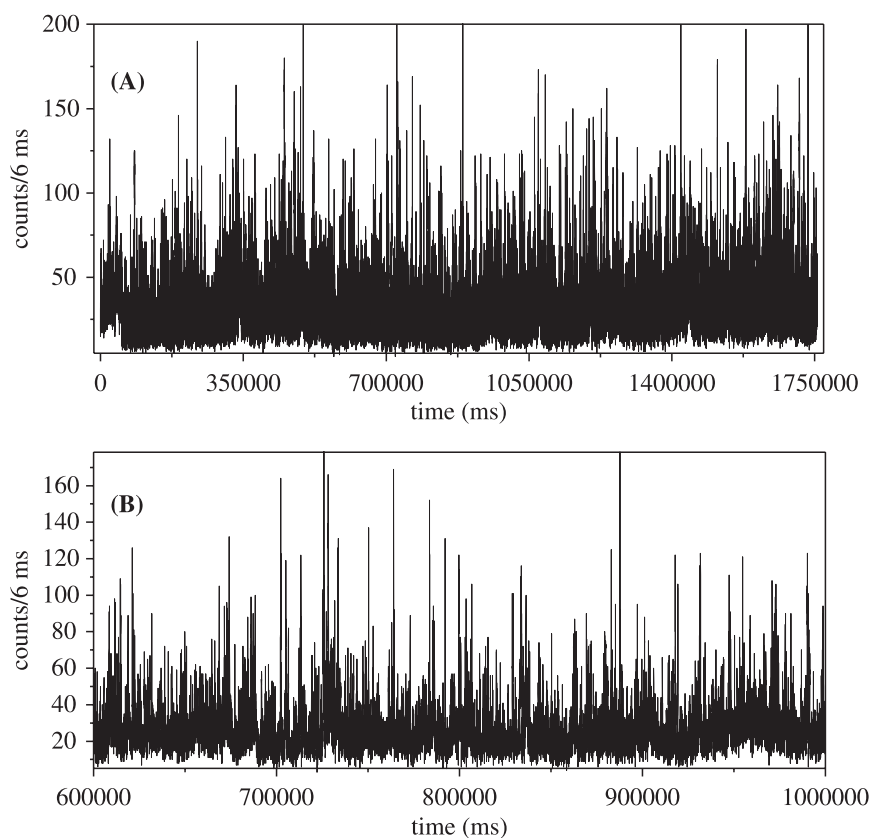


**Figure 7.5** Example of a fluorescence transient corresponding with an enzymatic turnover cycle. (A) A substrate concentration of 400 nM was added to the sample after photobleaching of the alexa-labels. (B) Zoom on the region from 600,000–1,000,000 ms

turnover event, one can gain information about the activity of a single enzyme molecule by simply counting the number of events (spikes) in a given time interval.

### 7.3.4 Analysis of the Fluorescence Intensity Transients

#### Substrate Concentration Dependency

Once an enzyme was found that displayed measurable activity, fluorescence transients were measured using different substrate concentrations applied to the same single enzyme, from 200 nM to 1.4  $\mu$ M. The number of turnover events in a time interval of 20 minutes was counted and plotted as a function of substrate concentration which reveals a saturation behaviour at a substrate concentration of approximately

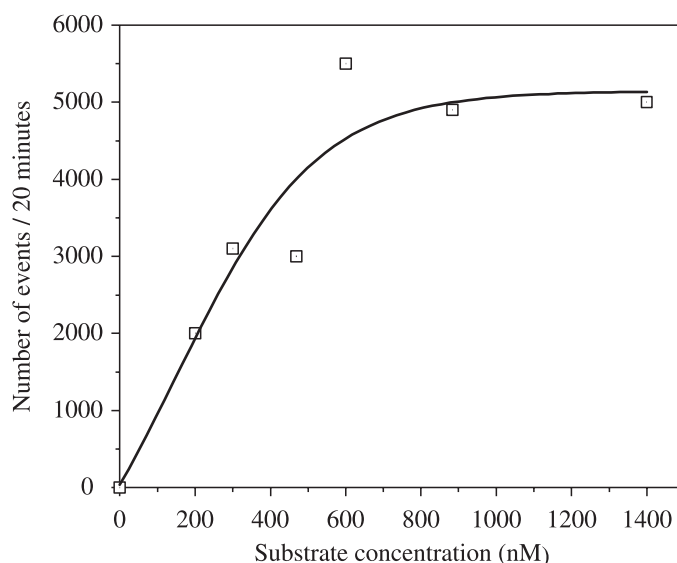


**Figure 7.6** Plot of the number of events counted in a time-interval of 20 minutes as a function of the substrate concentration. The plot reveals a saturation profile that is reached at a substrate concentration of approximately 600 nM

600 nM (Figure 7.6). Below a substrate concentration of 600 nM, the reaction is diffusion-controlled. The saturation level shows roughly 5000 events in a time interval of 20 minutes, resulting in approximately 4 turnovers per second. For the detection of dynamic disorder, it is important to perform all single enzyme experiments using conditions where always enough substrate is present in the vicinity of the enzyme and fluctuations in the off-times cannot be attributed to different or anomalous diffusion times of the substrate into the active site of the enzyme, that is, at substrate concentrations higher than 600 nM. Therefore, fluorescence transients were recorded using three different substrate concentrations (0.6, 0.9, and 1.4  $\mu\text{M}$ ), each of them above the saturation threshold level.

Interestingly, the activity of a single enzyme molecule as a function of substrate concentration showed a saturation behaviour similar to the ensemble Michaelis–Menten saturation curve. The origin of this behaviour is probably different for the ensemble and single-molecule conditions. At the ensemble level, the levelling off of the rate of the enzymatic reaction is due to the occupation of all enzymes as the substrate concentration increases whereas at the single-molecule level at a substrate concentration of 600 nM, there are always enough substrate molecules present in the vicinity of the enzyme molecule to allow it eventually to work at its maximum rate. A further increase of the substrate concentration does not result anymore in an increase in the enzymatic rate. To our knowledge, this is one of the few examples where saturation behaviour is reported for a single enzyme molecule and this opens up new questions for the field of enzymology as to whether Michaelis–Menten kinetics, which is a typical ensemble outcome, still appropriately describes the kinetics of a single enzyme molecule.

### The Local Threshold Method

In order to analyze the recorded fluorescence transients, the enzymatic turnover cycle is considered to be a two-state process (Velonia et al. 2005; Flomenbom et al. 2005). When the substrate molecule is bound in the active site, no fluorescence is observed and when the substrate molecule has been turned into a product molecule, fluorescence can be observed. When the product molecule exits the active site, the enzymatic cycle starts all over again.

Enzymatic dynamics can be studied by constructing the on- and off-time histograms (Lu et al. 1998; Xie and Lu 1999). In the text that follows, the on-time histogram is designated as  $P_{\text{on}}(t)$  and the off-time histogram is designated as  $P_{\text{off}}(t)$ . However, a suitable method is necessary to discriminate between on- and off-states. Usually a threshold level is set whereby states that are situated above the threshold level are designated as on-states and states that are situated below the threshold level are designated as off-states. In order to estimate the threshold level for each transient, a photon count value was assigned to each given time interval of the transient and these photon count values were histogrammed (Yip et al. 1998).

Furthermore, the increasing background level as a result of product formation as can be seen in Figure 7.4 is also taken into account. In order to achieve this, a local treatment is performed on the fluorescence transient (Flomenbom et al. 2005). Briefly, the difference between the local threshold and the average photon count number of the off-states is fixed in each interval of the fluorescence transient. This results in a local threshold that shifts to higher values as a function of time and thus compensating the increasing background fluorescence.

### Off-Time Histograms

Using this threshold-method, off-time histograms ( $P_{\text{off}}(t)$ ) were constructed. Examples of three different concentrations are shown in Figure 7.7A–C. The logarithmic-linear scale emphasizes the nonexponential relaxation pattern. The histograms could be fitted best with a stretched exponential function, also known as the Kohlrausch–Williams–Watts (KWW)-function shown in Equation (7.1) (Lindsey and Patterson 1980). This KWW-function is often used to describe heterogeneous systems showing a continuous distribution of the investigated parameter rather than a discrete set of exponentials.

$$P_{\text{off}}(t) = P_0 e^{-\left(\frac{t_{\text{off}}}{\tau}\right)^\alpha} \quad (7.1)$$

where  $0 < \alpha \leq 1$  is a so-called width or stretch parameter that may be interpreted either as a measure of the nonexponential character of  $P_{\text{off}}(t)$ , or as a measure of the width of the underlying distribution of relaxation times. When  $\alpha$  is close to one, the deviation from monoexponential decay is minimal and consequently, the decay may be approximated by a sum of a few exponential terms. A value  $\alpha$  close to zero indicates a large deviation from exponential behaviour and hence a real continuous distribution of off-times. The parameter  $\tau$  is the time at which  $P_{\text{off}}(t)$  falls to  $1/e$  of its initial value. The term  $P_0$  is a normalization factor. Rewriting this equation gives:

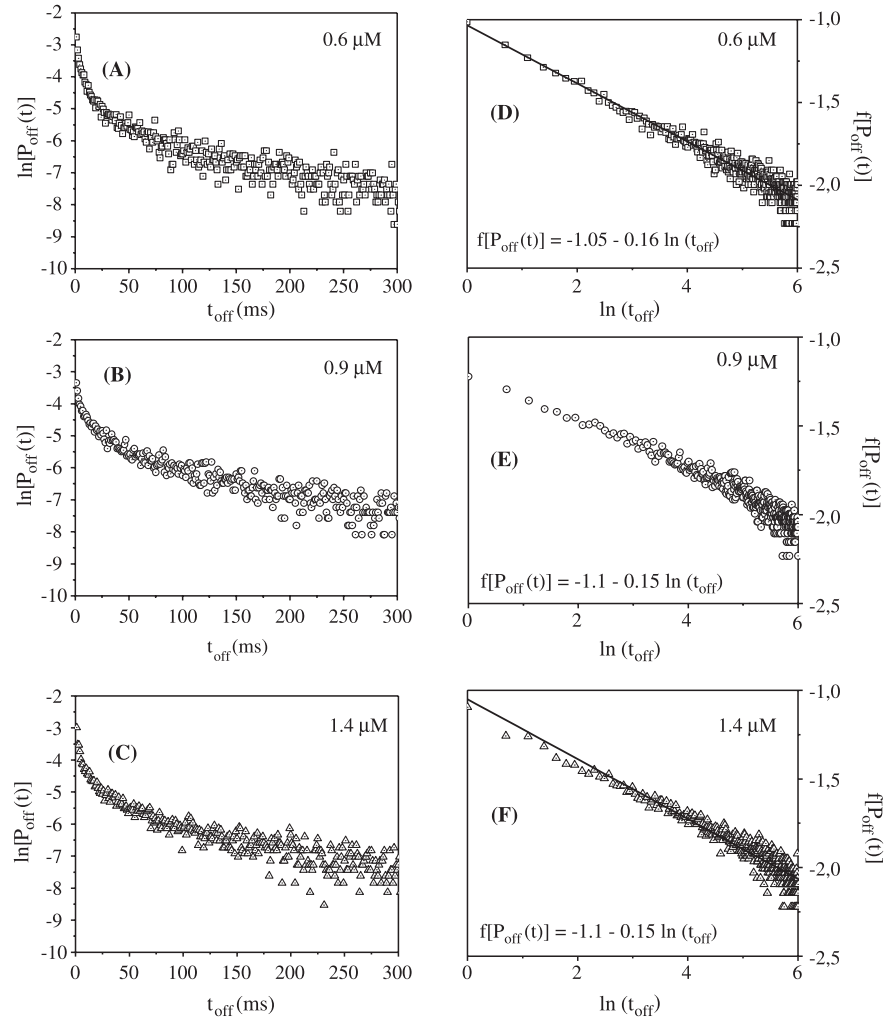


**Figure 7.7** (A–C) Off-time histograms for three different substrate concentrations (0.6, 0.9, and 1.4 μM) that were added sequentially on top of the same enzyme. (D–F) Double logarithmic plots of  $P_{\text{off}}(t)$  for the three substrate conditions, respectively. Here  $f(P_{\text{off}}(t)) = -\ln[-\ln(P_{\text{off}}(t))]$  is plotted versus  $\ln(t)$ . The slope is equal to  $-\alpha$  resulting in a value of  $\alpha = 0.15$  for the three substrate concentrations

$$f(P_{\text{off}}(t)) = -\ln[-\ln(P_{\text{off}}(t))] = \alpha \ln \tau - \alpha \ln t_{\text{off}}. \quad (7.2)$$

The function  $f(P_{\text{off}}(t))$  depends linearly on  $\ln(t_{\text{off}})$  with a slope  $-\alpha$ . The double logarithmic plots allow the extraction of the parameters  $\alpha$  and  $\tau$  (Figure 7.7D–F). The exponential term  $\alpha$  and the parameter  $\tau$  appear to be independent of the substrate concentration, with  $\alpha = 0.15$  and  $\tau = 1.15 \mu\text{s}$ .

The two extracted parameters  $\alpha$  and  $\tau$  allow the calculation of the average off-time, which is 235 ms for all substrate concentrations. This corresponds with 4

turnovers per second on average. It is known from other systems such as glassy materials that a stretched exponential decay pattern can arise from contributions of a large number of weighted exponentials due to an inhomogeneous environment (Metzler et al. 1999; Dubreuil 2003).

In our case, the stretched exponential decay of  $P_{\text{off}}(t)$  indicates that the enzyme exhibits dynamic disorder in its catalytic activity, with identical fitting parameters ( $\alpha$  and  $\tau$ ) and hence also the average off-times for all substrate concentrations. Hence, the dynamic disorder, which leads to a stretched exponential decay of  $P_{\text{off}}(t)$ , is an inherent property of the enzyme under study, originating from different enzyme conformations which each contribute with an exponential term to the overall decay of  $P_{\text{off}}(t)$ .

### Autocorrelation Analysis (Data Not Shown)

In order to obtain information on the time scales on which fluctuations occur, autocorrelation analysis was performed on the digitized traces (Flomenbom et al. 2005). The best fit to the autocorrelation decay was again a stretched exponential function. The decay was spread over three orders of time (fluctuations ranging from 1–1000 ms) and the fit parameters were:  $\alpha = 0.085$  and  $\tau = 0.356 \mu\text{s}$ .

The experimentally obtained autocorrelation trace was compared with a simulated autocorrelation trace, constructed based on a two-state (on and off) model. The simulated trace also displayed a stretched exponential decay with the same  $\alpha$ -value ( $\alpha \sim 0.08$ ) but different  $\tau$ -value ( $\tau = 0.141 \text{ ns}$ ) as for the experimental one. The fact that the experimental autocorrelation decay relaxes slower than the simulated one serves as an indication that the enzymatic turnover cycle is more complex than the assumed two-state model. Furthermore, the finding that the autocorrelation decay is best fit with a stretched exponential function suggests that fluctuations exist in different time scales and hence it also indicates that dynamic disorder exists in this enzyme system.

### Off-Times as a Function of Time

It is interesting to see how the off-times fluctuate as a function of time (or event index) (Figure 7.8). A similar trajectory has been used in the literature to calculate the autocorrelation function of the off-times and obtain information about conformational changes (Lu et al. 1998; Schenter et al. 1999; Cao 2000; Yang and Cao 2002). The trajectory shows that the off-times fluctuate as a function of the event index but what is particularly interesting is that there are local trends visible. Events of similar time duration follow each other; that is, a long off-time tends to be followed by another long off-time. Short off-times tend to be followed by other short off-times. Clearly visible in this trace are groups of very short off-times (shorter than 35 ms) that are clustered together with an average of 3.5 events per group and an average duration time of 8 ms per event in the group. This is very reminiscent of the memory effect as it was described by Xie and coworkers (Lu et al. 1998). Clearly, CalB also shows a similar effect.

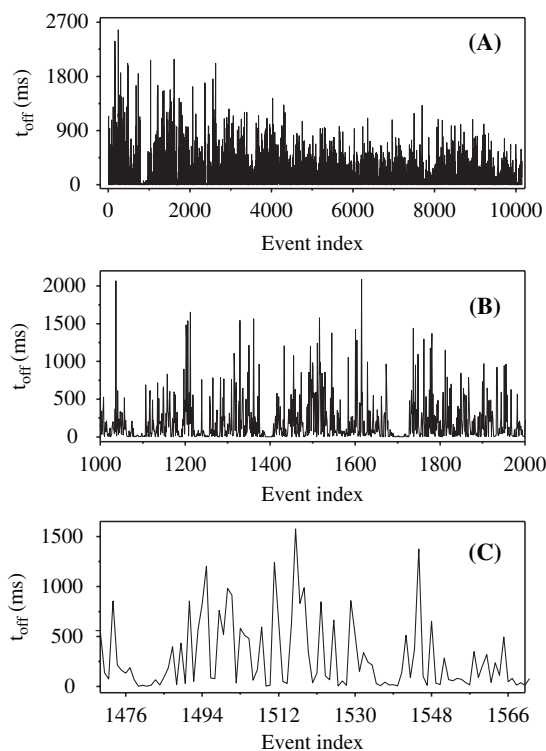


**Figure 7.8** (A) Time-duration of the off-events as a function of event index. Groups of very fast events (less than 35 ms) are visible along this trajectory. Furthermore, events of similar time duration seem to be localized in groups. (B) Zoom on a part of the trace in panel A (from events 1000–2000). (C) Further zoom on the trace from panel A, from events 1470–1570

The events of short time duration were binned and subsequently histogrammed (Figure 7.9). The histogram represents the probability that the enzyme occupies a ‘fast’ (or in other words: a very reactive) conformation (or conformations) for a given time  $t$  before a transition to a less reactive conformational state occurs. Fitting this histogram yields an average time of 27 ms which is the average time the enzyme spends in its ‘fast’ conformation before conformational changes occur.

We cautiously interpret the off-times in terms of a turnover rate of the enzyme on a surface. On average, the short events have a duration time of 8 ms, corresponding with 125 turnovers per second. The maximum off-times of 2575 ms correspond with roughly 0.4 turnovers per second. The average off-time of 235 ms corresponds with roughly 4 turnovers per second. Considering the fact that roughly 10,000 events can be counted in a time-interval of 20 minutes, it is obvious that the enzyme is catalytically ‘silent’ during long periods of time before acquiring a reactive conformation. Once in this reactive state, the enzyme performs on average three turnovers before acquiring a less reactive conformational state again.

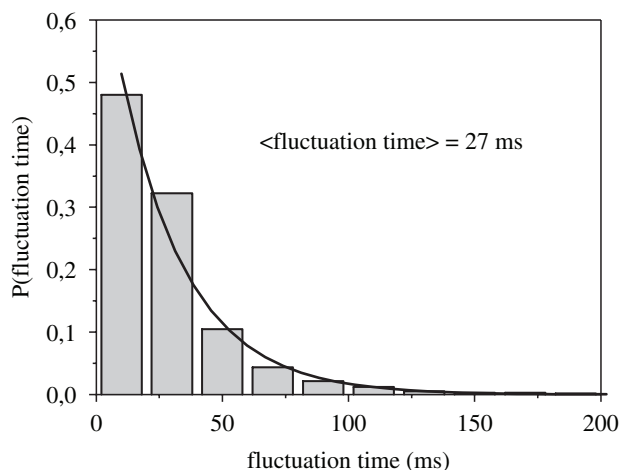
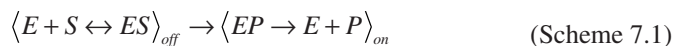


**Figure 7.9** The histogram of the binned ‘fast’ events. Fitting the histogram gives an average time the enzyme spends in its ‘fast’ conformation (27 ms)

Note that there is a large discrepancy between the number of turnovers per second at the single-molecule level and the ones obtained by bulk measurements. Several factors can be considered to explain this observation. Although CalB doesn’t have a real ‘lid’, still a certain extent of interfacial activation can be observed which will increase the working speed of the enzymes when exposed to a surface compared to the bulk activity. Furthermore, from the large number of single molecules measured, only a few seem to be active, indicating that the commercially available enzyme samples might contain a lot of nonactive enzymes. A third explanation is that in the single-molecule approach only the most active ones are measured because these are the most easily seen.

### 7.3.5 The Model

Consider a general Michaelis–Menten scheme:



where  $E$ ,  $S$ , and  $P$  stand for the enzyme, substrate, and product molecules whereas  $ES$  and  $EP$  stand for the enzyme–substrate and enzyme–product complexes. Also indicated are the fluorescent properties of the species during all stages of the reaction cycle. The expected off-time histograms for the scheme above are not stretched exponentially. They are expected to be biexponential. In this case, fitting the histogram gives an off-time that can unambiguously be related to a reaction rate. Therefore, the current observations force us to propose a model that goes beyond the Michaelis–Menten type of description. The stretched exponential decay pattern

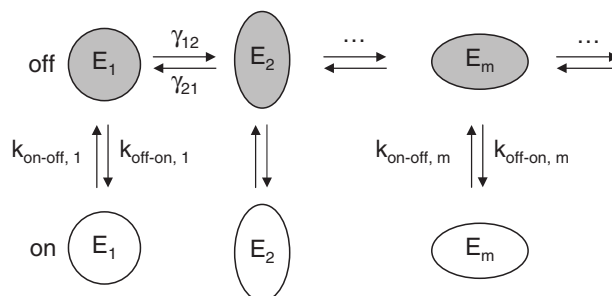


**Figure 7.10** The model for the enzyme behaviour. The enzyme explores its conformational space ( $E_1, \dots, E_m$ ). Each conformational substate can catalyze the reaction possibly with a different rate. When a substrate molecule is converted into a product molecule, the off-state turns into an on-state. When the product molecule diffuses out of the enzyme, the on-state turns into the corresponding off-state again

of the off-time histograms indicates that the system exhibits dynamic disorder, meaning that multiple conformations of the enzyme are involved in the catalytic cycle. In this case, however, it is less obvious to extract unambiguously a turnover rate because each conformation has its own turnover rate.

We therefore propose a model that involves both conformational changes as well as catalysis. The model describes an off-state that consists of a broad spectrum of conformations (Figure 7.10).

Each conformation  $m$  has its own reaction rate  $k_{\text{on-off}, m}$ . The interconversions between the different conformations are described by the rate constants  $\gamma_{12}$  and  $\gamma_{21}$  for interconversion between substate 1 and 2 and so on. How can one imagine these multiple conformations? As already said in the introductory part of this chapter, enzymes are complex molecules, possessing many degrees of motional freedom. Therefore, conformational changes in its structure occur constantly. Not all of these ‘small’ conformational changes necessarily affect the enzymatic activity. Some of them may be totally unimportant. Conformational changes also keep on happening while the enzyme–substrate complex is being formed.

It is not fully clear at this moment which processes of the enzymatic cycle are rate limiting. One of the possibilities is the diffusion and docking of the substrate into the active site of the enzyme, a process that possibly is dependent on the conformation of the enzyme.

## 7.4 Conclusions and Perspectives

Nonexponential behaviour of biomolecules has been reported for several systems. However, stretched exponential off-time histograms in the enzymatic catalytic activity at the level of a single molecule are much less documented (Jia et al. 1997). A possible explanation regarding the origin of the nonexponential character of  $P_{\text{off}}(t)$  is that the enzymatic kinetics involve a broad conformational spectrum,



where each conformation contributes an exponential factor to the overall turnover cycle. Both the smaller value of the characteristic time parameter of the experimental correlation function relative to the theoretical one and the local temporal trend of the off-state events suggest that a single molecule scheme consisting of a spectrum of conformations that are interconverting, best describes the enzymatic turnover cycle. The ability to measure the activity of a single enzyme for long periods of time as shown and analyzed in this chapter offers a powerful tool for the investigation of other enzymes.

**Acknowledgements** We thank Prof. Nolte (Nijmegen), Prof. Rowan (Nijmegen), Prof. Velonia (Lausanne), Prof. Klafter (Tel Aviv), Dr. Flomenbom (Tel Aviv), and Dr. Svenson (Novozymes) for their fruitful collaboration. Financial support from the KULeuven research fund (GOA 2/06, Center of Excellence CECAT), the Federal Science Policy of Belgium (Grant IAP-V-03 and IAP-VI-27), the FWO (G.0366.06 and G.0229.07) and from the IWT through ZWAP04/007 is acknowledged. This research was conducted in the Framework of the European projects Sisitomas and the STREP project Bioscope.

## References

- Adelhorst K, Björkling F, Godtfredsen SE, Kirk O (1990) Enzyme catalyzed preparation of 6-O-acylglucopyranosides. *Synthesis-Stuttgart* (2): 112–115.
- Agmon N (2000) Conformational cycle of a single working enzyme. *J. Phys. Chem. B*, 104: 7830–7834.
- Anderson EM, Larsson KM, Kirk O (1998) One biocatalyst - Many applications: The use of *Candida antarctica* B-lipase in organic synthesis. *Biocatal. Biotransfor.*, 16: 181–204.
- Ansari A, Berendzen J, Bowne SF, Frauenfelder H, Iben IET, Sauke TB, Shyamsunder E, Young RD (1985) Protein states and proteinquakes. *Proc. Natl. Acad. Sci. USA*, 82: 5000–5004.
- Astumian RD (2002) Protein conformational fluctuations and free-energy transduction. *Appl. Phys. A*, 75: 193–206.
- Berezhkovskii AM, Boguñá M, Weiss GH (2001) Evaluation of rate constants for conformational transitions using single-molecule fluorescence spectroscopy. *Chem. Phys. Lett.*, 336: 321–324.
- Berezhkovskii AM, Szabo A, Weiss GH (1999) Theory of single-molecule fluorescence spectroscopy of two-state systems. *J. Chem. Phys.*, 110: 9145–9150.
- Bosley JA, Peilow AD (1997) Immobilisation of lipases on porous polypropylene: reduction in esterification efficiency at low loading. *J. Am. Oil Chem. Soc.*, 74: 107–111.
- Brady L, Brzozowski AM, Derewenda ZS, Dodson E, Dodson G, Tolley S, Turkenburg JP, Christiansen L, Høge-Jensen B, Nørskov L, Thim L, Møgelvang U (1990) A serine protease triad forms the catalytic center of a triacylglycerol lipase. *Nature*, 343: 767–770.
- Cao J (2000) Event-averaged measurements of single-molecule kinetics. *Chem. Phys. Lett.*, 327: 38–44.
- Cao LQ, Bornscheuer UT, Schmid RD (1996) Lipase-catalyzed solid phase synthesis of sugar esters. *Fett-Lipid*, 98(10): 332–335.
- Cao LQ, Fischer A, Bornscheuer UT, Schmid RD, (1997) Lipase-catalyzed. solid phase synthesis of sugar fatty acids esters. *Biocatal. Biotransfor.*, 14(4): 269–283.
- Córdova A, Hult K, Iversen T (1997) Esterification of methyl glycoside mixtures by lipase catalysis. *Biotechnol. Lett.*, 19(1): 15–18.
- Dubreuil A-C, Doumenc F, Guerrier B, Johannsmann D, Allain C (2003) Analysis of the solvent diffusion in glassy polymer films using a set inversion method. *Polymer*, 44: 377–387.
- Edman L, Földes-Papp Z, Wennmalm S, Rigler R (1999) The fluctuating enzyme: A single molecule approach. *Chem. Phys.*, 247: 11–22.

- Edman L, Rigler R (2000) Memory landscapes of single-enzyme molecules. *Proc. Natl. Acad. Sci. USA*, 97: 8266–8271.
- Fernández-Lorente G Terreni M, Mateo C, Bastida A, Fernández-Lafuente R, Dalmases P, Huguet J, Guisán JM (2001) Modulation of lipase properties in macro-aqueous systems by controlled enzyme immobilization: Enantioselective hydrolysis of a chiral ester by immobilized *Pseudomonas* lipase. *Enzyme Microb. Tech.*, 28: 389–396.
- Fersht A (1985) *Enzyme Structure and Mechanism*, 2nd edition, W.H. Freeman, New York
- Flomenbom O, Klafter J, Szabo A (2005) What can one learn from two-state single molecule trajectories? *Biophys. J.*, 88: 3780–3783.
- Flomenbom O, Velonia K, Loos D, Masuo S, Cotlet M, Engelborghs Y, Hofkens J, Rowan A, Nolte R.J.M, Van der Auweraer M, De Schryver FC, Klafter J (2005) Stretched exponential decay and correlations in the catalytic activity of fluctuating single lipase molecules. *Proc. Natl. Acad. Sci. USA*, 102, 7: 2368–2372.
- Frauenfelder H, McMahon BH, Austin RH, Chu K, Groves JT (2001) The role of structure, energy landscape, dynamics, and allostery in the enzymatic function of myoglobin. *Proc. Natl. Acad. Sci. USA*, 98: 2370–2374.
- Frauenfelder H, Sligar SG, Wolynes PG (1991) The energy landscapes and motions of proteins. *Science*, 254: 1598–1603.
- Garcia HS, Yang B, Parkin KL (1996) Continuous reactor for enzymic glycerolysis of butter oil in the absence of solvent. *Food Res. Int.*, 28: 605–609
- Geva E, Skinner JL (1998) Two-state dynamics of single biomolecules in solution. *Chem. Phys. Lett.*, 288: 225–229.
- Geyer U, Klemm D, Pavel K, Ritter H (1995) Enzymes in polymer chemistry. 8. Chemoenzymatic synthesis of polymerizable 11-meth acryloyl-amino-undecanoic ester of 1- and 3-O-methyl- $\alpha$ -D-glucose in 6-O-position. *Macromol. Chem. Rapid Comm.*, 16: 337–341.
- Heldt-Hansen HP, Ishii M, Patkar S, Hansen TT, Eigtred P (1989) In: *Biocatalysis in Agricultural Biotechnology* (eds.) Whitaker J.R. and Sonnet P.E., Am. Chem. Soc., Washington D.C.: pp 158–172.
- Jensen MØ, Jensen TR, Kjaer K, Bjørnholm T, Mouritsen OG, Peters GH, (2002) Orientation and conformation of a lipase at an air–water interface: Molecular dynamics simulations. *Biophys. J.*, 83: 98–111.
- Jia Y, Sytnik A, Li L, Vladimirov S, Cooperman BS, Hochstrasser RM (1997) Nonexponential kinetics of a single tRNA<sup>Phe</sup> molecule under physiological conditions. *Proc. Natl. Acad. Sci. USA*, 94: 7932–7936.
- Kirk O, Christensen MW, Beck F, Damhus T (1995) Lipase catalyzed regioselective acylation and deacylation of glucose derivatives. *Biocatal. Biotransfor.*, 12: 91–97.
- Kou SC, Cherayil BJ, Min W, English BP, Xie XS (2005) Single-Molecule Michaelis–Menten Equations. *J. Phys. Chem. B*, 109: 19068–19081.
- Lee AI, Brody JP (2005) Single-molecule enzymology of chymotrypsin using water-in-oil emulsion. *Biophys. J.*, 88: 4303–4311.
- Lerch H-P, Rigler R, Mikhailov AS (2005) Functional conformational motions in the turnover cycle of cholesterol oxidase. *Proc. Natl. Acad. Sci. USA*, 102, 31: 10807–10812.
- Lindsey CP, Patterson GD (1980) Detailed comparison of the Williams–Watts and Cole–Davidson functions. *J. Chem. Phys.*, 73: 3348–3357.
- Ljunger G, Adlercreutz P, Mattiasson B (1994) Lipase-catalyzed acylation of glucose. *Biotechnol. Lett.*, 16(11): 1167–1172.
- Lu HP, Xun L, Xie XS (1998) Single-molecule enzymatic dynamics. *Science*, 282: 1877–1882.
- Mahapatro A, Kumar A, Kalra B, Gross RA (2004) Solvent-free adipic acid/1,8-octanediol condensation polymerizations catalyzed by *Candida antarctica* lipase B. *Macromolecules*, 37: 35–40.
- Martinelle M, Hult K (1995) Kinetics of acyl transfer reactions in organic media catalysed by *Candida antarctica* lipase B. *Biochim. Biophys. Acta*, 1251: 191–197.
- Matthews CK, Van Holde KE (1996) *Biochemistry*, 2nd edition, Benjamin-Cummings, CA: 208–210.

- Mattson A, Öhrner N, Hult K, Norin T (1993) Resolution of diols with C<sub>2</sub>-symmetry by lipase catalysed transesterification. *Tetrahedr. Asymm.*, 4: 925–930.
- Metzler R, Klafter J, Jortner J (1999) Hierarchies and logarithmic oscillations in the temporal relaxation patterns of proteins and other complex systems. *Proc. Natl. Acad. Sci. USA*, 96: 11085–11089.
- Nelson LA, Foglia TA, Marmer WN (1996) Lipase-catalyzed production of biodiesel. *J. Am. Chem. Oil. Soc.*, 73: 1191–1195.
- Ollis DL, Cheah E, Cygler M, Dijkstra B, Frolow F, Franken SM, Harel M, Remington SJ, Silman I, Schrag J, Sussman JL, Verschuere KHG, Goldman A (1992) The alpha/beta hydrolase fold. *Protein Eng.*, 5: 197–211.
- Onuchic JN, Wang J, Wolynes PG (1999) Analyzing single molecule trajectories on complex energy landscapes using replica correlation function. *Chem. Phys.*, 247: 175–184.
- Partali V, Waagen V, Alvik T, Anthonsen T (1993) Enzymatic resolution of butanoic esters of 1-phenylmethyl and 1-[2-phenylethyl] ethers of 3-chloro-1,2-propanediol. *Tetrahedr. Asymm.*, 4: 961–968.
- Rogalska E, Cudrey C, Ferrato F, Verger R (1993) Stereoselective hydrolysis of triglycerides by animal and microbial lipases. *Chirality*, 5: 24–30.
- Ross J, Vlad MO (1999) Nonlinear kinetics and new approaches to complex reaction mechanisms. *Ann. Rev. Phys. Chem.*, 50: 51–78.
- Rotman B (1961) Measurement of activity of single molecules of  $\beta$ -D-galactosidase. *Proc. Nat. Acad. Sci. U.S.A.*, 47, 1981–1991.
- Rotman, B (1973) in *Fluorescence Techniques in Cell Biology* (eds.) Thier AA, Sernetz M, Springer, New York, pp. 333–337.
- Schenter GK, Lu HP, Xie XS (1999) Statistical analyses and theoretical models of single-molecule enzymatic dynamics. *J. Phys. Chem. A*, 103: 10477–10488.
- Taylor A, Binns F (1994) Enzymatic synthesis. World Patent WO 94/12625.
- Van Tilbeurgh H, Egloff M-P, Martinez C, Rugani N, Verger R, Cambillau C (1993) Interfacial activation of the lipase-procolipase complex by mixed micelles revealed by X-ray crystallography. *Nature*, 362: 814–820.
- Velonia K, Flomenbom O, Loos D, Masuo S, Cotlet M, Engelborghs Y, Hofkens J, Rowan AE, Klafter J, Nolte RJM, De Schryver FC (2005) Single enzyme kinetics of CALB catalyzed hydrolysis. *Angew. Chem. Int. Ed.* 44: 560–564.
- Xie XS (2002) Single-molecule approach to dispersed kinetics and dynamic disorder: Probing conformational fluctuation and enzymatic dynamics. *J. Chem. Phys.* 117: 11024–11032.
- Xie XS, Lu HP (1999) Single molecule enzymology. *J. Biol. Chem.*, 274: 15967–15970.
- Xue Q, Yeung ES (1995) Differences in the chemical reactivity of individual molecules of an enzyme. *Nature*, 373: 681–683.
- Yang H, Xie XS (2002) Statistical approaches for probing single-molecule dynamics photon-by-photon. *Chem. Phys.*, 284: 423–437.
- Yang S, Cao J (2002) Direct measurements of memory effects in single molecule kinetics. *J. Chem. Phys.*, 117: 10996–11009.
- Yip W-T, Hu D, Yu J, Vanden Bout DA, Barbara PF (1998) Classifying the photophysical dynamics of single- and multiple-chromophoric molecules by single molecule spectroscopy. *J. Phys. Chem. A*, 102: 7564–7575.

# Chapter 8

## Protein Folding and Dynamics from Optical Single Molecule Spectroscopy

Benjamin Schuler(✉) and Gilad Haran(✉)

8.1	Introduction.....	182
8.2	The Protein Folding Problem.....	182
8.2.1	Current Questions in Protein Folding.....	183
8.3	Single-Molecule Spectroscopy.....	184
8.3.1	Free Diffusion Experiments.....	188
8.3.2	Experiments on Immobilized Proteins.....	190
8.4	Single-Molecule Protein Folding.....	195
8.4.1	Studies on Freely Diffusing Protein Molecules.....	195
8.4.2	Immobilized Protein Molecules.....	202
8.5	Perspective.....	207
	References.....	208

**Abstract** Protein folding is an intrinsically heterogeneous process, taking a protein from a large ensemble of unfolded conformations to an essentially unique three-dimensional structure. Single molecule spectroscopy is thus a promising technique for mapping the structural and dynamic aspects of this reaction that have eluded experimental investigation by ensemble methods. Here, we summarize recent progress in this area, with a focus on Förster resonance energy transfer (FRET) studies of individual protein molecules. In experiments on freely diffusing molecules, folded and unfolded subpopulations co-existing at equilibrium can be separated. Most importantly, this has opened the possibility to study the dimensions and dynamics of the unfolded state even under near-native conditions, which are physiologically most relevant, but difficult to study with ensemble methods. Experiments on immobilized molecules have led to the direct observation of the stochastic signature of the protein folding reaction and the identification of signs of unexpected heterogeneity in the unfolded state and during the folding process.

---

Benjamin Schuler  
Biochemisches Institut, Universität Zürich, Winterthurerstr. 190, 8057 Zürich, Switzerland  
schuler@bioc.unizh.ch

Gilad Haran  
Chemical Physics Department, Weizmann Institute of Science, Rehovot 76100, Israel  
gilad.haran@weizmann.ac.il

## 8.1 Introduction

The folding of a protein is the first part of its function: it has to find its native three-dimensional structure—encoded in the amino acid sequence—to be able to act as an enzyme, a signal transducer, a membrane channel, or a stabilizing element of a cell, to name but a few of the many roles that proteins can take. Contrary to widespread belief, folding is not a unique singular event in the life of a protein. Many proteins are marginally stable and will fold and unfold many times during their functional life. A large class of proteins even fold only in the presence of stabilizing ligands or binding partners (Dyson and Wright 2005), illustrating the close coupling of folding and function.

On a microscopic level, protein folding is a highly heterogeneous process, owing to the large complexity of the many-body interactions involved, typically between thousands of protein and solvent atoms. We can get an idea of this “molecular dance” from simulations, but the drastic simplifications of force fields necessary to make them computationally feasible have been limiting their predictive power. Experimentally, chemical kinetics and thermodynamics have revealed an impressive variety of mechanisms, reflected in a wide range of relevant time scales from nanoseconds to years, but much of the underlying heterogeneity has remained buried in the ensemble-averaged signal of most measurements. The availability of methods to probe individual biomolecules, especially force microscopy and fluorescence spectroscopy, now provide an opportunity to avoid ensemble averaging and gain a new perspective on protein folding.

This chapter focuses on single-molecule fluorescence studies of the dynamics and thermodynamics of protein folding. We start with a brief discussion of the protein folding problem, then introduce the various methods employed to address this problem on the single-molecule level. This is a budding field, and a rather small number of proteins have been studied so far; each of them is described in light of the particular methodology used. We also try to illuminate particular aspects of folding that each of these experiments attempts to answer, and finally suggest where this field may be heading in the coming years.

## 8.2 The Protein Folding Problem

Experiments in the 1930s and 1940s had already indicated that protein folding is autonomous and reversible, that is, that a protein’s specific structure can be restored after denaturation (Anson and Mirsky 1934; Anson 1945; Neurath et al. 1944; Wu 1931). Anfinsen’s classical work on the reduction and reoxidation of ribonuclease supplied clear evidence that the amino acid sequences selected through evolution contain all necessary information for attaining their native structures (Anfinsen 1972, 1973; Sela et al. 1957). The hierarchic patterns found in crystal structures of proteins had already suggested that folding might also be a hierarchic process, and

the developing concept of nucleation events emphasized the importance of local interactions for the early stages of protein folding, with a subsequent condensation of substructures (Anfinsen 1973; Levinthal 1968; Tsong and Baldwin 1972; Wetlaufer 1973). The following work of the 1970s and 1980s was dominated by the hunt for folding intermediates on the pathway from the unfolded to the native state, and led to the identification of structurally and spectroscopically distinct intermediate states in the folding of a large number of proteins (Creighton 1992; Jaenicke 1980; Kim and Baldwin 1982). This was accompanied by the development of a range of phenomenological models of folding (Fersht 1995; Go et al. 1980; Harrison and Durbin 1985; Kanehisa and Tsong 1979; Karplus and Weaver 1976; Kim and Baldwin 1982; Ptitsyn and Rashin 1975) that differ in the degree of parallel formation of substructures, their interactions on the way to more complex assemblies and the assignment of the rate limiting step, but these theories are difficult to distinguish experimentally (Karplus and Weaver 1994).

### 8.2.1 Current Questions in Protein Folding

Two important developments in the 1990s were the discovery of small proteins that fold very fast ( $\sim 10^3 \text{ s}^{-1}$  and faster) without populating stable intermediates (Jackson and Fersht 1991; Jackson 1998), and the introduction of the concepts of statistical mechanics into the theory of protein folding (Figure 8.1) (Bryngelson and Wolynes 1987; Dill and Chan 1997; Dobson et al. 1998; Onuchic et al. 1997; Shakhnovich 1997). The identification of “two-state folders” very clearly demonstrated that stable

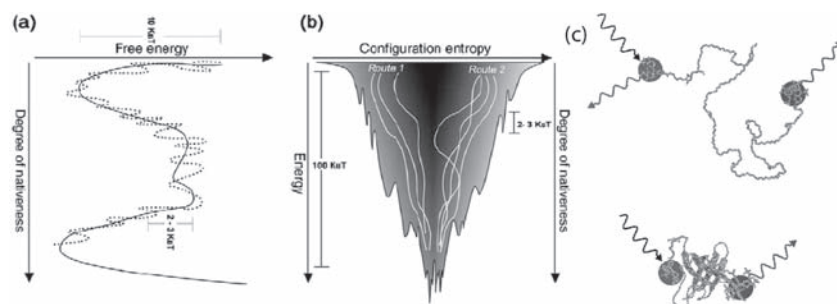


**Figure 8.1** Schematic depiction of a protein’s conformational energy landscape. (a) Projection on a single reaction coordinate yields the classical two-state picture with a native and an unfolded state. (b) The energy landscape theory of folding considers folding as the progressive organization of an ensemble of partially folded structures through which the protein passes on its way to the natively folded structure on a rugged, funnel-like energy landscape. (c) Cartoon of a small protein (*CspTm*) in its unfolded and folded state, respectively. The protein is terminally labeled with fluorophores for FRET, illustrating how different energy transfer efficiencies can be used to distinguish folded and unfolded molecules in single molecule spectroscopy. (Panels a and b reprinted from Onuchic and Wolynes (2004), with permission)

intermediates are not a general prerequisite for folding, and demanded different approaches to solving the protein folding problem. One such strategy is the characterization of transition states for folding by protein engineering methods (Fersht 1998; Serrano et al. 1992), another the analysis of elementary processes of protein folding, such as the formation of loops (Bieri and Kiefhaber 1999; Bieri et al. 1999; Hagen et al. 1996; Lapidus et al. 2000, Neuweiler et al. 2003; Neuweiler and Sauer 2004) or isolated secondary structure elements (Krieger et al. 2003; Munoz et al. 1997; Scholtz and Baldwin 1992; Thompson et al. 1997). Whereas the “new view” (Baldwin 1995) of protein folding introduced from statistical thermodynamics (Bryngelson and Wolynes 1987; Dill and Chan 1997; Onuchic et al. 1997; Shakhnovich 1997) was sometimes perceived to be in contradiction to the “classical view” of folding pathways, it can rather be considered more general (Pande et al. 1998), and it contributed to a range of new questions, which are currently under intense investigation. These include the hunt for a protein folding “speed limit” (Bieri and Kiefhaber 1999; Hagen et al. 1996; Kubelka et al. 2004) and “downhill” (or barrierless) folding (Eaton 1999; Sabelko et al. 1999; Yang and Gruebele 2003), the importance of unfolded state dynamics (Fitzkee and Rose 2004; Frieden et al. 2002; Kohn et al. 2004; Shortle 1996; Zagrovic et al. 2002) and the prediction of protein folding rates (Alm and Baker 1999, Galzitskaya and Finkelstein 1999; Munoz and Eaton 1999; Plaxco et al. 1998). Another boom for the field of protein folding has come from the realization that misfolding and aggregation (Jaenicke and Seckler 1997) of many proteins—for years disregarded as an irrelevant side reaction—are of great medical relevance and a probable cause of a wide range of diseases, especially neurodegenerative disorders (Dobson 2003) such as Alzheimer’s, Parkinson’s, or Huntington’s disease.

Common to protein folding and misfolding is the large degree of structural or conformational heterogeneity, both during structure formation and, particularly in the case of aggregates, in the final structures. In many cases, obtaining a detailed structural understanding of the processes involved is difficult or even impossible with classical methods investigating large ensembles of molecules. Therefore, it is a promising new opportunity in the search for a more fundamental understanding of protein folding to turn to the study of individual molecules, with the ultimate goal of identifying the distributions of microscopic pathways an unfolded protein can take to its final state, be it correctly or incorrectly folded.

### 8.3 Single-Molecule Spectroscopy

Several different modalities of fluorescence spectroscopy have been used for the study of folding of individual protein molecules, although this field has been dominated by Förster resonance energy transfer (FRET), which is due to the ability of this technique to provide structure-related information in the form of intramolecular distances. We start by briefly discussing the more common fluorescence techniques as they are applied to single-molecule spectroscopy.

The simplest observable in fluorescence spectroscopy is the emission intensity. The time-dependence of the intensity can yield important information about biomolecular dynamics. As an example note the work of Xie and coworkers, in which an enzymatic cycle was probed by following changes in fluorescence intensity of a fluorescent flavin cofactor (Lu et al. 1998). Another example is the blinking of fluorescent proteins, which is a manifestation of the complex photophysics of their intrinsic chromophore (Dickson et al. 1997; Garcia-Parajo et al. 2000). Intensity fluctuations mirror changes in the quantum yield of a fluorophore, which can sometimes be obtained more accurately from measurements of fluorescence lifetimes (Eggeling et al. 2001). Such fluctuations can be due to intermittent quenching through interaction with another molecule, and can therefore be used to measure the time scales of chain dynamics (Buscaglia et al. 2003; Neuweiler et al. 2005). Another manifestation of the time-varying interaction of a fluorophore with its environment is spectral fluctuations (Wazawa et al. 2000).

The reorientational motion of a fluorophore is one of the richest sources of dynamic information, and it can be followed using fluorescence polarization techniques (Forkey et al. 2000; Ha et al. 1999). By modulating the polarization of the excitation light, splitting the emitted light into two polarization components or a combination of the two, one can obtain accurate information about the orientation of an individual fluorophore. A particularly illuminating example is provided by the recent study of Goldman and coworkers, in which a special bidentate fluorophore was rigidly attached to the protein myosin V, and its three-dimensional orientation was followed in time to show switching between two conformations during translational jumps on actin (Forkey et al. 2003). Polarization spectroscopy can also be performed on diffusing molecules, using either CW (Boukobza et al. 2001) or pulsed excitation (Schaffer et al. 1999), and information about the rotational freedom of a fluorophore attached to a biomolecule can be obtained. This information might be important for the evaluation of FRET data.

Because, as noted above, FRET has been a dominant modality in the single-molecule field, we discuss here in some detail its essentials and how it is applied (a more general review of the modern application of FRET in biophysics can be found in Selvin (2000)). The usefulness of this method stems from the fact that it enables measuring distances within a macromolecule. FRET spectroscopy thus projects all the dynamics of a biomolecule onto a single distance coordinate. FRET was discovered in 1948 by Förster (1948), who showed that the interaction between the transition dipoles of two molecules, a donor and an acceptor, can lead to an efficient transfer of excitation energy from one molecule to the other. Using Fermi's golden rule he showed that the rate of energy transfer could be written in the form

$$k_{ET} = \frac{1}{\tau} \left( \frac{R_0}{R} \right)^6,$$

where  $\tau$  is the fluorescence lifetime of the donor molecule,  $R$  is the distance between the two molecules, and  $R_0$ , the "Förster distance," is a constant (given in Å) which depends on their spectral characteristics in the following way.



$$R_0^6 = (8.79 \times 10^{23}) \kappa^2 n^{-4} Q_D \int d\lambda \lambda^4 F_D(\lambda) A_A(\lambda)$$

In this expression  $F_D(\lambda)$  is the normalized emission spectrum of the donor as a function of the wavelength  $\lambda$ , and  $A_A(\lambda)$  is the absorption spectrum of the acceptor.  $Q_D$  is the fluorescence quantum yield of the donor.  $\kappa^2$  is the so-called orientational factor, which depends on the relative orientation of the donor and acceptor transition dipole moments, and may take any value between 0 and 4, and  $n$  is the refractive index of the medium.

The strong dependence on distance makes FRET an optimal method to determine intramolecular distances in biological molecules (Stryer 1978). The useful range for FRET with the dyes that are typically being used for single molecule experiments is 20–100 Å. An accurate determination of the Förster distance for a particular donor–acceptor pair is required in order to enable distance measurements, and the largest uncertainty is due to the difficulty in estimating the orientational factor. It can be shown though that if the donor and acceptor reorient on a time scale faster than the donor lifetime, an averaged value of 2/3 can be used (van der Meer 1999). This averaged value is broadly used in the literature, although its application has to be justified in each case separately, as it depends crucially on the freedom of motion of the two fluorescent molecules. Schemes have been developed that allow putting limits on the possible error arising from the use of the averaged in cases where the orientational motion of the donor and acceptor is limited. These schemes rely on the values of the fluorescence anisotropy of the fluorophores. The interested reader is referred to the original literature (Dale et al. 1979; Haas et al. 1978).

$k_{ET}$  can be determined in a time-resolved fluorescence experiment by measuring the change in the donor lifetime. Under steady-state illumination conditions one measures the FRET efficiency:

$$E_{ET} = \frac{R_0^6}{R^6 + R_0^6}$$

which can be obtained from the reduction in donor fluorescence intensity in the presence of the acceptor, from the increase in acceptor fluorescence intensity in the presence of the donor or best, by taking into account both intensities in the following manner,

$$E_{ET} = \frac{I_A}{I_A + I_D}$$

where  $I_A$  and  $I_D$  are the donor and acceptor intensities. This expression must be corrected for differences in donor and acceptor quantum yields, cross-talk between the detection channels, and direct acceptor excitation, as well as differences in the detection efficiencies at the respective wavelengths (Ha et al. 1999; Jia et al. 1999).

If the distance between donor and acceptor fluctuates, for example, due to conformational dynamics in a large biomolecule, an analysis of the type described above provides only the average FRET efficiency in ensemble experiments. Haas

and coworkers devised a method to obtain a parameterized distance distribution from time-resolved fluorescence experiments (Haas et al. 1975). This method has been extensively applied to study intramolecular dynamics, including protein folding (Haas 1996; Ratner et al. 2000).

Single-molecule experiments provide a more direct way to obtain the FRET efficiency distribution. The FRET efficiency can be calculated from each burst in a diffusion experiment or from each point in a single-molecule trajectory obtained from an immobilized molecule. A histogram is then constructed from the series of values obtained in this way. Based on some knowledge on the dynamics of the system, it is possible to invert the histogram and construct a distance distribution (Gopich and Szabo 2003). In particular, if the dynamics of the system are slow on the observation time scale, one can calculate the distance directly from each FRET efficiency value, and create the distance histogram in that way. Broadening of this distribution can be caused by static or dynamic variations in the donor–acceptor distance, which in turn can be related to structural and functional properties of a biomolecule under study. However, several other factors contribute to the width of this distribution, including photon shot noise (Gopich and Szabo 2005), slow reorientational dynamics of the probes, and conformation-dependent quantum efficiencies.

The problem of specific chemical labeling of a biomolecule with two fluorescent probes does not have a universal solution. This problem is simplified in the case of nucleic acids, because separate oligonucleotide chains can be labeled and then hybridized (Deniz et al. 1999). Techniques of a similar spirit can be devised for proteins as well, especially if they are not too large. For example, Jia et al. (1999) synthesized and labeled separately the two helices of the GCN4 peptide they used in their single-molecule folding study, then ligated them together with a disulfide bond. In fact, peptide synthesis offers several options for the simplification of double labeling scheme (Bark and Hahn 2000; Deniz et al. 2000). Such techniques cannot be applied to larger proteins that cannot be chemically synthesized.

Haas and coworkers have devised a multistep process for specific labeling with two fluorophores (Ratner et al. 2002), and have applied this process over the years to several different proteins (Amir and Haas 1987; Haran et al. 1992; Ratner et al. 2000; Sinev et al. 1996). Their process relies on a careful application of chemical separation techniques to first prepare populations of protein molecules which are specifically labeled with a fluorophore at a unique position on the protein, typically a cysteine residue (Ratner et al. 2002). In a subsequent step a second residue is labeled with the different fluorophore. In some cases this general method can be simplified by the use of an *N*-terminal cysteine residue which can be labeled very specifically with a thioester-containing fluorescent probe (Schuler and Pannell 2002).

It should be noted that proteins can also be labeled with genetically encoded fluorophores, that is, fluorescent proteins (Guerrero and Isacoff 2001). A FRET pair can be obtained by attaching two different fluorescent proteins to the same biomolecule (Brasselet et al. 2000). However, this approach does not seem to be universally useful for folding studies, not only because of the large size of the probes, but also because they might be severely affected by the denaturing or partially denaturing conditions of such experiments. Another new type of fluorescent markers, semiconductor

nanocrystals (Chan et al. 2002), already begin to find application in single biomolecule spectroscopy, especially due to their high photostability.

### 8.3.1 *Free Diffusion Experiments*

Studying individual molecules diffusing freely in solution is convenient, as it allows measuring a variety of molecular properties (some of which were mentioned above), and changing solution conditions quickly. Furthermore, and most important, this method minimizes perturbations from surface interactions, although the observation time is limited by the diffusion times of the molecules through the confocal volume. Typically, every molecule is observed for no more than a few milliseconds.

In the most common type of single-molecule spectrometer (Böhmer and Enderlein 2003; Ha 2001; Michalet et al. 2003) a laser is focused into a dilute solution of the freely diffusing molecule of interest. A confocal optical setup is used in order to limit the observation volume in a liquid sample to  $<1 \mu\text{m}^3$ . This is achieved by inserting a pinhole in the image plane of the microscope, which efficiently rejects out-of-focus light (Pawley 1995). If the concentration of fluorescing molecules is kept in the picomolar range, the probability of having more than one molecule in the focal volume of the laser beam is negligible. When a molecule traverses the beam, a burst of photons is emitted. A single-photon counter detects this burst of photons. Detection is typically done with single-photon-counting avalanche photodiodes, as these devices show a high quantum yield, as well as fast temporal response. The number of photons detected during a single burst (i.e., a single pass of a molecule through the laser beam) depends on several factors. The most important of these is the dwell time, which is the overall time it takes a molecule to cross the illuminated region. The dwell time is distributed exponentially (Ko et al. 1997), and for a typical confocal setup, its average value is of the order of a millisecond. The laser power used and the photophysics of the molecule will also affect the number of photons collected, but typically several tens of photons are detected. A thorough analysis of the statistics of fluorescence bursts can be found in Enderlein et al. (1997) and references therein.

There are two possible ways to collect photons in this experiment. First, the photons can be binned during data acquisition into time bins with predefined widths, using a multichannel scaler or a similar device. In this case a photon burst is discriminated from the background by setting a certain threshold, which is defined according to the statistics of the measurement. A second option is to measure the relative arrival time of photons at the detector (Fries et al. 1998). A trajectory of arrival times is then obtained, and the passage of a molecule through the beam is marked by a sharp reduction in the time lag between photons. The advantage of this method is that it makes use of the full time resolution of the detectors, a factor which might be important, for example, if one would like to calculate correlation functions from the data.

Several modifications are possible that make the type of experiment described above even more informative. First, a pulsed source of excitation can be used in

place of a CW source, allowing for the time delay between a pulse and the arrival of an emitted photon at the detector to be measured. This type of experiment is called time-correlated single photon counting. By constructing histograms of photon delay times one can obtain the fluorescence lifetime. Seidel and coworkers showed that this method can be combined with measurements on diffusing molecules and that the fluorescence lifetime of a single molecule can be obtained from as few as 100 photons (Eggeling et al. 2001).

Another modification of the free diffusion experiment is achieved by flowing molecules in capillaries (Dorre et al. 2001), or in the channels of microfluidic devices (Effenhauser et al. 1997). Flowing can improve the sampling rate of single molecules in solution. Furthermore, devices that quickly mix two solutions can be constructed (Knight et al. 1998), thereby opening the way to nonequilibrium experiments. Such devices have been used for ultrarapid (submillisecond) ensemble folding experiments (Pollack et al. 2001), and recently also for single-molecule folding studies (Lipman et al. 2003). Finally, the dwell time of diffusing molecules in the beam can be increased, either by using viscogenic agents to slow down the diffusion, or by actually immobilizing the molecules on a surface. The spectroscopy of immobilized molecules is discussed in the next section.

Two typical methods for analysis of signals from freely diffusing individual molecules are described here. First, in the case of a two-color FRET experiment, fluorescence emission of donor and acceptor dyes is collected separately. Intermittent photon bursts, corresponding to individual molecules diffusing through the confocal volume, are identified using a suitable combination of thresholds. From each burst, the FRET efficiency is calculated as discussed above after background subtraction, and entered into a histogram. Typically, several thousand bursts are used to obtain reliable statistics. A histogram of FRET efficiencies is then constructed. Some of the observables that can be extracted from such a histogram are discussed in connection with particular experiments below.

More generally, the correlation function of the fluctuating fluorescence signal can be calculated. This method is known as fluorescence correlation spectroscopy (FCS; Eigen and Rigler 1994; Hess et al. 2002). The correlation function contains information about the diffusion time of molecules through the laser beam ( $\sim 100 \mu\text{s}$  under regular solution conditions), as well as about any fast intramolecular dynamic processes that modify the intensity of fluorescence (on the nanosecond to microsecond time scales). An analytical form can be derived for the correlation function and fitted to the experimental curve. In the case of a single intramolecular kinetic process, such as folding, where one state is fluorescent and the other is not, the normalized fluorescence correlation function for a Gaussian volume element is of the following form.

$$G(t) = \frac{1}{N} \cdot \left(1 + \frac{t}{\tau_d}\right)^{-1} \cdot \left(1 + \frac{t}{\omega^2 \tau_d}\right)^{-1/2} \cdot (1 + K \exp(-t / \tau_r)),$$

where  $N$  is the average number of fluorescent molecules in the confocal spot,  $\tau_d$  is the diffusion time of a molecule across the observed volume,  $\omega$  is a parameter that

characterizes the shape asymmetry of the laser focus, and  $K$  and  $\tau_r$  are the equilibrium constant and overall relaxation time of the kinetic process (Krichevsky and Bonnet 2002). For two-state folding, for example,  $K = k_{\text{folding}}/k_{\text{unfolding}}$ , and  $\tau_r = 1/(k_{\text{folding}} + k_{\text{unfolding}})$ , with  $k_{\text{folding}}$  and  $k_{\text{unfolding}}$  the rates for folding and unfolding, respectively.

### 8.3.2 Experiments on Immobilized Proteins

The study of molecules immobilized near a surface offers some unique advantages. Most important, the time-dependent behavior of each molecule can be tracked for a long time, from seconds to many minutes, under equilibrium or nonequilibrium conditions. In addition, immobilized molecules can in principle be manipulated using external force (an issue outside the premises of the current review). Many techniques have been devised in order to bind macromolecules on surfaces, single-molecule experiments being only one of many incentives for their developments. Here we discuss some of those techniques that have been employed to study biomolecular dynamics.

Biomolecules tend to adsorb passively to surfaces typically used in the laboratory, such as glass. This adsorption is based on short-range van der Waals forces or longer range electrostatic interactions between a molecule and the surface (Safran 2003). Although passive adsorption provides the simplest means to prepare a sample for single-molecule spectroscopy, it does not allow for control of the orientation of an adsorbed molecule. Furthermore, in some cases the interaction of a macromolecule with the surface can lead to partial denaturation, possibly through stabilization of intermediate structures that expose hydrophobic surfaces (Engel et al. 2004; Talaga et al. 2000).

In cases where the orientation of the molecule on the surface is important, it is possible to use specific tethering methods to control the way a biomolecule is attached to the surface. A simple, but elegant, method is based on the introduction of a sequence of charged residues into the molecule, and makes use of the specific electrostatic interactions between that segment and a treated surface to bind the molecule in a defined orientation. Jia et al. (1999) used such a technique to attach a polypeptide to a glass surface. The peptide was constructed with a patch of negatively charged amino acids, allowing for its specific adsorption to a positively charged amino-silane treated surface. It is also possible to covalently attach a macromolecule to a surface using a linker with a functional group. A common technique for the introduction of linkers onto a surface is the preparation of a self-assembled monolayer or a similar structure on the surface (Wink et al. 1997). Bonding of the functional group to a macromolecule is then achieved by flowing in the macromolecule in the presence of a chemical coupler. For example, a self-assembled monolayer with carboxy groups on the surface can be used to immobilize proteins by forming a peptide bond between these groups and amino side chains of the protein (Johnsson et al. 1991). This and similar techniques are used extensively in the context of surface plasmon resonance spectroscopy (McDonnell 2001) and quartz crystal microbalance sensing (Wegener et al. 2001) of biomolecular interactions.

Biotin–avidin chemistry has also been employed to attach biomolecules specifically to surfaces (Turkova 1999). This method relies on the extremely strong interaction between biotin and the proteins avidin or streptavidin. A biotin moiety is introduced onto the surface of the macromolecule that needs to be immobilized. A ‘sandwich’ structure is formed by preparing a biotinylated surface, covering it with avidin molecules, and finally attaching biotinylated macromolecules to the avidin.

Another useful approach is to employ the strong interaction between nickel ions and multihistidine sequences in proteins. This interaction is commonly used in protein purification protocols; a tail including 6–10 histidine residues is introduced into the amino-terminus of a protein, and the protein is then purified on an affinity column containing nickel ions. The same method can be used to immobilize protein molecules on nickelated surfaces. Single-molecule studies of rotational motion of the protein  $F_1$ -ATPase have utilized this technique (Noji et al. 1997).

A completely different approach involves trapping of biomolecules within the pores of gels or glasses (Figure 8.3C). A thin layer of a gel, with fluorescent molecules already incorporated, can be prepared on a surface (Chirico et al. 2002; Dickson et al. 1996; Lu et al. 1998; Mei et al. 2003). An advantage of gels is that they usually contain a large fraction of water, thus providing a suitably hydrating environment to molecules trapped within them. Furthermore, the size of the pores in these gels can in principle be engineered to match the size of the trapped proteins. The compatibility of gels with biomolecules was demonstrated nicely in a study on green fluorescent protein (GFP) molecules trapped in a silica gel, which were found to rotate in a similar fashion to their rotation in free solution, even as their translational motion was essentially frozen (Chirico et al. 2002).

Although the above methods can provide suitable means for immobilizing biomolecules for functional studies on the single-molecule level, some care should be exerted in applying them to folding studies. The main difficulty arises from surface interactions of partially unfolded states of a macromolecule. Such interactions can significantly modify the energy landscape of a protein (Engel et al. 2004; Talaga et al. 2000). In fact, even the pure entropic effect of confinement in a cavity on the thermodynamics and kinetics of folding can be significant (Eggers and Valentine 2001; Klimov et al. 2002). Interestingly, RNA molecules seem to suffer less from this problem, and their adsorption on a surface does not change their properties significantly (Zhuang et al. 2000).

An immobilization method that might overcome this difficulty was recently developed (Boukobza et al. 2001). The method is based on the trapping of single protein molecules within 100 nm lipid vesicles prepared by extrusion and tethered to glass using biotin-avidin chemistry (Figure 8.2). The large size of the vesicles compared to a protein allows ample volume for free rotational motion. This has been shown using a single-molecule fluorescence polarization technique (Boukobza et al. 2001). Furthermore, single-molecule measurements of the FRET efficiency distributions of labeled molecules of the proteins adenylate kinase (Rhoades et al. 2003) and the cold shock protein (Rhoades et al. 2004) under native and fully denatured conditions showed that these distributions are consistent with ensemble measurements, and so the influence of the vesicles on the energy landscape of

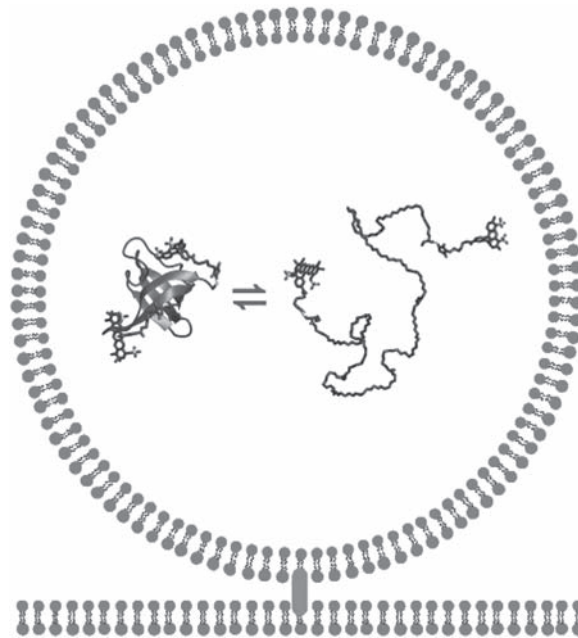


**Figure 8.2** Trapping within the water compartment of a surface-tethered lipid vesicle is a useful technique for studying protein folding on the single-molecule level, inasmuch as it allows minimal interference with the conformational equilibrium and dynamics of a protein molecule. The size of the vesicle ( $\sim 100$  nm) is selected to be much larger than a typical trapped protein, but much smaller than the diffraction-limited laser beam used for excitation

the protein is probably minimal (see more in Section 8.4.2). The vesicle encapsulation method was also used recently to study the folding of RNA molecules (Okumus et al. 2004).

Adsorption of proteins on surfaces densely covered with polyethylene glycol molecules was also shown to enable folding studies with minimal perturbation. Indeed, individual RNaseH molecules withstood many cycles of chemical unfolding and refolding on such surfaces (Groll et al. 2004).

Two basic microscopy methods are used for studying individual immobilized molecules. The first technique is a variant of confocal microscopy in which the molecules are not diffusing in solution but are attached on a glass surface. Typically, the surface is scanned in order to identify fluorescent molecules. Photons are collected from each molecule until it photobleaches. As above, avalanche photodiodes are used as detectors. Typically, a single molecule emits  $\sim 1$  million photons before photobleaching, out of which up to 10% can be detected. Again, the detected photons can be binned on-the-fly or else their arrival times at the detector can be recorded (Kim et al. 2002). Xie and coworkers have recently elaborated the methodology for analysis of photon arrival trajectories and showed how correlation

functions can be used to significantly improve the time-resolution of single-molecule experiments (Yang and Xie 2002a,b).

The second technique is total internal reflection fluorescence microscopy (Axelrod 1989; TIRFM). A laser beam is totally reflected at the interface between glass and the water comprising the sample, and an evanescent wave is formed within the sample. The excitation light is introduced either through a prism (Conibear and Bagshaw 2000) or through the objective (Tokunaga et al. 1997). Specialized objectives with numerical apertures of 1.45 and 1.65 can be used for the latter configuration. The evanescent wave in TIRFM excites molecules that are either at the surface or within  $\sim 100$  nm of the surface. There are two advantages to this type of illumination. First, if the interaction of a diffusing fluorescent molecule with a molecule adsorbed on the surface is studied, then the fluorescent molecule concentration can be kept rather high without introducing a large background signal (Yamasaki et al. 1999). This advantage is not so important for the typical folding experiment. A second benefit of TIRFM is the ability to illuminate a large area on the surface, even in excess of  $50\mu\text{m}$  in diameter. Thus many adsorbed molecules are illuminated at once. The signals from these molecules can be collected using a CCD camera, and so a large number of trajectories can be obtained in a short time. However, it should be noted that the time resolution of a CCD camera is significantly lower than that of an avalanche photodiode, which limits the experiment to slower events.

The analysis of noisy single-molecule trajectories presents challenges that researchers are only starting to tackle. Some of the pertinent issues were already dealt with in the literature of single ion channel recording (Sakmann and Neher 1995), a technique that has been around for more than 20 years. Here we focus briefly on two aspects of the problem: the reduction of noise in time-dependent trajectories, and the extraction of rate constants from stochastic trajectories.

It is possible to devise several different types of filters that will reduce the noise in trajectories and expose some of the information that might be hidden behind this noise, while causing minimal distortion to the data. The simplest procedure that can be applied is a running-average procedure, in which each data point in the averaged trajectory is represented by the average of  $N$  points preceding it in the original trajectory. A more sophisticated linear filtering procedure, the so-called Wiener filter, was used by Talaga et al. (2000). This filter is applied in Fourier space, and uses knowledge about the power spectrum of the photon noise to optimally filter it out (Press et al. 2003).

Unfortunately, all linear low-pass filters tend to smear and even distort fast jumps in the data. The forward-backward nonlinear filter developed by Chung and Kennedy (1991) was specifically adapted for single-molecule FRET experiments (Haran 2004), and was recently used by Rhoades et al. to analyze single-molecule trajectories (Rhoades et al. 2003). This filter builds on the simple running-average procedure and significantly improves it by generating a set of predictors and adaptively weighting them in a way that ensures that fast jumps in the data are not smeared. An example of the result of operation of this filter on a simulated dataset



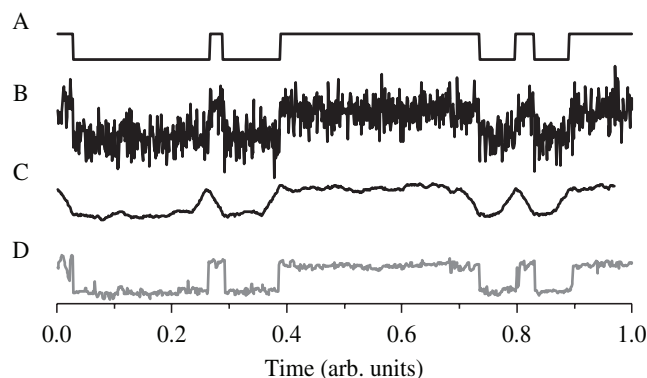


**Figure 8.3** Filtering of a single-molecule trajectory with the nonlinear forward–backward filter. **(A)** Simulated data showing stochastic transitions between two states. **(B)** The same data with added noise. **(C)** A running-average filter can reduce the noise significantly but it also distorts the rising and falling edges of the transitions. **(D)** The adaptive nonlinear filter recovers the original data without distorting sharp transitions. (Reprinted from Haran (2004), with permission)

is given in Figure 8.3. It is seen that the filter reconstructs the data out of the noise in a way that allows clear identification of transitions.

Other methods to expose data under noise have been suggested. Talaga and coworkers introduced methods built on hidden Markov techniques, allowing them to test kinetic models directly on the photon data, without any pretreatment (Andrec et al. 2003). Watkins and Yang (2004) used information theory to develop an algorithm for optimal analysis of single-molecule data. This algorithm identifies the minimal number of photons required to compute a certain physical property (such as FRET or electron transfer efficiency), thus extracting the maximal information from the experimental data.

A detailed analysis of conformational fluctuations in single-molecule folding trajectories requires a model to describe the underlying dynamics. One way to describe single-molecule dynamics relies on partitioning of the molecular conformational space into discrete states, with rate constants that describe the transitions between them. The problem then reduces to the evaluation of these rate constants from stochastic trajectories. If the various states can be clearly delineated in each trajectory, which is the situation when transition rates between states are slow compared to the time resolution of the experiment, then the evaluation of the rate constants can be done using histograms of dwell times in the various states (see, e.g., Lu et al. (1998)), or by computing certain statistical moments from the trajectories (Berezhkovskii et al. 2001; Boguna et al. 2001; Gopich and Szabo 2003a). More generally, rate constants can be evaluated by computing correlation functions of the experimental signals (Yang and Xie 2002a; Yang and Cao 2001), a method akin to the established fluorescence correlation spectroscopy (Eigen and Rigler 1994; Hess et al. 2002).

## 8.4 Single-Molecule Protein Folding

### 8.4.1 *Studies on Freely Diffusing Protein Molecules*

#### 8.4.1.1 Chymotrypsin Inhibitor 2

Deniz et al.(2000) pioneered the investigation of freely diffusing single protein molecules with their study of the protein chymotrypsin inhibitor 2 (CI-2), a two-state folder well characterized by ensemble techniques (Jackson and Fersht 1991). Molecules of CI-2 were made from two peptides that corresponded to the N- and C-terminal parts of the protein, respectively, which were prepared using solid-phase peptide synthesis methodology and subsequent native chemical ligation. This technique facilitated specific labeling of the protein with tetramethylrhodamine as the donor molecule and Cy5 as the acceptor. FRET efficiency distributions were obtained at a range of denaturant concentrations. The distributions nicely showed two subpopulations, one corresponding to the native conformation and one to the unfolded one (Figure 8.4). Properties of the subpopulations were analyzed to extract an unfolding curve, as well as a possible small expansion in the unfolded state as a function of increasing denaturant.

#### 8.4.1.2 Cold Shock Protein

A protein extensively studied with optical single-molecule methods is the cold shock protein from the hyperthermophilic bacterium *Thermotoga maritima* (CspTm). It forms a simple five-stranded beta barrel structure, and by all criteria investigated to date it behaves as a perfect two-state folding system (Perl et al. 1998; Schuler et al. 2002a; Wassenberg et al. 1999). For single-molecule studies, the protein sequence was modified using site-directed mutagenesis, expressed with two cysteine residues close to the termini and labeled with maleimide derivatives of the Alexa Fluors 488 and 594 as donor and acceptor, respectively (Schuler et al. 2002b).

From transfer efficiency histograms measured at different concentrations of the denaturant guanidinium chloride (GdmCl), it was obvious that the mean transfer efficiency of the subpopulation of unfolded proteins shows a clear shifting of the peak with decreasing GdmCl concentration, whereas the mean efficiency of folded molecules remained constant (Figure 8.5). In order to account for possible effects of the solvent on the photophysics or photochemistry of the fluorophores, the same denaturant dependence was analyzed with a control molecule, an icosaproline peptide labeled with the same dyes as the protein. In this case, only a very slight shift of the efficiency peak was observed, which can be accounted for by the change in refractive index of the solution. Consequently, the much larger decrease in transfer efficiency observed for unfolded CspTm molecules at low GdmCl concentrations corresponds to a real distance change: a collapse in response to the change in solvent conditions. Collapsed CspTm only becomes noticeable under conditions where the

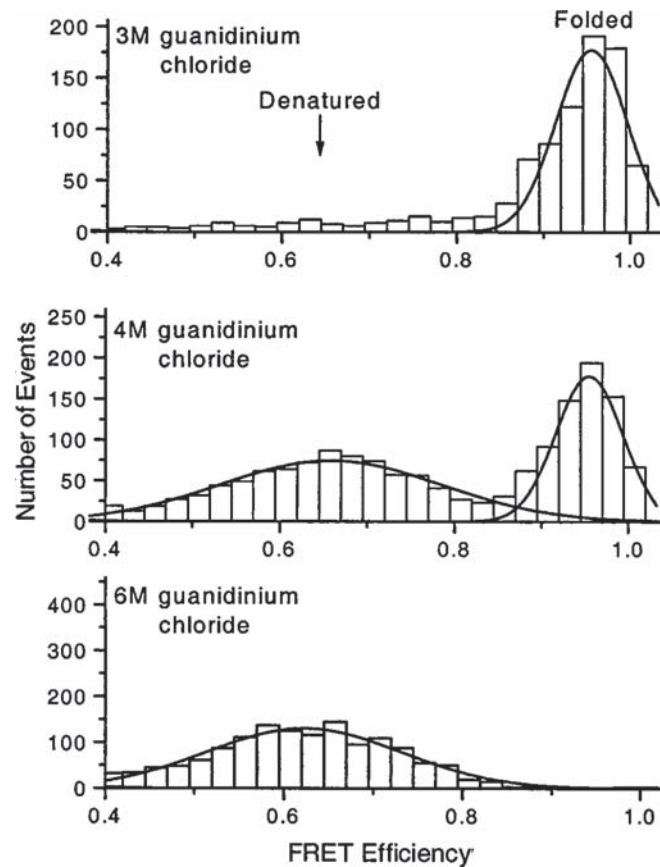


**Figure 8.4** FRET histograms of the small protein CI2 at different denaturant concentrations obtained from confocal single molecule experiments. Note that folded and unfolded molecules can be clearly separated even close to the midpoint of unfolding (middle panel). (Reprinted from Deniz et al. (2000), with permission)

large majority of molecules are folded, and therefore it could not be observed in a corresponding equilibrium ensemble experiment. The strength of the single-molecule approach is that the subpopulations can be separated, and investigated independently.

A shortcoming of the equilibrium experiment is that due to the small population of unfolded molecules at low denaturant concentrations, their mean transfer efficiency cannot be determined with high accuracy over the entire concentration range. A way to solve this problem is the transient population of the unfolded state in a kinetic experiment. In view of the optical requirements of confocal detection, microfluidic mixing devices (Kauffmann et al. 2001; Knight et al. 1998) provide an ideal technical solution to this problem (Lipman et al. 2003). The confocal volume is positioned downstream of the mixing region at distances chosen to correspond,

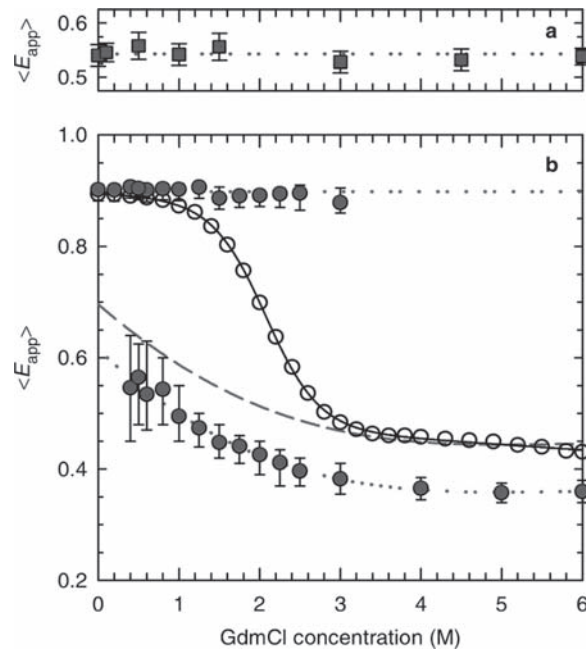


**Figure 8.5** Dependence of the means of the measured FRET efficiency  $\langle E_{app} \rangle$  on the concentration of GdmCl (a) for Pro<sub>20</sub> and (b) for CspTm. Single-molecule mean values (filled circles), ensemble FRET efficiencies (open circles), and associated two-state fit (unbroken curve) for CspTm are given. The increase of the transfer efficiency at low GdmCl concentrations corresponds to a collapse of unfolded molecules. (Reprinted from Schuler et al. (2002b), with permission)

via the flow rate, to the desired delays following mixing (Figure 8.6). Data are acquired analogous to equilibrium experiments on freely diffusing molecules, and transfer efficiency histograms are accumulated at different times after mixing.

After initiation of the reaction, a redistribution of the populations is observed with time (Figure 8.6). The positions of the peaks, however, remain constant, indicating that the average end-to-end distances of the molecules in the subpopulations do not change during the course of the reaction. The lower denaturant concentration after dilution results in more compact unfolded molecules, which are populated within 50 ms (the dead time of the mixer) and exhibit higher FRET efficiencies (Lipman et al. 2003). It is noteworthy that qualitatively different signal changes result from collapse and folding. Collapse of the unfolded state causes a shift of the corresponding peak to higher efficiency, whereas folding increases the folded state population (as measured by peak area) and depopulates the unfolded state. In an ensemble FRET experiment, both collapse and folding would result in an overall increase of the transfer efficiency, and the respective contributions could be identified only indirectly by kinetic modeling. It remains to be established whether this

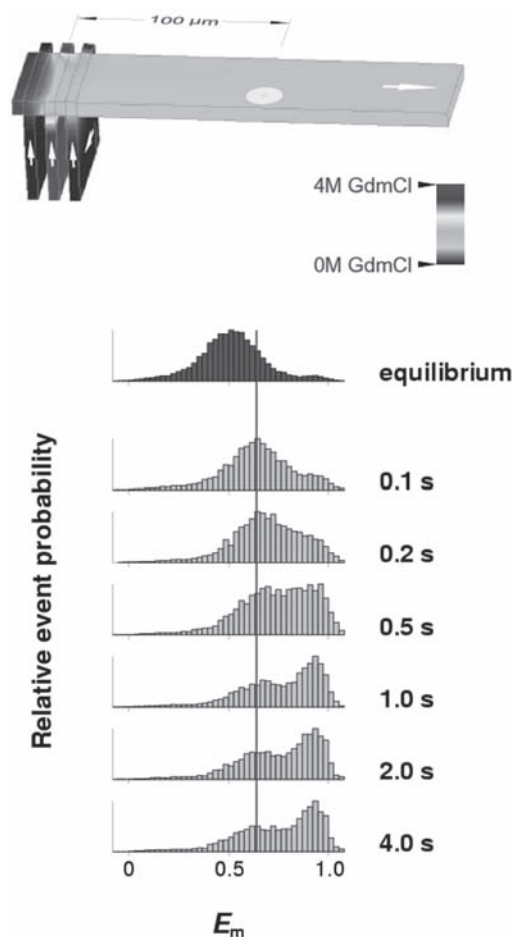


**Figure 8.6** Protein folding kinetics studied by microfluidic mixing. (a) Schematic of the mixing area, with the three inlet channels coming in from the bottom. Calculated GdmCl concentrations are indicated on a colour scale. The  $1/e^2$  intensity contour of the laser beam is illustrated along with the cone of fluorescence emission collected by the microscope objective (light circle). (b) Histograms of measured FRET efficiencies before (topmost panel) and at different distances downstream of the mixing area, corresponding to different times after mixing. The vertical red line indicates the mean FRET efficiency value in the unfolded state after mixing. (Reprinted from Lipman et al. (2003), with permission)

reaction is merely a nonspecific heteropolymer collapse in response to altered solvent conditions or whether specific parts of the polypeptide chain become structured under native conditions prior to the actual folding process. The transient population of unfolded molecules under native conditions additionally allows a more accurate determination of their mean FRET efficiencies at low denaturant concentrations (Lipman et al. 2003), taking us closer to the physiologically relevant conditions, that is, in the absence of denaturants.

Equilibrium single-molecule experiments provide the opportunity to obtain information on protein dynamics, particularly those of the unfolded state, from the width of the transfer efficiency histograms (Chattopadhyay et al. 2005; Gopich and Szabo 2003b; Schuler et al. 2002b). However, as outlined above, the issue is complicated by the fact that even for a molecule with a single fixed distance or very rapid conformational averaging, the experimental FRET efficiency histogram does not resemble a delta function. Therefore, polyproline peptides, which have a narrow end-to-end distance distribution due to their large persistence length, were used as a reference (Schuler et al. 2002b, 2005). Similar results were obtained with labeled double-stranded DNA (B. Schuler, unpublished observation). The conformational dynamics in the unfolded state are closely related to the maximum rate at which the protein could fold in the absence of an activation barrier, the protein folding “speed limit,” and could therefore be used to obtain an estimate for the elusive pre-exponential factor in a description of protein folding kinetics using reaction rate theory (Portman et al. 2001).

#### 8.4.1.3 FynSH3 Domain

Due to the relatively large distances that can be probed with Förster transfer, it is an ideal method to study the unfolded state at high concentrations of denaturant, which is usually assumed to be devoid of persistent regular structure. Using small angle X-ray scattering (SAXS), the radius of gyration of proteins unfolded in 6 M GdmCl has been shown to exhibit the length scaling expected for a random coil over a large range of molecular weights (Kohn et al. 2004). To probe whether the same scaling law is found for residue-to-residue separations within a denatured polypeptide chain, McCarney et al. (2005) placed Alexa 488 and Alexa 594 as donor and acceptor chromophores, respectively, at a series of positions within the FynSH3 domain and determined the transfer efficiencies between five residue pairs within the protein. By and large, they found the length dependence of the transfer efficiency expected for a random coil, but some site-specific deviations are suggestive of residual structure. This might be another indication that random coil behavior of unfolded polypeptide chains in the sense of polymer physics does not necessarily require truly random structure (McCarney et al. 2005). This conclusion is corroborated by another interesting observation of McCarney and colleagues: in trifluoroethanol, a denaturant known to induce helical structure, the dimensions of the unfolded state are essentially identical to those in GdmCl (McCarney et al. 2005).

This work illustrates an important point concerning the current state of single molecule spectroscopy. Some experiments that could in principle be done with ensemble methods are now more accurately and reliably done with single-molecule spectroscopy, which allows molecules lacking an active acceptor chromophore to be excluded from the analysis (and thus simplifies labeling and sample purification, but also reveals possible complications from photochemistry), and is able to detect heterogeneity of the sample through the separation of subpopulations.

#### 8.4.1.4 Calmodulin

The equilibrium folding of Calmodulin, a  $\text{Ca}^{2+}$ -binding two-domain protein, was recently investigated in free diffusion experiments (Slaughter et al. 2005). Positions 34 and 110 were labeled via Cysteine residues with Alexa 488 and Texas Red, respectively, and unfolding of calmodulin was followed with increasing concentrations of urea. Previous ensemble studies had indicated the existence of populated folding intermediates (Masino et al. 2000; Sorensen and Shea 1998). This conclusion is consistent with the single-molecule experiments of Slaughter et al. (2005), who found their apparent distance distributions obtained from single-molecule transfer efficiency measurements to be in agreement with either a three-state model involving a folding intermediate or an unfolded state continuously expanding with increasing denaturant concentration. In view of the evidence for unfolded state expansion in experiments on two-state folders (Kuzmenkina et al. 2005; Schuler et al. 2002), the inference of a third state seems somewhat ambiguous based on the single molecule data (Slaughter et al. 2005) alone, but with the background of other data, it is the interpretation suggested by the authors.

In this context, we would like to stress that calculating distance distributions directly from a burstwise analysis of free diffusion experiments requires detailed information about the dynamics of the system. As shown by Gopich and Szabo (2003b, 2005), the observation time must be approximately an order of magnitude smaller than the relaxation time of the donor–acceptor distance to obtain physically meaningful distance distributions or corresponding potentials of mean force. Otherwise, only the mean value of the transfer efficiency of the respective subpopulation can be used to get information about the distance distribution, and an independent model of the distance distribution is needed. In practice, this means that distance distributions can be determined from typical free diffusion experiments on proteins only if the underlying dynamics are on a time scale greater than about 10 ms. A noticeable influence of dynamics on the width, however, is already expected for fluctuations in the 10 to 100  $\mu\text{s}$  time scale (Gopich and Szabo 2003b, Schuler et al. 2002b).

#### 8.4.1.5 Fluorescence Correlation Spectroscopy of Fast Dynamics

FCS has recently been shown to be a useful tool for probing folding-related dynamics. Frieden and coworkers used FCS to study the dynamics of the denatured state of the intestinal fatty acid binding protein (Chattopadhyay et al. 2005). This 131 amino-acid protein was labeled with two tetramethylrhodamine chromophores 48 residues apart from each other. In the denatured state these probes could transiently meet and self-quench, however, this quenching reaction was missing in the folded state. Indeed, a fast exponential component in the correlation function was shown to grow in as the protein was denatured further and further. At 3 M GdmHCl the relaxation time extracted from the fast component was 1.6  $\mu\text{s}$ . The authors noted that this time is significantly longer than predicted from the dynamics of Gaussian chain, suggesting that conformational mobility of the protein is retarded at 3 M

GdmHCl compared to a random coil. It is possible, however, that the measured relaxation time is also influenced by the quenching reaction itself, whose contribution was not assessed by the authors.

Neuweiler et al. (2005) used a similar technique to study the dynamics of a 20 amino-acid polypeptide, the Trp-cage. Here the quencher was a tryptophan residue, and the chromophore molecule was MR121, a nice probe for FCS because it does not show a contribution from intersystem crossing, the involvement of which might mar the interpretation of fast dynamics. The fluorescence correlation curve of the polypeptide exhibits a temperature-dependent relaxation component on the microsecond time scale, which is ascribed to the folding reaction (Figure 8.7). A shorter fragment, as well as a control peptide, presents only a faster, nanosecond-time relaxation component, which is missing in the full protein and is assigned to dynamics in the fully unfolded state. Further analysis suggests that the inability to observe a fast component in the full protein is due to an intermediate, molten globulelike state, which is the only denatured state that can be seen under the conditions of the experiment. In this intermediate the quenching by tryptophan is so efficient that it occurs on time scales too fast to be accessed by FCS. Indeed, a single mutation can destabilize this intermediate, leading to the appearance of the nanosecond relaxation component. FCS thus nicely reveals the hierarchical nature of the folding reaction of the Trp-cage, which was hidden in previous experiments. A complication in this experiment was the complex formation of tryptophan and MR121 in the denatured state, whose dissociation kinetics may influence the fastest time scales investigated.

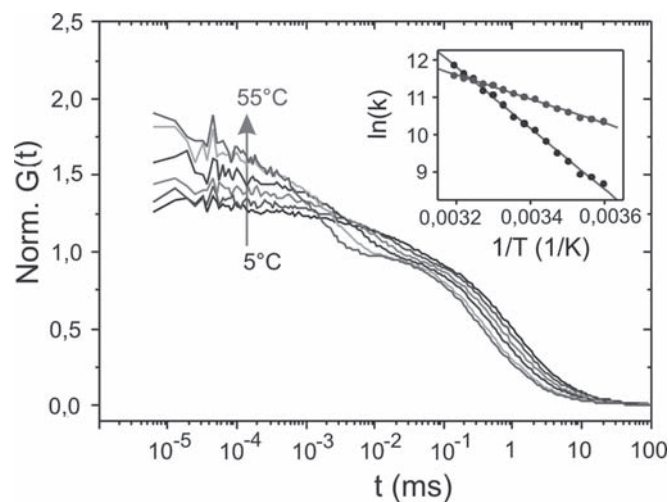


**Figure 8.7** Correlation functions of the protein Trp-cage labeled with a single chromophore, showing a kinetic component at short times that corresponds to the folding dynamics of the peptide. From fits to the correlation functions it is possible to extract the folding and unfolding rates as a function of temperature (inset). (From Neuweiler et al. (2005), with permission)



These two studies demonstrate the power of FCS to probe dynamics on time scales relevant to protein folding. The equilibrium technique therefore competes with nonequilibrium methods that have been developed in the last decade for probing fast protein folding, such as temperature and pressure jump experiments, as well as ultrafast mixing techniques. A fluorescence correlation spectrometer is easier to set up and operate than most of the equipment required for nonequilibrium experiments. A major disadvantage of FCS is that it cannot probe regions of parameter space in which there is a large difference in population between states, because in these cases the kinetic flux that leads to meaningful fluorescence fluctuations vanishes.

## **8.4.2 *Immobilized Protein Molecules***

### **8.4.2.1 GCN4**

Hochstrasser and coworkers (Jia et al. 1999; Talaga et al. 2000) were the first to investigate the folding dynamics of immobilized molecules. They studied a peptide prepared from the yeast transcription factor GCN4, which forms a cooperatively folded helical dimer. A version of the peptide in which the two helices are connected by a disulphide bond was prepared. One of the helices was labeled at its N-terminus with rhodamine 6G as a FRET donor, and the other helix was labeled with Texas Red as a FRET acceptor. The rate of folding of the labeled dimer was measured to be  $150 \text{ sec}^{-1}$ . A negatively charged stretch of amino acids was inserted at the C-terminus of each helix to facilitate oriented attachment to an aminosilanized glass surface. FRET trajectories of single molecules were collected with a confocal microscope. Some of the trajectories showed fluctuations in FRET efficiency, which were attributed to the folding/unfolding dynamics of the dimer. Correlation analysis showed that the time scale of these fluctuations indeed matched the ensemble time scale. However, analysis of FRET efficiency distributions, especially in comparison to similar distributions obtained on freely diffusing molecules, showed that surface attachment significantly affects the distribution. This effect was especially significant at high urea concentration, and the distribution of surface-attached molecules was much broader than the distribution obtained in solution.

### **8.4.2.2 Adenylate Kinase**

A first step towards solving the above-mentioned problem was made by studying protein molecules trapped within surface-tethered lipid vesicles (Boukobza et al. 2001). The 214-amino acid protein adenylate kinase was used in this study (Rhoades et al. 2003) and was labeled with Alexa 488 as the donor and Texas Red as the acceptor, which were specifically attached to cysteine residues inserted into the polypeptide

chain. The FRET efficiency distributions obtained from trajectories of trapped molecules under native or fully denatured conditions match the ensemble-measured values. At the midpoint of the denaturation curve the distribution is clearly bimodal, indicating the existence of one dominant free energy barrier under these conditions. This barrier separates two subpopulations of the protein, even though adenylate kinase is certainly not a two-state folder. The peak values of the two subdistributions are shifted from the corresponding values in the fully folded or fully denatured distributions. The shift of the denatured distribution is again an indication of chain collapse due to change in solvent conditions. The shift in the 'folded' distribution suggests that partially open conformations of the protein are populated under midtransition conditions.

The distribution is broadened by transitions between these substates of the protein, as can be verified by examining the trajectories themselves. Indeed, the trajectories show that some of these transitions transfer a molecule over the large free energy barrier mentioned above, whereas other transitions maintain the molecule within the same side of the barrier. Sample trajectories are shown in Figure 8.8. Panels A and B show a trajectory with several jumps between a fully folded state of the protein (FRET efficiency of  $\sim 0.8$ ) and a partially folded state (FRET efficiency of  $\sim 0.5$ ). Panels C and D show an example of a "slow transition," a transition between two states of the protein that does not occur instantaneously on the time scale of the measurement, as opposed to the transitions shown in A and B. Such a slow transition, the like of which are seen quite frequently in the AK trajectories, actually allows tracing the conformation of the molecule as it changes from one state to another. It is hard to imagine that it can be due to a barrier-crossing event, though, and a molecular picture of the origin of such slow motion on the energy landscape is still missing. One possibility is that it arises from very slowed-down intrachain diffusion experienced by this large protein on certain regions of its energy landscape.

A two-dimensional map of the transitions seen in the trajectories, with the initial FRET efficiency value (i.e., the value before the transition) as one coordinate, and the final value (after the transition) as the other coordinate, shows a large dispersion of the points, indicating that the dynamics of the protein are very heterogeneous (Rhoades et al. 2003). Furthermore, the distribution of transition sizes suggests that these dynamics involve motion between neighboring intermediate states rather than large jumps between very different conformations. This picture is as expected for a rugged energy landscape, on which many local traps and barriers dictate the motion (Onuchic et al. 1997).

#### 8.4.2.3 Cold Shock Protein

The vesicle encapsulation method was also applied to *CspTm* (Rhoades et al. 2004). Labeled molecules of this protein were encapsulated in unilamellar lipid vesicles in aqueous buffer containing 2 M GdmCl. At this denaturant concentration, the rates of folding and unfolding are equal, and consequently folded and unfolded states are equally populated (Schuler et al. 2002b). A sample-scanning confocal microscope

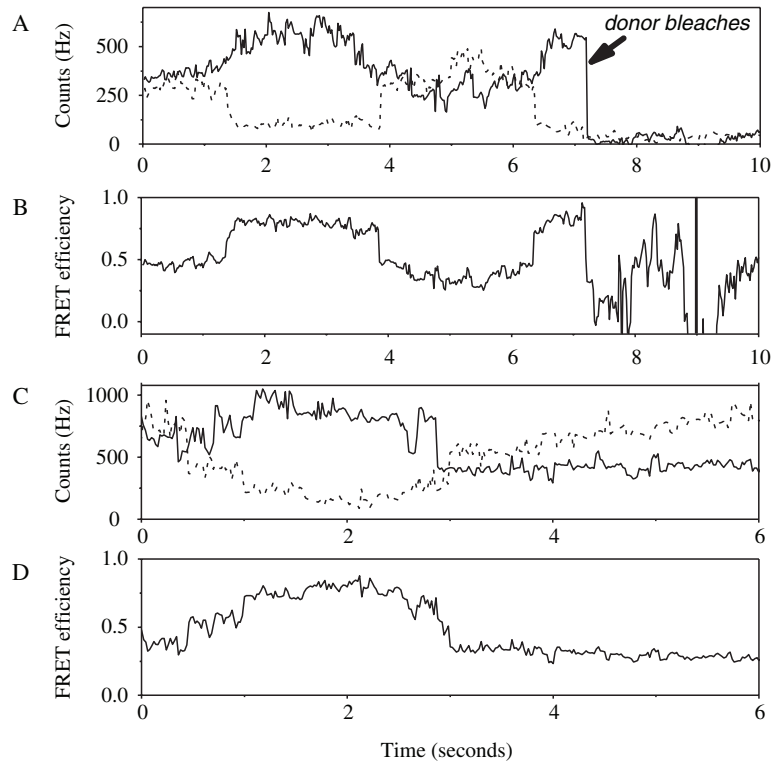


**Figure 8.8** (A) Time traces of an individual vesicle-trapped AK molecule under midtransition conditions, showing the acceptor signal (solid line) and the donor signal (dashed line). The traces were collected with 20 millisecond time bins, and smoothed using the forward-backward nonlinear filter described in the text. (B) FRET efficiency trajectory calculated from the signals. (C), (D) A single-molecule trajectory showing a slow transition between two states of the molecule, starting at  $\sim 0.5$  seconds and ending at  $\sim 2$  seconds. Donor and acceptor time traces in (C), FRET efficiency trajectory in (D). (Reprinted from Rhoades et al. (2003), with permission)

was used to record fluorescence intensity traces. As in the case of AK, some trajectories showed steady levels of FRET efficiency followed by rapid jumps, until photobleaching of one of the dyes occurs. Based on the previous FRET experiments with *CspTm*, (Schuler et al. 2002b) high transfer efficiencies were identified with the folded state and low transfer efficiencies with the unfolded state of the protein. Consequently, abrupt changes in the FRET efficiency represent folding or unfolding events. The actual transitions were too rapid to be time-resolved, even with a sampling period of  $100\mu\text{s}$ . The simplicity of the trajectories and the stochastic occurrence of folding and unfolding permitted a quantitative comparison with ensemble stopped-flow experiment under identical solution conditions, validating the single molecule result. Consequently, the simple two-state behavior of *CspTm* inferred from ensemble-averaged experiments is reflected quantitatively in the folding trajectories of individual molecules.

#### 8.4.2.4 Ribonuclease HI

Nienhaus and coworkers established an immobilization scheme based on star-shaped polyethylene glycol polymer-covered surfaces (Amirgoulova et al. 2004; Groll et al. 2004; Heyes et al. 2004). This scheme was used for studying the folding of individual molecules of ribonuclease HI (RNase H) (Kuzmenkina et al. 2005). Even though the biotin used for immobilization of RNase HI via streptavidin is attached nonspecifically to lysine side chains of the protein, cooperative and reversible folding in good agreement with ensemble experiments was observed in confocal experiments, suggesting minimal perturbation of the protein by interaction with the surface. An advantage of this scheme is that the solution conditions can be exchanged easily and rapidly. Immobilized RNase H also shows an equilibrium collapse of the unfolded state with decreasing denaturant concentrations, which has been analyzed in terms of a model including a continuous range of unfolded substates (Kuzmenkina et al. 2006).

Fluorescence trajectories of individual immobilized RNase HI molecules were followed on time scales up to several minutes by intermittent excitation, and heterogeneous transitions of the transfer efficiency on time scales ranging from microseconds to minutes were observed (Kuzmenkina et al. 2005; Figure 8.9). The rate constants of transitions between folded and unfolded molecules at the unfolding midpoint of 1.7 M GdmCl ( $\sim 10^{-2} \text{ s}^{-1}$ ) were in agreement with ensemble experiments. Cross-correlation analysis of donor and acceptor emission exhibited an anticorrelation term with a time constant of 20  $\mu\text{s}$ , which was interpreted as the polypeptide reconfiguration time in the unfolded state. Another component of the correlation on a time scale of about 100  $\mu\text{s}$  was taken to originate from intrinsic emission fluctuations of the fluorophores unrelated to folding. Most surprisingly, transitions of the transfer efficiency within the range assigned to the unfolded state occurred with characteristic times of about 2 s. The authors concluded that such slow transitions must be due to high free energy barriers originating from substantial structure in the denatured state. Such pronounced features of the energy landscape in the unfolded state have not been observed for other proteins, and their structural basis remains to be understood.

#### 8.4.2.5 Green Fluorescent Protein

Chirico and coworkers performed a series of interesting studies on individual GFP encapsulated in wet silica gels (Campanini et al. 2005; Cannone et al. 2005; Chirico et al. 2002). Because the rotational motion of the molecules within the gel were similar to bulk rotation (Chirico et al. 2002), and because ensemble folding/unfolding studies of encapsulated molecules also showed similar behavior to solution, the authors concluded that the gel environment does not perturb the protein and that its folding behavior can be studied on the single-molecule level. GFP can exist in two major states, anionic or neutral, whose interconversion rates and equilibrium depend on pH. These states can be distinguished based on their excitation and

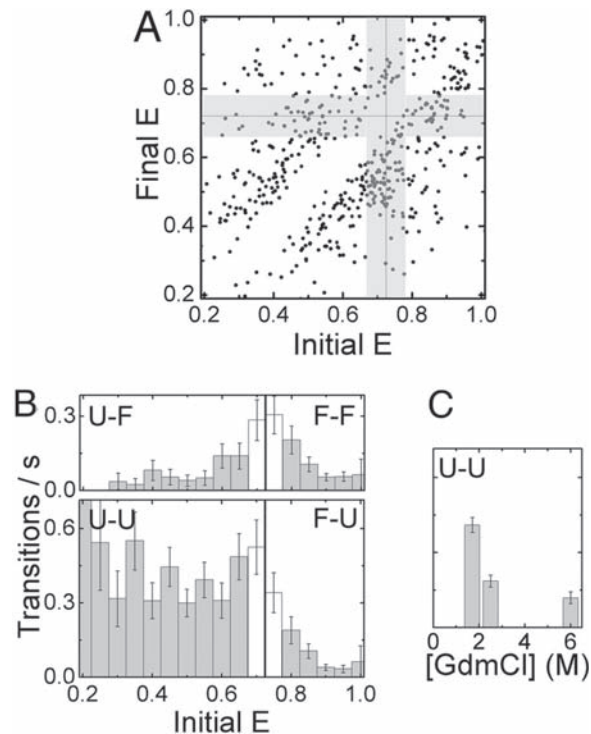


**Figure 8.9** A map of the FRET efficiency changes in transitions within trajectories of individual RnaseH molecules is shown in panel A. The large number of transitions observed allowed the authors to construct histograms of the rates of transitions as a function of initial efficiency for jumps within the unfolded ensemble (U–U), within the folded ensemble (F–F) or between the two (U–F and F–U). (Reprinted from Kuzmenkina et al. (2005), with permission)

emission spectra. Single-molecule fluorescence images of gel-encapsulated GFP molecules were therefore obtained in two detection channels, enabling simultaneous tracking of the two states. It is important that, by employing weak excitation intensities and long delays between observations Cannone et al (2005) could watch the same molecules for many hours. Repetitive alternating addition of GdmCl solution and buffer allowed observation of reversible unfolding and refolding cycles, with rather slow time constants.

A curious phenomenon reported in this work was that a significant retention of the original state of the molecule upon unfolding and refolding was observed. It was found that this “memory effect” was slightly more significant in the neutral state than in the anionic state. This imbalance led to a different-than-equilibrium distribution of the occupancy in the two states. The difference was maximal right after refolding, but decayed back to the equilibrium ratio with a slow relaxation time. The authors suggested that the memory effect might be related to constraints posed by caging in a gel. It is possible that unfolding in the gel is not complete,

even though CD studies on large ensembles of molecules indicated loss of secondary structure (Campanini et al. 2005). Another possibility is that heterogeneity of the ionic state of gel pores leads to variation of the local pH at the position of different molecules.

## 8.5 Perspective

As is evident from the discussion above, single-molecule fluorescence spectroscopy is starting to contribute substantially to our understanding of biomolecular folding. Here we outline some of the questions that will be of interest for this field in the coming years, and suggest where it might make its largest contributions.

First, as discussed in Section 8.4, the opportunity to probe the unfolded state under native conditions with ensemble techniques is rare, and in most proteins one has to be content with the availability of data on the structure under denaturing conditions. On the other hand, single-molecule experiments are able to separate those molecules that are denatured from those that are folded, or to probe one molecule as it undergoes transitions between these states. Thus it should be possible to directly probe dynamics in the unfolded state of a protein, identify the appearance of fleeting structure elements, and measure the rates of their formation and disappearance. An interesting recent suggestion, based on molecular dynamics simulations of small denatured proteins under native conditions, is that although each molecule retains a random conformation, the average topology is similar to the native state (Zagrovic et al. 2002). To verify this assertion experimentally one needs to build the average structure from its constituents, a natural exercise for single-molecule studies. As it is expected that dynamics in the unfolded state will be rather fast, one will have to rely on more sophisticated analysis techniques such as correlation functions (Yang and Xie 2002a,b). It is possible that modalities of fluorescence spectroscopy other than FRET will be useful here, in particular polarization spectroscopy that might pick up changes in segmental rigidity or transient formation of secondary-structure elements. Further development of instrumentation and data analysis techniques will be crucial for a wide range of questions, as illustrated by the recent development of alternating laser excitation (Kapanidis et al. 2004; Muller et al. 2005) in combination with multiparameter detection for the investigation of fluctuations in biopolymers (Laurence et al. 2005).

Second, it is highly desirable to develop the ability to directly detect multiple folding pathways and a broad distribution of substates. This ability should allow us to more fully characterize the free energy landscape of the folding molecule, and characterize its level of ruggedness. Technically, the possibility of identifying heterogeneous pathways (Kuzmenkina et al. 2005; Rhoades et al. 2003) relies on a rather slow interconversion between intermediate states formed on the way to folding. It is feasible that in small proteins which show two-state folding behavior on the ensemble level, the rate of interconversion between various substates in the ensemble of structures describing the folded or unfolded states will be too fast for

direct probing. This rate can in principle be slowed down using viscogenic reagents, with the caveat that these chemicals might also affect the overall stability of a protein (Jacob et al. 1999).

Another important issue related to folding pathways is the ability to probe the actual transition between folded and unfolded states, or in other words to resolve the motion of a molecule over the folding barrier. Although methods such as  $\phi$ -value analysis provide indirect information about the structure of the transition state, it will definitely be of high interest to directly probe this structure, and this is not generally possible with ensemble kinetic methods. Again, a judicious application of viscogenic reagents can lead to slowing down of the folding dynamics to the extent that motion over the folding barrier can possibly be directly probed.

Some general statistical mechanical aspects of the folding dynamics of individual biomolecules are also worthwhile studying. For example, the question of the approach to ergodic behavior (Straub and Thirumalai 1993) is quite intriguing, and might shed some more light on the rate of sampling of substates, as well as on the accessibility of different regions on the energy landscape. Short-time deviations from ergodic behavior are commonly observed in disordered systems, especially close to the glass transition. Single-molecule experiments have already suggested deviations from ergodicity in the conformational dynamics of DNA molecules (Wennmalm et al. 1999) and enzymes (Edman and Rigler 2000; Lu et al. 1998).

Single-molecule experiments should also be useful for studying folding in more complex environments. For example, cotranslational folding, that is, coupling of folding to the synthesis of the amino-acid chain on the ribosome, is still a rather mysterious and poorly studied process. Recent work suggests that some polypeptides can form compact states already within the ribosomal exit tunnel (Woolhead et al. 2004; Ziv et al. 2005). The dynamics of tRNA molecules during translation were studied by single-molecule techniques (Blanchard et al. 2004). Similar experiments that target the nascent chain could provide significant insight on the translation process, and might open the way to studies of folding within cells.

## References

- Alm, E. and Baker, D. (1999) Prediction of protein-folding mechanisms from free-energy landscapes derived from native structures. *Proc Natl Acad Sci USA* 96:11305–11310
- Amir, D. and Haas, E. (1987) Estimation of intramolecular distance distributions in bovine pancreatic trypsin inhibitor by site-specific labeling and nonradiative excitation energy-transfer measurements. *Biochemistry* 26:2162–2175
- Amirgoulova, E. V., Groll, J., Heyes, C. D., Ameringer, T., Rocker, C., Moller, M. and Nienhaus, G. U. (2004) Biofunctionalized polymer surfaces exhibiting minimal interaction towards immobilized proteins. *Chem Phys Chem* 5:552–555
- Andrec, M., Levy, R. M. and Talaga, D. S. (2003) Direct determination of kinetic rates from single-molecule photon arrival trajectories using hidden Markov models. *J Phys Chem A* 107:7454–7464

- Anfinsen, C. B. (1972) The formation and stabilization of protein structure. *Biochem J* 128:737–749
- Anfinsen, C. B. (1973) Principles that govern the folding of protein chains. *Science* 181:223–230
- Anson, M. L. (1945) Protein denaturation and the properties of protein groups. *Adv Protein Chem* 2:361–384
- Anson, M. L. and Mirsky, A. E. (1934) *J Gen Physiol* 17:393–408
- Axelrod, D. (1989) Total internal reflection fluorescence microscopy. *Meth Cell Biol* 30:245–270
- Baldwin, R. L. (1995) The nature of protein folding pathways: The classical versus the new view. *J Biomol NMR* 5:103–109
- Bark, S. J. and Hahn, K. M. (2000) Fluorescent indicators of peptide cleavage in the trafficking compartments of living cells: Peptides site-specifically labeled with two dyes. *Methods* 20:429–435
- Berezhtkovskii, A. M., Boguna, M. and Weiss, G. H. (2001) Evaluation of rate constants for conformational transitions using single-molecule fluorescence spectroscopy. *Chem Phys Lett* 336:321–324
- Bieri, O. and Kiefhaber, T. (1999) Elementary steps in protein folding. *Biol Chem* 380:923–929
- Bieri, O., Wirz, J., Hellrung, B., Schutkowski, M., Drewello, M. and Kiefhaber, T. (1999) The speed limit for protein folding measured by triplet–triplet energy transfer. *Proc Natl Acad Sci USA* 96:9597–9601
- Blanchard, S. C., Gonzalez, R. L., Kim, H. D., Chu, S. and Puglisi, J. D. (2004) tRNA selection and kinetic proofreading in translation. *Nat Struct Mol Biol* 11:1008–1014
- Boguna, M., Berezhtkovskii, A. M. and Weiss, G. H. (2001) Rate constants for slow conformational transitions and their sampling errors using single-molecule fluorescence spectroscopy. *J Phys Chem A* 105:4898–4901
- Böhmer, M. and Enderlein, J. (2003) Fluorescence spectroscopy of single molecules under ambient conditions: Methodology and technology. *Chem Phys Chem* 4:793–808
- Boukoubza, E., Sonnenfeld, A. and Haran, G. (2001) Immobilization in surface-tethered lipid vesicles as a new tool for single biomolecule spectroscopy. *J Phys Chem B* 105:12165–12170
- Brasselet, S., Peterman, E. J. G., Miyawaki, A. and Moerner, W. E. (2000) Single-molecule fluorescence resonant energy transfer in calcium concentration dependent cameleon. *J Phys Chem B* 104:3676–3682
- Bryngelson, J. D. and Wolynes, P. G. (1987) Spin glasses and the statistical mechanics of protein folding. *Proc Natl Acad Sci USA* 84:7524–7528
- Buscaglia, M., Schuler, B., Lapidus, L. J., Eaton, W. A. and Hofrichter, J. (2003) Kinetics of intramolecular contact formation in a denatured protein. *J Mol Biol* 332:9–12
- Campanini, B., Bologna, S., Cannone, F., Chirico, G., Mozzarelli, A. and Bettati, S. (2005) Unfolding of green fluorescent protein mut2 in wet nanoporous silica gels. *Protein Sci* 14:1125–1133
- Cannone, F., Bologna, S., Campanini, B., Diaspro, A., Bettati, S., Mozzarelli, A. and Chirico, G. (2005) Tracking unfolding and refolding of single GFPmut2 molecules. *Biophys J* 89:2033–2045
- Chan, W. C., Maxwell, D. J., Gao, X., Bailey, R. E., Han, M. and Nie, S. (2002) Luminescent quantum dots for multiplexed biological detection and imaging. *Curr Opin Biotechnol* 13:40–46
- Chattopadhyay, K., Elson, E. L. and Frieden, C. (2005) The kinetics of conformational fluctuations in an unfolded protein measured by fluorescence methods. *Proc Natl Acad Sci USA* 102:2385–2389
- Chirico, G., Cannone, F., Beretta, S., Diaspro, A., Campanini, B., Bettati, S., Ruotolo, R. and Mozzarelli, A. (2002) Dynamics of green fluorescent protein mutant2 in solution, on spin-coated glasses, and encapsulated in wet silica gels. *Protein Sci* 11:1152–1161
- Chung, S. H. and Kennedy, R. A. (1991) Forward-backward non-linear filtering technique for extracting small biological signals from noise. *J Neurosci Meth* 40:71–86
- Conibear, P. B. and Bagshaw, C. R. (2000) A comparison of optical geometries for combined flash photolysis and total internal reflection fluorescence microscopy. *J Microscopy* 200:218–229
- Creighton, T. E. (1992) *Protein Folding* (W.H. Freeman, New York)



- Dale, R. E., Eisinger, J. and Blumberg, W. E. (1979) The orientational freedom of molecular probes. The orientation factor in intramolecular energy transfer. *Biophys J* 26:161–193
- Deniz, A. A., Dahan, M., Grunwell, J. R., Ha, T., Faulhaber, A. E., Chemla, D. S., Weiss, S. and Schultz, P. G. (1999) Single-pair fluorescence resonance energy transfer on freely diffusing molecules: observation of Forster distance dependence and subpopulations. *Proc Natl Acad Sci USA* 96:3670–3675
- Deniz, A. A., Laurence, T. A., Beligere, G. S., Dahan, M., Martin, A. B., Chemla, D. S., Dawson, P. E., Schultz, P. G. and Weiss, S. (2000) Single-molecule protein folding: Diffusion fluorescence resonance energy transfer studies of the denaturation of chymotrypsin inhibitor 2. *Proc Natl Acad Sci USA* 97:5179–5184
- Dickson, R. M., Cubitt, A. B., Tsien, R. Y. and Moerner, W. E. (1997) On/off blinking and switching behaviour of single molecules of green fluorescent protein. *Nature* 388:355–358
- Dickson, R. M., Norris, D. J., Tzeng, Y.-L. and Moerner, W. E. (1996) Three-dimensional imaging of single molecules solvated in pores of poly(acrylamide) gels. *Science* 274:966–969
- Dill, K. A. and Chan, H. S. (1997) From Levinthal to pathways to funnels. *Nature Struct Biol* 4:10–19
- Dobson, C. M., Sali, A. and Karplus, M. (1998) Protein folding: A perspective from theory and experiment. *Angew Chem-Int Edit* 37:868–893
- Dobson, C. M. (2003) Protein folding and misfolding. *Nature* 426:884–890
- Dorre, K., Stephan, J. and Eigen, M. (2001) Highly efficient single molecule detection in different micro and submicrometer channels with cw-excitation. *Single Mol* 2:165–175
- Dyson, H. J. and Wright, P. E. (2005) Intrinsically unstructured proteins and their functions. *Nat Rev Mol Cell Bio* 6:197–208
- Eaton, W. A. (1999) Searching for “downhill scenarios” in protein folding. *Proc Natl Acad Sci USA* 96:5897–5899
- Edman, L. and Rigler, R. (2000) Memory landscapes of single-enzyme molecules. *Proc Natl Acad Sci USA* 97:8266–8271
- Effenhauser, C. S., Bruin, G. J. M., Paulus, A. and Ehrat, M. (1997) Integrated capillary electrophoresis on flexible silicon microdevices: Analysis of DNA restriction fragments and detection of single DNA molecules on microchips. *Anal Chem* 69:3451–3457
- Eggeling, C., Berger, S., Brand, L., Fries, J. R., Schaffer, J., Volkmer, A. and Seidel, C. A. (2001) Data registration and selective single-molecule analysis using multi-parameter fluorescence detection. *J Biotechnol* 86:163–180
- Eggers, D. K. and Valentine, J. S. (2001) Crowding and hydration effects on protein conformation: A study with sol-gel encapsulated proteins. *J Mol Biol* 314:911–922
- Eigen, M. and Rigler, R. (1994) Sorting single molecules: Application to diagnostics and evolutionary biotechnology. *Proc Natl Acad Sci USA* 91:5740–5747
- Enderlein, J., Robbins, D. L., Ambrose, W. P., Goodwin, P. M. and Keller, R. A. (1997) The statistics of single molecule detection: An overview. *Bioimaging* 5:88–98
- Engel, M. F., Visser, A. J. and van Mierlo, C. P. (2004) Conformation and orientation of a protein folding intermediate trapped by adsorption. *Proc Natl Acad Sci USA* 101:11316–11321
- Fersht, A. R. (1995) Optimization of rates of protein folding: The nucleation-condensation mechanism and its implications. *Proc Natl Acad Sci USA* 92:10869–10873
- Fersht, A. R. (1998) *Structure and Mechanism in Protein Science* (W.H. Freeman and Company, New York)
- Fitzkee, N. C. and Rose, G. D. (2004) Reassessing random-coil statistics in unfolded proteins. *Proc Natl Acad Sci USA* 101:12497–12502
- Forkey, J. N., Quinlan, M. E. and Goldman, Y. E. (2000) Protein structural dynamics by single-molecule fluorescence polarization. *Prog Biophys Mol Biol* 74:1–35
- Forkey, J. N., Quinlan, M. E., Shaw, M. A., Corrie, J. E. and Goldman, Y. E. (2003) Three-dimensional structural dynamics of myosin V by single-molecule fluorescence polarization. *Nature* 422:399–404
- Förster, T. (1948) Zwischenmolekulare Energiewanderung und Fluoreszenz. *Ann Phys* 2:55–75
- Frieden, C., Chattopadhyay, K. and Elson, E. L. (2002) What fluorescence correlation spectroscopy can tell us about unfolded proteins. *Adv Protein Chem* 62:91–109

- Fries, J. R., Brand, L., Eggeling, C., Kollner, M. and Seidel, C. A. M. (1998) Quantitative identification of different single molecules by selective time-resolved confocal fluorescence spectroscopy. *J Phys Chem A* 102:6601–6613
- Galzitskaya, O. V. and Finkelstein, A. V. (1999) A theoretical search for folding/unfolding nuclei in three-dimensional protein structures. *Proc Natl Acad Sci USA* 96:11299–11304
- Garcia-Parajo, M. F., Segers-Nolten, G. M., Veerman, J. A., Greve, J. and van Hulst, N. F. (2000) Real-time light-driven dynamics of the fluorescence emission in single green fluorescent protein molecules. *Proc Natl Acad Sci USA* 97:7237–7242
- Go, N., Abe, H., Mizuno, H. and Taketomi, H. (1980) in *Protein Folding* (ed. Jaenicke, R.) 167–181 (Elsevier/North-Holland Biomedical Press, Amsterdam/New York)
- Gopich, I. V. and Szabo, A. (2003a) Statistics of transitions in single molecule kinetics. *J Chem Phys* 118:454–455
- Gopich, I. V. and Szabo, A. (2003b) Single-macromolecule fluorescence resonance energy transfer and free-energy profiles. *J Phys Chem B* 107:5058–5063
- Gopich, I. V. and Szabo, A. (2005) Theory of photon statistics in single-molecule Förster resonance energy transfer. *J Chem Phys* 122:1–18
- Groll, J., Amirgoulova, E. V., Ameringer, T., Heyes, C. D., Rocker, C., Nienhaus, G. U. and Moller, M. (2004) Biofunctionalized, ultrathin coatings of cross-linked star-shaped poly(ethylene oxide) allow reversible folding of immobilized proteins. *J Am Chem Soc* 126:4234–4239
- Guerrero, G. and Isacoff, E. Y. (2001) Genetically encoded optical sensors of neuronal activity and cellular function. *Curr Opin Neurobiol* 11:601–607
- Ha, T. (2001) Single-molecule fluorescence resonance energy transfer. *Methods* 25:78–86.
- Ha, T., Laurence, T. A., Chemla, S. S. and Weiss, S. (1999) Polarization spectroscopy of single fluorescent molecules. *J Phys Chem B* 103:6839–6850
- Ha, T., Ting, A. Y., Liang, J., Caldwell, W. B., Deniz, A. A., Chemla, D. S., Schultz, P. G. and Weiss, S. (1999) Single-molecule fluorescence spectroscopy of enzyme conformational dynamics and cleavage mechanism. *Proc Natl Acad Sci USA* 96:893–898
- Haas, E. (1996) The problem of protein-folding and dynamics-time-resolved dynamic nonradiative excitation-energy transfer measurements. *IEEE J Sel Top Quantum Elect* 2:1088–1106
- Haas, E., Katchalskikatzir, E. and Steinberg, I. Z. (1978) Brownian-motion of ends of oligopeptide chains in solution as estimated by energy-transfer between chain ends. *Biopolymers* 17:11–31
- Haas, E., Wilchek, M., Katchalski-Katzir, E. and Steinberg, I. Z. (1975) Distribution of end-to-end distances of oligopeptides in solution as estimated by energy transfer. *Proc Natl Acad Sci USA* 72:1807–1811
- Hagen, S. J., Hofrichter, J., Szabo, A. and Eaton, W. A. (1996) Diffusion-limited contact formation in unfolded cytochrome c: Estimating the maximum rate of protein folding [see comments]. *Proc Natl Acad Sci USA* 93:11615–11617
- Haran, G. (2004) Noise reduction in single-molecule fluorescence trajectories of folding proteins. *Chem Phys* 307:137–145
- Haran, G., Haas, E., Szpikowska, B. K. and Mas, M. T. (1992) Domain motions in phosphoglycerate kinase: Determination of interdomain distance distributions by site-specific labeling and time-resolved fluorescence energy transfer. *Proc Natl Acad Sci USA* 89:11764–11768
- Harrison, S. C. and Durbin, R. (1985) Is there a single pathway for the folding of a polypeptide chain? *Proc Natl Acad Sci USA* 82:4028–4030
- Hess, S. T., Huang, S., Heikal, A. A. and Webb, W. W. (2002) Biological and chemical applications of fluorescence correlation spectroscopy: A review. *Biochemistry* 41:697–705.
- Heyes, C. D., Kobitski, A. Y., Amirgoulova, E. V. and Nienhaus, G. U. (2004) Biocompatible surfaces for specific tethering of individual protein molecules. *J Phys Chem B* 108:13387–13394.
- Jackson, S. E. (1998) How do small single-domain proteins fold. *Fold Des* 3:r81–r91
- Jackson, S. E. and Fersht, A. R. (1991) Folding of chymotrypsin inhibitor 2. 1. Evidence for a two-state transition. *Biochemistry* 30:10428–10435.

- Jacob, M., Geeves, M., Holtermann, G. and Schmid, F. X. (1999) Diffusional barrier crossing in a two-state protein folding reaction. *Nat Struct Biol* 6:923–926.
- Jaenicke, R. (1980) *Protein Folding: Proceedings of the 28th Conference of the German Biochemical Society*, held at the University of Regensburg, Regensburg, West Germany, September 10–12, 1979, Elsevier, Amsterdam.
- Jaenicke, R. and Seckler, R. (1997) Protein misassembly in vitro. *Adv Protein Chem* 50:1–59
- Jia, Y., Talaga, D. S., Lau, W. L., Lu, H. S. M., DeGrado, W. F. and Hochstrasser, R. M. (1999) Folding dynamics of single GCN-4 peptides by fluorescence resonant energy transfer confocal microscopy. *Chem Phys* 247:69–83
- Johnsson, B., Lofas, S. and Lindquist, G. (1991) Immobilization of proteins to a carboxymethyl-dextran-modified gold surface for biospecific interaction analysis in surface plasmon resonance sensors. *Anal Biochem* 198:268–277
- Kanehisa, M. I. and Tsong, T. Y. (1979) Dynamics of the cluster model of protein folding. *Biopolymers* 18:1375–1388
- Kapanidis, A. N., Lee, N. K., Laurence, T. A., Doose, S., Margeat, E. and Weiss, S. (2004) Fluorescence-aided molecule sorting: Analysis of structure and interactions by alternating-laser excitation of single molecules. *Proc Natl Acad Sci USA* 101:8936–8941
- Karplus, M. and Weaver, D. L. (1976) Protein-folding dynamics. *Nature* 260:404–406
- Karplus, M. and Weaver, D. L. (1994) Protein folding dynamics: The diffusion-collision model and experimental data. *Protein Sci* 3:650–668
- Kauffmann, E., Darnton, N. C., Austin, R. H., Batt, C. and Gerwert, K. (2001) Lifetimes of intermediates in the beta-sheet to alpha-helix transition of beta-lactoglobulin by using a diffusional IR mixer. *Proc Natl Acad Sci USA* 98:6646–6649
- Kim, H. D., Nienhaus, G. U., Ha, T., Orr, J. W., Williamson, J. R. and Chu, S. (2002) Mg<sup>2+</sup>-dependent conformational change of RNA studied by fluorescence correlation and FRET on immobilized single molecules. *Proc Natl Acad Sci USA* 99:4284–4289
- Kim, P. S. and Baldwin, R. L. (1982) Specific intermediates in the folding reactions of small proteins and the mechanism of protein folding. *Ann Rev Biochem* 51:459–489
- Klimov, D. K., Newfield, D. and Thirumalai, D. (2002) Simulations of beta-hairpin folding confined to spherical pores using distributed computing. *Proc Natl Acad Sci USA* 99:8019–8024
- Knight, J. B., Vishwanath, A., Brody, J. P. and Austin, R. H. (1998) Hydrodynamic focusing on a silicon chip: Mixing nanoliters in microseconds. *Phys Rev Lett* 80:3863–3866
- Ko, D. S., Sauer, M., Nord, S., Muller, R. and Wolfrum, J. (1997) Determination of the diffusion coefficient of dye in solution at single molecule level. *Chem Phys Lett* 269:54–58
- Kohn, J. E., Millett, I. S., Jacob, J., Zagrovic, B., Dillon, T. M., Cingel, N., Dothager, R. S., Seifert, S., Thiagarajan, P., Sosnick, T. R., Hasan, M. Z., Pande, V. S., Ruczinski, I., Doniach, S. and Plaxco, K. W. (2004) Random-coil behavior and the dimensions of chemically unfolded proteins. *Proc Natl Acad Sci USA* 101:12491–12496
- Krichevsky, O. and Bonnet, G. (2002) Fluorescence correlation spectroscopy: The technique and its applications. *Rep Prog Phys* 65:251–297
- Krieger, F., Fierz, B., Bieri, O., Drewello, M. and Kiefhaber, T. (2003) Dynamics of unfolded polypeptide chains as model for the earliest steps in protein folding. *J Mol Biol* 332:265–274
- Kubelka, J., Hofrichter, J. and Eaton, W. A. (2004) The protein folding ‘speed limit’. *Curr Opin Struct Biol* 14:76–88
- Kuzmenkina, E. V., Heyes, C. D. and Nienhaus, G. U. (2005) Single-molecule Forster resonance energy transfer study of protein dynamics under denaturing conditions. *Proc Natl Acad Sci USA* 102:15471–15476
- Kuzmenkina, E. V., Heyes, C. D. and Nienhaus, G. U. (2006) Single-molecule FRET study of denaturant induced unfolding of RNase H. *J Mol Biol* 357:313–324
- Lapidus, L. J., Eaton, W. A. and Hofrichter, J. (2000) Measuring the rate of intramolecular contact formation in polypeptides. *Proc Natl Acad Sci USA* 97:7220–7225

- Laurence, T. A., Kong, X. X., Jager, M. and Weiss, S. (2005) Probing structural heterogeneities and fluctuations of nucleic acids and denatured proteins. *Proc Natl Acad Sci USA* 102:17348–17353
- Levinthal, C. (1968) Are there pathways for protein folding? *J Chim Phys* 65:44–45
- Lipman, E. A., Schuler, B., Bakajin, O. and Eaton, W. A. (2003) Single-molecule measurement of protein folding kinetics. *Science* 301:1233–1235
- Lu, H. P., Xun, L. and Xie, X. S. (1998) Single-molecule enzymatic dynamics. *Science* 282:1877–1882
- Masino, L., Martin, S. R. and Bayley, P. M. (2000) Ligand binding and thermodynamic stability of a multidomain protein, calmodulin. *Protein Sci* 9:1519–1529
- McCarney, E. R., Kohn, J. E. and Plaxco, K. W. (2005) Is there or isn't there? The case for (and against) residual structure in chemically denatured proteins. *Crit Rev Biochem Mol* 40:181–189
- McCarney, E. R., Werner, J. H., Bernstein, S. L., Ruczinski, I., Makarov, D. E., Goodwin, P. M. and Plaxco, K. W. (2005) Site-specific dimensions across a highly denatured protein; a single molecule study. *J Mol Biol* 352:672–682
- McDonnell, J. M. (2001) Surface plasmon resonance: Towards an understanding of the mechanisms of biological molecular recognition. *Curr Opin Chem Biol* 5:572–577
- Mei, E., Tang, J., Vanderkooi, J. M. and Hochstrasser, R. M. (2003) Motions of single molecules and proteins in trehalose glass. *J Am Chem Soc* 125:2730–2735
- Michalet, X., Kapanidis, A. N., Laurence, T., Pinaud, F., Doose, S., Pflughoeft, M. and Weiss, S. (2003) The power and prospects of fluorescence microscopies and spectroscopies. *Ann Rev Biophys Biomol Struct* 32:161–182
- Muller, B. K., Zaychikov, E., Brauchle, C. and Lamb, D. C. (2005) Pulsed interleaved excitation. *Biophys J* 89:3508–3522
- Munoz, V. and Eaton, W. A. (1999) A simple model for calculating the kinetics of protein folding from three-dimensional structures. *Proc Natl Acad Sci USA* 96:11311–11316
- Munoz, V., Thompson, P. A., Hofrichter, J. and Eaton, W. A. (1997) Folding dynamics and mechanism of beta-hairpin formation. *Nature* 390:196–199
- Neurath, H., Greenstein, J. P., Putnam, F. W. and Erickson, J. O. (1944) *Chem Rev* 34:157–265
- Neuweiler, H. and Sauer, M. (2004) Using photoinduced charge transfer reactions to study conformational dynamics of biopolymers at the single-molecule level. *Curr Pharm Biotechnol* 5:285–298
- Neuweiler, H., Doose, S. and Sauer, M. (2005) A microscopic view of miniprotein folding: enhanced folding efficiency through formation of an intermediate. *Proc Natl Acad Sci USA* 102:16650–16655
- Neuweiler, H., Schulz, A., Bohmer, M., Enderlein, J. and Sauer, M. (2003) Measurement of sub-microsecond intramolecular contact formation in peptides at the single-molecule level. *J Am Chem Soc* 125:5324–5330
- Noji, H., Yasuda, R., Yoshida, M. and Kinosita, K. (1997) Direct observation of the rotation of F<sub>1</sub>-ATPase. *Nature* 386:299–302
- Okumus, B., Wilson, T. J., Lilley, D. M. and Ha, T. (2004) Vesicle encapsulation studies reveal that single molecule ribozyme heterogeneities are intrinsic. *Biophys J* 87:2798–2806
- Onuchic, J. N. and Wolynes, P. G. (2004) Theory of protein folding. *Curr Opin Struct Biol* 14:70–75
- Onuchic, J. N., Luthey Schulten, Z. and Wolynes, P. G. (1997) Theory of protein folding: The energy landscape perspective. *Ann Rev Phys Chem* 48:545–600
- Pande, V. S., Grosberg, A., Tanaka, T. and Rokhsar, D. S. (1998) Pathways for protein folding: Is a new view needed? *Curr Opin Struct Biol* 8:68–79
- Pawley, J. B. (ed.) (1995) *Handbook of Biological Confocal Microscopy* (Plenum, New York)
- Perl, D., Welker, C., Schindler, T., Schröder, K., Marahiel, M. A., Jaenicke, R. and Schmid, F. X. (1998) Conservation of rapid two-state folding in mesophilic, thermophilic and hyperthermophilic cold shock proteins. *Nat Struct Biol* 5:229–235
- Plaxco, K. W., Simons, K. T. and Baker, D. (1998) Contact order, transition state placement and the refolding rates of single domain proteins. *J Mol Biol* 277:985–994

- Pollack, L., Tate, M. W., Finnefrock, A. C., Kalidas, C., Trotter, S., Darnton, N. C., Lurio, L., Austin, R. H., Batt, C. A., Gruner, S. M. and Mochrie, S. G. (2001) Time resolved collapse of a folding protein observed with small angle x-ray scattering. *Phys Rev Lett* 86:4962–4965
- Portman, J. J., Takada, S. and Wolynes, P. G. (2001) Microscopic theory of protein folding rates. II. Local reaction coordinates and chain dynamics. *J Chem Phys* 114:5082–5096
- Press, W. H., Teukolsky, S. A., Vetterling, W. T. and Flannery, B. P. (2003) *Numerical Recipes, the Art of Scientific Computing* (Cambridge University Press, Cambridge, UK)
- Pitsyn, O. B. and Rashin, A. A. (1975) A model of myoglobin self-organization. *Biophys Chem* 3:1–20
- Ratner, V., Kahana, E., Eichler, M. and Haas, E. (2002) A general strategy for site-specific double labeling of globular proteins for kinetic FRET studies. *Bioconjug Chem* 13:1163–1170
- Ratner, V., Sinev, M. and Haas, E. (2000) Determination of intramolecular distance distribution during protein folding on the millisecond timescale. *J Mol Biol* 299:1363–1371
- Rhoades, E., Cohen, M., Schuler, B. and Haran, G. (2004) Two-state folding observed in individual protein molecules. *J Am Chem Soc* 126:14686–14687
- Rhoades, E., Gussakovskiy, E. and Haran, G. (2003) Watching proteins fold one molecule at a time. *Proc Natl Acad Sci USA* 100:3197–3202
- Sabelko, J., Ervin, J. and Gruebele, M. (1999) Observation of strange kinetics in protein folding. *Proc Natl Acad Sci USA* 96:6031–6036
- Safran, S. (2003) *Statistical Thermodynamics of Surfaces, Interfaces, and Membranes* (Westview, Cambridge, MA)
- Sakmann, B. and Neher, E. (1995) *Single Channel Recording* (Plenum, New York)
- Schaffer, J., Volkmer, A., Eggeling, C., Subramaniam, V., Striker, G. and Seidel, C. A. M. (1999) Identification of single molecules in aqueous solution by time-resolved fluorescence anisotropy. *J Phys Chem A* 103:331–336
- Scholtz, J. M. and Baldwin, R. L. (1992) The mechanism of alpha-helix formation by peptides. *Ann Rev Bioph Biom* 21:95–118
- Schuler, B. and Pannell, L. K. (2002) Specific Labeling of polypeptides at amino-terminal cysteine residues using Cy5-benzyl thioester. *Bioconjugate Chem* 13:1039–1043
- Schuler, B., Kremer, W., Kalbitzer, H. R. and Jaenicke, R. (2002a) Role of entropy in protein thermostability: Folding kinetics of a hyperthermophilic cold shock protein at high temperatures using F-19 NMR. *Biochemistry* 41:11670–11680
- Schuler, B., Lipman, E. A. and Eaton, W. A. (2002b) Probing the free-energy surface for protein folding with single-molecule fluorescence spectroscopy. *Nature* 419:743–747
- Schuler, B., Lipman, E. A., Steinbach, P. J., Kumke, M. and Eaton, W. A. (2005) Polyproline and the “spectroscopic ruler” revisited with single molecule fluorescence. *Proc Natl Acad Sci USA* 102:2754–2759
- Sela, M., White, F. H., Jr. and Anfinsen, C. B. (1957) Reductive cleavage of disulfide bridges in ribonuclease. *Science* 125:691–692
- Selvin, P. R. (2000) The renaissance of fluorescence resonance energy transfer. *Nat Struct Biol* 7:730–734
- Serrano, L., Matouschek, A. and Fersht, A. R. (1992) The folding of an enzyme. III. Structure of the transition state for unfolding of barnase analysed by a protein engineering procedure. *J Mol Biol* 224:805–818
- Shakhnovich, E. I. (1997) Theoretical studies of protein-folding thermodynamics and kinetics. *Curr Opin Struct Biol* 7:29–40
- Shortle, D. (1996) The denatured state (the other half of the folding equation) and its role in protein stability. *Faseb J* 10:27–34
- Sinev, M. A., Sineva, E. V., Ittah, V. and Haas, E. (1996) Domain closure in adenylate kinase. *Biochemistry* 35:6425–6437
- Slaughter, B. D., Unruh, J. R., Price, E. S., Huynh, J. L., Urbauer, R. J. B. and Johnson, C. K. (2005) Sampling unfolding intermediates in calmodulin by single-molecule spectroscopy. *J Am Chem Soc* 127:12107–12114
- Sorensen, B. R. and Shea, M. A. (1998) Interactions between domains of apo calmodulin alter calcium binding and stability. *Biochemistry* 37:4244–4253

- Straub, J. E. and Thirumalai, D. (1993) Exploring the energy landscape in proteins. *Proc Natl Acad Sci USA* 90:809–813
- Stryer, L. (1978) Fluorescence energy transfer as a spectroscopic ruler. *Ann Rev Biochem* 47:819–846
- Talaga, D. S., Lau, W. L., Roder, H., Tang, J. Y., Jia, Y. W., DeGrado, W. F. and Hochstrasser, R. M. (2000) Dynamics and folding of single two-stranded coiled-coil peptides studied by fluorescent energy transfer confocal microscopy. *Proc Natl Acad Sci USA* 97:13021–13026
- Thompson, P. A., Eaton, W. A. and Hofrichter, J. (1997) Laser temperature jump study of the helix-coil kinetics of an alanine peptide interpreted with a 'kinetic zipper' model. *Biochemistry* 36:9200–9210
- Tokunaga, M., Kazuo, K., Saito, K., Iwane, A. H. and Yanagida, T. (1997) Single molecule imaging of fluorophores and enzymatic reactions achieved by objective-type total internal reflection fluorescence microscopy. *Biochem Biophys Res Com* 235:47–53
- Tsong, T. Y. and Baldwin, R. L. (1972) A sequential model of nucleation-dependent protein folding: Kinetic studies of ribonuclease A. *J Mol Biol* 63:453–469
- Turkova, J. (1999) Oriented immobilization of biologically active proteins as a tool for revealing protein interactions and function. *J Chromatogr B* 722:11–31
- van der Meer, B. W. (1999) in *Resonance Energy Transfer* (eds. Andrews, D. L. and Demidov, A. A.) 1–64 (Wiley, Chichester)
- Wassenberg, D., Welker, C. and Jaenicke, R. (1999) Thermodynamics of the unfolding of the cold-shock protein from *Thermotoga maritima*. *J Mol Biol* 289:187–193
- Watkins, L. P. and Yang, H. (2004) Information bounds and optimal analysis of dynamic single molecule measurements. *Biophys J* 86:4015–4029
- Wazawa, T., Ishii, Y., Funatsu, T. and Yanagida, T. (2000) Spectral fluctuation of a single fluorophore conjugated to a protein molecule. *Biophys J* 78:1561–1569
- Wegener, J., Janshoff, A. and Steinem, C. (2001) The quartz crystal microbalance as a novel means to study cell-substrate interactions in situ. *Cell Biochem Biophys* 34:121–151
- Wennmalm, S., Edman, L. and Rigler, R. (1999) Non-ergodic behavior in conformational transitions of single DNA molecules. *Chem Phys* 247:61–67
- Wetlaufer, D. B. (1973) Nucleation, rapid folding, and globular intrachain regions in proteins. *Proc Natl Acad Sci USA* 70:697–701
- Wink, T., van Zuilen, S. J., Bult, A. and van Benkom, W. P. (1997) Self-assembled monolayers for biosensors. *Analyst* 122:43R–50R
- Woolhead, C. A., McCormick, P. J. and Johnson, A. E. (2004) Nascent membrane and secretory proteins differ in FRET-detected folding far inside the ribosome and in their exposure to ribosomal proteins. *Cell* 116:725–736
- Wu, H. (1931) Studies on denaturation of proteins. XIII. A theory of denaturation. *Chin J Physiol* 5:321–344
- Yamasaki, R., Hoshino, M., Wazawa, T., Ishii, Y., Yanagida, T., Kawata, Y., Higurashi, T., Sakai, K., Nagai, J. and Goto, Y. (1999) Single molecular observation of the interaction of GroEL with substrate proteins. *J Mol Biol* 292:962–972
- Yang, H. and Xie, X. S. (2002a) Probing single-molecule dynamics photon by photon. *J Chem Phys* 117:10965–10979
- Yang, H. and Xie, X. S. (2002b) Statistical approaches for probing single-molecule dynamics photon-by-photon. *Chem Phys* 284:423–437
- Yang, S. L. and Cao, J. S. (2001) Two-event echos in single-molecule kinetics: A signature of conformational fluctuations. *J Phys Chem B* 105:6536–6549
- Yang, W. Y. and Gruebele, M. (2003) Folding at the speed limit. *Nature* 423:193–197
- Zagrovic, B., Snow, C. D., Khaliq, S., Shirts, M. R. and Pande, V. S. (2002) Native-like mean structure in the unfolded ensemble of small proteins. *J Mol Biol* 323:153–164
- Zhuang, X. W., Bartley, L. E., Babcock, H. P., Russell, R., Ha, T. J., Herschlag, D. and Chu, S. (2000) A single-molecule study of RNA catalysis and folding. *Science* 288:2048
- Ziv, G., Haran, G. and Thirumalai, D. (2005) Ribosome exit tunnel can entropically stabilize alpha helices. *Proc Natl Acad Sci USA* 102:18956–18961

## Chapter 9

# Single Molecules and Nanoscale Surfactant Networks

Aldo Jesorka, Michal Tokarz, and Owe Orwar(✉)

9.1	Introduction.....	218
9.2	Phospholipid Membranes and Vesicles.....	219
9.2.1	Physicochemical Properties of Phospholipid Membranes.....	219
9.2.2	Membrane Surface Properties Defined by Phospholipid Composition.....	221
9.2.3	Mechanical Properties of Phospholipid Membranes.....	222
9.2.4	Self-Assembly of Vesicular Systems.....	224
9.2.5	Membrane Biofunctionalization of Liposomes.....	224
9.3	Fabrication, Transformations, and Modifications of Nanotube–Vesicle Networks.....	225
9.3.1	Fabrication of Nanotube–Vesicle Networks, Forced Shape Transitions.....	225
9.3.2	Complex Network Geometries Caused by Self-Organization.....	227
9.3.3	Internal Functionalization, Mixing, and Compartmentalization of Nanotube–Vesicle Networks.....	228
9.4	Single Molecule Applications in Nanotube–Vesicle Networks.....	230
9.4.1	Mass Transport in Nanotube–Vesicle Networks.....	230
9.4.2	Tension-Controlled (Marangoni) Lipid Flow and Intratubular Liquid Flow in Nanotubes.....	232
9.4.3	Electrophoretic Transport.....	238
9.4.4	Diffusive Transport.....	242
9.5	Summary.....	244
	References.....	246

**Abstract** Networks of giant phospholipid vesicles and nanotubes are new sophisticated model systems for studies of transport phenomena and chemical reactions in ultrasmall volumes in a biomimetic environment. The unique soft matter properties of the phospholipid material led to novel bottom-up fabrication methods, enabling the controlled construction of complex container–nanotube assemblies. Active and passive transport of submicron particles and biopolymers through nanotubes in such networks, including electrophoretic transport and detection of single DNA molecules, was demonstrated. The insights into biological and biophysical principles gained from these studies lead to better understanding of biological transport

---

Owe Orwar  
Department of Chemistry and Bioscience, Chalmers University of Technology, Kemivägen 10,  
SE-41296 Göteborg, Sweden  
orwar@chembio.chalmers.se

R. Rigler and H. Vogel (eds.), *Single Molecules and Nanotechnology*. 217  
*Springer Series in Biophysics 12*.  
© Springer-Verlag Berlin Heidelberg 2008

and reaction phenomena, such as the function of natural and artificial ion channels on the single molecule level.

## 9.1 Introduction

The investigation of physical and chemical processes occurring in biocompatible systems providing confinement of, and control over single molecules has developed into a major research field. The driving force for such investigations can be found in the desire to gain basic knowledge of, for example, rates and mechanisms of single molecule reactions or in the need for novel applications and technologies such as nanoscale analytical and separation devices or biocomputing systems (Zauner 2005).

In biology, nanoscale chemical reactors featuring mechanisms for transport, storage, release, and mixing of reactants, catalysts, and products down to the single-molecule level are abundant. So far, artificially created systems are lagging behind both in terms of material properties, functionality, and structural complexity. However, new advances using soft materials to create cell-like artificial environments can open pathways to new technologies, making possible the construction of functional devices that can be dynamically controlled, modified, and restructured in order to operate with single or very small numbers of molecules. The desired initiation and control of chemical processes at this scale in artificial environments can be achieved by combining biologically inspired materials and principles with manmade materials (Wu and Payne 2004).

One example of such new technologies reviewed here are soft-matter nanotube-vesicle networks (NVNs) constructed from self-assembled bilayer membranes of surfactant materials such as phospholipids.

From a materials science perspective, phospholipid membranes are unconventional liquid crystalline materials (2-D fluids) with attractive physical and chemical properties such as high mechanical strength, extraordinary elasticity, and compatibility with a wide range of biomaterials. Although the number of available soft materials with dynamic functions is rapidly growing (Hamley 2005; Kato and Kishimoto 2006; Kato et al. 2006; Hall et al. 2005), phospholipids are the most widely applied bilayer-forming material in the biosciences. Phospholipids are successfully used in the assembly of fluid, biocompatible supported membranes (Groves and Dustin 2003; Sackmann and Tanaka 2000; Zana 2005), membrane-enclosed pico- to femtoliter volumes (vesicles; Houser 1993; Lasic 2000; Robinson and Rogerson 2002), and geometrically complex networks of vesicles interconnected by tubular structures (Karlsson et al. 2001). The physical—most importantly structural and elastic—properties of these network systems are largely defined by the membrane itself. The structure and the amphiphilic properties of the individual molecular building blocks result in ordered aggregation controlled by the so-called hydrophobic effect. The self-assembly of such low molecular weight building blocks into fluid-state nanoscale molecular objects has recently attracted large interest in terms of systematic bottom-up fabrication of nanomaterials, often in the context of biomimetic functional devices and artificial cells.



Due to their small size and favorable material properties, nanotube-vesicle networks allow for controlled transport of ultrasmall amounts of materials down to the single-molecule level by, for example, diffusion or field-driven transport. Furthermore, size and optical properties of these structures allows for direct determination of the properties and behavior of single molecules. In Figure 9.1, the fundamental aspects of the creation and modification of NVNs and their application for studies of single molecule processes are depicted.

In the following chapter we outline properties, assembly methods, and means of manipulation of such networks and their use and functionality for single molecule transport and manipulation, focusing on

- Self-assembly and membrane modification (Level 1)
- Forced shape transformations and modification of the internalized volume (Level 2)
- Fabrication of biophysical devices suitable for single molecule studies (Level 3)

A recent review provides a detailed introduction into general aspects of fabrication, topology and modification of NVNs (Karlsson et al. 2004).

## 9.2 Phospholipid Membranes and Vesicles

### 9.2.1 *Physicochemical Properties of Phospholipid Membranes*

As depicted at the first level in Figure 9.1, aggregation and membrane functionalization of phospholipid membranes are used as tools for the formation of spherical surface-immobilized vesicles which are precursors to NVNs. Vesicle formation is driven by self-assembly and self-organization, and can be controlled both by physical and chemical means. Most phospholipids as amphiphilic molecules spontaneously aggregate to ~5 nm thick bilayer membranes when suspended in an aqueous solution. Depending on the assembly conditions and the chemical structure of the phospholipids, planar bilayers, spherical vesicles (liposomes), or more complex aggregates such as cubosomes can be obtained (Barauskas et al. 2005). Phospholipid membranes are thermotropic two-dimensional fluids with a low dielectric constant ( $\epsilon \sim 2$ ) as compared to the mostly high dielectric surrounding media (e.g., water with  $\epsilon \sim 80$ ) and feature limited permeability to charged species (Lipowsky and Sackmann 1995).

Morphologically, liposomes are classified according to their size and the number of bilayers of which they are composed. The latter parameter is generally referred to as “lamellarity.” Vesicles composed of only one bilayer (unilamellar vesicles) are divided into three size regimes: small (10–50 nm), large (50–1000 nm), and giant (>1  $\mu\text{m}$ ). Lipid vesicles have gained much attention in the fields of medical and biophysical chemistry and applied material science. Drug delivery in combination with controlled release from liposomes (Dhoot and Wheatley 2003), material transport through lipid membranes, and lipid membrane-based biosensors (Schmidt et al. 2000) as well as bioelectronic applications (Fromherz et al. 1999) are some

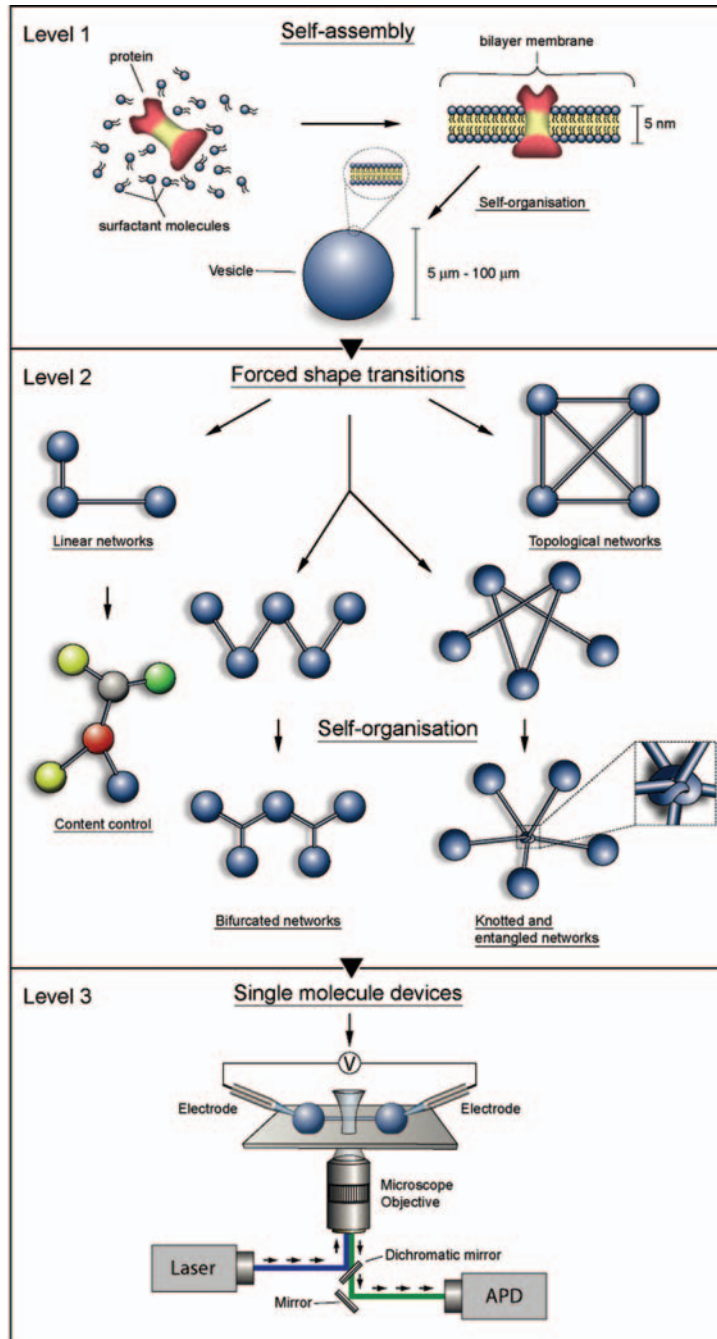


**Figure 9.1** Construction, evolution, and application of nanotube–vesicle networks in biophysical devices for single-molecule analysis. The methodology reaches from the molecular level via a variety of transformation stages to the level of complex biophysical devices. The figure shows a setup for electrophoretic transport of biomacromolecules combined with optical single-molecule detection

intensively researched areas in this field. The great diversity in size and physical parameters combined with biocompatibility and opportunity for chemical modification render lipids a very versatile material. The general structural and biophysical aspects of lipid vesicle uses in pharmaceutical and biochemical applications have appeared in a recent review (Plempers van Balen et al. 2004).

### ***9.2.2 Membrane Surface Properties Defined by Phospholipid Composition***

The lipid bilayer of biomembranes found in nature is nonhomogeneous and composed of a variety of lipids. Besides bulk amounts of uncharged zwitterionic species, a small quantity of charged phospholipids is present in biological membranes, which is highly relevant for cell functions, for example, for signal transduction and interaction with other complex molecular systems. Electrostatic properties and behavior of phospholipids, self-assembled bilayers, and biologically relevant membranes have been intensively studied. Macroscopic properties of bilayer membranes such as adhesion, interaction with proteins and other species, permeability, and wetting have been found to be highly dependent on the presence of charged lipids, their local density, and location with respect to the interface and to the properties of their neighboring membrane constituents (Langner and Kubica 1999).

Much research has been focused on the development of functionalized membranes, both utilizing and mimicking natural systems as well as introducing artificial functionality. Examples of such systems are abundant, leading to, for example, catalytic activity functionalities (Terlecki et al. 2002), site- and molecule-specific binding (Pick et al. 2005), sensor functionalities (Costello et al. 1998), enhanced surface adhesion (Sott et al. 2003), transmembrane material transport (Steinberg-Yfrach et al. 1997), and protein crystallization (Misquitta et al. 2004). Active species utilized to introduce functionality include peptides, carbohydrates, antibodies and antigens, DNA, ATP, biotin, and different cofactors. Immobilization of those species in the membrane has been achieved either specifically (chemisorption) or unspecifically (physisorption). Unspecific binding is generally based on tail group hydrophobicity and electrostatic forces modulated through the lipid headgroup charge, whereas specific binding mainly relates to techniques of chemical transformation, typically applied to lipids or lysolipids before membrane assembly (Schmitt and Tampe 1996). Specific modifications of lipid tail or headgroups have led to new materials, for example, polymerized membranes (Hentze and Kaler 2003) or metal chelating headgroups (Roy et al. 2003), and a number of novel applications, extending the systematic physicochemical determinations of structure–function relationships, most notably here in biomedical applications as well as model studies of cellular membranes. Of particular relevance in the medical field is the interaction of lipid vesicles with biological cells, such as the transfer of membrane proteins from cells into artificial bilayers, membrane fusion, and stimulation of cell functions by liposome-reconstituted active species. This has, for example, been

achieved through cationic lipid-mediated migration (Lindner et al. 2006) or through electroinsertion/ electrotransformation (Raffy and Teissie 1997).

Composition, morphology, and phase behavior of phospholipid bilayer membranes are closely interrelated (Mason 1998), and can be controlled by the chemical and physical environment, for example, temperature and solvent composition (Li and Schick 2000). Local domains are formed if lipid bilayer membranes composed of more than one individual lipid component are forced into a multiphase coexistence region of the phase diagram, such as by a change in temperature (Lipowsky and Dimova 2003).

This results in localized patches of membrane material that differ significantly from their surrounding area. Domain formation parameters such as temperature-dependent phase transitions, curvature, and volume-to-area ratio, vesicle tension, and membrane composition are conveniently controlled and modified (Anyarambhatla and Needham 1999) in giant unilamellar vesicles (Bagatooli and Grattan 1999) and in free standing bilayers (Bagatolli 2003) of lipid mixtures. In natural membranes microdomains (rafts) are linked to specific cellular functions, such as cholesterol transport (Fielding and Fielding 1997), endocytosis (Nabi and Le 2003), and signal transduction (Simons and Toomre 2000). Lipids with long straight chains, such as glycosphingolipids, are preferentially incorporated into these microdomains, allowing for tighter packing and somewhat higher order. Therefore, rafts exist as separate, more ordered phases within the assembly of rather poorly ordered lipids.

### 9.2.3 Mechanical Properties of Phospholipid Membranes

A theoretical framework for describing the elastic properties of vesicles has been developed and gradually improved (Evans and Skalak, 1980; Dobereiner et al., 1997). The most important macroscopic property of lipid bilayers is the surface bending elasticity, which is closely related to the overall vesicle shape, the chemical properties of individual phospholipids in the membrane, and the nature of structural phases and their transitions (Evans and Needham, 1987; Needham and Zhelev, 1996).

The total surface free energy  $F$  of a fluid-state membrane is a linear combination of the elastic relations representing bending and stretching integrated over the entire membrane surface:

$$F = \frac{K_a}{2A_0}(A - A_0)^2 + \frac{K_c}{2} \int (c_1 + c_2)^2 dA + \kappa_g \int c_1 c_2 dA - \phi A^* \quad (9.1)$$

The first term represents the area dilation where  $A$  is the area of a stretched membrane,  $A_0$  the area of the unstretched surface, and  $K_a$  is the elastic modulus, typically about 240 mN/m for a lipid bilayer (Evans and Needham, 1987). The second and third terms describe bending deformations where  $k_c$  is the bending modulus with a characteristic value of  $10^{-19}$  J. The two principal curvatures are  $c_1$  and  $c_2$ . The fourth term is the Gaussian curvature contribution, adjusting the bending energy in saddle points on a unit area membrane element with  $k_g$  as the Gaussian bending modulus.

A parameter that strongly affects the surface free energy of membrane structures is adhesion to surfaces. Adhesive behavior is promoted by the attractive potential between the membrane and the surface and is balanced by the elastic energy of the membrane (Seifert and Lipowsky 1990). In the case of an immobilized vesicle, contributes to Equation (9.1) as the effective contact potential and  $A^*$  is the contact area of the adhered part of the membrane.

In addition to the vesicular compartments, lipid nanotubes with a diameter of ~100 nm range are the other important constituent of NVNs. Lipid nanotubes form when a point load is applied to a vesicle (Heinrich et al. 1999), involving first-order shape transitions, where the obtained shape represents a minimum in surface free energy; that is, the surface-to-volume ratio of the structure is optimized. For a membrane part that is pulled away from the planar surface, the minimum surface area is reached when the point of pulling is connected to the surface by an infinitesimally narrow tether. During the process of pulling, the curvature of the membrane increases as the extending membrane part shrinks towards this tether. Eventually, a narrow tube is formed with a radius that is determined by the balance between the membrane surface tension and the bending rigidity, which prevents the collapse of the extended membrane part to an infinitesimally narrow size. Surface tension  $\sigma$  can be introduced to describe the interface between a vesicle and its surrounding environment. A reflection interference microscopy technique to directly estimate the surface tension of adhered vesicles under various conditions was described by Puech and Brochard-Wyart (2004).  $\sigma$  can be employed because only a very small part of the membrane is involved in the tube formation, and therefore the term  $\sigma A$  contributes to the system's free energy the free energy for a (cylindrical) nanotube is:

$$F = \sigma A + \frac{\kappa_c}{2} \int (c_1 + c_2)^2 dA = 2\pi L_{tube} \left( \frac{\kappa_c}{2R_{tube}} + \sigma R_{tube} \right). \quad (9.2)$$

The free energy contribution of the differential stretching is much smaller than the other terms and can be omitted, likewise the Gaussian curvature contribution and the contribution of bilayer surface adhesion. The force required for pulling out a tube is:

$$f = 2\pi \sqrt{2\sigma\kappa_c} \quad (9.3)$$

which is typically on the order of a few pN. Importantly, the (steady-state) radius of a lipid nanotube  $R_{tube}$  is a force balance between lateral membrane tension and curvature energy (Evans and Yeung 1994) and results from minimizing Equation (9.2) with respect to  $R$ :

$$R_{tube}^2 = \frac{\kappa_c}{2\sigma}. \quad (9.4)$$

Because the tube-vesicle system consists of one single continuous membrane, the tube radius can be modulated dynamically in an existing structure by controlling the lateral membrane tension in the vesicle.

#### **9.2.4 Self-Assembly of Vesicular Systems**

Giant unilamellar vesicles (GUVs) with sizes ranging from 5 to 100  $\mu\text{m}$  are intensely studied in diverse areas, focusing on membrane functions such as adhesion, fusion, fission (Luisi and Walde 1999), or generation and properties of nanotubes and network assemblies. A number of methods to create giant vesicles have been reported. One of the methods is based on a dehydration–rehydration procedure described by Criado and Keller (1987). As a variant, the rehydration of thin dried films obtained after evaporation of the solvent from lipid–protein complexes solubilized in organic solvents has been used to produce giant proteoliposomes (Darszon et al. 1980). The advantage of the dehydration/rehydration method is the compatibility with a large range of buffer compositions, specifically with high ionic strength buffers. This method produces, however, a large proportion of multilamellar vesicles related to the uncontrolled rehydration process. This disadvantage has been removed in the electroformation technique Angelova and Dimitrov (1986), in which a lipid film is rehydrated in the presence of an alternating current (AC) electric field, and GUVs with a more homogeneous size distribution around 25  $\mu\text{m}$  in diameter can be generated. Reconstitution of membrane proteins by electroformation is possible only with limitations, given the use of organic solvents, for example, diethyl ether, that are not compatible with amphiphilic membrane proteins.

#### **9.2.5 Membrane Biofunctionalization of Liposomes**

The implementation of complex functions with a focus on the simulation and investigation of cellular reaction mechanisms requires functionalization of the networks, which can be based on functional materials embedded in the membrane, for example, membrane proteins or synthetic multifunctional pores (SMPs; Sorde et al. 2003), or the modification of the vesicle's interior volume, for example, by compartmentalization or internalization of functional polymers.

As depicted in Figure 9.1, membrane functionality is introduced at the membrane self-assembly level by addition of functional entities, whereas modification or exchange of internalized contents is carried out after the formation of the NVN, using membrane-penetrating electroinjection methods.

For example, to enable communication between the interior and exterior of a vesicle–nanotube network, mediation of a chemical signal through the membrane is of special importance. Using membrane proteins (i.e., transporters and channels) as highly selective signal mediators due to inherent molecular recognition and permeability properties, selectivity over the transported chemical species can be achieved. Many membrane proteins also have an additional gating function controlled by membrane potential or specific ligands. Membrane-based devices of this kind can be advantageously used where a series of manipulations has to be performed on an initially extremely small volume containing a signalling molecule or an analyte, for example, in analytical, biosensor, and computational devices. By combining

biological and micromanipulation techniques, a new method for producing NVNs using reconstituted proteins have also been developed. Proteins (i.e., ion transporters) can be introduced to the networks either in their outer membranes or as integrated parts of organelles and/or catalytically active particles, which can be confined in individual containers. Patch clamp measurements confirmed the activity of the proteins in the membrane, and LIF microscopy yielded evidence for mobility of the membrane proteins over an extended network structure (Davidson et al. 2003).

### **9.3 Fabrication, Transformations, and Modifications of Nanotube–Vesicle Networks**

The second level in Figure 9.1 depicts geometries that are available through forced shape transformations and structural self-organization. Several molecular systems such as microemulsions (Hentze et al. 2003; Jang and Yoon 2003), surfactant membranes (Seifert 1997), and some polymer systems (Ghadiri et al. 1993) aggregate or self-organize through noncovalent interactions into micro- and nanoscale structures with predetermined shapes. None of these spontaneous shapes is directly applicable for building nanoscale devices with complex geometries and function.

#### ***9.3.1 Fabrication of Nanotube–Vesicle Networks, Forced Shape Transitions***

We have developed a set of experimental techniques to control geometry, dimensionality, topology, and functionality in surfactant membranes to be directly useful in nanoscale network and device fabrication (Karlsson et al. 2001, 2002a; Sott et al. 2003). In particular, methods based on self-organization, and forced shape transformations using novel micromanipulation tools, have been designed and optimized to form synthetic or semisynthetic enclosed lipid bilayer structures with several properties similar to biological micro- and nanocompartments. These procedures represent unconventional fabrication routes to yield three-dimensional soft-matter devices of different function and geometries at a length scale and flexibility that are difficult to reach with modern clean room technology.

Nanotube-conjugated vesicle networks terminated at the ends by surface-immobilized vesicles are most advantageously formed using a microelectroinjection technique (Karlsson et al. 2001). This method can produce unilamellar (or thin-walled) vesicles (1 to 50  $\mu\text{m}$  in diameter,  $10^{-15}$  to  $10^{-12}$  liters) interconnected by lipid nanotubes ( $\sim 25$  to 300 nm in diameter; Figure 9.2f). Our techniques are generally related to the variety of experimental micromanipulation techniques developed for tether formation (Derenyi et al. 2002), such as pulling with pipettes (Evans and Yeung 1994), optical tweezers (Dai and Sheetz 1999), pulling by hydrodynamic force (Rossier et al. 2003), pulling by action of polymers (Fygenson et al. 1997), and pulling by action of molecular motors (Koster et al. 2003).

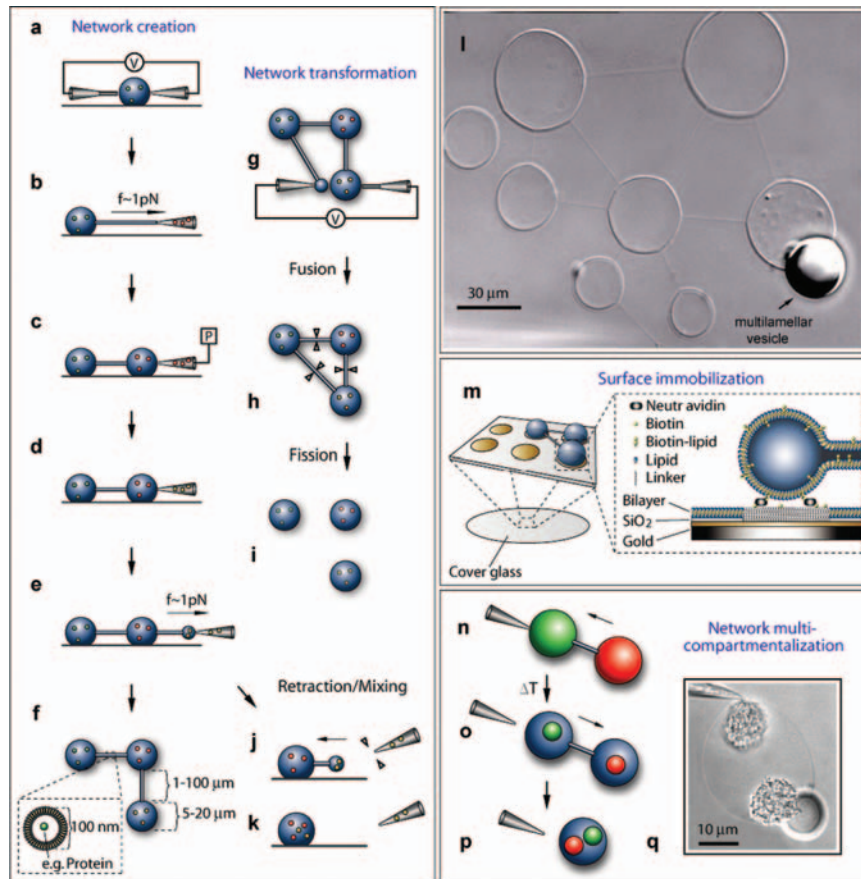


**Figure 9.2** (a)–(f). Schematic representation of micropipette-assisted formation and internal functionalization of networks of vesicles and nanotubes. A micropipette is inserted into a unilamellar vesicle by means of electroinjection (a) using a carbon fiber microelectrode. The pipette is then pulled away forming a lipid nanotube (b). A new vesicle is formed by injecting buffer into the nanotube orifice at the tip of the pipette (c). Repeating this procedure can be used to form networks of vesicles. By exchanging the solution in the pipette during the network formation, the interior contents of the vesicles can be differentiated (d)–(f). Image (f) provides size measures of the individual components (g)–(i): network transformation and fission is depicted, using electrical pulses to fuse vesicles (g) or cut nanotubes (h),(i), as well as contents mixing by formation and subsequent release of a vesicle of different internalized material (j), (k). (l) Nomarski micrograph of a multivesicle network. (m) Patterned surface (having both membraneophilic and membraneophobic parts) used for attaching the network vesicles to specific sites. (n)–(q): Schematic representation of a two-vesicle network (n)–(p) and the micrograph of a vesicle (q) with multiple dynamically created, hydrophobic polymer compartments

To create liposome–lipid nanotube networks, a unilamellar liposome is first penetrated by microelectroinjection of a small, buffer-filled glass pipette (Figure 9.2a). The lipid is then allowed to reseal around the injection tip, which is followed by a retraction of the injection tip away from the liposome. This results in a lipid tube



that is connected between the injection tip and the original liposome (Figure 9.2b). By slowly injecting buffer (tens of femtoliters per second), the nanotube expands at the injection tip, thereby forming a new liposome connected to the original liposome via a lipid nanotube (Figure 9.2c). The required extra lipid material for growth of the liposome ultimately comes from an attached multilamellar liposome (see Figure 9.2l), which flows to the unilamellar liposome and along the nanotube. This flow of lipid is required to alleviate the stress imposed on the bilayer membrane when the membrane is expanded and stretched at the injection tip and the membrane tension is increased. It has been demonstrated that a gradient or difference in membrane tension across a lipid membrane surface drives the lipids to flow from regions of low tension to regions of high tensions, in order to eliminate the tension difference (Karlsson et al. 2002b). When the expanding liposome growing on the injection tip has reached the desired size, it can be adhered to a glass surface and the pipette can be removed (Figure 9.2d). The procedure is repeated until a network of the desired size and complexity is obtained (Figure 9.2e,f).

Additionally, Karlsson et al. demonstrated a micropipette-assisted electrofusion protocol, for formation of networks having complex geometries and higher-order topologies (Karlsson et al. 2002a). Such structures include circular networks as well as fully connected networks with three-dimensional nanotube layers. Fusion of the vesicle containers was stimulated by application of one or several transient rectangular DC-voltage pulses of field strengths between 40-to-80 V/cm and duration of 1-to-4 ms over the micropipette (Figure 9.2g). Alternatively, pulses of the same type applied directly to the nanotubes leads to fission of networks and consequently restructuring of individual vesicles (Figure 9.2h,i). The bright-field micrograph (Figure 9.2l) shows a network resulting from this procedure, consisting of eight unilamellar containers, one multilamellar reservoir vesicle, and nine interconnecting nanotubes. A tenth tube is connected to a micropipette.

Specialized surfaces such as streptavidin-coated gold surfaces can be used to create particular patterns for vesicle adhesion in which the coordinates for individual nodes can be defined with great precision (Sott et al. 2003; Figure 9.2m). Other chemical or physical patterning or surface-treatment techniques can be employed in order to create substrates with differential adhesion characteristics towards lipid material or vesicles, for example, surfaces decorated with biofunctionalized beads (Abdelghani-Jacquín et al. 2002). Moreover, techniques for formation of three-dimensional topographic substrates have been developed (Hurtig et al. 2004).

### ***9.3.2 Complex Network Geometries Caused by Self-Organization***

An important feature of a fluid-state continuum membrane structure is the property of structural self-organization. In the case of nanotube-vesicle networks, surface energy is inhomogeneously distributed due to the extreme difference in curvature (by a factor 10 to 100) between the vesicle containers and the lipid nanotubes. Furthermore, a distance at the vesicle-nanotube interface must separate two or sev-

eral nanotubes emanating from a common vesicle container in order to preserve the geometry of the system (Karlsson et al. 2002a). Otherwise, the tubes will coalesce in order to reduce surface energy of the system, and form a three-way junction that self-organizes by means of the minimum pathway solution of the specific geometry set by the vertex coordinates of the connected containers, eventually leading to a situation when the angle between tubes equals  $120^\circ$ . As displayed in Figure 9.1, level 2, this self-organization capability can be directly exploited to create structured networks of bifurcating lipid nanotubes with the surface-immobilized vesicles arranged at the periphery. It is initiated by mechanical or electromechanical action using micropipettes to merge two nanotubes and is driven by spontaneous minimization of surface free energy. Length and diameter of the participating nanotubes, network connectivity, size, location, and contents of the vesicle containers can be controlled with high precision. Thus, it is possible to create well-defined branching nanometer-scale subdomain networks with controlled geometry and topology within a nanotube-vesicle network. (Lobovkina et al. 2004).

### ***9.3.3 Internal Functionalization, Mixing, and Compartmentalization of Nanotube-Vesicle Networks***

Independently or in addition to a prenetwork membrane functionalization, the internalized volumes of the network can be exchanged or new reactants such as aqueous salt solutions, soluble proteins, or protein-functionalized catalytically active nanoparticles (hard nanospheres, suspensions of nanosized liposomes) can be added to the interiors of vesicles or nanotubes. Unlike the membrane functionalization, which is linked to membrane/vesicle formation (Level 1), this step occurs either at the same time or subsequent to the formation of NVNs (Level 2).

In order to inject controlled amounts of material into surface-adhered giant unilamellar vesicles, the method that is depicted in Figure 9.2a–f can be applied. During the sequential network formation steps, injection needles can be changed after each newly created vesicle; each vesicle will consequentially contain a new material, whereas the interconnecting tubes allow for transport between the vesicles. In principle, this method allows for investigation of complex chemical reactions in ultra-small volumes, for example, of coupled reaction pathways ubiquitous in biological cells, where substrates and products of a reaction in networks of a certain geometry and topology are shuttled between different membrane-bound reaction centers. The nanotube connecting two given containers represents a diffusion pathway for substrates and products between two reaction locations, separated in space. Davidson et al. (2003) demonstrated this concept of particle-mediated reaction confinement by injecting proteoliposomes into separate containers after formation of a surface-immobilized vesicle network. Thus, networks were the internal volume of each vesicle is unique and tightly controllable.

When a solvent A in the injection needle and the medium (solvent B) in the vesicle from which material is extracted through a nanotube are different, mixing of the

two solutions will take place in the growing daughter vesicle. Thus, when the solutes are smaller than the nanotube diameter, they will be carried by the solvent flow. When they are larger, such as, for example, colloidal particles and organelles, they will be retained. The growth of the vesicle generates a Marangoni flow of surfactants in the nanotube which in turn generates a flow of solvent *B* inside the nanotube counterdirectional to the pressure-injected solvent *A*. The volume ratio  $\psi$  between solvent *A* and *B* inside the mixing vesicle depend only on geometrical quantities. In the simplest case it is:

$$\Psi = \frac{V_B}{V_A} = \frac{3a}{2R}, \quad (9.5)$$

where *a* is the nanotube radius and *R* is the vesicle radius. This equation is valid when  $R \gg a$  and assumes plug flow. It is remarkable that the mixing ratio only depends on geometrical quantities. With a tube radius  $a = 100$  nm, and vesicle radius  $R = 3 \mu\text{m}$ , there will be 5% of solvent *B* in the mixing vesicle. Thus, the majority of fluid injected to the growing daughter vesicle comes from the pressure-based injection, and for large vesicle sizes it dominates. When several vesicles are formed sequentially, controlled mixing can occur spanning several orders of magnitude (Davidson et al. 2005).

An alternative retraction/mixing method has been developed by Karlsson et al. (2005) as displayed in Figure 9.2j,k. A vesicle that has been inflated from a nanotube and is still attached to a pipette, can be released by applying an electric pulse through the pipette (Figure 9.2j). The network immediately seeks to minimize its surface energy by retracting the nanotube between the immobilized and the released vesicle. The released vesicle is pulled toward the target vesicle until both merge. The contents mix by diffusion, which at the short length scales in question is a very fast process (Figure 9.2k). This procedure has been successfully used to initiate enzymatic reactions in lipid vesicles (Karlsson et al. 2005).

In contrast to dilute bulk solutions in which enzyme kinetics studies are conducted, the interior of biological cells represents a very dense and crowded environment. In a real cell, even though the concentration of molecular species is usually low (submicromolar range), the combined density of macromolecular components in the cytoplasm can reach high values (200–300 mg protein/ml). Networks of vesicles and nanotubes have the potential to house such an environment, provided macromolecular crowding conditions can be established in a controlled manner. Moreover, the complexity of a cell is very much related to the existence of internal compartments, a feature that is normally absent in vesicular systems. Internal functionalization and compartmentalization of GUV-nanotube networks using hydrogel-forming macromolecular systems has recently been reported (Long et al, 2005; Jesorka et al. 2005a,b). Furthermore, temperature-induced reversible, and therefore easily controllable compartmentalization is achieved using the hydrogel-forming LCST polymer poly(*N*-isopropyl acrylamide) in the internal volume of a network.

In a high ionic strength buffer, an internally formed hydrogel collapses into a hydrophobic compartment that reaches a density which is typical for macromolecular crowding in living cells (Ellis 2001). Such compartmentalization and density control in NVNs is an important prerequisite for the modeling and study of cellular reaction rates and mechanisms. (Figure 9.2 n–p) schematically depicts multicompartmentalization using an internalized water-soluble LCST polymer. A two-vesicle nanotube-interconnected network is constructed (Figure 9.2n); a hydrogel forms and collapses upon heating (Figure 9.2o). Co-injected material that is larger than the pore size of the collapsed gel, for example, nanosized beads or DNA, is trapped inside. Subsequently, both vesicles are allowed to join through tension-driven nanotube retraction (Figure 9.2p), leading to the presence of several hydrophobic sub-compartments of different composition in a single vesicle. Figure 9.2q shows an example of a container with two internal gel compartments created by this procedure.

## 9.4 Single Molecule Applications in Nanotube–Vesicle Networks

### 9.4.1 Mass Transport in Nanotube–Vesicle Networks

In order to take full advantage of lipid nanotube–vesicle networks (NVNs) as systems for performing operations with single molecules, including initiating and controlling chemical reactions, ways to transport materials through the nanotubes are of central importance. There are three fundamental transport mechanisms available (Figure 9.3). The first, Marangoni transport, is based on membrane tension gradients and utilizes the dynamic and fluid character of the bilayer membrane. The second is electrophoresis, a well-established way of moving fluids and solutes in micro- and nanofluidic devices. The third is based on diffusion, which is a very effective means of transport over short distances. Diffusion can be an asset or a limitation and careful experimental design is needed for diffusion to be beneficial. In this section the implementation of these three transport methods in NVNs is discussed.

To be able to track and interrogate single molecules, a sensitive detection technique must be used. Fluorescence is the most common method used for detection of single particles and molecules in NVNs as well as in solid material devices. The choice of detector is related to the size of the structure or network. Fluorescence detection at a fixed point along a nanotube is best performed using an avalanche photodiode (APD) coupled to a confocal microscope (Karlsson et al. 2003; Tokarz et al. 2005). The excitation light is focused into a very small volume ( $\sim 10^{-15} \text{ dm}^3$ ) and the fluorescence is detected from the same volume, as shown in Figure 9.3. The

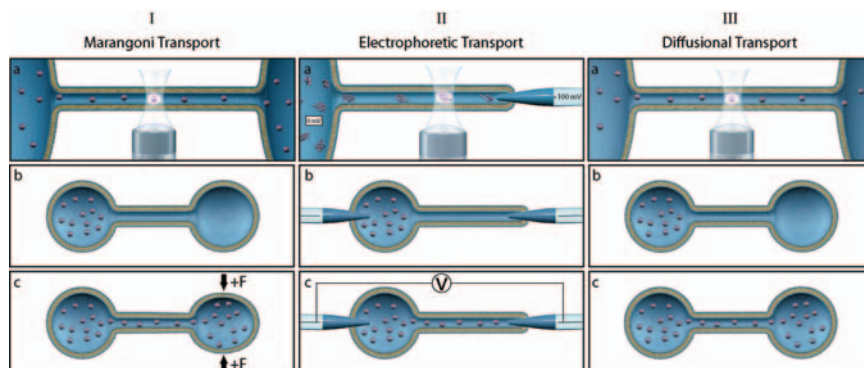


**Figure 9.3** Three different mechanisms for nanotube-mediated transport combined with singlepoint detection along the nanotube. **(I)** Tension-driven lipid flow by Marangoni-flow. **(Ia)** Schematic of a cross-section of two vesicles connected by a lipid nanotube. **(Ib)** Schematic illustrating a network at rest. **(Ic)** Schematic showing Marangoni transport. The right vesicle is deformed, creating a tension gradient in the network. Fluid and particles trapped in the nanotube are transported in the direction of the gradient. **(II)** Electrophoretic transport. **(IIa)** Schematic of a cross-section of a vesicle connected to a pipette via a lipid nanotube. **(IIb-c)** By applying an electric field across the lipid nanotube, charged species, such as DNA, can be made to move through the nanotube. **(III)** Diffusional transport **(IIIa)** Schematic of a cross-section of two vesicles connected by a lipid nanotube. **(IIIb-c)** The diffusional transport driven by the difference in chemical potential between the two vesicles

dimensions of the excitation/detection volume are such that the whole cross-section of the nanotube is illuminated, resulting in a detection efficiency close to unity. APDs have very high quantum yields and are capable of detecting single fluorophores with excellent time resolution as long as care is taken to reduce background fluorescence to a minimum.

For molecule tracking in a vesicle, nanotube, or small NVN, the detector of choice is a back-illuminated electron multiplying charge-coupled device (EMCCD). This device combines excellent sensitivity with high operating speeds, suitable for high-speed imaging of medium-to-large structures. Imaging of large networks requires a confocal scanning microscope, preferably with APD detectors, and a motorized stage for lateral sample movement. The confocal microscope gives good spatial resolution in both two and three dimensions, the APDs give excellent sensitivity, and the motorized stage allows large structures to be scanned. An added advantage of an integrated confocal microscope is the automation that simplifies experiments. The main drawback of confocal scanning microscopy is the low time resolution which makes it unsuitable for tracking requiring high time resolution. It is, however, ideally suited for long-time tracking. In all single-molecule experiments it is vital to reduce background noise which can usually be done with careful sample preparation and experimental design (Dimalanta et al. 2004; McCain et al. 2003; Stevens and Ha 2004).

### 9.4.2 Tension-Controlled (Marangoni) Lipid Flow and Intratubular Liquid Flow in Nanotubes

If there is a tension difference along the interface of a fluid system, this can give rise to a flow (Bloom et al. 1991; Dommersnes et al. 2005; Finkelstein 1987). Interfacial tension-driven flows are generally called Marangoni flows and examples of this flow behavior are spreading of a film on an air–water interface or wetting of a dry solid substrate by a film (de Gennes 1985; Probst 1994). For a film of thickness  $e$ , a shear flow in the direction of the tension gradient is given by:

$$V_x(z) = (z/\eta)(\delta\sigma/\delta x). \quad (9.6)$$

where  $z$  is the coordinate orthogonal to the film surface,  $\eta$  is the viscosity of the film and  $\delta\sigma/\delta x$  is the tension gradient tangential to the film surface. The liquid flux is given by

$$J = \frac{1}{2}(e^2/\eta)(\delta\sigma/\delta x). \quad (9.7)$$

In a bilayer membrane, forces can generate surface tension gradients (Probst 1994) leading to membrane flow. Examples of such forces are fluid convection, temperature gradients, electric fields, laser light, or mechanical forces. If the surface tension is increased at some point in a lipid membrane, it will respond to this perturbation by transporting lipid material from regions of lower tension to the point of higher tension until the tension gradient disappears; that is, the tension is uniform in the whole membrane. Mechanical perturbations, using micropipettes, have been used to locally increase the surface-to-volume ratio in vesicles conjugated by nanotubes (Figure 9.4; Karlsson et al. (2003b, 2001, 2002b)). Another way of inducing tension gradients is to inflate a single vesicle by injecting fluid into it (Davidson et al. 2005; Karlsson et al. 2003c).

Local deformations, that is, deformations of individual vesicles, induce tension gradients in the whole network, which responds by transporting lipid material from all vesicles with low tension toward the perturbed vesicle. Because the liquid within the nanotube is viscously coupled to the lipid membrane of which the nanotube is comprised, it too will be transported in the same direction as the membrane. This fact has been used to transport and detect individual 30 nm fluorescent latex beads in a network (Karlsson et al. 2003b). A network was constructed in which one vesicle was filled with fluorescent beads. Two closely spaced vesicles functioned as anchors for a short stretch of nanotube along which a confocal detection spot was aligned, as shown in Figure 9.5. A fourth vesicle was continuously inflated in order to create a tension gradient in the network thus causing particle transport. At higher concentrations, the fluorescence bursts from beads are more frequent as expected. The burst times are also increased several milliseconds, indicating that cluster formation and simultaneous detection of several beads is possible at high concentrations. The flow velocity can be calculated using the burst time and the radius of the probe volume.

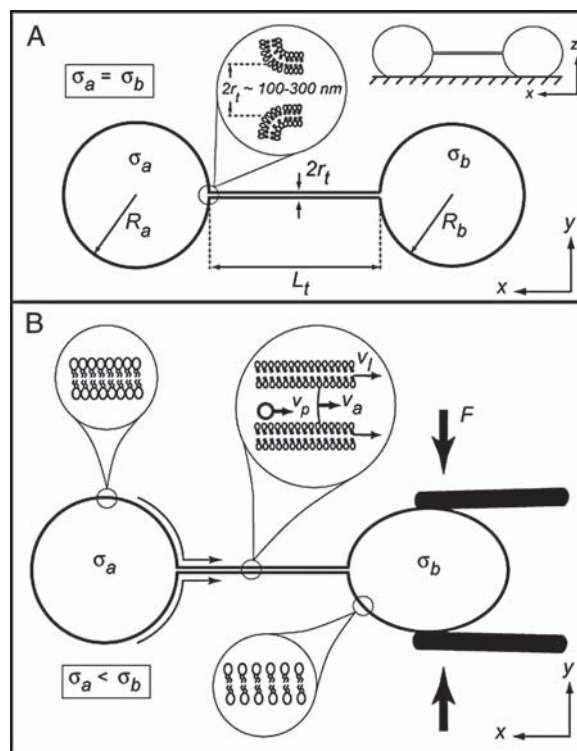


**Figure 9.4** Schematic showing two surface-immobilized unilamellar vesicles, with radius  $R_a$  and  $R_b$ , connected by a nanotube of radius  $r_t$  and length  $L_t$ . The size of the vesicles was typically 5–25  $\mu\text{m}$  in diameter, and the diameter of the nanotube was in the range of 100–300 nm. **(A)** Axial view and sideview (inset), where the surface tension  $\sigma$  in both vesicles is the same and no net lipid flow occurs. **(B)** Lipid flow induced through a deformation of a vesicle (axial view). By applying a force,  $F$ , using two carbon fibers, the surface-to-volume ratio increases and the membrane in the deformed vesicle is stretched, resulting in an increased surface tension. To eliminate this tension gradient, lipid flows from regions of lower tension,  $\sigma_a$ , to regions of higher tension,  $\sigma_b$ , with velocity  $v_l$ . Because the fluid and the particles are dragged along the lipid flow, the lipid velocity in practice sets an upper limit for the velocity of the particles  $v_p$  and the fluid  $v_a$ . Zero or small pressure differences result in flat (pluglike) flow profiles

Figure 9.5E-G shows avalanche photodiode traces (photon counts vs time) with high intensity signals as fluorescent nanoparticles pass through the detector probe volume. Figure 9.5E,F shows two different concentrations of nanoparticles flowing through the tube. The solutions were diluted from a stock solution of 2% solids: (E) diluted 100 times; (F) diluted 1000 times; (G) control experiment with a flow of buffer solution through the nanotube containing no beads.

A theoretical description for Marangoni flow in a simple network (two vesicles connected by a nanotube) has been developed by Dommersnes et al. (2005), and is briefly summarized below.

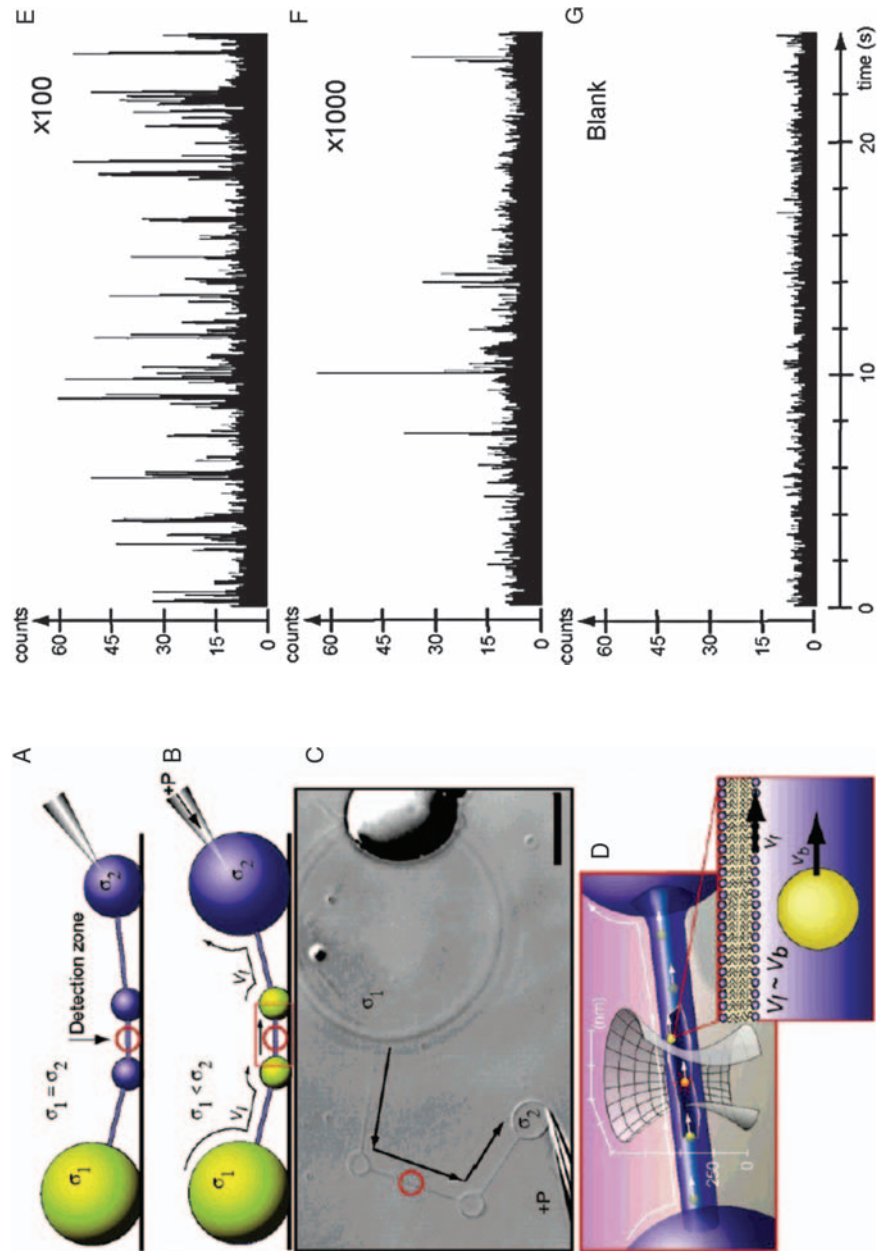




**Figure 9.5** (A) Network consisting of four vesicles interconnected by nanotubes that is used in combination with fluorescence detection. The two small vesicles are included to be able to position the nanotube close to the substrate surface. Fluorescent beads were injected into the system as flow markers. (B) When buffer (same as the surrounding medium) is injected into the vesicle to the right, a lipid flow is created over the system to eliminate the membrane tension difference that arises. The lipid flows from the vesicle to the left, over the two small vesicles and all interconnecting nanotubes. The lipid flow creates a flow of fluid and particles inside the tube through viscous coupling. (C) Normarski image of a four-container network similar to that described in (A) and (B). The injection needle continuously injects buffer into the attached vesicle, thereby creating a lipid flow in the system from the vesicle that is attached to the multilamellar vesicle. The multilamellar part donates lipid into the network on demand when, for example, the membrane tension is increased in a vesicle container in the system. The detection volume is positioned between the two smaller vesicles (red ring), to be able to detect particles that flow inside the nanotube. Scale bar 10  $\mu\text{m}$ . (D) Schematic of part of the vesicle–nanotube system, the nanoparticles that flow inside the tube, and the laser focus used for fluorescence excitation of the fluorescent beads. Due to the restricted geometry of the nanotube the particles pass through the detector probe volume when a lipid flow is created. (E–F) Avalanche photodiode detector (photon counts vs. time) traces with signals of high intensity as the fluorescent particles pass through the detector probe volume. (E) High concentration of nanoparticles (100 times diluted 2% stock solution) (F) Low concentration of nanoparticles (1000 times diluted 2% stock solution) (G) Control experiment without fluorescent beads.

The flux of liquid driven by Marangoni flow is given by

$$J_M \propto \frac{r^3}{\eta} \frac{d\sigma}{dx}, \quad (9.8)$$

where  $r$  is the nanotube radius and  $d\sigma/dx$  is the tension gradient along the nanotube.

Because the tension gradient has been achieved through the deformation of a vesicle, the hydrostatic pressure in that vesicle has increased. The pressure difference between vesicles will thus give rise to a Poiseuille flow given by

$$J_p = \frac{\pi r^4}{8\eta L} \Delta P, \quad (9.9)$$

where  $L$  is the length of the nanotube and  $\Delta P$  is the pressure difference between two vesicles.

For large vesicles, the internal pressure is extremely weak and the Poiseuille flow is dominated by the Marangoni flow. In general the balance between Marangoni and Poiseuille flow can be found from the following approximation,

$$\frac{J_M}{J_p} \propto \frac{R_v}{r} \approx 10^3, \quad (9.10)$$

where  $R_v$  is the vesicle radius. The expression states that as long as the radius of the vesicle is much larger than the nanotube radius, the Marangoni effect will be the dominant contribution to transport in nanotubes

When a tension difference is applied between two vesicles connected by a nanotube, a tension gradient is established very quickly with a relaxation time  $\tau_\sigma \sim 1$  ms. This is associated with stretching out the small variations in lipid density. As this happens the tension gradient increases (Dommersnes et al. 2005). This is a transient state where the radius of the nanotube is unchanged. As the lipid membrane is stretched, the nanotube starts to change shape. This is called the peristaltic mode where fluctuations in tube diameter relax with a relaxation time  $\tau_r$  until the tube reaches the final stationary state as long as the tension gradient is kept constant. The second relaxation time can be thousands of times longer than  $\tau_\sigma$ , meaning that although the tension gradient relaxes very quickly, the tube shape changes slowly.

#### 9.4.2.1 Marangoni Transport in Large Networks

In order to transport material between two selected containers in a complex network without affecting the rest of the network, a two-point perturbation technique needs to be employed where both containers between which transport is to be achieved are manipulated (Karlsson et al. 2003b,c). The membrane tension

in one surface-immobilized liposome (from which material is to be taken) is decreased by donating membrane material to it by injecting vesicles. At the same time, the membrane tension in another surface-immobilized liposome (to which material is to be transported) is increased by a shape deformation using carbon fibers. With the two-point perturbation technique, a tension gradient between two containers can be created that is much larger than gradients between all other connected containers and therefore, the transport preferentially takes place through the nanotube connecting these two containers. This technique makes it possible to use the phenomenon of tension-driven lipid flow in complex networks having many containers with an intricate connectivity, even containing three-way nanotube junctions.

#### 9.4.2.2 Marangoni Transport of Nanotube-Integrated Vesicles

Nanotube-integrated vesicles, also known as pearl-chain liposomes, were described by Bar-Ziv and co-workers (Bar-Ziv and Moses 1994; Bar-Ziv et al. 1998, 1999). These pearling states have been induced in liposomes by optical tweezers or in cells by gradual disruption of the cytoskeleton. Tsafirir et al. (2001) report on a pearling instability caused by anchoring polymers in lipid bilayer vesicles. For vesicle networks, the method for creating nanotube-integrated vesicles has been developed by Karlsson et al. (2003b). In an approach similar to the one described in the previous section, the surface tension is decreased in one of the surface-adhered liposomes, by injecting vesicles, and it is increased in another. In this case, however, large vesicles are added to the network. The change in surface-to-volume ratio of the receiving vesicle is so large that the excess membrane material cannot be accommodated by the vesicle itself, but flows into the nanotube. Membrane material is donated from a donor liposome to the target liposome by coalescence. The sudden addition of excess membrane material results in an expanded tube diameter. Approximately tenfold (from 0.2  $\mu\text{m}$  to 2  $\mu\text{m}$ ) expansion is observed at the point of maximum expansion.

As the tension equilibrates across the entire network, micrometer-sized vesicles are created on the nanotube. Note that these are not a result of Rayleigh instabilities, which are created at high tensions, but formed as a result of a drop in tension. These nanotube-integrated vesicles are mobile and can be transported by applying tension gradients, analogous to the previously described methodology, between the two surface-adhered liposomes. Upon arrival they merge with the immobilized vesicle and release their contents. This means that material, contained within small vesicles, is transported from the surface-adhered liposome where the small vesicles originate, along the lipid nanotube, to a neighboring surface-adhered liposome with which they merge. Each vesicle moves femtoliter to picoliter volumes ( $10^{-15}$  to  $10^{-12}$  liters), much larger than those moved by intratubular transport. Using this method it is possible to achieve an extraordinary level of control of transport and mixing of small volumes in confined geometries (Karlsson et al. 2003b,c).

### 9.4.2.3 Marangoni Transport of Nanotube Knots

Entanglements and trefoil knots on surfactant nanotubes can be produced by a combination of network self-organization, and advanced micromanipulation (Lobovkina et al. 2004). The resulting knots are self-tightening, and the tightening is driven by minimization of surface free energy of the lipid membrane. The knots always tighten to a size approximately  $R = 1.3r$ , where  $R$  is the knot radius (approximated as a torus) and  $r$  is the nanotube radius. This is valid for any curvature modulus and tension, with the result that the knots are always tight and have a size comparable to that of the nanotube. Knots formed by self-organization can be moved back and forth along a nanotube by using a surface tension gradient created by vesicle deformation, as shown in the previous sections. Using the knots, high-aspect-ratio nanometer- and micrometer-sized objects, such as other nanotubes, can be trapped and manipulated along a predetermined trajectory defined by the nanotube axis.

### 9.4.3 Electrophoretic Transport

Standard capillary electrophoresis (CE) is performed in narrow-bore fused-silica capillaries, with a typical inner diameter of 25–75  $\mu\text{m}$ , and capillary lengths of tens of centimeters (Beale 1998). It is a technique for analyzing relatively large sample volumes, typically several nanoliters. Downsizing the separation channels by various microfabrication methods, combined with sensitive detection schemes, has led to chip-based devices, using electrophoretic transport, capable of analyzing picoliter volumes and detecting single molecules (Chou et al. 1999; Filippova et al. 2003; Lyon and Nie 1997). Extremely narrow channels (10  $\times$  50 nm) have been fabricated in silicon by Cao and co-workers (Cao et al. 2002), in which double-stranded DNA molecules are forced to stretch by the confinement of the channels.

Generating high electric fields in fused-silica capillaries several tens of centimeters in length, or in microfabricated channels several centimeters in length, is trivial and requires only a high-power voltage source and, ideally, high-quality platinum electrodes. Working with liposome networks, where distances between containers are typically in the micrometer range, the application of electric fields requires a different approach. There are two main problems to overcome: controlled field strength over a very short distance and the need for ultra-small electrodes. The technique described below has been developed by Tokarz and co-workers (Tokarz et al. 2005).

As only small ( $\sim 100$  mV) voltages need to be applied in order to reach field strengths on the order of  $\sim 10$  V/cm, the voltage drop at the electrode surface becomes of paramount importance. At low voltages, the electrode surfaces will become charged and the ions in solution will form an electric double layer in order to neutralize the charge. Consequently, the field strength will be zero only a few nanometers away from the electrode surfaces. Using Ag/AgCl electrodes, the electric charge can be driven through the solution with negligible potential loss.

Addressing the size of the electrodes, micropipettes with inserted Ag/AgCl electrodes are used. The chloride ions needed for the electrochemical reactions are included in the buffer in the pipettes. In order to suppress electro-osmotically driven volume flow through the pipette tips, the surface of the pipettes is modified with hexamethyl disilazane (HMDS), a hydrophobic agent, and the pipette tips are capped with 20% cross-linked acrylamide gel, polymerized in situ.

These pipettes are inserted into liposomes using electroporation (Karlsson et al. 2000). As with the electroinjection protocol, the membrane pore closes over the electrode and forms a high electrical resistance seal. Subsequently, one of the electrodes is withdrawn from the liposome, pulling a tube. Both the electrodes and the membrane seals have electric resistances, which can be measured accurately with patch-clamp amplifiers. The resistance of the lipid nanotube can be calculated from buffer conductivity and tube geometry. Knowing these resistances, it is possible to calculate the electric field inside the nanotube (Figure 9.6).

A positive potential is applied at the pipette holding the nanotube and the lipid membrane is pulled by the electric field towards this electrode. The moving membrane causes the liquid inside the tube to move along with it. However, because an electric field is also applied inside the tube, the resulting electro-osmotic flow counters this movement to a very large degree. In fact, there is only a ~10% velocity difference between the membrane wall movement and the electro-osmotic flow, resulting in a velocity profile across the nanotube, dominated by the electro-osmotic flow close to the walls and by the Poiseuille flow in the middle of the tube. In a closed network there is, however, no net liquid flow.

This technique, in conjunction with confocal microscopy and single-molecule fluorescence detection using APDs, has been used to transport and detect large (5.4–166 kbp) double-stranded DNA molecules with a detection efficiency close to unity. The size-dependence of the DNA conformation inside the nanotube can be elucidated from the fluorescence bursts originating from the individual DNA molecules as they are detected during transport (Tokarz et al. (2005); Figure 9.7a). Three parameters were extracted from the electropherograms: the maximum fluorescence signal detected from each DNA molecule (peak intensity  $I_p$ ), the duration of the peak (transit time  $\Delta t$ ), and the integrated fluorescence intensity (peak area  $A_p$ ). The average parameter values for each DNA size are plotted in Figure 9.7b–d.

The fact that the average peak area increases linearly with increasing DNA size is consistent with a strong confinement inside the nanotube because it ensures that the entire molecule passes through the detection volume. This is an important result, because it demonstrates that the system is capable of single-file transport and counting of DNA molecules. Notably, the average peak intensity is observed to increase linearly with DNA size as well. Finally, the transit time also exhibits a linear dependence on DNA size, but in this case with an intercept with the ordinate axis at  $t_0 = 20.0$  ms. This corresponds to the transit time for a small DNA molecule across the finite detection volume (0.8  $\mu\text{m}$  in diameter), yielding a velocity of 40  $\mu\text{m/s}$  toward the positive electrode. From these parameters it is possible to characterize the electrophoretic system and to interrogate the conformation of the DNA molecules during transport.

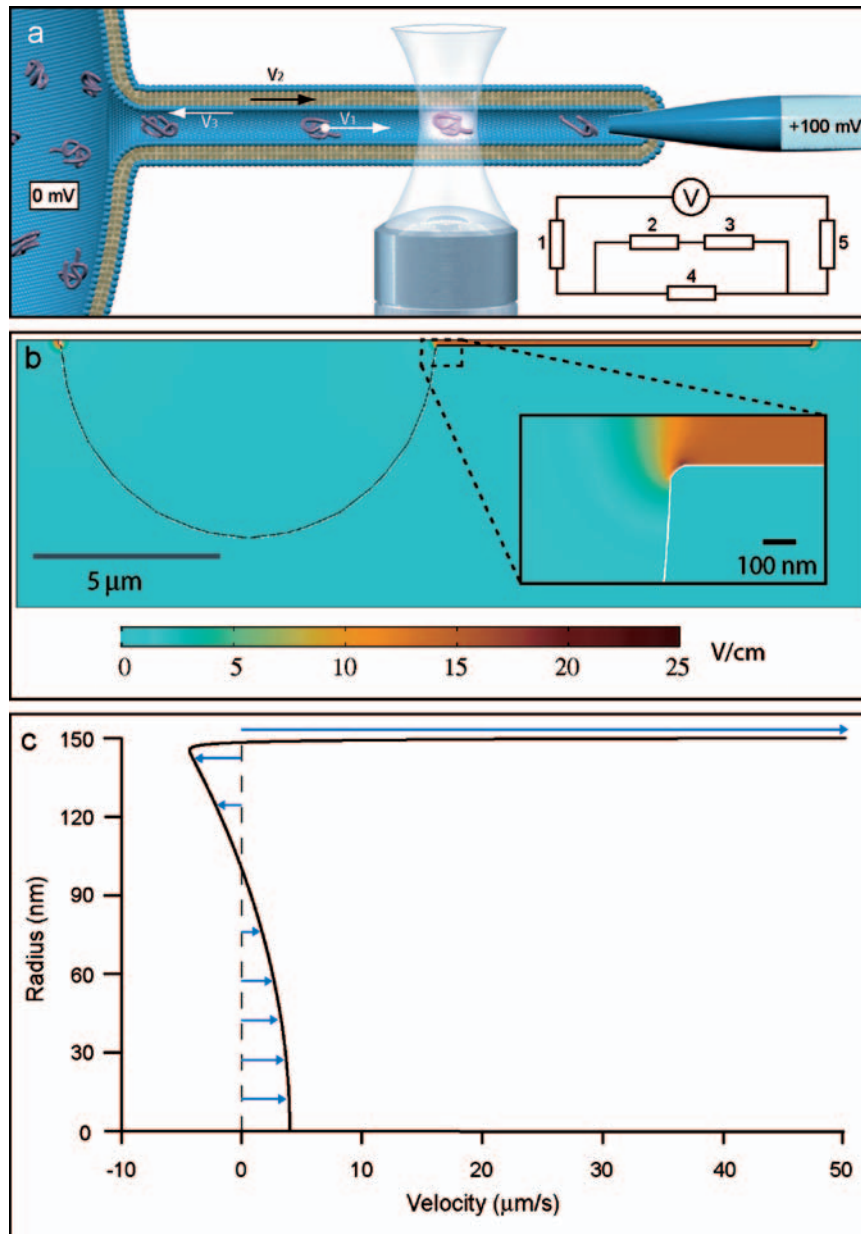


**Figure 9.6** Schematic describing the geometry of the NVN system and fluorescence detection used in the experiments, simulations of the field distribution and flow profile. **(a)** Schematic picture of the NVN. The nanotube is aligned across the confocal excitation/detection spot of the confocal microscopy setup and an electric potential is applied between the electrodes, with the nanotube-coupled electrode having positive potential. The fluorescence signal from the DNA molecules is detected as they pass the excitation/detection spot.  $V_1$  is the velocity of the DNA molecules,  $V_2$  is

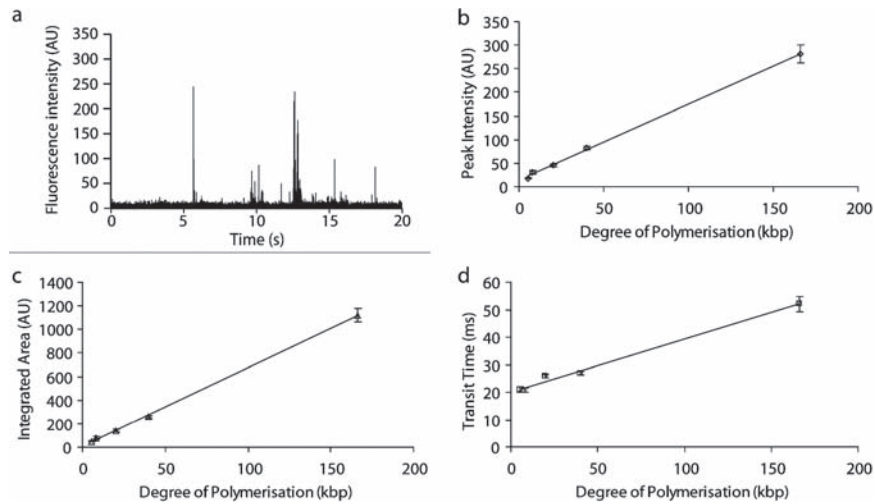


**Figure 9.7** Example of electrophoretic DNA transport and plots of peak parameters for different DNA sizes. (a) Time trace of T7 DNA transport. The DNA molecules were transported through  $40\ \mu\text{m}$  long lipid membrane nanotubes, and detected at its midpoint. The effective field strength was  $\sim 15\ \text{V}/\text{cm}$  in all experiments. Mean values of (b) peak intensity ( $I_p$ ), (c) integrated peak area ( $A_i$ ) and (d) transit time ( $\Delta t$ ) versus DNA size (number of base pairs). Error bars correspond to the standard error. Where the error bars are not clearly visible, they are equal to or smaller than the data points

A theoretical description of semi-flexible polymers, such as DNA, in soft tubes has been proposed by Brochard-Wyart et al. (2005). They predict that small polymers will be squeezed by the tube into an elongated shape that can be described by the blob model (de Gennes 1979), but if a polymer is large enough it will deform the tube and retain a globulelike conformation. The coil is spherical in shape, but compacted compared with the unconfined polymer coil because of forces arising from the wall of the expanded tube. Given the membrane tension in the NVNs, Brochard-Wyart et al. predict that the transition from the blob behavior in an unperturbed nanotube to the compressed globule in an expanded tube occurs for a polymer size of  $\sim 150$  persistence lengths. The experimental results of Tokarz et al., described above, support this theory.

**Figure 9.6** (continued) the velocity of the membrane, and  $V_3$  is the velocity of the electro-osmotic flow. Because  $V_2$  and  $V_3$  cancel each other out, no net liquid flow occurs in the nanotube. The inset shows the equivalence circuit of the electrophoretic system; 1 and 5 represent the electrode resistance ( $\sim 50\ \text{M}\Omega$ ), 2 and 3 represent the vesicle–electrode seal resistance ( $\sim 50\ \text{M}\Omega$ ) and the nanotube–electrode seal resistance ( $\sim 100\ \text{M}\Omega$ ). 4 represents the nanotube resistance ( $> 1\ \text{G}\Omega$ ), calculated from the buffer conductivity ( $0.5\ \text{S}/\text{m}$ ) and the nanotube dimensions ( $L = 40\ \mu\text{m}$  and  $R = 150\ \text{nm}$ ). Evaluation of the equivalence circuit gives a potential drop of  $60\ \text{mV}$  over the nanotube. (b) Field strength distribution inside and outside the NVN, modeled with the finite element method program FEMLAB 3.0. (c) Flow profile of axial velocity inside nanotube, drawn from the nanotube center line to the membrane surface

#### 9.4.4 Diffusive Transport

Diffusion of molecules in micro- and nanofluidic systems can be an advantage or a handicap. It may be desirable to mix several species in a channel or chamber or avoid diffusive mixing between separate compartments. It is therefore important to be aware of the time scale on which diffusive mixing as well as diffusive transport occurs. The mixing time of molecules in any volume can be given as

$$t_{mix} = \frac{L^2}{D}, \quad (9.11)$$

where  $L$  is the linear size of the volume and  $D$  is the diffusion coefficient (Stange et al. 1998). The molecules will mix more slowly if they are large (proteins and DNA) compared with small molecules because of the effect of size on the diffusion coefficient. Similarly, slower mixing will occur in a large volume than in a small. Thus, care should be taken when designing micro- and nanofluidic systems where mixing of fluids is desirable.

For a common case of two chambers filled with different solutions and connected with a channel, one must consider the time it takes for molecules from each chamber to move to the other. The driving force for concentration equilibration is the chemical potential difference between the two chambers. Dagdug and co-workers considered how the concentration difference between two chambers connected with a cylindrical tube changes with time (Dagdug et al. 2003). The concentration decays exponentially, with a characteristic relaxation time

$$\tau_{relax} = \frac{L_{tube}}{\pi D R_{tube}^2} \times \frac{V_1 V_2}{V_1 + V_2}, \quad (9.12)$$

where  $L_{tube}$  is the length of the tube connecting the containers,  $R_{tube}$  is its the radius, and  $V_1$  and  $V_2$  are the volumes of the containers. In this case, not only the tube length but also its size profoundly affects the characteristic relaxation time. This process is very slow in a typical microfluidic device, with relaxation times ranging from days to years for a molecule with  $D \sim 10^{-11}$  m<sup>2</sup>/s (such as a protein). In nanofluidic devices, with narrow channels and small chambers, this time is on the order of hours. These time scales should be considered when designing fluidic devices and can readily be used to predict the behavior of different designs, allowing quantitative comparison.

##### 9.4.4.1 Diffusion in NVNs

In the nanotube vesicle networks, diffusion is an important factor governing the movement of molecules. The contents of vesicles can be initially differentiated, thus the chemical potential in each container can be set, but this state lasts only



for a limited time span. In complex networks, composed of many containers of different sizes and lipid nanotubes of different length and connectivity, the time-dependent concentration variation of molecular species in each separate container is not trivial to predict. However, one can derive a closed set of equations that describe how the number of particles in each vesicle evolves over time as described by Lizana and Konkoli (2005). The problem is solved numerically based on the geometry of the network, its connectivity, and the bulk diffusion coefficients of the molecular species. By varying the initial conditions it is possible to induce wavelike concentration behavior, with concentration maxima and minima, in selected vesicles. This approach has been exploited in reaction–diffusion networks, in which it is possible to predict the time-dependent concentration changes of several species—enzyme(s), substrate(s), and product(s)—in each container in the network. Sott and coworkers performed experiments in which an enzyme is diffusing through linear and branched networks filled with substrate. As the enzyme diffuses into consecutive vesicles the substrate is consumed and a fluorescent product is formed and detected (Figure 9.8A–D). The dynamics of enzyme diffusion can be controlled by geometry and initial conditions. The diffusion is slowed by longer nanotubes (Figure 9.8E–H) as well as by the presence of vesicles along the path (Figure 9.8 I–L). The experimental results coincide very well with the theoretical description (Karlsson et al. 2005).

#### 9.4.4.2 Diffusion in Membranes

Diffusion is of course also present in the lipid membrane inasmuch as it is effectively a two-dimensional fluid. Davidson and co-workers reconstituted membrane proteins in soybean lipid vesicles (Davidson et al. 2003). The membrane protein functionality was preserved in the lipid membrane. The liposomes were used to build both simple and complex networks and protein diffusion in the membrane was confirmed using fluorescence recovery after photobleaching (FRAP). The proteins were fluorescently labeled and one part of the network was bleached using an Ar<sup>+</sup> laser. After some time, the unbleached protein diffused along the nanotube to the bleached vesicle (Figure 9.9).

It is possible to control the diffusion of molecules by attaching them to structures that are too large to move through the channels connecting the containers in a network. Biomolecules (DNA and proteins) have been attached to particles (Karhanek et al. 2005; Wolf et al. 2004) or lipid vesicles (Alfonta et al. 2001; Jung et al. 2000; Yegneswaran et al. 2003) with preserved functionality. Membrane proteins can be embedded into vesicles (Davidson et al. 2003; Kahya et al. 2001, 2003), which subsequently can be sized in such a way that vesicles smaller than the channels function as carriers and large vesicles are localized to selected chambers. This approach can be used to create well-defined reaction chambers into which reactants can be introduced by diffusion or other forms of transport and then moved away for detection, collection or to other reaction sites.

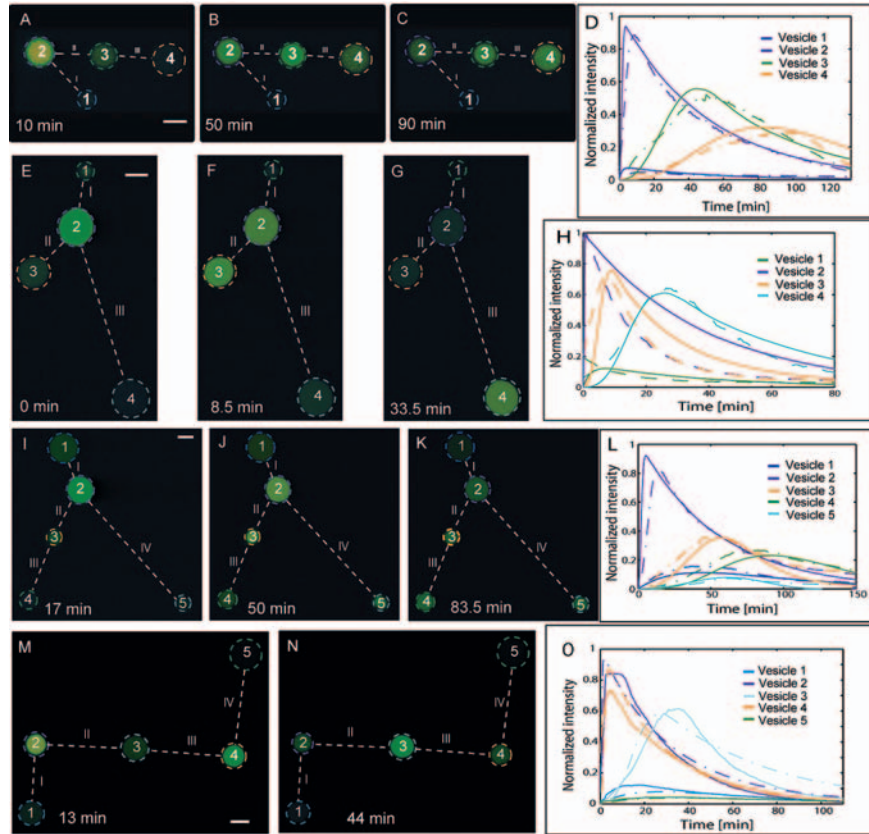


**Figure 9.8** Fluorescence microscopy images (A–C, E–G, I–K, M, and N) showing product formation in networks with different geometries. Graphs D, H, L, and O show the normalized fluorescence intensities of the corresponding measurements plotted versus time. Initially, the enzyme-filled vesicles are vesicle 1 in panels A–C, E–G, and I–K, and vesicles 1 and 5 in M–N. The rest of the vesicles are filled with substrate. The dash-dotted lines in graphs D, H, L, and O show the theoretical fit to the experimentally measured product formation. Fluorescence images were digitally edited to improve image quality. The scale bar represents 10  $\mu\text{m}$

## 9.5 Summary

Networks of phospholipid nanotubes, and giant unilamellar vesicles represent novel model systems for studies of transport phenomena in ultrasmall volumes, especially in a biomimetic environment. The unique soft matter properties of the phospholipid materials, allow for novel bottom-up fabrication methods that enable the controlled construction of complex container–nanotube assemblies. Several means of membrane functionalization, direct internalization, and manipulation of materials including (bio-)polymers such as poly-isopropylacrylamide or DNA were

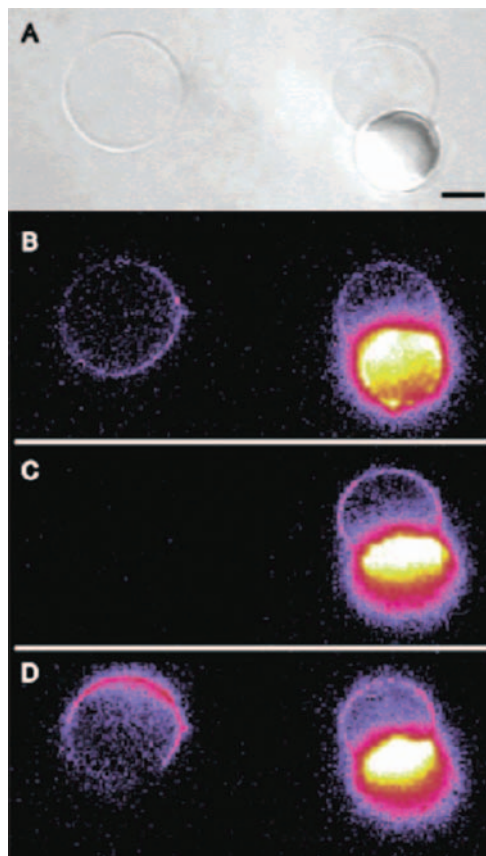


**Figure 9.9** Membrane protein in a vesicle network diffuses freely between containers connected by a lipid nanotube. (A) Brightfield image of the network. (B) EMA-labeled AE1 distribution after the formation of the network was homogeneous. (C) AE1-associated EMA was bleached in the left vesicle and was recovered, (D) after diffusion of EMA-labeled AE1 from the right vesicle via the nanotube. The fluorescence images were intensity-indexed for clarity. Scale bar is 5  $\mu\text{m}$

established, leading to a complex, highly versatile biomimetic chemical reactor model. Active and passive transport of submicron particles and biomacromolecules through nanotubes in such networks could be demonstrated, including electrophoretic transport and detection of single DNA molecules. The insights into biological and biophysical principles gained from these studies lead to better understanding of cellular transport and reaction phenomena, for example, macromolecular crowding phenomena or the function of natural and artificial ion channels on the single molecule level, and can be expected to lead to entirely new nanoscale fabrication technologies that can generate functional biomimetic devices of very high complexity. Furthermore, the functions and properties of naturally occurring nanotubes and their functions in biological systems are now intensively studied (Iglıc et al.

2003; Koster et al. 2005; Onfelt et al. 2004; Onfelt et al. 2005; Rustom et al. 2004), and it can be expected that hybrid devices with membrane nanotubes interconnecting vesicles and living cells will eventually lead to new insights into natural transport and reaction phenomena.

## References

- Abdelghani-Jacquin C, Abdelghani A, Kantlehner M, Sackmann E (2002) Decorated surfaces by biofunctionalized gold beads: Application to cell adhesion studies. *Eur. Biophys. J.* 2:102–110.
- Ajouz B, Berrier C, Besnard M, Martinac B, Ghazi A (2000) Contributions of the different extramembranous domains of the mechanosensitive ion channel MscL to its response to membrane tension. *J. Biol. Chem.* 275:1015–1022.
- Alfonta L, Singh AK, Willner I (2001) Liposomes labeled with biotin and horseradish peroxidase: A probe for the enhanced amplification of antigen-antibody or oligonucleotide-DNA sensing processes by the precipitation of an insoluble product on electrodes. *Anal. Chem.* 73(1): 91–102.
- Angelova M I, Dimitrov DS (1986) Liposome electroformation. *Faraday Discuss.* 81:303–311.
- Anyarambhatla GR, Needham DJ (1999) Enhancement of the phase transition permeability of DPPC liposomes by incorporation of MPPC: A new temperature-sensitive liposome for use with mild hyperthermia. *J. Liposome Res.* 9: 491–506.
- Bagatolli LA (2003) Direct observation of lipid domains in free standing bilayers: From simple to complex lipid mixtures. *Chem. Phys. Lipids* 122:137–145.
- Bagatolli LA, Gratton E (1999) Two-photon fluorescence microscopy observation of shape changes at the phase transition in phospholipid giant unilamellar vesicles. *Biophys. J.* 77(4):2090–2101.
- Barauskas J, Johnsson M, Tiberg F (2005): Self-assembled lipid superstructures: Beyond vesicles and liposomes. *Nano Lett.* 5:1615–9.
- Bar-Ziv R, Moses E (1994) Instability and “pearling” states produced in tubular membranes by competition of curvature and tension. *Phys. Rev. Lett.* 73(10): 1392–1395.
- Bar-Ziv R, Moses E, Nelson P (1998) Dynamic excitations in membranes induced by optical tweezers. *Biophys. J.* 75(1): 294–320.
- Bar-Ziv R, Tlusty T, Moses E, Safran SA, Bershadsky A (1999) Pearling in cells: A clue to understanding cell shape. *Proc. Natl. Acad. Sci. USA* 96(18): 10140–10145.
- Beale, SC (1998) Capillary electrophoresis. *Anal. Chem.* 70(12): 279r–300r.
- Bloom, M, Evans, E, Mouritsen, OG (1991) Physical-properties of the fluid lipid-bilayer component of cell-membranes - a perspective. *Q. Rev. Biophys.* 24(3): 293–397.
- Brochard-Wyart, F, Tanaka, T, Borghi, N, de Gennes, PG (2005) Semiflexible polymers confined in soft tubes. *Langmuir* 21(9): 4144–4148.
- Cao, H, Yu, ZN, Wang, J, Tegenfeldt, JO, Austin, RH, Chen, E, Wu, W, Chou, SY (2002) Fabrication of 10 nm enclosed nanofluidic channels. *Appl. Phys. Lett.* 81(1): 174–176.
- Chou, HP, Spence, C, Scherer, A, Quake, S (1999) A microfabricated device for sizing and sorting DNA molecules. *Proc. Natl. Acad. Sci. USA* 96(1): 11–13.
- Costello RF, Peterson IP, Heptinstall J, Byrne NG, Miller LS (1998) A robust gel-bilayer channel biosensor. *Adv. Mater. Opt. Electr.* 8 (2): 47–52.
- Criado M, Keller BU (1987) A membrane-fusion strategy for single-channel recordings of membranes usually non-accessible to patch-clamp pipette electrodes. *FEBS Lett.* 224(1): 172–176.
- Dagdug, L, Berezhkovskii, AM, Shvartsman, SY, Weiss, GH (2003) Equilibration in two chambers connected by a capillary. *J. Chem. Phys.* 119(23): 12473–12478.
- Dai J, Sheetz MP (1999). Membrane tether formation from blebbing cells. *Biophys. J.* 77(6): 3363–70.
- Davidson M, Dommersnes P, Markstrom M, Joanny JF, Karlsson M, Orwar O (2005) Fluid mixing in growing microscale vesicles conjugated by surfactant nanotubes. *J. Am. Chem. Soc.* 127(4): 1251–1257.

- Davidson M, Karlsson M, Sinclair J, Sott K, Orwar O (2003) Nanotube-vesicle networks with functionalized membranes and interiors. *J. Am. Chem. Soc.* 125(2): 374–378.
- Darszon A, Vandenberg CA, Schonfeld M, Ellisman MH, Spitzer NC, Montal M (1980) Reassembly of Protein-Lipid Complexes into Large Bilayer Vesicles - Perspectives for Membrane Reconstitution. *Proc. Natl. Acad. Sci. USA* 77(1): 239–243.
- De Gennes P-G (1979) *Scaling Concepts in Polymer Physics*, Ithaca, NY: Cornell University Press.
- De Gennes P-G (1985) Wetting-statics and dynamics. *Rev. Mod. Phys.* 57(3): 827–863.
- Derenyi I, Jülicher F, Prost J (2002) Formation and interaction of membrane tubes. *Phys. Rev. Lett.* 88(23): 238101-1–238101-4.
- Dhoot NO, Wheatley MA (2003) Microencapsulated liposomes in controlled drug delivery: Strategies to modulate drug release and eliminate the burst effect. *J. Pharm. Sci.* 92(3): 679–689.
- Dimalanta ET, Lim A, Runnheim R, Lamers C, Churas C, Forrest DK, de Pablo JJ, Graham MD, Coppersmith SN, Goldstein S, Schwartz DC (2004) A microfluidic system for large DNA molecule arrays. *Anal. Chem.* 76(18): 5293–5301.
- Dobereiner HG, Evans E, Kraus M, Seifert U, Wortis M (1997) Mapping vesicle shapes into the phase diagram: A comparison of experiment and theory. *Phys. Rev. E* 55:4458–4474.
- Dommersnes PG, Orwar O, Brochard-Wyart F, Joanny JF (2005) Marangoni transport in lipid nanotubes. *Europhys. Lett.* 70(2): 271–277.
- Ellis RJ (2001) Macromolecular crowding: Obvious but underappreciated. *Trends Biochem. Sci.* 26(10): 597–604.
- Evans E, Needham D (1987) Physical properties of surfactant bilayer membranes: Thermal transitions, elasticity, rigidity, cohesion, and colloidal interactions. *J. Phys. Chem.* 91: 4219–4228.
- Evans E, Skalak R (1980) *Mechanics and Thermodynamics of Biomembranes*. Boca Raton, FL: CRC Press.
- Evans E, Yeung A. (1994) Hidden dynamics in rapid changes of bilayer shape. *Chem. Phys. Lipids.* 73(1–2): 39–56.
- Fielding C J, Fielding PE (1997) Intracellular cholesterol transport. *J. Lipid Res.* 38(8): 1503–1521.
- Filippova EM, Monteleone DC, Trunk JG, Sutherland BM, Quake SR, Sutherland JC (2003) Quantifying double-strand breaks and clustered damages in DNA by single-molecule laser fluorescence sizing. *Biophys. J.* 84(2): 1281–1290.
- Finkelstein A (1987) *Water Movement Through Lipid Bilayers, Pores, and Plasma Membranes: Theory and Reality*. New York: John Wiley and Sons.
- Fromherz P, Kiessling V, Kottig K, Zeck G (1999) Membrane-transistor with giant lipid vesicle touching a silicon chip. *Appl. Phys. A* 69: 571–576.
- Fygenson DK, Elbaum M, Shraiman B, Libchaber A (1997) Microtubules and vesicles under controlled tension. *Phys. Rev. E* 55: 850–859.
- Ghadiri MR, Granja JR, Milligan RA, McRee DE, Khazanovich N (1993) Self-assembling organic nanotubes based on a cyclic peptide architecture. *Nature* 366:324–327.
- Groves JT, Dustin ML (2003) Supported planar bilayers in studies on immune cell adhesion and communication. *J. Immunol. Meth.* 278: 19–32.
- Hamley IW (2005) Nanoshells and nanotubes from block copolymers. *Soft Matter* 1: 36–43.
- Hall AJ, Emgenbroich M, Sellergren B (2005) Imprinted polymers. Templates in chemistry II; *Top. Cur. Chem.* 249: 317–349.
- Heinrich V, Bozic B, Svetina S, Zeks B (1999) Vesicle deformation by an axial load: From elongated shapes to tethered vesicles. *Biophys. J.* 76(4): 2056–2071.
- Hentze H, Co CC, McKelvey CA, Kaler EW (2003) Templating vesicles, microemulsions, and lyotropic mesophases by organic polymerization processes. *Top. Curr. Chem.* 226: 197–223.
- Hentze HP, Kaler EW (2003) Polymerization of and within self-organized media. *Curr. Opin. Colloid Int. Sci.* 8:164–78.
- Houser H. (1993) Phospholipid vesicles. *Phospholipids Handb.* 603–637.
- Hurtig J, Karlsson M, Orwar O (2004) Topographic SU-8 substrates for immobilization of three-dimensional nanotube vesicle networks. *Langmuir* 20(13): 5637–5641.

- Iglic A, Hagerstrand H, Bobrowska-Hagerstrand M, Arrigler V, Kraij-Iglic V (2003) Possible role of phospholipid nanotubes in directed transport of membrane vesicles. *Phys. Lett. A* 310 (5–6): 493–497.
- Jang J, Yoon H. 2003. Facile fabrication of polypyrrole nanotubes using reverse microemulsion polymerization. *Chem. Comm.* 6:720–721.
- Jesorka A., Markstrom M., Karlsson M., Orwar O (2005a) Controlled hydrogel formation in the internal compartment of giant unilamellar vesicles. *J. Phys. Chem. B* 109(31): 14759–14763.
- Jesorka A., Markstrom M., Orwar O (2005b) Controlling the internal structure of giant unilamellar vesicles by means of reversible temperature dependent sol-gel transition of pnternalized poly(*N*-isopropyl acrylamide). *Langmuir* 21(4): 1230–1237.
- Jung LS, Shumaker-Parry JS, Campbell CT, Yee SS, Gelb MH (2000) Quantification of tight binding to surface-immobilized phospholipid vesicles using surface plasmon resonance: Binding constant of phospholipase A(2). *J. Am. Chem. Soc.* 122(17): 4177–4184.
- Kahya N, Pecheur EI, de Boeij WP, Wiersma DA, Hoekstra D (2001) Reconstitution of membrane proteins into giant unilamellar vesicles via peptide-induced fusion. *Biophys. J.* 81(3): 1464–1474.
- Kahya N, Scherfeld D, Bacia K, Poolman B, Schwille P (2003) Probing lipid mobility of raft-exhibiting model membranes by fluorescence correlation spectroscopy. *J. Biol. Chem.* 278(30): 28109–28115.
- Karhanek M, Kemp JT, Pourmand N, Davis RW, Webb CD (2005) Single DNA molecule detection using nanopipets and nanoparticles. *Nano Lett.* 5(2): 403–407.
- Karlsson A, Karlsson M, Karlsson R, Sott K, Lundqvist A, Tokarz M, Orwar O (2003a) Nanofluidic networks based on surfactant membrane technology. *Anal. Chem.* 75(11): 2529–2537.
- Karlsson A, Karlsson R, Karlsson M, Cans AS, Stromberg A, Ryttsen F, Orwar O (2001) Molecular engineering - Networks of nanotubes and containers. *Nature* 409(6817): 150–152.
- Karlsson A, Sott K, Markstrom M, Davidson M, Konkoli Z, Orwar O (2005) Controlled initiation of enzymatic reactions in micrometer-sized biomimetic compartments. *J. Phys. Chem. B* 109(4): 1609–1617.
- Karlsson M, Davidson M, Karlsson R, Karlsson A, Bergenholtz J, Konkoli Z, Jesorka A, Lobovkina T, Hurtig J, Voinova M, Orwar O (2004) Biomimetic nanoscale reactors and networks. *Ann. Rev. Phys. Chem.* 55: 613–649.
- Karlsson M, Nolkranz K, Davidson MJ, Stromberg A, Ryttsen F, Akerman B, Orwar O (2000) Electroinjection of colloid particles and biopolymers into single unilamellar liposomes and cells for bioanalytical applications. *Anal. Chem.* 72(23): 5857–5862.
- Karlsson M, Sott K, Davidson D, Cans AS, Linderholm P, Chiu D, Orwar O (2002a) Formation of geometrically complex lipid nanotube-vesicle networks of higher-order topologies. *Proc. Natl. Acad. Sci. USA* 99:11573–78.
- Karlsson R, Karlsson M, Karlsson A, Cans AS, Bergenholtz J, Akerman B, Ewing AG, Voinova M, Orwar O (2002b) Moving-wall-driven flows in nanofluidic systems. *Langmuir* 18(11): 4186–4190.
- Karlsson R, Karlsson A, Orwar O (2003b) Formation and transport of nanotube-integrated vesicles in a lipid bilayer network. *J. Phys. Chem. B* 107(40): 11201–11207.
- Karlsson R, Karlsson A, Orwar O (2003c) A nanofluidic switching device. *J. Am. Chem. Soc.* 125(28): 8442–8443.
- Kato T, MN, Kishimoto K (2006) Functional liquid-crystalline assemblies: Self-organized soft materials. *Angew Chem. Int. Ed.* 45:1 38–68.
- Koster G, VanDuijn M, Hofs B, Dogterom M (2003) Membrane tube formation from giant vesicles by dynamic association of motor proteins. *Proc. Natl. Acad. Sci. USA* 100 (26): 15583–15588.
- Koster G, Cacciuto A, Derenyi I, Frenkel D, Dogterom M (2005) Force barriers for membrane tube formation. *Phys. Rev. Lett.* 94(6):068101.
- Langner M, Kubica K (1999) The electrostatics of lipid surfaces. *Chem. Phys. Lipids* 101(1):3–35.
- Lasic DD (2000) Giant vesicles - A historical introduction. *Perspect. Supramol. Chem.* 6: 11–24.

- Li XJ, Schick M (2000) Theory of lipid polymorphism: Application to phosphatidylethanolamine and phosphatidylserine. *Biophys. J.* 78(1): 34–46.
- Lindner LH, Brock R, Arndt-Jovin D, Eibl H (2006) Structural variation of cationic lipids: Minimum requirement for improved oligonucleotide delivery into cells. *J. Controlled Release* 110(2): 444–456.
- Lipowsky R, Dimova R (2003) Domains in membranes and vesicles. *J. Phys. Condens. Mat.* 15(1): S31–S45.
- Lipowsky R, Sackmann E (1995). *Structure and Dynamics of Membranes*. Amsterdam: Elsevier.
- Lizana L, Konkoli Z (2005) Diffusive transport in networks built of containers and tubes. *Phys. Rev. E* 72(2): 026305.
- Lobovkina, T, Dommersnes, P, Joanny, JF, Bassereau, P, Karlsson, M, Orwar, O (2004) Mechanical tweezer action by self-tightening knots in surfactant nanotubes. *Proc. Natl. Acad. Sci. USA* 101(21): 7949–7953.
- Long MS, Jone CD, Helfrich MR, Mangeney-Slavin LK, Keating CD (2005) Dynamic microcompartmentation in synthetic cells. *Proc. Natl. Acad. Sci. USA* 102(17): 5920–5925.
- Luisi PL, Walde P (1999) *Giant Vesicles*. New York: John Wiley and Sons.
- Lyon, WA, Nie, SM (1997) Confinement and detection of single molecules in submicrometer channels. *Anal. Chem.* 69(16): 3400–3405.
- Mason JT (1998) Investigation of phase transitions in bilayer membranes. *Energ. Biol. Macromol. B Meth. Enzymol.* 295:468–494.
- McCain, KS, Hanley, DC, Harris, JM (2003) Single-molecule fluorescence trajectories for investigating molecular transport in thin silica sol-gel films. *Anal. Chem.* 75(17): 4351–4359.
- Misquitta LV, Misquitta Y, Cherezov V, Slattery O, Mohan JM, Hart D, Zhahnina M, Cramer WA, Caffrey M (2004) Membrane protein crystallization in lipidic mesophases with tailored bilayers. *Structure.* 12(12): 2113–2124.
- Nabi IR, Le PU (2003) Caveolae/raft-dependent endocytosis. *J. Cell Biol.* 161(4): 673–677.
- Needham D, Zhelev D V (1996) The mechanochemistry of lipid vesicles examined by micropipet manipulation techniques. In *Vesicles* (M. Rosoff ed.), Surface Science Series, New York: Marcel Dekker, 62:373–443.
- Onfelt B, Nedvetzki S, Yanagi K, Davis DM (2004) Cutting edge: Membrane nanotubes connect immune cells. *J. Immunol.* 173(3):1511–1513.
- Onfelt B, Purbhoo MA, Nedvetzki S, Sowinski S, Davis DM (2005) Long distance calls between cells connected by tunneling nanotubes. *Science* STKE PE55: 1–3.
- Pick H, Schmid EL, Tairi AP, Ilegems E, Hovius R, Vogel H (2005) Investigating cellular signaling reactions in single attoliter vesicles *J. Am. Chem. Soc.* 127 (9): 2908–2912.
- Plempers van Balen GP, Martinet CAM, Caron G, Bouchard G, Reist M, Carrupt PA, Fruttero R, Gasco A, Testa B (2004) Liposome/water lipophilicity: Methods, information content, and pharmaceutical applications. *Med. Res. Rev.* 24 (3): 299–324.
- Probstein, RF (1994) *Physicochemical Hydrodynamics*. New York: John Wiley and Sons.
- Puech PH, Brochard-Wyart F (2004) Membrane tensiometer for heavy giant vesicles. *Eur. Phys. J. E* 15(2), 127–132.
- Raffy S, Teissie J (1997) Electroinsertion of glycophorin A in interdigitation-fusion giant unilamellar lipid vesicles. *J. Biol. Chem.* 272(41): 25524–30.
- Robinson, BH, Rogerson, M. (2002) Vesicles. *Handb. Appl. Surface Colloid Chem.* 2: 45–53.
- Rossier O, Cuvelier D, Borghi N, Puech PH, Derényi I, Buguin A, Nassoy P, Brochard-Wyart F (2003) Giant vesicles under flows: Extrusion and retraction of tubes. *Langmuir* 19(3): 575–584.
- Roy BC, Santos M, Mallik S, Campiglia AD (2003) Synthesis of metal-chelating lipids to sensitize lanthanide ions. *J. Org. Chem.* 68(10): 3999–4007.
- Rustom A, Saffrich R, Markovic I, Walther P, Gerdes HH (2004) Nanotubular highways for intercellular organelle transport. *Science* 303 (5660): 1007–1010.
- Sackmann E, Tanaka M (2000) Supported membranes on soft polymer cushions: Fabrication, characterization and application. *Trends Biotechnol.* 18 (2): 58–64.
- Schmidt C, Mayer M, Vogel H (2000) A chip-based biosensor for the functional analysis of single ion channels. *Angew Chem. Int. Ed. Engl.* 39:3137–3140.

- Schmitt L, Tampe R, (1996) ATP-lipids-protein anchor and energy source in two dimensions. *J. Am. Chem. Soc.* 118(24): 5532–43.
- Seifert, U (1997) Configurations of fluid membranes and vesicles. *Adv. Phys.* 46:13–137.
- Seifert U, Lipowsky R (1990) Adhesion of vesicles. *Phys. Rev. A* 42: 4768–4771.
- Simons K, Toomre D (2000) Lipid rafts and signal transduction. *Nature Rev. Mol. Cell Biol.* 1(1), 31–39.
- Sorde N, Das G, Matile, S (2003) Enzyme screening with synthetic multifunctional pores: Focus on biopolymers. *Proc. Natl. Acad. Sci. USA* 100(21), 11964–11969.
- Sott K, Karlsson M, Pihl J, Hurtig J, Lobovkina T, Orwar O (2003) Micropipet writing technique for production of two-dimensional lipid bilayer nanotube-vesicle networks on functionalized and patterned surfaces. *Langmuir* 19(9): 3904–3910.
- Sott K, Lobovkina T, Lizana L, Tokarz M, Bauer B, Konkoli Z, Orwar, O (2006) Controlling enzymatic reactions by geometry in a biomimetic nanoscale network. *Nano Lett.* 6(2): 209–214.
- Stange P, Zanette D, Mikhailov A, Hess B (1998) Self-organizing molecular networks. *Biophys. Chem.* 72(1–2): 73–85.
- Steinberg-Yfrach G, Liddell PA, Hung S-C, Moore AL, Gust D, Moore TA (1997) Conversion of light energy to proton potential in liposomes by artificial photosynthetic reaction centres. *Nature* 385: 239–241.
- Stevens BC, Ha T (2004) Discrete and heterogeneous rotational dynamics of single membrane probe dyes in gel phase supported lipid bilayer. *J. Chem. Phys.* 120(6): 3030–3039.
- TerleckiG, Czapinska E, Gutowicz J (2002) The role of lipid phase structure in the interaction of lactate dehydrogenase with phosphatidylserine. *Cell Mol. Biol. Lett.* 7: 895–903.
- Tokarz M, Akerman B, Olofsson J, Joanny JF, Dommersnes P, Orwar, O (2005) Single-file electrophoretic transport and counting of individual DNA molecules in surfactant nanotubes. *Proc. Natl. Acad. Sci. USA* 102(26): 9127–9132.
- Tsafrir I, Sagi D, Arzi T, Guedeau-Boudeville MA, Frette V, Kandel D, Stavans J (2001) Pearling instabilities of membrane tubes with anchored polymers. *Phys. Rev. Lett.* 86(6): 1138–1141.
- Wolf LK, Gao Y, Georgiadis RM (2004) Sequence-dependent DNA immobilization: Specific versus nonspecific contributions. *Langmuir* 20(8): 3357–3361.
- Wu LQ, Payne GF (2004) Biofabrication: Using biological materials and biocatalysts to construct nanostructured assemblies. *Trends Biotechnol.* 22 (11): 593–599.
- Yegneswaran S, Deguchi H, Griffin JH (2003) Glucosylceramide, a neutral glycosphingolipid anticoagulant cofactor, enhances the interaction of human- and bovine-activated protein C with negatively charged phospholipid vesicles. *J. Biol. Chem.* 278(17): 14614–14621.
- Zana R ed. (2005) *Dynamics of Surfactant Self-Assemblies: Micelles, Microemulsions, Vesicles and Lyotropic Phases*. Boca Raton, FL: CRC Press.
- Zauner, KP (2005) Molecular information technology. *Crit. Rev. Solid State* 30 (1): 33–69.



## Chapter 10

# Single-Molecule Covalent Chemistry in a Protein Nanoreactor

Hagan Bayley(✉), Tudor Luchian, Seong-Ho Shin,  
and Mackay B. Steffensen

10.1	The Nanoreactor Approach to Single-Molecule Chemistry .....	252
10.2	Properties of the $\alpha$ HL Nanoreactor .....	254
10.3	Early Related Work.....	256
10.4	Irreversible Single-Molecule Covalent Chemistry.....	258
10.5	Reversible Single-Molecule Covalent Chemistry.....	259
10.6	Turnover of Irreversible Reactions in a Two-Compartment System.....	261
10.7	Examining a Polymerization One Step at a Time.....	262
10.8	Single-Molecule Experiments are Capable of Revealing Information that Would be Obscured in Ensemble Measurements.....	264
10.9	Alternative Approaches to Single-Molecule Chemistry .....	265
10.10	Problematic Issues and Present Limitations of the Approach .....	269
10.11	Future Directions .....	272
	References.....	274

**Abstract** Covalent chemistry can be observed at the single-molecule level by using engineered protein pores as “nanoreactors”. By recording the ionic current driven through single engineered alpha-hemolysin ( $\alpha$ HL) pores in a transmembrane potential, individual bond-making and bond-breaking steps that occur within the pore and perturb the current are monitored with sub-millisecond time-resolution. Recently, a variety of covalent reactions of small molecules have been observed by this approach including irreversible light-activated chemistry, multiple turnovers of reversible reactions, the turnover of normally irreversible reactions in a two-compartment system and a step-by-step polymerization. These single-molecule experiments are revealing information about fundamental chemical processes that cannot be extracted from ensemble measurements. Further, the approach can be used to examine the effects of the local environment on chemistry and catalysis, and to construct sensors for reactive molecules based on covalent chemistry rather than non-covalent binding interactions. Alternative approaches to small molecule covalent chemistry at the single-molecule level are described in the review, as well as the problems and present limitations of the nanoreactor approach.

---

Hagan Bayley  
Department of Chemistry, University of Oxford, Oxford, OX1 3TA, UK  
hagan.bayley@chem.ox.ac.uk

R. Rigler and H. Vogel (eds.), *Single Molecules and Nanotechnology*.  
*Springer Series in Biophysics 12*.  
© Springer-Verlag Berlin Heidelberg 2008

## 10.1 The Nanoreactor Approach to Single-Molecule Chemistry

We have been developing a means to examine the covalent chemistry of small molecules in aqueous solution at the single-molecule level. Our goals are to use the approach to study fundamental chemical processes, to investigate the effects of the local environment on chemistry and catalysis, and to construct sensors for reactive molecules based on covalent chemistry rather than noncovalent binding interactions. Although many of the experiments described in this volume use optical or force measurements to examine individual molecules, we have taken a different and, in origin, an older approach. We use the interior of a protein pore as a “nanoreactor”; chemistry occurring inside the pore alters an ionic current flowing through it and, thereby, the intermediates in a reaction are registered and their lifetimes recorded.

The ability to measure the movement of ions through individual channels and pores in planar lipid bilayers was developed in the 1960s and brought to fruition when currents were recorded flowing through single channels of known chemical structure, formed by the antibiotic gramicidin A (Hladky and Haydon, 1970). Soon afterwards, current recording was used to observe the noncovalent block of channels by ions and small molecules that lodge within them and it is this capability that forms the foundation of the work described here.

Our measurements are made by bilayer recording (Figure 10.1A). A typical recording cell contains two chambers separated by a thin plastic partition, often teflon, which has been breached by a single tiny hole, generally  $\sim 100\mu\text{m}$  in diameter. A lipid bilayer is deposited across the hole. One way to do this is to form a “folded bilayer”. For example, the hole is first pretreated with hexadecane. Then, by adding a lipid dissolved in pentane, a monolayer is formed on the surface of a small amount of electrolyte that has been placed in each chamber. When the pentane has evaporated, the level of the electrolyte in each chamber is raised above the aperture and a bilayer is formed. The lipid is often 1,2-diphytanoyl-*sn*-glycero-3-phosphocholine, which is chemically stable and shows no phase transition over the temperature range of 0 to  $100^\circ\text{C}$  (it is in the disordered liquid crystalline phase). The electrolyte is typically a buffered 1 M salt solution.

The protein pore we use is that formed by staphylococcal  $\alpha$ -hemolysin ( $\alpha\text{HL}$ ). A single preformed pore can be introduced into the planar bilayer, simply by adding a minute amount, less than  $1\text{ ng mL}^{-1}$ , to one of the chambers (the *cis* side) and waiting for the current, in a fixed applied potential, to jump from zero to the accepted value for the pore. Chemical reactions can be encouraged to occur inside various engineered  $\alpha\text{HL}$  pores (see below) and a reaction is monitored by recording the modulation of the current that flows through an individual pore, for example, 30 pA at +40 mV in 1 M NaCl.  $\alpha\text{HL}$  is a bacterial toxin that is normally secreted as a 293-residue monomeric polypeptide, which assembles into a pore containing seven identical subunits (Figure 10.1B). As very little protein is needed for the types of experiment described here, it is made in our laboratory in a convenient cell-free expression system, assembled on red cell membranes, solubilized in detergent,

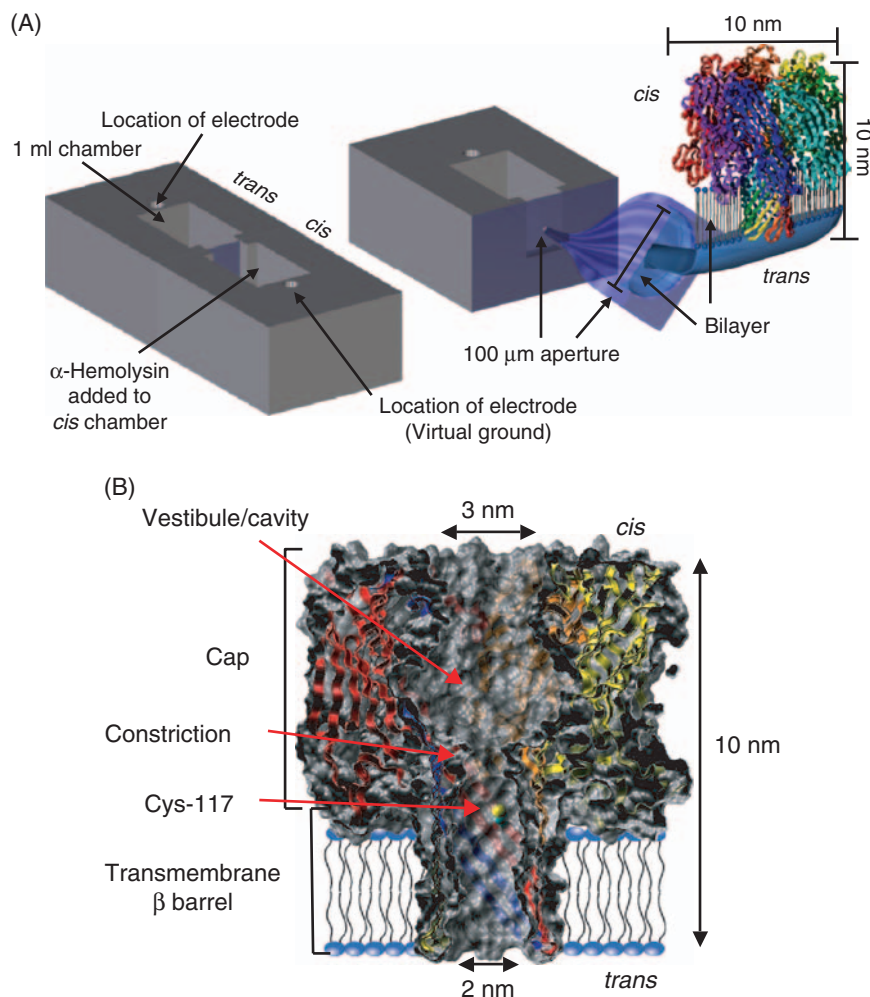


**Figure 10.1** Observation of single molecule covalent chemistry in a protein nanoreactor. **(A)** Typical apparatus for bilayer recording. Two chambers, *cis* and *trans*, are separated by a thin (e.g., 25  $\mu\text{m}$  thick) teflon barrier (mauve). A bilayer is formed across a hole in the teflon, which is typically 100  $\mu\text{m}$  in diameter.  $\alpha$ -Hemolysin ( $\alpha\text{HL}$ ) pores are added to the *cis* chamber. Measurements of current flow are made after a single pore inserts spontaneously into the bilayer. The *cis* chamber is at ground, and the applied potential is that at the *trans* side. A positive current is defined as cations flowing through the pore from *trans* to *cis* (or anions from *cis* to *trans*). **(B)** A sagittal section through the  $\alpha$ -hemolysin pore, which acts as a protein nanoreactor. The chemistry we examine takes place within the transmembrane  $\beta$  barrel of the  $\alpha\text{HL}$  pore, which has a volume of  $\sim 16 \text{ nm}^3$  and contains  $\sim 500$  water molecules

and purified by electrophoresis. The details have been described elsewhere, but it is important to note that this method permits the formation and purification of heteromeric  $\alpha\text{HL}$  pores, which have been crucial for the success of our work (Braha et al., 1997). Very often, we need pores with six natural (or “wild-type”, WT) subunits

and one engineered subunit containing one or more amino acid substitution or a residue with a chemically modified sidechain.

$\alpha$ HL has several properties that make it almost ideal as a nanoreactor. It is robust; for example, it is stable over a wide range of pH values (Gu and Bayley, 2000) and at temperatures close to the boiling point of water (Kang et al., 2005). The pore remains open at transmembrane potentials below 100 mV in the commonly used buffered salt solutions. The annoying “gating” transitions seen in many other related  $\beta$ -barrel proteins are absent. A high-resolution X-ray structure has been determined, which greatly facilitates rational engineering (Bayley and Jayasinghe, 2004). Most important, as discussed below, the pore is of just the right dimensions for the work at hand: any smaller and the chemistry would be significantly perturbed, any larger and the current changes would not be observed.

## 10.2 Properties of the $\alpha$ HL Nanoreactor

Most of the chemistry we have examined has taken place within the transmembrane  $\beta$  barrel of the  $\alpha$ HL pore (Figure 10.1B). This volume of the lumen is roughly cylindrical with a diameter of 2 nm and a height of 5 nm. The top end is constricted to a diameter of about 1.4 nm and the migration of small molecules into the cylinder from this end is expected to be more hindered than it is from the bottom (*trans*) end. To a first approximation, we have assumed that there is free diffusion of molecules from the bulk phase through the *trans* entrance. The volume of the barrel forming the nanoreactor is then  $\sim 16 \text{ nm}^3$ , and it contains  $\sim 500$  water molecules. A single molecule located in the  $\beta$  barrel has an effective concentration of  $\sim 100 \text{ mM}$ . We suggest that the dimensions of the  $\alpha$ HL pore are well suited for the detection of chemical reactions through the perturbation of ionic currents. For example, a benzene ring is  $\sim 0.6 \text{ nm}$  in diameter, 30% of the diameter of the pore. Although the observed changes in current have a complex, and for the moment unresolved, dependence on the size, shape, charge, and location of the tethered reactant, it seems likely that if the pore were any smaller the chemistry would be perturbed, and if it were any larger the current changes could not be observed above the noise. Experiments in the  $\alpha$ HL nanoreactor can be carried out with excellent control of temperature (Kang et al., 2005), pH, and ionic strength. Irradiation with UV or visible light can be performed when required (Luchian et al., 2003a).

In the chemistry we have observed, one reactant is tethered to the surface of the nanoreactor. This is done because electrical detection is limited by instrument noise to the  $\mu\text{s}$  time domain (Mayer et al., 2003; Shapovalov and Lester, 2004). Ignoring, for the time-being, electrophoretic and electro-osmotic transport, a small molecule located at the midpoint of the nanoreactor ( $x = 2.5 \text{ nm}$ , from the *trans* entrance) would have a mean residence time ( $x^2/2D$ ) of only 6.25 ns, where  $D = 0.5 \times 10^{-9} \text{ m}^2\text{s}^{-1}$ , the value of the diffusion coefficient for a small molecule such as sucrose in

water. Therefore, a molecule free in solution within the pore would not be registered in the experiments we perform at  $\mu\text{s}$  to  $\text{ms}$  time resolution.

It is unlikely that  $\text{ns}$  time resolution can be achieved. For example, by taking special precautions, including the use of quartz micropipettes rather than a bilayer setup, rms noise was reduced to  $\sim 13\text{ pA}$  at a high bandwidth ( $B = 250\text{ kHz}$ ), which allows the detection of high amplitude events of a few  $\mu\text{s}$  (Shapovalov and Lester, 2004). It is also possible to facilitate work in the  $\mu\text{s}$  domain by correcting for “missed events” (Blatz and Magleby, 1986; Movileanu et al., 2003). However, even if all the instrument noise could be eliminated, a pore with a conductance of  $700\text{ pS}$  or a resistance ( $R$ ) of  $1.4\text{ G}\Omega$  (e.g., the  $\alpha\text{HL}$  pore in  $1\text{ M NaCl}$ ) at  $250\text{ kHz}$  would yield at room temperature thermal (Johnson) noise  $[(4kTB/R)^{1/2}]$  of  $1.7\text{ pA}$  rms and shot noise  $[(2q_eIB)^{1/2}]$  of  $1.5\text{ pA}$  rms for a total of  $2.3\text{ pA}$  rms or  $8\%$  of the single-channel current of  $28\text{ pA}$  at  $40\text{ mV}$ , making it difficult to discern transient appearances of molecules within the barrel or other rapid transitions associated with small current steps. It has proved possible to trap a small molecule in the  $\alpha\text{HL}$  pore between two cyclodextrins lodged at the top and bottom of the  $\beta$  barrel (Gu et al., 2001) and, by this or a related approach, it is likely that various untethered chemistries of trapped reactants can be observed, for example, reversible bimolecular chemistry.

The kinetic analysis of single-molecule reactions is closely related to that of ensemble systems. However, when a reaction within a single pore is envisioned, it can be hard to grasp that this is the case. For example, a reactant molecule equilibrated with the bulk phase at  $50\text{ }\mu\text{M}$  is located inside the nanoreactor for only about  $0.05\%$  of the time, and upon each visit it leaves within a few nanoseconds. In turn, it might react with a thiol on the wall of the nanoreactor that is in its deprotonated (thiolate) form for only  $1\%$  of the time. Nevertheless, after the reactant has visited the pore numerous times, the reaction will occur, and the time-averaged properties of the system over an extended period are equivalent to the ensemble-averaged properties (the condition of ergodicity). The length of the experiment will determine the confidence limits on the rate constants that are extracted from the data. In a single-molecule experiment, rate constants ( $k$ ) are related to the mean lifetimes ( $\tau$ ) of states (Moczydlowski, 1986). At any given moment, a chemical state of the system has a probability of existence ( $p$ ), rather than being manifested as a concentration. For a simple unimolecular reaction, such as the breakdown of a tethered intermediate,  $\tau = 1/k$ . For a unimolecular branching reaction,  $\tau = 1/(k_1 + k_2)$ . For a bimolecular reaction, for example, the reversible reaction of a tethered intermediate with a molecule, A, presented in solution,  $\tau = 1/k[A]$ ; the forward reaction is pseudo-first order because  $[A]$  does not change appreciably in the single-molecule case.

In single-molecule enzymology, there has been considerable interest in dynamic disorder, the idea that rate constants can vary with time (Min et al., 2005). This most likely arises from conformational changes of proteins taking place over a wide range of timescales (Min et al., 2005), and it is unlikely to occur in small molecule chemistry. However, we must remember that the nanoreactor itself is a protein, and could undergo time-dependent changes in its properties.

### 10.3 Early Related Work

The ability to observe the noncovalent block of ion channels by small molecules dates from the 1970s (Hille, 2001). Considerably later, in the 1990s, the availability of the structure of the  $\alpha$ HL pore allowed our group to engineer sites for specific blockers within its lumen with the idea of using current recording to study noncovalent interactions at the single-molecule level and to develop the concept of stochastic sensing, in which analytes are identified and quantified through their interactions with a single engineered pore (Bayley and Cremer, 2001). In some cases, protein engineering techniques were developed specifically for this purpose: for example, molecular adapters, which are host molecules that lodge in the pore and act as binding sites for analytes (Gu et al., 1999). Our experience in this area led to the realization that a similar approach might be used to observe covalent chemical reactions in aqueous solution under relatively nonperturbing conditions. Rather little related work had been done previously, and by now we have been able to explore a wide variety of reactions and conditions that have convinced us that this will continue to be a wonderfully fertile area.

In earlier work, there have been several interesting studies of the kinetics of protonation of amino acid sidechains in channels and pores dating back to the work of Peter Hess' group who observed the protonation and deprotonation of an amino acid side chain in an L-type  $\text{Ca}^{2+}$  channel (Prod'homme et al., 1987). They later discovered complexities in the kinetics and concluded that the two observable states reflect two channel conformations, both of which are protonatable at the same site (Pietrobon et al., 1988, 1989; Prod'homme et al., 1989). Protonation kinetics could nonetheless be extracted from the data, but the proton association rates were anomalously high at  $10^{12}$  to  $10^{13} \text{ M}^{-1}\text{s}^{-1}$ , even given the high mobility of "protons" in water. By using noise analysis, Bezrukov and Kasianowicz examined the protonation of an unidentified residue in the  $\alpha$ HL pore, which is a protein unlikely to undergo large conformational fluctuations, and obtained a more reasonable association rate constant of  $\sim 8 \times 10^9 \text{ M}^{-1}\text{s}^{-1}$  (Bezrukov and Kasianowicz, 1993; Kasianowicz and Bezrukov, 1995).

In a detailed study of resolvable pH-dependent current fluctuations in a cyclic-nucleotide-gated ion channel, Root and MacKinnon identified the protonated residue as Glu-333, found an association rate constant of  $\sim 6 \times 10^9 \text{ M}^{-1}\text{s}^{-1}$  and emphasized the effect of buffer-mediated proton transfer, which they felt would better explain the data of Hess and colleagues (Root and MacKinnon, 1994; Morrill and MacKinnon, 1999). It would be interesting to re-explore the issues raised in these early studies with structurally defined engineered forms of the  $\alpha$ HL pore. In a recent study, the electrostatic environment within the nicotinic acetylcholine receptor channel was investigated systematically by observing the protonation of lysine- and histidine-substituted subunits. Here, the focus was on the  $\text{pK}_a$  values of the amino acid sidechains rather than the protonation kinetics (Cymes et al., 2005).

In a pioneering study of the isomerization of a small molecule, Woolley and his colleagues covalently attached a carbamate at the mouths of the dimeric gramicidin A channel. By manipulating the applied potential, events occurring at just one of the two symmetry-related channel entrances were observed. *Cis-trans*

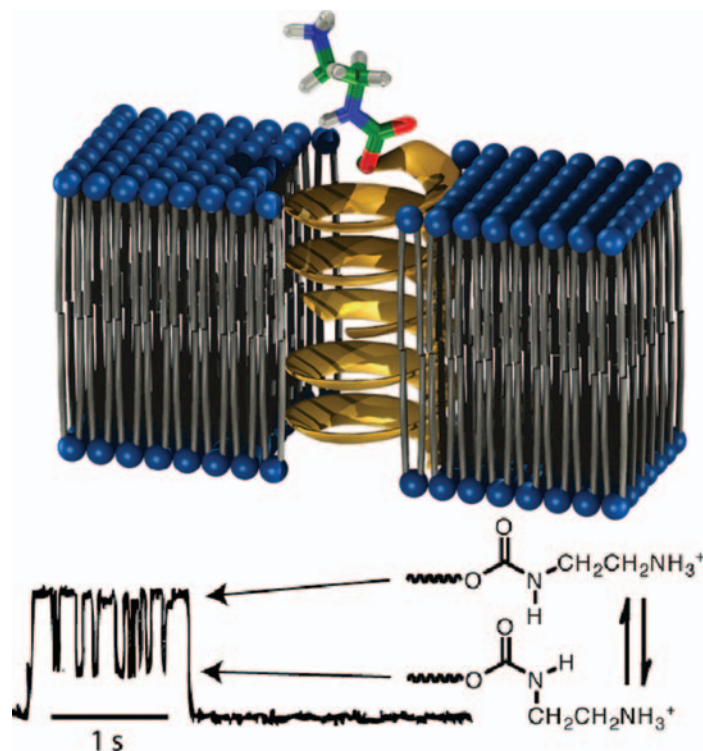


**Figure 10.2** A pioneering experiment in the field. The isomerization of a covalently attached carbamate at a mouth of the dimeric gramicidin A channel. *Cis-trans* isomerization at the carbamate CO–NH bond was reflected in the single-channel current (Jaikaran and Woolley, 1995; Woolley et al., 1995)

isomerization at the carbamate CO–NH bond was reflected in a modulation of the single-channel conductance (Jaikaran and Woolley, 1995; Woolley et al., 1995) (Figure 10.2). From an analysis of the intervals between the transitions over the temperature range 2°C to 37°C, it was possible to extract standard enthalpies and entropies, and activation enthalpies and entropies, for the isomerization. In an early example of a covalent reaction observed at the single-molecule level, Mindell and colleagues examined the reaction of a thiol with various methanethiosulfonates to form mixed disulfides. The thiol was presented in the channel-forming domain of diphtheria toxin (the T domain) as the side-chain of a cysteinyl residue (Cys; Mindell et al. (1994)). The reaction is irreversible and therefore the acquisition of statistically significant data would normally be tedious (see Section 10.4). But, because insertions of the T domain continued to occur from the *cis* compartment, the reactions of up to 15 channels with a methanethiosulfonate originating in the *trans* compartment could be observed sequentially in a single experiment. Analysis of the intervals between T domain insertion and reaction allowed the determination of a second-order rate constant for the reaction with

the methanethiosulfonate. In this case (compare  $\alpha$ HL, below), the rate constant was considerably lower than that observed for a similar reaction in solution, suggesting that there is steric hindrance in the relatively narrow channel. The authors envisioned the potential of the approach: in particular, they recognized that the ability to examine fast reactions is not limited by mixing, but by the acquisition time of the recording system.

These early studies suggested that an ideal nanoreactor for observing single-molecule covalent chemistry would be a pore with a diameter wide enough to accommodate rather than confine the reactants. The pore would be structurally defined at atomic resolution, exist in a single conformational state, and be amenable to precise protein engineering to allow positioning of the reactants within the pore. The  $\alpha$ HL pore fulfills this role.

#### 10.4 Irreversible Single-Molecule Covalent Chemistry

As outlined above, Mindell and colleagues examined the reaction of a thiol presented within a channel protein with a methanethiosulfonate to form a mixed disulfide (Mindell et al., 1994). This is a simple single-step reaction. We decided to look at a more complex reaction sequence at the single-molecule level (Luchian et al., 2003a). Both for convenience, and because of its relevance to “caged” reagents for biology (Lawrence, 2005; Ludwig and Bayley, 2005), photoinitiated chemistry was selected (Figure 10.3). A 3,4-dimethoxy-6-nitrobenzylcarbamate was attached to a cysteine mutant of the  $\alpha$ HL monomer through an oligo(ethylene glycol) linker that terminated in an iodoacetamide group. The modified subunit was assembled into a pore in the presence of WT  $\alpha$ HL subunits, and the heteroheptamer (WT<sub>6</sub>M<sub>1</sub>) containing just one modified (M) subunit in which the attached reagent projected into the lumen of the pore was purified by charge-shift SDS-polyacrylamide gel electrophoresis by means of an oligoaspartate tail on the M subunit (Bayley and Jayasinghe, 2004). The pore was examined in a modified recording cell in which the lipid bilayer can be irradiated with ultraviolet light. A sequence of three steps was expected after the absorption of a photon: rearrangement of the dimethoxynitrobenzyl group to form a nitronate, loss of the protecting group to yield a carbamate, and finally decarboxylation to reveal the deprotected amine. Three steps were indeed observed as reflected in the electrical signal (Figure 10.3).

A significant weak point of the present approach is the difficulty in identifying reaction intermediates (see below). In this case, the strong pH dependence of the final step is characteristic of the decarboxylation of carbamic acids. Using  $k_{\text{obs}} = k[\text{H}^+]/(K_a + [\text{H}^+])$ , we found  $k = 350 \text{ s}^{-1}$  and  $pK_a = 6.4$ , whereas literature values for the decarboxylation of similar carbamates in solution yield  $k = \sim 500 \text{ s}^{-1}$  and  $pK_a \sim 5.2$ . The discrepancy in the  $pK_a$  value is discussed later, but there is little doubt that the final step is the proposed decarboxylation, placing only the structure of the first intermediate, the proposed nitronate, in any doubt. The structure of this



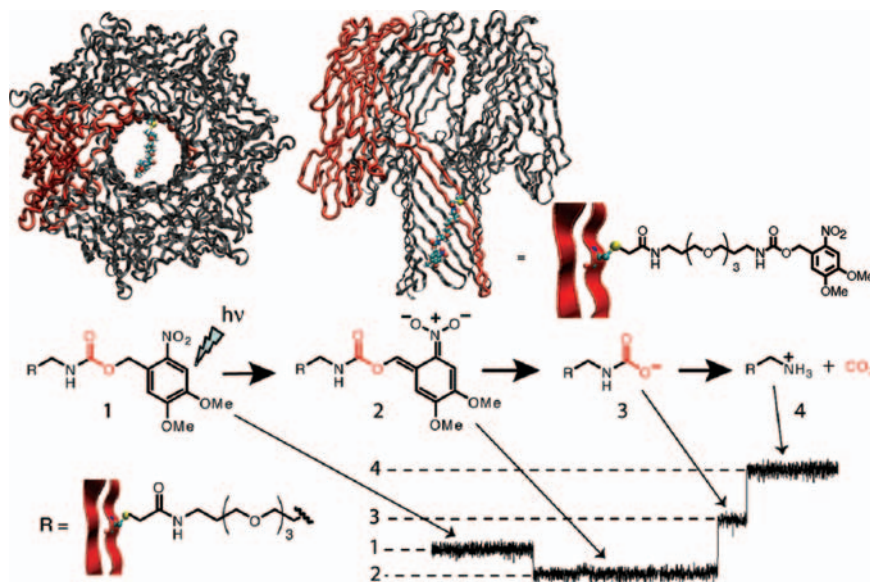


**Figure 10.3** Examination of a three-step photoinitiated reaction in the  $\alpha$ HL nanoreactor. A 3,4-dimethoxy-6-nitrobenzylcarbamate was attached to a cysteine residue within the pore through an oligo(ethylene glycol) linker. Three steps were observed after the absorption of a photon, which were assigned as the rearrangement of the dimethoxynitrobenzyl group to form a nitronate, loss of the protecting group to yield a carbamate and finally decarboxylation to reveal the deprotected amine

intermediate has indeed been debated, and we can at the least say that we have observed an intermediate with a lifetime of about 2 s (pH 7.0) that is only weakly pH dependent. Clearly, this form of 2-nitrobenzyl protection is unlikely to be useful in caging procedures where very rapid deprotection is required, such as in protein folding experiments (Loudwig and Bayley, 2005).

## 10.5 Reversible Single-Molecule Covalent Chemistry

Evidently, the examination of irreversible bond formation at the single-molecule level can be rewarding, but it is tedious because each experiment reveals only a single value of the lifetime for each event. Therefore, we sought to investigate interesting reversible covalent chemistry at the single-molecule level, where multiple events would be seen in each experiment permitting the rapid accumulation of reliable mean lifetimes. Organoarsenic(III) compounds have been used in basic science for tagging macromolecules, in medicine, and as chemical warfare and crowd-control agents. Organoarsenic(III) reagents, such as  $\text{RAs}(\text{OH})_2$ , react with dithiols to form stable cyclic  $-\text{S}-\text{As}(\text{R})-\text{S}-$  derivatives. Indeed,  $\text{As}(\text{III})$  compounds

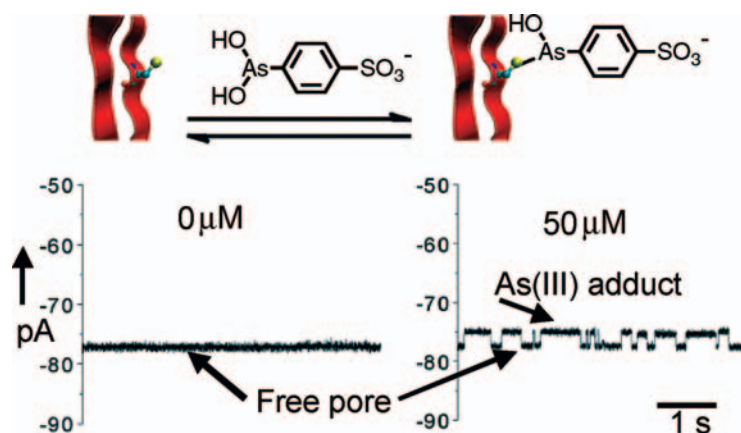


**Figure 10.4** Observation of reversible single-molecule covalent chemistry in the  $\alpha$ HL nanoreactor. A heteromeric  $\alpha$ HL pore was built with a single Cys residue within the lumen at position 117. The reaction of 4-sulfophenylarsonous acid with the thiol (S, yellow atom) of the Cys side chain was examined. A covalent As(III) adduct of the form  $R'SAs(OH)R$  was observed with a lifetime of  $\sim 700$  ms

are toxic because of their reactions with lipoyl cofactors and proteins that have two Cys residues at the active site.

We sought to investigate what must be the first step of this reaction, the reaction of As(III) molecules with monothiol. To this end, we built a heteromeric  $\alpha$ HL pore with a single Cys residue within the lumen at position 117 in the mutant subunit. Assembly of the pore was carried out along the lines used for the chemically derivatized pore described in Section 10.4. The interaction of this pore with a variety of arylarsonous acids has been investigated (S.-H.S., unpublished work) of which 4-sulfophenylarsonous acid has been examined in detail (Shin et al., 2002) (Figure 10.4). In this case, As–S bond formation occurs with a rate constant of  $1.4 \times 10^4 \text{ M}^{-1}\text{s}^{-1}$  in 2 M KCl at pH 8.4 at  $-50$  mV. To obtain this bimolecular rate constant, we assumed that the instantaneous probability that a 4-sulfophenylarsonous acid molecule is present in the pore directly reflects the bulk concentration; that is,  $p_A = V_p[A]N_{\text{avo}}$ , where  $V_p$  is volume of the nanoreactor;  $[A]$ , bulk concentration; and  $N_{\text{avo}}$ , Avogadro's number. The covalent adduct is quite short-lived under these conditions with a mean lifetime of  $\sim 700$  ms ( $k = 1.4 \text{ s}^{-1}$ ). It is important to note that it would be difficult to isolate the As–S adduct under normal conditions. Not only is it short-lived, but when an As(III) compound,  $RAs(OH)_2$ , reacts with a monothiol in bulk solution, the formation constant of the ternary product  $((R'S)_2AsR)$  is greater than that for the binary product  $(R'SAs(OH)R)$  (Spuches et al., 2005). By contrast, when the chemistry occurs with a thiol on the wall of the lumen of the  $\alpha$ HL pore, the product cannot be attacked by a second thiol and is therefore isolated within the nanoreactor.

## 10.6 Turnover of Irreversible Reactions in a Two-Compartment System

As noted earlier, the examination of an irreversible covalent reaction in the nanoreactor can be a protracted process. Based on the fact that electrical recording with planar bilayers is of necessity a two-compartment system, we felt that it might provide a means to allow turnover of what would normally be an irreversible process (Figure 10.5). One reactant would be introduced from the *trans* side of the bilayer and react at a defined site within the lumen of the pore. A second reactant would have access to the reaction site from the *cis* side of the bilayer and cleave the bond formed by the *trans* reagent.

In the example that was used to test the approach, 5,5'-dithiobis(2-nitrobenzoic acid) (DTNB) was introduced from the *trans* side of the bilayer to the  $\alpha$ HL pore carrying a single Cys at position 117. DTNB reacts with the thiol in the pore to form a mixed disulfide. Normally, the reaction would be irreversible, but in this case dithiothreitol (DTT) was present on the *cis* side of the bilayer and diffused into the reaction zone within the pore to cleave the disulfide. The initial product is a

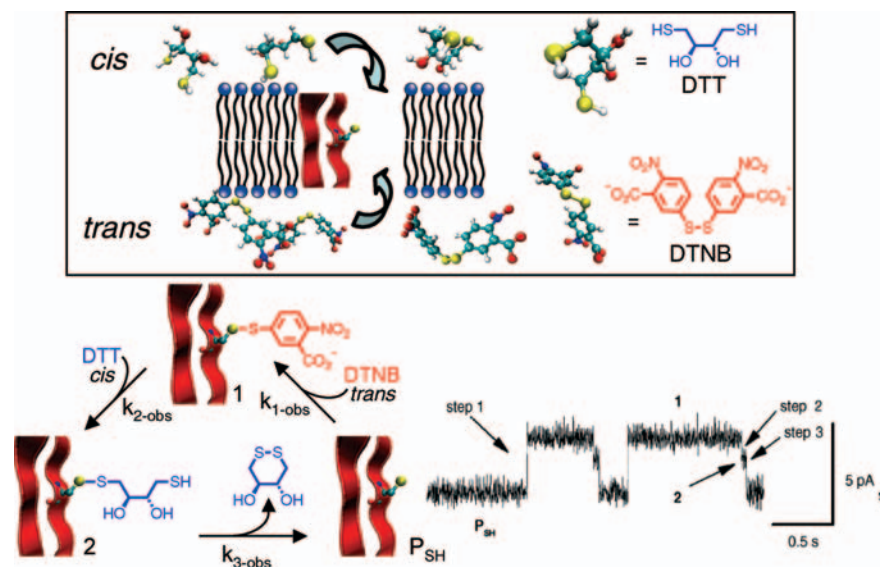


**Figure 10.5** Turnover of an irreversible reaction in a two-compartment system. By using the bilayer system, a reactant can be introduced from one side of the bilayer and react at a defined site within the lumen of the pore. A second reactant can access the reaction site from the other side. In the example shown, 5,5'-Dithiobis(2-nitrobenzoic acid) (DTNB) was introduced from the *trans* side of the bilayer to react with the  $\alpha$ HL pore carrying a single Cys at position 117. The reaction product, a mixed disulfide, was cleaved by dithiothreitol (DTT) entering from the *cis* side. A short-lived mixed disulfide intermediate can be observed in the current trace. The  $\alpha$ HL pore is released unchanged and is then free to undergo additional reaction cycles. The L-form of DTT is shown

short-lived mixed disulfide from which the oxidized form of DTT is released after closure to the 6-membered ring, which is highly favorable. The  $\alpha$ HL pore is released unchanged and is then free to undergo another reaction cycle. From the current traces, the mean interevent intervals required to determine the rate constants for all three reaction steps could be obtained.

To obtain the rate of reaction of DTNB with Cys-117 ( $4.9 \times 10^3 \text{ M}^{-1}\text{s}^{-1}$  in 2M KCl at pH 8.5 at  $-50\text{mV}$ ), we again assumed that the probability that the reagent is in the pore ( $p_A$ ) reflects the bulk concentration. In this case, it was also necessary to show that the DTT from the *cis* chamber, which can diffuse through the pore, did not alter the concentration of DTNB in the *trans* surface layer by reacting with it. At low concentrations of DTT, this problem was insignificant as the rate at which DTNB reacted in the pore did not vary with  $[\text{DTT}]_{\text{cis}}$  in the range 0 to  $50\mu\text{M}$ . To obtain the rate of reaction of DTT with the adduct at Cys-117 ( $1.1 \times 10^4 \text{ M}^{-1}\text{s}^{-1}$  in 2M KCl at pH 8.5 at  $-50\text{mV}$ ), we reversed the sidedness of the reagents and used  $\text{DTT}_{\text{trans}}$  and  $\text{DTNB}_{\text{cis}}$ , because we were afraid that the internal constriction in the pore might reduce the effective concentration (actually  $p_A$ ) of the *cis* reagent within the  $\beta$  barrel. Although it was not proven that this was necessary, it was reassuring that low concentrations of the *cis* reagent (in this case  $\text{DTNB} < 50\mu\text{M}$ ) did not affect the rate of reaction from the *trans* side, in this case with DTT.

Because the final step of the reaction is unimolecular, there is no difficulty regarding the  $p_A$  of one of the reactants, as considered for the bimolecular steps. Indeed, the rate constant for the final step  $k_3 = 23 \text{ s}^{-1}$  at pH 8.5 was independent of the concentration of both reactants. As expected the rate of this reaction was pH-dependent with  $k = k_3 K_a / (K_a + [\text{H}^+])$ . We found  $\text{p}K_a = 9.5$ , in keeping with the  $\text{p}K_a$  values of typical thiols, with  $k_3 = 250 \text{ s}^{-1}$ . This suggests, as expected, that the form of the adduct that cyclizes is the deprotonated form or thiolate.

The idea of using reagents presented from both sides of the bilayer to allow the turnover of chemical reactions should be generally applicable. In the immediate future, the chemistry is likely to be dictated by a nucleophile at the reaction site in the lumen of the pore, most often the thiolate of Cys, the most nucleophilic of the naturally occurring protein sidechains. This in turn dictates that the primary reactant will be an electrophile, and the secondary reagent that cleaves the initial product will be a nucleophile; that is, the primary and secondary reactants would react with each other and therefore must of necessity be separated. Alternative prospective combinations of reactants are likely to have the same "incompatibility" and require spatial separation. It is worth noting that two-compartment chemistry would not be possible with a narrow channel such as gramicidin A.

## 10.7 Examining a Polymerization One Step at a Time

An extension of the approach in which chemical reactants are spatially separated has permitted the examination of a polymerization reactant, one step at a time. The reaction was discovered accidentally. We had decided to examine the

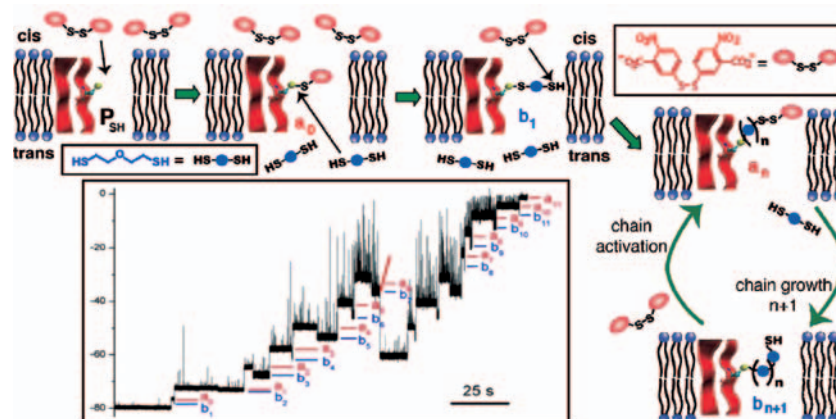


**Figure 10.6** Examination of a polymerization reactant, one step at a time. Here, bis(2-mercaptoethyl)ether (bMEE) enters from the *trans* side of the bilayer and reacts with the mixed disulfide formed at Cys-117 with DTNB (see Figure 10.5) entering from the *cis* side. The rate of cyclization of bMEE is slower than that of DTT (cf. Figure 10.5) and a second coupling with DTNB takes place before cyclization can occur. This is followed by reaction with a second bMEE, a third DTNB coupling, and so on, resulting in a polymerization. In the current trace that is shown, the red levels are those in which the polymer is terminated with the 5-mercapto-2-nitrobenzoic acid leaving group of DTNB and the blue levels are those terminated with bMEE. At the red arrow, the chain was broken as described in the text and immediately resumed growth

dependence of the rate of the cyclization step in the DTNB/dithiol reaction (Figure 10.6) on the chain length of the dithiol. One of the additional dithiols tested was bis(2-mercaptoethyl)ether (bMEE), but under the conditions of the experiment the rate of cyclization was sufficiently slow that a second coupling with DTNB took place before it occurred. This was followed by reaction with bMEE, a third DTNB coupling, and so on (Figure 10.6).

The current changes associated with the two steps in the polymerization were distinctive: disulfide formation at the end of the growing chain by reaction with DTNB caused a relatively large decrease in current that was followed by a smaller increase in current upon reaction with bMEE. Overall then, the current decreased as the chain lengthened and by the time  $\sim 11$  bMEE units had been added the polymerization could be followed no further. Incidentally, in single-molecule enzymology, it is only very recently that single-base incorporation by RNA polymerase has been made possible through the observation of the coupled base-pair stepping of the enzyme along the template DNA with improved optical trapping technology (Abbondanzieri et al., 2005).

Several interesting observations have resulted from an examination of the polymerization reaction. The mean rate constant for the reactions with DTNB (at all stages of the polymerization) was  $1.6 \times 10^4 \text{ M}^{-1}\text{s}^{-1}$  and that for the subsequent reactions with bMEE was  $2.7 \times 10^3 \text{ M}^{-1}\text{s}^{-1}$  (in 2 M KCl at pH 8.5 at  $-50 \text{ mV}$ ), which

are again similar to values in the literature for related reactions. The reaction rates increased as the polymer chain lengthened, but this was a modest effect and would require a more detailed investigation to confirm its validity and origin. It is reasonable to conclude that there is little hindrance to growth, with the possible exception of a small effect in the first couple of steps. The extents of current block at each step of the polymerization were roughly equal, except near the start and end of the process, which is in keeping with this conclusion. Occasionally, the polymer chain would break and then continue to grow (Figure 10.6). The chain break could occur by attack of bMEE on an internal disulfide, or with seemingly less likelihood an internal cyclization in which the terminal thiol of the growing chain attacks an internal disulfide.

As the polymer chain grows, spikes to lower conductance of increasing density and amplitude are seen. Similar spikes are seen when poly(ethylene glycol) (PEG; Howorka et al. (2000) and Movileanu et al. (2000)) or DNA (Howorka and Bayley, 2002) is confined within the pore. These spikes are likely to arise from movement of the polymer chains within the pore. The ability to form chains of defined length anchored at specific sites within the  $\alpha$ HL pore might constitute a sophisticated means for producing a collection of modified pores for the further investigation of the behavior of polymers under confinement. Protein pores with ligands for analytes attached through polymeric linkers have been used in stochastic sensing (Movileanu et al., 2000). In situ polymerization in the presence of a capping reagent (which could incorporate a ligand) might be a useful way to prepare polymer chains of defined length as polymer-based stochastic sensor elements.

## 10.8 Single-Molecule Experiments are Capable of Revealing Information that Would be Obscured in Ensemble Measurements

Single-molecule approaches can provide insight into chemistry that would not be forthcoming from ensemble experiments. All the intermediates in a reaction are revealed in the correct sequence. At the single-molecule level, a fast step that follows a slow one is readily observed and complex branched pathways can be dissected. The approach can also reveal dynamic disorder in reaction kinetics, but we have argued that this is less likely to be an issue in small molecule chemistry, compared with the chemistry of macromolecules, such as enzyme catalysis.

Current recording as a read-out has advantages over other single-molecule techniques, for the investigation of small molecule chemistry. For example, experiments carried out by current recording require no large tags, which is the case for single-molecule fluorescence. Clearly, some of the subtle changes we have monitored would be severely perturbed by the appendage of a molecule such as fluorescein. Most dyes also blink and bleach and therefore they often present problems for the observation of long reaction trajectories. For many chemical transformations, a

high reagent concentration is required, which cannot be achieved for most experiments involving single-molecule fluorescence. Electrical recording also has a relatively fast time response and in most cases the reactions are under stationary conditions, which means that the response of the system is not limited by bulk diffusion or mixing. An exception is the use of spatially separated reactants (Section 10.6), where transmembrane diffusion and reaction in the unstirred layer must be considered at high reagent concentrations.

Although we have so far been exploring the potential of the nanoreactor approach, the experiments we have performed have begun to yield findings that could not be obtained readily in ensemble measurements. First, it has indeed proved possible to observe short-lived intermediates that occur after a relatively long-lived state. Simple examples include the DTT adduct that is formed during the reductive cleavage of a disulfide (Figure 10.5), and at low pH the carbamate that decarboxylates after the photolysis of a 2-nitrobenzyl-protected carbamic acid (Figure 10.3). The intermediates that are observed during a step-by-step polymerization provide a more complex example (Figure 10.6). The ability to isolate a reactant within the nanoreactor has also been demonstrated in the case of organoarsenic(III) chemistry. The adduct that is formed by the reaction of a thiolate, provided by the sidechain of a Cys residue within the lumen of the  $\alpha$ HL pore, with 4-sulfophenylarsonous acid cannot react with a second thiolate (Figure 10.4).

Single-molecule experiments also allow the observation of branched pathways. For example, in one case (Figure 10.6) of the polymerization described above, the chain is broken after seven units have been added to form a chain with four units that then continues to grow to eleven units and beyond. The nature of the collection of routes taken during the polymerization can be clarified by such experiments. Finally, the ability to use spatially separated reactants opens up opportunities that are not available in homogeneous bulk solution. For example, reactions can be performed on a target within the nanoreactor with two reagents that would normally react quickly with each other. The problem is circumvented by presenting one reagent from each chamber (Figure 10.5). This approach has been used to induce the turnover of a chemical reaction, however, it could just as well have been used to trap a reactive intermediate.

## 10.9 Alternative Approaches to Single-Molecule Chemistry

At this point, it is instructive to compare alternatives to our nanoreactor approach to single-molecule chemistry. The present review has been limited to small molecule chemistry in aqueous solutions. Previous work in water has been largely confined to studies of biomacromolecules, especially enzymes. In these cases, the movement of proteins has been monitored by optical techniques or the binding and dissociation, or turnover, of small substrates has been observed through fluorescence measurements. For example, an ultra-stable optical trapping system has

allowed the monitoring of the processive movement of RNA polymerase in discrete 3.7 Å steps along a DNA template (Abbondanzieri et al., 2005).

In most cases, the visualization of single substrates requires fluorescent tagging. For example, the observation of the repeated incorporation of fluorescently labeled nucleotides into individual DNA strands with a DNA polymerase is a promising approach for the sequencing of single DNA molecules (Braslavsky et al., 2003). In a rare exception to the need for fluorescent tagging, the turnover of a natural fluorescent substrate, flavin adenine dinucleotide, has provided detailed information about the kinetics of individual cholesterol oxidase molecules (Lu et al., 1998). The kinetics of individual enzyme molecules have been examined in emulsion droplets (Lee and Brody, 2005; Musyanovych et al., 2005) or femtoliter chambers (Rondelez et al., 2005), but not yet at the single turnover level, and it is possible that such approaches can be adapted for small molecule chemistry, although it is likely that fluorescent reactants would again be required with the disadvantages discussed in Section 10.8 and below.

A great deal of work with small molecules has been confined to the gas phase or surfaces under ultrahigh vacuum, conditions that obviously affect the nature of the reactions that can be observed and the pathways that are taken. In the gas phase, crossed molecular beams have provided considerable insight into the chemical dynamics of elementary reactions (Herschbach, 2000). For relatively large objects, high-resolution transmission electron microscopy can be useful. For example, carbon nanofiber growth from a Ni nanoparticle catalyst has been observed at 500°C with subsecond time resolution revealing cyclical shape changes in the catalyst (Helveg et al., 2004). In several cases involving smaller molecules, scanning tunneling microscopy (STM) has permitted the visualization of reactions on surfaces in a vacuum with extraordinary spatial resolution (Ho, 2002; Otero et al., 2006). Examples include the isomerization of an azobenzene mediated by light or the applied tip potential (Yasuda et al., 2003; Henzl et al., 2006) (Figure 10.7A), and bond making and breaking reactions, for example, the stepwise synthesis of Fe(CO)<sub>2</sub> on a silver surface from an Fe atom and two CO molecules (Lee and Ho, 1999). The measurement of the conductance of individual molecules, which can be made in various ways including STM, is of major interest in the area of molecular electronics (Nitzan and Ratner, 2003; Selzer and Allara, 2006).

Single-molecule chemistry in condensed phases has required alternative approaches of which fluorescence has been the most generally useful. By using time-correlated photon counting, the photochemistry of individual fluorescent molecules can be examined. For example, intramolecular photoinduced electron transfer in a dendrimer diluted in a spin-coated polymer has been investigated. In this case, variations of the electron transfer rates (nanosecond) on the timescale of seconds were attributed to changes in the local environment and conformation of the dendrimer (Gronheid et al., 2003). Recently, Roeffaers and colleagues have used single-molecule fluorescence to show that the hydrolysis of fluorescein diacetate at room temperature occurs on a specific face of a catalytic Li/Al double hydroxide crystal, whereas transesterification occurs on all faces (Roeffaers et al., 2006). The use of fluorescence has limitations for the examination of small molecule chemistry, which have been discussed earlier in Section 10.8.



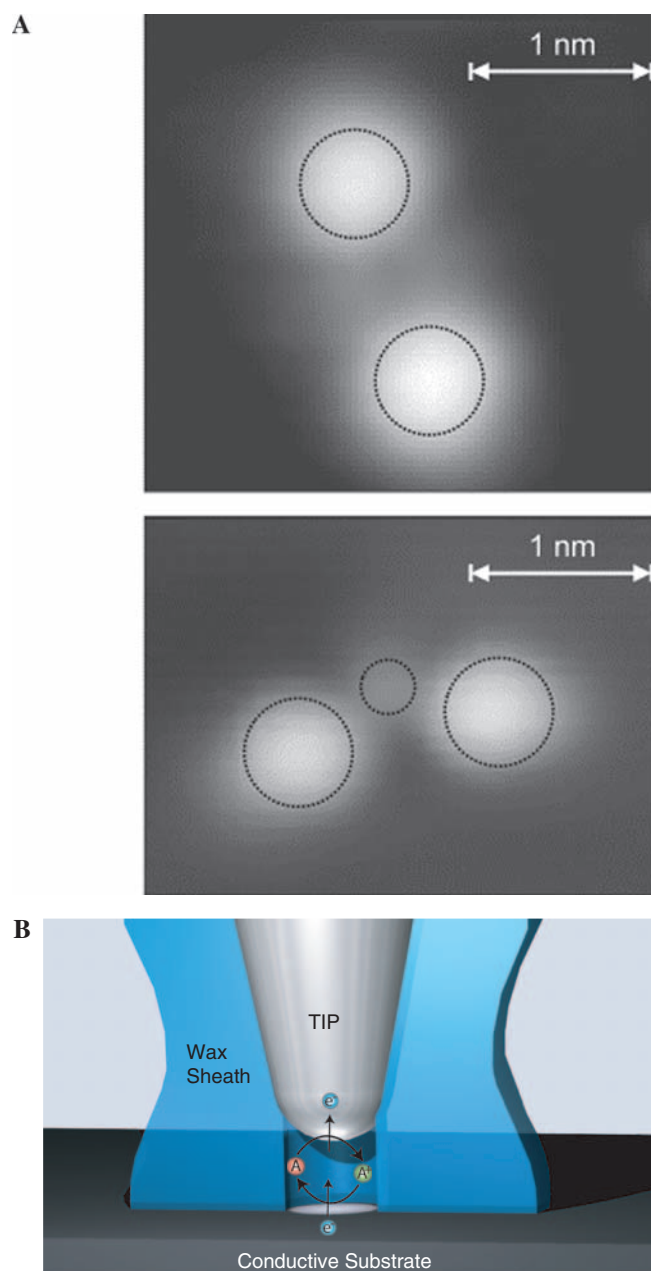


**Figure 10.7** Single-molecule chemistry of small molecules by alternative approaches. (A) Isomerization of an azobenzene in a scanning-tunneling microscope (STM) (Henzl et al., 2006). Top, the *trans* isomer; bottom, the *cis* isomer. One ring carried a 4-nitro group and the other a 4-amino group. (B) Fan and Bard observed the current produced by a single ferrocene derivative trapped in solution between a nanoelectrode and a conductive surface (Bard and Fan, 1996). In this case, the current represents multiple electrochemical turnovers of the same electroactive molecule.

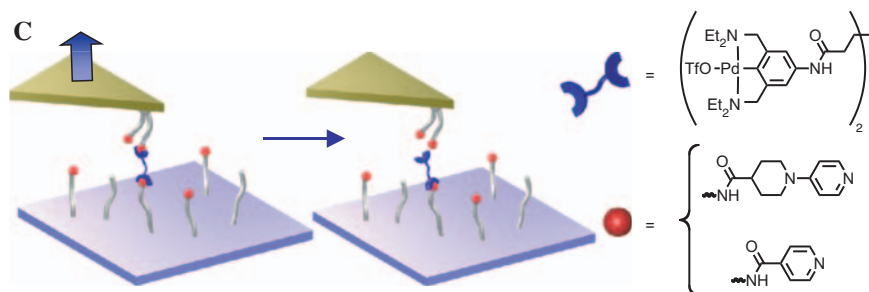


**Figure 10.7** (continued) (C) The cleavage of a Pd–N bond by mechanical activation with an atomic force microscope tip (Kersey et al., 2006)

Electrochemical approaches have been useful in particular circumstances. Fan and Bard observed the current produced by a single electroactive molecule trapped in solution between a nanoelectrode and a conductive surface (Bard and Fan, 1996). In this case, the current represented multiple electrochemical turnovers of the same molecule (Figure 10.7B). Collinson and Wightman generated, alternately, radical cations and radical anions from 9,10-diphenylanthracene in  $\sim 20$  fL of acetonitrile at a nanoelectrode surface and were able to observe the emission from individual excited singlet states formed after electron transfer between the radicals (Collinson and Wightman, 1995). The scope of the single-molecule chemistry that can be explored by electrochemical approaches is limited and it is rather difficult to obtain accurate rate constants in the experimental configurations that have been reported.

Force spectroscopy has been applied to examine bond breaking in a variety of situations. Noncovalent interactions are most readily investigated. For example, the dissociation kinetics of various ammonium cations from a resorc[4]arene that had been covalently bound to a gold substrate were investigated by force spectroscopy carried out in ethanol (Eckel et al., 2005). The cations were presented at the end of a PEG chain, the other end of which had been tethered to a  $\text{Si}_3\text{N}_4$  AFM tip. Dissociation rate constants could be obtained from the relationships between the dissociation force and the loading rate. The cleavage of the covalent bonds, Si–C and S–Au (Grandbois et al., 1999), and the rupture of Ni–nitriolotriacetate complexes (Conti et al., 2000) in aqueous solutions have been examined by a similar approach. Mechanical activation of a tip-linked leaving group has been shown to speed up nucleophilic attack of dimethylsulfoxide on a Pd(II) complex, involving the cleavage of a Pd–N bond and formation of a Pd–S bond (Kersey et al., 2006) (Figure 10.7C). At present, force spectroscopy is practical only for dissociative chemistry.

Finally, the chemistry of the superheavy elements (Schadel, 2006) is often explored one atom at a time. For example, element 108 was shown to have chemical properties similar to osmium on the basis of the temperature of adsorption of seven molecules of its oxide onto a silicon nitride surface (Düllmann and al., 2002).

## 10.10 Problematic Issues and Present Limitations of the Approach

The use of electrical recording to examine small molecule covalent chemistry in protein nanoreactors compares favorably with alternative techniques, as emphasized in Section 10.9. However, at this point, we have only sketched out part of the territory that can be explored by this means. Obviously, a more detailed quantitative analysis is warranted. Without doubt, chemistry observed inside a protein nanoreactor will differ from that in the bulk phase, although the extent to which it diverges is currently unclear. Whether the goal is to mimic reactions in solution faithfully or to investigate the effects of transport, confinement, and environment on small molecule chemistry, there remains a large number of issues that must be considered.

Is there evidence that chemistry in the  $\alpha$ HL nanoreactor differs from the same chemistry observed in the bulk phase? Where comparisons can be made, we can say that the differences are not great: within an order of magnitude for rate and equilibrium constants (Shin et al., 2002; Luchian et al., 2003a,b; Shin and Bayley, 2005). For example, we determined the  $pK_a$  value of a carbamate to be  $pK_a = 6.4$ , whereas the accepted literature value is  $pK_a = 5.2$  (Luchian et al., 2003a). There is, however, a need to study reactions where a direct comparison can be made under strictly equivalent conditions and, for the single-molecule experiments, where errors arising from limited sampling have been reduced to an acceptable level; this has not yet been done.

One factor that might influence chemistry in the nanoreactor is the small number of water molecules in the  $\beta$  barrel of the  $\alpha$ HL pore: about 500. Whether water confined in this way behaves “normally” is a topic of current theoretical, computational and experimental investigation (Zangi and Mark, 2003b,a; Beckstein and Sansom, 2004; Raviv et al., 2004). A study of water flow through  $\alpha$ HL pores in rabbit red blood cell membranes under an osmotic gradient supports the idea that the water in the pore behaves similarly to bulk water (Paula et al., 1999). The protonation kinetics of unidentified groups within the  $\alpha$ HL pore are also in keeping with this concept (Bezrukov and Kasianowicz, 1993; Kasianowicz and Bezrukov, 1995).

The walls of the nanoreactor might also affect the chemistry under observation. Surface forces and topology might serve to orient reactants in ways that could favor or disfavor a reaction. Fixed charges provided by amino acid sidechains are likely to present one of the strongest influences and here the ionic strength of the electrolyte is critical (Stauffer and Karlin, 1994; Hille, 2001). The effect of a fixed charge decays exponentially over a characteristic distance known as the Debye length ( $1/\kappa$ ), which is proportional to  $I^{-1/2}$ , where  $I$  is the ionic strength of a solution. The potential at  $1/\kappa$  from a single positive charge near a protein surface is about +10 mV (Hille, 2001). For a 100 mM NaCl solution  $1/\kappa$  is about 1 nm, the approximate radius of the lumen of the  $\alpha$ HL barrel domain, and for 1 M NaCl about 0.3 nm. The influence of engineered charged groups and the length and rigidity of the tethers that hold reactants in the pore, remains to be fully explored.

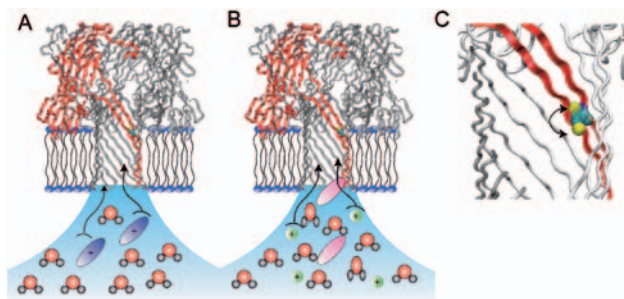


**Figure 10.8** The effect of the transmembrane potential on various aspects of chemistry in the  $\alpha$ HL nanoreactor. (A) The applied potential can drive charged reactants (blue ovals) into the reactor (or repel them). (B) The movement of neutral molecules (red ovals) can also be affected by the applied potential as a result of electroosmotic flow, the movement of solvent in response to the electrophoretic transport of ions. (C) The field within the pore arising from the applied potential is unlikely to orient tethered molecules with dipoles. The energy of orientation is well below  $kT$

The transmembrane potential, as opposed to a local potential, might also affect the course of a reaction by influencing the transport of reactants and products into and out of the nanoreactor. The voltage-dependent block of ion channels is a well-known phenomenon and has been analyzed by Woodhull in the context of proton binding sites within a channel lumen (Hille, 2001). Simply put, if a blocker binds at a site part of the way across the electric field maintained by the transmembrane potential, its dissociation constant from the site ( $K_d$ ) to the *trans* side of the bilayer will be altered:  $K_d(\Delta V) = K_d(0)\exp(-zF\delta\Delta V/RT)$ , where  $z$  is the charge on the blocker;  $\delta\Delta V$ , fractional drop of the membrane potential ( $\Delta V$ ) at the binding site (Moczydlowski, 1986; Hille, 2001). It follows that the on and off rates for the site will also be altered. For example, in a positive applied potential the on-rate for a positively charged molecule presented from the *trans* side of the bilayer will be increased (Figure 10.8A). The molecule is said to be “driven” into the pore. The effect can be large and it is an exponential function of the applied potential, for example, for +40 mV,  $\exp(-zF\delta\Delta V/RT) = 0.20$ ; +100 mV,  $\exp(-zF\delta\Delta V/RT) = 0.018$ .

The movement of neutral molecules into and out of a pore is also affected by the applied potential as a result of electro-osmotic flow, the movement of solvent in response to the electrophoretic transport of ions (Figure 10.8B). Because several water molecules are transported in association with each ion, the effect will be appreciable even for a weakly ion selective pore where there is still a significant net ion flux (i.e., more ions, of any type, moving in one direction). For example, we have studied the binding of  $\beta$ -cyclodextrin to a site within the  $\beta$  barrel of the  $\alpha$ HL pore. The rates of association and dissociation can be affected by more than 100-fold (Gu et al., 2003). In an additional consideration, when a reactant is transported through the membrane, net work is performed and equilibrium conditions (Section 10.6) are not fulfilled (Richard and Miller, 1990; Root and MacKinnon, 1994). These phenomena

associated with the transmembrane potential remain largely unexplored in the context of covalent chemistry. They can be ameliorated by working at low potential or by gathering data where extrapolations through 0 mV are possible. The potential drop in the *cis* cavity of the  $\alpha$ HL pore is lower than that in the  $\beta$  barrel (Howorka and Bayley, 2002), and it may be possible to compare chemistry carried out in the two compartments to ascertain the effects of an applied potential.

It is often asked whether the applied potential has an effect on the observed chemistry, as opposed to the transport of reactants. The local field arising from the applied potential is of the order of  $10^7 \text{ Vm}^{-1}$ . If we consider a molecule with a high dipole moment, such as the merocyanine form of a spiropyran at  $50\text{--}60 \times 10^{-30} \text{ Cm}$  (Sakata et al., 2005), the energy of orientation parallel to the field is  $DE = 0.36 \text{ kJ}$ , where  $D$  is the dipole moment;  $E$ , field strength. This value of  $\sim 0.14 \text{ kT}$  would produce only a weak orientation (Figure 10.8C). In cases where a tethered intermediate carries a full charge, it might be “pushed” or “pulled” from the reaction site and there are several ways in which this might affect the course of a reaction, for example, by moving the reaction center closer to a neighboring group on the wall of the nanoreactor. In the case of carbamate isomerization, as studied by Woolley and colleagues, a carbamate with a small positively charged group tethered at the entrance to the gramicidin pore can be pulled transiently into the pore in which case the overall *cis/trans* ratio and presumably the rates of interconversion of the two forms are altered, although the latter were not analyzed (Woolley et al., 1997). Local fields arising from fixed charge groups within a transmembrane pore can be strong compared with the field arising from the applied potential, and their effects were considered earlier (Stauffer and Karlin, 1994).

For a large reactant, the rate of entry into the pore and hence the rate of reaction at an internal site will depend on the size and flexibility of the molecule (Kong and Muthukumar, 2005). For example, large flexible molecules pay an entropic penalty for entry into the pore lumen. In the case of a PEG molecule, a 1000 Da polymer equipped with a pyridyl disulfide group reacts with an internal thiol group about 100 times more rapidly than a similarly equipped 5000 Da PEG (Movileanu and Bayley, 2001; Movileanu et al., 2001).

Chemistry within the pore might also be affected by pore-to-pore variation, which could arise from either dynamic or static “disorder”. Static disorder arises from fixed differences between pores that originate in mistranslation, misfolding, or posttranslational damage. Dynamic disorder, fluctuations in the functional properties of a protein with time, is thought to arise from conformational changes (Min et al., 2005), although other explanations are possible such as the existence of long-lived protonation states.

Of the practical issues arising from the nanoreactor approach, the ability to identify reaction intermediates by virtue of the associated current levels is of great importance. Much of the chemistry we are examining is quite subtle and the current steps can be small, sometimes less than 1 pA. The ability to observe these steps obviously depends on the current noise, as discussed earlier. Once this has been minimized, the experimenter must attempt to increase the magnitude of the steps themselves. Woolley and colleagues have nicely demonstrated that in the case of

gramicidin, a narrow, cation-selective channel, this can be done by carrying out the reaction at the opening through which ions enter, as determined by the applied potential (Jaikaran and Woolley, 1995). For a wider pore, such as  $\alpha$ HL, there is less logic to the selection of the reaction site and further exploration is needed. For the time being, we have chosen to use mainly the interior of the  $\beta$  barrel. Beyond that, the narrowest part of the lumen, near the constriction (as in position 117), and perhaps the *trans* entrance, based on the observations with gramicidin would seem to be reasonable choices as reaction sites.

It follows that it would be foolhardy to base the identification of intermediates on the sign or magnitude of small changes in current level, which are a poor indication of structure. Because individual molecules cannot be identified by spectroscopic techniques, with the possible exception of fluorescence spectroscopy, the “old-fashioned” tools of mechanistic chemistry must be employed, which include convergence on the same intermediate through different pathways, the chemical trapping or diversion of intermediates, the effects of pH, temperature, and so on on the reaction pathway, the appropriate use of substituent effects (e.g., linear-free energy relationships) and of isotope effects. Given the imprecision inherent in our approach, as presently implemented, only primary hydrogen isotope effects are likely to be of immediate use.

A final drawback of the technique is that it can only be used in water. Of course a great deal of interesting chemistry occurs in the aqueous phase (Lindström, 2002), which is relevant to pharmacology, biochemistry, “green” approaches, and so on. The possibility of carrying out similar experiments with stabilized bilayers (or alternative films) in nonaqueous solvents containing electrolytes or in ionic liquids (Baker et al., 2005) has not been explored.

## 10.11 Future Directions

As emphasized in the preceding text, we consider the work that has been done so far on single-molecule covalent chemistry in nanoreactors to be very much a first pass. Unexplored areas remain and in other cases there is a need for more detailed investigations. Certainly, many of the issues raised in Section 10.10 deserve further consideration. In particular, the environment within the nanoreactor requires additional investigation. How waterlike is the internal solvent? What are the effects of local potentials? The transport of reactants in and out of the nanoreactor is also poorly understood. Experiments designed to address these issues would be most informative if they were carried out in conjunction with theoretical and computational studies, where there is also progress to be made. In this context, computational studies of the fundamental functional properties of the  $\alpha$ HL pore are advancing (Noskov et al., 2004), and analyses of polymer transport have been carried out because of the interest in DNA sequencing (Mathé et al., 2005) and stochastic sensing (Kong and Muthukumar, 2005). By contrast, there has been little computational work on noncovalent or covalent interactions within the pore with the exception of a study of adapter (cyclodextrin) binding (Shilov and Kurnikova, 2003).

The desire to mimic chemistry in bulk solution, as far as possible, has already been mentioned. Here it is likely that resurfacing of the lumen of the  $\alpha$ HL pore will be required to minimize the interactions of reactants with the wall. The reaction conditions are also expected to be important; for example, the use of high ionic strength solutions will reduce electrostatic interactions and the application of the lowest possible transmembrane potentials will minimize the effects of the electrophoretic and electro-osmotic transport of reactants. The effects of tethering the reaction site to the wall of the reactor might be diminished by the development of untethered systems in which reactants are trapped between adapters, as proposed earlier (Gu et al., 2001), or locked within the nanoreactor, after they have entered, by a covalent reaction at the trans entrance.

The classes of chemistry that can be carried within the nanoreactor should be extended. Our work has largely been confined to the reactions of thiolates (i.e., deprotonated Cys sidechains) and of groups that can be attached to Cys residues. The latter is a versatile approach. Nonetheless, alternatives would facilitate the exploration of additional chemistry. An important option is the introduction of unnatural amino acids into the protein to provide a wider selection of reactive sidechains. We are applying both of the principal techniques for doing this to  $\alpha$ HL: the use of misacylated tRNAs (Wang and Schultz, 2004) and the introduction of synthetic peptide segments by native chemical ligation (Muir, 2003). For example, it would be interesting to explore the chemistry of a selenolate, provided by the sidechain of selenocysteine. Compared to thiols, selenols have a  $pK_a$  value that is reduced by about 3 units ( $pK_a \sim 6$ ) and the anion is possibly a better nucleophile than the thiolate (Johansson et al., 2005).

The potential applications of single-molecule covalent chemistry have not been reviewed here. Suffice it to say that stochastic sensing, a means to detect analytes at the single-molecule level, is a powerful emerging technology. Previous studies of stochastic sensing with engineered  $\alpha$ HL pores have focused on detection through noncovalent interactions (Bayley and Cremer, 2001). The chemistry demonstrated here offers the opportunity to detect molecules based on their reactivity rather than their size, shape and charge, as might be the case with conventional immunological detection, for example. Potential analytes include pesticides, chemical weapons, pharmaceuticals, and components of food (Figure 10.9).

The ability to carry out catalysis within the  $\alpha$ HL pore is an interesting proposition. Again this area has not been explored and the possibilities range from simple ideas such as the use of neighboring groups provided by amino acid sidechains to promote reaction to the introduction of more complex catalytic centers, such as coordinated metal ions. The ultimate goal would be to carry out a chemical transformation with coupled transmembrane translocation. In this regard, it is interesting that certain enzymes, such as carbamoyl phosphate synthase, carry out a series of transformations coordinated with vectorial movement of the substrate through a tunnel in the protein (Raushel et al., 2003). Another potential application is single-molecule synthetic chemistry, which offhand might be considered an esoteric pursuit. However, functionalized  $\alpha$ HL pores for stochastic sensing might be quickly built in situ, one step at a time, by monitoring the associated current.

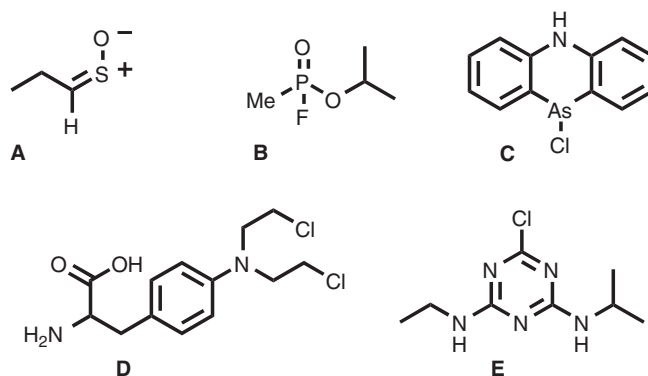


**Figure 10.9** Potential analytes for stochastic sensing based on single-molecule chemistry. **(A)** Propanthial S-oxide, found in chopped onions; **(B)** Sarin, a nerve “gas”; **(C)** Adamsite, former riot-control agent; **(D)** Melphalan, a chemotherapy agent; **(E)** Atrazine, a herbicide

## References

- Abbondanzieri, E. A., Greenleaf, W. J., Shaevitz, J. W., Landick, R., and Block, S. M. (2005). Direct observation of base-pair stepping by RNA polymerase. *Nature* *438*, 460–465.
- Baker, G. A., Baker, S. N., Pandey, S., and Bright, F. V. (2005). An analytical view of ionic liquids. *The Analyst* *130*, 800–808.
- Bard, A. J., and Fan, F.-R. F. (1996). Electrochemical detection of single molecules. *Acc Chem Res* *29*, 572–578.
- Bayley, H., and Cremer, P. S. (2001). Stochastic sensors inspired by biology. *Nature* *413*, 226–230.
- Bayley, H., and Jayasinghe, L. (2004). Functional engineered channels and pores. *Mol Membrane Biol* *21*, 209–220.
- Beckstein, O., and Sansom, M. S. (2004). The influence of geometry, surface character, and flexibility on the permeation of ions and water through biological pores. *Phys Biol* *1*, 42–52.
- Bezrukov, S. M., and Kasianowicz, J. J. (1993). Current noise reveals protonation kinetics and number of ionizable sites in an open protein ion channel. *Phys Rev Lett* *70*, 2352–2355.
- Blatz, A. L., and Magleby, K. L. (1986). Correcting single channel data for missed events. *Biophys J* *49*, 967–980.
- Braha, O., Walker, B., Cheley, S., Kasianowicz, J. J., Song, L., Gouaux, J. E., and Bayley, H. (1997). Designed protein pores as components for biosensors. *Chem Biol* *4*, 497–505.
- Braslavsky, I., Hebert, B., Kartalov, E., and Quake, S. R. (2003). Sequence information can be obtained from single DNA molecules. *Proc Natl Acad Sci USA* *100*, 3960–3964.
- Collinson, M. M., and Wightman, R. M. (1995). Observation of individual chemical reactions in solution. *Science* *268*, 1883–1885.
- Conti, M., Falini, G., and Samori, B. (2000). How strong is the coordination bond between a histidine tag and Ni-nitrilotriacetate? An experiment of mechanochemistry on single molecules. *Angew Chem Int Ed Engl* *39*, 215–218.
- Cymes, G. D., Ni, Y., and Grosman, C. (2005). Probing ion-channel pores one proton at a time. *Nature* *438*, 975–980.
- Düllmann, C. E., et al. (2002). Chemical investigation of hassium (element 108). *Nature* *418*, 859–862.



- Eckel, R., Ros, R., Decker, B., Mattay, J., and Anselmetti, D. (2005). Supramolecular chemistry at the single molecule level. *Angew Chem Int Ed Engl* 44, 484–488.
- Grandbois, M., Beyer, M., Rief, M., Clausen-Schaumann, H., and Gaub, H. E. (1999). How strong is a covalent bond? *Science* 283, 1727–1730.
- Gronheid, R., Stefan, A., Cotlet, M., Hofkens, J., Qu, J., Mullen, K., van der Auweraer, M., Verhoeven, J. W., and De Schryver, F. C. (2003). Reversible intramolecular electron transfer at the single-molecule level. *Angew Chem Int Ed Engl* 42, 4209–4214.
- Gu, L.-Q., and Bayley, H. (2000). Interaction of the non-covalent molecular adapter,  $\beta$ -cyclodextrin, with the staphylococcal  $\alpha$ -hemolysin pore. *Biophys J* 79, 1967–1975.
- Gu, L.-Q., Braha, O., Conlan, S., Cheley, S., and Bayley, H. (1999). Stochastic sensing of organic analytes by a pore-forming protein containing a molecular adapter. *Nature* 398, 686–690.
- Gu, L.-Q., Cheley, S., and Bayley, H. (2001). Capture of a single molecule in a nanocavity. *Science* 291, 636–640.
- Gu, L.-Q., Cheley, S., and Bayley, H. (2003). Electroosmotic enhancement of the binding of a neutral molecule to a transmembrane pore. *Proc Natl Acad Sci USA* 100, 15498–15503.
- Helveg, S., Lopez-Cartes, C., Sehested, J., Hansen, P. L., Clausen, B. S., Rostrup-Nielsen, J. R., Abild-Pedersen, F., and Nørskov, J. K. (2004). Atomic-scale imaging of carbon nanofibre growth. *Nature* 427, 426–429.
- Henzl, J., Mehlhorn, M., Gawronski, H., Rieder, K. H., and Morgenstern, K. (2006). Reversible cis-trans isomerization of a single azobenzene molecule. *Angew Chem Int Ed Engl* 45, 603–606.
- Herschbach, D. (2000). Fifty years in physical chemistry: Homage to mentors, methods, and molecules. *Annu Rev Phys Chem* 51, 1–39.
- Hille, B. (2001). *Ion Channels of Excitable Membranes*, 3rd edition, (Sunderland, MA, USA: Sinauer).
- Hladky, S. B., and Haydon, D. A. (1970). Discreteness of conductance change in biomolecular lipid membranes in the presence of certain antibiotics. *Nature* 225, 451–453.
- Ho, W. (2002). Single-molecule chemistry. *J Chem Phys* 117, 11033–11061.
- Howorka, S., and Bayley, H. (2002). Probing distance and electrical potential within a protein pore with tethered DNA. *Biophys J* 83, 3202–3210.
- Howorka, S., Movileanu, L., Lu, X., Magnon, M., Cheley, S., Braha, O., and Bayley, H. (2000). A protein pore with a single polymer chain tethered within the lumen. *J Am Chem Soc* 122, 2411–2416.
- Jaikaran, D. C. J., and Woolley, G. A. (1995). Characterization of thermal isomerization at the single molecule level. *J Phys Chem* 99, 13352–13355.
- Johansson, L., Gafvelin, G., and Arner, E. S. (2005). Selenocysteine in proteins-properties and biotechnological use. *Biochim Biophys Acta* 1726, 1–13.
- Kang, X., Gu, L.-Q., Cheley, S., and Bayley, H. (2005). Single protein pores containing molecular adapters at high temperatures. *Angew Chem Int Ed Engl* 44, 1495–1499.
- Kasianowicz, J. J., and Bezrukov, S. M. (1995). Protonation dynamics of the  $\alpha$ -toxin channel from spectral analysis of pH-dependent current fluctuations. *Biophys J* 69, 94–105.
- Kersey, F. R., Yount, W. C., and Craig, S. L. (2006). Single-molecule forces spectroscopy of bimolecular reactions: System homology in the mechanical activation of ligand substitution reactions. *J Am Chem Soc* 128, 3886–3887.
- Kong, C. Y., and Muthukumar, M. (2005). Simulations of stochastic sensing of proteins. *J Am Chem Soc* 127, 18252–18261.
- Lawrence, D. S. (2005). The preparation and in vivo applications of caged peptides and proteins. *Curr Opin Chem Biol* 9, 570–575.
- Lee, A. I., and Brody, J. P. (2005). Single-molecule enzymology of chymotrypsin using water-in-oil emulsion. *Biophys J* 88, 4303–4311.
- Lee, H. J., and Ho, W. (1999). Single-bond formation and characterization with a scanning tunneling microscope. *Science* 286, 1719–1722.
- Lindström, U. (2002). Stereoselective organic reactions in water. *Chem Rev* 102, 2751–2772.

- Ludwig, S., and Bayley, H. (2005). In *Light-Activated Proteins: An Overview Dynamic Studies in Biology: Phototriggers, Photoswitches and Caged Biomolecules*, M. Goeldner, and R. Givens, eds. (Weinheim, Germany: Wiley-VCH Verlag), pp. 253–304.
- Lu, H. P., Xun, L., and Xie, X. S. (1998). Single-molecule enzymatic dynamics. *Science* 282, 1877–1882.
- Luchian, T., Shin, S.-H., and Bayley, H. (2003a). Kinetics of a three-step reaction observed at the single molecule level. *Angew Chem Int Ed* 42, 1926–1929.
- Luchian, T., Shin, S.-H., and Bayley, H. (2003b). Single-molecule covalent chemistry with spatially separated reactants. *Angew Chem Int Ed* 42, 3766–3771.
- Mathé, J., Aksimentiev, A., Nelson, D. R., Schulten, K., and Meller, A. (2005). Orientation discrimination of single-stranded DNA inside the alpha-hemolysin membrane channel. *Proc Natl Acad Sci U S A* 102, 12377–12382.
- Mayer, M., Kriebel, J. K., Tosteson, M. T., and Whitesides, G. M. (2003). Microfabricated teflon membranes for low-noise recordings of ion channels in planar lipid bilayers. *Biophys J* 85, 2684–2695.
- Min, W., English, B. P., Luo, G., Cherayil, B. J., Kou, S. C., and Xie, X. S. (2005). Fluctuating enzymes: Lessons from single-molecule studies. *Acc Chem Res* 38, 923–931.
- Mindell, J. A., Zhan, H., Huynh, P. D., Collier, R. J., and Finkelstein, A. (1994). Reaction of diphtheria toxin channels with sulfhydryl reagents: Observation of chemical reactions at the single molecule level. *Proc Natl Acad Sci USA* 91, 5272–5276.
- Moczydlowski, E. (1986). In *Single-Channel Enzymology Ion Channel Reconstitution*, C. Miller, ed. (New York: Plenum Press), pp. 75–113.
- Morrill, J. A., and MacKinnon, R. (1999). Isolation of a single carboxyl-carboxylate proton binding site in the pore of a cyclic nucleotide-gated channel. *J Gen Physiol* 114, 71–83.
- Movileanu, L., and Bayley, H. (2001). Partitioning of a polymer into a nanoscopic protein pore obeys a simple scaling law. *Proc Natl Acad Sci USA* 98, 10137–10141.
- Movileanu, L., Cheley, S., and Bayley, H. (2003). Partitioning of individual flexible polymers into a nanoscopic protein pore. *Biophys J* 85, 897–910.
- Movileanu, L., Cheley, S., Howorka, S., Braha, O., and Bayley, H. (2001). Location of a constriction in the lumen of a transmembrane pore by targeted covalent attachment of polymer molecules. *J Gen Physiol* 117, 239–251.
- Movileanu, L., Howorka, S., Braha, O., and Bayley, H. (2000). Detecting protein analytes that modulate transmembrane movement of a polymer chain within a single protein pore. *Nature Biotechnology* 18, 1091–1095.
- Muir, T. (2003). Semisynthesis of proteins by expressed protein ligation. *Ann Rev Biochem* 72, 249–289.
- Musyanovych, A., Mailander, V., and Landfester, K. (2005). Miniemulsion droplets as single molecule nanoreactors for polymerase chain reaction. *Biomacromolecules* 6, 1824–1828.
- Nitzan, A., and Ratner, M. A. (2003). Electron transport in molecular wire junctions. *Science* 300, 1384–1389.
- Noskov, S. Y., Im, W., and Roux, B. (2004). Ion permeation through the alpha-hemolysin channel: Theoretical studies based on Brownian dynamics and Poisson-Nernst-Planck electrodiffusion theory. *Biophys J* 87, 2299–2309.
- Otero, R., Rosei, F., and Besenbacher, F. (2006). Scanning tunneling microscopy manipulation of complex organic molecules on solid surfaces. *Annu Rev Phys Chem* 57, 497–525.
- Paula, S., Akesson, M., and Deamer, D. (1999). Water transport by the bacterial channel  $\alpha$ -hemolysin. *Biochim Biophys Acta* 1418, 117–126.
- Pietrobon, D., Prod'hom, B., and Hess, P. (1988). Conformation changes associated with ion permeation in L-type calcium channels. *Nature* 333, 373–376.
- Pietrobon, D., Prod'hom, B., and Hess, P. (1989). Interactions of protons with single open L-type calcium channels: pH Dependence of proton-induced current fluctuations with Cs<sup>+</sup>, K<sup>+</sup>, and Na<sup>+</sup> as permeant ions. *J Gen Physiol* 94, 1–21.
- Prod'hom, B., Pietrobon, D., and Hess, P. (1987). Direct measurement of proton transfer rates to a group controlling the dihydropyridine-sensitive Ca<sup>2+</sup> channel. *Nature* 329, 243–246.

- Prod'hom, B., Pietrobon, D., and Hess, P. (1989). Interactions of protons with single open L-type calcium channels: Location of protonation site and dependence of proton-induced current fluctuations on concentration and species of permeant ion. *J Gen Physiol* 94, 23–42.
- Raushel, F. M., Thoden, J. B., and Holden, H. M. (2003). Enzymes with molecular tunnels. *Acc Chem Res* 36, 539–548.
- Raviv, U., Perkin, S., Laurat, P., and Klein, J. (2004). Fluidity of water confined down to subnanometer films. *Langmuir* 20, 5322–5332.
- Richard, E. A., and Miller, C. (1990). Steady-state coupling of ion-channel conformations to a transmembrane ion gradient. *Science* 247, 1208.
- Roeffaers, M. B., Sels, B. F., Uji, I. H., De Schryver, F. C., Jacobs, P. A., De Vos, D. E., and Hofkens, J. (2006). Spatially resolved observation of crystal-face-dependent catalysis by single turnover counting. *Nature* 439, 572–575.
- Rondelez, Y., Tresset, G., Tabata, K. V., Arata, H., Fujita, H., Takeuchi, S., and Noji, H. (2005). Microfabricated arrays of femtoliter chambers allow single molecule enzymology. *Nat Biotechnol* 23, 361–365.
- Root, M. J., and MacKinnon, R. (1994). Two identical noninteracting sites in an ion channel revealed by proton transfer. *Science* 265, 1852–1856.
- Sakata, T., Yan, Y., and Marriott, G. (2005). Optical switching of dipolar interactions on proteins. *Proc Natl Acad Sci U S A* 102, 4759–4764.
- Schadel, M. (2006). Chemistry of superheavy elements. *Angew Chem Int Ed Engl* 45, 368–401.
- Selzer, Y., and Allara, D. L. (2006). Single-molecule electrical junctions. *Annu Rev Phys Chem* 57, 593–623.
- Shapovalov, G., and Lester, H. A. (2004). Gating transitions in bacterial ion channels measured at 3 microseconds resolution. *J Gen Physiol* 124, 151–161.
- Shilov, I. Y., and Kurnikova, M. G. (2003). Energetics and dynamics of a cyclic oligosaccharide molecule in a confined protein pore environment. A molecular dynamics study. *J Phys Chem B* 107, 7189–7201.
- Shin, S.-H., and Bayley, H. (2005). Stepwise growth of a single polymer chain. *J Am Chem Soc* 127, 10462–10463.
- Shin, S.-H., Luchian, T., Cheley, S., Braha, O., and Bayley, H. (2002). Kinetics of a reversible covalent-bond forming reaction observed at the single molecule level. *Angew Chem Int Ed* 41, 3707–3709.
- Spuches, A. M., Kruszyna, H. G., Rich, A. M., and Wilcox, D. E. (2005). Thermodynamics of the As(III)-thiol interaction: Arsenite and monomethylarsenite complexes with glutathione, dihydrolipoic acid, and other thiol ligands. *Inorganic Chemistry* 44, 2964–2972.
- Stauffer, D. A., and Karlin, A. (1994). The electrostatic potential of the acetylcholine binding sites in the nicotinic receptor probed by reactions of binding-site cysteines with charged methanethiosulfonates. *Biochemistry* 33, 6840–6849.
- Wang, L., and Schultz, P. G. (2004). Expanding the genetic code. *Angew Chem Int Ed Engl* 44, 34–66.
- Woolley, G. A., Jaikaran, A. S. I., Zhang, Z., and Peng, S. (1995). Design of regulated ion channels using measurements of *cis-trans* isomerization in single molecules. *J Am Chem Soc* 117, 4448–4454.
- Woolley, G. A., Zunic, V., Karanicolas, J., Jaikaran, A. S. I., and Starostin, A. V. (1997). Voltage-dependent behavior of a ball-and-chain gramicidin channel. *Biophys J* 73, 2465–2475.
- Yasuda, S., Nakamura, T., Matsumoto, M., and Shigekawa, H. (2003). Phase switching of a single isomeric molecule and associated characteristic rectification. *J Am Chem Soc* 125, 16430–16433.
- Zangi, R., and Mark, A. E. (2003a). Bilayer ice and alternate liquid phases of confined water. *J Chem Phys* 119, 1694–1700.
- Zangi, R., and Mark, A. E. (2003b). Monolayer ice. *Phys Rev Lett* 91, 025502–025501 to 025502–025504.

# Chapter 11

## Single-Molecule Microscopy and Force Spectroscopy of Membrane Proteins

Andreas Engel(✉), Harald Janovjak, Dimtrios Fotiadis, Alexej Kedrov,  
David Cisneros, and Daniel J. Müller

11.1	Introduction .....	280
11.2	High-Resolution Imaging Using Atomic Force Microscopy.....	282
11.2.1	Sample Preparation.....	282
11.2.2	AFM Imaging .....	283
11.2.3	Optimizing Conditions for Contact Mode Imaging.....	283
11.2.4	Determining Oligomeric State and Assembly .....	286
11.2.5	Observing Native Membranes .....	287
11.2.6	AFM, a Structural Biology Method Complementing Biochemical Procedures .....	288
11.2.7	Observing the Diffusion of Single Membrane Proteins .....	288
11.2.8	Observing Structural Flexibility of Membrane Proteins .....	289
11.2.9	Imaging Conformational Changes of Native Membrane Proteins.....	292
11.2.10	Controlled Manipulation.....	292
11.3	Single-Molecule Force Spectroscopy of Membrane Proteins .....	294
11.3.1	Molecular Interactions Establish Stable Structural Segments Within Membrane Proteins .....	295
11.3.2	Mapping Molecular Interactions Stabilizing Structural Segments .....	297
11.3.3	Membrane Proteins Choosing Different Unfolding Pathways and Crossing Different Barriers .....	298
11.3.4	Protein–Protein Interactions Influence Stability and Unfolding Pathways of Membrane Proteins .....	299
11.3.5	Which Interactions Establish Stable Structural Segments?.....	299
11.3.6	Unfolding Pathways Depend on Temperature .....	300
11.3.7	How Do Secondary Structure Elements Unfold at Zero Force?.....	301
11.3.8	Probing the Energy Landscape of Secondary Structures.....	301
11.3.9	Determining Natural Unfolding Rates of Secondary Structure Elements.....	302
11.3.10	Dynamic Properties of Single Proteins.....	302
11.3.11	Observing Folding Steps and Kinetics of Single Membrane Proteins .....	304
11.5	Conclusion and Perspectives .....	305
	References.....	306

---

Andreas Engel  
M.E. Müller Institute for Structural Biology, Biozentrum, University of Basel,  
Klingelbergstrasse 70, 4056 Basel, Switzerland  
andreas.engel@unibas.ch

R. Rigler and H. Vogel (eds.), *Single Molecules and Nanotechnology*. 279  
*Springer Series in Biophysics 12*.  
© Springer-Verlag Berlin Heidelberg 2008

**Abstract** Single-molecule atomic force microscopy (AFM) provides novel ways to characterize the structure-function relationship of native membrane proteins. High-resolution AFM topographs allow observing the structure of single proteins at sub-nanometer resolution as well as their conformational changes, oligomeric state, molecular dynamics and assembly. We will review these feasibilities illustrating examples of membrane proteins in native and reconstituted membranes. Classification of individual topographs of single proteins allows understanding the principles of motions of their extrinsic domains, to learn about their local structural flexibilities and to find the entropy minima of certain conformations. Combined with the visualization of functionally related conformational changes these insights allow understanding why certain flexibilities are required for the protein to function and how structurally flexible regions allow certain conformational changes. Complementary to AFM imaging, single-molecule force spectroscopy (SMFS) experiments detect molecular interactions established within and between membrane proteins. The sensitivity of this method makes it possible to measure interactions that stabilize secondary structures such as transmembrane  $\alpha$ -helices, polypeptide loops and segments within. Changes in temperature or protein-protein assembly do not change the locations of stable structural segments, but influence their stability established by collective molecular interactions. Such changes alter the probability of proteins to choose a certain unfolding pathway. Recent examples have elucidated unfolding and refolding pathways of membrane proteins as well as their energy landscapes. Other examples show the capability of this approach to detect and to locate ligand and inhibitor binding to a protein. We review current and future potential of these approaches to reveal insights into membrane protein structure and function.

## 11.1 Introduction

Atomic force microscopy (AFM; Binnig et al., 1986; Drake et al., 1989) and single-molecule force spectroscopy (SMFS; Leckband, 2000; Zhuang and Rief, 2003) provide novel approaches to characterize membrane proteins under freely adjustable physiologically relevant environments. In contrast to most other microscopy techniques AFM does not require labeling or fixation of the biological sample. Instead the sample is exposed to buffer solution at ambient temperatures, which maintains its full biological activity and enables observation of dynamic processes. The outstanding signal-to-noise (S/N) ratio of AFM topographs allows us to locate single molecules and to observe their structural details. This offers new experimental possibilities; in particular, it has become possible to study the structural and functional individuality of biological molecules and to investigate factors stimulating their variability. In principle, every single component of a macromolecular assembly can be observed in an AFM topograph, opening new avenues to study pathways of molecular biological reactions.

Recently, fast scanning AFMs were developed that are able to record up to 200 AFM topographs within one second and allowing the observation of biological processes in real time (Ando et al., 2003; Hobbs et al., 2006; Humphris et al., 2005; Schitter et al., 2004; Viani et al., 2000). In all measurements reviewed here the membrane proteins were embedded in the native membrane or into reconstituted membrane bilayers. In the first part of this review, we provide an overview of high-resolution AFM imaging (vertical resolution  $\approx 0.1$  nm, lateral resolution  $\approx 0.5$  nm), which allows visualizing the oligomeric states and the structural assemblies of functional membrane proteins. At the same time, conformational fluctuations of delicate structures were mapped and local flexibilities of the protein surface determined. Examples demonstrate that functionally related conformational changes are directly observed on single native membrane proteins at molecular resolution using AFM.

The AFM stylus probes molecular surfaces at high resolution. However, interactions occurring between stylus and the biological object can have multiple origins and various interaction mechanisms may contribute on the molecular scale. To detect multiple biochemical and biophysical interactions and parameters of a membrane protein the AFM stylus can be freely modified (Frederix et al., 2003). We discuss perspectives of such a 'lab on the tip'. Although AFM allows the observation of single membrane proteins at subnanometer resolution (Czajkowsky and Shao, 1998; Engel and Müller, 2000; Frederix et al., 2004; Müller and Anderson, 2002), SMFS enables us to detect inter- and intramolecular interactions within and between proteins (Kellermayer et al., 1997; Marszalek et al., 1999; Oesterhelt et al., 2000; Rief et al., 1997). Additionally, we discuss recent advances in SMFS performed on membrane proteins. Such experiments detected the stability of membrane proteins (Müller et al., 2002c) and probed their energy landscape (Janovjak et al., 2004) and refolding pathways (Kedrov et al., 2004).

Structural segments within the protein establish stable units that may be represented by transmembrane  $\alpha$ -helices, polypeptide loops, or fragments hereof. It is assumed that all amino acids (aa) within such segments collectively establish stabilizing interactions. Once the externally applied force overcomes the stability of these segments its aa unfold spontaneously within the time resolution of the experiment. The first experiments allowed investigating how environmental variations such as the oligomeric assembly (Sapra et al., 2006a), temperature changes (Janovjak et al., 2003), point mutations (Müller et al., 2002c), or pH variations (Kedrov et al., 2005) influenced the stability of these structural segments and thereby the unfolding pathways of the protein. Comparing stable structural segments established within two different membrane proteins having almost identical structures allowed us to gain insights into the origin of these interactions (Cisneros et al., 2005).

Recently, it has become possible to observe the refolding of secondary structure elements into the final protein and to estimate their folding kinetics from single-molecule experiments (Kedrov et al., 2006a). Unfolding of bovine rhodopsin (Rho) revealed that molecular interactions establishing structurally stable segments have at least dual roles (Sapra et al., 2006b). First, they stabilize the entire membrane protein, which is a prerequisite for proper functioning of the

G-protein coupled receptor (GPCR). Second, they position highly conserved residues (>80%) within the protein. Based on these results, it became possible to set up SMFS experiments for detection and localisation of molecular interactions occurring upon ligand binding and protein activation (Kedrov et al., 2005) as well as upon inhibitor binding and protein deactivation (Kedrov et al. 2006b). Because molecular interactions drive all biological processes, future SMFS may be applied to break down the contribution of individual interactions driving these processes. Such approaches will assist in our understanding the molecular language of biological processes.

## 11.2 High-Resolution Imaging Using Atomic Force Microscopy

### 11.2.1 *Sample Preparation*

AFM and SMFS sample preparation methods of membrane proteins in buffer solutions all have the objective to attach the specimen to a supporting surface (Amrein and Müller, 1999; Cisneros et al., 2006; Karrasch et al., 1993). The immobilization strategies of membrane proteins for AFM imaging and SMFS only differ little. For imaging proteins have to be adsorbed tightly to the support. If this is not done, proteins will be displaced by the scanning AFM stylus or move during scanning impeding their high-resolution imaging. Lateral forces are largely eliminated by the dynamic (or tapping) imaging mode, where the stylus is oscillated vertically, touching the sample surface only at the very end of every downward movement. Alternatively, noncontact imaging may be applied to reduce lateral forces (Hogan, 2006; Hoogenboom et al., 2006).

For SMFS the vertical anchoring of a protein to the supporting surface is most important. This is facilitated by the surrounding membrane, which is adsorbed to the support and at the same time anchors the membrane protein by hydrophobic interactions. In most cases biological membranes are adsorbed to freshly cleaved mica by adjusting the electrolyte and pH of the buffer solution (Müller et al., 1997b). Whereas the pH determines the surface charge of the membrane, the electrolyte concentration shields the electrostatic double-layer repulsion between membrane and supporting surface (Müller et al., 1997a). This shielding is facilitated by a counterion layer being accumulated at a charged surface in solution (Israelachvili, 1991). The thickness of this counterion layer is characterized by the Debye length and depends on the electrolyte concentration of the buffer solution. At sufficiently high electrolyte concentration the Debye length gets small enough so that membrane and support can approach close enough to snap into van der Waals attraction. This attraction finally immobilizes the membrane. The minimal concentration of KCl or NaCl for adsorbing biological membranes to mica typically ranges between 50–100 mM. After the membranes have been adsorbed the buffer solution can be almost freely chosen and exchanged for imaging.

### 11.2.2 AFM Imaging

The AFM (Figure 11.1; (Binnig et al., 1986)) uses a piezo device to raster scan a sharp stylus mounted at the end of a flexible cantilever over the biological sample. A reflected laser beam detects cantilever deflections with resolution of  $<1 \text{ \AA}$ . These deflections are used by a feedback system to contour the biological object and to minimize the force applied between the stylus and the fragile object. While the stylus scans over corrugations, the feedback of the piezo scanner perpendicular to the  $x$ - $y$  raster plane minimizes the deviation of the cantilever deflection from a preset value. In this way, the cantilever stylus contours the sample surface at a preset force. Biomolecular forces lie between a few pN ( $1 \text{ pN} = 10^{-12} \text{ N}$ ), as generated, for example, by motor proteins, and 250 pN, as required to break the specific streptavidin–biotin bond. It is important to ensure that imaging forces between stylus and sample are sufficiently small to prevent sample distortion or disruption. Imaging forces ranging between 50 and 100 pN are sufficiently small to observe proteins in their native state. Delicate substructural details such as loops or peptide ends are traced with sufficient precision to directly compare structural models derived from X-ray and electron crystallography (Heymann et al., 1999; Schabert et al., 1995).

### 11.2.3 Optimizing Conditions for Contact Mode Imaging

A substantial number of membrane proteins were imaged with the AFM during the last decade (Czajkowsky et al., 2004,1998; Fotiadis et al., 2000, 2003, 1998, 2004b; Hoh et al., 1993; Karrasch et al., 1994; Mou et al., 1995; Müller et al., 1995;

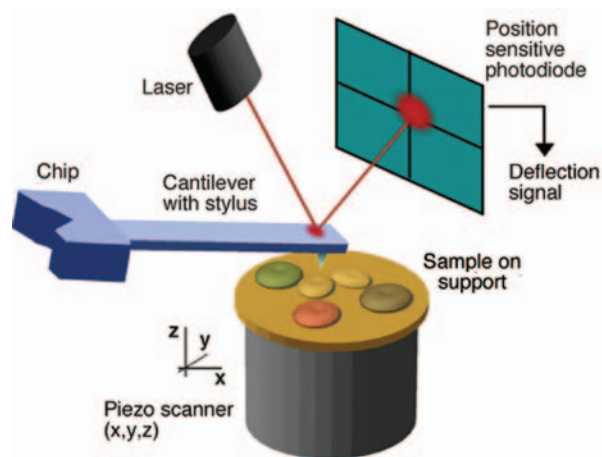


**Figure 11.1** Schematic AFM setup. The sample is mounted on a three-axis ( $x,y,z$ ) piezo scanner and raster-scanned by the stylus attached to the cantilever. A laser beam detects the deflection of the cantilever for each point of the raster-pattern



Pogoryelov et al., 2005; Schabert et al., 1995; Scheuring et al., 2001, 2004; Seelert et al., 2000; Stahlberg et al., 2001). Most of these high-resolution topographs have been acquired using contact mode AFM. While establishing AFM for high-resolution imaging of proteins the first question that arose was whether the topographs correlate to the native protein structure. Besides establishing immobilization strategies (Amrein and Müller, 1999; Wagner, 1998), imaging conditions had to be developed that prevent any functional or structural distortion of the sample. Experiments demonstrated that the relatively soft proteins could be easily deformed by the scanning AFM stylus (Fotiadis et al., 1998; Müller et al., 1995, 1999c).

The first successful approaches of reproducibly imaging protein substructures were focused on minimizing the interacting forces between the AFM stylus and the biological sample using tapping mode (Möller et al., 1999), or electrostatically controlled contact mode imaging (Müller et al., 1999b). Electrostatic interactions, van der Waals interaction, and Pauli repulsion are the major forces interacting between AFM stylus and a biological sample when imaging in buffer solution (Butt et al., 1995). Recording of a force–distance (F-D) curve between stylus and sample reveals the nature of these forces. Whereas Pauli repulsion and van der Waals interaction are determined by the surface properties of stylus and biological sample, the electrostatic double-layer interactions additionally depend on the pH and electrolyte of the buffer solution.

Similar to the procedure applied to adsorb membranes to a supporting surface the electrolyte concentration of the buffer solution can be adjusted to control the electrostatic repulsion between AFM stylus and sample. F-D curves directly reveal the amount of electrostatic repulsion. Best high-resolution topographs have been achieved by adjusting the long-range electrostatic repulsive force to about 50 pN while applying a force of  $\approx 100$  pN to the cantilever. As a result the net force interacting locally between the AFM stylus and local protein structures is  $\approx 50$  pN, which is sufficient to contour the sample without structural distortion (Fotiadis et al., 2002; Müller et al., 1995, 1999b). A positive side effect is achieved by pushing the AFM stylus against an electrostatic counterforce to the sample. It reduces the thermal noise of the cantilever because the stylus now builds a coupled system with the sample (unpublished results).

Besides controlling the interaction forces, AFM feedback parameters must be optimized to ensure distortion-free contouring of the sample. Thus, fast cantilever detection, fast feedback, and fast piezo movements are required to compensate changes in the cantilever deflection. So far, most high-resolution topographs could be obtained using 100  $\mu\text{m}$  long, V-shaped cantilevers exhibiting a force constant of  $\approx 0.1$  N/m and a resonance frequency around 9 kHz in aqueous solution (Olympus Ltd., Japan). Under such conditions, topographs of protein surfaces routinely revealed details with a lateral resolution of 5 Å and a vertical resolution of 1 Å (Müller and Anderson, 2002; Müller et al., 1999b).

Importantly, such topographs exhibit an outstanding S/N ratio, enabling recognition of single molecule structural features with unprecedented clarity. Figure 11.2 shows topographs of both cytoplasmic and extracellular surfaces of purple membranes (Müller et al., 1999c) from *Halobacterium salinarum*. This native 2D crystal is

composed of lipids and bacteriorhodopsin (BR), a light-driven proton pump (Oesterhelt and Stoeckenius, 1974). BR assembles into trimers, which assemble into a hexagonal arrangement. High-resolution AFM topographs of the cytoplasmic (Figure 11.2A) and extracellular (Figure 11.2B) BR surfaces reveal the structural details of the fully active BR trimers (see broken circles in Figure 11.2). The calculated 2D power spectrum of the extracellular side (Figure 11.2B) is displayed in Figure 11.2C. Sharp spots extend beyond the (1 nm) resolution limit (broken circle), for example, the spot (6,9) corresponds to a lateral resolution of 0.41 nm. Many grey levels are resolved in this topograph of the purple membrane, whose extracellular surface exhibits a corrugation of 0.6 nm, and thus the vertical resolution achieved in this case is better than 0.1 nm.

These AFM topographs of the native purple membrane correlated well with structural information elucidated using X-ray crystallography and electron microscopy (Heymann et al., 1999; Müller et al., 1999c). Such advanced studies showed that if sample preparation and imaging conditions were optimized structural details obtained from AFM and other conventional techniques could be correlated within a few Ångstroms deviation (Heymann et al., 1999; Karrasch et al., 1994; Schabert et al., 1995). However, AFM topographs also revealed that certain polypeptide loops of BR molecules assembled into dimers showed different conformations compared to loops of BR trimers (Müller et al., 1999c).

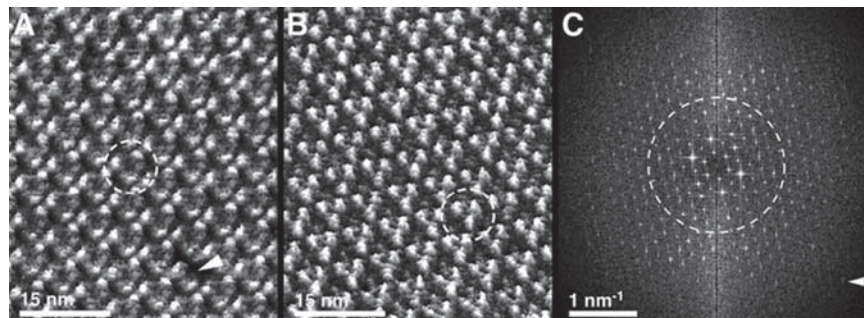


**Figure 11.2** High-resolution AFM topographs of the cytoplasmic (A) and the extracellular surface (B) of native purple membrane from *H. salinarum*. Dashed circles indicate single bacteriorhodopsin (BR) trimers. A trimer lacking a single missing BR monomer is indicated by an arrowhead (A). (C) Calculated power spectrum from the extracellular surface (B). The dashed circle represents the (1 nm) resolution limit. The arrow head points at diffraction spot (6,9) corresponding to a resolution limit of 0.41 nm. Imaging buffers: 20 mM Tris-HCl (pH 7.8), 150 mM KCl (cytoplasmic surface), and 20 mM Tris-HCl (pH 7.8), 150 mM KCl, 25 mM MgCl<sub>2</sub> (extracellular surface). Full gray levels of topographs correspond to a vertical range of 1.2 nm (A) and 0.8 nm (B)

### 11.2.4 Determining Oligomeric State and Assembly

AFM was applied to determine the oligomeric state or assembly of various membrane proteins. Figure 11.3A shows a densely packed assembly of sodium driven rotors of a bacterial  $F_0F_1$ -ATP synthase. Each rotor (diameter  $\approx 5.4$  nm) is assembled from eleven identical subunits (Figure 11.3B; (Stahlberg et al., 2001)). Surprisingly, AFM topographs recorded from ion-driven rotors of  $F_0F_1$ -ATP synthases from other species indicated a different number of subunits, for example, rotors from spinach chloroplast  $F_0F_1$ -ATP synthases: 14 subunits (Figure 11.3C; Seelert et al., (2000)) and rotors from *Spirulina platensis*: 15 subunits (Figure 11.3D; Pogoryelov et al., (2005)). Although most recent reviews report on the high-resolution AFM imaging of isolated human, vertebrate, bacterial, and plant membrane proteins (Czajkowsky, 2000, p.1581) a new era of observing the complex assemblies of native membrane proteins has begun (Fotiadis et al., 2004a; Scheuring et al., 2005). Highlights of some very recent examples show exciting insights into the oligomeric state and assembly of murine and bovine Rho (Fotiadis et al., 2003, 2004a), the cytolysin prepore formation (Czajkowsky et al., 2004), and into different supramolecular assemblies of light harvesting complexes from various organisms (Fotiadis et al., 1998, 2004b; Scheuring et al., 2005, 2004; Scheuring and Sturgis, 2005).

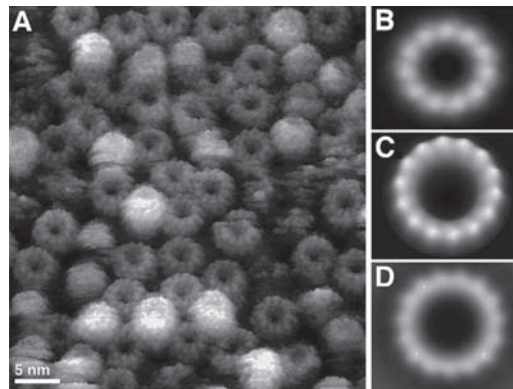


**Figure 11.3** Determining the oligomeric state of ion driven rotors from  $F_0F_1$ -ATP synthases using AFM. (A) AFM topography of sodium driven rotors of the F-ATP synthase from *Ilyobacter tartaricus* recorded in buffer solution (300 mM KCl, 10 mM Tris, pH 7.8) at room temperature. The upper right inset (B) shows the correlation averaged topograph of the raw data (A). The rotor has an outer diameter of  $\approx 5.4$  nm. Insets (C) and (D) represent correlation averages obtained from topographs of the proton-driven rotor of the spinach chloroplast (C) and of the sodium-driven rotor of the *Spirulina platensis* (D)  $F_0F_1$ -ATP synthases. To encompass the enhanced numbers of subunits the rotors have an outer diameter of 7.3 nm (C) and 6.3 nm (D). F-ATP synthase rotor shown in (C) is displayed in a perspective view ( $5^\circ$  tilt)

### 11.2.5 Observing Native Membranes

The best way to study membrane proteins under native or near-native conditions is to directly prepare and observe them in buffer solution. The AFM is currently the only instrument that allows imaging under these conditions with a resolution better than 2 nm. Recently, topographs of the native bacterial photosynthetic membrane of *Rhodospseudomonas viridis* have revealed the molecular organization of the photosynthetic core complex (Scheuring et al., 2003) and its changes during light adaptation (Scheuring and Sturgis, 2005). AFM topographs of disk membranes of murine retina have elucidated the native organization of Rho molecules, which are arranged in rows of dimers (Fotiadis et al., 2003) (Figure 11.4), in contrast to findings from early optical studies. These AFM data were further confirmed by electron microscopy, blue native- and sodium dodecyl sulphate-polyacrylamide gel electrophoresis, chemical crosslinking, limited proteolysis, and molecular modelling (Suda et al., 2004). The importance of this observation is remarkable because for a long time cross-linking and pharmacokinetic studies have suggested that GPCRs are working as dimers. Because Rho is the only GPCR with a known structure (Filipek et al., 2003; Palczewski et al., 2000), the AFM data now provide a solid basis to model a GPCR dimer and to discuss possible interactions with the cognate

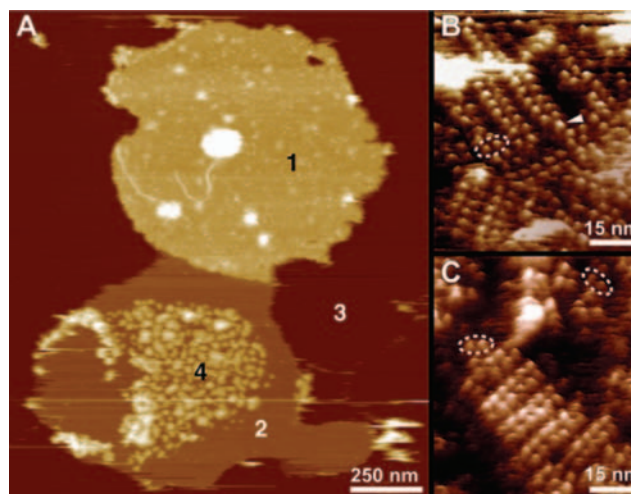


**Figure 11.4** AFM topographs of native disk membranes. (A) Height image of an open, spread-flattened disk. Four different surface types are evident: the disk membrane surface (types 1 and 4; thickness: 7–8 nm), lipid (type 2; thickness: ~3.7 nm) and mica (type 3). The topographies of regions 1 (B) and 4 (C) at higher magnification reveal densely packed rows of rhodopsin dimers protruding by ~1.4 nm out of the lipid bilayer and packing densities between 30,000 and 55,000 rhodopsin monomers per  $\mu\text{m}^2$ . Besides paracrystals (unit cell dimensions:  $a = 8.4 \text{ nm}$ ,  $b = 3.8 \text{ nm}$ ,  $\gamma = 85^\circ$ ), single rhodopsin dimers (broken ellipses) and occasional rhodopsin monomers (arrowhead) can be seen floating in the lipid bilayer. Vertical brightness ranges: 22 nm (A) and 2.0 nm (B) and (C)

proteins (Fotiadis et al., 2006), such as arrestin and the G-protein heterotrimer (Filipek et al., 2004; Liang et al., 2003).

### ***11.2.6 AFM, a Structural Biology Method Complementing Biochemical Procedures***

AFM has also been applied to verify biochemical results as exemplified by the studies of ion driven  $F_0F_1$ -ATP synthase rotors. Besides determining the stoichiometry of different  $F_0F_1$ -ATP synthases (Pogoryelov et al., 2005; Seelert et al., 2000; Stahlberg et al., 2001), it was possible to identify the presence of phospholipid headgroups in the central rotor cavity (Meier et al., 2001), to elucidate that rotor diameter and stoichiometry are determined by its subunits (Müller et al., 2001), to demonstrate that reconstituting the rotor in different detergents and lipids had no influence on its characteristic stoichiometry (Seelert et al., 2003), and to show that growing the biological organism at different conditions does not influence the rotor stoichiometry (Meier et al., 2005). The latter finding contradicted previous notions based on the analysis of biochemical data obtained from nonvisual bulk experiments (Schemidt et al., 1998). In summary, these examples indicate the high potential of the AFM in biology as well as its complementary to biochemical procedures.

### ***11.2.7 Observing the Diffusion of Single Membrane Proteins***

Time-lapse AFM imaging of membrane proteins allows dynamic processes to be observed (Engel and Müller, 2000; Müller et al., 1996, 2002a). An example is illustrated in Figure 11.5 where the movements of single rotor proteins were tracked. As seen in Figure 11.4 the unrivaled S/N ratio of the AFM allowed the visualization of all structures in the membrane irrespective of the packing density. The uncertainty of determining the position of a single rotor was  $<1$  nm, which is  $\approx 30$  times smaller than the accuracy of single-molecule optical methods, and  $\approx 200$ – $300$  times smaller than diffraction-limited optical resolution (Weiss, 1999, 2000). Trajectories of single sodium-driven rotors of the  $F_0F_1$ -ATP synthase from *Ilyobacter tartaricus* laterally moving through the membrane bilayer were observed directly in the topograph (Müller et al., 2003). Subsequent analysis of the protein trajectories combined with structural information of the surrounding environment allowed single protein movements to be classified. The two modes of lateral diffusion found were free-diffusion, in which the protein movement was apparently not confined by any other macromolecular structure, and constrained diffusion, where the protein movement was constrained by surrounding objects. It was possible to visualize how proteins switch between the two modes of lateral diffusion (Müller et al., 2003). In the future, this approach combined with fast-speed AFM imaging (Ando et al., 2003;

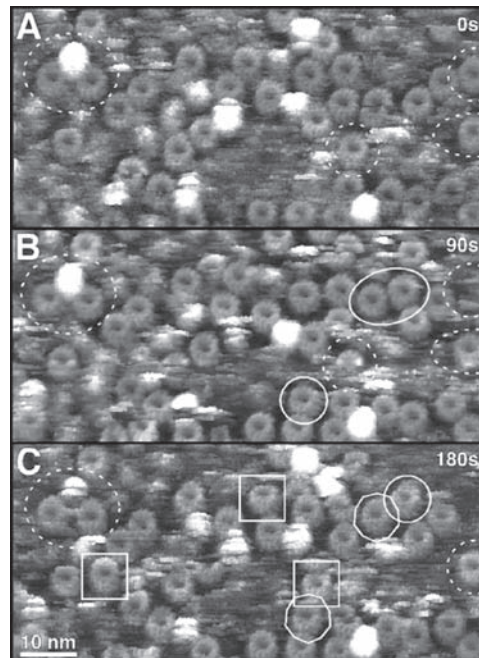


**Figure 11.5** Diffusion of single rotors observed at a lateral resolution of  $<1$  nm and a vertical resolution of  $\approx 0.2$  nm. (A) AFM topograph showing sodium driven rotors of  $F_0F_1$ -ATP synthases from *I. tartaricus* assembled in the membrane bilayer. One rotor has an outer diameter of about 5.4 nm. The eleven subunits of individual rotors were observed in the raw data. (B) Same area imaged after 90 seconds. Individual rotors changed their position (outlined white circles and dashed circles) whereas others remained at their location (outlined dashed ellipses). (C) Repeated imaging of the same area after additional 90 seconds. Although some proteins moving in the previous images interrupted their movement (outlined octahedron) others continued (outlined squares) or began to move (outlined circles). Vertical brightness range of topographs corresponds to 3 nm

Humphris et al., 2005; Viani et al., 2000) may provide novel insights into biomolecular interactions controlling the free motion of proteins through the membrane, and of interactions directing protein aggregation and assembly.

### 11.2.8 Observing Structural Flexibility of Membrane Proteins

Comparison of the surface structure of single membrane proteins on AFM topographs (Figure 11.6A) identified variable and invariable surface features (Müller et al., 1998). Correlation averaging of the protein surface enhanced common structural features (Figure 11.6D). Consequently, the corresponding standard deviation map assigned regions of enhanced structural flexibility (Figure 11.6E). Complementary

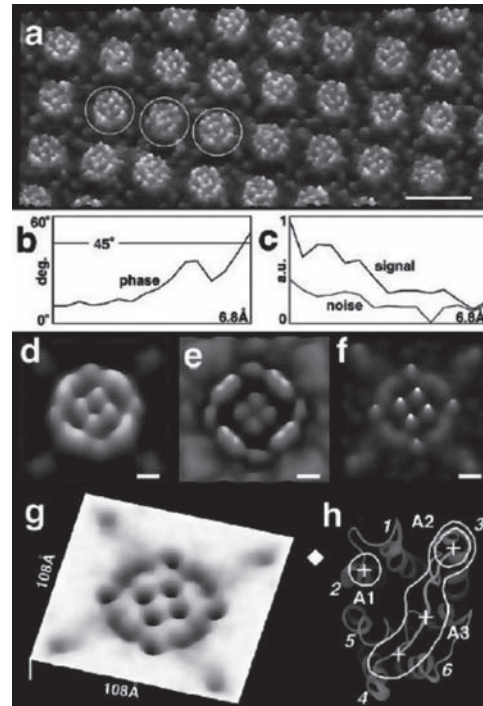


**Figure 11.6** Mapping local flexibilities and free energy states of the bacterial aquaporin (AqpZ) surface (Scheuring et al., 2002). AFM topographs were recorded at an applied force of 80 pN in 10 mM Tris-HCl, pH 7.8, 100 mM KCl. (a) Unprocessed AFM topograph of an AqpZ 2D-crystal. Circles indicate individual extracellular protein surfaces. (b) Phase residual analysis from averaging 1447 topographs of the extracellular AqpZ surface. The Nyquist frequency corresponds to  $1/(6.8 \text{ \AA})$ . (c) Spectral S/N ratio analysis from averaging the 1447 AqpZ topographs. The Nyquist frequency is  $1/(6.8 \text{ \AA})$ . (d) Average topograph calculated from a total of 1447 aligned tetramers. (e) Standard deviation map corresponding to (d). (f) Probability map calculated from peak position distribution of 1447 aligned tetramers. (g) Energy landscape as function of protrusion peak position. The image size corresponds to 10.8 nm and the full grayscale represents a vertical scale of  $\Delta kT = 6.6$ . (h) Overlay of the FWHM outline and a model of the AQP1 structure (Murata et al., 2000). The crosses indicate the highest probability positions, the outlines give the probability tracing line of loop C. Transmembrane  $\alpha$ -helices are numbered in italics (helices 1 and 2 connected by loop A (FWHM: A1); helices 3 and 4 connected by loop C (FWHM: A3); helices 5 and 6 are connected by loop E which folds back into the water channel). The diamond outside the monomer indicates the four-fold axis symmetry center of the AQP tetramer. Scale bars correspond to 10 nm (a) and 1 nm (d)–(f). Full grayscale represents vertical range of 1 nm (a), (d)

structural insights such as observed from NMR, electron microscopy, or X-ray crystallography confirmed the structural flexibility of the individual polypeptide loops (Heymann et al., 1999). Although some loops truncated from transmembrane  $\alpha$ -helices adopted their three-dimensional structure such as observed in the functional protein, others did not show any common structure (Bennett et al., 2004; Katragadda et al., 2000). Thus, it was concluded that polypeptide loops adopting an

intrinsic structure contribute to the folding and stability of membrane proteins. Furthermore, it was assumed that the rigidity or flexibility of loops was evolutionary optimized enabling a best possible membrane protein function. For example, flexible loops would provide the conformational motility necessary to allow the tilting of one helix relative to the other.

In agreement with these assumptions, the analysis of high-resolution AFM topographs indicated that structural regions which were of functional importance to BR (Heymann et al., 1999; Müller et al., 1999c), OmpF porin from *E. coli* (Müller and Engel, 1999), HPI-layer from *Deinococcus radiodurans* (Müller et al., 1996), and gap junctions from rat liver epithelial cells (Müller et al., 2002a), exhibited enhanced flexibilities. In further studies, AFM allowed the observation of these structural regions undergoing conformational changes (see next section). On the example of the gap junction forming connexins the conformational change of the inner pore lining structures changed from flexible (open pore) to rigid (closed pore) (Müller et al., 2002a).

In a different approach, the amplitudes of structural domain movements were estimated from a large number of single-molecule topographs using image processing. This approach allowed a variety of parameters describing the mechanical properties of a membrane protein surface to be extracted. First, the topographs of single proteins need to be aligned laterally and angularly. This can be accomplished to subnanometer accuracy with randomly oriented single particles as result of the high S/N ratio of the AFM topographs. As illustrated for the bacterial aquaporin, AqpZ, topographic averages and standard deviation of the protein surface are calculated pixel by pixel from aligned single molecules (Figure 11.6). Calculating two independent averages from all odd and all even numbered single particles allows the resolution to be determined by comparing the Fourier coefficients of these two averages. This yields the phase residual (Figure 11.6B) and the spectral S/N ratio (Figure 11.6C) as a function of resolution. Both analyses indicate a lateral resolution of 0.7 nm.

The vertical scale of Figure 11.6E documents that vertical resolutions can be better than 0.1 nm provided that the sample is sufficiently rigid. Larger vertical variations reflect changes of the sample flexibility. Vertical fluctuations were found emerging from lateral displacements of polypeptide loops connecting transmembrane  $\alpha$ -helices. Therefore, it is advantageous to characterize variations in the protein surface structure by calculating the probability  $p(x,y)_d$  to find a certain domain at a certain position  $(x,y)_d$  by mapping the corresponding peak positions of all individual AqpZ tetramers (Figure 11.6F). This map is readily converted to a free energy landscape  $G_d$  using Boltzmann's law (Figure 11.6G):  $G_d(r) = -k_B T \ln p(x,y)_d$ , where  $k_B T$  is the thermal energy ( $\approx 4.1 \cdot 10^{-21}$  J or 4.1 pN nm at room temperature). Interpretation of this map is facilitated by the 3D structure of AQP1: the long loop C spanning the entire molecule is likely to be flexible, although it is fixed to the C-terminal end of helix 3, whereas loop A is kept fixed by helices 1 and 2 (Figure 11.5H; Scheuring et al. (2002)). In the future, such approaches will enable us to investigate how environmental changes or ligand binding may influence the energy landscape of native protein surfaces.



### **11.2.9 Imaging Conformational Changes of Native Membrane Proteins**

AFM enables us to observe membrane proteins in physiological environments, and thus is a method of choice to directly visualize their conformational changes. An example reported thus far was the reversible deformation of single cytoplasmic polypeptide loops of BR (Müller et al., 1995). By slightly enhancing the force applied to the AFM stylus to values above 100 pN the loop EF could be bent away. This enhanced flexibility of the loop has a functional role because it enables helix F to bend away upon absorption of light by the BR retinal. Time-lapse AFM allowed the direct imaging of the reversible opening and closing of single pores of the surface layer from *D. radiodurans* (Müller et al., 1996). Conformational changes of voltage- and pH-gated channels in response to an applied electrical potential were firstly observed by AFM (Müller and Engel, 1999) and later confirmed by other studies on a related channel (Andersen et al., 2002). Figure 11.7 shows the  $\text{Ca}^{2+}$  induced gating of rat liver gap junctions (Hand et al., 2001) directly imaged by AFM (Müller et al., 2002a). Topographs show the extracellular surface of the Cx26 connexons in absence of  $\text{Ca}^{2+}$  ions. Each hexagonal pore exhibited a central channel in the open state (Figure 11.7A, top). As shown by the standard deviation map, the central cavity exhibited an increased flexibility in the open state. On addition of  $\text{Ca}^{2+}$  ( $\geq 0.5$  mM) to the buffer solution the channel entrance closed (Figure 11.7B, top). In contrast to the open state the closed channel showed no enhanced flexibility anymore. This channel closure was reversible and the channel opened again after removal of  $\text{Ca}^{2+}$  from the buffer solution.

An AFM requires about one minute to record a high-resolution AFM topograph. This time limitation builds the bottleneck for imaging fast conformational changes and other dynamic processes. Recent developments of fast scanning probe microscopes allow recording of up to 200 topographs per second (Ando et al., 2003; Humphris et al., 2005, 2003; Viani et al., 1999a). Viani and co-workers used a prototype small cantilever AFM (Viani et al., 1999b) to observe interactions between individual GroES and GroEL proteins in real-time (Viani et al., 2000). This pioneering work highlights that fast-scanning AFM will be a highly useful tool for studying protein dynamics at the single-molecule level. The adaptation of these technologies as a routine method for high-resolution imaging of biomacromolecular systems (Ando et al., 2003; Koder et al., 2003) will allow us to investigate many other functionally related conformational changes and dynamic processes of functional membrane proteins and native cell membranes apart from the static ones presented thus far.

### **11.2.10 Controlled Manipulation**

High-resolution AFM topographs are usually recorded at minimal forces ( $< 100$  pN) to prevent deformation of the molecules. Higher forces would not only reversibly or irre-

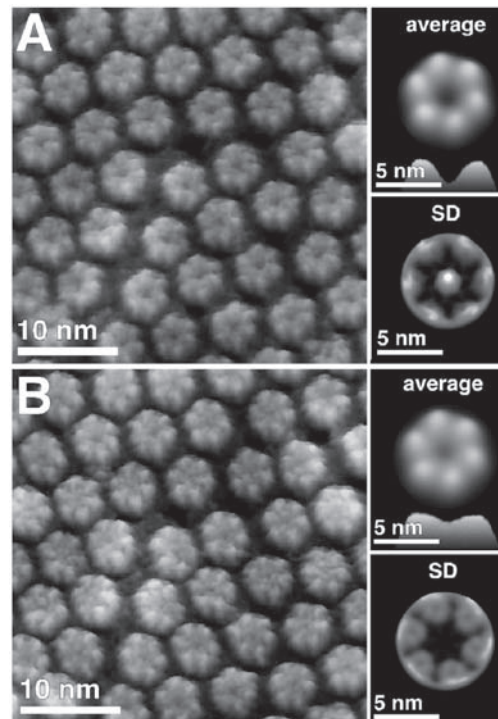


**Figure 11.7** Imaging the conformational change of connexons from rat liver epithelial cells. **(A)** Connexons imaged in buffer solution containing no calcium. The central channel entrance of every hexameric pore was clearly resolved. **(B)** Addition of 0.5 mM calcium induced the pores to close their channel. The central channel closure was reversible as proved by their opening upon removal of calcium from the buffer solution. The unprocessed topographs were recorded in buffer solution (1 mM phenyl methylsulfonyl fluoride (PMSF), 0.5 mM  $\text{CaCl}_2$  (for B), 5 mM Tris) and at room temperature. Upper right insets of **(A)** and **(B)** represent correlation averages of the topographs. Averages are displayed in a perspective view ( $5^\circ$  tilt). The lower right insets represent the corresponding standard deviation (SD) maps. Maxima of the SD maps indicate regions of the protein exhibiting an enhanced flexibility

versibly deform flexible biological structures but also increase the contact area between AFM stylus and object. This results in a reduced resolution (Weihs et al., 1991). However, it was shown that at higher forces the stylus may be used as a molecular tweezer to dissect supramolecular assemblies in a controlled manner (Fotiadis et al., 1998, 2002). After imaging individual photosystem I complexes at minimal force, the force applied to the AFM stylus was slightly increased until the first extrinsic proteins were removed from the complexes. Scanning of the complex at minimal force after depletion of the extrinsic proteins allowed the visualization of the dissected structures. The same process can be applied to dissect entire membranes or even larger complexes such as chromosomes or cells (Fotiadis et al., 2002; Ikai and Afrin, 2003). Small forces of  $\approx 1$  nN are sufficient to separate stacked layers of membranes or 2D

crystals (Fotiadis et al., 2000; Hoh et al., 1991; Müller et al., 2002d). The possibility of performing molecular dissections are of great use to unveil otherwise hidden surfaces and to estimate interaction forces holding subunits of a complex together.

### 11.3 Single-Molecule Force Spectroscopy of Membrane Proteins

Since the invention of the AFM, the AFM stylus has served as a nanotweezer, enabling us to manipulate biological objects at the molecular scale. The outstanding positioning precision ( $\approx 0.1$  nm) and force sensitivity ( $\approx 5$  pN) of the AFM has made even delicate single-molecule unfolding experiments using force spectroscopy possible. In these experiments, the force applied to a single protein acts as a denaturant leading to complete unfolding of its three-dimensional structure. In their initial studies, Rief and co-workers applied SMFS to the giant muscle protein titin, which consists of repeats of globular immunoglobulin and fibronectin domains (Rief et al., 1997; Zhuang and Rief, 2003). The continuous mechanical extension of the protein resulted in the subsequent unfolding of the globular domains allowing the unfolding force and pathway of each domain to be detected (Marszalek et al., 1999; Rief et al., 1997; Williams et al., 2003).

In contrast to many experiments performed on globular proteins, the combination of AFM imaging and SMFS (Müller et al., 1999a; Oosterhelt et al., 2000) yielded surprisingly detailed insights into molecular interactions stabilizing membrane proteins such as BR (Janovjak et al., 2003; Müller et al., 2002c), halorhodopsin (HR; Cisneros et al., 2005), human aquaporin-1 (AQP1) (Möller et al., 2003), bovine Rho (Sapra et al., 2006b), and the  $\text{Na}^+/\text{H}^+$  antiporter NhaA from *Escherichia coli* (Kedrov et al., 2004). To select a membrane protein for a force spectroscopy experiment, the protein membrane surface was first imaged at subnanometer resolution. Then the AFM stylus and the selected protein were brought into contact. Applying a force of 300–1000 pN resulted in attachment of one terminal end to the stylus either via a covalent bond (Oosterhelt et al., 2000) or enforced nonspecific adsorption (Müller et al., 2002c).

Withdrawal of the stylus from the membrane stretches the terminus of the protein and deflects the cantilever. Upon further separating the stylus and surface, the force pulling on the protein steadily increases. As soon as the force exceeds the stability of the protein it induces the sequential unfolding of its three-dimensional structure. Recording the force against stylus–surface separation yields a F-D spectrum characteristic of the unfolding of a single protein (Figure 11.8A, left frame). The presence of several distinct events in the force spectrum indicates that secondary structure elements of membrane proteins unfold in well-defined sequences (Figure 11.8A, right frame). As their characteristic sawtooth pattern stems from the extension of already unfolded polypeptide elements, the unfolding spectra are readily analyzed with the wormlike chain (WLC) model (Figure 11.8, solid red lines).

In addition to the detection of a reproducible peak pattern there are a few simple criteria to identify unfolding spectra originating from the manipulation of single molecules. Firstly, the overall length of the force curve is well suited to select molecules attached to the cantilever by one of its termini and not one of its loops (Müller et al., 2002c). In addition, a pickup frequency of <20% implies that nearly 90% of the events monitor single-molecule interactions (Williams and Evans, 2002). A higher adhesion frequency increases the statistical probability that events originate from multiple molecules and sometimes might indicate contamination of the AFM stylus. Recently we have presented a software solution that allows sorting F-D spectra by their similarity and removes highly deviant spectra, such as those originating from stylus contamination (Kuhn et al., 2005).

### ***11.3.1 Molecular Interactions Establish Stable Structural Segments Within Membrane Proteins***

The WLC model describes the force–extension relationship for the stretching of an unfolded polypeptide and hence can reveal the lengths of the mechanical unfolding intermediates of single proteins (Marko and Siggia, 1995; Rief et al., 1997). Consequently, each force peak fitted using the WLC model determines the position of a stable structural segment established in the protein against mechanical unfolding (Figure 11.8). The height of the force peak reflects the force required to break the molecular interactions that form that segment. Apparently, molecular interactions established by a variable number of aa act collectively to form a stable structural segment. As soon as an external force exceeds the mechanical strength of this structural segment, it unfolds in a cooperative event. It is difficult to determine how many aa are required to establish a stable structural segment within a protein. Our results indicate that the smallest segments contain only 6 aa whereas the largest ones are established by more than 20 aa. In addition, these segments do not necessarily correlate to the secondary structure elements of the protein. For example, it was observed that a transmembrane helix together with a polypeptide loop can establish a mechanical barrier as well.

These findings support recent assumptions that larger proteins (more than 100 residues) generally fold in modules and that the folding process takes place largely independently in different segments or domains of the protein (Dinner et al., 2000; Dobson, 2003). Interactions involving key residues are likely to establish the natively like fold within local regions or domains (Khan et al., 2003; Vendruscolo et al., 2001). Replacing the key proline (P50A) residue of the kinked BR helix B showed that neither the structure nor the stability of the membrane protein was changed significantly (Faham et al., 2004). It was shown that the bend of helix B did not depend on a single proline residue, but results from cumulative effects of adjacent residues. These results support that folded polypeptides interact collectively to establish stable structural modules or segments. Our measurements showed that



all aa of these segments unfolded cooperatively as soon as an externally applied force overcame their collective barrier.

### 11.3.2 Mapping Molecular Interactions Stabilizing Structural Segments

Although force measurements performed at a single pulling speed allow determining the position and length of stable structural segments, those performed at different pulling speeds or temperatures allow determining the widths and heights of their energetic barriers (see following sections). Thus far, most SMFS experiments performed on membrane proteins were recorded at only one pulling speed. After identification of all stable structural segments, a structural model of the protein was built using this information (Figures 11.8D and 11.9). From such representations it becomes clear which parts of the three-dimensional membrane protein structure are stabilized by collective molecular interactions (Cisneros et al., 2005; Kedrov et al., 2004; Möller et al., 2003; Sapa et al., 2006b).

**Figure 11.8** Unfolding of a single BR molecule from native purple membrane using single-molecule force spectroscopy. **(A)** Left side, the experimental force curve shows a representative unfolding spectrum of a single BR. Force peaks have been fitted with WLC model curves (red lines). On the right, the schematic unfolding pathway is sketched. The BR molecule was unfolded by mechanically pulling at its C-terminal end. The first force peaks occurring at stylus-sample separations below 15 nm indicate the unfolding of transmembrane helices F and G. After unfolding both helices, a 88 aa long polypeptide chain links the AFM stylus and membrane (a). Separating the stylus further from the membrane stretches the unfolded polypeptide (b) thereby exerting a force on helix E. At average forces of  $\approx 120$  pN, the mechanical stability of helices E and D is overcome and they unfold together with loop DE. As the number of aa linking the stylus and the protein structures anchored by the membrane increases to 148 and the AFM cantilever relaxes (c). In the forthcoming step, the unfolded 148 aa are stretched thereby pulling on helix C (d). After unfolding helices B and C and loop BC in a single step the molecular bridge between AFM stylus and membrane is lengthened to 219 aa (e). By further separating stylus and surface helix A unfolds (f) and the polypeptide is completely extracted from the membrane (g). In the unfolding pathway described two transmembrane  $\alpha$ -helices and their connecting loop unfold in a single step. **(B)** The first unfolding peak at 88 aa has a certain probability to show two shoulder peaks indicating the stepwise unfolding of the helical pair. This probability is driven by external experimental conditions such as temperature, pulling speed, assembly, and lipids. If both shoulders occur, the 88 aa peak indicates the unfolding of helix E, that at 94 aa represent unfolding of loop DE, and the 105 aa peak corresponds to unfolding of helix D. **(C)** The shoulder peaks of the second peak indicate the stepwise unfolding of helices C and B and loop BC. The 148 aa peak indicates the unfolding of helix C, the 158 aa peak unfolding of loop BC, and the 175 aa peak represents unfolding of helix B. This shows that although single transmembrane helices and polypeptide loops are sufficiently stable to unfold in individual steps, they exhibit a distinct probability to unfold groupwise with directly neighbored elements (black arrows). **(D)** Stable structural segments assign map regions in which molecular interactions collectively act to stabilize BR



**Figure 11.9** Mapping structural segments stabilized by molecular interactions acting within native HR. Being structurally very similar to BR, the molecular interactions within HR stabilized almost identical structural segments (compare to Figure 11.8). The broken circles frame regions encoding the ending and starting of structural segments as detected by force spectroscopy (Cisneros et al., 2005)

### 11.3.3 Membrane Proteins Choosing Different Unfolding Pathways and Crossing Different Barriers

The preceding analysis allowed the localization of stable structural segments in single transmembrane  $\alpha$ -helices and polypeptide loops. In some cases, it was observed that even fragments of secondary structure elements established sufficiently strong molecular interactions to act as independent stable units. However, even more information is buried in the individuality of the unfolding spectra, because each was obtained on a single protein. Firstly, the height of force peaks varied due to the stochastic nature of forced unfolding experiments far from equilibrium. The standard deviation of the most probable unfolding force corresponded to the ratio of the thermal energy and the width of the potential barrier (Evans,

1998). In addition, in some force curves distinct peaks appeared whereas they did not in other curves. This implied that several unfolding pathways exist for the same proteins differing in the potential barriers crossed during unfolding (Janovjak et al., 2004; Müller et al., 2002c). Certain unfolding pathways included several potential barriers, whereas in others the same elements unfolded by crossing a single barrier. Examples are shown in Figures 11.8B and C where two transmembrane helices either unfold in several pairwise steps as characterized by shoulder peaks or a single force peak. The analysis showed further, that every protein exhibits a well-defined probability of following each of these unfolding pathways (Cisneros et al., 2005; Kedrov et al., 2004; Möller et al., 2003; Müller et al., 2002c; Sapra et al., 2006b).

#### ***11.3.4 Protein–Protein Interactions Influence Stability and Unfolding Pathways of Membrane Proteins***

SMFS experiments on monomeric, dimeric, and trimeric BR revealed insights into how membrane protein assembly influences protein stability (Sapra et al., 2006a). First, it was shown that BR molecules of all three assemblies showed identical unfolding pathways and intermediates. However, the BR assembly influenced the stability of the secondary structure elements. BR molecules assembled into a trimer showed the highest unfolding forces and thus were the most stable ones. This stability of single BR molecules decreased if they were assembled into a dimer and even further decreased for the BR monomers. This result is in agreement with conventional thermal and chemical unfolding experiments that report a higher stability of BR molecules assembled into a trimer as compared to monomeric BR (Brouillette et al., 1989). However, analysis of the force spectra showed that the probability of BR molecules to select a certain unfolding pathway changed with the molecular assembly. All of these findings suggested that molecular interactions stabilizing BR were established intrinsically within the protein and that these interactions are increased by neighboring molecules. It was thus possible to dissect intra- and intermolecular interactions contributing to the protein stability. This example shows that SMFS provides unique insights into how the stability of individual secondary structure elements, for example, those involved in monomer–monomer contacts depend on oligomerisation or association with other molecules.

#### ***11.3.5 Which Interactions Establish Stable Structural Segments?***

HR and BR, the two light-driven ion pumps from *H. salinarum*, exhibit an extremely high structural similarity (Kolbe et al., 2000). SMFS was applied to detect the molecular interactions stabilizing the structures of both membrane



proteins HR and BR (Cisneros et al., 2005). As expected, the force spectra revealed that single HR molecules chose among different unfolding pathways such as previously detected for BR. In some unfolding pathways single secondary structure elements unfolded in separate events, whereas in other pathways these elements unfolded cooperatively. The stable structural segments found for HR are shown in Figure 11.9. Comparing the stability assignment of HR (Figure 11.9) and BR (Figure 11.8D) showed that the energetic barriers established against unfolding were located at similar structural regions.

These remarkable results revealed for the first time that two proteins having ~30 % sequence identity and an almost identical 3D structure unfold in almost identical pathways. They also suggest that different aa residues stabilize structural segments at the same structural positions within a membrane protein. It may be concluded that the stable structural segments are the result of comprehensive interactions between many different aa within a structural region. In apparent contrast, it was found that a localized Pi-bulk interaction not only structurally disrupts helix E of HR but also divides this transmembrane  $\alpha$ -helix into two cooperatively unfolding segments. Thus, it may be concluded that certain residues show a collective behavior contributing to the mechanical interactions stabilizing a structural segment, whereas other aa can behave as a stopping function braking a segment into two parts.

### ***11.3.6 Unfolding Pathways Depend on Temperature***

Small globular proteins such as immunoglobulin and fibronectin unfold at different forces although they show almost identical thermal stabilities (Rief et al., 1998). This indicates that SMFS detects intramolecular interactions that stabilize proteins, which are not revealed by thermal denaturation experiments. The question arising from such measurements was to what extent temperature influences intra- and intermolecular molecular interactions that stabilize membrane proteins? To answer this question, which is of high importance for classical unfolding experiments inducing membrane proteins by thermal denaturation, the molecular interactions stabilizing BR were characterized at different temperatures ranging within the physiologically relevant range (Janovjak et al., 2003).

Stepwise increasing the sample temperature from 8 to 52°C showed that the stabilization of transmembrane helices and peptide loops of BR significantly decreased by up to 50%. In spite of this the temperature apparently did not change the unfolding pathways; that is, every individual pathway was observed at each temperature examined. Most interestingly, however, the probability for a single BR molecule to follow a certain unfolding pathway depended sensitively on the temperature. This observation indicates relative probabilities of following unfolding pathways are sensitive to the strengths of stabilizing molecular interactions. Thus, these data provide direct evidence that the preferred unfolding pathway of a protein may change drastically within small environmental variations. Increasing tempera-

tures increased the probability of pairwise unfolding of transmembrane helices, however, decreasing temperatures increased the probability of single helices to unfold individually. It was further concluded that increasing the temperature lowered the energy barrier for pairwise unfolding more than that for unfolding of individual helices (Janovjak et al., 2003).

### ***11.3.7 How Do Secondary Structure Elements Unfold at Zero Force?***

Monitoring unfolding forces as a function of the cantilever pulling speed allows probing the energy landscape of biological interactions stabilizing a membrane protein. This approach is referred to as dynamic force spectroscopy (DFS; Evans (1998, 2001)), which already provided exciting relations between the biomolecular structure and lifetime of small globular proteins (Rief et al., 1997; Williams et al., 2003), receptor–ligand interactions (Merkel et al., 1999), and double-stranded nucleic acids (Strunz et al., 1999). Applied to membrane proteins, this approach revealed detailed insights into individual energy barriers stabilizing secondary structure elements. Such barriers are of fundamental relevance for the three-dimensional structure of a functional membrane protein (Janovjak et al., 2004).

As expected for a nonequilibrium process, it was observed that the pulling speed had a strong influence on the forces required to unfold single BR molecules. Additionally, it was observed that the unfolding pathway chosen by the BR molecule depended on the pulling speed. At fast pulling speeds, unfolding of individual transmembrane helices clearly dominated over pairwise unfolding of structural segments. Thus, at low pulling speeds a majority of the molecules followed pathways describing the groupwise unfolding of structural segments. Extrapolating the pulling speed to zero applied force showed that transmembrane helices almost exclusively unfolded pairwise in native BR (Janovjak et al., 2004). This indicates that in the absence of force, the energy barrier for pairwise unfolding is significantly smaller compared to the barrier for unfolding of the same helices in individual steps (Figure 11.10B). Such a pairwise association of transmembrane helices was previously suggested to play an important role in membrane protein folding (Engelman et al., 2003; Popot and Engelman, 2000, 1990) and has been now experimentally supported.

### ***11.3.8 Probing the Energy Landscape of Secondary Structures***

SMFS unfolding experiments of single BR molecules revealed that single transmembrane  $\alpha$ -helices establish sufficiently strong interactions to exist as independently stable domains. However, when interacting with each other, these segments can also show a cooperative behavior. For example, two helices and their connecting polypeptide loop can act as a group and establish a single barrier

against unfolding. Both cases can be described by a simple two-state model to approximate the energy landscape of unfolding based on the DFS data (Janovjak et al., 2004). An energy barrier located at the transition state ( $\ddagger$ ) separates the folded state (F) from the unfolded state (U) (Figure 11.10A).

The position of the energy barrier along the reaction coordinate is described by the potential barrier width ( $x_u$ ) and the end-to-end distance of the molecule was considered as the reaction coordinate. Extending the folded structure by a length  $\geq x_u$  initiates unfolding of the protein. We found that single and grouped structural segments unfolded cooperatively when they were extended by only  $x_u \approx 0.5$  nm. Therefore, the extension ruptured inter- or intramolecular bonds stabilizing structural segments such as transmembrane helices or groups hereof (Janovjak et al., 2004). This finding forms a strong argument against the hypothesis that transmembrane helices would be pulled from the membrane in a first step and then unfold in a second step. In the future, combined SMFS experiments and molecular dynamics simulations will provide more detailed information about the unfolding process, such as the exact sequence of events associated with the distortion of molecular interactions stabilizing of membrane proteins.

### ***11.3.9 Determining Natural Unfolding Rates of Secondary Structure Elements***

The spontaneous unfolding rate  $k_u^0$  (Figure 11.10A) determines the time required to cross the energy barrier of unfolding in the absence of an externally applied force. Thus the average stability of the folded structure corresponds to the inverse of the unfolding rate ( $1/k_u^0$ ). Using DFS, we found spontaneous unfolding rates of the order of  $10^{-2}$  s $^{-1}$  for single transmembrane helices and of the order of  $10^{-4}$  s $^{-1}$  for helical pairs of BR (Janovjak et al., 2004). Consequently, the typical stability of a single helix is  $\approx 100$  s and a pair of helices  $\approx 10^4$  s. Although membrane proteins are stabilized by completely different mechanisms (Haltia and Freire, 1995), these values are of comparable magnitude to water-soluble proteins such as barnase ( $1/k_u^0 \approx 10^5$  s) (Best et al., 2001) and the Ig27 domain of titin ( $1/k_u^0 \approx 10^4$  s) (Williams et al., 2003). This indicates that individual transmembrane helices can not only be considered as important folding intermediates but also exhibit a remarkable intrinsic stability.

### ***11.3.10 Dynamic Properties of Single Proteins***

Modified force spectroscopy measurements allow probing the dynamic viscoelastic properties of a wide class of single (bio-)molecules (Chtcheglova et al., 2004; Kawakami et al., 2004; Kienberger et al., 2000; Li and Fernandez, 2004; Mitsui et al., 2000; Okajima et al., 2004). In such force modulation spectroscopy (FMS)

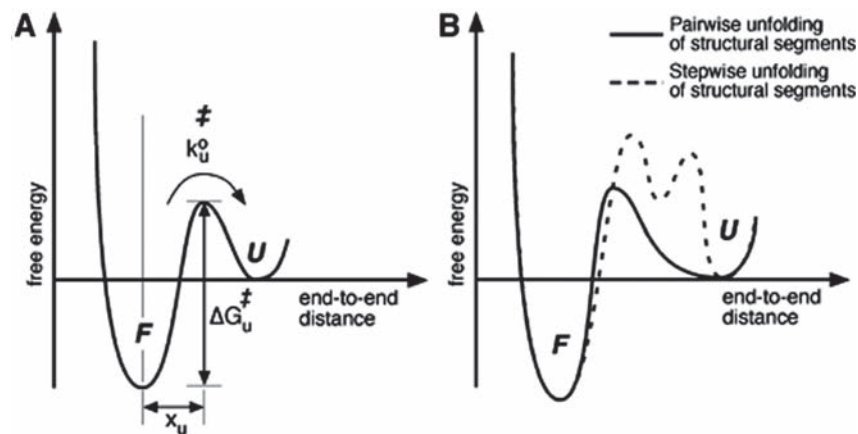


**Figure 11.10** Energy landscape of structural segments stabilizing a membrane protein. (A) A two-state potential describes the unfolding of single helices of BR using SMFS. A potential barrier separates the folded state ( $F$ ) from the unfolded state ( $U$ ).  $\Delta G_u^\ddagger$  represents the activation energy for unfolding,  $x_u$  the distance from the folded state to the transition state ( $\ddagger$ ), and  $k_u^0$  the natural (thermal) transition rate. Forced unfolding experiments at different pulling speeds allow determining the width of the potential barrier and the unfolding rate. (B) Two possible unfolding pathways were observed for structural segments stabilizing transmembrane helices in BR. In the first one (solid line), each structural segment established its own independent potential barrier and unfolded in an individual step. In the second pathway (dashed line), two structural segments grouped together to collectively establish a potential barrier. These structural segments unfolded pairwise

experiments, either the sample stage or the cantilever is sinusoidally oscillated while the oscillation amplitude and phase are monitored. Analyzing the amplitude and phase enables the separation of the elastic and dissipative contributions to the chair-boat transition of single dextran molecules (Humphris and Miles, 2002; Kawakami et al., 2004). In apparent contrast, the extension of nucleic acids and poly(ethyleneglycol) was found to be dominated by purely elastic interactions (Kienberger et al., 2000; Liu et al., 1999), and the stretching elasticity of single antibody–antigen bonds was determined (Chtcheglova et al., 2004). Okajima and co-workers constructed an oscillating sample stage to study the dynamic behavior of bovine carbonic anhydrase II in the millisecond domain (Mitsui et al., 2000; Okajima et al., 2004). An out-of-phase response of the partially unfolded molecule was observed and correlated to refolding of the hydrophobic protein core (Okajima et al., 2004).

FMS was also applied to probe the dynamic properties of BR (Janovjak et al., 2005). The damping of an oscillating cantilever stylus (amplitude  $\approx 5$  nm) allowed estimating the energy dissipation during unfolding of individual secondary structure elements. This approach allowed the quantification of the stability of secondary structure elements and provided a direct and continuous measurement of the elasticity of single polypeptide strands. The possibility to detect dissipative and elastic contributions during protein unfolding forms an important step to unravel the different interactions contributing to the structure–function relationship of proteins.

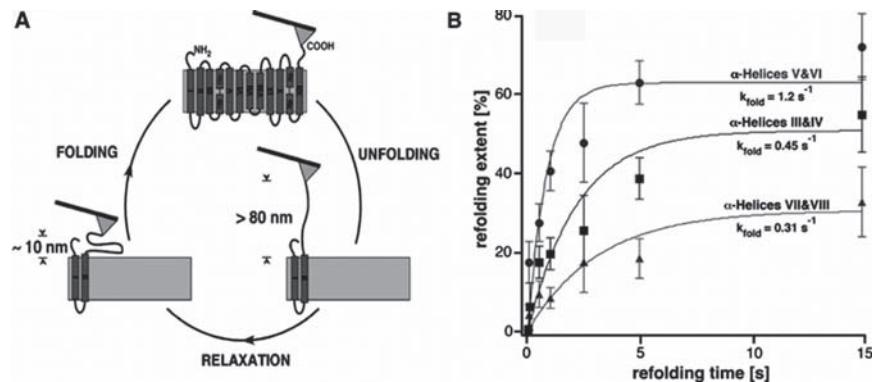


**Figure 11.11** Determining the refolding kinetics of structural segments into the final membrane protein. (A) schematic drawing of the experiment. After tethering the C-terminal end of a single NhaA to the AFM stylus, the protein was unfolded except for the last two helices, which were left in the membrane. The AFM stylus was then lowered towards the membrane surface thereby allowing the protein to refold. After a certain refolding time ranging between 10ms and 15s, the NhaA peptide was unfolded again to detect which structural regions had refolded. (B) Folding kinetics of helical pairs determined from the refolding experiment. The fastest folding segment of NhaA ( $k_{\text{fold}} = 47 \text{ s}^{-1}$ ) was the sodium-binding domain of helix V facing the cytoplasm (data not shown; Kedrov et al., 2006a, 2004)

### 11.3.11 Observing Folding Steps and Kinetics of Single Membrane Proteins

Since the pioneering work of Anfinsen (1973), protein folding has been an area of major interest in life sciences. Although most studies focused on small globular proteins, significant advances were also achieved on membrane proteins (Booth et al., 2001). However, these results were achieved on a few transmembrane proteins whereas most of the others have been largely excluded from folding studies because they are considerably more difficult to work with (Booth et al., 2001). This is mainly due to the difficulties in mimicking the native, anisotropic environment of the biological membrane (Haltia and Freire, 1995; White et al., 2001). Recently, refined single-molecule unfolding experiments have allowed us to describe the folding process of single transmembrane helices and to estimate their folding kinetics (Kedrov et al., 2006a, 2004). The Na<sup>+</sup>/H<sup>+</sup> antiporter NhaA from *E. coli* was chosen for these studies as it belongs to a large family of ion transporters ubiquitous in many prokaryots and eukaryots (Padan et al., 2001).

After imaging of the reconstituted NhaA molecules, proteins were partly unfolded by the AFM stylus leaving only two helices anchored in the lipid membrane (Figure 11.11A). The corresponding force spectrum exhibited a characteristic sequence of peaks indicating that a single NhaA molecule was pulled from its C-terminal end (Kedrov et al., 2006a; Kedrov et al., 2004). In a next step, the

AFM stylus was lowered to close proximity of the membrane thereby relaxing the unfolded polypeptide chain (Figure 11.11A). At this stage, the system was left to equilibrate for 0.02 to 15 seconds allowing the coiled polypeptide chain to assume its free energy minimum. The efficiency of the refolding process was estimated from repeated folding and unfolding cycles of the molecule. Usually, all major peaks observed during the initial unfolding were detected with intensities similar to original ones if the refolding time delay lasted for >15 s. This indicated that the secondary structures of NhaA refolded and supports the postulation that unfolding and folding of transmembrane helices may be fully reversible (Hunt et al., 1997; Popot et al., 1987).

Spontaneous folding and insertion of  $\alpha$ -helices into the hydrophobic core of a lipid bilayer was shown to be an energetically favorable process as the contacts between nonpolar aa residues and forcedly oriented molecules of the solvent decrease yielding an energy benefit of 20–40  $k_B T$  per helix (Engelman et al., 1986). Significantly reducing the refolding time allowed determining in which order structural segments of the protein folded. Most obviously it was found that certain structural segments folded before others. In particular the ligand (sodium ion) binding site of the protein was the fastest folding element. After this the helices embedding the ligand-binding site followed. Then the adjacent helices followed. Figure 11.11B gives the folding kinetics determined for the individual structural segments.

In the near future we will be able to quantify the folding kinetics of membrane proteins in their native environment: the lipid membrane. These experiments include the controlled refolding in a wide range of timescales followed by detailed analysis of the consecutive unfolding traces. Plotting the refolding probability as a function of time allows determining the folding rate of the corresponding structural element (Carrion-Vazquez et al., 1999). These methods allow us to detect refolding intermediates and thereby reconstruct the folding pathway of an unfolded polypeptide into the functional protein (Kedrov et al., 2006a, 2004; Kessler et al., 2006). An important application of this approach will be the study of misfolded membrane proteins, that is, those trapped in alternative kinetically stable conformations.

## 11.5 Conclusion and Perspectives

Single-molecule AFM imaging and force spectroscopy are powerful tools to analyze folding, interaction, structure, dynamics, and function of membrane proteins. These tools allow membrane proteins to be studied in their native environment, where their function is preserved. For the first decade there have been no strong developments in AFM instrumentation for biological applications. Small cantilevers, highly sensitive deflection measurements, conductive cantilevers, new imaging modes, and high-speed scanners are only slowly emerging in commercial instruments. However, it is only a matter of time until such progress occurs and is routinely applied to the study of membrane proteins

**Acknowledgments** We are grateful to our colleagues Ch. Bippes, P. Blasubramaniam, and T. Sapra, for inspiring discussions and comments. This work was supported by the Deutsche Forschungsgemeinschaft (DFG), the Bundesministerium für Bildung und Forschung (BMBF), the Free State of Saxony, the European Union, the Swiss National Research Foundation (grant 3100-059415), the M. E. Müller Foundation, the Swiss National Center of Competence in Research (NCCR) ‘Structural Biology,’ and the NCCR ‘Nanoscale Science’.

## References

- Amrein, M. and Müller, D.J. (1999) Sample preparation techniques in scanning probe microscopy. *Nanobiology*, **4**, 229–256.
- Andersen, C., Schiffler, B., Charbit, A. and Benz, R. (2002) PH-induced collapse of the extracellular loops closes Escherichia coli maltoporin and allows the study of asymmetric sugar binding. *J Biol Chem*, **277**, 41318–41325.
- Ando, T., Kodera, N., Naito, Y., Kinoshita, T., Furuta, K. and Toyoshima, Y.Y. (2003) A high-speed atomic force microscope for studying biological macromolecules in action. *Chemphyschem*, **4**, 1196–1202.
- Anfinsen, C.B. (1973) Principles that govern the folding of protein chains. *Science*, **181**, 223–230.
- Bennett, M., Yeagle, J.A., Maciejewski, M., Ocampo, J. and Yeagle, P.L. (2004) Stability of loops in the structure of lactose permease. *Biochemistry*, **43**, 12829–12837.
- Best, R.B., Li, B., Steward, A., Daggett, V. and Clarke, J. (2001) Can non-mechanical proteins withstand force? Stretching barnase by atomic force microscopy and molecular dynamics simulation. *Biophys J*, **81**, 2344–2356.
- Binnig, G., Quate, C.F. and Gerber, C. (1986) Atomic force microscope. *Phys Rev Lett*, **56**, 930–933.
- Booth, P.J., Templer, R.H., Meijberg, W., Allen, S.J., Curran, A.R. and Lorch, M. (2001) In vitro studies of membrane protein folding. *Crit Rev Biochem Mol Biol*, **36**, 501–603.
- Brouillette, C.G., McMichens, R.B., Stern, L.J. and Khorana, H.G. (1989) Structure and thermal stability of monomeric bacteriorhodopsin in mixed phospholipid/detergent micelles. *Proteins*, **5**, 38–46.
- Butt, H.-J., Jaschke, M. and Ducker, W. (1995) Measuring surface forces in aqueous solution with the atomic force microscope. *Bioelect Bioenerg*, **38**, 191–201.
- Carrion-Vazquez, M., Oberhauser, A.F., Fowler, S.B., Marszalek, P.E., Broedel, S.E., Clarke, J. and Fernandez, J.M. (1999) Mechanical and chemical unfolding of a single protein: a comparison. *Proc Natl Acad Sci U S A*, **96**, 3694–3699.
- Chitchevlova, L.A., Shubeita, G.T., Sekatskii, S.K. and Dietler, G. (2004) Force spectroscopy with a small dithering of AFM tip: A method of direct and continuous measurement of the spring constant of single molecules and molecular complexes. *Biophys J*, **86**, 1177–1184.
- Cisneros, D.A., Muller, D.J., Daud, S.M. and Lakey, J.H. (2006) An approach to prepare membrane proteins for single-molecule imaging. *Angew Chem Int Ed*, **45**, 3252–3256.
- Cisneros, D.A., Oesterhelt, D. and Muller, D.J. (2005) Probing origins of molecular interactions stabilizing the membrane proteins halorhodopsin and bacteriorhodopsin. *Structure (Camb)*, **13**, 235–242.
- Czajkowsky, D.M. and Shao, Z. (1998) Submolecular resolution of single macromolecules with atomic force microscopy. *FEBS Lett*, **430**, 51–54.
- Czajkowsky, D.M., Hotze, E.M., Shao, Z. and Tweten, R.K. (2004) Vertical collapse of a cytolysin prepore moves its transmembrane beta-hairpins to the membrane. *Embo J*, **23**, 3206–3215.
- Czajkowsky, D.M., Sheng, S. and Shao, Z. (1998) Staphylococcal alpha-hemolysin can form hexamers in phospholipid bilayers. *J Mol Biol*, **276**, 325–330.

- Dinner, A.R., Sali, A., Smith, L.J., Dobson, C.M. and Karplus, M. (2000) Understanding protein folding via free-energy surfaces from theory and experiment. *Trends Biochem Sci*, **25**, 331–339.
- Dobson, C.M. (2003) Protein folding and misfolding. *Nature*, **426**, 884–890.
- Drake, B., Prater, C.B., Weisenhorn, A.L., Gould, S.A.C., Albrecht, T.R., Quate, C.F., Cannell, D.S., Hansma, H.G. and Hansma, P.K. (1989) Imaging crystals, polymers, and processes in water with the atomic force microscope. *Science*, **243**, 1586–1588.
- Engel, A. and Müller, D.J. (2000) Observing single biomolecules at work with the atomic force microscope. *Nat Struct Biol*, **7**, 715–718.
- Engelman, D.M., Chen, Y., Chin, C.N., Curran, A.R., Dixon, A.M., Dupuy, A.D., Lee, A.S., Lehnert, U., Matthews, E.E., Reshetnyak, Y.K., Senes, A. and Popot, J.L. (2003) Membrane protein folding: Beyond the two stage model. *FEBS Lett*, **555**, 122–125.
- Engelman, D.M., Steitz, T.A. and Goldmann, A. (1986) Identifying nonpolar transbilayer helices in amino acid sequences of membrane proteins. *Annu Rev Biophys Biophys Chem*, **15**, 321–353.
- Evans, E. (1998) Energy landscapes of biomolecular adhesion and receptor anchoring at interfaces explored with dynamic force spectroscopy. *Faraday Discuss*, **111**, 1–16.
- Evans, E. (2001) Probing the relation between force-lifetime-and chemistry in single molecular bonds. *Annu Rev Biophys Biomol Struct*, **30**, 105–128.
- Faham, S., Yang, D., Bare, E., Yohannan, S., Whitelegge, J.P. and Bowie, J.U. (2004) Side-chain contributions to membrane protein structure and stability. *J Mol Biol*, **335**, 297–305.
- Filipek, S., Krzysko, K.A., Fotiadis, D., Liang, Y., Saperstein, D.A., Engel, A. and Palczewski, K. (2004) A concept for G protein activation by G protein-coupled receptor dimers: the transducin/rhodopsin interface. *Photochem Photobiol Sci*, **3**, 628–638.
- Filipek, S., Teller, D.C., Palczewski, K. and Stenkamp, R. (2003) The crystallographic model of rhodopsin and its use in studies of other G protein-coupled receptors. *Annu Rev Biophys Biomol Struct*, **32**, 375–397.
- Fotiadis, D., Hasler, L., Müller, D.J., Stahlberg, H., Kistler, J. and Engel, A. (2000) Surface tongue-and-groove contours on lens MIP facilitate cell-to-cell adherence. *J Mol Biol*, **300**, 779–789.
- Fotiadis, D., Jastrzebska, B., Philippsen, A., Muller, D.J., Palczewski, K. and Engel, A. (2006) Structure of the rhodopsin dimer: A working model for G-protein-coupled receptors. *Curr Opin Struct Biol*, **16**, 252–259.
- Fotiadis, D., Liang, Y., Filipek, S., Saperstein, D.A., Engel, A. and Palczewski, K. (2003) Atomic-force microscopy: Rhodopsin dimers in native disc membranes. *Nature*, **421**, 127–128.
- Fotiadis, D., Liang, Y., Filipek, S., Saperstein, D.A., Engel, A. and Palczewski, K. (2004a) The G protein-coupled receptor rhodopsin in the native membrane. *FEBS Lett*, **564**, 281–288.
- Fotiadis, D., Müller, D.J., Tsiotis, G., Hasler, L., Tittmann, P., Mini, T., Jenö, P., Gross, H. and Engel, A. (1998) Surface analysis of the photosystem I complex by electron and atomic force microscopy. *J Mol Biol*, **283**, 83–94.
- Fotiadis, D., Qian, P., Philippsen, A., Bullough, P.A., Engel, A. and Hunter, C.N. (2004b) Structural analysis of the reaction center light-harvesting complex I photosynthetic core complex of *Rhodospirillum rubrum* using atomic force microscopy. *J Biol Chem*, **279**, 2063–2068.
- Fotiadis, D., Scheuring, S., Muller, S.A., Engel, A. and Muller, D.J. (2002) Imaging and manipulation of biological structures with the AFM. *Micron*, **33**, 385–397.
- Frederix, P.L., Akiyama, T., Staufer, U., Gerber, C., Fotiadis, D., Muller, D.J. and Engel, A. (2003) Atomic force bio-analytics. *Curr Opin Chem Biol*, **7**, 641–647.
- Frederix, P.T., Hoogenboom, B., W., Fotiadis, D., Müller, D.J. and Engel, A. (2004) Atomic force microscopy of biological samples. *MRS Bulletin*, **29**, 449–455.
- Haltia, T. and Freire, E. (1995) Forces and factors that contribute to the structural stability of membrane proteins. *BBA-Bioenergetics*, **1228**, 1–27.
- Hand, G.M., Müller, D.J., Nicholson, B., Engel, A. and Sosinsky, G.E. (2001) Isolation and characterization of gap junctions from tissue culture cells. *J Mol Biol*, **315**, 587–600.
- Heymann, J.B., Müller, D.J., Landau, E., Rosenbusch, J., Pebay-Peroulla, E., Büldt, G. and Engel, A. (1999) Charting the surfaces of the purple membrane. *J Struct Biol*, **128**, 243–249.
- Hobbs, J.K., Vasilev, C. and Humphris, A.D. (2006) VideoAFM—a new tool for high speed surface analysis. *Analyst*, **131**, 251–256.



- Hogan, J. (2006) Focus on the living. *Nature*, **440**, 14–15.
- Hoh, J.H., Lal, R., John, S.A., Revel, J.-P. and Arnsdorf, M.F. (1991) Atomic force microscopy and dissection of gap junctions. *Science*, **253**, 1405–1408.
- Hoh, J.H., Sosinsky, G.E., Revel, J.-P. and Hansma, P.K. (1993) Structure of the extracellular surface of the gap junction by atomic force microscopy. *Biophys J*, **65**, 149–163.
- Hoogenboom, B.W., Hug, H.J., Pellmont, Y., Martin, S., Frederix, P.L.T.M., Fotiadis, D. and Engel, A. (2006) Quantitative dynamic-mode scanning force microscopy in liquid. *Appl Phys Lett*, **88**, 193109.
- Humphris, A.D. and Miles, M.J. (2002) Developments in dynamic force microscopy and spectroscopy. *Methods Cell Biol*, **68**, 337–355.
- Humphris, A.D., Miles, M. and Hobbs, J.K. (2005) A mechanical microscope: High-speed atomic force microscopy. *Appl Phys Lett*, **86**.
- Humphris, A.D.L., Hobbs, J.K. and Miles, M.J. (2003) Ultrahigh-speed scanning near-field optical microscopy capable of over 100 frames per second. *Appl Phys Lett*, **83**, 6–8.
- Hunt, J.F., Rath, P., Rothschild, K.J. and Engelman, D.M. (1997) Spontaneous, pH-dependent membrane insertion of a transbilayer alpha-helix. *Biochemistry*, **36**, 15177–15192.
- Ikai, A. and Afrin, R. (2003) Toward mechanical manipulations of cell membranes and membrane proteins using an atomic force microscope: An invited review. *Cell Biochem Biophys*, **39**, 257–277.
- Israelachvili, J. (1991) *Intermolecular & Surface Forces*. Academic Press, London.
- Janovjak, H., Kessler, M., Gaub, H., Oesterhelt, D. and Müller, D.J. (2003) Unfolding pathways of native bacteriorhodopsin depend on temperature. *EMBO J*, **22**, 5220–5229.
- Janovjak, H., Müller, D.J. and Humphris, A.D.L. (2005) Molecular force modulation spectroscopy revealing the dynamic response of single bacteriorhodopsins. *Biophys J*, **88**, 1423–1431.
- Janovjak, H., Struckmeier, J., Hubain, M., Kedrov, A., Kessler, M. and Müller, D.J. (2004) Probing the energy landscape of the membrane protein bacteriorhodopsin. *Structure (Camb)*, **12**, 871–879.
- Karrasch, S., Dolder, M., Hoh, J., Schabert, F., Ramsden, J. and Engel, A. (1993) Covalent binding of biological samples to solid supports for scanning probe microscopy in buffer solution. *Biophys J*, **65**, 2437–2446.
- Karrasch, S., Hegerl, R., Hoh, J., Baumeister, W. and Engel, A. (1994) Atomic force microscopy produces faithful high-resolution images of protein surfaces in an aqueous environment. *Proc Natl Acad Sci U S A*, **91**, 836–838.
- Katragadda, M., Alderfer, J.L. and Yeagle, P.L. (2000) Solution structure of the loops of bacteriorhodopsin closely resembles the crystal structure. *Biochim Biophys Acta*, **1466**, 1–6.
- Kawakami, M., Byrne, K., Khatri, B., Mcleish, T.C., Radford, S.E. and Smith, D.A. (2004) Viscoelastic properties of single polysaccharide molecules determined by analysis of thermally driven oscillations of an atomic force microscope cantilever. *Langmuir*, **20**, 9299–9303.
- Kedrov, A., Janovjak, H., Ziegler, C., Kuhlbrandt, W. and Müller, D.J. (2006a) Observing folding pathways and kinetics of a single sodium-proton antiporter from *Escherichia coli*. *J Mol Biol*, **355**, 2–8.
- Kedrov, A., Ziegler, C. and Müller, D.J. (2006b) Differentiating ligand and inhibitor interactions of a single antiporter. *J Mol Biol*, **362**, 925–932.
- Kedrov, A., Krieg, M., Ziegler, C., Kuhlbrandt, W. and Müller, D.J. (2005) Locating ligand binding and activation of a single antiporter. *EMBO Rep*, **6**, 668–674.
- Kedrov, A., Ziegler, C., Janovjak, H., Kuhlbrandt, W. and Müller, D.J. (2004) Controlled unfolding and refolding of a single sodium-proton antiporter using atomic force microscopy. *J Mol Biol*, **340**, 1143–1152.
- Kellermayer, M.S., Smith, S.B., Granzier, H.L. and Bustamante, C. (1997) Folding-unfolding transitions in single titin molecules characterized with laser tweezers. *Science*, **276**, 1112–1116.
- Kessler, M., Gottschalk, K.E., Janovjak, H., Müller, D.J. and Gaub, H.E. (2006) Bacteriorhodopsin folds into the membrane against an external force. *J Mol Biol*, **357**, 644–654.
- Khan, F., Chuang, J.I., Gianni, S. and Fersht, A.R. (2003) The kinetic pathway of folding of barnase. *J Mol Biol*, **333**, 169–186.
- Kienberger, F., Pastushenko, V.P., Kada, G., Gruber, H.J., Riener, C., Schindler, H. and Hinterdorfer, P. (2000) Static and dynamical properties of single poly(ethylene glycol) molecules investigated by force spectroscopy. *Single Mol*, **1**, 123–128.

- Kodera, N., Kinoshita, T., Ito, T. and Ando, T. (2003) High-resolution imaging of myosin motor in action by a high-speed atomic force microscope. *Adv Exp Med Biol*, **538**, 119–127.
- Kolbe, M., Besir, H., Essen, L.O. and Oesterhelt, D. (2000) Structure of the light-driven chloride pump halorhodopsin at 1.8 Å resolution. *Science*, **288**, 1390–1396.
- Kuhn, M., Janovjak, H., Hubain, M. and Müller, D.J. (2005) Automated alignment and pattern recognition of single-molecule force spectroscopy data. *J Microsc-Oxford*, **218**, 125–132.
- Leckband, D. (2000) Measuring the forces that control protein interactions. *Annu Rev Biophys Biomol Struct*, **29**, 1–26.
- Li, H.B. and Fernandez, J.M. (2004) Force-clamp spectroscopy monitors the folding trajectory of a single protein. *Science*, **303**, 1674–1678.
- Liang, Y., Fotiadis, D., Filipek, S., Saperstein, D.A., Palczewski, K. and Engel, A. (2003) Organization of the G protein-coupled receptors rhodopsin and opsin in native membranes. *J Biol Chem*, **278**, 21655–21662.
- Liu, Y.Z., Leuba, S.H. and Lindsay, S.M. (1999) Relationship between stiffness and force in single molecule pulling experiments. *Langmuir*, **14**, 8547–8548.
- Marko, J.F. and Siggia, E.D. (1995) Stretching DNA. *Macromolecules*, **28**, 8759.
- Marszalek, P.E., Lu, H., Li, H., Carrion-Vazquez, M., Oberhauser, A.F., Schulten, K. and Fernandez, J.M. (1999) Mechanical unfolding intermediates in titin modules. *Nature*, **402**, 100–103.
- Meier, T., Matthey, U., Henzen, F., Dimroth, P. and Müller, D.J. (2001) The central plug in the reconstituted undecameric c cylinder of a bacterial ATP synthase consists of phospholipids. *FEBS Lett*, **505**, 353–356.
- Meier, T., Yu, J., Raschle, T., Henzen, F., Dimroth, P. and Müller, D.J. (2005) Structural evidence for a constant c11 ring stoichiometry in the sodium F-ATP synthase. *FEBS J*, **272**, 5474–5483.
- Merkel, R., Nassoy, P., Leung, A., Ritchie, K. and Evans, E. (1999) Energy landscapes of receptor-ligand bonds explored with dynamic force microscopy. *Nature*, **397**, 50–53.
- Mitsui, K., Nakajima, K., Arakawa, H., Hara, M. and Ikai, A. (2000) Dynamic measurement of single protein's mechanical properties. *Biochem Biophys Res Commun*, **272**, 55–63.
- Möller, C., Allen, M., Elings, V., Engel, A. and Müller, D.J. (1999) Tapping mode atomic force microscopy produces faithful high-resolution images of protein surfaces. *Biophys J*, **77**, 1050–1058.
- Möller, C., Fotiadis, D., Suda, K., Engel, A., Kessler, M. and Müller, D.J. (2003) Determining molecular forces that stabilize human aquaporin-1. *J Struct Biol*, **142**, 369–378.
- Mou, J.X., Yang, J. and Shao, Z.F. (1995) Atomic force microscopy of cholera toxin B-oligomers bound to bilayers of biologically relevant lipids. *J Mol Biol*, **248**, 507–512.
- Müller, D.J. and Anderson, K. (2002) Biomolecular imaging using atomic force microscopy. *Trends Biotechnol*, **20**, S45–49.
- Müller, D.J. and Engel, A. (1999) Voltage and pH-induced channel closure of porin OmpF visualized by atomic force microscopy. *J Mol Biol*, **285**, 1347–1351.
- Müller, D.J., Amrein, M. and Engel, A. (1997a) Adsorption of biological molecules to a solid support for scanning probe microscopy. *J Struct Biol*, **119**, 172–188.
- Müller, D.J., Baumeister, W. and Engel, A. (1996) Conformational change of the hexagonally packed intermediate layer of *Deinococcus radiodurans* imaged by atomic force microscopy. *J. Bacteriol.*, **178**, 3025–3030.
- Müller, D.J., Baumeister, W. and Engel, A. (1999a) Controlled unzipping of a bacterial surface layer with atomic force microscopy. *Proc Natl Acad Sci U S A*, **96**, 13170–13174.
- Müller, D.J., Büldt, G. and Engel, A. (1995) Force-induced conformational change of bacteriorhodopsin. *J Mol Biol*, **249**, 239–243.
- Müller, D.J., Dencher, N.A., Meier, T., Dimroth, P., Suda, K., Stahlberg, H., Engel, A., Seelert, H. and Matthey, U. (2001) ATP synthase: constrained stoichiometry of the transmembrane rotor. *FEBS Lett*, **504**, 219–222.
- Müller, D.J., Engel, A. and Amrein, M. (1997b) Preparation techniques for the observation of native biological systems with the atomic force microscope. *Biosens Bioelect*, **12**, 867–877.
- Müller, D.J., Engel, A., Matthey, U., Meier, T., Dimroth, P. and Suda, K. (2003) Observing membrane protein diffusion at subnanometer resolution. *J Mol Biol*, **327**, 925–930.
- Müller, D.J., Fotiadis, D. and Engel, A. (1998) Mapping flexible protein domains at subnanometer resolution with the AFM. *FEBS Lett*, **430**, 105–111.

- Müller, D.J., Fotiadis, D., Scheuring, S., Müller, S.A. and Engel, A. (1999b) Electrostatically balanced subnanometer imaging of biological specimens by atomic force microscopy. *Biophys J*, **76**, 1101–1111.
- Müller, D.J., Hand, G.M., Engel, A. and Sosinsky, G. (2002a) Conformational changes in surface structures of isolated Connexin26 gap junctions. *EMBO J*, **21**, 3598–3607.
- Müller, D.J., Janovjak, H., Lehto, T., Kuerschner, L. and Anderson, K. (2002b) Observing structure, function and assembly of single proteins by AFM. *Prog Biophys Mol Biol*, **79**, 1–43.
- Müller, D.J., Kessler, M., Oesterhelt, F., Moeller, C., Oesterhelt, D. and Gaub, H. (2002c) Stability of bacteriorhodopsin alpha-helices and loops analyzed by single-molecule force spectroscopy. *Biophys J*, **83**, 3578–3588.
- Müller, D.J., Sass, H.-J., Müller, S., Büldt, G. and Engel, A. (1999c) Surface structures of native bacteriorhodopsin depend on the molecular packing arrangement in the membrane. *J Mol Biol*, **285**, 1903–1909.
- Müller, P.Y., Janovjak, H., Miserez, A.R. and Dobbie, Z. (2002d) Processing of gene expression data generated by quantitative real-time RT-PCR. *Biotechniques*, **32**, 1372–1380.
- Murata, K., Mitsuoka, K., Hirai, T., Walz, T., Agre, P., Heymann, J.B., Engel, A. and Fujiyoshi, Y. (2000) Structural determinants of water permeation through aquaporin-1. *Nature*, **407**, 599–605.
- Oesterhelt, D. and Stoekenius, W. (1974) Isolation of the cell membrane of *Halobacterium halobium* and its fraction into red and purple Membrane. *Methods Enzymol*, **31**, 667–678.
- Oesterhelt, F., Oesterhelt, D., Pfeiffer, M., Engel, A., Gaub, H.E. and Müller, D.J. (2000) Unfolding pathways of individual bacteriorhodopsins. *Science*, **288**, 143–146.
- Okajima, T., Arakawa, H., Alam, M.T., Sekiguchi, H. and Ikai, A. (2004) Dynamics of a partially stretched protein molecule studied using an atomic force microscope. *Biophys Chem*, **107**, 51–61.
- Padan, E., Venturi, M., Gerchman, Y. and Dover, N. (2001) Na<sup>(+)</sup>/H<sup>(+)</sup> antiporters. *Biochim Biophys Acta*, **1505**, 144–157.
- Palczewski, K., Kumasaka, T., Hori, T., Behnke, C.A., Motoshima, H., Fox, B.A., Le Trong, I., Teller, D.C., Okada, T., Stenkamp, R.E., Yamamoto, M. and Miyano, M. (2000) Crystal structure of rhodopsin: A G protein-coupled receptor. *Science*, **289**, 739–745.
- Pogoryelov, D., Yu, J., Meier, T., Vonck, J., Dimroth, P. and Muller, D.J. (2005) The c15 ring of the *Spirulina platensis* F-ATP synthase: F1/F0 symmetry mismatch is not obligatory. *EMBO Rep*, **6**, 1040–1044.
- Popot, J.-L., Gerchmann, S.-E. and Engelmann, D.M. (1987) Refolding of bacteriorhodopsin in lipid bilayers: A thermodynamically controlled two-stage process. *J Mol Biol*, **198**, 655–676.
- Popot, J.L. and Engelmann, D.M. (2000) Helical membrane protein folding, stability, and evolution. *Annu. Rev Biochem*, **69**, 881–922.
- Popot, J.L. and Engelmann, D.M. (1990) Membrane protein folding and oligomerization: The two stage model. *Biochemistry*, **29**, 4031–4037.
- Rief, M., Gautel, M., Oesterhelt, F., Fernandez, J.M. and Gaub, H.E. (1997) Reversible unfolding of individual titin immunoglobulin domains by AFM. *Science*, **276**, 1109–1112.
- Rief, M., Gautel, M., Schemmel, A. and Gaub, H.E. (1998) The mechanical stability of immunoglobulin and fibronectin III domains in the muscle protein titin measured by atomic force microscopy. *Biophys J*, **75**, 3008–3014.
- Sapra, K.T., Besir, H., Oesterhelt, D. and Muller, D.J. (2006a) Characterizing molecular interactions in different bacteriorhodopsin assemblies by single-molecule force spectroscopy. *J Mol Biol*, **355**, 640–650.
- Sapra, K.T., S.-H., P.P., Filipek, S., Engel, A., Palczewski, K. and Muller, D.J. (2006b) Detecting molecular interactions that stabilize bovine rhodopsin. *J Mol Biol*, **358**, 3252–3256.
- Schabert, F.A., Henn, C. and Engel, A. (1995) Native *Escherichia coli* OmpF porin surfaces probed by atomic force microscopy. *Science*, **268**, 92–94.
- Schmidt, R.A., Qu, J., Williams, J.R. and Brusilow, W.S. (1998) Effects of carbon source on expression of F0 genes and on the stoichiometry of the c subunit in the F1F0 ATPase of *Escherichia coli*. *J Bacteriol*, **180**, 3205–3208.
- Scheuring, S. and Sturgis, J.N. (2005) Chromatic adaptation of photosynthetic membranes. *Science*, **309**, 484–487.

- Scheuring, S., Levy, D. and Rigaud, J.L. (2005) Watching the components of photosynthetic bacterial membranes and their in situ organisation by atomic force microscopy. *Biochim Biophys Acta*, **1712**, 109–127.
- Scheuring, S., Müller, D.J., Stahlberg, H., Engel, H.A. and Engel, A. (2002) Sampling the conformational space of membrane protein surfaces with the AFM. *Eur Biophys J*, **31**, 172–178.
- Scheuring, S., Reiss-Husson, F., Engel, A., Rigaud, J.L. and Ranck, J.L. (2001) High-resolution AFM topographs of *Rubrivivax gelatinosus* light-harvesting complex LH2. *EMBO J*, **20**, 3029–3035.
- Scheuring, S., Rigaud, J.L. and Sturgis, J.N. (2004) Variable LH2 stoichiometry and core clustering in native membranes of *Rhodospirillum rubrum*. *Embo J*, **23**, 4127–4133.
- Scheuring, S., Seguin, J., Marco, S., Levy, D., Robert, B. and Rigaud, J.L. (2003) Nanodissection and high-resolution imaging of the *Rhodospseudomonas viridis* photosynthetic core complex in native membranes by AFM. *Proc Natl Acad Sci U S A*, **100**, 1690–1693.
- Schitter, G., Stark, R.W. and Stemmer, A. (2004) Fast contact-mode atomic force microscopy on biological specimen by model-based control. *Ultramicroscopy*, **100**, 253–257.
- Seelert, H., Dencher, N.A. and Müller, D.J. (2003) Fourteen protomers compose the oligomer III of the proton-rotor in spinach chloroplast ATP synthase. *J Mol Biol*, **333**, 337–344.
- Seelert, H., Poetsch, A., Dencher, N.A., Engel, A., Stahlberg, H. and Müller, D.J. (2000) Proton powered turbine of a plant motor. *Nature*, **405**, 418–419.
- Stahlberg, H., Müller, D.J., Suda, K., Fotiadis, D., Engel, A., Matthey, U., Meier, T. and Dimroth, P. (2001) Bacterial ATP synthase has an undecameric rotor. *EMBO Reports*, **21**, 1–5.
- Strunz, T., Oroszlan, K., Schafer, R. and Guntherodt, H.J. (1999) Dynamic force spectroscopy of single DNA molecules. *Proc Natl Acad Sci U S A*, **96**, 11277–11282.
- Suda, K., Filipek, S., Palczewski, K., Engel, A. and Fotiadis, D. (2004) The supramolecular structure of the GPCR rhodopsin in solution and native disc membranes. *Mol Membr Biol*, **21**, 435–446.
- Vendruscolo, M., Paci, E., Dobson, C.M. and Karplus, M. (2001) Three key residues form a critical contact network in a protein folding transition state. *Nature*, **409**, 641–645.
- Viani, M.B., Pietrasanta, L.I., Thompson, J.B., Chand, A., Gebeshuber, I.C., Kindt, J.H., Richter, M., Hansma, H.G. and Hansma, P.K. (2000) Probing protein–protein interactions in real time. *Nature Struct Biol*, **7**, 644–647.
- Viani, M.B., Schäfer, T.E., Chand, A., Rief, M., Gaub, H. and Hansma, P.K. (1999a) Small cantilevers for force spectroscopy of single molecules. *J Appl Phys*, **86**, 2258–2262.
- Viani, M.B., Schäfer, T.E., Palocz, G.T., Pietrasanta, L.I., Smith, B.L., Thompson, J.B., Richter, M., Rief, M., Gaub, H.E., Plaxco, K.W., Cleland, A.N., Hansma, H.G. and Hansma, P.K. (1999b) Fast imaging and fast force spectroscopy of single biopolymers with a new atomic force microscope designed for small cantilevers. *Rev Sci Ins*, **70**, 4300–4303.
- Wagner, P. (1998) Immobilization strategies for biological scanning probe microscopy. *FEBS Lett*, **430**, 112–115.
- Weih, T.P., Nawaz, Z., Jarvis, S.P. and Pethica, J.B. (1991) Limits of imaging resolution for atomic force microscopy of molecules. *Appl Phys Lett*, **59**, 3536–3538.
- Weiss, S. (1999) Fluorescence spectroscopy of single biomolecules. *Science*, **283**, 1676–1683.
- Weiss, S. (2000) Measuring conformational dynamics of biomolecules by single molecule fluorescence spectroscopy. *Nat Struct Biol*, **7**, 724–729.
- White, S.H., Ladokhin, A.S., Jayasinghe, S. and Hristova, K. (2001) How membranes shape protein structure. *J Biol Chem*, **276**, 32395–32398.
- Williams, P.M. and Evans, E. (2002) Dynamic Force Spectroscopy: II. Multiple Bonds. In Flyvbjerg, H., Jülicher, F., Ormos, P. and David, F. (eds.), *Physics of Bio-Molecules and Cells*. EDP Sciences – Springer-Verlag, Vol. Ecoles des HOUCHEs d'Ete, LXXV, pp. 186–203.
- Williams, P.M., Fowler, S.B., Best, R.B., Toca-Herrera, J.L., Scott, K.A., Steward, A. and Clarke, J. (2003) Hidden complexity in the mechanical properties of titin. *Nature*, **422**, 446–449.
- Zhuang, X. and Rief, M. (2003) Single-molecule folding. *Curr Opin Struct Biol*, **13**, 88–97.

# Index

## A

absorption cross-section 29, 55, 137  
aggregation 60, 84, 87, 95, 96, 125, 139, 184, 218, 289  
atomic force microscopy (AFM) 31, 32, 42, 268, 280ff  
  aquaporin 290, 291, 294  
  bacteriorhodopsin 285, 286, 292, 295, 297–303  
  cantilever 283, 284, 297, 303, 305  
  channel 290, 292, 293  
  conexin/connexons 291, 293  
  contact mode 283, 284  
   $F_0F_1$ -ATP synthase 286, 288, 289  
  imaging 282–289, 292, 293, 305  
  light harvesting complexes 31, 286  
  membrane protein reconstitution 304, 305  
  protein immobilization 282, 284  
  protein structure 284, 297  
  purple membrane 284, 285, 297  
  rhodopsin 287  
  scanner 283  
  signal-to-noise 280  
  single molecule trajectories 288  
  structural flexibility 289–293  
  topograph 280, 281, 284–293  
autocorrelation amplitude 86, 87, 94, 95  
autocorrelation function (ACF) 85–97, 100–103  
  angle dependent 92  
  stretchd exponential 174  
autofluorescence of cells 74, 112–115, 134, 137, 138, 140, 149  
avalanche photodiode (APD) 15, 34, 64, 65, 70, 98–100, 188, 192, 193, 230, 231, 239  
averaging 85–87, 90, 92, 102, 134, 135, 148, 182, 199, 289, 290

## B

binding 16, 63, 74, 94–96, 103  
  pocket 38, 39, 42  
  ligand 95, 125, 133, 140, 143, 144, 148–155  
biological cells  
  CHO 9, 97, 141, 153  
  Dictyostelium 110–112, 125, 126  
  HEK 149, 150  
  neurons 73, 132, 141, 152–154  
  purple bacteria 27, 30, 31  
Bohr radius 54, 57, 58  
bowtie nanoantenna  
  electric field enhancement 12, 15, 16  
  resonances 13, 14, 16, 19

## C

CCD 64–66, 73, 109, 111, 116, 136–139, 193, 231  
cell membrane 7, 8, 74, 96ff, 121, 132ff, 252, 269, 292  
  labeling 7, 73, 122, 137  
  lipid rafts 121, 133, 144, 152, 222  
  synapse 132, 151, 152, 155  
cell membrane protein imaging 66, 69, 73, 96, 122, 131, 137, 138, 143, 144, 149ff, 280ff  
  adenosin receptor 152  
  adrenergic receptor 152  
  agonist 149–154, 156  
  antagonist 150, 151, 153, 154, 156  
  aquaporin 290, 291, 294  
  bacteriorhodopsin 285, 286, 292, 295, 297–303  
  channel 109, 141, 143, 154, 290, 282, 293  
  estrogen receptor 134, 156  
   $F_0F_1$ -ATP synthase 286, 288, 289  
  GABA receptor 153

cell membrane protein imaging (*cont.*)  
 glutamate receptor 151, 154  
 glucocorticoid receptor 153  
 glycine receptor 73, 155  
 G protein coupled receptor (GPCR) 111,  
 121, 133, 141, 149ff, 282, 287  
 ligand-gated ion channel 143, 154ff  
 light harvesting complexes 30ff, 286  
 neurokinin receptor 149  
 NMDA receptor 154  
 nuclear receptor 131, 132, 142, 167, 168  
 odorant/olfactory receptor 132, 150, 151  
 opioid receptor 149  
 purple membrane 284, 285, 297  
 receptor internalization 126, 133,  
 150–152  
 receptor-ligand 109, 125, 152–154, 301  
 serotonin receptor 154  
 cellular imaging 149  
 cellular signaling 108ff, 131ff  
 chemotaxis 110, 121, 152  
 coincidence analysis 96  
 concanavilin 122  
 concentration measurements 88, 93–96  
 cooling rate 43, 45  
 correlator 100, 101  
 cross-correlation 88, 92, 94, 96, 100, 101,  
 103, 205  
 cryogenic temperature 25ff  
 cryogenic conditions 25ff  
 cryostat 34, 43–45

**D**  
 Debye length 269  
 dendrimer 266  
 diffusion 27–47, 69–75, 84–97, 107ff,  
 148–156, 167, 171, 177, 188ff, 219,  
 228–231, 242, 243, 254, 265, 288  
 confined 125, 144, 145, 147, 148, 150  
 coefficient/constant 9, 86, 88, 91, 95, 111,  
 116–125, 135, 144–152, 242, 254  
 subdiffusion 124, 146  
 time 29, 44, 90–94, 134, 135  
 diffusion time distribution analysis  
 (DDA) 148ff  
 dihydrolipoic acid 62  
 dipole moment 3–6, 37, 39, 186, 271  
 dipole-dipole interaction 14, 34  
 disorder  
 dynamic 164, 171, 174, 177, 255, 264,  
 271  
 static 164, 271  
 dithiol 259, 263

**E**  
 electric field 12, 14, 16, 19, 224, 231, 232,  
 238, 239, 270  
 electrochemistry 268  
 electron microscopy 55, 74, 266, 290  
 electro-osmosis 239, 241, 254, 270, 273  
 electrophile 262  
 electrophoresis 155, 230, 238, 253, 258  
 energy bandgap 56  
 energy landscape 27, 30, 41, 42, 47, 183, 191,  
 203, 205, 207, 208, 280, 281, 290, 291,  
 301–303  
 hierarchy 30, 41, 47  
 enhanced fields  
 chemical enhancement 15, 16, 19  
 electromagnetic enhancement 12, 16,  
 18, 19  
 optical enhancement 14, 15, 19  
 SERS enhancement 16  
 ensemble average 85–87  
 equilibrium 84, 96  
 exciton 35–37, 42, 58, 60

**F**  
 FCS, *see* fluorescence correlation  
 spectroscopy  
 flavin 10, 74, 112–114, 137, 164, 185, 266  
 flow 88–97, 189, 227, 229  
 fluorescence  
 anisotropy 44–47  
 background 10, 55, 74, 112, 114–116,  
 137, 138, 168, 231  
 correlation spectroscopy (FCS) 84–97,  
 101, 102, 132–135, 148ff, 200–202  
 fluctuations 84–87  
 intensity distribution analysis 14, 94, 119,  
 120  
 lifetime 7, 8, 31, 42, 45, 61, 74  
 photobleaching quantum yield 5  
 polarization 71, 185, 191  
 quantum yield 3, 5, 7, 59, 61, 67, 137,  
 139, 142, 185–188  
 quenching 28, 74, 185, 200, 201  
 reporter 2, 3, 6, 10, 19  
 resonance energy transfer (FRET) 42,  
 141–143, 156, 183–207  
 recovery after photobleaching (FRAP) 84,  
 132, 135, 156, 243  
 total photons 6  
 Förster resonance energy transfer 184  
 Förster distance 185, 186  
 FRET efficiency 186, 187, 189, 197–199,  
 202–206

- FRET efficiency distribution 187, 191, 195, 202, 203
  - FRET efficiency histogram 196, 199
  - orientational factor 186
  - finite-difference time domain (FDTD) 12–14, 17
  - force spectroscopy 268, 280ff
  - FRET, *see* fluorescence resonance energy transfer, *and* Förster resonance energy transfer
  - freeze-quenching 27, 48
  - Frenkel exciton 35, 37, 42
    - diagonal disorder 33, 38
    - off-diagonal disorder 33, 38
    - strong coupling 35
    - weak coupling 35
- G**
- glycerol 44, 45, 47
  - gramicidin 252, 256, 257, 262, 271, 272
- H**
- hemolysin 251ff
    - $\beta$  barrel 253–255, 262, 269–272
- I**
- image correlation spectroscopy (ICS) 84, 86, 102
    - higher-order correlation 94
  - imaging
    - animal 54, 55
    - cell surface receptor 64, 73
    - fluorescence 64, 122
    - multiplexing 70
    - resolution 2, 11, 12, 26ff, 55, 65, 67–74, 84ff, 110ff, 231, 266, 280ff
- L**
- labels and tags
    - acyl carrier protein (ACP) 142, 149, 150
    - Alexa 122, 152, 153, 168–170, 195, 199, 200, 202
    - alkylguanine-DNA alkyltransferase (AGT) 142
    - autofluorescent protein (AFP) 64, 67, 109, 113, 114, 139, 140, 142, 187
    - avidin 66, 191
    - biotin 63, 66, 109, 140, 191, 205, 221, 283
    - bowtie nanoantenna 3, 12–15, 19
    - Cy3 29, 73, 111
    - Cy5 9, 111, 125, 142, 149, 154, 195
    - dicyanodihydrofuran (DCDHF) 3–11, 19
    - green fluorescent protein (GFP) 72, 96, 97, 102, 109, 113, 138, 140, 150, 191, 205, 206
    - nanoantennas 12
    - nanoparticle 131, 132, 136, 144
    - native protein ligation 143, 195, 273
    - nitrilotriacetate (NTA) 119, 140, 143
    - p-mercaptoaniline (pMA) 16–18, 30
    - polyhistidine 140, 143
    - semiconducting quantum dot, *see* quantum dot
    - semiconductor nanocrystal, *see* quantum dot
    - reversal labeling 140, 143
    - rhodamine 5, 45, 108, 154, 195, 200, 202
    - suppressor tRNA technology 140–142, 273
    - streptavidin 63, 109, 140, 218, 227, 283
    - Texas Red 5, 6, 200, 202
    - unnatural amino acid 63, 141, 142, 273
    - yellow fluorescent protein (YFP) 113–117, 119–121, 123, 124, 126, 134, 138, 148, 156
  - light-harvesting complex 1 (LH1) 30ff
  - light-harvesting complex 2 (LH2) 31ff
    - B800 31–35, 38
    - B850 31–33, 35–38, 42
    - electronic structure 33, 34
    - pigment-pigment interaction 36, 38, 39
    - pigment pool 31, 36, 42
    - pigment-protein interaction 32, 34, 40, 41, 42
    - structure 31, 32, 34, 42
  - lipid 9, 108–110, 121, 122, 218–245, 252ff, 284ff
    - bilayer/membrane 9, 95, 218ff, 252ff, 300ff
    - cholesterol 121, 152, 222
    - fluorescent 122
    - giant unilamellar vesicle (GUV) 96, 224, 229
    - membrane surface tension 223, 232, 237, 238
    - monolayer 95
    - multilamellar 224, 227
    - nanotube 223ff
    - phospholipid 61–63, 231ff, 288
    - raft 121, 133, 144, 152, 222
    - vesicle 9, 95, 96, 115, 122, 191, 192, 202–204, 231ff

**M**

mean square displacement (MSD) 117, 145ff  
 microfluidic devices 189, 196, 198, 242  
   on-chip analysis 144, 238  
 microscopy  
   confocal 55, 64, 122, 153, 192, 239  
   confocal laser scanning (CLSM) 65, 91ff, 135  
   epifluorescence 4, 5, 9, 54, 64–66  
   near-field 11, 108  
   resolution 20, 67–70  
   scanning tunneling microscopy (STM) 266, 261  
   single-molecule 2, 20, 30, 55, 64ff, 107ff, 131ff, 167, 202ff, 230ff, 279ff  
   STED, *see* stimulated emission depletion  
   TIR, *see* total internal reflexion  
   two-photon 10, 11, 55, 97, 98, 100

**N**

nanoreactor 251 ff  
   arsenic 259, 265  
   arsonous acid 260, 265  
   azobenzene 266, 267  
   carbamate 256–259, 265, 269, 271  
   channel protein 252, 255–258, 270  
   confinement 238, 239, 264, 269  
   cyclization 263, 264  
   cyclodextrin 255, 270, 272  
   decarboxylation 258, 259  
   disulfide 257, 258, 261–265, 271  
   enthalpy 257  
   entropy 257, 271  
   enzyme 263–266, 273  
   ergodicity 255  
   hemolysin 251ff  
   intermediate 252, 255, 258, 259, 261, 264, 265, 271, 272  
   irradiation 254, 258  
   isomerization 256, 257, 266, 267, 271  
   kinetics 256, 266, 268, 269  
   methanethiosulfonate 257, 258  
   nanotube-vesicle networks 218ff  
   nitronate 258, 259  
   noise 254–256, 271  
   nucleophile 262, 268, 273  
   pH 254ff  
   photolysis 265  
    $pK_a$  256ff  
   polymerization 262–265  
   protonation 255ff  
   steric hindrance 258  
   water 253–256, 269, 272

nanotube-vesicle networks (NVN) 218ff  
   biosensor 219, 224  
   branching 228  
   electrophoretic transport 220, 231, 238, 245  
   enzyme kinetics 229  
   diffusive transport 242ff  
   fabrication 225ff  
   FRAP 243  
   functionalization 219, 224ff  
   immobilization 219, 221, 223, 225, 228, 229, 233, 237  
   nanotube radius 223, 229, 233, 236, 238, 242  
   Marangoni flow 229ff  
   microinjection 225ff  
   micropipette 226–228, 232, 239  
   self-organization 225ff  
   single-molecule experiments 218–220, 231, 239  
   surfactant 225, 238  
   topograph 227  
   vesicle size 219ff  
 near-field imaging 11ff

**P**

photobleaching 5, 6, 10, 29, 43, 55, 67, 69, 73, 93, 96, 98, 113, 119, 121, 139, 144, 168, 170, 192  
 photoblinking 29, 45  
 photochemistry 195, 199, 266  
   nitrobenzyl 258, 259, 265  
 photon counting histogram 94  
 photostability 3, 30, 55, 60, 66, 71–75, 134, 139, 140, 168, 188  
 photosynthesis 30  
 pinhole 98, 134, 188  
 point spread function (PSF) 68–70, 146  
 Poisson distribution 86, 95  
 polymerization 20, 166, 262–265  
 position-sensitive fluorescence correlation spectroscopy (PSFCS) 92, 93, 97, 102  
 potential hypersurface 41  
 protein  
   adenylate kinase 191, 202  
   bacteriorhodopsin 285  
    $\beta$  barrel 195, 253–255, 262, 269–272  
   calmodulin 200  
   cholesterol oxidase (COx) 164, 266  
   chymotrypsin inhibitor 195  
   cold shock protein 191, 195, 203  
   conformational substate 27, 41, 47, 164, 177, 203, 207, 208



- dynamics 40, 42, 132, 199, 292  
 energy landscape 27, 30, 41, 42, 47,  
 183, 191, 203, 205, 207, 208, 280,  
 281, 290, 291, 301–303  
 engineering 140, 184, 258  
 folding 181ff  
 FynSH3 domain 199  
 GCN4 187, 202  
 heteropolymer collapse 198  
 immobilization 151, 168, 191, 205,  
 282, 284  
 intestinal fatty acid binding  
 protein 200  
 labeling 61, 73, 139ff, 168, 187  
 lactate dehydrogenase (LDH) 164  
 lipase 165  
 myosin 71, 72, 185  
 radius of gyration 199  
 random coil 199, 201, 305  
 ribonuclease 182, 205  
 small angle X-ray scattering 199  
 unfolded state 183ff  
 unfolded state collapse 197, 205
- Q**  
 quantum confinement 54, 57  
 quantum dot  
 animal imaging 54, 55  
 blinking 59, 69  
 cell tracking 66, 73  
 colloid 53ff  
 conjugation strategies 61  
 core materials 60, 61  
 electrical properties 56  
 fluorescence in situ hybridization  
 (FISH) 71  
 functionalization 62  
 imaging 55, 61, 71, 72  
 immunoassays 55  
 labeling 63  
 near-infrared fluorescence 54, 55, 62,  
 74, 75  
 optical properties 58  
 Ostwald ripening 60  
 phytochelatin peptide 63  
 preparation 60  
 quantum yield 59  
 shell growth 60  
 singleness 69  
 size 54, 58–61  
 solubilization 61  
 targeting 56  
 tracking 66, 69, 73, 133, 155
- R**  
 random walk 116, 145  
 Rayleigh criterion 68  
 scanning fluorescence correlation  
 spectroscopy (SFCS) 83, 87  
 image correlation spectroscopy (ICS) 84,  
 86, 102  
 measurement volume 85ff  
 normalization 85, 97, 96  
 particle imaging velocimetry (PIV) 91  
 particle number 86, 95  
 photon counting histogram 94  
 Poisson distribution 86, 95  
 position-sensitive fluorescence correlation  
 spectroscopy (PSFCS) 92, 93, 97, 102  
 synchronization 91, 97, 100, 101  
 scanner 97–101
- S**  
 scanning pattern 90, 91, 96  
 circle 90–93, 96  
 line 88ff  
 random 96  
 raster 90, 91, 97  
 spiral 90, 91, 93, 96  
 SERS, *see* surface-enhanced Raman  
 spectroscopy  
 single-molecule  
 chemistry 252ff  
 conformational fluctuations 26, 164,  
 194, 292  
 conformational substates 27, 47, 164,  
 203, 207  
 detection 53ff, 116, 134ff  
 enzyme kinetics 163ff  
 fluorescence 4, 16, 29, 64, 73, 108ff, 131,  
 206, 207, 264–266  
 FRET 193  
 imaging 3, 5, 53ff, 64, 66, 71, 107ff, 122,  
 133, 141, 144, 149, 157  
 localization 67, 96, 110, 123, 152  
 memory effect 47, 164, 174, 206  
 Michaelis-Menten equations 164,  
 171, 176  
 microscopy 30, 55, 64, 67, 113, 125,  
 141, 279  
 protein folding 181ff  
 resolution 67, 85, 108, 135, 136ff  
 sensitivity 63  
 subpopulations 55, 108, 123, 147, 195ff  
 single molecule force spectroscopy  
 (SMFS) 280ff  
 aquaporin 294

- single molecule force spectroscopy (SMFS)
    - (*cont.*)
    - bacteriorhodopsin (BR) 285, 287, 289–297
    - energy landscape 290, 301
    - GPCR 287
    - halorhodopsin (HR) 294, 298, 299
    - kinetics of (un)folding 304
    - membrane protein 294
    - molecular interactions 295
    - protein folding 294ff
    - protein unfolding 294ff
    - purple membrane 285
    - secondary structural elements 295ff
    - wormlike chain model 294
  - single-molecule trajectory 117, 118, 123, 132, 145–149, 151, 192–194, 288
    - hidden Markov techniques 194
    - information theory 194
    - time-dependent 190
    - single particle tracking (SPT) 66, 73, 132, 136, 137, 139, 141, 144–147
    - stochastic 193, 194
    - noise reduction 193, 194
  - signal-to-background 66, 149
  - signal-to-noise ratio 28, 42, 65–68, 91, 93, 98, 102, 116, 154, 280
  - spatiotemporal image correlation spectroscopy (STICS) 87–91
  - spectral diffusion 33, 38, 41
  - spectral selection 30
  - spectral traces 38
  - stimulated emission depletion (STED) 69
  - stochastic sensing 264, 272–274
  - stoichiometry states of receptors 119–121, 288
  - stretched exponential 174, 176
  - surface-enhanced Raman spectroscopy (SERS) 16–19
- T**
- temperature cycles 43
  - temperature gradient 45
  - time-correlated single photon counting (TCSPC) 7, 86, 100
  - TIR, *see* total internal reflection
  - thiol 255ff
  - total internal reflection (TIR) 13, 64, 67, 71, 137, 138, 193
  - transition dipole 37, 39, 185, 186
  - trapping 191, 192
    - chemical 27, 272
    - optical 263, 265
    - physical 27, 42
  - two-photon
    - absorption 10, 14
    - excitation 10, 93, 96, 98, 102
    - fluorescence 9, 10
    - imaging 97
    - microscopy 10, 11, 55, 97, 98, 100
    - photoluminescence 14